PROCEEDINGS OF THE SIXTEENTH WORKSHOP ON GENERAL RELATIVITY AND GRAVITATION in JAPAN

NIIGATA PREFECTURAL CIVIC CENTER, NIIGATA, JAPAN
NOVEMBER 27 – DECEMBER 1, 2006

Edited by
Ken-ichi Oohara, Tetsuya Shiromizu, Kei-ichi Maeda and Misao Sasaki

Preface

The sixteenth workshop on General Relativity and Gravitation (the 16th JGRG meeting) was held at Niigata Prefectural Civic Center, from 27 November to 1 December, 2006.

There has been impressive progress in astrophysical/cosmological observation in recent years, including CMB, black holes and gamma-ray bursts. On the theory side, motivated by unified theories of fundamental interactions, especially string theory, physics in higher dimensional spacetimes has been studied intensively. There has been also important developments in various areas of GR, including alternative theories of gravity, quantum gravity, spacetime singularities, etc.

This year, we invited ten speakers from various countries, who gave us clear overview of recent developments and future perspectives. We witnessed active discussions among the participants during the meeting. We would like to thank all the participants for their earnest participation.

Ken-ichi Oohara, Tesuya Shiromizu, Kei-ichi Maeda and Misao Sasaki   28 January 2007

Organising Committee

H. Asada (Hirosaki), T. Chiba (Nihon), A. Hosoya (Titech),
K. Ioka (Kyoto), H. Ishihara (Osaka City), M. Kawasaki (Tokyo),
H. Kodama (YITP, Kyoto), Y. Kojima (Hiroshima), K. Maeda (Waseda),
S. Mukoyama (Tokyo), T. Nakamura (Kyoto), K. Nakao (Osaka City),
Y. Nambu (Nagoya), R. Nishi (Niigata), K. Oohara (Niigata),
M. Sasaki (YITP, Kyoto), M. Shibata (Tokyo), T. Shiromizu (Titech),
J. Soda (Kyoto), N. Sugiyama (Nagoya), S. Yamada (Waseda),
T. Tanaka (YITP, Kyoto), J. Yokoyama (Tokyo), K. Watanabe (Niigata)

Table of Contents

Oral Presentation

Poster Presentation

Post-Friedmannian effects of inhomogeneities in observational cosmology
— Apparent Acceleration through Large-Scale Inhomogeneities? —

Masumi Kasai[1]

Faculty of Science and Technology, Hirosaki University, Hirosaki 036–8561, Japan

Abstract

There have been suggestions that the apparent acceleration of the cosmic expansion is not driven by *dark energy*, but is a consequence of large-scale inhomogeneities in the universe. Previous works, however, deeply depend on the simplified toy models, such as the spherically symmetric Lemaître-Tolman models. In this article, we demonstrate a method to describe phenomenologically the effects of the large-scale inhomogeneities in the universe, without depending on the specific toy models. This clearly illustrate how the post-Friedmannian effects of inhomogeneities, *i.e.*, the effects due to the deviations from the perfectly homogeneous Friedmann models, change the cosmological parameters, in particular q_0.

1 Introduction

The Cosmological Principle, which states that the universe is described by the perfectly homogeneous and isotropic Friedmann model, is a working hypothesis which has been widely accepted among current cosmologists. The present, past, and future evolution of the Friedmann model is determined by a few constant parameters, such as the Hubble parameter H_0 and the deceleration parameter q_0. The determination of the cosmological parameters is one of the main purposes in observational cosmology.

The recent observations of type Ia supernovae (SNIa) [1] now strongly suggests the negative deceleration parameter, $q_0 < 0$. As long as we stick to the perfectly homogeneous Friedmann models, this requires *dark energy*, an exotic energy component which accelerates the cosmic expansion with its negative pressure.

Instead of introducing such a mysterious energy component, there have been attempts to explain the apparent accelerated expansion of the universe as a result of the large-scale inhomogeneities in the universe. For example, Tomita [2], using his local void model, and Iguchi et al. [3], using the Lemaître-Tolman model, discussed the possibility of explaining the observed magnitude-redshift (m-z) relation of SNIa. Moreover, recently Alnes et al. [4] have concluded that not only the m-z relation of SNIa but also the position of the first peak in the CMB anisotropy can be explained due to the inhomogeneity in the Lemaître-Tolman model.

Previous works, however, depend specifically on the simplified toy models. Therefore, due to the lack of strong support for such toy models as a realistic description of our universe, the study of the inhomogeneous effects of the universe is not the main stream of the research subjects, compared to that of *dark energy*.

In this article, we demonstrate a method to describe phenomenologically the effects of the large-scale inhomogeneities in the universe, without depending on the specific toy models. This method clearly illustrate how the post-Friedmannian effects of inhomogeneities, *i.e.*, the effects due to the deviations from the perfectly homogeneous Friedmann models, change the cosmological parameters, in particular q_0.

---

[1]E-mail: kasai@phys.hirosaki-u.ac.jp

2 The magnitude-redshift relation of SNIa

Before describing the effects of inhomogeneities, let us summarize the magnitude-redshift relation in the Friedmann universe:

$$m = M + 5\log_{10}\frac{D_L(z)}{D_{10}}, \tag{1}$$

where m is the apparent magnitude, M is the absolute magnitude of SNIa which is defined as the apparent magnitude at a distance $D_L(z) = D_{10} \equiv 10\mathrm{pc}$, and $D_L(z)$ is the luminosity distance at redshift z. All SNIa we will consider in this article have the redshift $z < 1$, therefore, we can use the approximate formula for $D_L(z)$ as a power series:

$$D_L(z) = \frac{c}{H_0}\left\{z + \frac{1}{2}(1 - q_0)z^2 + \cdots\right\} \tag{2}$$

Putting this into Eq. (1), we obtain

$$m = M + 5\log_{10}\frac{c}{H_0\,D_{10}} + 5\log_{10}\left\{z + \frac{1}{2}(1 - q_0)z^2\right\} \equiv \mathcal{M} + 5\log_{10}\left\{z + \frac{1}{2}(1 - q_0)z^2\right\}, \tag{3}$$

where $\mathcal{M}$ is often called as the "Hubble-constant-free" absolute magnitude [1], or the magnitude "zero-point" [5]. The problem is now to obtain the best fit parameters $\mathcal{M}$ and q_0 from observational data.

As an illustration, we use the observed SNIa data given in the paper by Perlmutter et al.[1]. In Figure 1, we plot the Hubble diagram for 42 high-redshift ($0.172 \leq z \leq 0.830$) type Ia supernovae from the Supernova Cosmology Project and 18 low-redshift ($0.018 \leq z \leq 0.101$) supernovae from the Calán/Tolont Supernova Survey. Also plotted is the best fit m-z curve with the parameters $\mathcal{M} = 24.01, q_0 = -0.32$.
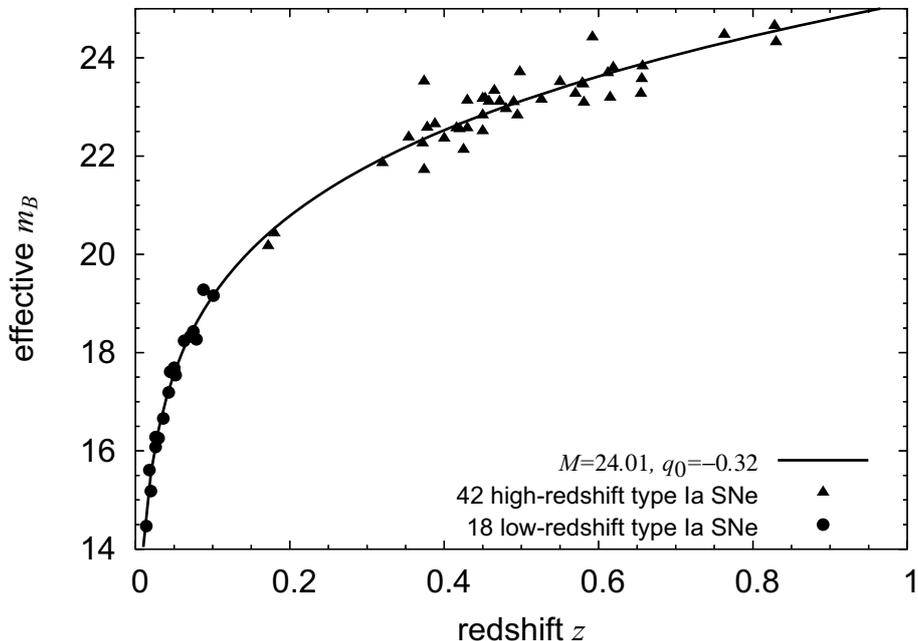
Figure 1: Hubble diagram for 42 high-redshift type Ia supernovae from the Supernova Cosmology Project and 18 low-redshift supernovae from the Calán/Tolont Supernova Survey (data taken from [1]). The solid curve is the best fit m-z relation with $\mathcal{M} = 24.01, q_0 = -0.32$.

3   Different $\mathcal{M}$ for different data sets?

Before concluding "OK, q_0 is negative. We need *dark energy*. That's all", let us remark that the data consists of two different data sets, by different groups, of different distances and epochs of SN formation. In the two sets, the low-redshift data set essentially determines the value of $\mathcal{M}$ irrespectively of q_0, whereas the other, the high-redshift data set, plays the role of determining the best fit q_0 for the given value of $\mathcal{M}$.

In order to make an alternative interpretation without *dark energy*, let us perform the following experimental fitting for each data set: What happens if we fit the only high-redshift SN data, or the only low-redshift SN data, with the m-z relation assuming, say, $q_0 = 1/2$? Figure 2 shows the results of such experimental fittings.
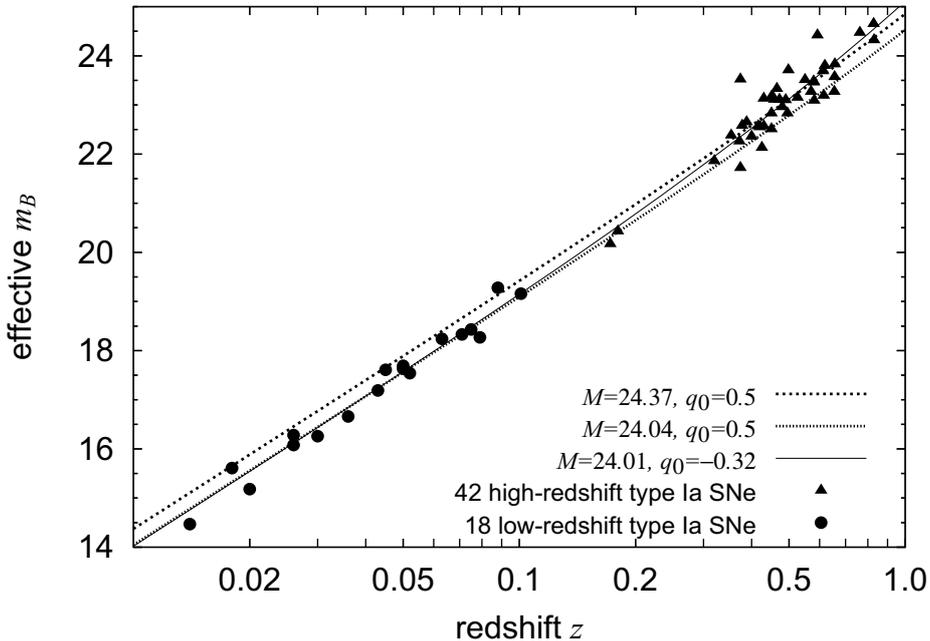
Figure 2: Hubble diagram for 42 high-redshift type Ia supernovae from the Supernova Cosmology Project and 18 low-redshift supernovae from the Calán/Tolont Supernova Survey (data taken from [1]). The upper dashed curve ($\mathcal{M} = 24.37, q_0 = 0.5$) fits with the high-redshift SN data, the lower dashed curve ($\mathcal{M} = 24.04, q_0 = 0.5$) fits with the low-redshift SN data.

4   Inhomogeneous interpretation?

Since $\mathcal{M} = M + 5 \log_{10} (c/H_0 D_{10})$, the result that the different values of $\mathcal{M}$ fit with the different redshift data sets may imply the following possibilities of inhomogeneous interpretation:

1. The absolute magnitude M of the high-redshift SNIa is systematically different from that of the low-redshift SNIa.

2. The speed of light c is different in different redshift regions;-)

3. H_0 in the high-redshift region is slightly different from that in the low-redshift region.

In the following, we examine further the third possibility of the inhomogeneous interpretation. If the difference in $\mathcal{M}$ is due to the inhomogeneous expansion rate H_0, we can estimate as follows:

$$24.37 - 24.04 = 5 \log_{10} \frac{H_0(z \leq 0.1)}{H_0(0.2 \leq z)}, \tag{4}$$

which yields $H_0(0.2 \leq z) = 0.86 H_0(z \leq 0.1)$, *i.e.*, 14% smaller value of H_0 in the high-redshift region compared to that in the low-redshift region may explain the observed *m-z* relation of SNIa, without introducing *dark energy*.

5   Post-Friedmannian effects of large-scale inhomogeneities

In the perfectly homogeneous Friedmann models, H_0 denotes the expansion rate at the present time t_0, and is constant all over the $t = t_0$ hypersurface. In generally inhomogeneous universes, however, the expansion rate is naturally dependent on the spatial positions, through which H_0 becomes dependent on z:

$$H_0 = H(t_0, x^i) = H_0(t_0, x^i(z)) \Rightarrow H_0(z). \tag{5}$$

In the same way, q_0 can also be dependent on z:

$$q_0 = q(t_0, x^i) = q_0(t_0, x^i(z)) \Rightarrow q_0(z). \tag{6}$$

Since $z < 1$, these are expanded as power series:

$$H_0(z) = \bar{H}_0 \left(1 + h_1 z + h_2 z^2 + \cdots \right), \tag{7}$$
$$q_0(z) = \bar{q}_0 \left(1 + \omega_1 z + \omega_2 z^2 + \cdots \right). \tag{8}$$

The coefficients $h_1, h_2, \ldots, \omega_1, \omega_2, \ldots$ represent the post-Friedmannian corrections due to spatial inhomogeneities. Including the post-Friedmannian corrections, we may describe the luminosity distance as

$$D_L(z) = \frac{c}{\bar{H}_0} \left\{ z + \frac{1}{2} \left(1 - (\bar{q}_0 + 2h_1) \right) z^2 + \cdots \right\}. \tag{9}$$

Therefore, negative values of the post-Friedmann term h_1 can contribute to decrease the apparent deceleration parameter $q_0 \equiv \bar{q}_0 + 2h_1$.

6   Conclusion

We have pointed out the possibility that the apparent accelerated expansion of the universe, which derived from the observed *m-z* relation of SNIa, may be explained by the large-scale inhomogeneities in the cosmological parameters. In generally inhomogeneous universes, the expansion rate are naturally dependent on spatial coordinates, therefore the redshift z. A simple phenomenological method to treat the post-Friedmannian effects, *i.e.*, the effects of the deviations from the perfectly homogeneous Friedmann models due to spatial inhomogeneities, is shown. This method clearly illustrates how the post-Friedmannian corrections affect the apparent cosmological parameters, in particular q_0.

In order to examine the more detail, we need to expand higher order. The detail will be published elsewhere in the forthcoming paper.

References

[1] S. Perlmutter et al., ApJ 517, 565 (1999).

[2] K. Tomita, ApJ 529, 38 (2000); K. Tomita, MNRAS 326, 287 (2001); K. Tomita, PTP 106, 929 (2001).

[3] H. Iguchi et al., PTP 108, 809 (2002).

[4] H. Alnes et al., PRD 73, 083519 (2006).

[5] M.-N. Célérier, AA 353, 63 (2000).

Can inhomogeneities accelerate the cosmic volume expansion?

Tomohiro Kai[1],Hiroshi Kozaki[2], Kenichi Nakao[3],Chul-Moon Yoo[4] and Yasusada nambu[5]

[1~4]*Graduate School of Science, Osaka City University, Osaka 558-8585, Japan*
[5]*Graduate School of Science,Nagoya University,Chikusa,Nagoya 464-8602,Japan*

Abstract

if the expanding and contracting regions coexist in the universe, the speed of cosmic volume expansion can be accelerated. We construct simple inhomogeneous dust-filled universe models of which the speed of cosmic volume expansion is accelerated for finite periods. We find that the the acceleration of the cosmic volume expansion is realized when the size of the contracting region is comparable to the horizon radius of the Einstein-de Sitter universe. This result implies that general relativistic non-linear effects of inhomogeneities are very important for the realization of the acceleration of the cosmic volume expansion.

1 Introduction

The accelerated expansion of the universe indicated by the observational data of the luminosity distance of Type Ia supernovae and the cosmic microwave background radiation is a great mystery in modern cosmology. The acceleration of a homogeneous and isotropic Friedmann-Robertson-Walker (FRW) universe implies the existence of the dark energy component of the matter fields which violates the energy conditions and we do not know their true character. Conversely, if the universe is not homogeneous and isotropic, the observational data does not necessarily indicate the accelerated expansion of the universe, or even if the cosmic expansion is accelerated, it does not necessarily mean the existence of the dark energy. Thus to explain the observational data without introducing the dark energy, the argument about the effects of the inhomogeneities has been arisen.

One of the present authors, Nambu, and his collaborator, Tanimoto pointed out the possibility that the non-perturbative features of inhomogeneities are crucial to realize the accelerated expansion of the universe by the backreaction effects.[1] They proposed a model of the universe containing both expanding and contracting regions and the spatially averaged scale factor defined through the volume of a spatial domain can show accelerated expansion if the size of each region is properly chosen.

As Nambu and Tanimoto have adopted a over-simplfied model of the accelerated universe, we modify their model and check whether their mechanism really works. Hence, in this paper, in order to check it, we study the comoving volume of the highly inhomogeneous dust-filled universe.

2 The mechanism of the accerelation

We consider a compact spatial domain D in each t =constant hypersurface by assuming that D is dust-comoving. By its definition, D contains fixed rest mass of dust. We assume that the domain D is so large that the spatial periodicity is recognizable in this domain. The volume V_D of D is defined by

$$V_D = \int_D \sqrt{\gamma}\, d^3x, \tag{1}$$

where γ is the determinant of the spatial metric γ_{ij}. Following Ref. [2, 3], we define the spatially averaged scale factor $a_D(t)$ of the domain by $3\dot{a}_D/a_D = \dot{V}_D/V_D$, where the dot $\dot{}$ means the derivative with respect to t. This definition is equivalent to $a_D(t) \propto V_D^{1/3}(t)$.

Since we assume that the expanding and contracting domains coexist within this domain D, we rewrite the volume V_D in the form

$$V_D = V_e + V_c, \tag{2}$$

where V_e and V_c are the comoving volume of the union of the expanding domains and that of the contracting domains, respectively. The time derivative of the volume is written as

$$\dot{V}_D = \dot{V}_e + \dot{V}_c = |\dot{V}_e| - |\dot{V}_c|. \tag{3}$$

We see from the above equation that even though $\dot{V}_D$ is initially positive, once $\dot{V}_c$ becomes dominant, $\dot{V}_D$ can almost vanish or be negative. In other words, due to the appearances of the contracting domains in D, the cosmic volume expansion of D can strongly slow down or the volume V_D of D can decrease. However, the contracting domains will collapse and then their contributions to the volume V_D necessarily become negligible. This means that $\dot{V}_e$ will be dominant in $\dot{V}_D$ and the volume V_D begins increasing again. Here it should be noted that the acceleration of volume expansion is realized around the end of the slowdown or contraction stage. In this period, the second order time derivative of the effective scale factor $a_D(t)$ becomes positive and thus the acceleration of cosmic expansion will be realized. This is the mechanism of the acceleration of the cosmic volume expansion pointed out by Nambu and Tanimoto[1].

3 An inhomogeneous universe witu expanding and contracting region

We consider an inhomogeneous dust-filled universe which is initially expanding everywhere. We assume that at some stage, the dust begins contracting in some domains and continues expanding elsewhere. Such a situation agrees with our conventional picture of the real universe (stars, galaxies, etc).

To describe this universe by the exact solution of Einstein equation, we consturuct a simple inhomogeneous dust filled model. This model is made by removing spherical region from Einstein-de-sitter universe (EDS) and filling each region by Lamaître-Tolman-Bondi (LTB) dust sphere with the same gravitational mass.

The line element of the LTB region is given by

$$ds^2 = -dt^2 + \frac{Y'^2(t,\chi)}{1-k(\chi)\chi^2}d\chi^2 + Y^2(t,\chi)(d\theta^2 + \sin^2\theta d\varphi^2), \tag{4}$$

where the prime $'$ denotes the differentiation with respect to the radial coordinate χ. This coordinate system is dust-comoving Gaussian normal coordinate. Einstein equations lead to the equations for the areal radius $Y(t,\chi)$ and the rest mass density $\rho(t,\chi)$ of the dust;

$$\dot{Y}^2 = -k(\chi)\chi^2 + \frac{2M(\chi)}{Y}, \tag{5}$$

$$\rho = \frac{M'(\chi)}{4\pi Y'Y^2}, \tag{6}$$

where $k(\chi)$ and $M(\chi)$ are arbitrary functions of the radial coordinate. We assume the non-negativity of ρ and monotonicity of Y with respect to χ, i.e., $Y' > 0$ in the regular region. This assumption leads $M' \geq 0$ and thus we can set $M(\chi) = 4\pi\rho_0\chi^3/3$, where ρ_0 is a non-negative arbitrary constant. This choice of $M(\chi)$ does not loose any generality. As equations (4)-(6) are invariant under the rescaling of the radial coordinate χ, we can choose the above form of $M(\chi)$ generally.

The solution of Eq.(5), (6) is given by

$$Y = \frac{4\pi\rho_0}{3k(\chi)}\left(1 - \cos\left(\sqrt{k(\chi)}\,\eta\right)\right)\chi, \tag{7}$$

$$t - t_i(\chi) = \frac{4\pi\rho_0}{3k(\chi)}\left(\eta - \frac{1}{\sqrt{k(\chi)}}\sin\left(\sqrt{k(\chi)}\,\eta\right)\right), \tag{8}$$

where $t_i(\chi)$ is an arbitrary function. We can use this expression of the solution for any sign of $k(\chi)$. Here note that the time $t = t_i$ corresponds to the Big Bang singularity. Hereafter, we assume a simultaneous Big Bang $t_i = 0$.

For $k(\chi) = 0$, this model corresponds to EDS universe that scale factor is given by $a_e(t) = (6\pi\rho_0 t^2)^{1/3}$. So, we need to set $k(\chi)$ so that LTB region smoothly mathed to EDS region. We denote the boundary between the LTB region and the EdS region by $\chi = \chi_b$. Then dividing the LTB region into four regions by using the following spatial profile of the curvature function:

$$k(\chi) = \begin{cases} k_0 & \text{for} \quad 0 \leq \chi < \chi_1 \\[2mm] \frac{k_0}{2\chi^2}\left\{\frac{(\chi^2-\chi_2^2)^2}{\chi_1^2-\chi_2^2} + \chi_1^2 + \chi_2^2\right\} & \text{for} \quad \chi_1 \leq \chi < \chi_2 \\[2mm] \frac{k_0}{2\chi^2}\left(\chi_1^2 + \chi_2^2\right) & \text{for} \quad \chi_2 \leq \chi < \chi_3 \\[2mm] \frac{k_0}{2\chi^2}\left(\chi_1^2 + \chi_2^2\right)\left\{\left(\frac{\chi^2-\chi_3^2}{\chi_b^2-\chi_3^2}\right)^2 - 1\right\}^2 & \text{for} \quad \chi_3 \leq \chi < \chi_b \end{cases}, \tag{9}$$

where k_0 is constant, and we are interested in the case that LTB regions will cotract, we assume $k_0 > 0$.

In the case of the present model, the singularity formed at the origin $\chi = 0$ is spacelike, since the innermost region $[0, \chi_1)$ is a Friedman universe with a positive spatial curvature. Therefore there is no causal influence of the spacelike singularities on the regular region This property allows us to ignore the contribution of the singularity in the calculation of the volume V_D of the domain D.

We see from Eq. (8) that the singularity formation time is given by $t = 8\pi^2\rho_0/(3k^{3/2})$. Since k is monotonically decreasing with respect to χ, the singularity formation time is monotonically increasing with respect to χ and thus the shell crossing singularity does not occur in the present model.

4 Numerial result

We first consider the model with one LTB region of $\chi_b = l$ in the domain D (see FIG. 1).
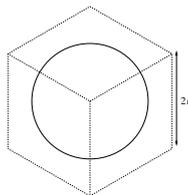
Figure 1: The compact domain D of the one-scale SSC model is depicted.

Thus in this model, the identical LTB regions are ranged in close order. The volume V_D of the domain D is given by

$$V_D = \left(8 - \frac{4\pi}{3}\right) a_e^3(t)l^3 + 4\pi \int_0^{a_e(t)l} \frac{Y^2 dY}{\sqrt{1 - k(\chi)\chi^2}}. \tag{10}$$

The integral in the right hand side of the above equation corresponds to the comoving volume of the LTB region. It should be noted that χ in this integral is the function of the areal radius Y at time t through Eqs. (7) and (8). Thus this integration covers the only region which has not yet collapsed to the singularity, i.e., the domain of $Y > 0$ at time t. In Fig.(2) we show several examples of the evolution of the scale factor $a_D(t)$. Here, $a_D(t) \equiv V_D^{1/3}/2l$.

The necessary condition for the appearance of the acceleration period is that the volume of the LTB region becomes dominant in V_D. In this case, if the parameter κ is almost equal to unity, the contribution of $\chi_2 \leq \chi < \chi_3$ is dominant in the volume of the LTB region and further makes the volume of the LTB region dominant in V_D for a long time before the domain $\chi \leq \chi_3$ completely collapses. So acceleraion
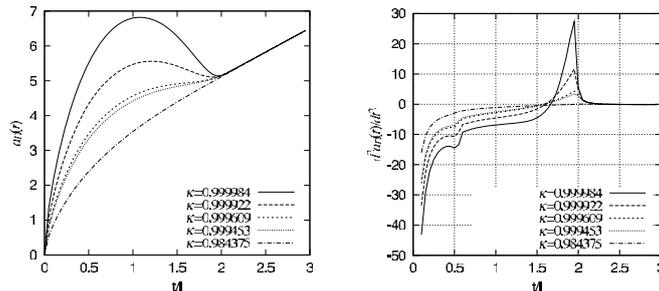
Figure 2: The left panel shows the evolution of the averaged scale factor a_D of one scale SSC model for various values of κ. The right panel shows the acceleration of the averaged scale factor a_D.

is realized. Especially, for two cases of $\kappa \geq 0.999609$, $\kappa \geq 0.999453$, do not have the contraction period although the acceleration occurs. this case is consitent with our real universe.

It should be noted that when the volume of the domain $\chi < \chi_3$ is dominant in the volume V_D and is contracting, the volume expansion of the domain D strongly slows down or the domain D contracts. The acceleration of the volume expansion is realized when the volume of the domain $\chi < \chi_3$ becomes so small that its contribution to V_D is negligible. In other words, the acceleration period appears around the time at which the dust in the domain $\chi < \chi_3$ collapses to the singularity and this time is given by

$$t_{\mathrm{ac}} := \frac{8\pi^2}{3} \frac{\rho_0 \chi_3^3}{\kappa^{3/2}}. \tag{11}$$

At $t = t_{\mathrm{ac}}$, the ratio of the areal radius of the boundary of a LTB region $a_{\mathrm{e}}(t)l$ to the Hubble horizon radius of EdS region $H^{-1}(t) := a_{\mathrm{e}}/\dot{a}_{\mathrm{e}} = 3t/2$ becomes

$$\frac{a_{\mathrm{e}}(t_{\mathrm{ac}})l}{H^{-1}(t_{\mathrm{ac}})} = \left(\frac{2}{3\pi}\right)^{1/3} \kappa^{1/2} \frac{l}{\chi_3} \simeq 0.60 \, \kappa^{1/2} \left(\frac{l}{\chi_3}\right). \tag{12}$$

Here it should be noted that κ has to be almost equal to unity so that the acceleration of the cosmic volume expansion is realized. Therefore the size of the LTB region is comparable to the horizon radius of EdS region in the acceleration period. This means that general relativistic non-linear effects are important for the realization of the acceleration period.

5   summary and future work

We indicated that the cosmic volume expansion can be accelerated by inhomogeneities in the dust-filled universe. Moreover, the existence of the cotracting region comparable to the Hubble horizon scale is necessarry condition to realize the acceleration. this fact is very different from the universe observed today in the period of the accelerating cosmic volume expansion. However, for the model with various scales of inhomogeneities, the temporal variation of the cosmic volume expansion is nontrivial from a theoretical point of view, and the complete analysis is left as a future work.

Here we should note that the issue of the cosmic acceleration has first been arisen from the observational data of the distance-redshift relation and that we have not directly observed the acceleration of the 'volume' expansion. So we need to investigate the distance-redshift relation in the inhomogeneous model. This is also our future work.

References

[1] Y. Nambu and M. Tanimoto, gr-qc/0507057 (2005).

[2] M. Kasai, Phys. Rev. Lett. 69 (1992), 2330.

[3] M. Kasai, H. Asada and T. Futamase, Prog. Theor. Phys. 115 (2006), 827.

Higgs phase of gravity

Shinji Mukohyama[1]

Department of Physics and Research Center for the Early Universe,
The University of Tokyo, Tokyo 113-0033, Japan

Abstract

Dark energy indicated by the current acceleration of our universe is one of the greatest mysteries in modern cosmology. Although more than 70% of our universe is thought to be dark energy, we do not know what it really is. In this situation, it seems natural to ask whether we can modify gravity at long distances to address the mystery. Ghost condensation is an analog of Higgs mechanism in general relativity, and modifies gravity at long distances without pathologies like ghost instability or strong coupling. In this presentation I discuss gravity and cosmology with ghost condensate.

1 Introduction

Acceleration of the cosmic expansion today is one of the greatest mysteries in both cosmology and fundamental physics. Assuming that Einstein's general relativity is the genuine description of gravity all the way up to cosmological distance and time scales, the so called concordance cosmological model requires that about 70% of our universe should be some sort of energy with negative pressure, called dark energy. However, since the nature of gravity at cosmological scales has never been probed directly, we do not know whether the general relativity is really correct at such infrared (IR) scales. Therefore, it seems natural to consider modification of general relativity in IR as an alternative to dark energy. Dark energy, IR modification of gravity and their combination should be tested and distinguished by future observations and experiments.

2 EFT of ghost condensation

Ghost condensation is an analogue of the Higgs mechanism in general relativity and modifies gravity in IR in a theoretically controllable way [1]. Its basic idea can be pedagogically explained by comparison with the usual Higgs mechanism as in the table shown below. First, the order parameter for ghost condensation is the vacuum expectation value (vev) of the derivative $\partial_\mu \phi$ of a scalar field ϕ, while the order parameter for Higgs mechanism is the vev of a scalar field Φ itself. Second, both have instabilities in their symmetric phases: a tachyonic instability around $\Phi = 0$ for Higgs mechanism and a ghost instability around $\partial_\mu \phi = 0$ for ghost condensation. In both cases, because of the instabilities, the system should deviate from the symmetric phase and the order parameter should obtain a non-vanishing vev. Third, there are stable points where small fluctuations do not contain tachyons nor ghosts. For Higgs mechanism, such a point is characterized by the order parameter satisfying $V' = 0$ and $V'' > 0$. On the other hand, for ghost condensation a stable point is characterized by $P' = 0$ and $P'' > 0$. Fourth, while the usual Higgs mechanism breaks usual gauge symmetry and changes gauge force law, the ghost condensation spontaneously breaks a part of Lorentz symmetry (the time translation symmetry) and changes linearized gravity force law in Minkowski background. Finally, generated corrections to the standard Gauss-law potential is Yukawa-type for the usual Higgs mechanism but oscillating for ghost condensation.

At this point one might wonder if the system really reach a configuration where $P' = 0$ and $P'' > 0$. Actually, it is easy to show that this is the case. For simplicity let us consider a Lagrangian $L_\phi = P(-(\partial\phi)^2)$ in the expanding FRW background with P of the form shown in the upper right part of the table. We assume the shift symmetry, the symmetry under the constant shift $\phi \to \phi + c$ of the scalar field. This symmetry prevents potential terms of ϕ from being generated. The equation of motion for ϕ

---

is simply $\partial_t[a^3 P'\dot\phi] = 0$, where a is the scale factor of the universe. This means that $a^3 P'\dot\phi$ is constant and that

$$P'\dot\phi \propto a^{-3} \to 0 \quad (a \to \infty) \tag{1}$$

as the universe expands. We now have two choices: $P' = 0$ or $\dot\phi = 0$, namely one of the two bottoms of the function P or the top of the hill between them. Obviously, we cannot take $\dot\phi = 0$ since it is a ghosty background and anyway unstable. Thus, we are automatically driven to $P' = 0$ by the expansion of the universe. In this sense the background with $P' = 0$ is an attractor.

	Higgs Mechanism	**Ghost Condensation**
Order Parameter	$\langle \Phi \rangle$ $V(\Phi)$ vs Φ	$\langle \partial_\mu \phi \rangle$ $P(X)$ vs $\dot\phi$, $X \equiv -(\partial \phi)^2$
Instability	Tachyon $-m^2 \Phi^2$	Ghost $-\dot\phi^2$
Condensate	V'=0, V''>0	P'=0, P''>0
Spontaneous breaking	Gauge symmetry	Lorents symmetry (Time translation)
Modifying	Gauge force	Gravitational force (in flat background)
New potential	Yukawa-type	Oscillating
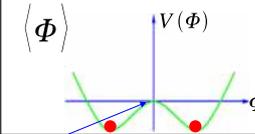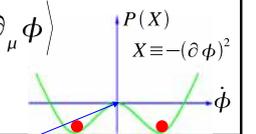
Having shown that the ghost condensate is an attractor, let us construct a low energy effective field theory around this background. For this purpose the most straightforward approach is to expand a general Lagrangian consistent with the shift symmetry. An alternative, more powerful way is to use the symmetry breaking pattern. In this approach, we actually do not need to specify a concrete way of the spontaneous symmetry breaking.

Here, let us briefly review this approach based on the symmetry breaking pattern. This is more universal and can be applied to any situations as far as the symmetry breaking pattern is the same. We assume that (i) $\langle \partial_\mu \phi \rangle$ is non-vanishing and timelike and that (ii) the background spacetime metric is maximally symmetric, either Minkowski or de Sitter. With the assumption (i), the 4-dimensional Lorentz symmetry is spontaneously broken down and we are left with the 3-dimensional spatial diffeomorphism $\vec{x} \to \vec{x}'(t, \vec{x})$. Our strategy here is to write down the most general action invariant under this residual symmetry. After that, the action for the Nambu-Goldstone (NG) boson π is obtained by undoing the unitary gauge.

For simplicity let us consider the Minkowski background plus perturbation: $g_{\mu\nu} = \eta_{\mu\nu} + h_{\mu\nu}$. The infinitesimal gauge transformation is $\delta h_{\mu\nu} = \partial_\mu \xi_\nu + \partial_\nu \xi_\mu$, where ξ^μ is a 4-vector representing the gauge freedom. Under the residual gauge transformation ξ^i ($i = 1, 2, 3$), the metric perturbation transforms as

$$\delta h_{00} = 0, \quad \delta h_{0i} = \partial_0 \xi_i, \quad \delta h_{ij} = \partial_i \xi_j + \partial_j \xi_i. \tag{2}$$

Now let us seek terms invariant under this residual gauge transformation. They must begin at quadratic order since we assumed that the flat spacetime is a solution to the equation of motion. The leading term (without derivatives acted on the metric perturbations) is $\int dx^4 M^4 h_{00}^2$. This is indeed invariant under the residual gauge transformation (2). From this term, we can obtain the corresponding term in the effective action for the NG boson π. Since $h_{00} \to h_{00} + 2\partial_0\xi_0$ under the broken symmetry transformation ξ^0, by promoting ξ^0 to a physical degree of freedom π, we obtain the term $\int dx^4 M^4 (h_{00} - 2\dot\pi)^2$. This includes a time kinetic term for π as well as a mixing term. At this point we wonder if we can get the usual space kinetic term $(\vec\nabla \pi)^2$ or not. The only possibility would be from $(h_{0i})^2$ since $h_{0i} \to h_{0i} - \partial_i\pi$ under the broken symmetry transformation $\xi^0 = \pi$. However, this term is not invariant under the residual spatial diffeomorphism ξ^i and, thus, cannot enter the effective action. Actually, there are combinations invariant

under the spatial diffeomorphism. They are made of the geometrical quantity called extrinsic curvature. The extrinsic curvature K_{ij} in the linear order is $K_{ij} = (\partial_0 h_{ij} - \partial_j h_{0j} - \partial_i h_{0j})/2$ and transforms as a tensor under the spatial diffeomorphism. Thus, $\int dx^4 \tilde{M}^2 K^2$ and $\int dx^4 \bar{M}^2 K^{ij} K_{ij}$ are invariant under spatial diffeomorphism and can be used in the action, where $K = K_i^i$. Since $K_{ij} \to K_{ij} + \partial_i \partial_j \pi$ under the broken symmetry $\xi^0 = \pi$, we obtain $\int dx^4 (\tilde{M}^2 + \bar{M}^2)(\vec{\nabla}^2 \pi)^2$. Combining these terms with the above time kinetic term and properly normalizing the definition of π and M, we obtain

$$L_{eff} = M^4 \left\{ \frac{1}{2} \left(\dot{\pi} - \frac{1}{2} h_{00} \right)^2 - \frac{\alpha_1}{M^2} \left(K + \vec{\nabla}^2 \pi \right)^2 - \frac{\alpha_2}{M^2} \left(K^{ij} + \vec{\nabla}^i \vec{\nabla}^j \pi \right) \left(K_{ij} + \vec{\nabla}_i \vec{\nabla}_j \pi \right) + \cdots \right\}, \quad (3)$$

where α_1 and α_2 are dimensionless constants of order unity. Note that, in deriving the effective action, all we needed was the symmetry breaking pattern. Thus, the low energy EFT of the ghost condensation is universal and should hold as far as the symmetry breaking pattern is the same.

In ghost condensation the linearized gravitational potential is modified at the length scale r_c in the time scale t_c, where r_c and t_c are related to the scale of spontaneous Lorentz breaking M as

$$r_c \simeq \frac{M_{\text{Pl}}}{M^2}, \quad t_c \simeq \frac{M_{\text{Pl}}^2}{M^3}. \quad (4)$$

Note that r_c and t_c are much longer than $1/M$. The way gravity is modified is peculiar. At the time when a gravitational source is turned on, the potential is exactly the same as that in general relativity. After that, however, the standard form of the potential is modulated with oscillation in space and with exponential growth in time. This is an analogue of Jeans instability, but unlike the usual Jeans instability, it persists in the linearized level even in Minkowski background. The length scale r_c and the time scale t_c above are for the oscillation and the exponential growth, respectively. At the time $\sim t_c$, the modification part of the linear potential will have an appreciable peak only at the distance $\sim r_c$. At larger distances, it will take more time for excitations of the Nambu-Goldstone boson to propagate from the source and to modify the gravitational potential. At shorter distances, the modification is smaller than at the peak position because of the spatial oscillation with the boundary condition at the origin. The behavior explained here applies to Minkowski background, but in ref. [1] the modification of gravity in de Sitter spacetime was also analyzed. It was shown that the growing mode of the linear gravitational potential disappears when the Hubble expansion rate exceeds a critical value $H_c \sim 1/t_c$. Thus, the onset of the IR modification starts at the time when the Hubble expansion rate becomes as low as H_c.

If we take the $M/M_{\text{Pl}} \to 0$ limit then the Higgs sector is completely decoupled from the gravity and the matter sectors and, thus, the general relativity is safely recovered. Therefore, cosmological and astrophysical considerations in general do not set a lower bound on the scale M of spontaneous Lorentz breaking, but provide upper bounds on M. If we trusted the linear approximation for all gravitational sources for all times then the requirement $H_c \lesssim H_0$ would give the bound $M \lesssim (M_{\text{Pl}}^2 H_0)^{1/3} \simeq 10 MeV$, where H_0 is the Hubble parameter today [1]. However, for virtually all interesting gravitational sources the nonlinear dynamics dominates in time scales shorter than the age of the universe. As a result the nonlinear dynamics cuts off the Jeans instability of the linear theory, and allows $M \lesssim 100 GeV$ [2].

Note that the ghost condensate provides the second most symmetric class of backgrounds for the system of field theory plus gravity. The most symmetric class is of course maximally symmetric solutions: Minkowski, de Sitter and anti-de Sitter. The ghost condensate minimally breaks the maximal symmetry and introduces only one Nambu-Goldstone boson.

3 Cosmological applications

Now let us discuss some applications to cosmology.

Inflation: We can consider inflation with ghost condensation in the regime of validity of the EFT. In the very early universe where H is higher than the cutoff M, we do not have a good EFT describing the sector of ghost condensation. However, the contribution of this sector to the total energy density ρ_{tot} is naturally expected to be negligible: $\rho_{ghost} \sim M^4 \ll M_p^2 H^2 \simeq \rho_{tot}$. As the Hubble expansion rate decreases, the sector of ghost condensation enters the regime of validity of the EFT and the Hubble

friction drives P' to zero. If we take into account quantum fluctuations then P' is not quite zero but is $\sim (H/M)^{5/2} \sim (\delta\rho/\rho)^2 \sim 10^{-10}$ in the end of ghost inflation. In this way, we have a consistent story, starting from the outside the regime of validity of the EFT and dynamically entering the regime of validity. All predictions of the ghost inflation are derived within the validity of the EFT, including the relatively low-H de Sitter phase, the scale invariant spectrum and the large non-Gaussianity [3].

Dark energy: In the usual Higgs mechanism, the cosmological constant (cc) would be negative in the broken phase if it is zero in the symmetric phase. Therefore, it seems difficult to imagine how the Higgs mechanism provides a source of dark energy. On the other hand, the situation is opposite with the ghost condensation: the cc would be positive in the broken phase if it is zero in the symmetric phase. Hence, while this by itself does not solve the cc problem, this can be a source of dark energy.

Dark matter: If we consider a small, positive deviation of P' from zero then the homogeneous part of the energy density is proportional to a^{-3} and behaves like cold dark matter (CDM). Inhomogeneous linear perturbations around the homogeneous deviation also behaves like CDM. However, at this moment it is not clear whether we can replace the CDM with ghost condensate. We need to see if it clumps properly. Ref. [2] can be thought to be a step towards this direction.

Cosmological perturbation: By using the formalism of the cosmological perturbations developed in [4], the theory of ghost condensation can be tested by dynamical information of large scale structure in the universe such as cosmic microwave background anisotropy, weak gravitational lensing and galaxy clustering.

4 UV completion via gauged ghost condensation

To realize the ghost condensation without fine-tuning, we need to spontaneously break the 4-dimensional diffeomorphism invariance times a global shift symmetry down to the 3-dimensional spatial diffeomorphism invariance times an unbroken global shift symmetry. The latter global shift is a combination of the former global shift and the time shift. However, it is generally believed that all symmetries in string theory are gauged. Therefore, it seems more plausible to obtain the ghost condensation as the neutral limit of the gauged version of the ghost condensation, i.e. the gauged ghost condensation [5]. To obtain the gauged ghost condensation from the ghost condensation we replace the global shift symmetry with a minimal gauge symmetry, i.e. $U(1)$ gauge symmetry, so that no global symmetry is needed. The ghost condensation can be obtained from the gauged ghost condensation if we can fine-tune the gauge coupling to a sufficiently small value. Thus, it is likely that, without fine-tuning, the gauged ghost condensation is the simplest Higgs phase of gravity in string theory. An attempt to realize the gauged ghost condensation in string theory has been made in ref. [6].

References

[1] N. Arkani-Hamed, H. C. Cheng, M. A. Luty and S. Mukohyama, "Ghost condensation and a consistent infrared modification of gravity," JHEP **0405**, 074 (2004) [arXiv:hep-th/0312099].

[2] N. Arkani-Hamed, H. C. Cheng, M. A. Luty, S. Mukohyama and T. Wiseman, "Dynamics of gravity in a Higgs phase," JHEP **0701**, 036 (2007) [arXiv:hep-ph/0507120].

[3] N. Arkani-Hamed, P. Creminelli, S. Mukohyama and M. Zaldarriaga, "Ghost Inflation," JCAP **0404**, 001 (2004) [arXiv:hep-th/0312100].

[4] S. Mukohyama, "Accelerating universe and cosmological perturbation in the ghost condensate," JCAP **0610**, 011 (2006) [arXiv:hep-th/0607181].

[5] H. C. Cheng, M. A. Luty, S. Mukohyama and J. Thaler, "Spontaneous Lorentz breaking at high energies," JHEP **0605**, 076 (2006) [arXiv:hep-th/0603010].

[6] S. Mukohyama, "A Higgs phase of gravity in string theory," arXiv:hep-th/0610254.

Accelerated Cosmological Parameter Estimation using Neural Networks

Tom Auld[1] and Michael Bridges[2]

Cambridge University, Cavendish Laboratory, J J Thomson Avenue, Cambridge CB3 0HE, UK

Abstract

We present a method for accelerating the calculation of CMB power spectra, matter power spectra and likelihood functions for use in cosmological parameter estimation. The algorithm, called COSMONET, is based on training a multilayer perceptron neural network. We demonstrate the capabilities of COSMONET by computing CMB power spectra over a box in the parameter space of both a flat ΛCDM model and non-flat cosmology (with tensor modes, varying equation of state of dark energy and massive neutrinos) containing the 4σ WMAP 3-year + (high resolution CMB experiments plus 2dF and SDSS surveys) confidence region. We also use COSMONET to compute the WMAP 3-year, 2dF and SDSS likelihoods and demonstrate that marginalised posteriors on parameters derived are very similar to those obtained using CAMB and the likelihood codes in the normal way. COSMONET and an interface to COSMOMC are publically available at `www.mrao.cam.ac.uk/software/cosmonet`.

1 Introduction

In the analysis of increasingly high-precision data sets, it is now common practice in cosmology to constrain cosmological parameters using sampling based methods, most notably Markov chain Monte Carlo (MCMC) techniques (Christensen et al. 2001; Knox, Christensen & Skordis 2001; Lewis & Bridle 2002). This approach typically requires one to calculate theoretical CMB power spectra (i.e. some subset of the TT, TE, EE and BB C_ℓ spectra) and/or the matter power spectrum $P(k)$ at a large number of points (typically $\sim 10^5$ or more) in the cosmological parameter space. In addition, one must also evaluate at each point the corresponding (combined) likelihood function for the data set(s) under consideration. As a result, the process can be computational very demanding.

MCMC parameter estimation codes such as COSMOMC (Lewis & Bridle 2002) attempt to decrease the overall computational burden by dividing the cosmological parameter space into 'fast' parameters (governing the initial primoridal power spectra of scalar and tensor perturbations) and 'slow' parameters (governing the perturbation evolution).

There are a number of ways in which suitably accurate spectra can be generated somewhat more rapidly. For small parameter spaces, it is possible simply to create spectra for a regular grid of models in parameter space and interpolate between them in some way, such as the ℓ-splitting scheme of Tegmark & Zaldarriaga (2000). Nevertheless, the pre-compute of the grid of models remains extremely time-consuming.

Analytic and semi-analytic approximations can reduce the required number of pre-computed models. The DASH code of Kaplinghat, Knox & Skordis (2002), stores a sparse grid of transfer functions (rather than C_ℓ) and uses efficient choices for grid parameters and makes considerable use of analytic approximations.

More recently, the need to pre-compute a grid of models has been removed in the CMBWARP package (Jimenez et al. 2004), which builds on the method introduced by Kosowsky, Milosavljevic & Jimenez (2002). In this approach, a new set of nearly uncorrelated 'physical parameters' are introduced upon which the CMB power spectra have a simple dependence. CMBWARP uses a modified polynomial fit in these parameters in which the coefficients are based on the spectra C_ℓ^{TT}, C_ℓ^{TE} or C_ℓ^{EE} for just a single fiducial model in the parameter space.

Although the above methods have proved extremely useful in performing cosmological parameter estimation, they do exhibit a number of drawbacks, including time consuming grid calculations, loss of accuracy and lack of generality. Most recently, this has led Fendt & Wandelt (2006) to propose a more flexible and robust machine-learning approach (called PICO) to accelerating both power spectra and likelihood evaluations. The basic algorithm used by PICO consists of three major parts. First, the training set is compressed using Karhunen–Loève eigenmodes which results in a reduction in the dimensionality of around two. Second, the training set is used to divide the

---

[1] E-mail:tauld@mrao.cam.ac.uk
[2] E-mail:mb435@mrao.cam.ac.uk

parameter space into (~ 100) smaller regions using a k-means clustering algorithm (see e.g. MacKay 1997). Finally, a (4th order) polynomial is fitted within each cluster to provide a local interpolation of the power spectra within the cluster as a function of cosmological parameters. The reason for dividing up the parameter space in the second step is that the interpolation method used fails to model accurately the power spectra over the entire parameter space.

We present an independent approach to using machine-learning techniques for accelerating both power spectra and likelihood evaluations. Our approach is based on training a neural network in the form of a 3-layer perceptron. The resulting COSMONET code has additional benefits over PICO in terms of simplicity, computational speed, accuracy, memory requirements and ease of training.

2   Neural Networks

2.1   Multilayer perceptron networks

Multilayer perceptron neural networks (MLPs) are a type of feed-forward network composed of a number of ordered layers of perceptron (Rosenblatt 1958) neurons that pass scalar messages from one layer to the next. We will work with a 3-layer network, which consists of an input layer, a hidden layer and an output layer, as illustrated in Fig. **??**.

In such a network, the outputs of the nodes in the hidden and output layers take the form

$$\text{hidden layer:} \quad h_j = g^{(1)}(f_j^{(1)}); \quad f_j^{(1)} = \sum_l w_{jl}^{(1)} x_l + \theta_j^{(1)}, \tag{1}$$

$$\text{output layer:} \quad y_i = g^{(2)}(f_i^{(2)}); \quad f_i^{(2)} = \sum_j w_{ij}^{(2)} h_j + \theta_i^{(2)}, \tag{2}$$

where the index l runs over input nodes, j runs over hidden nodes and i runs over output nodes. $w_{jl}^1, \theta_j^1, w^2 ij, \theta_i^2$ are the set of parameters that define the network that we will collectively refer to as the weights, $\mathbf{w}$ here. The functions $g^{(1)}$ and $g^{(2)}$ are called activation functions. We use $g^{(1)}(x) = \tanh x$ and $g^{(2)}(x) = x$.

According to a 'universal approximation theorem' (Leshno et al. 1993), a standard multilayer feed-forward network with these activation functions can approximate any continuous function to *any* degree of accuracy, given sufficient hidden nodes.

2.2   Network training

We build an empirical model of the CAMB mapping using a 3-layer MLP as described above (a model of the WMAP3 likelihood code can be constructed in an analogous manner). The number of nodes in the input layer will correspond to the number of cosmological parameters, and the number in the output layer will be the number of uninterpolated C_ℓ values output by CAMB. A set of training data $D = \{\mathbf{x}^{(k)}, \mathbf{t}^{(k)}\}$ is provided by CAMB and the problem now reduces to choosing the appropriate weights $\mathbf{w}$ that best fit this training data. We do this by minimising the 'error' term $\chi^2(\mathbf{w})$ on the training set given by

$$\chi^2(\mathbf{w}) = \tfrac{1}{2} \sum_k \sum_i \left[t_i^{(k)} - y_i(\mathbf{x}^{(k)}; \mathbf{w}) \right]^2. \tag{3}$$

This is, however, a highly non-linear, multi-modal function in many dimensions whose optimisation is achieved using the MEMSYS package (Gull & Skilling 1999).

3   Results

We demonstrate our approach by training networks to replace the CAMB package for the evaluation of the CMB power spectra C_ℓ^{TT}, C_ℓ^{TE}, C_ℓ^{EE} (and C_ℓ^{BB}) for two separate cosmological models within a box in parameter space that encompasses the 4σ confidence region as determined using a typical mixture of CMB and large scale structure experiments; WMAP 3-year + higher resolution CMB observations (ACBAR; Kuo et al. 2004; BOOMERang; Piacentini et al. 2003; CBI; Readhead et al. 2004 and the VSA; Dickinson C., et al. 2004) and galaxy surveys;

2dF; Cole et al. 2005 and SDSS; Tegmark et al. 2004. The first model; Model A, is a flat ΛCDM model, the second; model B, is a 10-parameter non-flat cosmology that includes tensor modes, massive neutrinos and a varying equation of state of dark energy. We also train networks to replace the WMAP 3-year, 2dF and SDSS likelihood codes for model A within the same 4σ region.

The training data for the spectra interpolation is produced by uniformly sampling models over the 4σ parameter region. It was found that up-to 5000 models are required in training for the various networks. Using less, led to a loss in accuracy, and more, led to a slower training time. The physical parameters (ω_b, ω_{cdm}, θ,...) are converted back to cosmological parameters (Ω_b, Ω_{cdm}, H_0,...) and used as input to CAMB to produce the training set of CMB power spectra out to $\ell_{max} = 1500$. The WMAP 3-year likelihood was also generated for model A, but for model B, this was problematic, due to the WMAP likelihood code producing no finite value for very non-physical models in certain regions at the edges of the 4σ region. A further set of 10^4 samples were generated as testing data.

It was found that between 50 and 100 nodes in the hidden layer were sufficient to provide good results. The results of comparing the COSMONET output with CAMB over the testing set are shown in Figures 1 and 2.

For all but the very low values of l in the EE spectrum the average error is under 10% of cosmic variance. The 99th percentiles are comfortably below unit cosmic variance. A comparison of output of the COSMONET likelihood network with the WMAP 3-year likelihood code over the testing set reveals a mean error of roughly 0.2 ln units close to the likelihood peak for model A.

4 Application to cosmological parameter estimation

To illustrate the usefulness of COSMONET in cosmological parameter estimation we perform an analysis of the WMAP 3-year TT, TE and EE data using COSMOMC in three separate ways: (i) using CAMB power spectra and the WMAP 3-year, 2dF and SDSS likelihood codes; (ii) using COSMONET power spectra and the likelihood codes; and (iii) using the COSMONET likelihoods. The resulting marginalised parameter constraints for each method are shown in figures 3, and are clearly very similar.

In each case 4 parallel MCMC chains were run on Intel Itanium 2 processors at the COSMOS cluster (SGI Altix 3700) at DAMTP, Cambridge. The wall-clock computational time (the total CPU time is 4 times longer) required to gather ~ 20000 post burn-in MCMC samples was ~ 12 hours for model A and ~ 20 hours for model B using method (i) (with CAMB further parallelised over 3 additional processors per chain, therefore totalling 16 CPUs), 8 hours (model A and model B) for method (ii) and for model A roughly 35 ± 5 minutes using the interpolated likelihood for method (iii).

5 Conclusions

We have presented a method for accelerating power spectrum and likelihood evaluations based on the training of multilayer perceptron neural networks, which we have shown to be fast, robust and accurate. The method is demonstrated with applications to a 6-parameter ΛCDM model and a 10-parameter non-flat cosmology. The parameter constraints generated with COSMONET are very similar to those produced from the existing methods, but took significantly less time to compute.

The homepage for the COSMONET package is located at `www.mrao.cam.ac.uk/software/cosmonet` and provides a simple interpolation routine that interfaces with COSMOMC.

References

[] Bennett C. et al., 2003, ApJS, 148, 1

[] Christensen N., Meyer R., Knox L., Luey B., 2001, Class. Quant. Grav., 18, 2677

[] Cole, S., 2005, MNRAS, 362, 505-534

[] Dickinson, C. et al. 2004, MNRAS, 353, 732

[] Fendt W., Wandelt B., 2006, ApJ, submitted (astro-ph/0606709)
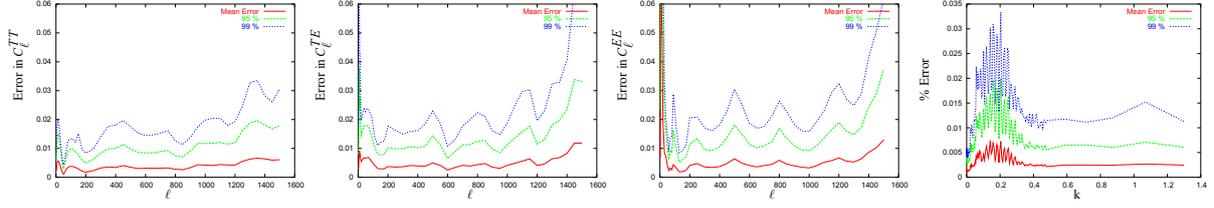
Figure 1: Comparison of the performance of COSMONET versus CAMB for TT, TE and EE power spectra and matter transfer function in a 6 parameter flat ΛCDM model. The plots show the average error together with the 95 and 99 percentiles in units of cosmic variance in the case of the CMB spectra and % error in the matter transfer function case.
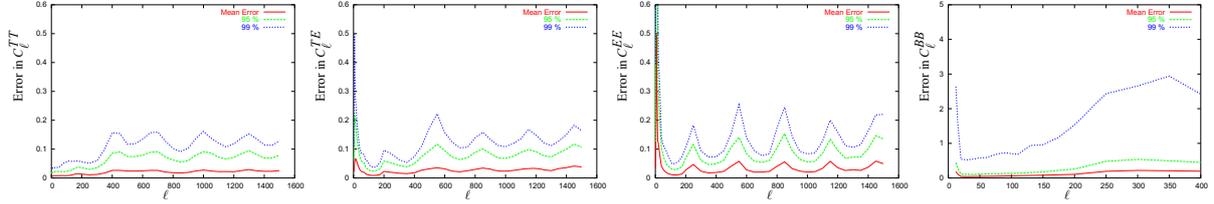
Figure 2: Comparison of the performance of COSMONET versus CAMB for TT, TE, EE and BB power spectra in a 10 parameter non-flat cosmological model. The plots shows the average error together with the 95 and 99 percentiles in units of cosmic variance.
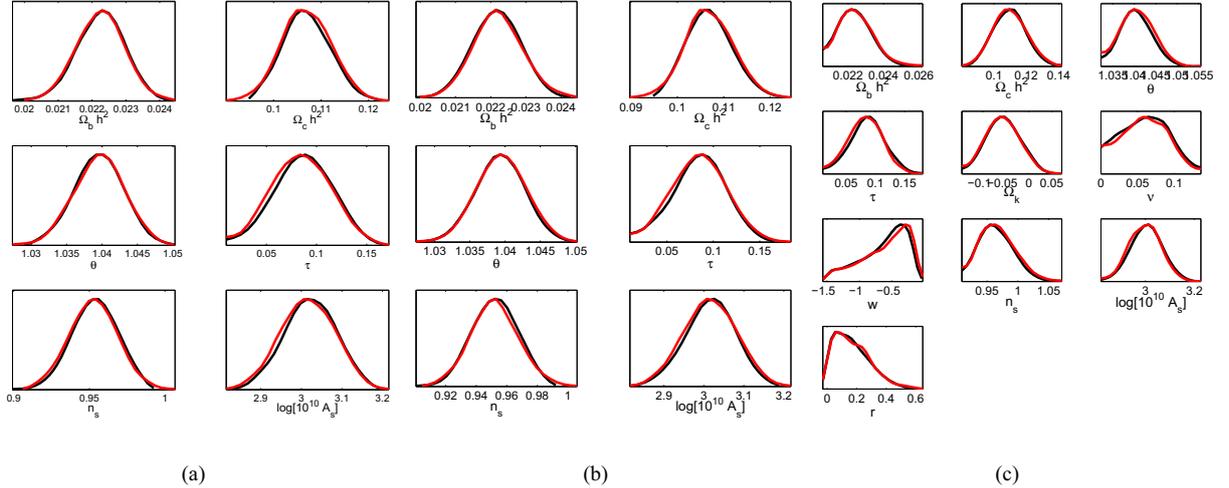
Figure 3: The one-dimensional marginalised posteriors on the cosmological parameters within the 6-parameter flat ΛCDM model comparing: CAMB power-spectra and WMAP3, 2dF and SDSS likelihoods (red) with COSMONET power spectra and WMAP3, 2dF and SDSS likelihoods (black) in (a) while (b) shows CAMB power-spectra and WMAP3, 2dF and SDSS likelihoods (red) with COSMONET likelihoods (black). The 10-parameter non-flat cosmology is shown in (c) comparing: CAMB power-spectra and WMAP3, 2dF and SDSS likelihoods (red) with COSMONET power spectra and WMAP3, 2dF and SDSS likelihoods (black).

[] Gull S.F., Skilling J., 1999, Quantified maximum entropy: MemSys 5 users' manual. Maximum Entropy Data Consultants Ltd, Royston

[] Jimenez R., Verde L., Peiris H., Kosowsky A., 2004, PRD, 70, 023005

[] Kaplinghat M., Knox L., Skordis C., 2002, ApJ, 578, 665

[] Kosowsky A., Milosavljevic M., Jimenez R., 2002, PRD, 66, 063007

[] Knox L., Christensen N., Skordis C., 2001, ApJ, 563, L95

[] Kuo, Chao-lin et al., 2004, ApJ, 600, 32-51

[] Lewis A., Bridle S., 2002, PRD, 66, 103511

[] Leshno M., Ya. Lin V., Pinkus A., Schocken S., 1993, Neural Netw., 1993, 6, 861

[] MacKay D.J.C., 2003, Information theory, inference and learning algorithms. Cambridge University Press

[] Piacentini F. et al., 2006, 647, 833-839

[] Readhead A., et al. 2004, ApJ, 498-512

[] Rosenblatt F., 1958, Psychological Review, 65, 386

[] Tegmark M., Zaldarriaga M., 2000, ApJ, 544, 30

[] Tegmark M., et al. 2004, ApJ, 2004, 606, 702-740

Neutrino Mass Constraints from WMAP and SDSS

Kazuhide Ichikawa[1]

Institute for Cosmic Ray Research, University of Tokyo,
Kashiwa 277-8582, Japan

Abstract

We discuss the constraints on the neutrino mass from recent cosmological data. Assuming the flat LCDM model with power-law adiabatic perturbations, we find $m_\nu < 0.7$ eV (95% C.L.) from the WMAP data alone, without the aid of any other cosmological data. We also investigate how much the SDSS LRG power spectrum can improve this WMAP limit.

1   Introduction

The neutrino mass is directly searched by tritium β-decay experiments and the current upper bound for the electron neutrino mass is 2 eV (95% C.L.) [1]. At present, it is difficult to push down the limit in this way, but, as is well known, cosmological considerations give more stringent constraints.

For example, Ref. [2] obtained $m_\nu < 0.21$ eV and Ref. [3] obtained $m_\nu < 0.58$ eV, using the WMAP 1st year data combined with the galaxy power spectrum (the former used the data from the 2dFGRS and the latter from the SDSS main sample. The difference can be ascribed to the use of the bias information by Ref. [2]). By contrast, we found $m_\nu < 0.66$ eV from the WMAP 1st year data alone as reported in Ref. [4]. We note that this is the first to point out CMB data (the WMAP 1st year data) alone can give a sub-eV upper bound on the neutrino mass, which is comparable to the limits obtained from the CMB and galaxy clustering data combined.

Before Ref. [4] (and some time after that too), there seems to be a lack of consensus about whether the CMB experiment with the WMAP-level precision can derive a sub-eV neutrino mass limit and, in fact, the WMAP alone limit reported in Ref. [3], $m_\nu < 3.8$ eV, which allows 100% HDM was somewhat accepted (incidentally, the WMAP group did not report the WMAP 1st year data alone limit on the neutrino mass). We, on the contrary, have derived the upper limit 0.66 eV as quoted above from the same data by the χ^2 minimization method which is independent from the MCMC method adopted by Ref. [3]. Our conclusion is later confirmed by Refs. [5–7] (Ref. [5] does not report the WMAP alone limit in a number but judging from their likelihood figure, it looks less than 1 eV. Refs. [6] and [7] gives $m_\nu < 0.70$ eV and $m_\nu < 0.63$ eV respectively).

Below, we first discuss the WMAP alone limit comparing results from 1st year data and 3rd year data. Then, we will see how the limit is tightened by the SDSS Luminous Red Galaxy (LRG) power spectrum [8] which is obtained from a galaxy sample with the largest effective volume to date (about 6 times larger than that of the main sample).

We here summarize our notations. We derive neutrino mass constraint in the flat ΛCDM model with the power-law adiabatic perturbations. Namely, cosmological parameters we consider are: baryon density ω_b, matter density ω_m, hubble parameter h, reionization optical depth τ, spectral index of primordial spectrum n_s, its amplitude A and massive neutrino density ω_ν. Here, $\omega \equiv \Omega h^2$ where Ω is the energy density normalized to the critical density and $\omega_m \equiv \omega_b + \omega_c$ where ω_c is cold dark matter density [2]. ω_ν is related to neutrino masses by $\omega_\nu = \sum m_\nu/(94.1 \text{ eV})$ and we assume three generations of massive neutrinos with degenerate masses so that $\omega_\nu = m_\nu/(31.4 \text{ eV})$. The flatness condition is expressed as $\omega_m + \omega_\nu + \omega_\Lambda = h^2$ where ω_Λ is the cosmological constant energy density.
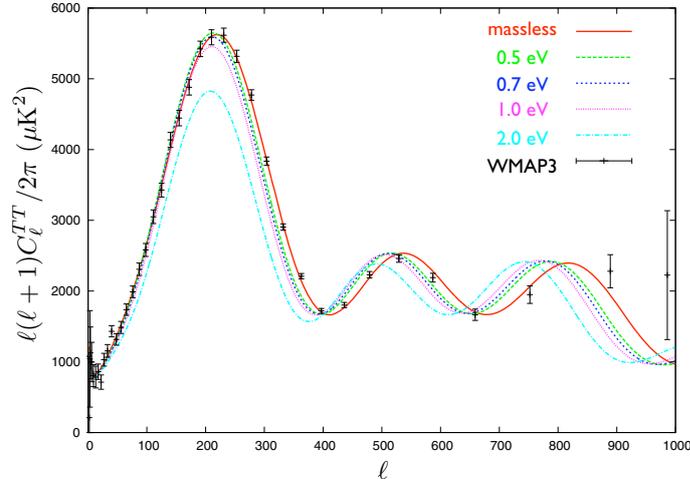
Figure 1: Effects of massive neutrinos on the CMB TT power spectrum. The labels denote the neutrino mass for single species m_ν and we assume three degenerate species. When we vary the neutrino mass, we fix ω_b, ω_c, h and $\Omega_{\rm tot} = 1$ so that Ω_Λ varies. We also fix the amplitude (normalization) for the primordial power spectrum A. Errorbars are from the WMAP 3-year observation.

2   WMAP alone limit

We begin with showing how CMB power spectrum is modified by increasing neutrino mass in Fig. 1. The other cosmological parameters are fixed here. Also, we assume equal mass m_ν for three neutrino species, which is justified because, from the oscillation experiments, the mass differences are known to be much smaller than one eV. In this figure, we see horizontal shift, and suppression around the first peak. We will briefly discuss whether these variations are degenerate with other cosmological parameters.

As for the horizontal shift, this comes from the fact that the larger m_ν implies smaller amount of cosmological constant, since we assume that the universe is flat. Then the distance to the last scattering surface is shorter and the peaks move to smaller ℓ (to larger angular scales). However, this shift is easily cancelled by the shift in the hubble parameter. Therefore this does not produce a neutrino mass signal.

Next, the suppression of the 1st peak takes place only when m_ν is larger than about 0.6 eV. This corresponds to 0.3 eV in terms of photon temperature T. Meanwhile, the recombination takes place at $z \approx 1088$ or $T \approx 0.3$ eV. In other words, massive neutrinos become non-relativistic before the epoch of recombination if they are heavier than 0.6 eV. Therefore, only in this case, the neutrino mass can imprint a characteristic signal in acoustic peaks (to be specific, the matter-radiation equality occurs earlier due to less relativistic degrees of freedom and the enhancement of the 1st peak by the early-integrated Sachs-Wolfe effect is smaller).

In passing, notice that such separation of the neutrino mass effect into the horizontal shift and the suppression of the 1st peak for $m_\nu > 0.6$ eV can be accomplished by our parametrization that $\omega_m \equiv \omega_b + \omega_c$ is fixed (Ω_Λ is varied) when m_ν is varied.

This signal, however, could be accidentally mimicked by some combination of other cosmological parameters. So we searched a large cosmological parameter space in order to find the degree of degeneracy between m_ν and the other cosmological parameters. The results are shown in Fig. 2. We calculated WMAP χ^2 (log likelihood) as functions of m_ν. For each value of m_ν, we varied 6 other ΛCDM cosmological parameters to find minimum χ^2. In Fig. 2, the different lines represent different data sets. The blue dotted line is the WMAP 1st year result which I mentioned in the introduction. The others use WMAP 3-year data. The red solid line uses full data sets including temperature and polarization and the green dashed line uses only temperature power spectrum. We find that three lines are quite similar.

---

[1] E-mail:kazuhide@icrr.u-tokyo.ac.jp

[2] Caution that many literatures define $\omega_m \equiv \omega_b + \omega_c + \omega_\nu$ to include the massive neutrino in the matter density.
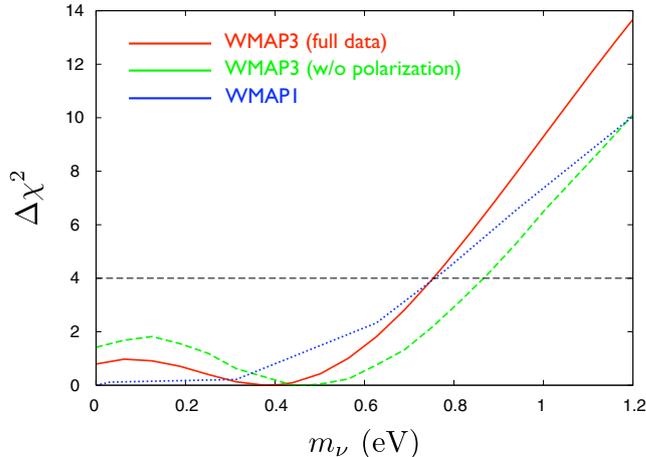
Figure 2: $\Delta\chi^2$ of WMAP data as functions of the neutrino mass m_ν [4,9]. $\Delta\chi^2 = 4$ roughly corresponds to 95% C.L. limit. Each curve represents different data sets. The blue dotted line use the WMAP 1st year data (TT+TE), the red solid line uses the full WMAP 3-year data including temperature and polarization and the green dashed line uses only temperature power spectrum of the WMAP 3-year data.

In summary, we obtained the upper bound of 0.7 eV from WMAP alone and two points are worth mentioning. First is that the WMAP 3-year constraint is not improved from the 1st year limit. Next is that the polarization data does not contribute to the limit much. These results are reasonable because the neutrino mass (larger than 0.6 eV) characteristically modifies the acoustic peaks around 1st and 2nd peaks in the temperature power spectrum and these regions are already well measured by the WMAP 1st year.

We stress that this bound is robust in a sense that it is obtained from CMB data of the WMAP which is considered to be the cleanest cosmological data and that it is obtained from a single experiment. Also, CMB can be dealt with the linear perturbation theory so it does not suffer from non-linearity or biasing which appear in galaxy clustering data.

However, we have to combine other data sets to improve this limit. This is because, as we mentioned earlier, CMB is insensitive to the neutrino mass lighter than 0.6 eV [3] , whose effects being absorbed in the shift of the hubble parameter.

3   WMAP + SDSS LRG limit

Now, we try to improve the WMAP alone limit by combining with the newest galaxy power spectrum data of SDSS based on the luminous red galaxy samples. We are mostly interested in how combined limit is affected by systematic effects, especially by uncertainties in non-linear modeling. We show the result of the χ^2 analysis first in Fig. 3. We find SDSS data improves the limit down to 0.2 eV shown by the light-blue dot-dashed line from 0.7 eV of the WMAP alone limit shown by the red solid line. Here, when we marginalize over the other cosmological parameters, we marginalized also over two parameters for non-llinear modeling following the SDSS group's analysis [8]. Next I will explain non-linear modeling we adopted.

Our non-linear modeling follows a simple model of Ref. [10]: $P_{gal}(k) = (1 + \mathcal{Q}k^2)/(1 + Ak)P_{lin}(k)$, where k is the wavenumber. P_{lin} is the linear power spectrum computed by *e.g.* CMBFAST and P_{gal} is the galaxy power spectrum to be compared with the observation. A is fixed to 1.4 and we marginalize over $\mathcal{Q}$. We also marginalize over scale-independent "bias factor" b in addition to the above correction factor for Fig. 3.

---

[3]The lensed CMB is known to be sensitive to smaller neutrino masses if we obtained polarization data of next (or next-to-next) generation experiments, but we do not discuss this possibility here.
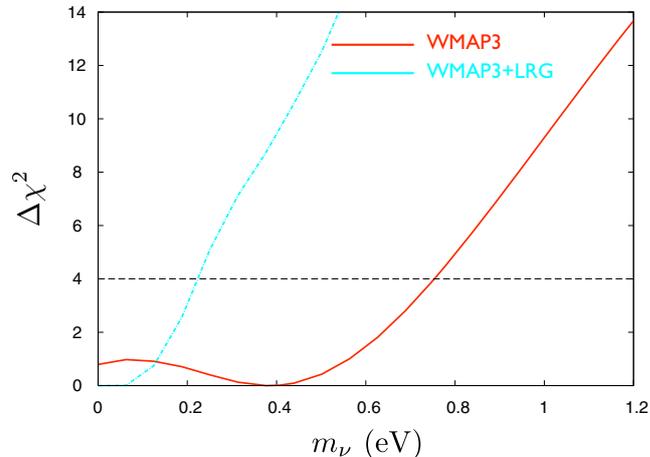
Figure 3: $\Delta\chi^2$ of WMAP 3-year and SDSS LRG power spectrum data as functions of the neutrino mass m_ν. The red solid line uses the full WMAP 3-year data and the light-blue dot-dashed line uses the WMAP 3-year + LRG.

To investigate how the neutrino mass and the non-linear correction are correlated, as a very simple test, we begin by fixing $\mathcal{Q}$. This is because the value such as $\mathcal{Q}$ is in principle determined by theoretical calculation if we could calculate how galaxies form in the dark matter halo. We performed χ^2 analysis with several fixed values of $\mathcal{Q}$ and we found that the upper bound does not move very much from 0.2 eV (0.2-0.25 eV for $\mathcal{Q}$ =25-35). However, note that, in such a simple way, systematic effects of non-linear corrections can not be fully investigated, of course.

In conclusion, the WMAP 3-year alone limit is 0.7 eV and the SDSS new galaxy data of LRG improves this limit down to around 0.2 eV. This combined limit does not seem to change much by simple systematic effects of non-linear correction like the one explained above. However, we need to investigate more the effects of the non-linear modeling on the neutrino mass constraints to increase the robustness of limits from the galaxy clustering data.

References

[1] W. M. Yao *et al.* [Particle Data Group], J. Phys. G **33**, 1 (2006).

[2] D. N. Spergel *et al.* [WMAP Collaboration], Astrophys. J. Suppl. **148**, 175 (2003).

[3] M. Tegmark *et al.* [SDSS Collaboration], Phys. Rev. D **69**, 103501 (2004).

[4] K. Ichikawa, M. Fukugita and M. Kawasaki, Phys. Rev. D **71**, 043001 (2005).

[5] C. J. MacTavish *et al.*, Astrophys. J. **647**, 799 (2006).

[6] S. Hannestad, arXiv:hep-ph/0602058.

[7] J. Lesgourgues and S. Pastor, Phys. Rept. **429**, 307 (2006).

[8] M. Tegmark *et al.*, Phys. Rev. D **74**, 123507 (2006).

[9] M. Fukugita, K. Ichikawa, M. Kawasaki and O. Lahav, Phys. Rev. D **74**, 027302 (2006).

[10] S. Cole *et al.* [The 2dFGRS Collaboration], Mon. Not. Roy. Astron. Soc. **362**, 505 (2005).

Spontaneous Baryogenesis, CPT Violations and the Observational Imprints

Bo Feng[1]

[1] *Research Center for the Early Universe(RESCEU), Graduate School of Science, The University of Tokyo, Tokyo 113-0033, Japan*

Abstract

We realize the model of spontaneous baryogenesis in the framework of dynamical dark energy. This will lead to dynamical cosmic CPT violations and leave imprints in the universe. Using the CMB observations of WMAP and Boomerang we get a mild preference of such kind of cosmic CPT violations.

The origin of the baryon number asymmetry in the universe remains a big puzzle in cosmology and particle physics. Sakharov's original proposal for a dynamical generation of the baryon asymmetry requires three ingredients [1]: (1) baryon number violation; (2) C and CP non-conservation; and (3) out of thermal equilibrium. Note that the Sakharov's conditions were originally concerned for models where the CPT is conserved. If the CPT is violated the baryogenesis (or leptogenesis) could happen in thermal equilibrium[2, 3, 4], such as the spontaneous baryogenesis[3].

The current observations show strong evidence that our Universe is in a stage of accelerated expansion. One interesting candidate for the acceleration is the dynamical scalar field dubbed Quintessence[5]. Quintessence is expected to have interactions with the ordinary matter, however for most of cases the couplings are strongly constrained[6]. Nevertheless there could be some exceptions, and here we introduce the following interaction of Quintessence with the matter, which in terms of an effective lagrangian is given by[7]

$$\mathcal{L}_{eff} = \frac{c}{M} \partial_\mu Q \; J^\mu, \tag{1}$$

where M is the cut-off scale, and c is the coupling constant which characterizes the strength of Quintessence interacting with the ordinary matter in the Standard Model. J^μ can be the baryon current J_B^μ or the current of baryon number minus lepton number J_{B-L}^μ.

The term in Eq.(1), when $\dot{Q}$ is non-zero during the evolution of spatial flat Friedmann-Robertson-Walker Universe, violates CPT invariance and generates an effective chemical potential μ_b for baryons[3], *i.e.*, $\frac{c}{M}\partial_\mu Q J_B^\mu \to c \; \frac{\dot{Q}}{M} n_B = c \; \frac{\dot{Q}}{M}(n_b - n_{\bar{b}})$, $\mu_b = c \; \frac{\dot{Q}}{M} = -\mu_{\bar{b}}$. In thermal equilibrium the baryon number asymmetry is given by (when $T \gg m_b$) $n_B = \frac{g_b T^3}{6}(\frac{\mu_b}{T} + \mathcal{O}(\frac{\mu_b}{T})^3) \simeq c\frac{g_b \dot{Q} T^2}{6M}$, where g_b counts the internal degree of freedom of the baryon. The final expression for the baryon to entropy ratio would be $n_B/s \simeq \frac{15c}{4\pi^2} \frac{g_b \dot{Q}}{g_\star MT}$, where $\dot{Q}$ can be obtained by solving the equation of motion of Quintessence. Without fine tuning of the parameters, we find there are viable Quintessence models which lead to the observed baryon number asymmetry[7]

$$\frac{n_B}{s}|_{T_D} \sim 0.01 \; c \; \frac{T_D}{M} \tag{2}$$

with T_D being the decoupling temperature. In this picture the baryon number asymmetry and the current accelerated expansion of the Universe have been described in a unified way.

In general the scalar field Q in Eq.(1) could be the function of a scalar field as extended models of spontaneous baryogenesis[8, 9]. Meanwhile from naive dimensional analysis for the interaction with the photon sector one would expect to have the Chern-Simons(CS) term:

$$\mathcal{L}_{int} = -\frac{1}{2}\delta \; \partial_\mu Q K^\mu \;, \tag{3}$$

---

[1] E-mail:fengbo@resceu.s.u-tokyo.ac.jp

where $K^\mu = A_\nu \widetilde{F}^{\mu\nu}$, $F_{\mu\nu}$ is the electromagnetic field strength tensor, and $\widetilde{F}^{\mu\nu} \equiv \frac{1}{2}\epsilon^{\mu\nu\rho\sigma}F_{\rho\sigma}$ is its dual. The coefficients between c/M in Eq.(1) and δ could be naturally related when J^μ is anomalous with respect to the electromagnetic interaction[9].

With the presence of the CS term the equations of motion for the electromagnetic field are now

$$\nabla_\mu F^{\mu\nu} = \delta\ \partial_\mu Q \widetilde{F}^{\mu\nu}\ , \nabla_\mu \widetilde{F}^{\mu\nu} = 0\ . \tag{4}$$

In a FRW cosmology we can write the electromagnetic field strength tensor in terms of $\mathbf{E}$ and $\mathbf{B}$:

$$F^{\mu\nu} = a^{-2} \begin{bmatrix} 0 & -E_x & -E_y & -E_z \\ E_x & 0 & -B_z & B_y \\ E_y & B_z & 0 & -B_x \\ E_z & -B_y & B_x & 0 \end{bmatrix}\ . \tag{5}$$

The dual tensor $\widetilde{F}^{\mu\nu}$ can be obtained from $F^{\mu\nu}$ by replacing $\mathbf{E}$ and $\mathbf{B}$ with $\mathbf{B}$ and $-\mathbf{E}$ respectively. In terms of the notations given by Ref.[10]:

$$\begin{aligned} \mathbf{B}(\vec{\mathbf{x}}, \eta) &= \mathrm{e}^{-\mathbf{ik\cdot x}}\mathbf{B}(\eta)\ , \\ F_\pm &= a^2 B_\pm(\eta) = a^2(B_y \pm iB_z)\ , \end{aligned} \tag{6}$$

we have the equation of motion for a given mode $\mathbf{k}$,

$$F''_\pm + (k^2 \pm \delta k Q')F_\pm = 0\ , \tag{7}$$

where the prime represents the derivative with respect to the conformal time η and k is the modulus of $\mathbf{k}$. In the equation above, we have assumed the wave vector $\mathbf{k}$ is along the x axis, and $+$ and $-$ denote right- and left-handed circular polarization modes respectively. The non-vanishing Q' induces a difference between the dispersion relations for the modes with different handedness. This will rotate the direction of the polarization of light from distant sources. For a source at a redshift z, the rotation angle is

$$\Delta\alpha = \frac{1}{2}\delta\ \Delta Q\ , \tag{8}$$

where ΔQ is the change in Q between the redshift z and today, i.e., $\Delta Q = Q|_z - Q|_{z=0}$.

The CMB polarization can be described with two Stokes parameters of Q and U, which can be spherically expanded to get a gradient (G) and a curl (C) component [11]. If the temperature/polarization distribution does not violate parity, one gets vanished CMB TC and GC due to the intrinsic properties of the tensor spherical harmonics. The interaction in Eq.(3) violates P, CP and also CPT. In our case the polarization vector of each photon is rotated by a same angle $\Delta\alpha$ everywhere and one would get nonzero TC and GC correlations with[12, 9]

$$\begin{aligned} C_l'^{TC} &= C_l^{TG}\sin 2\Delta\alpha\ , \tag{9} \\ C_l'^{GC} &= \frac{1}{2}(C_l^{GG} - C_l^{CC})\sin 4\Delta\alpha. \tag{10} \end{aligned}$$

The rotated quantities have been denoted with primes. Meanwhile the original TG,GG and CC are also modified as[13]

$$\begin{aligned} C_l'^{TG} &= C_l^{TG}\cos 2\Delta\alpha\ , \tag{11} \\ C_l'^{GG} &= C_l^{GG}\cos^2 2\Delta\alpha + C_l^{CC}\sin^2 2\Delta\alpha\ , \tag{12} \\ C_l'^{CC} &= C_l^{CC}\cos^2 2\Delta\alpha + C_l^{GG}\sin^2 2\Delta\alpha\ . \tag{13} \end{aligned}$$

As implied above, the rotation angel $\Delta\alpha$ can be used as a model independent parameter for the cosmological probe of the CPT violations, namely independent of the form of the scalar in Eq.(3). We use the WMAP observations and the data from the January 2003 Antarctic flight of BOOMERANG[19] (Hereafter B03) for the measurement of this rotation angel[13]. To break possible degeneracy between this term and the variation of other parameters, we make a global fit to the CMB data with the publicly
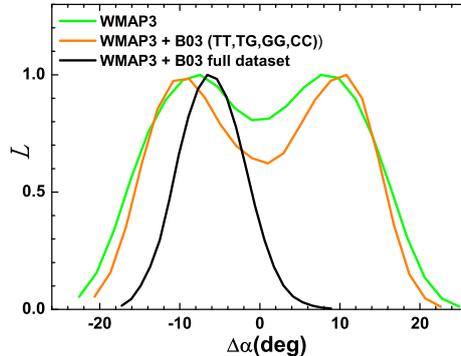
Figure 1: One dimensional constraints on the rotation angle $\Delta\alpha$ from WMAP data alone (Green or light gray line), WMAP and the 2003 flight of BOOMERANG B03 TT, TG, GG and CC(Orange or gray line), and from WMAP and the full B03 observations (TT, TG, GG, CC, TC, GC) (Black line)[13].

available Markov Chain Monte Carlo package `cosmomc`[14, 15], which has been modified to allow the rotation of the power spectra discussed above, with a new free parameter $\Delta\alpha$.

In Fig. 1 we plot our one dimensional constraints on $\Delta\alpha$ from the WMAP data alone, and from the combined WMAP and B03 data. "WMAP3" here denotes the three year WMAP observations[16] and previously we have also performed our analysis on the first year WMAP(WMAP1)[17, 18] combined with B03. We have assumed that the cosmic rotation is not too large and imposed a flat prior $-\pi/2 \le \Delta\alpha \le \pi/2$. Using the data from WMAP alone, for both the first and three year data set, we obtain a null detection within the error limits. For WMAP3 the 1, 2 σ constraints are $\Delta\alpha = 0.0^{+11.6}_{-11.7}\,^{+5.9}_{-5.9}$ deg and for WMAP1 $\Delta\alpha = -0.1^{+11.6}_{-11.6}\,^{+7.5}_{-7.4}$ deg. In the likelihood of Fig. 1 we have gained double peaks, which can be easily understood from Eqs.(11,12,13) due to the symmetry around $\Delta\alpha = 0$. For the first year WMAP while only TT and TG data were available, an indirect measurement on $\Delta\alpha$ could still be worked out with Eq.(11). WMAP3 constraints are a bit more stringent than WMAP1 results.

With the inclusion of the B03 data, the measurement could be improved dramatically. In a first step we also consider the indirect measurements only by including the B03 TT, TG, GG and CC data. We find the constraint on $\Delta\alpha$ becomes a bit more stringent compared with WMAP only, a nonzero $\Delta\alpha$ is slightly favored and the double peaks are still present. When the B03 TC and GC data are also included the degeneracy around $\Delta\alpha = 0$ is broken. We get the 1, 2 σ constraints to be $\Delta\alpha = -6.0^{+4.0}_{-4.0}\,^{+3.9}_{-3.7}$ deg with WMAP3 and the B03 full data set. And for the first year WMAP combined with B03 the constraint is $\Delta\alpha = -5.3^{+3.9}_{-4.0}\,^{+4.1}_{-3.5}$ deg. The mild preference on the nonzero rotation angel lies on the fact that for B03 there are several GC bands where the center values are below zero[19]. Future CMB polarization experiments like Planck and CMBpole will help significantly to detect such kind of effects[9].

In summary the current CMB polarization experiments have opened a new window to search the signature of cosmic P and CPT violations mentioned above and this can help to understand the nature of the dark energy which gives rise to the accelerated expansion of our Universe. Yet we need to understand better the inherited possible systematics and the degeneracy among the various cosmological parameters and difference physical processes, which are necessary to be explored in more details in the coming precision cosmology.

References

[1] A. D. Sakharov, Pis'ma Zh. Eksp. Teor. Fiz. **5**, 32 (1967).

[2] A. D. Dolgov and Y. B. Zeldovich, Rev. Mod. Phys. **53**, 1 (1981).

[3] A. Cohen and D. Kaplan, Phys. Lett. B **199**, 251 (1987).

[4] O. Bertolami, D. Colladay, V. A. Kostelecky and R. Potting, Phys. Lett. B **395**, 178 (1997).

[5] R. D. Peccei, J. Sola and C. Wetterich, Phys. Lett. B **195**, 183 (1987); C. Wetterich, Nucl. Phys. B **302**, 668 (1988); B. Ratra and P. J. E. Peebles, Phys. Rev. D **37**, 3406 (1988).

[6] S. M. Carroll, Phys. Rev. Lett. **81**, 3067 (1998).

[7] M. Li, X. Wang, B. Feng, and X. Zhang, Phys. Rev. D **65**, 103511 (2002).

[8] See e.g. A. De Felice, S. Nasri and M. Trodden, Phys. Rev. D **67**, 043509 (2003); M. Li and X. Zhang, Phys. Lett. B **573**, 20 (2003); M. Yamaguchi, Phys. Rev. D **68**, 063507 (2003); T. Chiba, F. Takahashi and M. Yamaguchi, Phys. Rev. Lett. **92**, 011301 (2004); H. Davoudiasl, R. Kitano, C. Kribs, H. Murayama, and P. J. Steinhardt, Phys. Rev. Lett. **93**, 201301 (2004); T. Shiromizu and K. Koyama, JCAP **0407**, 011 (2004); H. Li, M. z. Li and X. m. Zhang, Phys. Rev. D **70**, 047302 (2004); A. De Felice and M. Trodden, Phys. Rev. D **72**, 043512 (2005); C. Y. Chen, Y. G. Shen and B. Feng, High Energy Phys. Nucl. **29**, 1033 (2005); S. M. Carroll and J. Shu, Phys. Rev. D **73**, 103515 (2006); G. Lambiase, Phys. Lett. B **642**, 9 (2006); M. Li, J. Q. Xia, H. Li and X. Zhang, arXiv:hep-ph/0611192.

[9] B. Feng, H. Li, M. Li, and X. Zhang, Phys.Lett. B **620**, 27 (2005).

[10] S. M. Carroll and G. B. Field, Phys. Rev. D **43**, 3789 (1991).

[11] See *e.g.* W. Hu and M. White, New Astron. **2**, 323 (1997). Their E and B are in this paper G and C respectively.

[12] A. Lue, L. M. Wang, and M. Kamionkowski, Phys. Rev. Lett. **83**, 1506 (1999).

[13] B. Feng, M. Li, J. Q. Xia, X. Chen and X. Zhang, Phys. Rev. Lett. **96**, 221302 (2006).

[14] A. Lewis and S. Bridle, Phys. Rev. D **66**, 103511 (2002).

[15] Available from `http://cosmologist.info`.

[16] D. N. Spergel *et al.*, arXiv:astro-ph/0603449; L. Page *et al.*, astro-ph/0603450; G. Hinshaw *et al.*, astro-ph/0603451; N. Jarosik *et al.*, astro-ph/0603452.

[17] L. Verde *et al.*, Astrophys. J. Suppl. **148**, 195 (2003).

[18] G. Hinshaw *et al.*, Astrophys. J. Suppl. **148**, 345 (2003).

[19] W. C. Jones *et al.*, astro-ph/0507494; F. Piacentini *et al.*, astro-ph/0507507; T.E. Montroy *et al.*, astro-ph/0507514.

[20] Available from `http://cmb.phys.cwru.edu/boomerang/`.

Measurement of Extra Dimension by Kaluza-Klein Black Holes

Ken Matsuno[1], Hideki Ishihara[2], Masashi Kimura[3] and Shinya Tomizawa[4]

Department of Mathematics and Physics, Graduate School of Science,
Osaka City University, Sugimoto, Sumiyoshi-ku, Osaka 558-8585, Japan

Abstract

We apply an five-dimensional squashed Kaluza-Klein black hole solution to the outer region of the Earth and consider an evaluating of the size of an extra dimension by a measurement of the geodetic effect with the Gravity Probe B experiment.

1 Introduction

Brane world scenarios suggest the spacetime has large scale extra dimensions, such as a sub-millimeter scale. Based on this idea, there are many studies on higher-dimensional black objects : black holes, black rings and black branes, etc. In these scenarios, one of the most interesting problem is a verification of the size of extra dimensions from physical phenomena in higher-dimensional spacetimes [1,2]. Especially, we focus the Gravity Probe B experiment [3], here.

The Gravity Probe B satellite moves along a stable circular orbit around the Earth and collect data about two effects, the geodetic effect and the frame dragging effect. We focus on the geodetic effect, which is the leading effect, by the static Schwarzschild black hole. We expect that the geodetic effect is suffered from a correction by the existence of extra dimensions.

We apply an five-dimensional squashed Kaluza-Klein black hole solution with a compact extra dimension to the outer region of the Earth. We estimate the size of an extra dimension by the higher-dimensional correction to the geodetic precession angle.

2 Kaluza-Klein Black Hole with Squashed Horizon

We start from the five-dimensional Einstein system with the action :

$$S = \frac{1}{16\pi G_5} \int d^5 x \sqrt{-g} R, \tag{1}$$

where G_5 and R are the five-dimensional gravitational constant and the Ricci scalar curvature. From this action, we write down the Einstein equation

$$R_{\mu\nu} = 0. \tag{2}$$

The Kaluza-Klein black hole with a squashed S^3 horizon [4–6] is an exact solution of (2). The metric is written as

$$ds^2 = -V dt^2 + U \left(V^{-1} d\rho^2 + \rho^2 d\Omega_{S^2}^2 \right) + \left(\frac{r_\infty}{2} \right)^2 U^{-1} \chi_{S^1}^2, \tag{3}$$

where

$$d\Omega_{S^2}^2 = d\theta^2 + \sin^2\theta d\phi^2, \quad \chi_{S^1} = d\psi + \cos\theta d\phi, \tag{4}$$

and

$$V(\rho) = 1 - \frac{\rho_+}{\rho}, \quad U(\rho) = 1 + \frac{\rho_0}{\rho}, \quad r_\infty^2 = 4\rho_0 \left(\rho_+ + \rho_0 \right), \tag{5}$$

[1]E-mail: matsuno@sci.osaka-cu.ac.jp
[2]E-mail: ishihara@sci.osaka-cu.ac.jp
[3]E-mail: mkimura@sci.osaka-cu.ac.jp
[4]E-mail: tomizawa@sci.osaka-cu.ac.jp

with constants ρ_+ and ρ_0. The range of coordinates are $-\infty < t < \infty$, $0 < \rho < \infty$, $0 \le \theta < \pi$, $0 \le \phi < 2\pi$ and $0 \le \psi < 4\pi$.

This black hole (3) is static and has a squashed S^3, a twisted S^1 fiber bundle over a base space S^2, regular horizon at $\rho = \rho_+ > 0$, which covers up a timelike singularity at $\rho = 0$. The shape of horizon ρ_+ is oblate, the base space S^2 is larger than the fiber space S^1.

Asymptotic structure is a locally flat, a twisted constant S^1 fiber bundle over the four-dimensional Minkowski spacetime, at $\rho = \infty$. The size of extra dimension is $2\pi r_\infty$ at the spatial infinity. We also find a relation between the five-dimensional gravitational constant, G_5, and the four-dimensional one, G_4, as $G_5 = 2\pi r_\infty G_4$.

We discuss the physical meanings of the parameter ρ_0 in (3), shortly. When $\rho_0 \ll \rho_+$ then $V(\rho)$ becomes more effectively than $U(\rho)$ and the function $U(\rho)$ is almost constant. Thus distant observers at $\rho_0 \ll \rho_+ < \rho$ feel this black hole as the four-dimensional Schwarzschild black hole with a constant S^1 fiber. On the other hand, when $\rho_+ \ll \rho_0$ then $U(\rho)$ becomes more effectively than $V(\rho)$ near the horizon ρ_+. Thus observers at $\rho_+ < \rho \ll \rho_0$ feel this black hole as the five-dimensional Schwarzschild black hole. Therefore, the parameter ρ_0 denotes a typical scale between the four-dimensional black hole spacetime and the five-dimensional one.

Here, we consider the limit for parameters ρ_0 and ρ_+ with $\rho_0 \to \infty$ and $\rho_+ \to 0$ while $\rho_0\rho_+ \to$ finite. The metric (3) takes the form of the five-dimensional Schwarzschild black hole for this limit with a coordinate transformation $r = 2\sqrt{\rho_0\rho}$ and $r_g = 2\sqrt{\rho_0\rho_+}$ as

$$ds^2 = -\left[1 - \left(\frac{r_g}{r}\right)^2\right]dt^2 + \left[1 - \left(\frac{r_g}{r}\right)^2\right]^{-1} dr^2 + r^2 d\Omega_{S^3}^2, \quad d\Omega_{S^3}^2 = \frac{1}{4}\left(d\Omega_{S^2}^2 + \chi_{S^1}^2\right), \qquad (6)$$

where $d\Omega_{S^3}^2$ denotes the metric of unit S^3 sphere. This spacetime (6) is an asymptotically flat and is valid if the gravitational radius is much smaller than the size of an extra dimension.

3 Size of Extra Dimension Measured by Geodetic Effect

3.1 Geodesics in Higher-dimensional Black Holes

First, we consider timelike geodesics in the five-dimensional Schwarzschild black hole spacetime with no compactified extra dimension (6). We restrict ourselves to a motion in an equatorial plane, that is, $\theta = \pi/2$, then the geodesic equation and the effective potential with a proper time τ become

$$\left(\frac{dr}{d\tau}\right)^2 = E_S^2 - V_S, \quad V_S(r) = \left[1 - \left(\frac{r_g}{r}\right)^2\right]\left[1 + \left(\frac{L_S}{r}\right)^2\right], \qquad (7)$$

where $E_S = \left[1 - (r_g/r)^2\right](dt/d\tau)$ and $L_S = r^2\sqrt{(d\phi/d\tau)^2 + (d\psi/d\tau)^2}/2$ are the energy and the total angular momentum of a particle, respectively [7]. A typical shape of an effective potential V_S with $L_S = 2.1r_g$ is drawn in the left of Figure 1. We find that there is no stable circular orbit and this spacetime (6) does not give any description around the Earth.

Next, we consider timelike geodesics in the five-dimensional squashed Kaluza-Klein black hole spacetime with a compact extra dimension (3). We can restrict ourselves to a motion in an equatorial plane, $\theta = \pi/2$, as before, and we assume that there is no motion toward the extra direction. Then the geodesic equation and the effective potential with a proper time λ are given by

$$\left(\frac{d\rho}{d\lambda}\right)^2 = \left(E^2 - V_{KK}\right)\left(1 + \frac{\rho_0}{\rho}\right)^{-1}, \quad V_{KK}(\rho) = \left(1 - \frac{\rho_+}{\rho}\right)\left[1 + \frac{L^2}{\rho(\rho + \rho_0)}\right], \qquad (8)$$

where $E = (1 - \rho_+/\rho)(dt/d\lambda)$ and $L = \rho(\rho + \rho_0)(d\phi/d\lambda)$ denote the energy and the angular momentum of a particle. A typical shape of an effective potential V_{KK} with $L = 2.1\rho_+$ and $\rho_0 = 10^{-2}\rho_+$ is given in the right of Figure 1. It is easy to see there is a stable circular orbit at the local minimum of an effective potential.
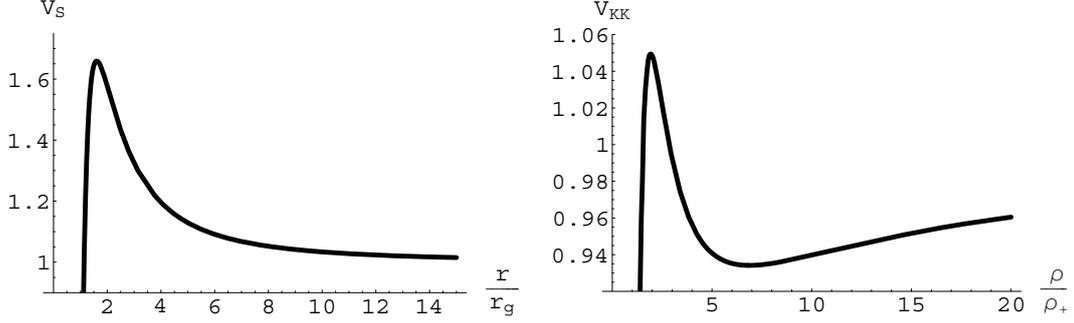
Figure 1: Effective potentials for a particle moving around the five-dimensional Schwarzschild black hole spacetime (7) with $L_S = 2.1 r_g$ (left) and around the five-dimensional squashed Kaluza-Klein black hole spacetime (8) with $L = 2.1 \rho_+$ and $\rho_0 = 10^{-2} \rho_+$ (right).

So, we apply the metric (3) with a condition $\rho_0 \ll \rho_+$ as a spacetime around the Earth and consider the higher-dimensional correction appears in the geodetic precession effect. Here, the mass of this black hole is given by

$$M = \frac{\rho_+}{2 G_4}. \tag{9}$$

3.2   Geodetic Precession

We regard an axes of a gyroscope of the Gravity Prove B satellite as a spacelike spin-vector S^μ which is parallelly transported along a timelike geodesic with a five-velocity $u^\mu = dx^\mu/d\lambda$ where λ denotes a proper time of the satellite.

We consider the geodesic equation for u^μ,

$$u^\mu \nabla_\mu u^\nu = 0, \tag{10}$$

the parallel transporting equation of S^μ along u^μ,

$$u^\mu \nabla_\mu S^\nu = 0, \tag{11}$$

and the orthogonality condition between u^μ and S^μ,

$$u^\mu S_\mu = 0. \tag{12}$$

Here, we set the following assumptions for u^μ and S^μ. First, we restrict ourselves to a stable circular orbit in an equatorial plane with a condition $\theta = \pi/2$, i.e.,

$$u^\rho = u^\theta = 0. \tag{13}$$

Next, we assume the matter is confined in a $\psi = \text{const.}$ plane, i.e.,

$$u^\psi = S^\psi = 0. \tag{14}$$

With these assumptions, we can write down the five-velocity u^μ of the satellite for a stable circular orbit with a radius R in a five-dimensional squashed Kaluza-Klein black hole spacetime (3) as

$$\frac{1}{u^t} = \sqrt{1 - \frac{3R + 2\rho_0}{2R + \rho_0} \frac{\rho_+}{R}}, \quad u^\phi = \frac{u^t}{R} \sqrt{\frac{\rho_+}{2R + \rho_0}}, \quad u^\rho = u^\theta = u^\psi = 0, \tag{15}$$

where u^μ is normalized as $u^\mu u_\mu = -1$.

Suppose the spin-vector S^μ is initially oriented in a radial ρ-direction at $\lambda = 0$. Then we get an expression of S^μ, which is normalized as $S^\mu S_\mu = 1$, as

$$S^t = C_t \sin(\Omega\lambda), \quad S^\rho = C_\rho \cos(\Omega\lambda), \quad S^\phi = \frac{C_\phi}{R} \sin(\Omega\lambda), \quad S^\theta = S^\psi = 0, \tag{16}$$

where C_t, C_ρ, C_ϕ and Ω are given by

$$C_t = \mp u^t \sqrt{\frac{\rho_+(R+\rho_0)}{(R-\rho_+)(2R+\rho_0)}}, \quad C_\rho = \pm\sqrt{\frac{R-\rho_+}{R+\rho_0}}, \quad C_\phi = \mp u^t \sqrt{\frac{R-\rho_+}{R+\rho_0}}, \tag{17}$$

$$\Omega = \frac{\sqrt{\rho_+(2R+\rho_0)}}{2R(R+\rho_0)}. \tag{18}$$

During one orbital period, ϕ goes from 0 to 2π and a proper time λ goes from 0 to $\lambda_f = 2\pi/u^\phi$, the geodetic precession angle $\Delta\Theta$ raises from a difference between these two angular displacements, ϕ and $\Omega\lambda$, as

$$\Delta\Theta = |\Omega\lambda_f - 2\pi| = \left| 2\pi \left(\frac{\Omega}{u^\phi} - 1 \right) \right|. \tag{19}$$

Thus we obtain the geodetic precession angle in a weak-field limit as follows

$$\triangle\Theta = \triangle\Theta_{4D}(1 + \delta) + O\left(R^{-2}\right), \tag{20}$$

where

$$\triangle\Theta_{4D} = \frac{3\pi G_4 M}{R} \tag{21}$$

is the predicted value by the four-dimensional Einstein theory and

$$\delta = \left(\frac{r_\infty}{2\sqrt{6}G_4 M} \right)^2 \tag{22}$$

is the higher-dimensional correction. We can estimate the size of an extra dimension by a measurement of a difference of the geodetic effect from $\triangle\Theta_{4D}$.

Even if, the result of the Gravity Probe B measurement gives the predicted value $\triangle\Theta_{4D} = 6.6144$ arcsec/yr with an expected accuracy of 0.5 marcsec/yr, this accuracy of an observation gives an upper limit of the size of an extra dimension as $|2\pi r_\infty| < 1$ mm.

References

[1] H. Liu and P.S. Wesson, Class. Quantum Grav. **13**, 2311 (1996).

[2] H. Liu and J.M. Overduin, Astrophys. J. **538**, 386 (2000).

[3] http://einstein.stanford.edu/

[4] P. Dobiasch and D. Maison, Gen. Rel. Grav. **14**, 231 (1982).

[5] G.W. Gibbons and D.L. Wiltshire, Ann. Phys. **167**, 201 (1986).

[6] H. Ishihara and K. Matsuno, Prog. Theor. Phys. **116**, 417 (2006).

[7] V. Frolov and D. Stojkovic, Phys. Rev. D **68**, 064011 (2003).

Kaluza-Klein Multi-Black Holes

Masashi Kimura[1], Hideki Ishihara[2], Ken Matsuno[3], and Shinya Tomizawa[4]

Department of Mathematics and Physics, Graduate School of Science, Osaka City University, 3-3-138 Sugimoto, Sumiyoshi, Osaka 558-8585, Japan

Abstract

We construct Kaluza-Klein multi-black hole solutions on the Gibbons-Hawking multi-instanton space in the five-dimensional Einstein-Maxwell theory. We study geometric properties of the multi-black hole solutions. In particular, the spatial cross section of each horizon is admitted to have the topology of a different lens space $L(n;1) = \mathrm{S}^3/\mathbb{Z}_n$ in addition to S^3.

1 Introduction

The large extra dimension sinario suggests the production of a mini-black hole at an accelerator. A mini-black hole probably have the property such that it behaves like a higher-dimensional black hole in the near region but like a four-dimensional black hole in the far region. Recently a black hole solution which has such a property were analyzed [1] in the five dimensional Einstein-Maxwell theory. Since the black hole has a compactified extra-dimension, we call this Kaluza-Klien black hole. In this article we generalize the black hole solution to multi-black hole solution, and investigate the geometrical structure [2].

2 Construction of Kaluza-Klein Multi-Black Hole solution

2.1 single black hole solution

The metric and the gauge potential one-form of the maximally charged limit of the Kaluza-Klein black hole [1] are

$$ds^2 = -H^{-2}dT^2 + Hds^2_{\mathrm{TN}}, \tag{1}$$

$$A = \pm\frac{\sqrt{3}}{2}H^{-1}dT, \tag{2}$$

where ds^2_{TN} denotes the metric of the Taub-NUT space which is given by

$$ds^2_{\mathrm{TN}} = V^{-1}\left(dR^2 + R^2 d\Omega^2_{\mathrm{S}^2}\right) + V\left(d\zeta + N\cos\theta d\phi\right)^2, \tag{3}$$

$$d\Omega^2_{\mathrm{S}^2} = d\theta^2 + \sin^2\theta d\phi^2, \tag{4}$$

$$V^{-1}(R) = 1 + \frac{N}{R}, \tag{5}$$

with

$$0 \le \theta \le \pi, \quad 0 \le \phi \le 2\pi, \quad 0 \le \zeta \le 2\pi L, \tag{6}$$

and the function H is given by

$$H(R) = 1 + \frac{M}{R}, \tag{7}$$

---

[1] E-mail:mkimura@sci.osaka-cu.ac.jp

[2] E-mail:ishihara@sci.osaka-cu.ac.jp

[3] E-mail:matsuno@sci.osaka-cu.ac.jp

[4] E-mail:tomizawa@sci.osaka-cu.ac.jp

where L, M and N are positive constants.

Regularity of the spacetime requires that the nut charge, N, and the asymptotic radius of S^1 along ζ, L, are related by

$$N = \frac{L}{2}n, \tag{8}$$

where n is an natural number.

We can see that a degenerated horizon exists at $R = 0$, where the nut singularity of the Taub-NUT space were located. Although the Taub-NUT space is regular only when $n = 1$ on the conditions (6), the nut singularity with $n \geq 2$ is resolved by the event horizon in the black hole solution.

In the case of $n = 1$, the horizon has the shape of round S^3 in a static time-slice in contrast to the non-degenerated case, where the horizon is squashed [1]. The spacetime is asymptotically locally flat, i.e., a constant S^1 fiber bundle over the four-dimensional Minkowski spacetime at $R \to \infty$. Therefore, the spacetime behaves as a five-dimensional black hole near horizon, while the dimensional reduction to four-dimension is realized in a far region. In the case of $n \geq 2$, the horizon is in shape of lens space $L(n; 1) = \mathrm{S}^3/\mathbb{Z}_n$.

2.2 multi-black hole solution

When we generalize the single black hole solution (1) to the multi-black holes, it is natural to generalize the Taub-NUT space to the Gibbons-Hawking space [3] which has multi-nut singularities. The metric form of the Gibbons-Hawking space is

$$ds_{\mathrm{GH}}^2 = V^{-1} \left(d\boldsymbol{x} \cdot d\boldsymbol{x} \right) + V \left(d\zeta + \boldsymbol{\omega} \right)^2, \tag{9}$$

$$V^{-1} = 1 + \sum_i \frac{N_i}{|\boldsymbol{x} - \boldsymbol{x}_i|}, \tag{10}$$

where $\boldsymbol{x}_i = (x_i, y_i, z_i)$ denotes position of the i-th nut singularity with nut charge N_i in the three-dimensional Euclid space, and $\boldsymbol{\omega}$ satisfies

$$\boldsymbol{\nabla} \times \boldsymbol{\omega} = \boldsymbol{\nabla} \frac{1}{V}. \tag{11}$$

We can write down a solution $\boldsymbol{\omega}$ explicitly as

$$\boldsymbol{\omega} = \sum_i N_i \frac{(z - z_i)}{|\boldsymbol{x} - \boldsymbol{x}_i|} \frac{(x - x_i)dy - (y - y_i)dx}{(x - x_i)^2 + (y - y_i)^2}. \tag{12}$$

If we assume the metric form (1) with the Gibbons-Hawking space instead of the Taub-NUT space, the Einstein equation and the Maxwell equation reduce to

$$\triangle_{\mathrm{GH}} H = 0, \tag{13}$$

where $\triangle_{\mathrm{GH}}$ is the Laplacian of the Gibbons-Hawking space. In general, it is difficult to solve this equation, but if one assume ∂_ζ to be a Killing vector, as it is for the Gibbons-Hawking space, then Eq.(13) reduces to the Laplace equation in the three-dimensional Euclid space,

$$\triangle_{\mathrm{E}} H = 0. \tag{14}$$

We take a solution with point sources to Eq.(14) as a generalization of Eq.(7), and we have the final form of the metric

$$ds^2 = -H^{-2}dT^2 + Hds_{\mathrm{GH}}^2, \tag{15}$$

$$H = 1 + \sum_i \frac{M_i}{|\boldsymbol{x} - \boldsymbol{x}_i|}, \tag{16}$$

where M_i are positive constants.

We note that the singular points of the harmonic function H are same points to the singular points of V^{-1}. If these points were not same points, curvature singularities would appear. This is the the reason why we extend the base space to Gibbons-Hawking space.

3 Property

Next we investigate near horizon geometry. For simplicity, we restrict ourselves to the solution with two black holes. In order to examine that the geometry near the horizon $\boldsymbol{x} = \boldsymbol{x}_1$, we make the coordinate transformation such that the point source $\boldsymbol{x}_1$ is the origin of the three-dimensional Euclid space and $\boldsymbol{x}_2 = (0, 0, -a)$. In this case, from Eqs.(15) and (16) the metric can take the following simple form,

$$
\begin{aligned}
ds^2 &= -H(R,\theta)^{-2}dT^2 \\
&\quad + H(R,\theta)\left[V(R,\theta)^{-1}(dR^2 + R^2 d\Omega_{\mathrm{S}^2}^2) + V(R,\theta)\left(d\zeta + \omega_\phi(R,\theta)d\phi\right)^2\right],
\end{aligned} \tag{17}
$$

with

$$
H(R,\theta) = 1 + \frac{M_1}{R} + \frac{M_2}{\sqrt{R^2 + a^2 + 2aR\cos\theta}}, \tag{18}
$$

$$
V(R,\theta)^{-1} = 1 + \frac{N_1}{R} + \frac{N_2}{\sqrt{R^2 + a^2 + 2aR\cos\theta}}, \tag{19}
$$

$$
\omega_\phi(R,\theta) = N_1\cos\theta + \frac{N_2(a + R\cos\theta)}{\sqrt{R^2 + a^2 + 2aR\cos\theta}}, \tag{20}
$$

where the parameter a denotes the separation between two point sources $\boldsymbol{x}_1$ and $\boldsymbol{x}_2$ in the three-dimensional Euclid space.

If we take the limit $R = |\boldsymbol{x} - \boldsymbol{x}_1| \to 0$, we can see the leading behavior of the metric as follows,

$$
ds^2 \simeq -\left(\frac{R}{M_1}\right)^2 dT^2 + \frac{M_1}{R}\left[\frac{R}{N_1}\left(d\zeta + N_1\cos\theta d\phi\right)^2 + \frac{N_1}{R}\left(dR^2 + R^2 d\Omega_{\mathrm{S}^2}^2\right)\right]. \tag{21}
$$

We should note that the other black holes does not contribute to this behavior of the metric in the leading order. Therefore, the form of each black hole is equivalent with the single extremal black hole (1) in the vicinity of the horizon. The Kretschmann invariant near the horizon $R = 0$ can be computed as,

$$
R_{\mu\nu\lambda\rho}R^{\mu\nu\lambda\rho} = \frac{19}{4M_1^2 N_1^2} + O\left(\frac{R}{a}\right), \tag{22}
$$

which suggests the horizon $R = 0$ is regular. In fact, under the coordinate transformation,

$$
u = T - F(R), \tag{23}
$$

$$
\frac{dF(R)}{dR} = \left(1 + \frac{M_1}{R} + \frac{M_2}{a}\right)^{3/2}\left(1 + \frac{N_1}{R} + \frac{N_2}{a}\right)^{1/2}, \tag{24}
$$

the metric near the horizon $R = 0$ has the following form

$$
ds^2 \simeq -2\sqrt{\frac{N_1}{M_1}}\,dudR + M_1 N_1\left[\left(\frac{d\zeta}{N_1} + \cos\theta d\phi\right)^2 + d\Omega_{\mathrm{S}^2}^2\right]. \tag{25}
$$

Here, we note that the black hole horizon is regular if and only if $2N_1/L$ is positive integer, then spatial cross section of the horizon is the lens space. The lens space is the quotient of S^3 by the discrete subgroup of the isometry generated by ∂_ζ. In a special case $2N_1/L = 1$, the shape of the horizon is S^3. Of course, from the similar discussion, the regularity of the other black hole horizon at $\boldsymbol{x} = \boldsymbol{x}_2$ is also assured. Outside the black holes, there is evidently no singular point from the explicit form of the metric. Even if we consider the situations with more than two black holes, these properties do not change in such spacetimes.

We saw the i-th black hole admits a lens space as a horizon in addition to S^3 by choosing parameter $2N_i/L$ to be an arbitrary positive integer. Since each black hole can take a different parameter N_i, each horizon of the black hole can be the lens space with a different index. Namely, black holes with different lens spaces can coexist in a spacetime.

Finally we comment that if 1 in V^{-1} (5) disappears then the base space is Eguchi-Hanson space which is asymptotically locally Euclidean. We can also construct multi-black hole solution on Eguchi-Hanson space in a similar way discussed here [4, 5].

References

[1] H. Ishihara and K. Matsuno, Prog.Theor.Phys. **116**, 417 (2006).

[2] H. Ishihara, M. Kimura, K. Matsuno and S. Tomizawa, Class.Quant.Grav.**23**,6919 (2006).

[3] G.W. Gibbons , S.W. Hawking , Phys. Lett. **78B** 430, (1978).

[4] H. Ishihara, M. Kimura, K. Matsuno and S. Tomizawa, Phys.Rev.D **74**, 047501 (2006).

[5] H. Ishihara, M. Kimura and S. Tomizawa, Class.Quant.Grav.**23**,L89 (2006).
See also the report by S. Tomizawa in this volume.

Coalescing Black Holes on Eguchi-Hanson Space

Shinya Tomizawa[1], Hideki Ishihara[2] and Masashi Kimura[3]

Department of Mathematics and Physics, Graduate School of Science, Osaka City University, 3-3-138 Sugimoto, Sumiyoshi, Osaka 558-8585, Japan

Abstract

We construct multi-black hole solutions in the five-dimensional Einstein-Maxwell theory with a positive cosmological constant on the Eguchi-Hanson space, which is an asymptotically locally Euclidean space. The solutions describe the physical process such that two black holes with the topology of S^3 coalesce into a single black hole with the topology of the lens space $L(2;1) = S^3/Z_2$. We discuss how the area of the single black hole after the coalescence depends on the topology of the horizon.

1   Introduction and summary

Black hole spacetime which has asymptotically Euclidean time slices, AE black holes in short, would be a good idealization in the situation such that we can ignore the tension of the brane and the curvature radius of the bulk, or the size of extra dimensions. However, from more realistic view point, we need not impose the asymptotic Euclidean condition toward the extra dimensions. In fact, higher dimensional black holes admit a variety of asymptotic structures: Kaluza-Klein black hole solutions [1, 2] have the spatial infinity with compact extra dimensions; Black hole solutions on the Eguchi-Hanson space [3] have the spatial infinity of topologically various lens spaces $L(2n; 1) = S^3/\mathbb{Z}_{2n}$ (n:natural number). The latter black hole spacetimes are asymptotically locally Euclidean, i.e., ALE black holes. In spacetimes with such asymptotic structures, furthermore, black holes have the different structures from the black hole with the asymptotically Euclidean structure. For instance, the Kaluza-Klein black holes [1, 2] and the black holes on the Eguchi-Hanson space [3] can have the horizon of lens spaces in addition to S^3.

We compare five-dimensional static and vacuum AE black holes (Schwarzschild black holes) with ALE black holes which has the spatial infinity with the topology of a lens space $L(2; 1) = S^3/\mathbb{Z}_2$. The metric of an ALE black hole we consider is given by

$$ds^2 = -\left(1 - \frac{r_g^2}{r^2}\right)dt^2 + \left(1 - \frac{r_g^2}{r^2}\right)^{-1}dr^2 + r^2 d\Omega_{S^3/\mathbb{Z}_2}^2, \tag{1}$$

where r_g is a constant, and the metric of the S^3 in the Schwarzschild spacetime is replaced by the metric of the lens space, which has the locally same geometry as S^3. The ADM mass of the ALE black hole (1) is half of the mass of Schwarzschild black hole with the same r_g. It means that the area of horizon of the ALE black hole is $\sqrt{2}$ times that of the Schwarzschild black hole with the same ADM mass. This fact would cause the difference of the coalescence process of higher dimensional black holes with non trivial asymptotic structure.

To observe this, we compare the ALE multi-black hole solutions constructed on the Eguchi-Hanson space with the five-dimensional version of Majumdar-Papapetrou solutions [4], which has AE structure. We can prepare a pair of black holes with the same mass and area of S^3-horizons in both ALE and AE solutions. If the black holes with S^3 topology coalesce into a single black holes, it would be natural that the resultant black hole has S^3-horizon in the AE case while $L(2; 1)$-horizon in the ALE case, because there are closed surfaces with S^3 topology surrounding two black holes in the AE case, while $L(2; 1)$ topology in the ALE case. If we assume the total mass of black holes is conserved through the whole process, the area of the final black hole in the ALE case is larger than that in the AE case.

Kastor and Traschen [5] constructed multi-black hole solutions with a positive cosmological constant, and London [6] extend it to five-dimensional solutions. If we consider a contracting phase derived by

---

[1]E-mail:tomizawa@sci.osaka-cu.ac.jp
[2]E-mail:ishihara@sci.osaka-cu.ac.jp
[3]E-mail:mkimura@sci.osaka-cu.ac.jp

the cosmological constant, the solution can describe a coalescence of black holes in an asymptotically de Sitter spacetime [7, 8]. Analogously, we investigate the coalescence of the ALE black holes by using new multi-black hole solutions on the Eguchi-Hanson space with a positive cosmological constant which is asymptotically locally de Sitter (Let us see Ref. [9] for the detail).

2   Solutions and their properties

We consider the five-dimensional Einstein-Maxwell system with a positive cosmological constant. In the previous work [3], we gave a metric of a pair of maximally charged black holes on the Eguchi-Hanson space as a solution in the five-dimensional Einstein-Maxwell theory without a positive cosmological constant. The Einstein equation with a positive cosmological constant and the Maxwell equation admit a new solution whose metric and gauge potential one-form are

$$ds^2 = -H^{-2}d\tau^2 + H ds_{\mathrm{EH}}^2, \quad \boldsymbol{A} = \pm \frac{\sqrt{3}}{2} H^{-1} d\tau, \tag{2}$$

with

$$ds_{\mathrm{EH}}^2 = \left(1 - \frac{a^4}{r^4}\right)^{-1} dr^2 + \frac{r^2}{4}\left[\left(1 - \frac{a^4}{r^4}\right)(d\tilde{\psi} + \cos\tilde{\theta}d\tilde{\phi})^2 + d\tilde{\theta}^2 + \sin^2\tilde{\theta}d\tilde{\phi}^2\right], \tag{3}$$

$$H = \lambda\tau + \frac{2m_1}{r^2 - a^2\cos\tilde{\theta}} + \frac{2m_2}{r^2 + a^2\cos\tilde{\theta}}, \tag{4}$$

where a and m_j ($j = 1, 2$) are positive constants, λ is a constant related to the cosmological constant by $\lambda^2 = 4\Lambda/3$, $-\infty < \tau < \infty$, $a \le r < \infty$, $0 \le \tilde{\theta} \le \pi$, $0 \le \tilde{\phi} \le 2\pi$ and $0 \le \tilde{\psi} \le 2\pi$. Equation (3) is the metric form of the Eguchi-Hanson space [10]. As is seen later, this solution describes coalescing two black holes.

In order to obtain the physical interpretation about this solution, let us introduce the following coordinate [11, 3],

$$R = a\sqrt{\frac{r^4}{a^4} - \sin^2\tilde{\theta}}, \ \tan\theta = \sqrt{1 - \frac{a^4}{r^4}}\tan\tilde{\theta}, \quad \phi = \tilde{\psi}, \ \psi = 2\tilde{\phi}, \tag{5}$$

where $0 \le R < \infty$, $0 \le \theta \le \pi$, $0 \le \phi \le 2\pi$, $0 \le \psi \le 4\pi$. Then, the metric takes the form of

$$ds^2 = -H^{-2}d\tau^2 + H\left[V^{-1}dR^2 + V^{-1}R^2(d\theta^2 + \sin^2\theta d\phi^2) + V\left(\frac{a}{8}d\psi + \omega_\phi d\phi\right)^2\right], \tag{6}$$

with

$$H = \lambda\tau + \frac{2m_1/a}{|\boldsymbol{R} - \boldsymbol{R}_1|} + \frac{2m_2/a}{|\boldsymbol{R} - \boldsymbol{R}_2|}, \quad V^{-1} = \frac{a/8}{|\boldsymbol{R} - \boldsymbol{R}_1|} + \frac{a/8}{|\boldsymbol{R} - \boldsymbol{R}_2|}, \quad \omega_\phi = \frac{a}{8}\left(\frac{z - a}{|\boldsymbol{R} - \boldsymbol{R}_1|} + \frac{z + a}{|\boldsymbol{R} - \boldsymbol{R}_2|}\right),$$

where $\boldsymbol{R} = (x, y, z)$ is the position vector on the three-dimensional Euclid space and $\boldsymbol{R}_1 = (0, 0, a)$, $\boldsymbol{R}_2 = (0, 0, -a)$. In order to focus our attention on the coalescence of two black holes, we consider only the contracting phase $\lambda = -\sqrt{4\Lambda/3}$ throughout below. Though τ runs the range $(-\infty, \infty)$, we investigate only the region $-\infty < \tau \le 0$.

For later convenience, we mention the global structure of the five-dimensional Reissner-Nordström-de Sitter solution with $m = \sqrt{3}|Q|/2$. This solution is static, spherically symmetric and has the horizons with the topology of S^3. By the coordinate transformation into the cosmological coordinate, the metric is given by [6],

$$ds^2 = -\left(\lambda\tau + \frac{m}{r^2}\right)^{-2}d\tau^2 + \left(\lambda\tau + \frac{m}{r^2}\right)\left[dr^2 + \frac{r^2}{4}d\Omega_{\mathrm{S}^2} + \frac{r^2}{4}(d\psi + \cos\theta d\phi)^2\right], \tag{7}$$

where each coordinate runs the range of $-\infty < \tau < \infty$, $0 \le r < \infty$, $0 \le \theta \le \pi$, $0 \le \phi \le 2\pi$, $0 \le \psi \le 4\pi$, m is a constant, λ is the constant related to the cosmological constant by $\lambda^2 = 4\Lambda/3$. The ingoing

and outgoing expansions of the null geodesics orthogonal to three-dimensional surfaces, $\tau = $ const and $r = $ const are given by

$$\theta_{\text{in}} = \lambda - \frac{2x}{\sqrt{(x+m)^3}}, \quad \theta_{\text{out}} = \lambda + \frac{2x}{\sqrt{(x+m)^3}}, \tag{8}$$

respectively, where $x := \lambda \tau r^2$. There is a curvature singularity at $x + m = 0$. Horizons occur at x such that

$$\lambda^2(x+m)^3 - 4x^2 = 0. \tag{9}$$

For $m < m_{\text{ext}} \equiv 16/(27\lambda^2)$, there are three horizons, which are three real roots $x_{\text{in}}[m] < x_{\text{BH}}[m] < x_{\text{dS}}[m]$, the inner and outer black hole horizons and the de Sitter horizon, respectively. We see that $\theta_{\text{out}} = 0$ at $x = x_{\text{BH}}[m]$ and $x = x_{\text{dS}}[m]$, and $\theta_{\text{in}} = 0$ at $x = x_{\text{in}}[m]$. When $m = m_{\text{ext}}$, the outer black hole horizon and the de Sitter horizon coincides with each other ($x_{\text{BH}}[m_{\text{ext}}] = x_{\text{dS}}[m_{\text{ext}}]$). In the case of $m > m_{\text{ext}}$ there is only a naked singularity.

Let us investigate the global structure of the solution (6) following the discussion of Ref.[7]. As mentioned below, in order to consider the coalescence of two black holes we must choose the parameters such that $m_1 + m_2 < 8/(27\lambda^2)$, $m_i > 0$. Therefore, in this letter, we assume such range of these parameters.

First, let us choose the origin on the three-dimensional Euclid space to be $\boldsymbol{R} = \boldsymbol{R}_i$ ($i = 1, 2$) in Eqs.(6). In the neighborhood of $R = 0$ the metric becomes

$$ds^2 \simeq -\left(\lambda\tau + \frac{m_i}{\tilde{r}^2}\right)^{-2} d\tau^2 + \left(\lambda\tau + \frac{m_i}{\tilde{r}^2}\right)\left[d\tilde{r}^2 + \frac{\tilde{r}^2}{4}d\Omega_{\text{S}^2}^2 + \frac{\tilde{r}^2}{4}(d\psi + \cos\theta d\phi)^2\right], \tag{10}$$

where the origin of τ is appropriately shifted by a constant and we used the coordinate $\tilde{r}^2 = aR/2$. This is identical to the metric of the five-dimensional Reissner-Nordström-de Sitter solution (7) which has mass equal to m_i which is written in the cosmological coordinate. If $m_i < 16/(27\lambda^2)$, which is automatically satisfied as long as we assume $m_1 + m_2 < 8/(27\lambda^2)$ and $m_i > 0$, at early time $\tau \ll 0$, sufficiently small spheres with the topology of S^3 centered at $\boldsymbol{R} = \boldsymbol{R}_i$ are always outer trapped, since there are solutions for $\theta_{\text{out}} = 0$ at $\tilde{r}^2 = x_{\text{BH}}[m_1]/(\lambda\tau)$ and $\tilde{r}^2 = x_{\text{BH}}[m_2]/(\lambda\tau)$, which denote an approximate small sphere, respectively.

Next, we study the asymptotic behavior of the metric for large $R := |\boldsymbol{R}|$, where we assume that R is much larger than the coordinate distance $|\boldsymbol{R}_1 - \boldsymbol{R}_2|$ between the two masses $2m_1/a$ and $2m_2/a$. In this region, the metric behaves as

$$ds^2 \simeq -\left(\lambda\tau + \frac{2(m_1+m_2)}{r^2}\right)^{-2} d\tau^2 + \left(\lambda\tau + \frac{2(m_1+m_2)}{r^2}\right)\left[dr^2 + \frac{r^2}{4}d\Omega_{\text{S}^2}^2 + \frac{r^2}{4}\left(\frac{d\psi}{2} + \cos\theta d\phi\right)^2\right],$$

where we introduced a new coordinate $r^2 := aR$. This resembles the metric of the five-dimensional Reissner-Nordström-de Sitter solution (7) with mass equal to $2(m_1 + m_2)$. Like the five-dimensional Reissner-Nordström solution, if we assume $2(m_1 + m_2) < 16/(27\lambda^2)$, at late time $\tau \to -0$, sufficiently large spheres becomes outer trapped, since $\theta_{\text{out}} = 0$ at $r^2 = x_{\text{BH}}[2(m_1+m_2)]/(\lambda\tau)$, which is approximately a sphere. However, we see that this solution differ from the five-dimensional Reissner-Nordström-de Sitter solution in the following point; Each $r = $ const surface is topologically a lens space $L(2;1) = \text{S}^3/\mathbb{Z}_2$, while in the five-dimensional Reissner-Nordström-de Sitter solution, it is diffeomorphic to S^3. We can regard S^3 and a lens space $L(2;1) = \text{S}^3/\mathbb{Z}_2$ as examples of Hopf bundles i.e. S^1 bundle over S^2. The difference between these metrics appears in Eqs.(10) and (11): $d\psi$ in S^3 metric (10) is replaced by $d\psi/2$ in $L(2;1)$ metric (11). Therefore, at late time, the topology of the trapped surface is a lens space $L(2;1) = \text{S}^3/\mathbb{Z}_2$.

From these results, we see that if $m_1 + m_2 < 8/(27\lambda^2)$ (in this letter, we consider only this case), this solution describes the dynamical situation such that two black black holes with the spatial topologies S^3 coalesce and convert into a single black hole with the spatial topologies of a lens space $L(2;1) = \text{S}^3/\mathbb{Z}_2$. We should note that in the case of the five-dimensional Kastor-Traschen solution [5, 6], in the contracting phase, two black holes with the topology of S^3 coalesce into a single black hole with the topology of S^3.

Finally, in order to compare the area of a single black hole formed by the coalescence of two black holes at late time, let us consider the five-dimensional Kastor-Traschen solution [5, 6] which has the two black holes with the masses m_1 and m_2 at early time,

$$ds^2 = -\left(\lambda\tau + \frac{m_1}{|\boldsymbol{r} - \boldsymbol{r}_1|^2} + \frac{m_2}{|\boldsymbol{r} - \boldsymbol{r}_2|^2}\right)^{-2} d\tau^2 + \left(\lambda\tau + \frac{m_1}{|\boldsymbol{r} - \boldsymbol{r}_1|^2} + \frac{m_2}{|\boldsymbol{r} - \boldsymbol{r}_2|^2}\right)(dr^2 + r^2 d\Omega^2_{\mathrm{S}^3}), \quad (11)$$

where $\boldsymbol{r} = (x, y, z, w)$ is the position vector on the four-dimensional Euclid space, and $\boldsymbol{r}_1$ and $\boldsymbol{r}_2$ denote the position vectors of the two black holes on the four-dimensional Euclid space.

Since this metric near the black horizon is equal to that of Eq.(10) at early time ($\tau \to -\infty$), each black hole has the same area as that in our solution. Using Eq.(9), the areas $\mathcal{A}^{\mathrm{KT}}_{\mathrm{late}}$ and $\mathcal{A}^{\mathrm{EH}}_{\mathrm{late}}$ of them at the late time can be computed as follows,

$$\mathcal{A}^{\mathrm{KT}}_{\mathrm{late}} = \frac{2}{\lambda} x_{\mathrm{BH}}[m_1 + m_2]\mathcal{A}_{\mathrm{S}^3}, \quad \mathcal{A}^{\mathrm{EH}}_{\mathrm{late}} = \frac{2}{\lambda} x_{\mathrm{BH}}[2(m_1 + m_2)]\frac{\mathcal{A}_{\mathrm{S}^3}}{2}, \quad (12)$$

respectively. Here, KT and EH denote the quantities of the Kastor-Traschen solutions and our solutions, respectively and $\mathcal{A}_{\mathrm{S}^3}$ is the area of a three-dimensional sphere with unit radius. We should note that $\mathcal{A}_{\mathrm{S}^3}/2$ in Eq.(12) reflects the fact that the black hole at late time after the coalescence of the two black holes is topologically a lens space $L(2;1) = \mathrm{S}^3/\mathbb{Z}_2$. Thus, we see that if each black holes at early time in our solution have the same area with that in the Kastor-Traschen solution, the ratio of the area of the single black hole at late time in our solution to that in the five-dimensional Kastor-Traschen solution is given by

$$\frac{\mathcal{A}^{\mathrm{EH}}_{\mathrm{late}}}{\mathcal{A}^{\mathrm{KT}}_{\mathrm{late}}} = \frac{x_{\mathrm{BH}}[2(m_1 + m_2)]}{2x_{\mathrm{BH}}[m_1 + m_2]}, \quad (13)$$

which is larger than one regardless of the values of m_1, m_2, since $x_{\mathrm{BH}}[m]$ is the concave downward and increasing function of m. The ratio $\mathcal{A}^{\mathrm{EH}}_{\mathrm{late}}/\mathcal{A}^{\mathrm{KT}}_{\mathrm{late}}$ is monotonically increasing function of the initial total mass of two black holes. We also see that this ratio has the range of $\sqrt{2} < \mathcal{A}^{\mathrm{EH}}_{\mathrm{late}}/\mathcal{A}^{\mathrm{KT}}_{\mathrm{late}} \leq 4$.

There are two main differences between our solution and the Kastor-Traschen solution [5, 6]: Firstly, two black holes with the topology of S^3 coalesce and change into a single black hole with the topology of $L(2;1) = \mathrm{S}^3/\mathbb{Z}_2$, while for the Kastor-Traschen solution, two black holes with the topology with S^3 coalesce into a single black hole with the topology of S^3. Secondly, after two black holes coalesce, where we assume that each black hole in our solution has the same mass and area as that in the Kastor-Traschen solution initially, the area of the single black hole formed by the coalescence at late time in our solution is larger than that in the Kastor-Traschen solution. These differences are essentially due to the asymptotic structure. While the Kastor-Traschen solution is asymptotically de Sitter and each $r = $ const surface has the topological structure of S^3, our solution is asymptotically locally de Sitter and $R = $ const surface is topologically $L(2;1) = \mathrm{S}^3/\mathbb{Z}_2$.

References

[1] H.Ishihara and K.Matsuno, Prog.Theor.Phys. **116**, 417 (2006).

[2] H. Ishihara, M. Kimura, K. Matsuno and S. Tomizawa, Class. Quantum Grav. **23**, 6919 (2006).

[3] H. Ishihara, M. Kimura, K. Matsuno and S. Tomizawa, Phys.Rev.D **74**, 047501 (2006).

[4] S.D.Majumdar, Phys.Rev.**72**, 390 (1947);
    A. Papapetrou, Proc.R.Ir.Acad.Sect. **A51**, 191 (1947);
    R. C. Myers, Phys.Rev.**D 35**, 455 (1987).

[5] D. Kastor and J. Traschen, Phys.Rev.D, **47**, 5370 (1993).

[6] L.A.J. London, Nucl.Phys.B **434**, 709 (1995).

[7] D. Brill, G. Horowitz, D. Kastor, J. Traschen, Phys.Rev. **D 49**, 840 (1994)

[8] K. Nakao, T. Shiromizu, and S. A. Hayward, Phys. Rev. D **52**, 796, (1995);
    D. Ida, K. Nakao, M. Siino and S. A. Hayward, Phys. Rev. D **58**, 121501, (1998).

[9] H. Ishihara, M. Kimura and S. Tomizawa, Class. Quantum Grav. **23**, L89 (2006).

[10] T. Eguchi and A. J. Hanson, Phys.Lett.**74B**, 249 (1978).

[11] M. K. Prasad, Phys.Lett.**83B**, 310 (1979).

Homogeneous and cohomogeneity-one objects in the five-dimensional anti-de-Sitter spacetime

Tatsuhiko Koike[1], Hiroshi Kozaki[2] and Hideki Ishihara[3]

[1]*Department of Physics, Keio University, Yokohama 223–8522 Japan*
[2,3]*Department of Mathematics and Physics, School of Science, Osaka City University, Osaka 558–8585 Japan*

Abstract

We classify all cohomogeneity-one cosmic strings in the five-dimensionalanti-de-Sitter space, by classifying the Killing vector fields up to isometry. The local isomorphism of $SO(4,2)$ and $SU(2,2)$ and the notion of H-similarity are effectively used. The result is useful also for the classification of higher-dimensional objects.

1   Introduction and summary

In cosmology, extended objects in the universe has been attracting long-lasting attention and it is still growing. The examples of extended objects are the topological defects, such as cosmic strings and membranes, and the universe as a whole which is embedded in a higher-dimensional spacetime in the context of the brane world universe model. The trajectory of an extended object forms a hypersurface in the spacetime which is described by some partial differential equation (PDE). For example, a test cosmic string in the spacetime is governed by the Nambu-Goto equation. The simplest solutions to those PDE are homogeneous ones, in which case the problem reduces to an algebraic one. However, these solutions usually do not have a wide variety and tend to be too simple to contain nontrivial dynamics.

One may expect that if we assume "less" homogeneity, the equation still remains to be tractable and the solutions has enough variety to show physically interesting properties and dynamics of those extended objects. The class of cohogeneity-one objects gives such a condition. We say that a hypersurface is of *cohomoneneity-one* if it is foliated by codimension-one submanifolds with each of them being embedded homogeneously in the whole spacetime. A cohomoneneity-one object has a world sheet which is a cohomoneneity-one hypersurface. Any covariant PDE governing such an object reduces to an ordinary differential equation (ODE), which can be easily solved analytically, or at least, numerically. A solution expresses a spatially homogeneous object with a nontrivial dynamics if the above-mentioned homogeneous submanifolds are spacelike, or a spatially nontrivial object with a trivial dynamics if the homogeneous submanifolds are timelike. The case with the null homogeneous submanifolds will also give new intriguing models. In the case of the Minkowski space, there are many nontrivial examples of Nambu-Goto strings [1].

With the application in brane world or string theory in mind, we shall focus on the extended objects in the five-dimensional anti-de-Sitter space AdS^5. In this talk, we shall classify (Theorem 1) the one-dimensional subalgebras of the Lie algebra of the isometry (equivalently, the Killing vector fields) up to isometry, because the classification of all cohomoneneity-one cosmic strings reduces to that problem. Finding solutions for the dynamics is another problem which depends on the PDE governing these objects; the case of Nambu-Goto string will be presented elsewhere. The classification presented here will also be the basis for that of higher-dimensional cohomoneneity-one objects in AdS^5.

In the classification we will make use of the local isomorphism between $SO(4,2)$ and $SU(2,2)$ (Sec. 2). The reason is, roughly speaking, that lower dimensional, complex matrices are easier to deal with, especially in the context of Jordan decomposition. The notion of H-selfadjoint matrices and the classification of the pair (A, H) of a H-selfadjoint matrix A and a Hermitian matrix H (Sec. 3) turn out to be essential.

---

[1]E-mail: koike@phys.keio.ac.jp
[2]E-mail: furusaki@sci.osaka-cu.ac.jp
[3]E-mail: ishihara@sci.osaka-cu.ac.jp

2 $SO(4,2)$ and $SU(2,2)$

Our aim is to classify Killing vector fields in the five-dimensional anti-de-Sitter space AdS^5 up to isometry, so we consider two Killing vector fields ξ and ξ' equivalent if there is an isometry ϕ (connected to the identity) such that $\xi' = \phi \circ \operatorname{Exp} t\xi \circ \phi^{-1}$, or $\xi' = \phi_* \xi$. The isometry group of AdS^5 is $SO(4,2)$, because AdS^5 is a hypersurface $-s^2 - t^2 + w^2 + x^2 + y^2 + z^2 = -l^2$ in the peudo-Euclidean space $E^{4,2}$ whose metric is $dS^2 = -ds^2 - dt^2 + dw^2 + dx^2 + dy^2 + dz^2$. Thus we shall classify $\mathfrak{so}(4,2)/\operatorname{Ad}_{SO(4,2)_0}$. To do so, we take advantage of the isomorphism $SO(4,2)_0 \simeq SU(2,2)/\{\pm 1\}$. This isomorphism implies in particular a Lie algebra isomporphism $\mathfrak{so}(4,2) \simeq \mathfrak{su}(2,2)$ and a Lie group isomorphism $\operatorname{Ad}_{SO(4,2)_0} \simeq \operatorname{Ad}_{SU(2,2)}$. Thus we have an isomorphism $\mathfrak{so}(4,2)/\operatorname{Ad}_{SO(4,2)_0} \simeq \mathfrak{su}(2,2)/\operatorname{Ad}_{SU(2,2)}$, which will be resolved in Sec. 3.

Let us give a concrete expression of the $SO(4,2)_0$ transformation by $SU(2,2)$. The action of an element of $SO(4,2)_0$ on $(s,t,x,y,z,w) \in E^{4,2}$ is expressed by the action of $U \in SU(2,2)$ on V in the following way:

$$p \mapsto UpU^T,$$
$$V \ni p = si\sigma_z \otimes \sigma_y + t1 \otimes \sigma_y + xi\sigma_y \otimes \sigma_x + y\sigma_x \otimes \sigma_y - zi\sigma_y \otimes \sigma_z + w\sigma_y \otimes 1. \tag{1}$$

The infinitesimal transformation for (1) is given by the action of $X \in \mathfrak{su}(2,2)$ as

$$p \mapsto Xp + pX^T = \{X_S, p\} + [X_A, p], \tag{2}$$

where $X_S := (X + X^T)/2$ and $X_A := (X - X^T)/2$ are the symmetric and antisimmetric parts, respectively, of X. Let us express the correspondence in terms of a basis of $\mathfrak{su}(2,2)$. A convenient basis for $\mathfrak{su}(2,2)$ is $\{1/i, \sigma_x, \sigma_y, \sigma_z/i\} \otimes \{1, \sigma_x, \sigma_y, \sigma_z\}$ with $(1/i) \otimes 1$ being omitted. [Including $(1/i) \otimes 1$ would yield a basis for $\mathfrak{u}(2,2)$.] Then the infinitesimal transformation are expressed by a commutator $[X, \bullet]$ for $X = \{1/i, \sigma_x, \sigma_z/i\} \otimes \{1, \sigma_x, \sigma_z\}$ and for $X = \sigma_y \otimes \sigma_y$, and by an anticommutator $\{X, \bullet\}$ for $X = \sigma_y \otimes \{1, \sigma_x, \sigma_z\}$ and for $X = \{1/i, \sigma_x, \sigma_z/i\} \otimes \sigma_y$. The corresponding $SO(4,2)_0$ infinitesimal transformations (Killing vectors on AdS^5) are given in Table 1, with X being $(e_1 \otimes e_2)/2$. In the table, xy denotes the rotation in the xy plane, st denotes the rotation in the st plane, tx denotes the t-boost in the x direction, $-sw$ denotes the s-boost in the $-w$ direction, and so forth.

e_1 \ e_2	1	σ_x	σ_y	σ_z
$1/i$		yz	zx	xy
σ_x	tw	sx	sy	sz
σ_y	$-sw$	tx	ty	tz
σ_z/i	st	wx	wy	wz

Table 1: Correspondence between the $\mathfrak{su}(2,2)$ and $\mathfrak{so}(4,2)$ transformations.

3 The classification

Let us introduce the useful terms in the classification. Let H be an invertible Hermitian matrix. The H-adjoint of a square matrix A is defined by $A^\star := H^{-1}A^\dagger H$. A matrix A is called H-selfadjoint when $A^\star = A$, H-anti-selfadjoint when $A^\star = -A$, and H-unitary when $AA^\star = A^\star A = 1$. Let us say that matrices A and B are H-unitarily similar and denote by $A \overset{H}{\sim} B$ if there exists an H-unitary matrix W satisfying $B = WAW^{-1}$. In this terminology, $SU(2,2)$ is the group of unimodular η-unitary matrices with $\eta = \operatorname{diag}[1,1,-1,-1]$. The Lie algebra $\mathfrak{su}(2,2)$ of $SU(2,2)$ consists of traceless η-anti-selfadjoint matrices

$$X = \begin{bmatrix} p & r \\ r^\dagger & q \end{bmatrix}, \tag{3}$$

where r is a 2×2 complex matrix and p and q are 2×2 anti-Hermitian matrices. The task of finding $\mathfrak{su}(2,2)/\operatorname{Ad}_{SU(2,2)}$ is equivalent to classifying elements of $\mathfrak{su}(2,2)$ up to equivalence relation $\overset{\eta}{\sim}$.

We shall now find out the equivalence classes of $\mathfrak{su}(2,2)/\mathrm{Ad}_{SU(2,2)} = \mathfrak{su}(2,2)/\overset{\eta}{\sim}$. Let (A, H) be a pair of a complex matrix and an invertible Hermitian matrix H. The pairs (A, H) and (A', H') are said unitarily similar if there is a complex matrix W such that $A' = WAW^{-1}, H' = WHW^{\dagger}$ [2]. This is an equivalence relation and will be denoted by $(A, H) \sim (A', H')$. Note that $A \overset{\eta}{\sim} A'$ is equivalent to $(A, \eta) \sim (A', \eta)$. Let A be an H-selfadjoint matrix. Then if λ is an eigenvalue of A, so is its complex conjugate λ^*. Let $J_0(\lambda)$ be the Jordan block with eigenvalue λ and let

$$J(\lambda) := \begin{cases} J_0(\lambda), & \lambda \text{ is real,} \\ J_0(\lambda) \oplus J_0(\lambda^*), & \lambda \text{ is non-real.} \end{cases} \tag{4}$$

We shall make use of the canonical forms of the pairs (A, H) [2]:

Lemma. *If A is H-selfadjoint, then (A, H) is unitarily similar to (J, P) with*

$$J = \bigoplus_{j=1}^{\beta} J(\lambda_j); \quad P = \Big(\bigoplus_{j=1}^{\alpha} c_j P_j\Big) \oplus \Big(\bigoplus_{j=\alpha+1}^{\beta} P_j\Big); \quad c_j = \pm 1, \quad P_j = \begin{bmatrix} 0 & & 1 \\ & \cdot^{\cdot^{\cdot}} & \\ 1 & & 0 \end{bmatrix}, \tag{5}$$

where $\lambda_1, \ldots, \lambda_\alpha$ are the real eigenvalues of A, $\lambda_{\alpha+1}, \lambda_{\alpha+1}^*, \ldots, \lambda_\beta, \lambda_\beta^*$ are the non-real eigenvalues of A, and the size of P_j is the same as that of $J(\lambda_j)$.

We will denote the type of of the generator X by the dimensions of J_j for the real and non-real eigenvalues of X, namely, by $(d_1, \ldots d_\alpha | d_{\alpha+1}/2, \ldots, d_\beta/2)$ with $d_j := \dim J(\lambda_j)$. [If there is either no real or no non-real eigenvalues, we put a 0 in the corresnponding slot.] We also define the subtype of each type by the signs of $(c_1, \cdots, c_\alpha)$. We sometimes denote the subtype as a subscript such as $(3, 1|0)_+$. In the theorem below, J_{xy} denotes spatial rotations in the xy plane, K_z denotes the boost with respect to the time t in the z direction, $\widetilde{K}_w$ denotes the boost with respect to the time s in the w direction, L denotes the rotation in the st plane, and so forth.

Theorem 1. *Any one-dimensional homogeneously embedded submanifold of AdS^5 is generated by one of the nine types of ξ in Table 2 up to isometry of AdS^5, where a, b, c are real numbers, the double-signs must be taken in the same order in each expression.*

Type	Killing vector field ξ
$(4\|0)$	$K_x + \widetilde{K}_y + J_{xy} + L + 2(J_{yz} + K_z)$
$(3, 1\|0)_\pm$	$K_x + \widetilde{K}_y + J_{yz} \pm J_{xw} + a(J_{xy} - L \mp J_{zw})$
$(2, 2\|0)_{++}$	$K_x + L + aJ_{yz}$
$(2, 2\|0)_{+-}$	$K_x + J_{xy} + aJ_{zw}$
$(2, 1, 1\|0)$	$K_x + \widetilde{K}_y + J_{xy} + L + a\,J_{wz} + b\,(J_{xy} - L)$
$(1, 1, 1, 1\|0)$	$a\,L + b\,J_{xy} + c\,J_{wz}\ (a^2 + b^2 + c^2 = 1)$
$(2\|1)$	$K_x + \widetilde{K}_y + L + J_{xy} + aJ_{zw} + b(K_y + \widetilde{K}_x)$
$(1, 1\|1)$	$K_x + \widetilde{K}_y + b\,(L - J_{xy}) + c\,J_{zw}$
$(0\|2)$	$K_x + J_{xy} + a\,\widetilde{K}_z\ (a \neq 0)$
$(0\|1, 1)$	$aK_x + b\,\widetilde{K}_y + c\,J_{zw}\quad (b \neq \pm a,\ a^2 + b^2 + c^2 = 1)$

Table 2: The types of the generator of $SU(2,2)$ and the corresponding Killing vector fields ξ.

Proof. Let X be an η-anti-selfadjoint matrix X. Let us first show that η-unitarily similar to $X_0 := iWJW^{-1}$ with some J in the Lemma and with an arbitrary complex matrix W satisfying $\eta = WPW^{\dagger}$. By the Lemma, we have $(X/i, \eta) \sim (J, P)$ with some (J, P) because X/i is η-selfadjoint. [This also implies that there exists at least one W' satisfying $\eta = W'PW'^{\dagger}$.] On the other hand, if $\eta = WPW^{\dagger}$ holds, we have $(J, P) \sim (WJW^{-1}, \eta)$ by the definition of unitary similarity. Then we have $(X/i, \eta) \sim (WJW^{-1}, \eta)$, which implies $X \overset{\eta}{\sim} iWJW^{-1}$. Thus we can carry out the classification by the following procedure.
(1) Enumeratete P such that there is some W satisfying $\eta = WPW^{\dagger}$.

(2) For each P and the corresponding W, construct $X_0 = iWJW^{-1}$.

(3) Translate X_0 back to the Killing vector field ξ in $SO(4,2)_0$.

In some cases, however, the canonical pairs (J,P) and (J',P') correspond to X_0's which generate an identical Lie group. This happens when $(J',P') \sim (\alpha J,P)$ holds with a nonzero real number α. To find nontrivial identifications and clarify the relation between subtypes, it is useful to know how a pair $(\alpha J_j(\lambda_j),P_j)$ can be canonicalized. For $\alpha > 0$, we simply have $(\alpha J_j(\lambda_j),P_j) \sim (J_j(\alpha\lambda_j),P_j)$. Therefore we focus on $(-J_j(\lambda_j),P_j)$.

(i) When d_j is odd, we have

$$(-J(\lambda_j),P_j) \sim (J(-\lambda_j),P_j). \tag{6}$$

This can be seen by applying a similarity transformation by $\mathrm{diag}[-1,1,-1]$, etc.

(ii) When d_j is even, we have

$$(-J(\lambda_j),P_j) \sim (J(-\lambda_j),-P_j). \tag{7}$$

Apply a similarity transformation by $\mathrm{diag}[-1,1,-1,1]$, etc.

(iii) In the special case of $d_j = 2$ and $\lambda_j \in \mathbb{C}$, not only (7) but also (6) holds because $-J(\lambda_j) = J(-\lambda_j)$.

Another useful relation is that of (J,P) and $(J,-P)$. Let us show that the corresponding Killing vector fields ξ are related by a reflection $r: (t,x) \mapsto (-t,-x)$, which is a transformation in $SO(4,2)$ which is not connected to the identity. When $(J,P) \sim (X_0,\eta)$, we have $(J,-P) \sim (-X_0',\eta)$ with $X_0' = -\Sigma X \Sigma^{-1}$ and $\Sigma = \sigma_y \otimes \sigma_x$, because $\Sigma\eta\Sigma^\dagger = -\eta$ holds. On the other hand, one can read off from (1) that the transformation $p \mapsto -\Sigma p(\Sigma^{-1})^T = -\Sigma p\Sigma^T$ is a reflection along the t and x axes. Thus the Killing vector field ξ' corresponding to X_0' is the one ξ corresponding to X_0 with the t and x axes reversed.

Let us find the relation of the subtypes within each type by using the results above. For Type $(4|0)$, by (7), the subtypes $(+)$ are $(-)$ identical and there is a unique subtype, which is invariant under r (though the parameters change). For Type $(3,1|0)$, there are two subtypes $(++)$ and $(--)$, which we shall simply call $(+)$ and $(-)$. They are related to each other by the reflection r. For Type $(2,2|0)$, by (7), the subtypes $(++)$ and $(--)$ are identical which is invariant under r. The subtype $(+-)$ is distinct but is the same as $(-+)$ (by a simple reordering) which is invariant under r. For Type $(2,1,1|0)$, because of reordering, there are at most two subtypes $(++-)$ and $(--+)$. However, they are identical, by (7) for the first block and by exchange of the second and the third blocks. It is invariant under r. Type $(1,1,1,1|0)$ has only one subtype (by reordering). For Type $(2|1)$, the subtypes $(+)$ and $(-)$ generates an identical group and fall into a unique subtype. This can be seen by applying (ii) to the first block and (iii) to the second, yielding $(\mathrm{diag}[J_1,J_2],\mathrm{diag}[-P_1,P_2]) \sim (-\mathrm{diag}[J_1,J_2],\mathrm{diag}[P_1,P_2])$. Type $(1,1|1)$ has a unique subtype (by reordering). Type $(0|2)$ and type $(0|1,1)$ have a unique subtype.

Let us demonstrate the concrete calculation for Type $(2|1)$ (the other types can be found in a similar manner). We have, because J is traceless, $J = \mathrm{diag}\left[\begin{bmatrix} a & 1 \\ 0 & a \end{bmatrix}, -a+bi, -a-bi\right]$, where a and b are real numbers, and $P = \mathrm{diag}\left[\pm\begin{bmatrix} 0 & 1 \\ 1 & 0 \end{bmatrix}, \begin{bmatrix} 0 & 1 \\ 1 & 0 \end{bmatrix}\right]$. As discussed above, however, it suffices to consider the plus sign. Let us choose $W = S_{23} \cdot \mathrm{diag}[R(\pi/2),R(-\pi/2)]$ where $R(\theta) = \begin{bmatrix} \cos\theta & -\sin\theta \\ \sin\theta & \cos\theta \end{bmatrix}$ and $S_{23} = \begin{bmatrix} 1 & 0 & 0 & 0 \\ 0 & 0 & 1 & 0 \\ 0 & 1 & 0 & 0 \\ 0 & 0 & 0 & 1 \end{bmatrix}$. Then $X_0 = iWJW^{-1} = \begin{bmatrix} i(a+1/2) & 0 & i/2 & 0 \\ 0 & -ia & 0 & b \\ -i/2 & 0 & i(a-1/2) & 0 \\ 0 & b & 0 & -ia \end{bmatrix} = -a\,(1/i) \otimes \sigma_z +$ $b\,\sigma_x \otimes \frac{1-\sigma_z}{2} - \frac{(\sigma_y+(\sigma_z/i))\otimes(1+\sigma_z)}{4}$. By Table 1, we find that X_0 corresponds to the $\mathfrak{so}(4,2)$ operation $\xi = -\widetilde{K}_w + K_z + L + J_{wz} + aJ_{xy} + b(K_w - \widetilde{K}_z)$, where we have rescaled ξ (by -4) and redefined a and b. $\qquad \square$

References

[1] K. Ogawa, JGRG14; *id.*, JGRG15.

[2] L. Gohberg, P. Lancaster and L. Rodman, *Matrices and indefinite scalar products*, (Birkhäuser Verlag, 1983).

Cosmological perturbations in Stochastic gravity
— Beyond the linear perturbations —

Yuko Urakawa[1] and Kei-ichi Maeda[2]

Department of Physics, Waseda University,Ohkubo 3-4-1 Shinjuku-ku, Tokyo 169–8555, Japan

Abstract

Base on the formalism in Stochastic gravity, we study the nonlinear quantum effect of the scalar field during inflation. We have shown as long as the slow-roll condition is satisfied, Einstein-Langevin equation, which describes the quantum correction of the scalar field to the gravitational field, can be solved iteratively. In these quantum corrections, there exist two different order parts; the leading part induces the equivalent effect to the linear analysis and the other part induces the nonlinear effect.

1 Introduction

The issue of calculating nonlinearity and the consequent non-Gaussianity in the primordial universe has been attracting increasing attention, recently. Nevertheless, since the second order gauge invariant perturbation equation is so complicated that it is difficult to quantize the gauge invariant variables in the similar way to the linear analysis. It is why we consider the alternative approach by Stochastic gravity to estimate this nonlinear effect.

2 Stochastic gravity

Since the Planck scale is so small, we expect that there exist some region where only the quantum effect of the matter field is essential. Based on this idea, in Stochastic gravity, we treat the gravitational field as a classical external field to pick up the quantum effect of the matter field. In particular, from the effective action given by Feynman-Vernon's Influence function or Closed time path formalism, we can derive the equation for gravitational field which includes also the nonlinear quantum correction of the matter field. [1]

$$G_{ab}[g+h](x) = \langle \hat{T}_{ab} \rangle_R[g+h](x) + 2\xi_{ab}(x)$$

$$\langle \hat{T}_{ab} \rangle_R[g+h](x) = \langle \hat{T}_{ab} \rangle_R[g] + \langle \hat{T}_{ab}^{(1)}[g;h] \rangle_R - 2\int d^4y \sqrt{-g} H_{abc'd'}[g](x,y) h^{cd}(y) + O(h^2) \quad (1)$$

This equation is called Einstein-Langevin equation and let me note next three points about it.

(1) Expectation value of the energy momentum tensor

This expectation value of the energy momentum tensor depends on both the gravitational field and the scalar field. The scalar field also depends on the gravitational filed. In other words, this energy momentum tensor depends on the gravitational field not only directly, but also indirectly through the scalar field. These two effects can be seen in the expectation value, $\langle \hat{T}_{ab} \rangle_R[g+h]$, respectively. We can see that the second term in Eq.(1) is induced from the change of the gravitational field from g to g+h directly. On the other hand, the third term, which represents the non-Markovian nature, is induced from the change of the gravitational field indirectly. The second term is given by the next equation, in case we consider minimal coupling scalar field

$$\langle \hat{T}_{ab}^{(1)}[g;h] \rangle_R = \left(\frac{1}{2} g_{ab} h^{cd} - \delta^c_a h^d_b - \delta^d_b h^c_a \right) \langle \hat{T}_{cd} \rangle_R[g] - \frac{1}{4} \left(h_{ab} - \frac{1}{2} g_{ab} h^c_c \right) \bigtriangledown_c \bigtriangledown^c \langle \hat{\phi}^2 \rangle_R[g] \quad (2)$$

---

[1] E-mail:yuko@gravity.phys.waseda.ac.jp
[2] E-mail:maeda@gravity.phys.waseda.ac.jp

(2) Stochastic variable ξ_{ab}

This classical noise represents the quantum fluctuation of the energy momentum tensor, the deviation from the expectation value. Here I neglect the non-Gaussianity of this noise term, but if necessary we can consider this effect in the formalism of Stochastic gravity. The correlation function of this stochastic variable, ξ_{ab}, is given by the next bi-tensor $N_{abc'd'}(x,y)$

$$N_{abc'd'}[g](x,y) \equiv \frac{1}{8}\langle\{(\hat{T}_{ab} - \langle\hat{T}_{ab}\rangle)(x), (\hat{T}_{c'd'} - \langle\hat{T}_{c'd'}\rangle)(y)\}\rangle = \langle\xi_{ab}(x)\xi_{c'd'}(y)\rangle_s \tag{3}$$

Here I put index "s" to distinguish the ensemble average from the expectation value of operators.

(3) General covariance

Einstein-Langevin equation satisfies the general covariance, as long as a background metric,g, is a solution of the semi-classical Einstein equation. To confirm this general covariance, let me consider the gauge transformation by a stochastic variable ζ. Under this transformation, any tensors which depends on the metric of the perturbed space time transform as follows to linear order,

$$R_{ab}[g + h'] = R_{ab}[g + h] + \mathcal{L}_\zeta R_{ab}[g] \tag{4}$$

Suppose that in one gauge (the perturbed metric $\rightarrow g + h$) Einstein-Langevin equation is satisfied, then under the gauge transformation to another gauge (the perturbed metric $\rightarrow g+h'$) this equation transforms as follows to linear order,

$$\left\{G_{ab}[g + h](x) - \langle\hat{T}_{ab}\rangle_R[g + h](x) - 2\xi_{ab}(x)\right\} - \mathcal{L}_\zeta\left\{G_{ab}[g](x) - \langle\hat{T}_{ab}\rangle_R[g](x)\right\} = 0 \tag{5}$$

Since the stochastic variable ξ_{ab} has no background part, there is no contribution from ξ_{ab} in second curly bracket. Then, in case a background metric g is a solution of the semi-classical Einstein equation, Einstein-Langevin equation is still valid after an arbitrary gauge transformation. From this fact, we can consider the right hand side of Einstein-Langevin equation as one ordinary energy momentum tensor.

3 Cosmological perturbations in Stochastic gravity

We shall consider a minimal coupling scalar field with mass term $\frac{1}{2}m^2\phi^2$. As a state of the quantum fluctuation, we choose Bunch-Davies vacuum. [2]

3.1 Background

To guarantee the general covariance, we have to consider a background space time as a solution of the semi-classical Einstein equation. Here I decomposed the scalar field into the classical part and the fluctuation part, $\hat{\phi} = \phi_{cl} + \hat{\psi}$. To substitute this decomposition into the semi classical Einstein equation, the back ground equation is

$$G_{ab}[g](x) = \kappa^2\{T_{ab}^{(cl)}(x) + \langle\hat{T}_{ab}\rangle_R(x)\} \tag{6}$$

Second term in the right hand side is composed of the fluctuation term,$\hat{\psi}^2(x)$. To compare the order of these two terms,

$$\text{1st term/2nd term} \sim \phi_{(cl)}^2/\langle\hat{\psi}^2\rangle_R \sim \phi_{(cl)}^2/H^2 \sim (m_{pl}/m)^2 \sim 10^{12} \tag{7}$$

The order of $\langle\hat{\psi}^2\rangle_R$ is essentially led by the Green function for Bunch-Davies vacuum.[2] The classical part of T_{ab},which is the leading term, induces a slow-roll inflationary stage.

3.2 Perturbed equations

Here, we shall consider the perturbation of Einstein-Langevin equation. As I already mentioned, since the right hand side of Einstein-Langevin equation can be considered as a single energy-momentum tensor,

although it includes a classical stochastic noise, this equation is just an ordinary Einstein equation. Then by solving this perturbed "Einstein equation", we can know the evolution of the gravitational field , affected by the quantum scalar filed.

At first we shall introduce the perturbed variables for the energy momentum tensor which corresponds to the right hand side of Einstein-Langevin equation.

$$
\begin{aligned}
\tilde{T}^0_{\ 0} &= -(\rho + \delta\rho Y) \\
\tilde{T}^j_{\ 0} &= -fY^j \\
\tilde{T}^i_{\ j} &= p\delta^i_{\ j} + \delta P Y \delta^i_{\ j} + p\pi Y^i_{\ j}
\end{aligned}
\tag{8}
$$

For the perturbed variables of the gravitational field, we use the same notation as [3]. Then, we can construct gauge invariant variables in the following, [3]

$$
\begin{aligned}
\rho\Delta &= \delta\rho + n(\rho + p)\mathcal{H}\frac{1}{k}\sigma_g \\
F &= f - (\rho + p)\frac{1}{k}\sigma_g \\
\widehat{\delta P} &= \delta P - p'\frac{1}{k}\sigma_g \\
p\Pi &= p\pi
\end{aligned}
\tag{9}
$$

,where n represents the spatial dimension. From now on, we will consider the evolution of two gauge invariant variables; one is the curvature perturbation in uniform density gauge $\mathcal{R}_{UD}$ and the other is the curvature perturbation in longitudinal gauge $\mathcal{R}_L$.

$$
\mathcal{R}_{UD} = \mathcal{R} + \frac{1}{n(\rho+p)}\delta\rho = \Phi + \frac{1}{n(\rho+p)}\rho\Delta
\tag{10}
$$

$$
\mathcal{R}_L = \mathcal{R} - \frac{\mathcal{H}}{k}\sigma_g = \Phi
\tag{11}
$$

The perturbed equations we shall solve are next four equations.

$$
(\rho\Delta)' + n\mathcal{H}\rho\Delta + kF + n\mathcal{H}\widehat{\delta P} + n(\rho+p)\Phi' = 0
\tag{12}
$$

$$
F' + (n+1)\mathcal{H}F - k\left(\widehat{\delta P} - \frac{n-1}{n}p\Pi\right) - (\rho+p)\Psi = 0
\tag{13}
$$

$$
\Phi = \frac{1}{n-1}\frac{\kappa^2 a^2}{k^2}\left(\rho\Delta + n\frac{\mathcal{H}}{k}F\right) = \frac{n}{2}\left(\frac{\mathcal{H}}{k}\right)^2\left\{\rho\Delta + n\left(\frac{\mathcal{H}}{k}\right)^2\frac{k}{\mathcal{H}}F\right\}
\tag{14}
$$

$$
\Psi = -(n-2)\Phi - \frac{a^2\kappa^2}{k^2}p\Pi
\tag{15}
$$

Once we know the evolution of $\rho\Delta$ and F, the evolution of $\mathcal{R}_{UD}$ and $\mathcal{R}_L$ is given by Eq.(10),Eq.(11),and Eq.(14). From Eq.(12) and Eq.(13), after transforming the variable from conformal time η into ζ, which satisfies $d\zeta/d\eta = \mathcal{H}\zeta$, $\rho\Delta$ and F are given by

$$
\begin{aligned}
\rho\Delta(\zeta) &= -\frac{n}{\zeta^n}\int_{\zeta_0}^{\zeta}d\zeta'\zeta'^{n-1}\widehat{\delta P} + \frac{1}{2\zeta^n}\int_{\zeta_0}^{\zeta}d\zeta'\left(\frac{k}{\mathcal{H}}\right)^2\zeta'^{n+1}\left(\frac{1}{\zeta^2} - \frac{1}{\zeta'^2}\right)\left(\widehat{\delta P} - \frac{n-1}{n}p\Pi\right) \\
&\quad + \frac{1}{2\zeta^n}\int_{\zeta_0}^{\zeta}d\zeta'\zeta'^{n+1}(1+w)\left(\frac{1}{\zeta^2} - \frac{1}{\zeta'^2}\right)\left(\frac{n}{2}\frac{k}{\mathcal{H}}F + \left(\frac{k}{\mathcal{H}}\right)^2\rho\Psi\right) - \frac{n}{\zeta^n}\int_{\zeta_0}^{\zeta}d\zeta'\zeta'^n(1+w)\rho\frac{d}{d\zeta'}\Phi \\
\frac{k}{\mathcal{H}}F(\zeta) &= \frac{1}{\zeta^{n+2}}\int_{\zeta_0}^{\zeta}d\zeta'\left(\frac{k}{\mathcal{H}}\right)^2\zeta'^{n+1}(\widehat{\delta P} - \frac{n-1}{n}p\Pi) + \frac{1}{\zeta^{n+2}}\int_{\zeta_0}^{\zeta}d\zeta'\zeta'^{n+1}(1+w)\left\{\frac{n}{2}\frac{k}{\mathcal{H}}F + \left(\frac{k}{\mathcal{H}}\right)^2\rho\Psi\right\}
\end{aligned}
\tag{16}
$$

Although $\rho\Delta$ and F have not been solved completely yet, using these equations, we can solve $\rho\Delta$ and F, and also $\mathcal{R}_{UD}$ and $\mathcal{R}_L$ iteratively during a slow-roll inflation.

---

[3]To compare the notation in [3], $f = (\rho+p)v$ and $F = (\rho+p)V$

Here we shall go back to the explicit form of Einstein-Langevin equation. From Eq.(1) and Eq.(2) in longitudinal gauge, $\widehat{\delta P}$ and $p\Pi$ are given by

$$
\begin{aligned}
\widehat{\delta P} &= \delta P_\xi - (1+w)(\rho\Phi + \delta P_m) + O((m/m_{pl})^4) \\
p\Pi &= p\pi_\xi - (1+w)p\pi_m
\end{aligned}
\tag{17}
$$

,where $\delta P_\xi, \delta P_m$ and $p\pi_\xi, p\pi_m$ represents the isotropic pressure part and the unisotropic pressure part for the stochastic variable ξ_{ab} and memory term, respectively.

Note that in case we consider the lowest order of $(1+w)$, the right hand side of $\rho\Delta$ and F are composed of δP_ξ and $p\pi_\xi$. Then, since the correlation function of δP_ξ and $p\pi_\xi$ are given by the bi-tensor $N_{abc'd'}$, the correlation function of $\rho\Delta, F, \mathcal{R}_{UD}$ and $\mathcal{R}_L$ are given in the lowest order of $(1+w)$ by these equations. Using the result of the lowest order,Eq.(16), and(17), we can find out the evolution of the correlation functions until any order of $(1+w)$. In other words, as long as $(1+w)$ is small, we can estimate the quantum correction of the scalar field to correlation functions, iteratively.

4   Nonlinear quantum effect of the scalar field

Since the perturbed equation which relates the stochastic terms and gauge invariant variables, what to do next is to estimate the correlation function of ξ_{ab} from $N_{abc'd}$. From Eq.(3), we can see that there are two order quantum corrections,

$$
N_{abcd}(x,y) \sim \mathcal{N}_{abcd}\langle\{\hat{\phi}^2(x) - \langle\hat{\phi}(x)\rangle^2, \hat{\phi}^2(y) - \langle\hat{\phi}(y)\rangle^2\}\rangle \sim \mathcal{N}_{abcd}[\phi_{cl}^2 G^+(x,y) + G^+(x,y)G^+(x,y)]
\tag{18}
$$

,where $G^+(x,y)$ is the Wightman function. In a similar way to Eq.(7), we can see that the first term is smaller than second one by order of $(m/m_{pl})^2$. Since the first term is equivalent to the linear perturbation and the second term corresponds to the nonlinear quantum effect of the scalar field, the quantum effect beyond the linear analysis is induced from the second term. Although this correction is much small, it is worth considering because it might represent a new physics which isn't included in the linear order. In particularly, we are considering two topics about this nonlinear effect; one is the contribution to the two point function and three point function and the other is the amplification of the tensor mode.

5   Summary

In the formalism of Stochastic gravity, the nonlinear quantum effect of the scalar field can be considered. We have shown that in case $1+w$ is small, we can solve Einstein-Langevin equation, iteratively. And there are two quantum corrections which have different order in the noise term(also in the memory term); the leading part corresponds to the linear effect and the other part corresponds to the nonlinear effect.

Acknowledgements

References

[1] B.L.Hu and E.Verdaguer,Living Rev.Rel.7:3(2004) gr-qc/0307032,
R.Martin and E.Verdaguer,Phys.Rev.D 60,084008(1999)

[2] N.D.Birrel and P.C.W. Davies, Quantum Fields in Curved Space (Cambridge University Press, Cambridge, England, 1982)

[3] H.Kodama and M.Sasaki, Prog.Theor.Phys.Supplement 78(1984)

Second-order gauge-invariant cosmological perturbation theory
— Einstein equations in terms of gauge invariant variables —

Kouji Nakamura[1]

Department of Astronomical Science, the Graduate University for Advanced Studies, 2-21-1, Osawa, Mitaka, Tokyo 181-8588, Japan

Abstract

The second order perturbations in Friedmann-Robertson-Walker universe filled with a perfect fluid are completely formulated in the gauge invariant manner without any gauge fixing. All components of the Einstein equations are derived neglecting the first order vector and tensor modes. These equations imply that the tensor and the vector mode of the second order metric perturbations may be generated by the non-linear effects of the Einstein equations from the first order density perturbations.

Recently, the first order approximation of the early universe from a homogeneous isotropic one is revealed by the observation of the CMB by Wilkinson Microwave Anisotropy Probe (WMAP)[1] and is suggested that fluctuations in the early universe are adiabatic and Gaussian at least in the first order approximation. One of the next theoretical tasks is to clarify the accuracy of these results, for example, through the non-Gaussianity. To do this, the second order cosmological perturbation theory is necessary.

In this article, we show the gauge invariant formulation of the general relativistic second order cosmological perturbations on the background Friedmann-Robertson-Walker (FRW) universe $\mathcal{M}_0$ filled with the perfect fluid whose metric is given by

$$g_{ab} = a^2(\eta) \left(-(d\eta)_a(d\eta)_b + \gamma_{ij}(dx^i)_a(dx^j)_b \right), \tag{1}$$

where γ_{ij} is the metric on maximally symmetric three space. The details of our formulation is given in Refs.[2].

The gauge transformation rules for the variable Q, which is expanded as $Q_\lambda = Q_0 + \lambda^{(1)}Q + \frac{1}{2}\lambda^2{}^{(2)}Q$, are given by

$$\overset{(1)}{\mathcal{Y}}Q - \overset{(1)}{\mathcal{X}}Q = \pounds_{\xi_{(1)}}Q_0, \quad \overset{(2)}{\mathcal{Y}}Q - \overset{(2)}{\mathcal{X}}Q = 2\pounds_{\xi_{(1)}}\overset{(1)}{\mathcal{X}}Q + \left\{ \pounds_{\xi_{(2)}} + \pounds^2_{\xi_{(1)}} \right\} Q_0, \tag{2}$$

where $\mathcal{X}$ and $\mathcal{Y}$ represet two different gauge choices, $\xi^a_{(1)}$ and $\xi^a_{(2)}$ are generators of the first and the second order gauge transformations, respectively.

The metric $\bar{g}_{ab}$ on the physical spacetime $\mathcal{M}_\lambda$ is expanded as $\bar{g}_{ab} = g_{ab} + \lambda h_{ab} + \frac{\lambda^2}{2}l_{ab}$. We decompose the components of the first order metric perturbation h_{ab} into the three sets of variables $h_{\eta\eta}, h_{(VL)}, h_{(L)}, h_{TL}$, $h_{(V)i}, h_{(TV)i}$, and $h_{(TT)ij}$, which are defined by

$$h_{\eta i} =: D_i h_{(VL)} + h_{(V)i}, \quad h_{ij} =: a^2 h_{(L)}\gamma_{ij} + a^2 h_{(T)ij}, \quad D^i h_{(V)i} = 0, \quad \gamma^{ij} h_{(T)ij} = 0, \tag{3}$$

$$h_{(T)ij} =: \left(D_i D_j - \frac{1}{3}\gamma_{ij}\Delta\right) h_{(TL)} + 2D_{(i}h_{(TV)j)} + h_{(TT)ij} \quad D^i h_{(TV)i} = 0, \quad D^i h_{(TT)ij} = 0. \tag{4}$$

Inspecting gauge transformation rules (2), we define a vector field X_a by

$$X_a := X_\eta(d\eta)_a + X_i(dx^i)_a, \quad X_\eta := h_{(VL)} - \frac{1}{2}a^2\partial_\tau h_{(TL)}, \quad X_i := a^2\left(h_{(TV)i} + \frac{1}{2}D_i h_{(TL)}\right), \tag{5}$$

where X_a is transformed as $\mathcal{Y}X_a - \mathcal{X}X_a = \xi_{(1)a}$ under the gauge transformation (2). We can also define the gauge invariant variables for the linear order metric perturbation by

$$\mathcal{H}_{ab} = -2a^2 \overset{(1)}{\Phi} (d\eta)_a(d\eta)_b + 2a^2 \overset{(1)}{\nu_i} (d\eta)_{(a}(dx^i)_{b)} + a^2\left(-2\overset{(1)}{\Psi}\gamma_{ij} + \overset{(1)}{\chi_{ij}}\right)(dx^i)_a(dx^j)_b, \tag{6}$$

---

[1] E-mail:kouchan@th.nao.ac.jp

where $D^i \overset{(1)}{\nu_i} = \overset{(1)}{\chi_{[ij]}} = \overset{(1)}{\chi^i{}_i} = D^i \overset{(1)}{\chi_{ij}} = 0$. In the cosmological perturbations[3], $\overset{(1)}{\Phi}, \overset{(1)}{\Psi}, \overset{(1)}{\nu_i}, \overset{(1)}{\chi_{ij}}$ are called the scalar, vector, and tensor modes, respectively. In terms of the variables $\mathcal{H}_{ab}$ and X_a, the original first order metric perturbation h_{ab} is given by

$$h_{ab} =: \mathcal{H}_{ab} + \pounds_X g_{ab}. \tag{7}$$

Since the scalar mode dominates in the early universe, we assume that $\overset{(1)}{\nu_i} = \overset{(1)}{\chi_{ij}} = 0$ in this article.

As shown in Ref.[2], through the above variables X_a and h_{ab}, the second order metric perturbation l_{ab} is decomposed as

$$l_{ab} =: \mathcal{L}_{ab} + 2\pounds_X h_{ab} + \left(\pounds_Y - \pounds_X^2 \right) g_{ab}. \tag{8}$$

The variables $\mathcal{L}_{ab}$ and Y^a are the gauge invariant and variant parts of l_{ab}, respectively. The vector field Y_a is transformed as ${}_y Y_a - {}_x Y_a = \xi_{(2)}^a + [\xi_{(1)}, X]^a$ under the gauge transformations (2). The components of $\mathcal{L}_{ab}$ are given by

$$\mathcal{L}_{ab} = -2a^2 \overset{(2)}{\Phi} (d\eta)_a (d\eta)_b + 2a^2 \overset{(2)}{\nu_i} (d\eta)_{(a}(dx^i)_{b)} + a^2 \left(-2 \overset{(2)}{\Psi} \gamma_{ij} + \overset{(2)}{\chi_{ij}} \right) (dx^i)_a (dx^j)_b, \tag{9}$$

where $D^i \overset{(2)}{\nu_i} = \overset{(2)}{\chi_{[ij]}} = \overset{(2)}{\chi^i{}_i} = D^i \overset{(2)}{\chi_{ij}} = 0$.

As shown in Ref.[2], by using the above variables X_a and Y_a, we can find the gauge invariant variables for the perturbations of an arbitrary field as

$$\overset{(1)}{\mathcal{Q}} := \overset{(1)}{Q} - \pounds_X Q_0,, \quad \overset{(2)}{\mathcal{Q}} := \overset{(2)}{Q} - 2\pounds_X \overset{(1)}{Q} - \left\{ \pounds_Y - \pounds_X^2 \right\} Q_0. \tag{10}$$

As the matter contents, in this article, we consider the perfect fluid whose energy-momentum tensor is given by $\bar{T}_a{}^b = (\bar{\epsilon} + \bar{p}) \bar{u}_a \bar{u}^b + \bar{p}\delta_a{}^b$. We expand these fluid components $\bar{\epsilon}, \bar{p}$, and $\bar{u}_a$ as

$$\bar{\epsilon} = \epsilon + \lambda \overset{(1)}{\epsilon} + \frac{1}{2}\lambda^2 \overset{(2)}{\epsilon}, \quad \bar{p} = p + \lambda \overset{(1)}{p} + \frac{1}{2}\lambda^2 \overset{(2)}{p}, \quad \bar{u}_a = u_a + \lambda \overset{(1)}{u}_a + \frac{1}{2}\lambda^2 \overset{(2)}{u}_a p. \tag{11}$$

Following the definitions (10), we easily obtain the corresponding gauge invariant variables for these perturbations of the fluid components:

$$\begin{aligned}
\overset{(1)}{\mathcal{E}} &:= \overset{(1)}{\epsilon} - \pounds_X \epsilon, \quad \overset{(1)}{\mathcal{P}} := \overset{(1)}{p} - \pounds_X p, \quad \overset{(1)}{\mathcal{U}}_a := \overset{(1)}{(u_a)} - \pounds_X u_a, \quad \overset{(2)}{\mathcal{E}} := \overset{(2)}{\epsilon} - 2\pounds_X \overset{(1)}{\epsilon} - \left\{ \pounds_Y - \pounds_X^2 \right\} \epsilon, \\
\overset{(2)}{\mathcal{P}} &:= \overset{(2)}{p} - 2\pounds_X \overset{(1)}{p} - \left\{ \pounds_Y - \pounds_X^2 \right\} p, \quad \overset{(2)}{\mathcal{U}}_a := \overset{(2)}{(u_a)} - 2\pounds_X \overset{(1)}{u}_a - \left\{ \pounds_Y - \pounds_X^2 \right\} u_a.
\end{aligned}$$

Through $\bar{g}^{ab}\bar{u}_a\bar{u}_b = g^{ab}u_a u_b = -1$ and neglecting the rotational part in $\overset{(1)}{\mathcal{U}}_a$, the components of $\overset{(1)}{\mathcal{U}}_a$ are given by $\overset{(1)}{\mathcal{U}}_a = -a \overset{(1)}{\Phi} (d\eta)_a + aD_i \overset{(1)}{v} (dx^i)_a$.

We also expand the Einstein tensor as $\bar{G}_a{}^b = G_a{}^b + \lambda^{(1)}G_a{}^b + \frac{1}{2}\lambda^2 {}^{(2)}G_a{}^b$. From Eqs.(7) and (8), each order perturbation of the Einstein tensor is given by

$${}^{(1)}G_a{}^b = {}^{(1)}\mathcal{G}_a{}^b [\mathcal{H}] + \pounds_X G_a{}^b, \quad {}^{(2)}G_a{}^b = {}^{(1)}\mathcal{G}_a{}^b [\mathcal{L}] + {}^{(2)}\mathcal{G}_a{}^b [\mathcal{H}, \mathcal{H}] + 2\pounds_X {}^{(1)}G_a{}^b + \left\{ \pounds_Y - \pounds_X^2 \right\} G_a{}^b \tag{12}$$

as expected from Eqs. (10). Here, ${}^{(1)}\mathcal{G}_a{}^b [\mathcal{H}]$ and ${}^{(1)}\mathcal{G}_a{}^b [\mathcal{L}] + {}^{(2)}\mathcal{G}_a{}^b [\mathcal{H}, \mathcal{H}]$ are gauge invariant parts of the frist and the second order perturbations of the Einstein tensor, respectively. On the other hand, the energy mometum tensor of the perfect fluid is also expanded as $\bar{T}_a{}^b = T_a{}^b + \lambda^{(1)}T_a{}^b + \frac{1}{2}\lambda^2 {}^{(2)}T_a{}^b$ and ${}^{(1)}T_a{}^b$ and ${}^{(2)}T_a{}^b$ are also given in the form

$${}^{(1)}T_a{}^b = {}^{(1)}\mathcal{T}_a{}^b + \pounds_X T_a{}^b, \quad {}^{(2)}T_a{}^b = {}^{(2)}\mathcal{T}_a{}^b + 2\pounds_X {}^{(1)}T_a{}^b + \left\{ \pounds_Y - \pounds_X^2 \right\} T_a{}^b \tag{13}$$

through the definitions (12) of the gauge invariant variables of the fluid components. Here, ${}^{(1)}\mathcal{T}_a{}^b$ and ${}^{(2)}\mathcal{T}_a{}^b$ are gauge invariant part of the first and the second order perturbation of the energy momentum

tensor, respectively. Then, the first and the second order perturbations of the Einstein equation are necessarily given in term of gauge invaraint variables:

$$^{(1)}\mathcal{G}_a{}^b\left[\mathcal{H}\right] = 8\pi G {}^{(1)}\mathcal{T}_a{}^b, \quad ^{(1)}\mathcal{G}_a{}^b\left[\mathcal{L}\right] + {}^{(2)}\mathcal{G}_a{}^b\left[\mathcal{H},\mathcal{H}\right] = 8\pi G {}^{(2)}\mathcal{T}_a{}^b. \tag{14}$$

The traceless scalar part of the spatial component of the first equation in Eq.(14) yields $\overset{(1)}{\Psi} = \overset{(1)}{\Phi}$, and the other components of Eq. (14) give well-known equations[3].

Since we neglect the first order vector and tensor modes, $\overset{(2)}{\mathcal{U}_a}$ is given by

$$\overset{(2)}{\mathcal{U}_a} = a\left(\left(\overset{(1)}{\Phi}\right)^2 - D_i \overset{(1)}{v} D^i \overset{(1)}{v} - \overset{(2)}{\Phi}\right)(d\eta)_a + a\left(D_i \overset{(2)}{v} + \overset{(2)}{\mathcal{V}_i}\right)(dx^i)_a, \tag{15}$$

where $D^i \overset{(2)}{\mathcal{V}_i} = 0$. All components of the second equation in Eq. (14) are summarized as follows: As the scalar parts, we have

$$4\pi G a^2 \overset{(2)}{\mathcal{E}} = \left(-3\mathcal{H}\partial_\eta + \Delta + 3K - 3\mathcal{H}^2\right)\overset{(2)}{\Phi} - \Gamma_0 + \frac{3}{2}\left(\Delta^{-1}D^i D_j \Gamma_i{}^j - \frac{1}{3}\Gamma_k{}^k\right)$$
$$-\frac{9}{2}\mathcal{H}\partial_\eta\left(\Delta + 3K\right)^{-1}\left(\Delta^{-1}D^i D_j\Gamma_i{}^j - \frac{1}{3}\Gamma_k{}^k\right), \tag{16}$$

$$8\pi G a^2(\epsilon+p)D_i \overset{(2)}{v} = -2\partial_\eta D_i \overset{(2)}{\Phi} - 2\mathcal{H}D_i \overset{(2)}{\Phi} + D_i\Delta^{-1}D^k\Gamma_k$$
$$-3\partial_\eta D_i\left(\Delta + 3K\right)^{-1}\left(\Delta^{-1}D^i D_j\Gamma_i{}^j - \frac{1}{3}\Gamma_k{}^k\right), \tag{17}$$

$$4\pi G a^2 \overset{(2)}{\mathcal{P}} = \left(\partial_\eta^2 + 3\mathcal{H}\partial_\eta - K + 2\partial_\eta\mathcal{H} + \mathcal{H}^2\right)\overset{(2)}{\Phi} - \frac{1}{2}\Delta^{-1}D^i D_j\Gamma_i{}^j$$
$$+\frac{3}{2}\left(\partial_\eta^2 + 2\mathcal{H}\partial_\eta\right)\left(\Delta + 3K\right)^{-1}\left(\Delta^{-1}D^i D_j\Gamma_i{}^j - \frac{1}{3}\Gamma_k{}^k\right), \tag{18}$$

$$\overset{(2)}{\Psi} - \overset{(2)}{\Phi} = \frac{3}{2}\left(\Delta + 3K\right)^{-1}\left(\Delta^{-1}D^i D_j\Gamma_i{}^j - \frac{1}{3}\Gamma_k{}^k\right). \tag{19}$$

where $\mathcal{H} = \partial_\eta a/a$ and

$$\Gamma_0 := 8\pi G a^2(\epsilon+p)D^i \overset{(1)}{v} D_i \overset{(1)}{v} - 3D_k\overset{(1)}{\Phi}D^k\overset{(1)}{\Phi} - 3\left(\partial_\eta\overset{(1)}{\Phi}\right)^2 - 8\overset{(1)}{\Phi}\Delta\overset{(1)}{\Phi} - 12\left(K + \mathcal{H}^2\right)\left(\overset{(1)}{\Phi}\right)^2,$$

$$\Gamma_i := -16\pi G a^2\left(\overset{(1)}{\mathcal{E}} + \overset{(1)}{\mathcal{P}}\right)D_i \overset{(1)}{v} + 12\mathcal{H}\overset{(1)}{\Phi}D_i\overset{(1)}{\Phi} - 4\overset{(1)}{\Phi}\partial_\eta D_i\overset{(1)}{\Phi} - 4\partial_\eta\overset{(1)}{\Phi}D_i\overset{(1)}{\Phi}, \tag{20}$$

$$\Gamma_i{}^j := 16\pi G a^2(\epsilon+p)D_i \overset{(1)}{v} D^j \overset{(1)}{v} - 4D_i\overset{(1)}{\Phi}D^j\overset{(1)}{\Phi} - 8\overset{(1)}{\Phi}D_i D^j\overset{(1)}{\Phi}$$
$$+2\left(3D_k\overset{(1)}{\Phi}D^k\overset{(1)}{\Phi} + 4\overset{(1)}{\Phi}\Delta\overset{(1)}{\Phi} + \left(\partial_\eta\overset{(1)}{\Phi}\right)^2 + 4\left(2\partial_\eta\mathcal{H} + K + \mathcal{H}^2\right)\left(\overset{(1)}{\Phi}\right)^2 + 8\mathcal{H}\overset{(1)}{\Phi}\partial_\eta\overset{(1)}{\Phi}\right)\gamma_i{}^j.$$

As the vector parts, we have

$$8\pi G a^2(\epsilon+p)\overset{(2)}{\mathcal{V}_i} = \frac{1}{2}\left(\Delta + 2K\right)\overset{(2)}{\nu_i} + \left(\Gamma_i - D_i\Delta^{-1}D^k\Gamma_k\right), \tag{21}$$

$$\partial_\eta\left(a^2 \overset{(2)}{\nu_i}\right) = 2a^2\left(\Delta + 2K\right)^{-1}\left\{D_i\Delta^{-1}D^k D_l\Gamma_k{}^l - D_k\Gamma_i{}^k\right\}. \tag{22}$$

As the tensor parts, we have the evolution equation of $\overset{(2)}{\chi_{ij}}$

$$\left(\partial_\eta^2 + 2\mathcal{H}\partial_\eta + 2K - \Delta\right)\overset{(2)}{\chi_{ij}}$$
$$= 2\Gamma_{ij} - \frac{2}{3}\gamma_{ij}\Gamma_k{}^k - 3\left(D_i D_j - \frac{1}{3}\gamma_{ij}\Delta\right)\left(\Delta + 3K\right)^{-1}\left(\Delta^{-1}D^k D_l\Gamma_k{}^l - \frac{1}{3}\Gamma_k{}^k\right)$$
$$+4\left(D_{(i}\left(\Delta + 2K\right)^{-1}D_{j)}\Delta^{-1}D^l D_k\Gamma_l{}^k - D_{(i}\left(\Delta + 2K\right)^{-1}D^k\Gamma_{j)k}\right), \tag{23}$$

Equations (22) and (23) imply that the second order vector and tensor modes may be generated due to the scalar-scalar mode coupling of the first order perturbation.

Further, the equations (16) and (19) are reduced to the single equation for $\overset{(2)}{\Phi}$

$$
\left(\partial_\eta^2 + 3\mathcal{H}(1+c_s^2)\partial_\eta - c_s^2\Delta + 2\partial_\eta\mathcal{H} + (1+3c_s^2)(\mathcal{H}^2 - K)\right) \overset{(2)}{\Phi}
$$
$$
= \quad 4\pi G a^2 \left\{ \tau \overset{(2)}{\mathcal{S}} + \frac{\partial c_s^2}{\partial\epsilon}\left(\overset{(1)}{\mathcal{E}}\right)^2 + 2\frac{\partial c_s^2}{\partial S}\overset{(1)}{\mathcal{E}}\overset{(1)}{\mathcal{S}} + \frac{\partial\tau}{\partial S}\left(\overset{(1)}{\mathcal{S}}\right)^2 \right\} + \frac{3}{2}\left(c_s^2 + \frac{1}{3}\right)\left(\Delta^{-1}D^i D_j \Gamma_i{}^j - \frac{1}{3}\Gamma_k{}^k\right)
$$
$$
- c_s^2\Gamma_0 + \frac{1}{6}\Gamma_k{}^k - \frac{3}{2}\left(\partial_\eta^2 + \left(2+3c_s^2\right)\mathcal{H}\partial_\eta\right)(\Delta+3K)^{-1}\left(\Delta^{-1}D^i D_j \Gamma_i{}^j - \frac{1}{3}\Gamma_k{}^k\right). \tag{24}
$$

Here, we have used the second order perturbation of the equation of state for the fluid components

$$
\overset{(2)}{\mathcal{P}} = c_s^2 \overset{(2)}{\mathcal{E}} + \tau \overset{(2)}{\mathcal{S}} + \frac{\partial c_s^2}{\partial\epsilon}\overset{(1)}{\mathcal{E}}{}^2 + 2\frac{\partial c_s^2}{\partial S}\overset{(1)}{\mathcal{E}}\overset{(1)}{\mathcal{S}} + \frac{\partial\tau}{\partial S}\overset{(1)}{\mathcal{S}}{}^2 , \tag{25}
$$

where $\overset{(1)}{\mathcal{S}}$ and $\overset{(2)}{\mathcal{S}}$ are the gauge invariant entropy perturbation of the first and second order, respectively, we denoted that $c_s^2 := \partial\bar{p}/\partial\bar{\epsilon}$ and $\tau := \partial\bar{p}/\partial\bar{S}$. The equation (24) will be useful to discus non-linear effects in the CMB physics[4]. We also derive the similar equations in the case where the matter content of the universe is a single scalar field[2].

Now, we are developing our formulation to the case in which the first order vector and tensor modes are not negligible. In some inflationary scenario, the tensor mode are also generated by the quantum fluctuations. This extension is necessary to clarify the evolution of the second order perturbation in the existence of the first order tensor mode. Further, to apply this formulation to clarify the non-linear effects in CMB physics[4], we have to extend our formulation to multi-field system and the Einstein Boltzmann system. This extension of our formulation is one of our future works.

Moreover, the rotational part of the fluid velocity in Eqs. (21) of the vector mode is also important in the early universe because this part of the fluid velocity is related to the generation of the magnetic field in the early universe[5]. The generation of the tensor mode by Eq. (23) is also interesting, since this is one of the generation process of gravitational waves. We have already known that the fluctuations of the scalar mode exist in the early universe from the anisotropy of the CMB[6]. Hence, the generation of the vector mode and tensor mode due to the second order perturbation will give the lower limit of these modes in the early universe.

References

[1] C.L. Bennett et al., Astrophys. J. Suppl. **148**, 1 (2003).

[2] K. Nakamura, Prog. Theor. Phys. **110**, 723 (2003); *ibid.* **113**, 481 (2005); K. Nakamura, Phys. Rev. D **74**, 101301; K. Nakamura, Prog. Theor. Phys. **117** (2007), in press [arXiv:gr-qc/0605108].

[3] J. M. Bardeen, Phys. Rev. D **22** (1980), 1882; H. Kodama and M. Sasaki, Prog. Theor. Phys. Suppl. No.78, 1 (1984); V. F. Mukhanov, H. A. Feldman and R. H. Brandenberger, Phys. Rep. **215**, 203 (1992).

[4] N. Bartolo, S. Matarrese and A. Riotto, JCAP **0401**, 003 (2004); N. Bartolo, S. Matarrese and A. Riotto, Phys. Rev. Lett. **93** (2004), 231301; N. Bartolo, E. Komatsu, S. Matarrese and A. Riotto, Phys. Rept. **402**, 103 (2004); N. Bartolo, S. Matarrese, and A. Riotto, arXiv:astro-ph/0512481.

[5] S. Matarrese, S. Mollerach, A. Notari, and A. Riotto, Phys. Rev. D **71** (2005), 043502; K. Takahashi, K. Ichiki, H. Ohno, and H. Hanayama, Phys. Rev. Lett. **95** (2005), 121301.

[6] S. Mollerach, D. Harari, and S. Matarrese, Phys. Rev. D **69** (2004), 063002; K.N. Ananda, C. Clarkson, and D. Wands, preprint [arXiv:gr-qc/0612013].

Gradient expansion approach to nonlinear superhorizon perturbations

Yoshiharu Tanaka[1] and Misao Sasaki[2]

Yukawa Institute for Theoretical Physics, Kyoto University, Kyoto 606–8502, Japan

Abstract

Using the gradient expansion approach, we formulate a nonlinear cosmological perturbation theory on super-horizon scales valid to $O(\epsilon^2)$, where ϵ is the expansion parameter associated with a spatial derivative. For simlicity, we focus on the case of a single perfect fluid, but we take into account not only scalar but also tensor modes. We derive the general solution under the uniform-Hubble time-slicing and identify the scalar, vector and tensor modes.

1 Introduction

The cosmic microwave background temperature anisotropy was found to be of order 10^{-5}, and the recent more accurate observation by WMAP was found to be perfectly consistent with the predictions of the inflationary universe, that the universe is spatially flat and that the primordial curvature perturbation is almost scale-invariant and statistically Gaussian [1]. Thus, it seems that the use of linear cosmological perturbation theory has been observationally justified. Nevertheless, the constraint obtained by WMAP on the deviation from Gaussianity is still very weak [1], and the next generation to WMAP, i.e. the PLANCK satellite may be able to detect non-Gaussianity. Also, on the theoretical side, many new types of inflationary models have been proposed in the last few years, motivated mainly by string theory, that predict rather large non-Gaussianity. Thus, to quantify the non-Gaussianity, it is important to develop a theory that can deal with nonlinear cosmological perturbations.

In this paper we take the gradient expansion approach [2] and formulate the cosmological perturbation to full nonlinear order in its amplitude but to second order in spatial gradients. In this approach, we introduce an expansion parameter, ϵ, and associate it with each spatial derivative, expand the field equations in terms of ϵ, and solve them order by order iteratively.

The most of the previous studies were, however, confined to the leading order approximation to gradient expansion. Although this leading order approximation seems to be justifiable for quite a large number of models, it can miss important points in some cases. A good example is the case studied by Leach et al. [3]. They considered the linear perturbation of a single-field inflation model which has a stage at which the slow-roll conditions are violated. It is then shown that the $O(k^2)$ corrections to the curvature perturbation on superhorizon scales, where k is the comoving wavenumber of the perturbation, plays a crucial role in the determination of the final curvature perturbation amplitude. To be a bit more precise, it is the decaying mode solution which becomes non-negligible and makes the $O(k^2)$ corrections important. If the $O(k^2)$ corrections are crucial already at linear order, one expects that they will affect the non-Gaussianity significantly. In gradient expansion, they correspond to $O(\epsilon^2)$ beyond the leading order. Thus it is important to include the $O(\epsilon^2)$ terms in gradient expansion.

There are still some issues to be clarified in the case of nonlinear, superhorizon perturbations. Among them are the issue of identifying the scalar, vector and tensor modes. At leading order of gradient expansion, the uniform density slicing (or equivalently uniform Hubble slicing) turns out to be convenient [4]. However, tensor modes which are to describe gravitational waves are not clearly seen at leading order. This is because of the general covariance that states that even if there exits a gravitational wave, spacetime can be made locally Minkowski within a region much smaller than the wavelength of the gravitational wave. Thus it seems necessary to go to higher orders to make clear distinction, if any, of tensor, scalar and vector modes. We shall formulate the gradient expansion to $O(\epsilon^2)$ beyond leading order in the uniform

---

Hubble slicing. We employ the $(3 + 1)$-decomposition of the Einstein equations and assume a perfect fluid equation of state $P = (\Gamma - 1)\rho$ with $\Gamma =$const.. We then derive the general solution for all the variables, focusing particularly on the correspondence between the degrees of freedom appearing in the general solution and those in the linear theory. We find that the identification of the tensor mode in the spatial metric is rather arbitrary, depending on how one fixes the spatial coordinates, as a reflection of the general covariance, while it can be unambiguously identified in the extrinsic curvature of the metric, albeit non-locally.

2   Gradient expnasion

In the $(3 + 1)$-decomposition, the metric is expressed as

$$
\begin{aligned}
ds^2 &= (-\alpha^2 + \beta_k\beta^k)dt^2 + 2\beta_i dx^i dt + \gamma_{ij}dx^i dx^j, & (1)\\
\gamma_{ij}(t, x^k) &= a^2(t)\,\psi^4(t, x^k)\,\tilde{\gamma}_{ij}(t, x^k)\,; \quad \det(\tilde{\gamma}_{ij}) = 1\,, & (2)
\end{aligned}
$$

where α, β^i $(\beta_i = \gamma^{ij}\beta^j)$, γ_{ij}, and $a(t)$ are the lapse function, shift vector, the 3-dimensional spatial metric, and the scale factor of a fiducial homogeneous and isotropic background universe respectively.

The extrinsic curvature K_{ij} of the $t =$const. hypersurface is defined by

$$
K_{ij} \equiv -\nabla_i n_j = -\alpha\Gamma^0{}_{ij}\,, \tag{3}
$$

where $n_\mu = (-\alpha, 0, 0, 0)$ is the vector unit normal to the time slices. We decompose the extrinsic curvature as

$$
K_{ij} = \frac{\gamma_{ij}}{3}K + \psi^4 a^2 \tilde{A}_{ij}\,; \quad K \equiv \gamma^{ij}K_{ij}\,, \tag{4}
$$

where $\tilde{A}_{ij}$ represents the traceless part of K_{ij}, and the indices of $\tilde{A}_{ij}$ are to be raised or lowered by $\tilde{\gamma}^{ij}$ and $\tilde{\gamma}_{ij}$. The stress-energy tensor for the fluid is

$$
T_{\mu\nu} = (\rho + P)u_\mu u_\nu + Pg_{\mu\nu}, \tag{5}
$$

where ρ, P and u^μ are the energy density, pressure, and the 4-velocity, respectively. We consider a perfect fluid with the barotropic equation of state $P/\rho = \Gamma - 1 =$const.. The components of the 4-velocity are expressed as

$$
\begin{aligned}
u^0 &= [\alpha^2 - (\beta_k + v_k)(\beta^k + v^k)]^{-1/2}, \quad u^i = u^0 v^i, \quad v^i \equiv \gamma^{ij}v_j, \\
u_0 &= -u^0[\alpha^2 - \beta^k(\beta_k + v_k)], \quad u_i = u^0(v_i + \beta_i).
\end{aligned} \tag{6}
$$

We consider nonlinear superhorizon perturbations in the spatial gradient expansion [2, 4] and assume that the characteristic length scale L of inhomogeneities is always much larger than the Hubble horizon scale, $L \gg H^{-1} \sim t$. We introduce a small parameter ϵ, and assume that L is of $O(1/\epsilon)$.

This assumption is equivalent to assuming that the magnitude of spatial gradients of the quantities is given by $\partial_i\psi = \psi \times O(\epsilon)$. In the limit $L \to \infty$, i.e., $\epsilon \to 0$, the universe looks locally like a FLRW spacetime, where 'locally' means as seen on the scale of the Hubble horizon volume. This implies that anisotropic quantities, i.e., β^i and v^i should be at least $O(\epsilon)$. Also, for the spatial metric to be locally homogeneous and isotropic, $\tilde{\gamma}_{ij}$ should be time independent in the limit $\epsilon \to 0$ [2]. This implies $\partial_t\tilde{\gamma}_{ij} = O(\epsilon)$. However, allowing it to be of $O(\epsilon)$ makes the analysis too complicated. We therefore require a bit tighter condition, $\partial_t\tilde{\gamma}_{ij} = O(\epsilon^2)$. Thus our basic assumptions are

$$
\beta^i = O(\epsilon)\,, \quad v^i = O(\epsilon)\,, \quad \partial_t\tilde{\gamma}_{ij} = O(\epsilon^2)\,. \tag{7}
$$

We note that from Eq. (4), the assumptions $\beta^i = O(\epsilon)$ and $\partial_t\tilde{\gamma}_{ij} = O(\epsilon^2)$ implies $\tilde{A}_{ij} = O(\epsilon^2)$. It is noted that physical quantities which are approximately homogeneous on each Hubble horizon scale can vary nonlinearly on very large scales.

We introduce $\delta \equiv \rho/\rho_0 - 1$, where ρ_0 is an energy density of a fiducial homogeneous and isotropic background universe. Then, using the Einstein equations and the hydrodynamic equations $\nabla^\mu T_{\mu\nu} = 0$ on uniform Hubble slicing, we can evaluate the order of magnitude of the basic variables as [4]

$$\psi = O(1), \quad \chi \equiv \alpha - 1 = O(\epsilon^2), \delta = O(\epsilon^2), \partial_t \tilde{\gamma}_{ij} = O(\epsilon^2),$$

$$\partial_t \psi = O(\epsilon^2), \quad \tilde{A}_{ij} = O(\epsilon^2), \quad u_i = O(\epsilon^3), \quad \beta^i + v^i = O(\epsilon^3). \tag{8}$$

An explicit demonstration of the above evaluation is given in [6].

3   General solution and identification of gravitational waves

Specifing the shift vector such that $\beta^i = O(\epsilon^3)$, we can find the general solutions valid up through $O(\epsilon^2)$ for all the physical quantities by solving the Einstein equations and the hydrodynamic equations, as follows.

$$\alpha = 1 + \chi = 1 - {}_{(2)}Q\,\frac{3\Gamma - 2}{3\Gamma}\,t^{2-\frac{4}{3\Gamma}}, \tag{9}$$

$$\psi = {}_{(0)}L\left(1 - {}_{(2)}Q\,\frac{1}{6\Gamma}t^{2-\frac{4}{3\Gamma}}\right) \tag{10}$$

$$\tilde{\gamma}_{ij} = {}_{(0)}f_{ik}\left(\delta_j^k - {}_{(2)}F^k{}_j\,\frac{9\Gamma^2}{9\Gamma^2 - 4}\,t^{2-\frac{4}{3\Gamma}} - {}_{(2)}C^k{}_j\,\frac{2\Gamma}{\Gamma - 2}\,t^{1-\frac{2}{\Gamma}}\right), \tag{11}$$

$$\tilde{A}_{ij} = {}_{(2)}F_{ij}\,\frac{3\Gamma}{3\Gamma + 2}\,t^{1-\frac{4}{3\Gamma}} + {}_{(2)}C_{ij}\,\frac{1}{a_f^3}\,t^{-\frac{2}{\Gamma}}, \tag{12}$$

$$\delta = {}_{(2)}Q\,t^{2-\frac{4}{3\Gamma}}, \tag{13}$$

$$u_i = {}_{(0)}L^{-6}\,\bar{D}^j\left[{}_{(0)}L^6{}_{(2)}F_{ij}\right]\,\frac{9\Gamma^2}{4(3\Gamma + 2)}\,t^{3-\frac{4}{3\Gamma}} + {}_{(0)}L^{-6}\,\bar{D}^j\left[{}_{(0)}L^6{}_{(2)}C_{ij}\right]\,\frac{3\Gamma}{4}\,t^{2-\frac{2}{\Gamma}}, \tag{14}$$

where ${}_{(0)}L$, ${}_{(0)}f_{ij}$ are $O(\epsilon^0)$ parts of ψ, $\tilde{\gamma}_{ij}$ respectively, and arbitrary, spatial functions, and ${}_{(2)}C_{ij}$ is an arbitrary, symmetric, and traceless function of $O(\epsilon^2)$, and $\bar{D}_i$ is the covariant derivative w.r.t. ${}_{(0)}f_{ij}$, and the prefix (n) means the quantity is of $O(\epsilon^n)$. The functions ${}_{(2)}F_{ij}$ and ${}_{(2)}Q$ are given as follows, respectively, as functions of ${}_{(0)}L$ and ${}_{(0)}f_{ij}$,

$$_{(2)}Q \equiv \frac{3\Gamma^2}{{}_{(0)}L^5}\left[-{}_{(0)}f^{ij}\bar{D}_i\bar{D}_{j\,(0)}L + \frac{1}{8}{}_{(0)}f^{kl}{}_{(2)}\bar{R}_{kl\,(0)}L\right], \tag{15}$$

$$_{(2)}F_{ij} \equiv \frac{1}{{}_{(0)}L^4}\left[{}_{(2)}\bar{R}_{ij} + {}_{(2)}R^L_{ij} - \frac{{}_{(0)}f_{ij}}{3}{}_{(0)}f^{kl}\left({}_{(2)}\bar{R}_{kl} + {}_{(2)}R^L_{kl}\right)\right], \tag{16}$$

where ${}_{(2)}\bar{R}_{ij}$ is the Ricci tensor w.r.t. ${}_{(0)}f_{ij}$, and ${}_{(2)}R^L_{ij}$ is defined as follows,

$$_{(2)}R^L_{ij} \equiv -\frac{2}{{}_{(0)}L}\bar{D}_i\bar{D}_{j\,(0)}L - \frac{2}{{}_{(0)}L}{}_{(0)}f_{ij}\bar{\Delta}_{(0)}L + \frac{6}{{}_{(0)}L^2}\bar{D}_{i\,(0)}L\bar{D}_{j\,(0)}L - \frac{2}{{}_{(0)}L^2}{}_{(0)}f_{ij}\bar{D}_{k\,(0)}L\bar{D}^k{}_{(0)}L, \tag{17}$$

where $\bar{\Delta}$ is the Laplacian w.r.t. ${}_{(0)}f_{ij}$. To clarify the physical role of these freely specifiable functions, let us first count the degrees of freedom. Since the determinant of ${}_{(0)}f_{ij}$ is unity, it has 5 degrees of freedom, and since ${}_{(2)}C_{ij}$ is traceless, it also has 5 degrees of freedom. So, together with the degree of freedom of ${}_{(0)}L$, the total number is $1 + 5 + 5 = 11$, while the true physical degrees of freedom are $4 + 2 + 2 = 8$, where 4 are of the fluid (1 from the density and 3 from the 3-velocity) and $2 + 2$ are of the gravitational waves (2 from the metric and 2 from the extrinsic curvature). This implies that there still remains 3 gauge degrees of freedom. It is easy to understand that these 3 gauge degrees come from spatial covariance, that is, from the gauge freedom of purely spatial coordinate transformations $x^i \to \bar{x}^i = f^i(x^j)$. Thus we may regard that ${}_{(0)}f_{ij}$ contains these 3 gauge degrees of freedom.

At this stage, it is useful to clarify the correspondence of the degrees of freedom counted as above, to those of linear theory. From the time-dependence associated with ${}_{(0)}L$, ${}_{(0)}f_{ij}$ and ${}_{(2)}C_{ij}$, one can identify

$_{(0)}L$ to the growing adiabatic mode of density perturbations, the 2 degrees in $_{(0)}f_{ij}$ to the growing modes of gravitational waves, the 3 degrees in $_{(2)}C_{ij}$ to 1 decaying scalar and 2 vector (vorticity) modes, and the remaining 2 in $_{(2)}C_{ij}$ to the decaying gravitational wave modes.

Now, returning to full nonlinear theory, it is generally impossible to identify uniquely the gravitational wave degrees of freedom in the metric because of general covariance. Nevertheless, if we focus on the extrinsic curvature K_{ij}, since its transverse-traceless part may be defined unambiguously, we may be able to single out the gravitational wave (tensor) degrees of freedom.

To show this is indeed the case, let us consider the momentum constraint [4, 6],

$$\bar{D}^j \left[_{(0)}L^6 \tilde{A}_{ij} \right] = 8\pi G \Gamma \rho_0 u_{i(0)} L^6 + O(\epsilon^5). \tag{18}$$

If we require the tensor modes to be transverse-traceless, an apparent candidate is the part of $_{(0)}L^6 \tilde{A}_{ij}$ that does not contribute to the right-hand side of the momentum constraint. Namely, we identify the transverse-traceless (TT) part of $_{(0)}L^6 \tilde{A}_{ij}$ with respect to the metric $_{(0)}f_{ij}$ as the tensor modes. Then the question is if the TT part can be uniquely determined. Fortunately, this is known to be possible [5]. For any symmetric traceless second rank tensor X_{ij}, we have the decomposition,

$$
\begin{aligned}
X_{ij} &= \tilde{D}_i W_j + \tilde{D}_j W_i - \frac{2}{3} \tilde{\gamma}_{ij} D^k W_k + X_{ij}^{TT} \\
(O\,W)_i &\equiv -\tilde{D}^j (\tilde{D}_i W_j + \tilde{D}_j W_i - \frac{2}{3} \tilde{\gamma}_{ij} D^k W_k) = -\tilde{D}^j (X_{ij}),
\end{aligned} \tag{19}
$$

where W_i satisfies the second-order differential equation (19). York showed that the solution is uniquely determined [5]. Thus, identifying X_{ij} with $_{(0)}L^6 \tilde{A}_{ij}$, we immediately see that the transverse parts of $_{(0)}L^6 {}_{(2)}F_{ij}$ and $_{(0)}L^6 {}_{(2)}C_{ij}$ represent the gravitational wave modes. Furthermore, from their time-dependence, it is clear that the former is the growing mode while the latter is the decaying mode, as in the case of linear theory.

4 Conclusion

In this paper, focusing on the simple case of a perfect fluid with constant adiabatic index, we have considered nonlinear perturbations on superhorizon scales in the context of (spatial) gradient expansion. We have adopted the uniform Hubble slicing, derived the general solution valid to second order in spatial gradients, and identified the physical meaning of those solutions. In particular, the relation of these degrees of freedom to those in the linear perturbation theory has been clarified. In doing this identification of various modes, we have found that the tensor modes contained in the extrinsic curvature (the time derivative of the metric) can be identified only non-locally.

We note that our result contains not only nonlinear scalar modes but also the nonlinear coupling of scalar, vector and tensor modes. Thus, if the framework we have developed is extended to the case of a (multi-component) scalar field, the resulting formalism will be a powerful tool to investigate various non-linear, non-local effects from the inflationary cosmology, especially non-Gaussianity of curvature perturbations from inflation.

References

[1] D. N. Spergel *et al.*, arXiv:astro-ph/0603449.

[2] D. H. Lyth, K. A. Malik and M. Sasaki, JCAP **0505**, 004 (2005) [arXiv:astro-ph/0411220].

[3] S. M. Leach, M. Sasaki, D. Wands and A. R. Liddle, Phys. Rev. D **64**, 023512 (2001) [arXiv:astro-ph/0101406].

[4] M. Shibata and M. Sasaki, Phys. Rev. D **60**, 084002 (1999) [arXiv:gr-qc/9905064].

[5] J. W. York, J. Math. Phys. **14**, 456 (1973).

[6] Y. Tanaka and M. Sasaki, arXiv:gr-qc/0612191.

The Engines behind Supernovae and Gamma-Ray Bursts
The Role of Convection and Rotation

Chris L. Fryer[1]

CCS Division, MS D409, Los Alamos National Laboratory, Los Alamos, NM 87545, USA

Abstract

We review the different engines behind supernova (SNe) and gamma-ray bursts (GRBs), focusing on those engines driving explosions in massive stars: core-collapse SNe and long-duration GRBs. Convection and rotation play important roles in the engines of both these explosions. We outline the basic physics behind convection in core-collapse and discuss the wide variety of ways scientists have proposed that this physics can affect the supernova explosion mechanism, concluding with a review of the current status in these fields.

1 Introduction

Supernovae and Gamma-Ray Bursts are the two most energetic explosions in the universe since the big bang. For a brief time, they outshine the galaxies in which they reside. Observations have led to the classification of these outbursts based on their observational properties. For supernovae, the classification is based primarily on their spectra: type II SNe have strong hydrogen lines, type I SNe exhibit hydrogen lines at late times if at all. Type I supernovae are further distinguished by the presence of strong silicon lines (Ia), absent in Ib/c supernovae; Ib supernovae have helium lines, absent in Ic supernovae. GRBs are differentiated by the duration of the burst and "hardness" of its spectra: long-hard bursts with durations above a few seconds and the short-soft bursts. A third intermediary category may exist. An additional feature of these observations is that long-duration GRBs have type Ic supernovae associated with them.

Theorists have proposed a wide variety of mechanisms for these explosions, from electrical storms in the earth's stratosphere to colliding strings in the early universe. Indeed, just 25 years after the discovery of GRBs, over 100 models existed for GRBs[50]. However, only a handful of models have emerged as "favorite" engines behind all the types of GRB and SN explosions. Figure 1 reviews the 3 main types of SN and 2 types of GRB and the energy source/mechanism behind the explosions. Type Ia SNe are produced by the thermonuclear explosion of a white dwarf. In the standard picture, the ignition of the white dwarf occurs when its mass exceeds the Chandrasekhar mass (generally through accretion from a binary companion). This is the only explosion powered by nuclear energy. All other explosions are produced by the release of gravitational energy. Short-Duration GRBs are believed to be produced by gravitational energy released during the merger of two neutron stars and the subsequent accretion onto the black hole formed during this merger.

Type Ib/c SNe, Type II SNe and long-duration GRBs are ALL believed to be produced in the collapse of a massive star down to a compact object. For most SNe, the outburst is produced when a massive star ($\gtrsim 9M_\odot$) collapses down to a neutron star. Long-duration GRBs are produced in the collapse of a very massive star ($\gtrsim 20M_\odot$) down to a black hole. Although the source of energy for both these explosions is the same potential energy released during the collapse, it is believed that the mechanism that converts this energy into an explosion is very different. The mechanism behind long-duration GRBs also produces associated type Ic SNe, so the line dividing these different explosions is not concrete, but we shall argue below that these "type Ic" SNe have different characteristics from "normal" type Ic SNe.

This paper reviews the role of convection in the explosion mechanisms of core-collapse SNe and GRBs. But before we focus on this particular piece of physics, let's review the basic engines involved.

---

[1]E-mail:fryer@lanl.gov
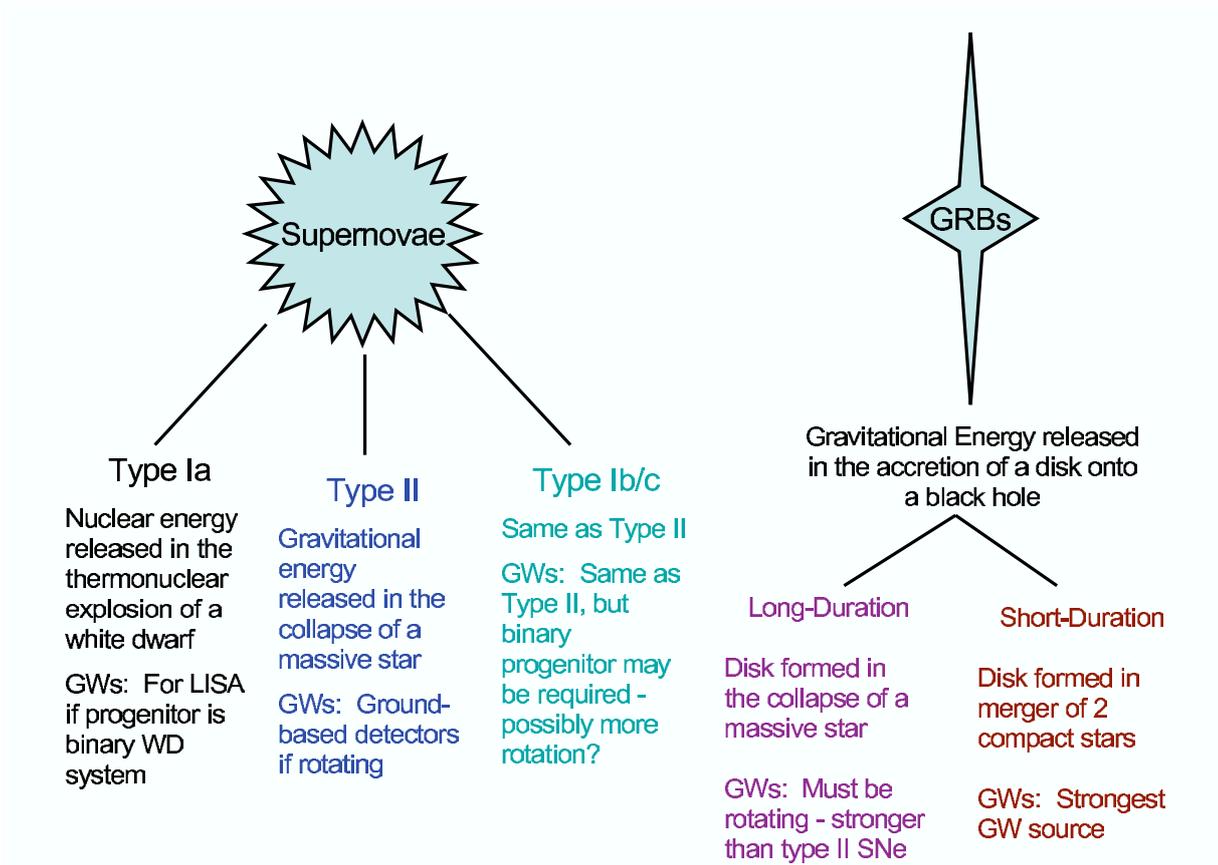
Figure 1: Three basic SN types and two primary GRB types. The basic SN types are distinguished based on the appearance of different elements (H, He, Si) in the spectra of the explosions. The GRB types are distinguished by the duration of the gamma-ray emission. Two SNe types (II,Ib/c) and one GRB class (long-duration) are believed to be produced by the collapse of massive stars. This paper focuses on the role of convection on the explosions behind these core-collapse events.

1.1 The Basic Engine Powering Core-Collapse Supernovae

Stars are powered by the nuclear fusion of material in their cores. For stars like the sun, this fusion stops after the core has "burned" its hydrogen into helium. But for more massive stars, the core is able to become sufficiently hot to fuse the helium ashes into carbon. In stars above $\sim 9 M_\odot$, this burning process continues through the fusion of silicon into iron. The fusion of iron to heavier elements does not release any further energy and the build up of an iron core marks the end of the life of even the most massive stars. When this core becomes so large that pressures and densities dissociate the iron to lighter atoms (removing thermal support) and induce the capture of electrons onto protons (removing electron degeneracy support), the core collapses.

The core collapses until it reaches nuclear densities where nuclear forces and neutron degeneracy pressure halt the collapse. This marks the initial formation of the proto-neutron star (roughly $0.9 M_\odot$) and sends a "bounce"-shock back through the star. This shock is extremely hot and most of its energy is stored in thermal energy. Initially, photons, and even neutrinos, are trapped in this shock. But as the shock moves to lower densities, the neutrinos can leak out of the shock, removing most of its energy and causing it to stall. This occurs roughly between 100-200 km. The stall leaves behind a region between the proto-neutron star and the stalled shock with a negative entropy gradient (high entropies below lower entropies) that initiates convection in this region. But this convection continues to be driven by a number of instabilities (to be discussed below) that Herant et al.[27] argued would allow the convective region to more-efficiently transfer the potential energy released (stored in the thermal energy of the proto-neutron star) to be converted to kinetic energy and ultimately drive a supernova explosion. After over a decade of debate, there is now a general consensus that this convective region is indeed critical to the supernova explosion engine. It allows the transfer of energy from the proto-neutron star to the stalled shock, pushing back against the infalling star and ultimately driving a supernova explosion.

1.2 The Basic Engine Powering Long-Duration GRBs

The engine behind both short and long-duration GRBs is powered by the accretion of matter onto a black hole. If this accreting matter has enough angular momentum to form a disk around the black hole, its energy can be extracted by first converting it into magnetic fields or neutrinos and then depositing this energy further out to drive a relativistic explosion[49]. A number of progenitor models exist to produce such black hole accretion disk (BHAD) systems and the relative merits of the two conversion mechanisms (neutrinos or magnetic fields) have been studied in detail assuming a simple disk picture[52, 17].

In 1993, Woosley[61] proposed that the BHAD engine could be produced in the collapse of a rotating massive star. MacFadyen & Woosley[42] modeled the first such collapse of a massive star in 2-dimensions and, using the simple disk models of Popham et al.[52] found that by injecting energy above the disk, they could produce a jet-like explosion that could explain the features of long-duration GRBs.

Let's outline the basic picture behind this collapsar engine. It begins with the same evolution as the stars we studied in our basic supernova engine. A massive star collapses, forms a proto-neutron star and this engine convects. However, if the star is more massive than roughly $20 M_\odot$[16], the supernova engine is unable to produce a strong explosion. If it produces a weak explosion, it is unable to disrupt the entire star and material will eventually fall back onto the proto-neutron star, causing it to collapse to a black hole. For extremely massive stars ($\gtrsim 40 M_\odot$), the supernova engine may not work at all, producing a black hole without any supernova explosion at all (but as we shall see, this collapse may still produce an explosion).

If the star is rotating, some of the material falling on the newly-formed black hole will hang up in an accretion disk around the black hole. Then it is assumed that either the neutrinos emitted from the hot disk or magnetic fields generated in the disk will convert the potential energy released into an explosion. Popham et al.[52] made a series of advection dominated accretion flow simulations to show that although both the neutrino and magnetic field conversion mechanisms are plausible, the magnetic field conversion mechanisms may well be required for the strong GRB explosions that are observed.

A series of papers have studied this disk picture in more detail. For the neutrino-annihilation transfer mechanism, semi-analytic calculations can provide quantitatively accurate estimates. di Matteo et al.[13] studied this mechanism at the highest accretion rates and found that neutrino trapping severely limited the amount of energy injected by neutrinos in this regime. Fryer & Mészáros[20] focused on progenitors,

finding that for massive stars, the black hole would become too massive by the time the axis above the disk cleared for the simple neutrino-annihilation disk-mechanism to work. All these studies agreed that it is unlikely that neutrino-annihilation will work for GRBs produced in stellar collapse. It is much more difficult to accurately estimate the role of magnetic fields. Although many papers exist predicting what magnetic fields can do for GRBs produced in stellar collapse[49, 35, 43] only a few quantitative calculations of these magnetic fields have been made[53]. Even these calculations are constrained by a number of assumptions and 2-dimensional calculations.

Three-dimensional calculations of these collapser models have shown us that the basic disk picture is far too simple and the behavior of matter near the black hole is much more similar to a supernova engine than that of an accretion disk[54]. Convective instabilities develop and dominate the flow of matter. Rockefeller et al. [54] also found that viscous forces may also be able to extract angular momentum energy driving outflows. How this leads to a GRB remains to be seem, but it is clear that nature is much more complex than we first imagined and a lot of work remains to fleshing out the GRB engine. But the first step is to understand this convection and we will focus on this aspect of the GRB engine here.

2 Convection in Supernovae

2.1 History

In 1979, Epstein[14] argued that lepton gradients in the proto-neutron star would drive convection that would help transport neutrinos deep in the proto-neutron star to its surface, allowing those neutrinos to better heat the material in the shocked region, driving an explosion[2]. Shortly thereafter, a more complete picture based on the first multi-dimensional calculations of convection in supernovae[41, 3, 57] argued that the convection was driven by the interplay between entropy and lepton gradients. These calculations also focused on the role of convection in the proto-neutron star core and the effect this convection would play on the neutrino flux, but they also realized that the role of convection might lead beyond just transporting neutrinos.

The research in the 1980s focused mostly upon the convection in the neutron star. Lattimer and collaborators[39, 7] took advantage of the latest advances in dense equations of state to better estimate the convection and hence the neutrino fluxes from the proto-neutron star. Burrows[8] argued, using semi-analytic calculations, that convection at the neutrinosphere would grow to encompass the entire proto-neutron star. This convection was later confirmed by multi-dimensional simulations[36]. With appropriate tweaking, Wilson & Mayle[59, 60] found that they could get explosions with this proto-neutron star convection, focusing on the doubly diffusive regime where heat diffusion removed the stable entropy gradient faster than lepton diffusion diminished the unstable lepton gradient. The increased neutrino flux from this convection was just enough to produce an explosion.

But all large-scale, multi-dimensional calculations since Herant et al.[27] that include the shocked region only exhibit weak convection in the proto-neutron stars. Whether or not strong convection occurs in the proto-neutron star is still a matter of debate. A very good review of our current understanding of this analysis has been done by Bruenn et al.[4].

However, in the 1990s, the focus of convection in supernovae turned to the region above the proto-neutron star. In trying to explain the mixing in the ejecta seen in SN 1987A, Herant et al.[26] argued that the convection above the proto-neutron star driven primarily by entropy gradients could be the key to the explosion. Despite discouraging results by Yamada et al.[62] and Miller et al.[45] arguing that the convection above the proto-neutron star was only a minor effect, the simulations of Herant et al.[27] argued that this convection actually played a key role in the explosion. Convection above the proto-neutron star converted thermal energy deposited by neutrinos just above the proto-neutron star to kinetic energy in the explosion.

The effects of convection above the proto-neutron star (PNS) outlined by Herant et al.[27] can be illustrated by comparing the differences between the 1-dimensional (fig. 2) and multi-dimensional (fig. 3) pictures. In the 1-dimensional scenario (fig. 2), material from the infalling star piles up on the stalled shock. For a successful explosion to develop, the engine must be able to push the matter outward. With

---

[2]At the PNS surface, electron neutrinos are no longer trapped and, because of this, this surface region becomes extremely electron poor, producing a gradient in the lepton number.

1-Dimensional Supernovae

PNS Surface
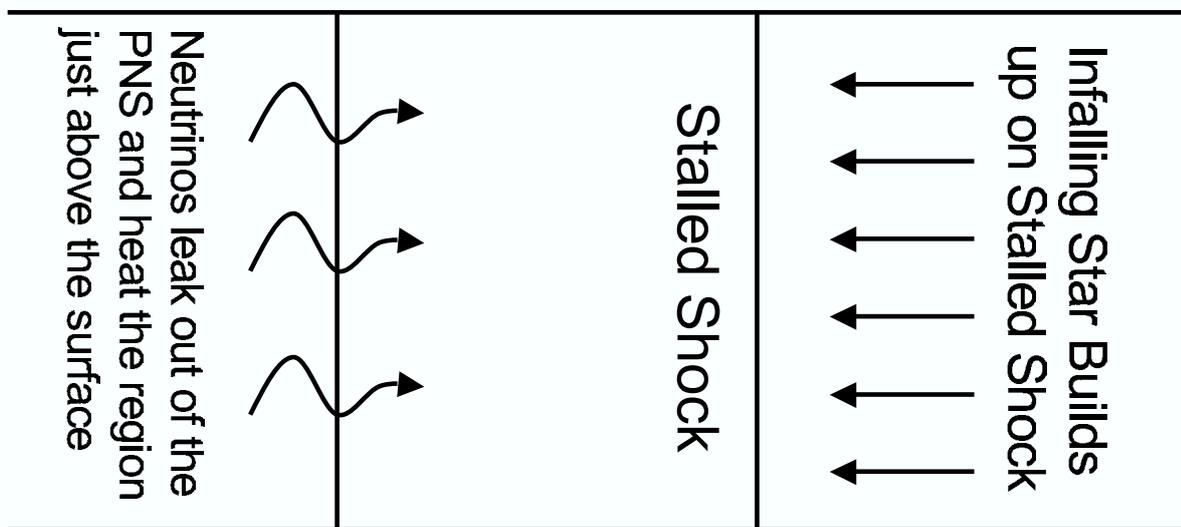
Neutrinos leak out of the PNS and heat the region just above the surface

Stalled Shock

Infalling Star Builds up on Stalled Shock

The neutrino-heated region becomes hot enough to emit neutrinos itself without pushing out the shock considerably.

Figure 2: Supernovae in the 1-dimensional picture. Matter is not allowed to mix, so the transfer of energy is much more difficult.

Convection Enhanced Supernovae

- **Neutrino Heated Material Rises, Cooling Adiabatically Before Losing Its Energy Via Neutrino Emission**

- **Infalling Material Convects Down to the Proto−Neutron Star. It Does NOT Pile Up at the Accretion Shock.**

Infalling Material Produces Accretion Shock

$$P_{shock} = \frac{1}{2}\, \rho_s\, v_{ff}^2$$

$\tau_\nu = 1$

Proto NS

~50km

Entropy Driven Convection

~100−300km

The Convective Region Must Overcome this Pressure to Launch an Explosion
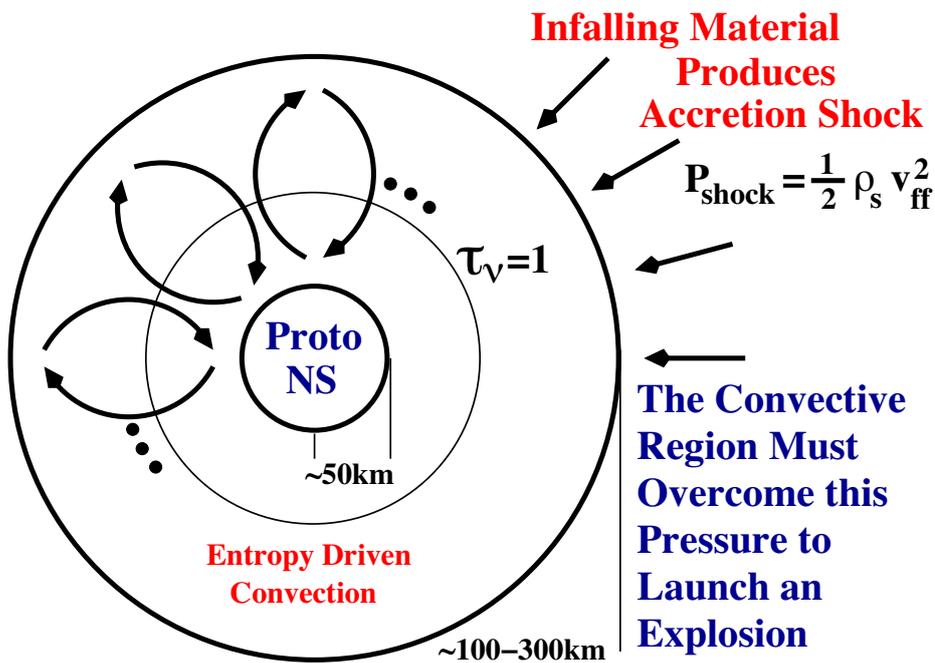
Figure 3: The convection picture from Herant et al.[27].

time, this material piles up on the shock, making the explosion harder and harder to explode. The neutrinos leaking out of the PNS primarily heat the region just above the PNS surface. If this region can not expand, it heats up so high that it too emits neutrinos, losing all of the energy it has gained from the PNS. These two issues make it very difficult for a 1-dimensional calculation to produce a successful explosion.

Convection above the PNS alleviates both of these issues. The infalling material falls onto the shock, but it does not build up on the shock(fig. 3). Instead, convection allows this material to flow down toward the PNS surface. This material does not build up on the shock, so does not contribute to the matter that must be pushed outward to drive a successful explosion. It accretes onto the PNS, depositing additional energy that can help drive a supernova explosion (possibly through neutrino emission). Both of these effects make it easier to produce an explosion. In addition, any heating just above the PNS surface causes the heated material to rise upward, converting its thermal energy into kinetic energy before it gets so hot that it re-emits that energy in the form of neutrinos. So convection also allows the region above the PNS to better convert its thermal energy into kinetic energy to drive an explosion.

What does this look like in a real simulation? Figure 4 shows a snapshot in time of the convective region above the proto-neutron star. The vectors show the direction and the shading denotes entropy. At roughly $300\,\mathrm{km}$ one can easily make out the edge of the shocked region where the infalling star hits the top of the convective region. The proto-neutron star ends roughly at 40-50 km. In this region, hot material at the base rises upward and pushes the shock outward. Infalling material pushes back and as it piles up, it flows down onto the proto-neutron star.

Although the Herant et al.[27] result was immediately corroborated by Burrows et al.[9], until recently, the debate about the role of convection met violent arguments. Janka & Müller[33] argued that convection could help the explosion, but only mildly. Mezzacappa et al.[44] argued that convection did not produce explosions. In 2003, Buras et al.[5] argued that explosions could not occur in collapsing stars, even with convection, without the invocation of new microphysics or magnetic fields. On the other extreme, Fryer and collaborators [16, 19, 21, 22, 24] produced explosions for all stars below about $20\,\mathrm{M}_\odot$ unless they artificially damped out convection. Arguments about numerical techniques ensued: e.g. hydrodynamic techniques, transport techniques, errors in the equation of state. Of the 4-5 supernova groups across the world, all but 1 focused on doing better neutrino transport.

In the past few years, this picture has changed. Blondin et al.[1] discovered that a number of instabilities exist in the region above the PNS. Burrows et al.[10] found that these instabilities could drive an explosion independent of neutrino transport scheme. The group led by Janka suddenly started to produce explosions[6]. At this point, over a decade after the Herant et al.[27] work proposed it, there is reasonable consensus in the field that convection above the PNS is critical in the supernova paradigm.

Why does it take so long for scientists to converge on this result? Because it is a difficult problem with a lot of interacting physics, core-collapse explosions must be modeled computationally, and this means scientists must be able to discern between numerical and real effects. And this can be difficult indeed. An example of how hard this is to do can be shown in the range of recent results from the Janka group. In 2003, they argued that convection could not produce explosions without new microphysics or magnetic fields. Two years later, they argued that they could get explosions for stars less massive than $12\,\mathrm{M}_\odot$, but nothing bigger could explode. At the Texas Symposium in Melbourne (Dec. 2006), they admitted that they could get $15\,\mathrm{M}_\odot$ stars to explode without new microphysics or magnetic fields. Issues in their numerics fooled them not once, but twice. This group is very strong in computational astrophysics and is considered by all to be excellent in both computational science and supernovae. But they, as we all do, struggle to disentangle the numerics from the physics. Bear this in mind when we discuss the current state-of-the-art results. What we believe now may be incorrect.

2.2 Convection Basics

The focus of most of the convective instabilities has been on either lepton or entropy gradients. These can be understood fairly easily by linear stability criteria and have been known since the 50s[40, 34]. To determine whether a region is Rayleigh-Taylor unstable to entropy gradients, let's examine a simple case of a homogeneous material with an entropy gradient and a constant gravity vector. Let's take a blob of material in this atmosphere with entropy $[S(r_0) = S_0]$ and slightly raise its entropy ($S_{\mathrm{bub}} = S_0 + \Delta S$).
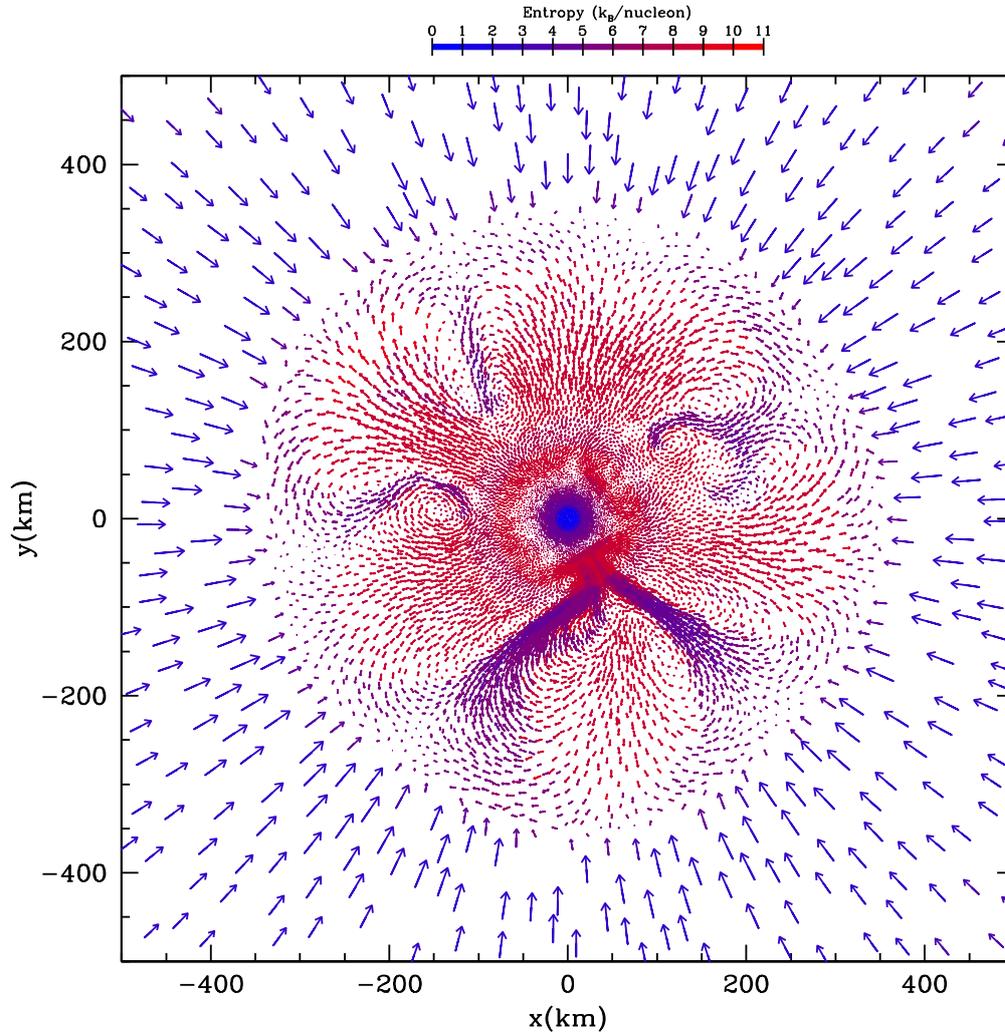
Figure 4: Convection in a core-collapse supernovae[19]. This plot shows a slice of a 3-dimensional simulation at a snapshot in time as the convective region starts to push the star outward[19]. The base of the convective region (surface of the PNS) is at roughly 40-50 km and the top of the convective region (position where the infalling stellar material shocks against the convective region).

As it evolves into pressure equilibrium with the material around it, its density will be lower than its surroundings (for most normal equations of state), and it will rise. If the entropy increases with increasing radius (r), then the bubble will only rise until $S_0 + \Delta S = S(r)$ where the density of the bubble and that of the atmosphere are the same. Such an atmosphere is stable to convection. If the entropy remains constant or decreases at increasing radius, the equilibrated bubble will always have a lower density than its surroundings and will continue to rise. Such an atmosphere is unstable to entropy gradients. Simply stated, the criterion for instability is:

$$dS/dr < 0. \tag{1}$$

If we include lepton (Y_L) gradients, the more general criterion for instability becomes:

$$(\partial P/\partial S)_{\rho,Y_L} dS/dr - (\partial P/\partial Y_L)_{\rho,S} dY_L/dr < 0 \tag{2}$$

where $(\partial P/\partial S)_{\rho,Y_L}$ is the partial derivative of the pressure with respect to the entropy and constant density ρ and lepton number Y_L and $(\partial P/\partial Y_L)_{\rho,S}$ is the corresponding partial derivative of the pressure with respect to the lepton number.

From this general equation, we can understand the bulk of the convective instabilities studied in core-collapse supernovae. The "Lepton-driven" instability is determined by the second term in equation 2. Essentially it says that if there is heavy material on top of light material, the light material will rise while the heavy material descends. The escape of the electron neutrinos at the surface of the PNS produces a region where there is a high neutron/electron ratio ($> 3 - 5$) above a region where this value is below 2.

In the region above the PNS, entropy-driven convection can dominate. As the initial bounce shock moves outward, it weakens and produces a lower shift in the entropy, leaving behind a negative entropy gradient. This starts entropy-driven convection. Heating near the PNS surface contines to maintain this entropy gradient, producing convection.

The electron neutrino emitted during electron capture is less energetic than the energy released during the capture. The neutron-rich region at the surface of the PNS tends to be hotter than the region below it. So although it is unstable to lepton gradients, the entropy gradient stabilizes against this convection. This leads to a doubly-diffusive or "salt-finger" instability[3]. It is this doubly-diffusive instability that must be understood if we are to solve whether convection within the PNS is important or not.

For the convection above the PNS, the lepton gradient is a negligible effect and we can estimate the convective instability (and timescale) on the entropy gradient alone. One way to estimate the timescale of this convection is to use the Brunt-Väisälä frequency ω[12]:

$$\omega^2 = g/\rho(\partial\rho/\partial S)_{\mathrm{P}}(\partial S/\partial r) \tag{3}$$

where $(\partial\rho/\partial S)_{\mathrm{P}}$ is the partial derivative of the density with respect to entropy at constant pressure, and $g \equiv GM_{\mathrm{enclosed}}/r^2$ is the gravitational acceleration. Here G is the gravitational constant and M_{enclosed} is the enclosed mass at radius r. If $(\partial S/\partial r)$ is negative, ω^2 is negative and the region is unstable. The timescale for this convection (τ_{conv}) is $(|1/\omega^2|)^{1/2}$.

In the limit where radiation pressure dominates the pressure term (reasonably true at the accretion shock), this equation becomes:

$$\omega^2 = g/S(\partial S/\partial r) \approx (1/S)(GM_{\mathrm{enclosed}})/r^2)(\Delta S/\Delta r) \tag{4}$$

where ΔS is the change in entropy over distance Δr. Here we used the following relations: $S \propto T^3/\rho$ and Pressure $\propto T^4$. For the massive $23\,\mathrm{M}_\odot$ star studied by Fryer & Young[25], where $g \approx 1.5 \times 10^{12}\,\mathrm{cm\,s^{-2}}$, $\Delta S/S \approx 0.2$, and $\Delta r \approx 10^7\mathrm{cm}$, the convective timescale is roughly $2\,\mathrm{ms}$. Even on core-collapse timescales, this is extremely rapid and most simulations do not reproduce this result, probably because numerical viscosity (either through SPH artificial viscosity or numerical advection in grid codes) damps out the convection.

Some scientists prefer to estimate the growth time of Rayleigh-Taylor instabilities based on a more simplified equation using the Atwood number A:

$$\omega^2_{\mathrm{Atwood}} = kgA \tag{5}$$

---

[3]So-named because it is like the hot Mediterranean Sea pouring into the Atlantic Ocean. The Sea is saltier but hotter than the Ocean. At first, the two fluids are stable, but as the heat from the Mediterranean diffuses into the water below it, lepton-driven gradients dominate over the stabilizing entropy gradient, allowing convection to develop.

where $A = (\rho_2 - \rho_1)/(\rho_2 + \rho_1)$ and k is the wave number. Such an equation is designed for simplistic examples of a two density fluid chamber. But, if we again assume a radiation pressure dominated gas, this equation becomes:

$$\omega_{\text{Atwood}}^2 = k(GM_{\text{enclosed}})/r^2)(\Delta S/S). \tag{6}$$

If we pick a wave number roughly of the size scale of our convective region, this equation is identical to our equation derived using the Brunt-Väisälä frequency.

2.3   Where Are We Now?

Blondin et al.[1] introduced a new feature into convection above the PNS. Building upon the work of Houck & Chevalier[28], they argued that advective-acoustic (or vortical-acoustic) instabilities would develop low-mode oscillations. This has become the focus of a lot of the multi-dimensional results in the past few years[55, 51, 10, 15] and has brought a new appreciation of the complexity of convection above the PNS.

There are some issues to this new convective instability that are still being realized by the supernova community. First and foremost, the existence of this instability does not preclude the existence of the Rayleigh-Taylor instabilities scientists have focused on in the past. Indeed, because the growth time of the accretion shock instabilities tend to be $> 100\,\text{ms}$, Rayleigh-Taylor instabilities will dominate at early times (Yamada, presented at this meeting[64, 65]). Figure 5 shows the explosion roughly $100\,\text{ms}$ after bounce. At this time, the only strong instabilities are Rayleigh-Taylor. As the edge of the shock front moves outward, the Rayleigh-Taylor instabilities will naturally develop lower order modes (Rayleigh-Taylor modes will have instabilities roughly the size of the convective region). Roughly $350\,\text{ms}$ after the explosion, the Rayleigh-Taylor instabilities still dominate (Fig. 6), but an $l = 1$ mode convection has developed that almost assuredly is an accretion instability. So this new instability will only play a role in extremely delayed explosions.

The long delay in the development of accretion shock instabilities places limits on the effectiveness of this instabilty in driving supernova explosions. The explosion energy is derived from the energy stored in the PNS or the convection region above the PNS. Once the explosion is launched, it is very difficult to inject further energy in the shock (unless we invoke magnetic fields). Fryer[23] made some simple estimates of the energy making the following assumptions: 1) the explosion energy is limited to the energy in the convective region, 2) the convective region can be mimicked by a radiation dominated gas ($\gamma = 4/3$), 3) the structure total energy in the convective region is not too different from the equilibrium solution. In pressure equilibrium, the pressure profile $[P(r)]$ of a radiation dominated gas is[11]:

$$P(r) = [1/4 M_{\text{NS}} G(S_{\text{rad}}/S_0)^{-1}(1/r - 1/r_{\text{shock}}) + P_{\text{shock}}^{1/4}]^4 \text{erg cm}^{-3}, \tag{7}$$

where M_{NS} is the mass of the proto-neutron star, G is the gravitational constant, S_{rad} is the entropy in Boltzmann's constant per nucleon, $S_0 = 1.5 \times 10^{-11}$ and $r_{\text{shock}}, P_{\text{shock}}$ are the radius and pressure of the accretion shock produced where the infalling stellar material hits the convective region. P_{shock} is set to the ram pressure of the infalling material $\equiv 1/2\rho v_{\text{ff}}^2$ where ρ is the density of the material and v_{ff} is the free-fall velocity at the shock. In our derivation, we will set our free parameter to the accretion rate ($\dot{M}_{\text{acc}}$) of the infalling material. Using mass continuity, $\rho = \dot{M}_{\text{acc}}/(4\pi r_{\text{shock}}^2 v_{\text{ff}})$, the pressure at the shock is:

$$P_{\text{shock}} = (2GM_{\text{NS}})^{0.5}\dot{M}_{\text{acc}}/(8\pi r_{\text{shock}}^{2.5}). \tag{8}$$

The energy density for a radiation dominated gas is just $3 \times P(r)$:

$$\begin{aligned}
u(r) &= 3\left[4.7 \times 10^8 \frac{M_{\text{NS}}}{M_\odot} \frac{10 k_{\text{B}}\text{nuc}^{-1}}{S_{\text{rad}}} \left(\frac{10^6\text{cm}}{r} - \frac{10^6\text{cm}}{r_{\text{shock}}}\right) \right. \\
&+ \left. 1.2 \times 10^6 \left(\frac{M_{\text{NS}}}{M_\odot}\frac{\dot{M}_{\text{acc}}}{M_\odot s^{-1}}\right)^{0.25} \left(\frac{2 \times 10^7\text{cm}}{r_{\text{shock}}}\right)^{5/8}\right]^4 \text{erg cm}^{-3}.
\end{aligned} \tag{9}$$

Note that the near the neutron star surface, the ram pressure is small compared to the pressure component compensating for the gravity of the neutron star. This means that the energy density in this region is
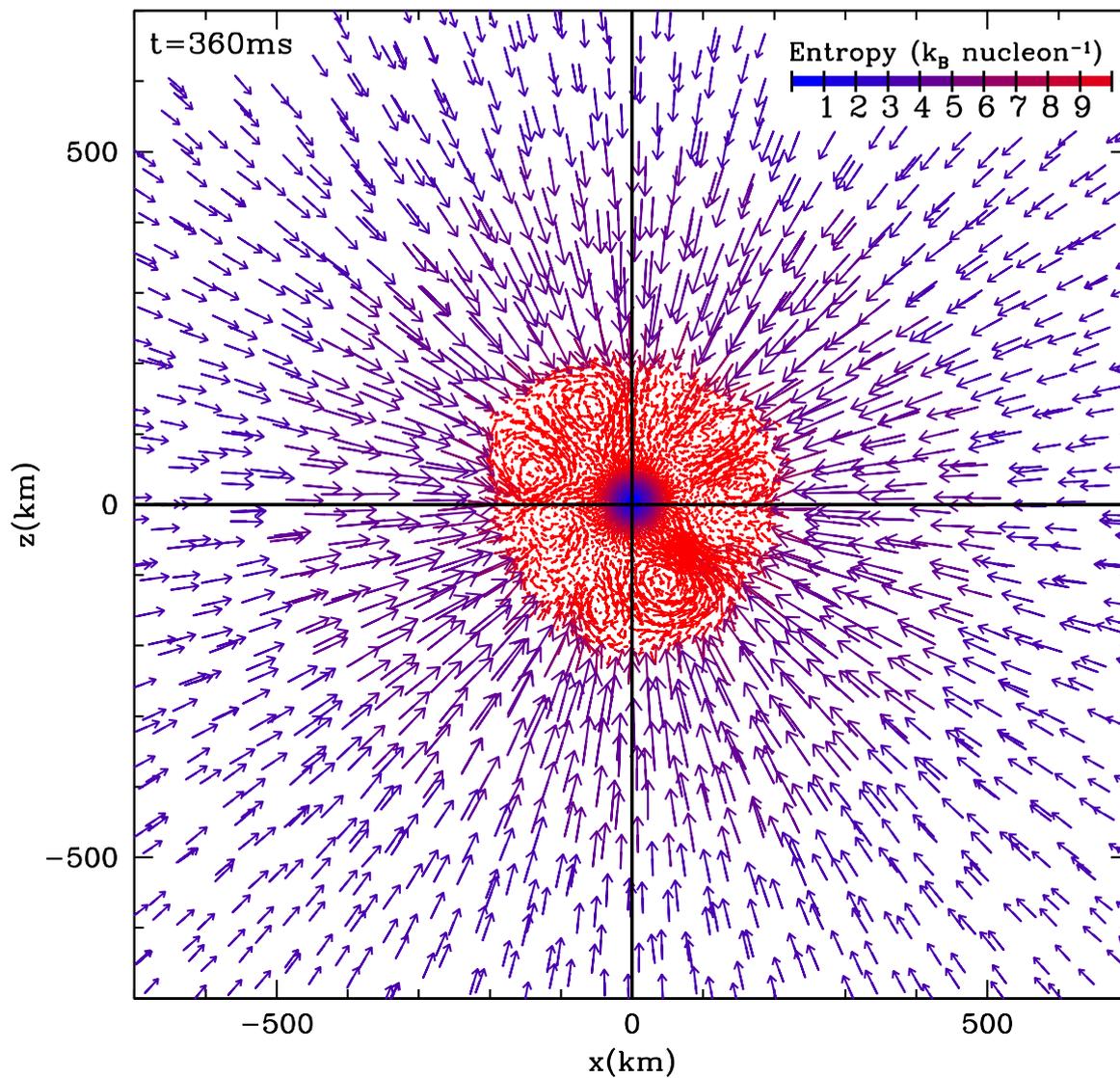
Figure 5: Slice of a 3-dimensional collapse of a $23\,M_\odot$ roughly $100\,\mathrm{ms}$ after bounce[25]. This quickly into the explosion, we do not expect any shock instabilities to have developed. Indeed, the the convective cycles, with sizes comparable to the size-scale of the convection region.
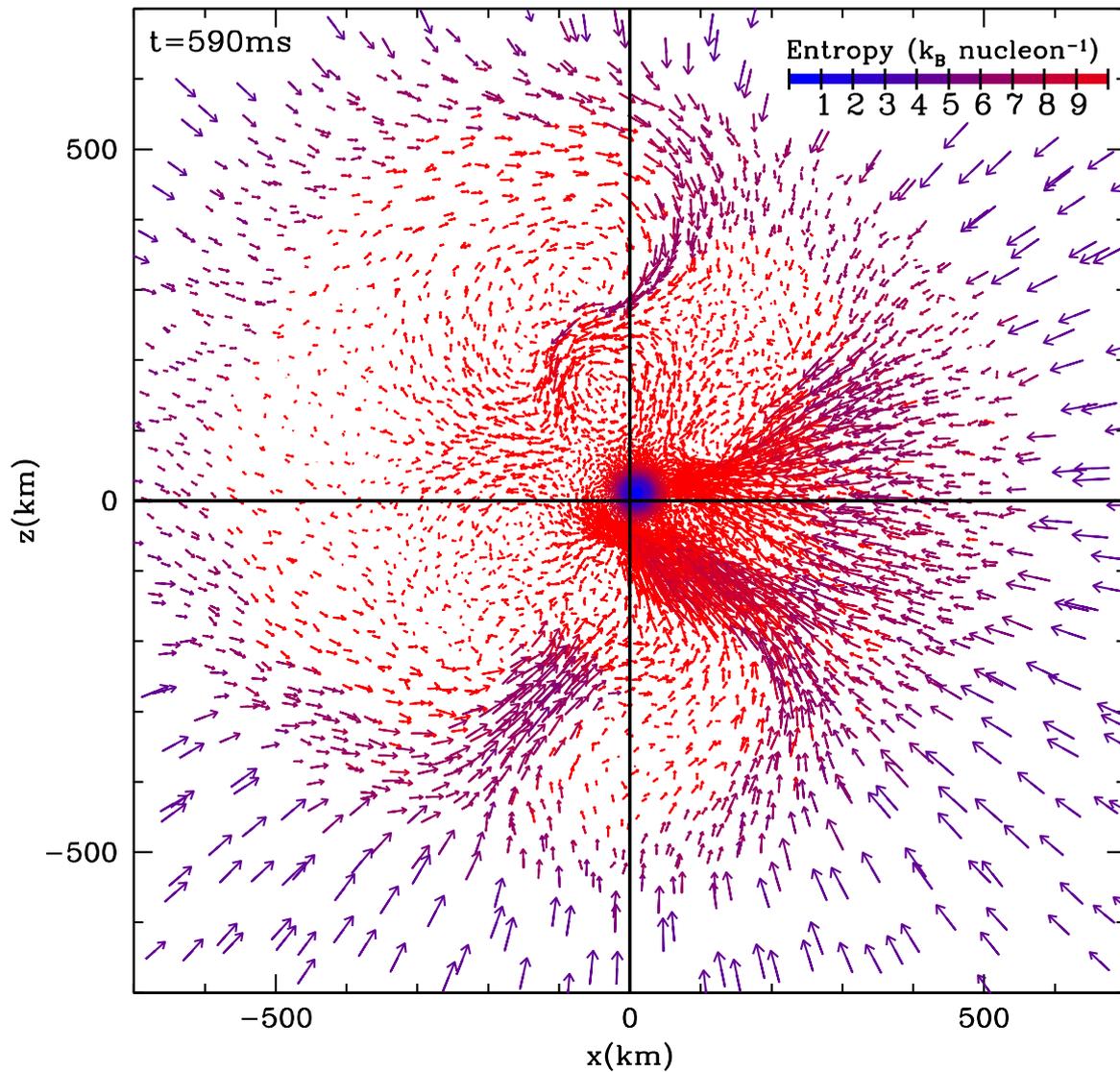
Figure 6: Slice of a 3-dimensional collapse of a $23\,M_\odot$ roughly $350\,\mathrm{ms}$ after bounce[25]. By this time, we expect shock instabilities to have developed, and an l=1 mode has developed that could well be caused by this instability. But Rayleigh-Taylor instabilities also exist.

dominated by the neutron star's mass. At higher radii, the energy density is set by the ram pressure. The ram pressure, in turn, is determined by the density structure of the star, but for stars less massive than 15-20 $M_\odot$, this infall rate drops considerably after the first 50-200 ms[16].

If the explosion has a long delay, there won't be much energy stored in the convection region (see Fryer 2006 for more details). It is possible that the explosion energy can be stored in the PNS and have it inject this energy even after the launch of the shock. Burrows et al.[10] suggested that accretion shocks could excite oscillations in the PNS. These oscillations could store energy to drive an explosion, but Yamasaki & Yamada[64, 65] found that this energy is less than 10^{50} erg (and is inefficient at imparting this energy into the envelope), a full order of magnitude less than what we need to produce a "normal" supernova explosion.

The long growth-time of the acoustic instabilities means both that Rayleigh-Taylor instabilities dominate at early times when we need to make the explosion occur if we want a strong explosion. For the accretion shock instabilities to be important for supernovae, we must find a different source for the explosion energy. One possible source is rotational energy in the PNS. With strong magnetic fields, a spinning neutron star can inject considerable energy into the expanding supernova ejecta. To understand that, we must understand the role of convection when rotation is added to the picture.

3 Convection with Rotation

3.1 History

Much of the early work studying rotation in stellar collapse focused on how rotation could drive an explosion[47, 2, 58, 46, 31, 32]. Most of these papers required extremely high rotation rates and strong magnetic fields. But these mechanisms generally predicted an explosion well before the core of the star reached nuclear densities and the neutrino fluxes from these explosion mechanisms fell far short of what was observed in SN 1987A. In addition, the angular momentum required far exceeded what current stellar evolution models could predict.

In the 90s, scientists started focusing on the role rotation played in modifying the convection above the PNS. Yamada and collaborators[56, 63] argued that neutrinos would heat along the rotation axis much more effectively than along the equator, driving stronger convection along this axis. Fryer and collaborators[18, 21] discussed a different effect, the fact that the angular momentum would stabilize against convection along the equator. Both of these effects lead to stronger convection along the rotation axis and a larger asymmetry in the explosion. This asymmetry has been used to explain many observational features of core-collapse supernovae[48, 37, 29, 30].

3.2 Basics of Convection with Rotation

To understand the effect of rotational gradients on convection, we can use a similar linear stability analysis to the one we used for lepton and entropy gradients 7. Let's consider the net force on the blob in a rotating atmosphere with an entropy gradient:

$$\Delta a = g\left(1 - \frac{\rho + \Delta\rho}{\rho_{\text{blob}}}\right) + \frac{j_{\text{blob}}^2 - (j + \Delta j)^2}{(r + \Delta r)^3} \tag{10}$$

where $j_{\text{blob}} = j$. For acceleration to remain positive (so the blob will continue to rise) any entropy gradient must overcome an angular momentum gradient. The corresponding Solberg-Høiland instability criterion is (Endal & Sofia 1978):

$$\frac{g}{\rho}\left[\left(\frac{d\rho}{dr}\right)_{\text{adiabat}} - \frac{d\rho}{dr}\right] > \frac{1}{r^3}\frac{dj^2}{dr} \tag{11}$$

The left half of this equation corresponds to the entropy gradient condition we've already studied. But the condition for instability set to zero is altered by the presence of an angular momentum gradient. If the angular momentum increases with increasing radius as it does for our core collapse models, then the entropy gradient must overcome the angular momentum gradient to drive convection. In our simulations,

Rotation

Models of Rotating Stars Now Exist!

Rotation Important for:

Neutron Star Spins and the Nature of Young Pulsars

Gravitational Wave Emission: Bar-Modes and R-modes

Asymmetric Supernova Explosions!
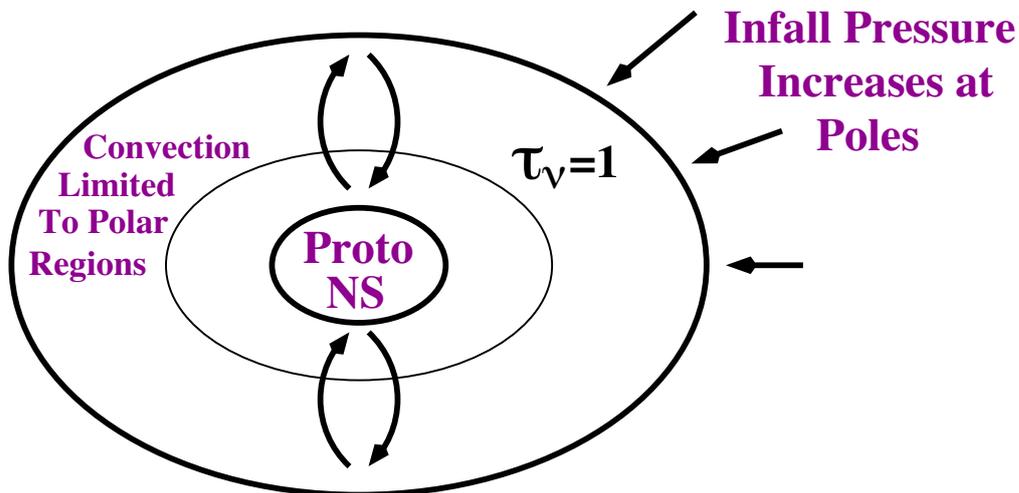
Figure 7: Rotation in Core-Collapse supernovae. Increased neutrino heating along the rotation axis and constraints on the convection in the equator combine to produce asymmetries in the supernova explosion.

the high entropy bubbles are unable to rise through the large angular momentum gradient and the convection is constrained to the polar region. The overwhelming effect of rotation on supernova models is this constraint on the convection and it causes weaker, asymmetric explosions.

But the pressure is also altered by the angular momentum. It produces a more condensed profile along the rotation axis and this will lead to more neutrino energy deposition along these poles[62, 56, 38].

3.3 Where We are Now?

Although rotation has been modeled in collapse extensively, we still do not have accurate progenitor models to definitively determine the role of rotation on convection. In addition, although estimates of the magnetic fields have been made, magnetic fields have not yet been modeled self-consistently. This is the next big step for rotation stellar collapse.

4 Rotation in GRBs

Right now, the history of GRB models is fairly limited. Only a handfull of calculations have been made[42, 53, 54]. The simple disk picture was shattered by the first set of 3-dimensional simulations. Angular momentum can help provide support around the black hole and convection cycles can develop. Figure 8 shows a slice of a 3D calculation where the y-axis is the rotation axis. Far from being a simple disk along the equatorial region, vigorous convection has developed. The angular momentum in this matter also contributes to additional instabilities, and this angular momentum can drive gravitational waves.

This problem is in its infancy, and much more work on any number of topics must be done before we know what issues must be studied and what physics is relevant. Among these is the role of magnetic fields and a better instability analysis of the Rockefeller et al.[54] simulations.

5 Gravitational Waves

Rotation clearly plays a key role in the explosions of GRBs, and because of this, we are also assured of producing gravitational waves (GWs). The signal peaks shortly after the collapse of the massive star and quickly drops off (9). The rotation provides an ideal way method to produce a time-varying quadruple moment in the mass motions. Even so, the GW signal from collapsars is strong enough for advanced LIGO to observe only if the GRB is very near to the earth (within the Galaxy or the local group).

In comparison, there is no guarantee that normal supernovae will produce a strong enough time-varying quadrupole moment to be observed at all. Conection alone produces a GW signal more than 100 times weaker than what is produced in collapsars (10). With rotation or asymmetries (especially in the neutrino emission), this signal could easily be an order of magnitude greater, detectable by advanced LIGO if the supernova occurs in the local group. Because of the much higher rate of supernovae over GRBs, we are more likely to detect supernovae in GWs than GRBs[4]. Despite the difficulty in detecting stellar collapse in GWs, GW observations will tell us much about the rotation and asymmetries in the mechanism itself.

References

[1] Blondin, J.M., Mezzacappa, A., DeMarino, C. 2003, ApJ, 584, 971

[2] Bodenheimer, P., & Woosley, S.E. 1983, ApJ, 269, 281

[3] Buchler, J.R., Livio, M., Colgate, S.A. 1980, Space Science Reviews, 27, 571

[4] Bruenn, S.W., Raley, E.A., Mezzacappa, A. 2004, astro-ph/0404099

---

[4]Note that short duration bursts are believed to be produced by the merger of two neutron stars. Such GRBs will be accompanied by strong GW emission.
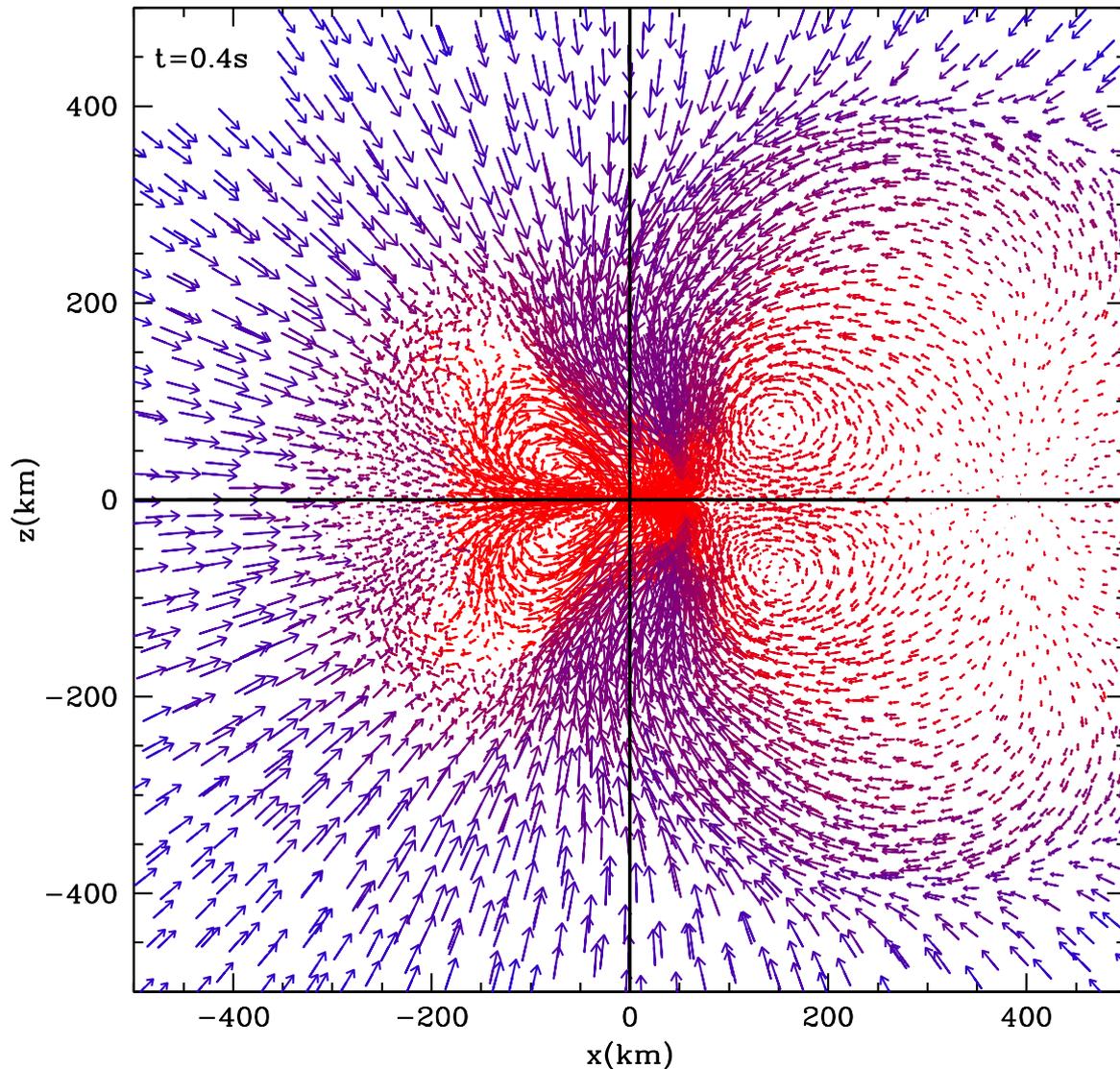
Figure 8: A 3-dimensional slice of a collapsar[54]. Angular momentum prevents direct accretion onto the black hole. Convective instabilities develop and move outward. It is hard to tell that angular momentum is even present in this calculation from this slice of the model. But angular momentum does more than prevent the accretion of material onto the black hole. It contains considerable energy, and viscous forces heat the material near the black hole considerably, driving an explosion.
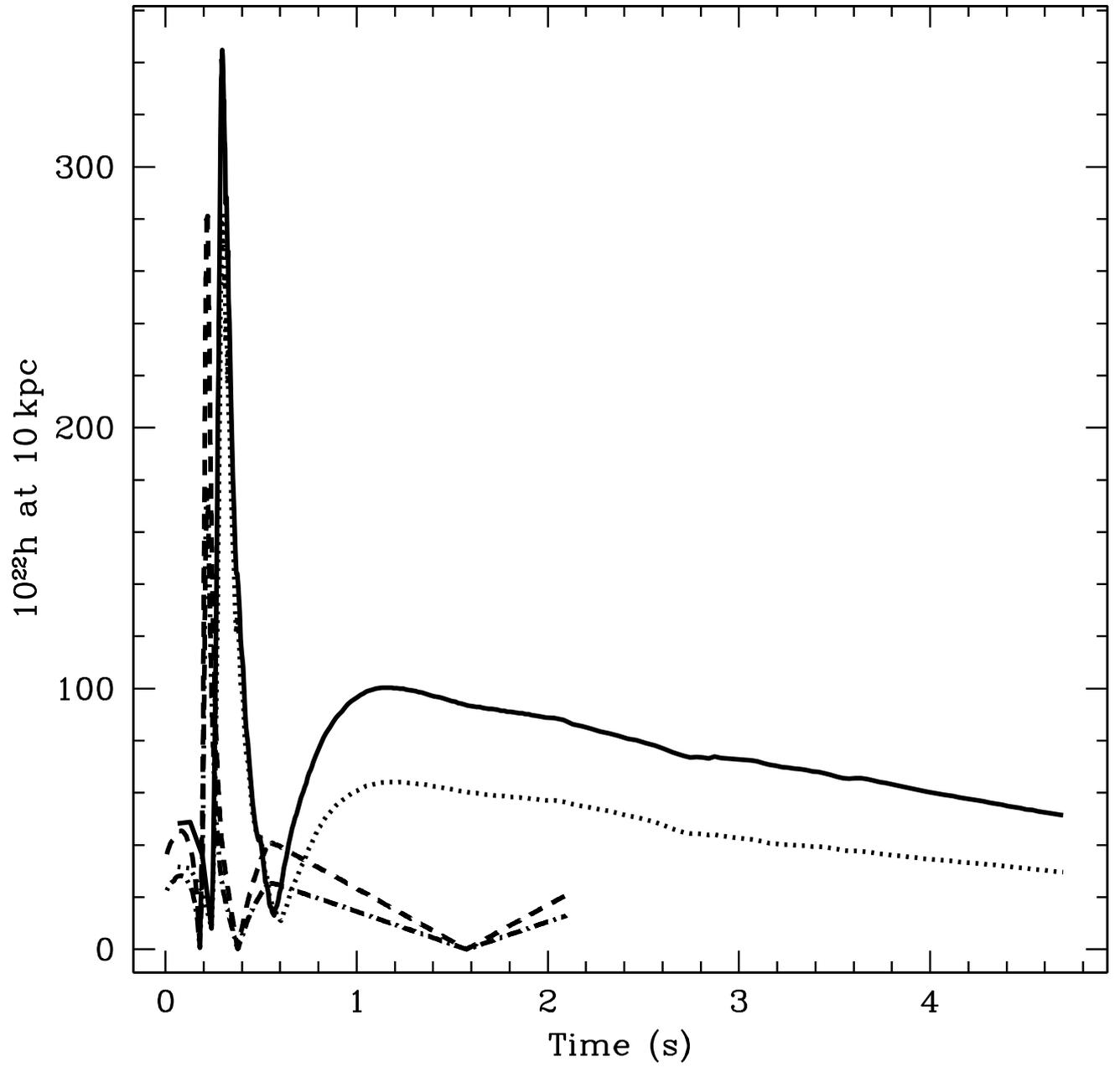
Figure 9: Gravitational wave emission from a $60 \, M_\odot$ star[54]. Angle-averaged wave amplitude of the gravitational wave emission arising from mass motions as a function of time for both a rapidly-rotating (solid/dotted lines for the two GW components) and slowly rotating (dashed/dot-dashed) simulations.
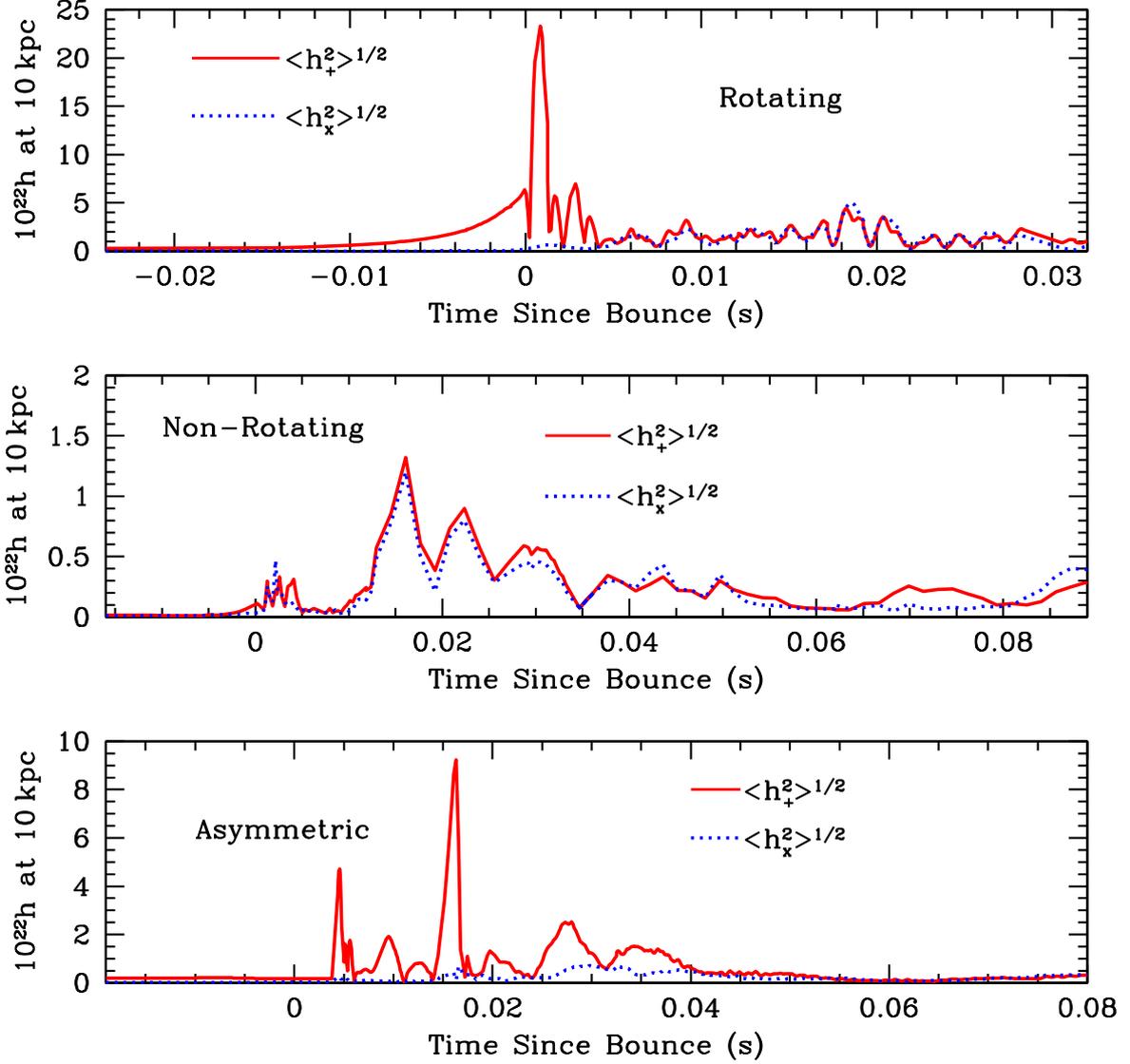
Figure 10: Angle averaged wave amplitudes from mass motions of 3 representative models of rotating, non-rotating, and asymmetric collapse supernovae. The fast-rotator produces the strongest signal, occuring at bounce. The asymmetric collapse simulation produces a reasonably strong signal, but not necessarily at bounce. The asymmetric neutrino signal will actually dominate the GW signal. The non-rotating case does not produce a strong signal.

[5] Buras, R., Rampp, M., Janka, H.-T., & Kifonidis, K. 2003, PRL, 90, 1101

[6] Buras, R., Janka, H.-T., Rampp, M., & Kifonidis, K. 2006, A&A, 457, 281

[7] Burrows, A., Mazuerk, T.J., Lattimer, J.M. 1981, ApJ, 251, 325

[8] Burrows, A. 1987, ApJ, 318, 57

[9] Burrows, A., Hayes, J., & Frxell, B.A. 1995, ApJ, 450, 830

[10] Burrows, A., Livne, E., Dessart, L., Ott, C.D., Murphy, J. 2006, ApJ, 640, 878

[11] Colgate, S.A., Herant, M., & Benz, W. 1993, Physics Reports, 227, 157

[12] Cox, A.N., Vauclair, S., & Zhahn,, J.P. 1983, Astrophysical Processes in Upper Main Sequence Stars (CH-1290 Sauverny: Geneva Observatory)

[13] di Matteo, T., Rosalba, P., & Narayan, R. 2002, ApJ, 579, 706

[14] Epstein, R.I. 1979, MNRAS, 188, 305

[15] Foglizzo, T., Galletti, P., Scheck, L., & Janka, H.-T. 2007, ApJ, 654, 1006

[16] Fryer, C.L. 1999, ApJ, 522, 413

[17] Fryer, C.L., Woosley, S.E., & Hartmann, D.H. 1999, ApJ, 550, 372

[18] Fryer, C.L., & Heger, A. 2000, ApJ, 541, 1033

[19] Fryer, C.L. & Warren, M.S. 2002, ApJ, 574, L65

[20] Fryer, C.L. & Mészáros P. 2003, ApJ, 588, L25

[21] Fryer, C.L. & Warren, M.S. 2004, ApJ, 601, 391

[22] Fryer, C.L. 2004, ApJ, 601, L175

[23] Fryer, C.L. 2006, New Astron. Rev., 50, 492

[24] Fryer, C.L. & Kusenko, A. 2006, ApJS, 163, 335

[25] Fryer, C.L. & Young, P.A. 2007, accepted by ApJ

[26] Herant, M., Benz, W., Colgate, S.A. 1992, ApJ, 395, 642

[27] Herant, M., Benz, W., Hix, W.R., Fryer, C.L., Colgate, S.A. 1994, ApJ, 435, 339

[28] Houck, J.C., & Chevalier, R.A. 1992, ApJ, 395, 592

[29] Hungerford, A.L., Fryer, C.L., & Warren, M.S. 2003, ApJ, 594, 390

[30] Hungerford, A.L., Fryer, C.L., & Rockefeller, G. 2005, ApJ, 635, 487

[31] Janka, H.-T. & Mönchmeyer, R. 1989, A&A, 209, L5

[32] Janka, H.-T., Zwerger, T. & Mönchmeyer, R. 1993, A&A, 268, 360

[33] Janka, H.-T. & Müller, E. 1996, A&A, 306, 167

[34] Kaniel, S., & Kovetz, A. 1967, Phys. Fluids, 10, 1186

[35] Katz, J. 1997, ApJ, 490, 633

[36] Keil, W., Janka, H.-T., Müller, E. 1996, ApJ, 473, L111

[37] Kifonidis, K., Plewa, T., Janka, H.-Th., & Müller, E. 2003, A&A, 408, 621

[38] Kotake, K., Yamada, S., & Sato, K. 2003, ApJ, 595, 304

[39] Lattimer, J.M. & Mazurek, T.J. 1981, ApJ, 246, 955

[40] Ledoux, P., & Walraven, Th. 1958, Handbuch der Physik, Vol 51 (Berlin; Springer-Verlag).

[41] Livio, M., Buchler, J.R., Colgate, S.A. 1980, ApJ, 238, L139

[42] MacFadyen, A. I., & Woosley, S. E. 1999, ApJ, 524, 262

[43] Meszaros, P., Rees, M. J. 1997, ApJ, 482, L29

[44] Mezzacappa, A., Calder, A.C., Bruenn, S.W., Blondin, J.M., Guidry, M.W., Strayer, M.R., & Umar, A.S. 1998, ApJ, 493, 848

[45] Miller, D.S., Wilson, J.R., & Mayle, R.W. 1993, ApJ, 415, 278

[46] Mönchmeyer, R. & Müller, E. 1989, in Timing Neutron Stars, ed. H. Ögelman & E.P.J. van den Heuvel (NATO ASI Ser. C, 262; New York: ASI), 549

[47] Müller, E. & Hillebrandt, W. 1981, A&A, 103, 358

[48] Nagataki, S. 2000, ApJS, 127, 141

[49] Narayan, R., Paczynski, B., & Piran, T. 1992, ApJ, 395, L83

[50] Nemiroff, R.J. 1994, Comments on Astrophysics, 17, 189

[51] Ohnishi, N., Kotake, K., & Yamada, S. 2006, ApJ, 641, 1018

[52] Popham, R., Woosley, S.E. & Fryer, C.L. 1999, ApJ, 518, 356

[53] Proga, D., MacFadyen, A. I., Armitage, P.J., Begelman, M.C. 2003, ApJ, 599, L5

[54] Rockefeller, G., Fryer, C.L., & Li, H. 2007, submitted to ApJ, astro-ph/0608028

[55] Scheck, L., Plewa, T., Janka, H.-T., & Müller, E. 2004, PRL, 92, 1

[56] Shimizu, T., Yamada, S., Sato, K. 1994, ApJ, 432, L119

[57] Smarr, L., Wilson, J.R., Barton, R.T., & Bowers, R.L. 1981, ApJ, 246, 515

[58] Symbalisty, E.M. 1984, ApJ, 285, 729

[59] Wilson, J.R. & Mayle, R. 1988, Phys. Rep., 163, 63

[60] Wilson, J.R. & Mayle, R. 1993, Phys. Rep., 227, 97

[61] Woosley, S.E. 1993, ApJ, 405, 273

[62] Yamada, S., Shimizu, T., Sato, K. 1993, Prog. in Theoretical Phys., 89, 1175

[63] Yamada, S., & Sato, K. 1994, ApJ, 434, 268

[64] Yamasaki, T., & Yamada, S. 2006, ApJ, 650, 291

[65] Yamasaki, T., & Yamada, S. 2006, submitted to ApJ, astro-ph/0606581

Low-Luminosity GRB 060218: A Collapsar Jet from a Neutron Star?

Kenji Toma[1], Kunihito Ioka[1], Takanori Sakamoto[2], Takashi Nakamura[1]

[1]*Department of Physics, Kyoto University, Kyoto 606–8502, Japan*
[2]*NASA - Goddard Space Flight Center, Greenbelt, Maryland 20771, USA*

Abstract

The gamma-ray burst (GRB) 060218 has $\sim 10^5$ times lower luminosity than typical long GRBs, and is associated with a supernova (SN). The radio afterglow displays no jet break, so that this burst might arise from a mildly-relativistic spherical outflow produced by the SN shock sweeping the stellar surface. Since this model is energetically difficult, we propose that the radio afterglow is produced by a non-relativistic phase of an initially collimated outflow (jet). Our jet model is supported by the detection of optical linear polarization in the SN component. We show analytically that the jet can penetrate a progenitor star. A possible engine of a neutron star is also discussed.

1   Introduction

The gamma-ray burst (GRB) 060218 is the second nearest event ($z = 0.033$) and it is spectroscopically associated with the supernova (SN) 2006aj [6]. Such a long GRB/SN association is common and this event further supports the established picture that all long GRBs are related to the deaths of massive stars [10]. However, the prompt and afterglow emission of GRB 060218 have many peculiarities [1, 7, 3]. Especially, the isotropic-equivalent luminosity of the prompt emission is extremely low $\sim 10^{47}$ erg s^{-1}, which is about 10^5 times lower than those of typical cosmological GRBs. Although such a low-luminosity event looks rare, the intrinsic event rate could be very high $R_{\rm LL} \sim 10^2$ Gpc^{-3} yr^{-1} compared with the local rate of typical long GRBs deduced from the BATSE data, $R_{\rm LG} \sim 1$ Gpc^{-3} yr^{-1} [7]. For this reason, it has been actively debated whether low-luminosity GRBs form a new GRB population and whether they have intrinsically different outflow mechanisms and emission mechanisms.

For GRB 060218, it has been widely suggested that the outflow is spherical since the radio afterglow has no jet break [7, 2]. If true, the collapsar model cannot be applied to this event because the outflow becomes non-relativistic by loading all the matter of a progenitor star. The relativistic spherical outflow might be produced by the outermost parts of the stellar envelope that the SN shock accelerates when propagating through the steep density gradient near the stellar surface [8]. However, Tan et al. [8] has shown that the energy $\sim 10^{48}$ erg is transferred to mildly relativistic material when the kinetic energy of the SN is $E_{\rm SN} \sim 10^{52}$ erg. For GRB 060218, $E_{\rm SN}$ is estimated as $\simeq 2 \times 10^{51}$ erg [6], so that it is quite unlikely that the prompt non-thermal emission with $E_{\gamma,\rm iso} \simeq 6 \times 10^{49}$ erg is produced by this type of the outflow [5].

Moreover, the detection of optical linear polarization in the SN component of this event has been recently reported [4]. This observation strongly suggests that GRB 060218 arises from a jet.

In this paper, we show that GRB 060218 can be produced by the standard collapsar jet model. We show that the available radio data may be interpreted as a non-relativistic phase of the external shock *after the jet break* within the standard model. We argue that the outflow with an initial opening angle $\theta_0 \simeq 0.3$ and Lorentz factor $\Gamma_0 \simeq 5$ can produce the synchrotron radiation which explains the radio afterglow and is compatible with the UV/optical and X-ray afterglow. We also examine whether such a wide and weak jet can penetrate a progenitor star by extending analytical considerations of the collapsar model by Matzner [5]. For details, please see Toma et al. [9].

---

[1] E-mail:toma@tap.scphys.kyoto-u.ac.jp

2 A Jet Model of the Radio Afterglow

The afterglow of this burst shows chromatic light curves. The UV/optical afterglow is quite dim and dominated by the thermal component and the SN component [1, 3]. The X-ray afterglow has a spectrum much steeper than those of typical GRB X-ray afterglows [7]. Only the radio afterglow seems rather typical and can be explained by the standard external shock synchrotron model [7, 2], but does not show a jet break until $t \simeq 22$ days.

The relativistic jet is decelerated and subsequently expands sideways, and finally becomes non-relativistic at a certain transition time t_s. The transition time is estimated by requiring that the speed of the Sedov-Taylor blastwave is close to the light speed, i.e., $\beta = \frac{2}{5c}[E_k/(nm_p t^3)]^{1/5} \sim 1$, where E_k is the kinetic energy of the spherical blastwave, and n is the number density of the circumburst medium:

$$t_s \simeq 7.5 \times 10^6 \text{ s} \left(\frac{E_{k,51}}{n} \right)^{1/3}. \tag{1}$$

Here (and hereafter) we have adopted the notation $Q = 10^x Q_x$ in cgs units. Since the available 8.46 GHz lightcurve does not show the sideways expanding relativistic phase $t^{-p} \sim t^{-2}$, we require $t_s \lesssim 2$ days.

We may model the synchrotron spectrum from the non-relativistic blastwave expanding into the constant density medium, and find the following physical parameters; $E_k \sim 2 \times 10^{48}$ erg, $n \sim 10^2$ cm^{-3}, and the ratios of the accelerated electrons energy and the magnetic energy to the shocked thermal energy $\epsilon_e \sim 10^{-1}$ and $\epsilon_B \sim 10^{-1}$, respectively. These satisfy the requirement of $t_s \lesssim 2 \times 10^5$ s.

Then the isotropic-equivalent kinetic energy before sideways expansion is estimated by $E_{k,\text{iso}} = 2E_k/\theta_0{}^2 \simeq 4 \times 10^{48} \theta_0{}^{-2}$ erg. To obtain a reasonable γ-ray efficiency $\eta_\gamma = E_{\gamma,\text{iso}}/(E_{\gamma,\text{iso}} + E_{k,\text{iso}}) \lesssim 0.5$, the opening angle $\theta_0 \lesssim 0.3$ is favorable.

In our model, the characteristic parameters at $t \simeq 5$ days are calculated as $F_{\nu,\text{max}} \sim 2 \times 10^{-25}$ erg cm^{-2} s^{-1} Hz^{-1}, $\nu_m \simeq 5 \times 10^6$ Hz, $\nu_a \simeq 4 \times 10^9$ Hz, and $\nu_c \simeq 7 \times 10^{13}$ Hz. Thus the optical νF_ν flux at this time is $\sim 10^{15} F_{\nu,\text{max}} (\nu_c/\nu_m)^{-0.5} (10^{15}/\nu_c)^{-1} \simeq 4 \times 10^{-15}$ erg cm^{-2} s^{-1}. If we trace back to earlier times through the standard jet model, the optical flux gets much higher than this value. The detected optical flux at $10^4 - 10^5$ s is dominated by the thermal component with $\nu F_\nu \sim 10^{-11}$ erg cm^{-2} s^{-1} [3, 1]. The requirement that the synchrotron flux from our jet should not exceed this flux gives constraints on the initial opening angle θ_0 and the initial Lorentz factor Γ_0 of the jet.

For $t \gtrsim 10^4$ s, the optical band is at the range $\nu > \nu_c$, and the optical energy flux evolves as t^{-1} at the Blandford-McKee phase, t^{-2} at the sideways expanding phase, and t^{-1} at the Sedov-Taylor phase. With these behaviors of the optical flux from the external shock, we can suggest a following possible jet scenario. The external shock of the jet is decelerated at $t_{\text{dec}} \simeq 6 \times 10^3$ s, begins to expand sideways at $t_j \simeq 2 \times 10^4$ s, and shifts to the Sedov-Taylor expansion at $t_s \simeq 2 \times 10^5$ s. The peak optical flux is $\nu F_\nu \simeq 3 \times 10^{-12}$, which is less than the observed one, so that the optical afterglow estimated within our jet model is not inconsistent with the available optical data.

Now we give the reasonable values of θ_0 and Γ_0. At the sideways expansion phase, the opening angle of the jet evolves as $\theta = \Gamma^{-1} \propto t^{1/2}$, and finally becomes $\theta \simeq 1$ at the transition time t_s to the Sedov-Taylor expansion phase. Thus the initial opening angle of the jet is determined by

$$\theta_0 \left(\frac{t_s}{t_j} \right)^{1/2} \simeq 1. \tag{2}$$

When $t_s \simeq 2 \times 10^5$ s and $t_j \simeq 2 \times 10^4$ s are adopted, we obtain $\theta_0 \simeq 0.3$. If θ_0 is smaller, the ratio t_s/t_j is larger. At the Blandford-McKee phase, the Lorentz factor of the jet evolves as $\Gamma \propto t^{-3/8}$, and finally becomes $\Gamma \simeq \theta_0{}^{-1}$ at the jet-break time t_j. Thus the initial Lorentz factor of the jet is determined by

$$\Gamma_0 \left(\frac{t_j}{t_{\text{dec}}} \right)^{-3/8} \simeq \theta_0{}^{-1}. \tag{3}$$

When $t_j \simeq 2 \times 10^4$ s and $t_{\text{dec}} \simeq 6 \times 10^3$ s are adopted, we obtain $\Gamma_0 \simeq 5$. If Γ_0 is larger, the ratio t_j/t_{dec} is larger. The upper bound of the optical data does not allow the values of t_s/t_j and t_j/t_{dec} larger than those we have adopted, and therefore it does not allow the smaller θ_0 and the larger Γ_0. Since the

consideration about the γ-ray efficiency requires $\theta_0 \lesssim 0.3$, the opening angle is restricted to a narrow range around $\theta_0 \simeq 0.3$.

In a summary, we have obtained a jet model for the radio afterglow of GRB 060218, with $\theta_0 \simeq 0.3$, $\Gamma_0 \simeq 5$, $E_{k,\mathrm{iso}} \simeq 4 \times 10^{49}$ erg, and $\eta_\gamma \simeq 0.6$, which is compatible with the UV/optical and X-ray data. The collimation-corrected energy of the jet is $E_j \simeq (E_{\gamma,\mathrm{iso}} + E_{k,\mathrm{iso}})\theta_0{}^2/4 \simeq 10^{48}$ erg. Assuming that the duration of the prompt non-thermal emission $\delta t \sim 10^3$ s is the active time of the central engine δT, the luminosity of the jet is estimated by $L_j \sim E_j/\delta T \sim 10^{45}$ erg s^{-1}.

3   A Collapsar Model of GRB 060218

In the previous section, we have obtained a possible jet model that is consistent with the available afterglow data. Our jet model requires an opening angle $\theta_0 \simeq 0.3$, which is somewhat larger than those of typical cosmological GRBs, and an extremely small luminosity $L_j \sim 10^{45}$ erg s^{-1}, which is about 10^5 times smaller than those of typical cosmological GRBs. Then one may wonder whether such a wide and low-luminosity jet can penetrate a progenitor star. It is possible that a jet becomes non-relativistic if it loads so much stellar matter with a large cross section. Matzner [5] has discussed analytically several conditions for making a hole in the collapsar model. We extend his theoretical considerations to conclude that an adiabatic cold jet is excluded, but a non-adiabatic hot jet is appropriate for this event.

The standard collapsar model assumes that a black hole or a neutron star with an accretion disk is formed after an iron core of the massive progenitor star collapses and that the system produces a jet [10]. Consider the progress of a relativistic jet outward through the stellar envelope. Two shocks form: a reverse shock reducing the jet speed and increasing its internal energy; and a forward shock that propagates into the surrounding stellar envelope giving it internal energy. As a result, there are four distinct regions in this system: the propagating jet; the head of the jet lying between the two shocks; the stellar envelope; and a cocoon consisting of shocked jet and shocked ambient material (see Figure 2 of [5]).

For a jet to break out the star relativistically, the speed of the jet head should be larger than that of the expanding cocoon,

$$\beta_h > \beta_c. \tag{4}$$

If this condition is violated, the cocoon expands spherically around the jet and finally explode the star, producing a non-relativistic dense spherical outflow. When the above condition is satisfied, we may consider the longitudinal balance of the momentum flux in the frame of the jet head,

$$w_j \Gamma_j{}^2 \Gamma_h{}^2 (\beta_j - \beta_h)^2 + p_j = w_a \Gamma_h{}^2 \beta_h{}^2 + p_a. \tag{5}$$

Here the subscripts j and h describe the jet and the jet head, respectively, and $w (\equiv e + p)$, p, and e are the enthalpy, the pressure, and the energy density including rest energy density ρc^2, respectively. For stellar envelopes, $p_a \ll \rho_a c^2$ and $w_a = \rho_a c^2$ are good approximations. The cocoon drives a shock into the stellar envelope, which expands non-relativistically at the velocity β_c given by the transverse balance of the cocoon pressure and the ram pressure of the stellar envelope,

$$p_c = \rho_a c^2 \beta_c{}^2. \tag{6}$$

Equations (5) and (6) give us the velocities of the jet head and the cocoon in terms of the parameters of the jet and the stellar envelope.

For the jet to drive an explosion, the consistency $\beta_h > \beta_c$ should be satisfied. This leads to the constraint on the opening angle of the jet,

$$\theta < \left(\frac{L_j}{\pi r^2 \rho_a c^3} \right)^{1/6}. \tag{7}$$

For GRB 060218, the underlying SN is Type Ic, which implies that the progenitor star is a C/O Wolf-Rayet star [6]. Its radius and mass are typically $R \sim 10^{11}$ cm and $M \sim 10^{34}$ g, respectively. Then the averaged mass density ρ_a is ~ 1 g cm^{-3}. For the luminosity $L_j \sim 10^{45}$ erg s^{-1}, the opening angle of the jet at the breakout (i.e., when $r = R$) is constrained to $\theta_{\mathrm{br}} < 0.03$, so that $\theta_0 < 0.03$ within the cold jet

scenario. The value of the opening angle suggested in our jet model ($\theta_0 \simeq 0.3$) violates this constraint. Therefore the cold jet scenario is excluded for this event. The jet of this burst may originate from a hot jet and obtain a wide opening angle by the free expansion after exiting the star.

4   Summary and Discussion

We have investigated whether GRB 060218 arises from a collimated jet. So far the lack of the jet break has led to the interpretation that the outflow of this event is spherical, and thereby the outflow is not the standard collapsar jet but the outermost parts of the stellar envelope that the SN shock accelerates to a mildly relativistic speed [7, 2]. However, we have shown that the available radio data may be interpreted as a non-relativistic phase of an initially collimated outflow within the standard external shock synchrotron model, and that the jet model with an initial opening angle $\theta_0 \simeq 0.3$, Lorentz factor $\Gamma_0 \simeq 5$, and a collimation-corrected luminosity $L_j \sim 10^{45}$ erg can explain the radio data and is compatible with the UV/optical and X-ray data. This model is more natural than the initially spherical outflow model, because in the latter model, the relativistic ejecta for the prompt and afterglow emission with $\simeq 10^{50}$ erg could not be produced by the underlying SN of the total kinetic energy $\simeq 10^{51}$ erg [6]. Furthermore, the jet model is supported by the recent report of the detection of optical linear polarization in the SN component of this event [4]. We also show that the jet of this event can penetrate the progenitor star by extending the analytical considerations by [5]. The jet would be relativistically hot in the progenitor star and hence expand freely outside the star into the relatively wide opening angle.

For the prompt emission, we analyzed the observational data of the prompt emission of this burst and obtained a smooth power-law light curve which might last longer than 10^6 s [9]. This behavior contrasts with the long intermittent activities with the X-ray flares of typical GRBs, implying that the engine of this burst is different from those of typical GRBs which are believed to be black holes. Mazzali et al. [6] have performed a detailed modeling of the spectra and light curve of the SN component and argued that the progenitor star of this event had a smaller mass than other GRB-SNe, suggesting that a neutron star rather than a black hole was formed as the central engine of the jet. The intrinsic rate of such low-luminosity GRBs would be larger than the local rate of typical cosmological GRBs [7]. For these reasons, low-luminosity GRBs might be a distinct GRB population involving neutron star engines. We speculate that massive progenitor stars form black holes at the core collapse which produce highly-relativistic jets making high-luminosity GRBs with strong spiky prompt emissions and flares, while less massive progenitor stars form neutron stars which produce mildly-relativistic jets making low-luminosity GRBs with weak smooth prompt emissions.

References

[1] Campana, S., et al. 2006, Nature, 442, 1008

[2] Fan, Y. Z., Piran, T., & Xu, D. 2006, JCAP, 9, 13

[3] Ghisellini, G., Ghirlanda, G., & Tavecchio, F. 2006b, MNRAS, in press (astro-ph/0608555)

[4] Gorosabel, J. et al. 2006, A&A, 459, L33

[5] Matzner, C. D. 2003, MNRAS, 345, 575

[6] Mazzali, P. A., Deng, J., Nomoto, K., et al. 2006, Nature, 442, 1018

[7] Soderberg, A. M., et al. 2006, Nature, 442, 1014

[8] Tan, J. C., Matzner, C. D., & McKee, C. F. 2001, ApJ, 551, 946

[9] Toma, K., Ioka, K., Sakamoto, T., & Nakamura, T. 2007, ApJ, in press (astro-ph/0610867)

[10] Woosley, S. E., & Bloom, J. S. 2006, A&ARA, 44, 507

Probing the Jet Structure of Gamma-Ray Bursts with Steep Decay Phase of their Early X-ray Afterglows

Kentaro Takami[1] and Ryo Yamazaki[2]

Department of Physics, Hiroshima University, Higashi-Hiroshima, Hiroshima 739-8526, Japan

Abstract

We show that the jet structure of gamma-ray bursts (GRBs) can be constrained by investigating the tail emission of the prompt GRB. The tail emission which we consider is identified as a steep-decay component of the early X-ray afterglow observed by the *Swift* X-ray Telescope. Using a Monte Carlo method, we derive, for the first time, the distribution of the decay index of the GRB tail emission for various jet models. The new definitions of the zero of time and the time interval of a fitting region are proposed. These definitions for fitting the light curve leads us an unique definition of the decay index, which is useful to investigate the structure of the GRB jet. We find that if the GRB jet has a core-envelope structure, the predicted distribution of the decay index of the tail has a wide scatter and has multiple peaks, which cannot be seen for the case of the uniform jet. Therefore, the decay index distribution tells us the information on the jet structure. Especially, if we observe events whose decay index is less than about 2, the uniform jet model will be disfavored according to our simulation study.

1 Introduction

Gamma-ray burst (GRB) jet structure, that is, the energy distribution $E(\theta)$ in the ultra-relativistic collimated outflow, is at present not yet fully understood . There are many jet models proposed in addition to the simplest uniform jet model; the power-law jet model and so on. The jet structure may depend on the generation process of the jet, and therefore, may tell us important information on the central engine of the GRB. For example, in collapsar model for long GRBs , the jet penetrates into and breakout the progenitor star, resulting $E(\theta) \propto \theta^{-2}$ profile [4]. For compact binary merger model for short GRBs, hydrodynamic simulations have shown that the resulting jet tends to have a flat core surrounded by the power-law like envelope [1].

In the *Swift* era, rapid follow up observation reveals prompt GRBs followed by the steep decay phase in the X-ray early afterglow [5]. Most popular interpretations of the steep decay component is the tail emission of the prompt GRB (so called high latitude emission), i.e., the internal shock origin [7] . Then, for the uniform jet case, predicted decay index is $\alpha = 1 - \beta$, where we use a convention $F_\nu \propto T^{-\alpha}\nu^{1+\beta}$ [3]. For power-law jet case ($E(\theta) \propto \theta^{-q}$), the relation is modified into $\alpha = 1 - \beta + (q/2)$. However, these simple analytical relations cannot be directly compared with observations because they are for the case in which the observer's line of sight is along the jet axis, and because changing the zero of time, which potentially lies anywhere within the epoch we see the bright pulses, substantially alters the early decay slope.

Recently, [6] investigated the tail emission of the prompt GRB, and found that the jet structure can be discussed, and that the global decay slope is not so much affected by the local angular inhomogeneity but affected by the global energy distribution. They also argued that the structured jet is preferable because steepening GRB tail breaks appeared in some events. In this paper, we calculate, for the first time, the distribution of the decay index of the prompt tail emission for various jet models, and find that derived distribution can be distinguished with each other, so that the jet structure can be more directly constrained than previous arguments.

---

[1]E-mail:takami@theo.phys.sci.hiroshima-u.ac.jp
[2]E-mail:ryo@theo.phys.sci.hiroshima-u.ac.jp

2 Tail Part of the Prompt GRB Emission

We consider the same model as discussed in the previous works [6]. The whole GRB jet, whose opening half-angle is $\Delta\theta_{\text{tot}}$, consists of N_{tot} emitting sub-shells. We introduce the spherical coordinate system $(r, \vartheta, \varphi, t)$ in the central engine frame, where the origin is at the central engine, and $\vartheta = 0$ is the axis of the whole jet. Each emitting sub-shell departs at time $t_{\text{dep}}^{(j)}$ ($0 < t_{\text{dep}}^{(j)} < t_{\text{dur}}$, where $j = 1, \cdots, N_{\text{tot}}$, and t_{dur} is the active time of the central engine) from the central engine in the direction of $\vec{n}^{(j)} = (\vartheta^{(j)}, \varphi^{(j)})$, and emits high-energy photons generating a single pulse as observed. The direction of the observer is denoted by $\vec{n}_{\text{obs}} = (\vartheta_{\text{obs}}, \varphi_{\text{obs}})$. The observed flux from the jth sub-shell is calculated when the following parameters are determined: the viewing angle of the sub-shell $\theta_v^{(j)} = \cos^{-1}(\vec{n}_{\text{obs}} \cdot \vec{n}^{(j)})$, the angular radius of the emitting shell $\Delta\theta_{\text{sub}}^{(j)}$, the departure time $t_{\text{dep}}^{(j)}$, the Lorentz factor $\gamma^{(j)} = (1 - \beta_{(j)}^2)^{-1/2}$, the emitting radius $r_0^{(j)}$, the low- and high-energy photon index $\alpha_B^{(j)}$ and $\beta_B^{(j)}$, the break frequency in the shell comoving frame $\nu_0'^{(j)}$ [2], the normalization constant of the emissivity $A^{(j)}$, and the source redshift z. The observer time $T = 0$ is chosen as the time of arrival at the observer of a photon emitted at the origin $r = 0$ at $t = 0$. Then, at the observer, starting and ending time of jth sub-shell emission are given by

$$T_{\text{start}}^{(j)} \quad \sim \quad t_{\text{dep}}^{(j)} + \frac{r_0^{(j)}}{2c\gamma_{(j)}^2}\left(1 + \gamma_{(j)}^2 \theta_-^{(j)\,2}\right) \quad , \tag{1}$$

$$T_{\text{end}}^{(j)} \quad \sim \quad t_{\text{dep}}^{(j)} + \frac{r_0^{(j)}}{2c\gamma_{(j)}^2}\left(1 + \gamma_{(j)}^2 \theta_+^{(j)\,2}\right) \quad , \tag{2}$$

where $\theta_+^{(j)} = \theta_v^{(j)} + \Delta\theta_{\text{sub}}^{(j)}$ and $\theta_-^{(j)} = \max\{0, \theta_v^{(j)} - \Delta\theta_{\text{sub}}^{(j)}\}$, and we use the formulae $\beta_{(j)} \sim 1 - 1/2\gamma_{(j)}^2$ and $\cos\theta \sim 1 - \theta^2/2$ for $\gamma^{(j)} \gg 1$ and $\theta \ll 1$, respectively. The whole light curve from the GRB jet is produced by the superposition of the sub-shell emission.

[6] discussed some of kinematical properties of prompt GRBs in our model and found that each emitting sub-shell with $\theta_v^{(j)} \gg \Delta\theta_{\text{sub}}^{(j)}$ produces a single, smooth, long-duration, dim, and soft pulse, and that such pulses overlap with each other and make the tail emission of the prompt GRB. Local inhomogeneities in the model are almost averaged during the tail emission phase, and the decay index of the tail is determined by the global jet structure, that is the mean angular distribution of the emitting sub-shell because in this paper all sub-shells are assumed to have the same properties until otherwise stated. Therefore, essentially we are also studying the tail emission from the usual continuous jets at once, i.e., from uniform or power-law jets with no local inhomogeneity. In the following, we study various energy distribution of the GRB jet through the change of the angular distribution of the emitting sub-shell.

3 Decay Index of the Prompt Tail Emission

In this section, we perform Monte Carlo simulations in order to investigate the jet structure through calculating the statistical properties of the decay index of the tail emission. For fixed jet model, we randomly generate 10^4 observers with their line of sights (LOSs) $\vec{n}_{\text{obs}} = (\vartheta_{\text{obs}}, \varphi_{\text{obs}})$. For each LOS, the light curve, $F(T)$, of the prompt GRB tail in the 15–25 keV band, is calculated, and the decay index is determined. The adopted observation band is the low-energy end of the BAT detector and near the high-energy end of the XRT on *Swift*. Hence one can observationally obtain continuous light curves beginning with the prompt GRB phase to the subsequent early afterglow phase , so that it is convenient for us to compare theoretical results with observation. However, our actual calculations have shown that our conclusion does not alter qualitatively even if the observation band is changed to, for example, 0.5–10 keV as usually considered for other references.

For each light curve, the decay index is calculated by fitting $F(T)$ with a single power-law form, $\propto (T - T_*)^{-\alpha}$ as in the following (see Fig. 1). The decay index α depends on the choice of T_* [6]. Let T_s and T_e be the start and the end time of the prompt GRB, i.e., $T_s = \min\{T_{\text{start}}^{(j)}\}$ and $T_e = \max\{T_{\text{end}}^{(j)}\}$. Then, we take T_* as the time until which 99% of the total fluence is radiated, that is

$$\frac{\int_{T_s}^{T_*} F(T')\, dT'}{\int_{T_s}^{T_e} F(T')\, dT'} = 0.99 \quad . \tag{3}$$
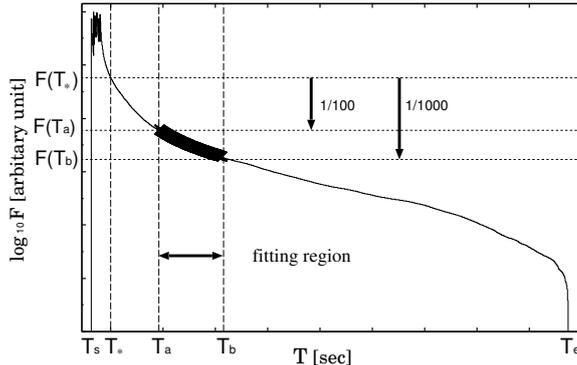
Figure 1: An example of how the decay index, α, is determined by the calculated light curve $F(T)$. The start and end time of the burst are denoted by T_s and T_e, respectively. The time T_* is determined by the Eq. (3). The decay index α is determined by fitting $F(T) \propto (T - T_*)^{-\alpha}$ in the time interval $[T_a, T_b]$.

Then, the prompt GRB is in the main emission phase for $T < T_*$, while in the tail emission phase for $T > T_*$. The time interval, $[T_a, T_b]$, in which the decay index α is determined assuming the form $F(T) \propto (T - T_*)^{-\alpha}$, is taken so as to satisfy $F(T_{a,b}) = q_{a,b} F(T_*)$, where we adopt $q_a = 1 \times 10^{-2}$ and $q_b = 1 \times 10^{-3}$ unless otherwise stated. We find that in this epoch, the assumed fitting form gives a well approximation.

At first, we consider the uniform jet case, in which the number of sub-shells per unit solid angle is approximately given by $dN/d\Omega = N_{\rm tot}/(\pi \Delta\theta_{\rm tot}^2)$ for $\vartheta < \Delta\theta_{\rm tot}$, where $\Delta\theta_{\rm tot} = 0.25$ rad is adopted. The departure time of each sub-shell $t_{\rm dep}^{(j)}$ is assumed to be homogeneously random between $t = 0$ and $t = t_{\rm dur} = 20$ sec. The central engine is assumed to produce $N_{\rm tot} = 1000$ sub-shells. In this section, we assume that all sub-shells have the same values of the following fiducial parameters: $\Delta\theta_{\rm sub} = 0.02$ rad, $\gamma = 100$, $r_0 = 6.0 \times 10^{14}$ cm, $\alpha_B = -1.0$, $\beta_B = -2.3$, $h\nu_0' = 5$ keV, and $A = $ constant.

For $\vartheta_{\rm obs} \lesssim \Delta\theta_{\rm tot}$ (on-axis case), α clusters around ~ 3. On the other hand, when $\vartheta_{\rm obs} \gtrsim \Delta\theta_{\rm tot}$ (off-axis case), α rapidly increases with $\vartheta_{\rm obs}$. The reason is as follows. If all sub-shells are seen sideways (that is $\theta_v^{(j)} \gg \Delta\theta_{\rm sub}^{(j)}$ for all j), the bright pulses in the main emission phase followed by the tail emission disappear because of the relativistic beaming effect, resulting smaller flux contrast between the main emission phase and the tail emission phase compared with the on-axis case. Then T_* becomes larger. Furthermore, in the off-axis case, the tail emission decays more slowly ($|dF/dT|$ is smaller) than in the on-axis case. Then both $T_a - T_*$ and $T_b - T_*$ are larger for the off-axis case than for the on-axis case. As can be seen in Fig. 3 of [7], the emission seems to decay rapidly, so that the decay index α becomes large.

Next, we consider the power-law distribution. In this case, the number of sub-shells per unit solid angle is approximately given by $dN/d\Omega = C[1 + (\vartheta/\vartheta_c)^2]^{-1}$ for $0 \le \vartheta \le \Delta\theta_{\rm tot}$, i.e., $dN/d\Omega \approx C$ for $0 \le \vartheta \ll \vartheta_c$ and $dN/d\Omega \approx C(\vartheta/\vartheta_c)^{-2}$ for $\vartheta_c \ll \vartheta \le \Delta\theta_{\rm tot}$, where $C = (N_{\rm tot}/\pi\vartheta_c^2)[\ln(1 + (\Delta\theta_{\rm tot}/\vartheta_c)^2)]^{-1}$ is the normalization constant and we adopt $\vartheta_c = 0.02$ rad and $\Delta\theta_{\rm tot} = 0.25$ rad. The other parameters are the same as for the uniform jet case.

When $\vartheta_{\rm obs} \lesssim \vartheta_c$, the observer's LOS is near the whole jet axis. Compared with the uniform jet case, α is larger because the power-law jet is dimmer in the outer region, i.e., emitting sub-shells are sparsely distributed near the periphery of the whole jet (see also the solid lines of Figs. 1 and 3 of [6]). If $\vartheta_{\rm obs} \gg \vartheta_c$, the scatter of α is large. Especially, some bursts have small α of around 2. This comes from the fact that the power-law jet has a core region ($0 < \vartheta \lesssim \vartheta_c$) where emitting sub-shells densely distributed compared with the outer region [6]. In the epoch before photons emitted by the core arrive at the observer , the number of sub-shells that contributes to the flux at time T, $N_{\rm sub}(T)$, increases with T more rapidly than in the case of the uniform jet case. Then, the light curve shows a gradual decay. If the fitting region $[T_a, T_b]$ lies in this epoch, the decay index α is around 2. In the epoch after the photons arising from the core are observed , the sub-shell emission with $\theta_v^{(j)} \gtrsim \vartheta_{\rm obs} + \vartheta_c$ is observed. Then $N_{\rm sub}(T)$ rapidly decreases with T and the observed flux suddenly drops. If the interval $[T_a, T_b]$ lies in this epoch, the decay index becomes larger than 4.

To compare the two cases considered above more clearly, we derive the distribution of the decay index α. Here we consider the events whose peak fluxes are larger than 10^{-4} times of the largest one in all
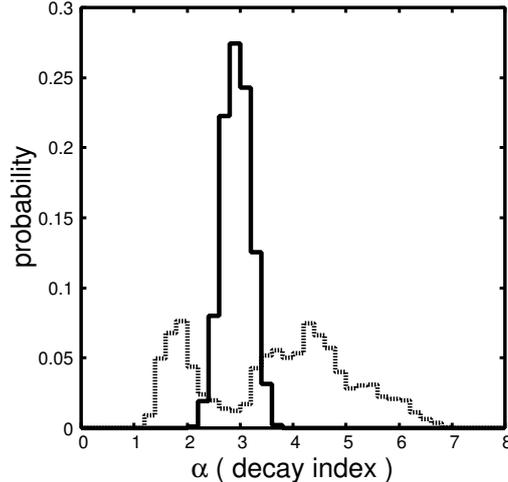
Figure 2: Solid and dotted lines show the distributions of the decay index, α, for uniform ($dN/d\Omega = const.$) and power-law jet ($dN/d\Omega \propto [1+(\vartheta/\vartheta_c)^2]^{-1}$) models, respectively. We assume that all sub-shells have the same values of the following fiducial parameters: $\Delta\theta_{\mathrm{sub}} = 0.02$ rad, $\gamma = 100$, $r_0 = 6.0 \times 10^{14}$ cm, $\alpha_B = -1.0$, $\beta_B = -2.3$, $h\nu'_0 = 5$ keV, and $A =$ constant. We consider events whose peak fluxes are larger than 10^{-4} times of the largest one in all simulated events .

simulated events, because the events with small peak fluxes are not observed. Fig. 2 shows the result. For the uniform jet case (the dotted line), α clusters around 3, while for the power-law jet case (the dashed line), the distribution is broad ($1 \lesssim \alpha \lesssim 7$) and has multiple peaks.

In summary, when we adopt model parameters within reasonable ranges, the decay index becomes larger than ~ 2 for the uniform jet case, while significant fraction of events with $\alpha \lesssim 2$ is expected for the power-law jet case. Therefore, if non-negligible number of events with $\alpha \lesssim 2$ are observed, uniform jet model will be disfavored. Furthermore, if we observationally derive the α-distribution, the structure of GRB jets will be more precisely determined.

4   Summary

We have calculated the distribution of the decay index α for the uniform and the power-law jet case, respectively. For the uniform jet case, α becomes larger than ~ 2, and its distribution has a single peak. On the other hand, for the power-law jet case, α ranges between ~ 1 and ~ 7, and its distribution has multiple peaks. Therefore we can decide the jet structure of GRBs with analyzing a lot of early X-ray data showing a steep decay component that is identified as a prompt GRB tail emission.

The details of this work will appear in the paper which we submitted to ApJ.

References

[1] Aloy, M. A., Janka, H.-T., & Müller, E. 2005, A&A, 436, 273

[2] Band, D. L. et al. 1993, ApJ, 413, 281

[3] Kumar, P. & Panaitescu, A. 2000, ApJ, 541, L51

[4] Lazzati, D. & Begelman, M. C. 2005, ApJ, 629, 903

[5] Tagliaferri, G. et al. 2005, Nature, 436, 985

[6] Yamazaki, R., Toma, K., Ioka, K., & Nakamura, T. 2006, MNRAS, 369, 311 (Y06)

[7] Zhang, B. et al. 2006, ApJ, 642, 354

Neutrino Emission from Stellar Core Collapse and Black Hole Formation

Ken'ichiro Nakazato[1], Kohsuke Sumiyoshi[2] and Shoichi Yamada[3]

[1] *Department of Physics, Waseda University, 3-4-1 Okubo, Shinjuku, Tokyo 169–8555, Japan*
[2] *Numazu College of Technology & Division of Theoretical Astronomy, National Astronomical Observatory of Japan, Ooka 3600, Numazu, Shizuoka 410–8501, Japan*
[3] *Department of Physics, Waseda University & Advanced Research Institute for Science & Engineering, Waseda University, 3-4-1 Okubo, Shinjuku, Tokyo 169–8555, Japan*

Abstract

In this study, we investigate the iron core collapses systematically for various masses, especially in the range which has not been studied well so far. Here, we solve the general relativistic hydrodynamics and neutrino transfer equations simultaneously, treating neutrino reactions in detail. We also estimate the neutrino event number from the black hole formation at the Galactic center for the currently operating detectors. As a result, we suggest that the probe into the black hole progenitors is possible by detecting the neutrinos emitted from them, because the more massive the progenitor is, the softer its $\bar{\nu}_e$ spectrum becomes. Further details of this study are seen in our lately submitted nanuscript [1].

1 Introduction

Various anomalous stars, such as the first stars in the universe (so-called Population III stars) or stars produced by stellar mergers in stellar clusters, are being studied recently. As for the Population III stars, it is suggested theoretically that they are much more massive ($M \gtrsim 100 M_\odot$) than stars of later generations. On the other hand, N-body simulations show that the runaway mergers of massive stars occur and the very massive ($M \gtrsim 100 M_\odot$) stars are formed in a young compact stellar cluster. It is noted especially that a new formation scenario of supermassive black holes is suggested nowadays, which requires the formation of intermadiate-mass black holes by the collapse of merged star in very compact stellar clusters [2]. If these anomalous stars collapse to black holes without supernova explosion, it is supposed to be hard to probe into their progenitors. One possibility is, we think, the neutrinos emitted from the black hole formation. For this purpose, systematical studies on the black hole formation including neutrinos are needed. In this study, we investigate the iron core collapses systematically for various masses and estimate the neutrino event number from the black hole formation at the Galactic center for the currently operating detectors. As a result, we suggest that we can probe into the black hole progenitors by the hardness of $\bar{\nu}_e$ spectrum because the more massive the progenitor is, the softer its $\bar{\nu}_e$ spectrum becomes.

2 Models and Methods

We construct the iron core models, which are used as initial models for the dynamical simulation of the collapse, solving the Oppenheimer-Volkoff equation under the assumption of the isentropy and the electron fraction $Y_e = 0.5$ throughout the core. For the systematic analysis, we set the initial central temperature as $T_{\mathrm{initial}} = 7.75 \times 10^9$ K, and generate 6 models with the values of entropy per baryon, $s_{\mathrm{initial}} = 3k_B$-$13k_B$. Since we define the mass of the iron core as the mass coordinate where the temperature is 5×10^9 K, the mass of the iron core is determined by the entropy in our models (Table 1). As for the numerical methods, we solve the general relativistic hydrodynamics and the neutrino transfer equations simultaneously, treating neutrino reactions in detail under spherical symmetry. We adopt a realistic equation of state [3,4] in order to obtain the initial models and follow the dynamics. Further details of

---

[1] E-mail:nakazato@heap.phys.waseda.ac.jp

numerical methods are given in our previous study [5]. It is noted that our method allows us to follow the dynamics with no difficulty up to the apparent horizon formation. The existence of the apparent horizon is the sufficient condition for the formation of a black hole (or, equivalently, of an event horizon).

3 Results and Discussions

It is known that the ordinary supernovae with $s_\text{initial} \sim 1k_\text{B}$ bounce because the central density exceeds the nuclear density ($\sim 2.5 \times 10^{14} \text{g/cm}^3$) and the pressure gets higher drastically. From our computations, we find that models with $3k_\text{B} \leq s_\text{initial} \leq 7.5k_\text{B}$ ($M_\text{iron} \leq 10.6 M_\odot$) have a bounce and they recollapse to black holes. On the other hand, models with $s_\text{initial} > 7.5k_\text{B}$ ($M_\text{iron} > 10.6 M_\odot$) collapse to black holes directly without bounce.

In the case of $3k_\text{B} \leq s \leq 7.5k_\text{B}$, it is noted that the bounce mechanism of the core with $s \geq 3k_\text{B}$ is not the same as that of the ordinary supernovae. The high entropy cores bounce by the thermal pressure of nucleons at sub-nuclear density. We can see this fact from the evolutions of central density and temperature in the phase diagram of the nuclear matter at $Y_e = 0.4$ and 0.2 (Figure 3). We note that for all models at the center, $Y_e \sim 0.4$ and $Y_e \sim 0.2$ when $T \sim 1$ MeV and $T \sim 10$ MeV, respectively. These figures show that the models with higher entropies go from the non-uniform mixed phase of nuclei and free nucleons to the classical ideal gas phase of thermal nucleons and α particles, whereas that of the ordinary supernova goes into the uniform nuclear matter phase. In the ideal gas phase, the number of non-relativistic nucleons and α particles is comparable to that of relativistic electrons. Since the adiabatic index of non-relativistic gas is $\gamma = \frac{5}{3}$ and that of relativistic gas is $\gamma = \frac{4}{3}$, the collapse is halted and bounce occurs. Because this bounce is weak, the shock is stalled and recollapses to black hole soon.
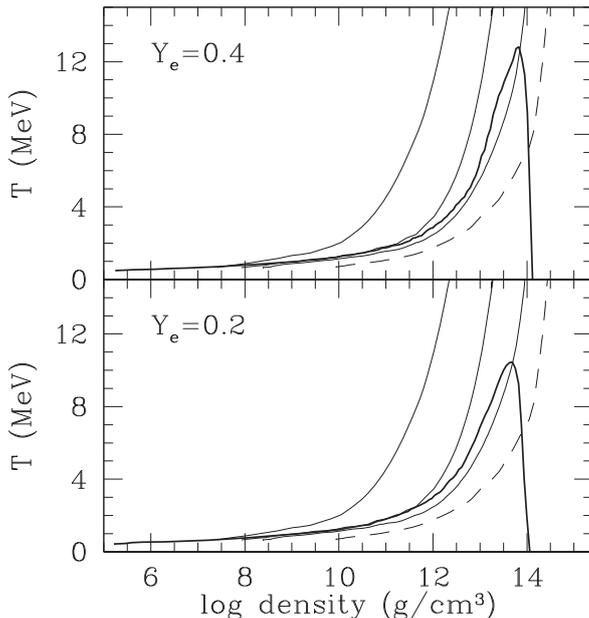
Figure 1: Phase diagram in $\rho - T$ plane from [4] for fixed electron fraction, Y_e (thick lines). The nucleus exist in the region below these thick lines. The phase boundaries depend on Y_e whereas the same trajectories are plotted for the upper panel and the lower panel. Dashed line represents the evolution of the central density and temperature for the ordinary supernova progenitor with the initial mass $15 M_\odot$ [6] and solid lines do that for the progenitors studied. Each line corresponds models with $s_\text{initial} = 3k_\text{B}$, $5k_\text{B}$ and $10k_\text{B}$ from right to left.

As for the neutrino emission during core collapse, we show the time-integrated neutrino spectra in the left panel of Figure 3. We can see that the spectra become softer for higher entropy models, especially

for $\bar{\nu}_e$ and ν_x. In order to investigate this tendency, we show the time-integrated spectra of the neutrino emitted before and after the shock formation each other in the right panel of Figure 3. We can see that, for higher entropy models, $\bar{\nu}_e$ and ν_x are emitted also before the shock formation. They are created by the electron-positron pair annihilation and their energy is relatively lower ($\lesssim$ several MeV) because the temperature is low ($T \lesssim 1$ MeV). On the other hand, for lower entropy models, $\bar{\nu}_e$ and ν_x can not be produced by the electron-positron pair process because positrons are absent owing to the Pauli blocking. As for $\bar{\nu}_e$ and ν_x emitted after the shock formation, they are mainly created by the bremsstrahlung. In this phase, the temperature near the neutrino sphere rises to $T \sim$ several MeV and it makes the neutrino energies relatively high ~ 10 MeV. Since the low energy ($\lesssim$ several MeV) neutrinos are not emitted so much and the spectra become harder for lower entropy models, the emission of low energy $\bar{\nu}_e$ and ν_x is characteristic for the collapse of high entropy cores.
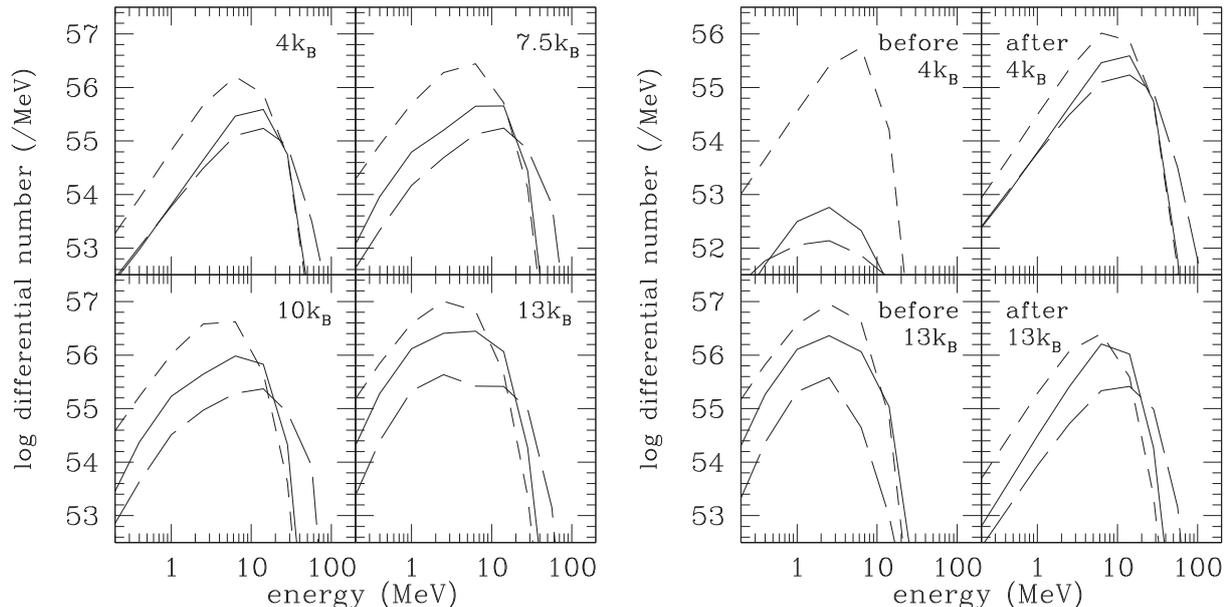
Figure 2: Spectra of time-integrated emissions of ν_e (short-dashed), $\bar{\nu}_e$ (solid) and ν_x (long-dashed). (*Left*) Upper left, upper right, lower left and lower right panels are for models with $s_{\mathrm{initial}} = 4k_{\mathrm{B}}$, $7.5k_{\mathrm{B}}$, $10k_{\mathrm{B}}$ and $13k_{\mathrm{B}}$, respectively. (*Right*) Upper left and upper right are the time-integrations of the emission before and after bounce, respectively, for the model with $s_{\mathrm{initial}} = 4k_{\mathrm{B}}$. Lower left and lower right panels are emission before and after shock formation, respectively, for the modell with $s_{\mathrm{initial}} = 13k_{\mathrm{B}}$.

Because lots of low energy $\bar{\nu}_e$ are emitted from the collapse of the high entropy cores and soften the spectrum, we may use this tendency in order to probe into the black hole progenitors. We estimate the $\bar{\nu}_e$ event number for Super Kamiokande III and KamLAND, currently operating neutrino detectors, under the assumption that the black hole formations considered above occur at the center of our Galaxy. For both detectors, the dominant reaction is the inverse beta decay,

$$\bar{\nu}_e + p \longrightarrow e^+ + n, \tag{1}$$

which we take into account only. We adopt the cross section for this reaction from [7]. For Super Kamiokande III, we assume that the fiducial volume is 22.5 kton and the trigger efficiency is 100% at 4.5 MeV and 0% at 2.9 MeV, which are the values at the end of Super Kamiokande I [8]. For KamLAND, we assume 1 kton fiducial mass, which means that 8.48×10^{31} free protons are contained [9]. We also assume that the trigger efficiency is 100% for all $\bar{\nu}_e$ energy larger than the threshold energy of the reaction.

The results are given in Table 1. The total event number does not change monotonically with the initial entropy of the core because the total number of neutrinos depends on both the core mass and the

duration time of neutrino emission. In order to investigate the hardness of $\bar{\nu}_e$ spectrum, we calculate the ratio of the event number by $\bar{\nu}_e$ with < 10 MeV to that for all events. The ambiguity about the distance of source is also canceled by this normalization. This ratio gets larger as the entropy of the core becomes higher. This suggests that we can probe the entropy of the black hole progenitor especially in higher regimes ($s_{\text{initial}} \geq 7.5 k_{\text{B}}$) because the event numbers of $\bar{\nu}_e$ with < 10 MeV are over 100 by Super Kamiokande III.

Table 1: Models and Results

s_{initial} (k_{B})	M_{iron} ($M_{\odot}$)	$t_{\text{recollapse}}$ (msec)	$\frac{N_{\bar{\nu}_e < 10\,\text{MeV,SK}}}{N_{\bar{\nu}_e,\text{SK}}}$	$N_{\bar{\nu}_e,\text{SK}}$	$\frac{N_{\bar{\nu}_e < 10\,\text{MeV,Kam}}}{N_{\bar{\nu}_e,\text{Kam}}}$	$N_{\bar{\nu}_e,\text{Kam}}$
3.0	2.44	96.7	3.3%	6163	3.3%	174
4.0	3.49	62.0	4.0%	4778	4.0%	135
5.0	4.97	52.6	4.6%	4319	4.6%	122
7.5	10.6	37.9	7.3%	4018	7.3%	114
10.0	19.3	—	11.8%	5326	12.0%	151
13.0	34.0	—	20.1%	9139	20.5%	259

Note: s_{initial}, M_{iron} and $t_{\text{recollapse}}$ are the initial value of the entropy par baryon, the iron core mass of the initial model and the interval time from the bounce to the apparent horizon formation, respectively. $N_{\bar{\nu}_e}$ represents the event number of $\bar{\nu}_e$ by Super Kamiokande III and KamLAND. The subscript "SK" and "Kam" means the prediction for Super Kamiokande III and KamLAND, respectively, and the subscript "< 10 MeV" means the event by $\bar{\nu}_e$ with < 10 MeV.

Acknowledgments

References

[1] Nakazato, K., Sumiyoshi, K., & Yamada, S. 2007, submitted to ApJ

[2] Ebisuzaki, T., et al. 2001, ApJ, 562, L19

[3] Shen, H., Toki, H., Oyamatsu, K., & Sumiyoshi, K. 1998a, Nucl. Phys., A637, 435

[4] Shen, H., Toki, H., Oyamatsu, K., & Sumiyoshi, K. 1998b, Prog. Theor. Phys., 100, 1013

[5] Nakazato, K., Sumiyoshi, K., & Yamada, S. 2006, ApJ, 645, 519

[6] Sumiyoshi, K., Yamada, S., Suzuki, H., Shen, H., Chiba, S., & Toki, H. 2005, ApJ, 629, 922

[7] Vogel, P., & Beacom, J. F. 1999, Phys. Rev. D, 60, 053003

[8] Hosaka, J., et al. 2006, Phys. Rev. D, 73, 112001

[9] Eguchi, K., et al. 2003, Phys. Rev. Lett., 90, 021802

Secular bar mode instabilities in rotating relativistic stars

Motoyuki Saijo[1] and Eric Gourgoulhon[2]

[1] *School of Mathematics, University of Southampton, Southampton SO17 1BJ, United Kingdom*
[2] *Laboratoire de l'Univers et de ses Théories, UMR 8102 du CNRS, Observatoire de Paris, F-92195 Meudon Cedex, France*

Abstract

We investigate the viscosity driven instability in rotating relativistic stars by means of an iterative approach. We focus on polytropic rotating equilibrium stars and impose an $m = 2$ perturbation in the lapse. We vary both the stiffness of the equation of state and the compactness of the star to study these factors on the critical value T/W for the instability. For a rigidly rotating star, the criterion T/W, where T is the rotational kinetic energy and W the gravitational binding energy, mainly depends on the compactness of the star and takes values around $0.13 \sim 0.16$, which slightly differ from that of Newtonian incompressible stars (~ 0.14). For differentially rotating stars, the critical value of T/W is found to span the range $0.17 - 0.25$. The value is significantly larger than in the rigidly rotating case with the same compactness of the star.

1 Introduction

Stars in nature are usually rotating and subject to nonaxisymmetric rotational instabilities. An analytical treatment of these instabilities exists only for Newtonian incompressible equilibrium fluids [e.g. 1]. For these configurations, global rotational instabilities arise from non-radial toroidal modes $e^{im\varphi}$ ($m = \pm 1, \pm 2, \ldots$) when $\beta \equiv T/W$ exceeds a certain critical value. Here φ is the azimuthal coordinate, while T and W are the rotational kinetic and gravitational binding energies. In the following we will focus on the $m = \pm 2$ bar-mode, since it is the fastest growing mode when the rotation is sufficiently rapid.

There exist two different mechanisms and corresponding timescales for bar-mode instabilities. Rigidly rotating, incompressible stars in Newtonian gravity are *secularly* unstable to bar formation when $\beta \gtrsim \beta_{\rm sec} \simeq 0.14$. This instability can grow in the presence of some dissipative mechanisms, such as viscosity or gravitational radiation, and the growth time is determined by the dissipative timescale, which is usually much longer than the dynamical timescale of the system. By contrast, a *dynamical* instability to bar formation sets in when $\beta \gtrsim \beta_{\rm dyn} \simeq 0.27$. This instability is independent of any dissipative mechanism, and the growth time is the hydrodynamic timescale of the system.

In the absence of thermal dissipation there are two dissipative mechanisms that can drive the secular bar instability; they are viscosity and gravitational radiation. The viscosity driven instability sets in when a mode has a zero-frequency in the frame rotating with the star, and the first unstable mode in terms of m is the $m = 2$ bar mode. Throughout the deformation process the circulation of a given closed curve at the beginning of deformation varies but the angular momentum is conserved. On the other hand, the instability induced by gravitational radiation sets in when the backward going mode is dragged forward in the inertial frame, and the modes are all unstable when m exceeds a certain value. Throughout the deformation process the star's angular momentum varies but the circulation of a given closed curve at the beginning of deformation is conserved.

The purpose of the paper is twofold. Firstly, we investigate the critical value T/W of the viscosity-driven instability for a rigidly rotating compressible star. The argument that the viscosity-driven instability can deform a star from a Maclaurin spheroid to a Jacobi ellipsoid is valid if the star has no internal energy. Otherwise the total energy can be converted into the internal energy without any emission from the star. Here we assume that the cooling timescale of the star is shorter than the thermal heating

---

[1] E-mail:ms1@maths.soton.ac.uk
[2] E-mail:eric.gourgoulhon@obspm.fr

timescale so that the thermal energy generated by viscosity is immediately radiated away. Therefore the picture of the deformation process due to viscosity is quite similar to the case of incompressible stars.

Our other main purpose in this paper is to investigate the effect of differential rotation on the secular bar instabilities driven by viscosity. For high viscosity or a strong magnetic field, the star maintains rigid rotation. However, in nature, the star may rotate differentially, as is the case for the Sun. Therefore it is worthwhile taking differential rotation into account to study instabilities driven by viscosity in rotating relativistic stars.

This paper is organized as follows. In Sec. 2 we present the iterative evolution approach to determine the stability due to viscosity in relativistic rotating stars. We discuss our numerical results in Sec. 3, and briefly summarize our findings in Sec. 4. Throughout this paper, we use the geometrized units with $G = c = 1$ and adopt polar coordinates (r, θ, φ) with the coordinate time t. A more detailed discussion is presented in Ref. [2].

2 Iterative evolution approach

We follow an iterative evolution approach [3] to investigate the viscosity-driven instability in rotating relativistic stars. The physical viewpoint of this approach can be understood in Newtonian gravity by considering the transition between a rigidly rotating incompressible axisymmetric star (Maclaurin spheroid) to a nonaxisymmetric star (Jacobi ellipsoid). The above deformation process is driven by viscosity, since viscosity causes the circulation to vary but keeps the angular momentum constant in the Newtonian incompressible star. From a computational viewpoint, the key theme of this approach is that, instead of performing a time evolution of the star to investigate its stability, we treat the iteration number as an evolutional time and determine the stability of the star with respect to this iteration. The advantage of this approach is that there is no restriction on the evolutional time-step even in a star with high compactness.

To determine the stability of a rotating relativistic star driven by viscosity, we follow a computational procedure to construct an equilibrium configuration until we reach a relative error in the enthalpy norm of 1.5×10^{-7}. At this iteration step, we put the following $m = 2$ perturbation in the logarithmic lapse ν to enhance the growth of the bar mode instability as

$$\nu = \nu_{\mathrm{eq}}(1 + \varepsilon_{\mathrm{amp}} \sin^2 \theta \cos 2\varphi), \tag{2.1}$$

where ν_{eq} is the logarithmic lapse in the equilibrium, and $\varepsilon_{\mathrm{amp}}$ is the amplitude of the perturbation. We diagnose the maximum logarithmic lapse of the $m = 2$ coefficients $\hat{\nu}_2$ in terms of mode decomposition as

$$q = \max |\hat{\nu}_2|. \tag{2.2}$$

We also define the logarithmic derivative of q in the iteration step $\mathcal{N}_i$ as

$$\frac{\dot{q}}{q} = \frac{q_i - q_{i-1}}{q_{i-1}}, \tag{2.3}$$

where q_i denotes q at the iteration step $\mathcal{N}_i$. We then determine the stability of the star as follows. When the diagnostic q grows exponentially after we impose a bar mode perturbation in the logarithmic lapse, we conclude that the star is unstable. On the other hand when the diagnostic decays after we introduce the perturbation, the star is stable. Finally we determine the critical value of β as the minimum one in the unstable branch. We also confirm our argument that in all equilibrium stars there is a continuous transition between stable and unstable stars as a function of β [2].

3 Numerical Results

We study the critical value of β for the viscosity-driven instability in rigidly rotating stars (see Figure 1). We have found that relativistic gravitation tends to stabilizes the star, and that the critical value of β for each compactness is almost insensitive to the stiffness of the equation of state. Our computational results (Figure 1) show that the critical β is ~ 0.137 for $M/R = 0.01$ (where M is the gravitational mass, R the
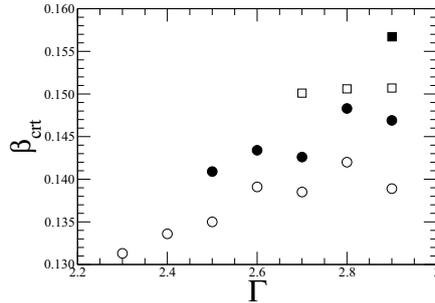
Figure 1: Critical value of β as a function of an adiabatic index Γ for four different compactness of rigidly rotating stars (see Table II of Ref. [2]). Open circles, filled circles, open squares, and filled squares refer to the compactness M/R of 0.01, 0.05, 0.1, and 0.15, respectively. The star whose adiabatic index is $\Gamma = \Gamma_{\text{low}} - 0.1$, where Γ_{low} is the lowest Γ of an unstable star for any compactness in this figure, is stable.

Table 1: Critical value of the viscosity-driven instability in differentially rotating relativistic stars. We choose $\Gamma = 2$ for the polytropic equation of state and $\hat{A}_{\text{rot}} = 1$ as the degree of differential rotation.

R_p/R_e[1]	H_{max}[2]	β_{crt}	M/R
0.4458	7.594×10^{-3}	0.1828	0.01000
0.3985	3.830×10^{-2}	0.1999	0.05000
0.3820	7.492×10^{-2}	0.2186	0.1000
0.3457	1.116×10^{-1}	0.2354	0.1500
0.2982	1.581×10^{-1}	0.2496	0.2000

circumferential radius), ~ 0.145 for $M/R = 0.05$, ~ 0.150 for $M/R = 0.1$, and ~ 0.157 for $M/R = 0.15$, respectively. The critical value of β monotonically increases when increasing the compactness of the star. For the case of Newtonian compressible stars it was shown in Fig. 3 of Ref. [3] that the critical value of β is ~ 0.134, and is not very sensitive to the stiffness of the star.

We now investigate the threshold for the viscosity-driven instability in differentially rotating stars. First we show the result of a fixed rotation profile throughout the evolution (Table 1). We find that both relativistic gravitation and differential rotation tend to stabilize the star. The critical value is $\beta_{\text{crt}} \sim 0.13 - 0.16$ for a rigidly rotating star depending on the compactness of the star, while $\beta_{\text{crt}} \sim 0.18 - 0.25$ for a differentially rotating star with a moderate degree of differential rotation.

Next we study the variation of the rotation profile as viscosity also plays a significant role in changing the angular momentum distribution of the star. In order to mimic this process, after we impose a perturbation we vary slightly the parameter which represents the degree of differential rotation $\hat{A}_{\text{rot}}$ and the central angular velocity Ω_{c}

$$\hat{A}_{\text{rot}}^{-1} = \hat{A}_{\text{rot}}^{-1 \, \text{(eq)}}[1 - \epsilon_{\text{rot}}(\mathcal{N} - \mathcal{N}_{\text{ptb}})], \tag{3.1}$$

$$\Omega_{\text{c}} = \Omega_{\text{c}}^{\text{(eq)}}[1 - \epsilon_{\text{omg}}(\mathcal{N} - \mathcal{N}_{\text{ptb}})], \tag{3.2}$$

$\hat{A}_{\text{rot}}^{\text{(eq)}}$ the degree of differential rotation in the equilibrium state, ϵ_{rot} the degree of the variation of the rotation profile which we set to be 1.0×10^{-4}, $\mathcal{N}$ the iteration number, $\mathcal{N}_{\text{ptb}}$ the iteration number when we impose the perturbation, $\Omega_{\text{c}}^{\text{(eq)}}$ is the central angular momentum in the equilibrium state, and ϵ_{omg} the degree of the variation of the central angular velocity required in order to (approximately) conserve the total angular momentum.

Taking into account the change of rotational profile, we show our numerical results for β_{crt} in Figure 2. We find that all stars with $\beta \approx \beta_{\text{crt}}$ and a fixed rotation profile become unstable. In fact, the plateau stage of $\dot{q}/q$ for a fixed rotation profile in Fig. 7 of Ref. [2] becomes increase one in our Figure 2. Therefore, we estimate two relevant timescales, the growth time of the bar mode due to viscosity and the variation time of the rotation profile due to viscosity, based on the analytical estimation [2]. The timescales used
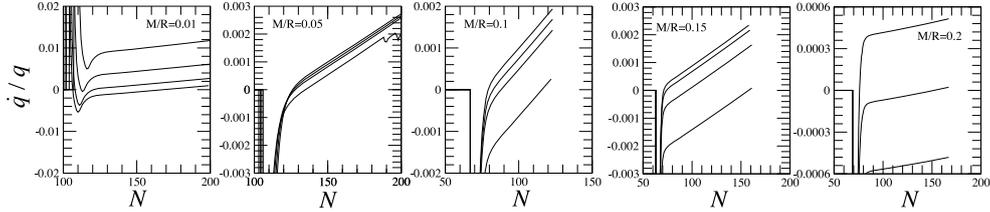
Figure 2: Diagnostic $\dot{q}/q$ as a function of iteration step $\mathcal{N}$ for five different differentially rotating stars. Solid, dashed, dotted, and dashed lines denote $\beta = (0.1825, 0.1828, 0.1834, 0.1844)$ and $\varepsilon_{\mathrm{omg}} = 0.8 \times 10^{-4}$ for $M/R = 0.01$; $\beta = (0.1993, 0.1996, 0.1998, 0.1999)$ and $\varepsilon_{\mathrm{omg}} = 0.9 \times 10^{-4}$ for $M/R = 0.05$; $\beta = (0.2180, 0.2184, 0.2185, 0.2186)$ and $\varepsilon_{\mathrm{omg}} = 1.3 \times 10^{-4}$ for $M/R = 0.1$; $\beta = (0.2348, 0.2352, 0.2353, 0.2354)$ and $\varepsilon_{\mathrm{omg}} = 1.1 \times 10^{-4}$ for $M/R = 0.15$; and $\beta = (0.2494, 0.2495, 0.2496)$ and $\varepsilon_{\mathrm{omg}} = 1.0 \times 10^{-4}$ for $M/R = 0.2$, respectively. Note that $\dot{q}/q$ is always increasing around the critical value of β in differentially rotating stars. We see that variations of rotation profile due to viscosity unstabilize the star.

in our numerical results should be described as

$$\tau_{\mathrm{ang}} \quad \approx \quad \varepsilon_{\mathrm{omg}}^{-1}, \tag{3.3}$$

$$\tau_{\mathrm{bar}} \quad \approx \quad \varepsilon_{\mathrm{omg}}^{-1} \left(\frac{\Omega_{\mathrm{c}} - \Omega_{\mathrm{s}}}{\Omega_{\mathrm{c}}} \right) \left(\frac{\beta_{\mathrm{sec}}}{\beta - \beta_{\mathrm{sec}}} \right), \tag{3.4}$$

where Ω_{s} is the equatorial surface angular velocity, and β_{sec} is the critical value β_{crt} of the secular bar mode instability driven by viscosity. We confirm that differential rotation tends to stabilize the star. Also, Eq. (3.4) shows that the timescale of the bar growth becomes short as the viscosity reduces the degree of differential rotation. The critical value β_{crt} changes from the value computed for a fixed rotation profile, but the change is roughly of the same order of magnitude as for differential rotation profile (Eq. [3.1]), which means $\approx \varepsilon_{\mathrm{omg}} (\approx \varepsilon_{\mathrm{rot}})$.

4   Conclusion

We have studied the viscosity-driven instability in both rigidly and differentially rotating polytropic stars by means of iterative evolution approach in general relativity. We have focused on the threshold of the instability driven by viscosity.

We find that relativistic (rather than Newtonian) gravitation stabilizes the star, preventing the onset of a viscosity-driven instability. Also, the critical value T/W is not sensitive to the stiffness of the polytropic equation of state for a given compactness of the star. In a previous study devoted to compressible stars, Bonazzola, Frieben and Gourgoulhon [3] investigated a sequence of mass-shedding stars and showed that relativistic gravitation does stabilize rigidly rotating polytropic stars. In our study we have calculated the value of β_{crt} for rigidly rotating stars.

We have also found that differential rotation stabilizes a star against the instability driven by viscosity. If we fix the compactness of the star, we find a significant increase of the critical value β_{crt}, which supports the above statement. We have also confirmed the above statement by changing the rotation profile due to viscosity and found that differential rotation still significantly stabilizes the instability driven by viscosity.

References

[1] S. Chandrasekhar, Ellipsoidal Figures of Equilibrium, Yale Univ. Press, New York, Chap. 5 (1969).

[2] M. Saijo and E. Gourgoulhon, Phys. Rev. D**74**, 084006 (2006).

[3] S. Bonazzola, J. Frieben and E. Gourgoulhon, Astrophys. J. **460**, 379 (1996); Astron. Astrophys. **331**, 280 (1998).

Self-similar homogeneous collapse of a perfect fluid and new critical phenomena

Eiji Mitsuda[1] and Akira Tomimatsu[2]

Department of Physics, Graduate School of Science, Nagoya University, Nagoya 464–8602, Japan

Abstract

Assuming that the collapsing matter is a perfect fluid with the equation of state $P = \alpha\rho$, we study spherically symmetric non-self-similar perturbations in homogeneous self-similar collapse described by the flat Friedmann solution. In the low pressure approximation $\alpha \ll 1$, we analytically derive an infinite set of the normal modes and their growth (or decay) rate. The existence of one unstable normal mode is found to suggest that new critical phenomena occur which result from the development of a certain inhomogeneous density profile with the lapse of time in homogeneous self-similar collapse of a sufficiently low pressure perfect fluid.

1   Introduction

Spherically symmetric self-similar gravitational collapse of a perfect fluid with pressure P given by the equation of state $P = \alpha\rho$ is one of the most extensively-studied phenomena in general relativity. Many efforts have been made to solve the Einstein's equations governing its dynamics, which are reduced to a set of ordinary differential equations with respect to the single variable $z \equiv r/t$. The flat Friedmann solution is well known as the unique analytically-found exact self-similar solution regular at the center and has played an important role in finding a family of solutions regular at the center. The homogeneous collapse described by this solution has been considered as the most basic process to spacelike singularity formation in the self-similar dynamics, while essential features of inhomogeneous self-similar collapse have been understood mainly through the detailed analysis of the general relativistic Larson-Penston solution. In addition, it is also noteworthy that the perfect fluid critical collapse corresponding to the threshold of black hole formation has been confirmed to be described by the self-similar solution called as the general relativistic Hunter(a) solution.

By means of renormalization group ideas, critical phenomena in spherically symmetric gravitational collapse are well explained in terms of time evolution of spherically symmetric non-self-similar perturbations of matter and metrics in spherically symmetric self-similar gravitational collapse [1]. An essential point of such an explanation is that a self-similar solution relevant to critical phenomena gives the single unstable normal mode. In fact, it was numerically found for $0 < \alpha \lesssim 0.89$ that the single normal mode is allowed to grow with the lapse of time in the self-similar collapse described by the general relativistic Hunter(a) solution [2]. In addition it was claimed through the numerical analysis of the perturbations for $0 < \alpha \lesssim 0.036$ that the flat Friedmann solution and the general relativistic Larson-Penston solution are stable and act as an attractor in general gravitational collapse [3]. Therefore the self-similar solution relevant to critical phenomena has been believed to be only the general relativistic Hunter(a) solution.

Recently, we have developed an analytical scheme to treat the stability problem by constructing the single wave equation governing non-self-similar spherically symmetric perturbations [4], which is reduced to the ordinary differential equation if we assume the perturbations to have the time dependence given by $\exp(i\omega \log|t|)$. In this paper, using this analytical scheme, we study the stability problem for the flat Friedmann solution in the low pressure limit, i.e., $0 < \alpha \ll 1$ (see [5] for details of this analysis). Fortunately, in the expansion with respect to the small parameter α, we can explicitly solve the master ordinary differential equation for the normal modes and consequently find the single unstable normal mode, which was not found in the numerical analysis [3]. This result strongly suggests that new critical phenomena relevant to the flat Friedmann solution occur in general gravitational collapse which starts from a nearly homogeneous density profile.

---

[1] E-mail:emitsuda@gravity.phys.nagoya-u.ac.jp

[2] E-mail:atomi@gravity.phys.nagoya-u.ac.jp

2 Perturbation theory for self-similar homogeneous perfect fluid collapse

In this section, we briefly illustrate our analytical scheme to treat spherically symmetric non-self-similar perturbations in homogeneous self-similar perfect fluid collapse described by the flat Friedmann solution. The line element considered throughout this paper is given by

$$ds^2 = -e^{2\nu(t,r)}dt^2 + e^{2\lambda(t,r)}dr^2 + R^2(t,r)\left(d\theta^2 + \sin^2\theta d\varphi^2\right) \tag{1}$$

with the comoving coordinates t and r. As was mentioned in Sec. 1, the equation of state is assumed to be $P = \alpha\rho$ with a constant α lying in the range $0 < \alpha \leq 1$. To discuss the self-similar behavior later, we use a new variable z defined by $z \equiv r/t$, instead of r. In addition, instead of the four unknown functions ν, λ, R and ρ, we introduce the following dimensionless functions:

$$S(t,r) \equiv \frac{R}{r} , \qquad \eta(t,r) \equiv 8\pi r^2 \rho , \qquad M(t,r) \equiv \frac{2m}{r} , \qquad V(t,r) \equiv ze^{\lambda-\nu} , \tag{2}$$

where the function $m(t,r)$ is the Misner-Sharp mass. The function V is interpreted as the velocity of a $z = $ const surface relative to the fluid element.

Now we consider spherically symmetric non-self-similar perturbations in the flat Friedmann background by expressing the solutions for the Einstein's equations as

$$S(t,z) = S_B(z)\left\{1 + \epsilon S_1(t,z) + O(\epsilon^2)\right\} , \qquad \eta(t,z) = \eta_B(z)\left\{1 + \epsilon\eta_1(t,z) + O(\epsilon^2)\right\} ,$$
$$M(t,z) = M_B(z)\left\{1 + \epsilon M_1(t,z) + O(\epsilon^2)\right\} , \qquad V(t,z) = V_B(z)\left\{1 + \epsilon V_1(t,z) + O(\epsilon^2)\right\} \tag{3}$$

with a small parameter ϵ. The functions S_B, η_B, M_B and V_B for the flat Friedmann solution are given by

$$S_B(z) \propto (-z)^{-p} , \qquad \eta_B(z) \propto z^2 , \qquad M_B(z) \propto (-z)^{2-3p} , \qquad V_B(z) \propto (-z)^{1-p} \tag{4}$$

with the constant p defined as $p \equiv 2/3(1+\alpha)$. From the perturbation equations for S_1, η_1 and M_1, we can obtain the single wave equation for the function Ψ defined as

$$\Psi(t,z) = S_1(t,z) - f(z)M_1(t,z) , \tag{5}$$

where the function f is explicitly written by the background flat Friedmann solution. The perturbations S_1, η_1, M_1 and V_1 are determined by the solution Ψ for the wave equation.

The wave equation allows us to consider the modes ϕ defined as

$$\Psi(t,z) = \phi(z,\omega)g(z)e^{i\omega\log(-t)} \tag{6}$$

with the spectral parameter ω, where the function g is also explicitly written by the background flat Friedmann solution. Then the equation for ϕ is found to be

$$\phi_{,xx} + \frac{2i\omega x - 2(1-p)x^2 - F(x,\alpha)}{(1-p)x(1-x^2)}\phi_{,x} - \frac{i\omega(F(x,\alpha) + W(x,\alpha)) + U(x,\alpha)}{(1-p)^2 x^2 (1-x^2)^2}\phi = 0 , \tag{7}$$

where the new variable x used instead of z is defined as

$$x = -V_B/\sqrt{\alpha} , \tag{8}$$

and the functions F, W and U are explicitly written as the functions of the variable x and regular both at $x = 0$ and $x = 1$. Note that the regular center $z = 0$ and the sonic point defined as a point at which the velocity of a $z = $ const surface relative to the fluid is equal to the sound speed, i.e., $V_B = -\sqrt{\alpha}$ correspond to $x = 0$ and $x = 1$, respectively. We require the boundary conditions such that ϕ is analytic both at the regular center $x = 0$ and at the sonic point $x = 1$ to set up the eigenvalue problem for Eq. (7) and to obtain the normal modes and the discrete eigenvalues denoted by ϕ_n and ω_n.

Here we would like to note that there exists an exact solution $\phi = \phi_g$ for Eq. (7) if the spectral parameter ω is equal to ω_g defined as $\omega_g = (1-\alpha)i/(1+\alpha)$. This solution ϕ_g is one of the normal modes ϕ_n but corresponds to a gauge mode due to an infinitesimal transformation of t. In fact, all the perturbations η_1, S_1 and M_1 obtained from ϕ_g are found to be independent of z. Although the gauge mode is obviously unphysical, the presence of such an exact solution will be mathematically useful for checking the validity of the analysis of Eq. (7).

3 Result and its implications

As was mentioned in Sec. 1, we consider the low pressure limit $\alpha \to 0$, keeping the variable x finite in the range $0 \le x \le 1$ and expanding the solution $\phi(x, \omega, \alpha)$ analytic at $x = 0$ as follows,

$$\phi(x, \omega, \alpha) = \phi^{(0)}(x, \omega) + O(\alpha) . \tag{9}$$

For the lowest-order solution $\phi^{(0)}$ we obtain the equation

$$\frac{d^2\phi^{(0)}}{dx^2} + \frac{3}{1-x^2}\left\{2i\omega + \frac{2x^3 + 3x^2 + 10x + 3}{3x(1+2x)}\right\}\frac{d\phi^{(0)}}{dx}$$
$$-\frac{3}{x(1+2x)(1+x)(1-x^2)}\left\{2i\omega(2x^2 - 2x - 1) - \frac{2x^4 + 4x^3 - x^2 - 2x - 1}{x}\right\}\phi^{(0)} = 0 . \tag{10}$$

We would like to emphasize that this limit does not mean to consider an exactly pressureless fluid (i.e., a dust fluid) because the requirement of the analyticity of ϕ at the sonic point $x = 1$ is not missed. The crucial point in this approach is that we can explicitly derive general solutions for Eq. (10). In particular, the solution $\phi^{(0)}$ satisfying the boundary condition at $x = 0$ is written as

$$\phi^{(0)}(x, \omega) = Z_1(x, \omega) - Z_2(x, \omega) , \tag{11}$$

where the functions Z_1 and Z_2 are the two independent solutions for Eq. (10) and given by

$$Z_1(x, \omega) = (1+x)^3\left\{-6x^2\omega^2 - 4x(x^2 - 3x + 1)i\omega + (1-x)^4\right\}/x^3(1+2x) , \tag{12}$$

$$Z_2(x, \omega) = (1-x)^{4+3i\omega}(1+x)^{1-3i\omega}\left\{x^2 + 2(1+i\omega)x + 1\right\}/x^3(1+2x) . \tag{13}$$

It is clear that this solution $\phi^{(0)}$ becomes analytic also at the sonic point $x = 1$ if the spectral parameter ω is equal to ω_n given by

$$\omega_n = \omega_n^{(0)} + O(\alpha) , \qquad \omega_n^{(0)} = (4 - n)i/3 \tag{14}$$

with n defined as non-negative integers. However, for $n = 0$, 2 and 4, the function $\phi^{(0)}$ turns out to vanish. Hence, the values of $\omega_n^{(0)}$ are given only for $n = 1, 3, 5, 6, \cdots$. It can be easily found that the value of $\omega_1^{(0)}$ and the function $\phi^{(0)}(x, \omega_1^{(0)})$ are identical with the value of ω_g and the gauge mode ϕ_g in the limit $\alpha \to 0$.

The most important result is that the imaginary part of $\omega_3^{(0)}$ given by Eq. (14) is positive, namely, there exists one unstable normal mode, at least for sufficiently small values of α. Hence the flat Friedmann solution does not act as an attractor in inhomogeneous collapse of a sufficiently low pressure perfect fluid. Moreover, it is also interesting that there exists an infinite set of the stable normal modes (i.e., ϕ_n for $n \ge 5$).

Let us denote the perturbed density η_1 corresponding to the normal modes ϕ_n by $\eta_{1(n)}$, which is expanded with respect to α as follows,

$$\eta_{1(n)}(t, x, \alpha) = \eta_{1(n)}^{(0)}(x) \exp\left\{i\omega_n^{(0)} \log(-t)\right\} + O(\alpha) . \tag{15}$$

Here we focus our attention on the leading term $\eta_{1(n)}^{(0)}$ depending on x. Using Eqs. (11), (6) and (5) in the limit $\alpha \to 0$ for the eigenvalues $\omega = \omega_n^{(0)}$, we obtain

$$\eta_{1(n)}^{(0)}(x) = \frac{2+n}{6x}\left[(1-x)^{n-2}\left\{3x^2 + 3(n-2)x + (n-1)(n-3)\right\}\right.$$
$$\left. -(1+x)^{n-2}\left\{3x^2 - 3(n-2)x + (n-1)(n-3)\right\}\right] . \tag{16}$$

In Fig. 1, we show the configuration of the density perturbation $\eta_{1(n)}^{(0)}(x)$ normalized by its value at $x = 0$ for $n = 1, 3, 5, 6, 7, 8, 9$ and 10 in the range $0 \le x \le 1$. It is shown in this figure that the normal mode
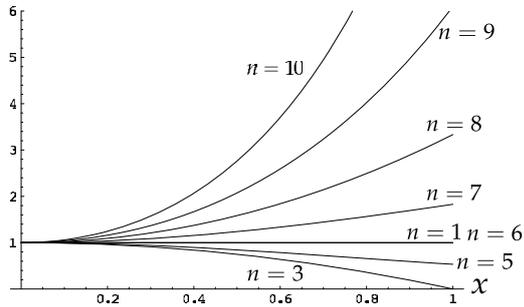
Figure 1: Configuration of the density perturbation given by $\eta_{1(n)}^{(0)}(x)/\eta_{1(n)}^{(0)}(0)$.
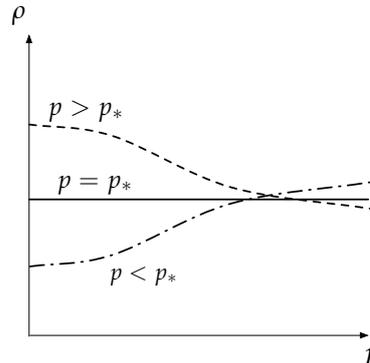
Figure 2: one parameter p family of the initial density profile which should be set up to see new critical phenomena relevant to the homogeneous self-similar collapse.

$\eta_{1(1)}^{(0)}$ corresponds to the gauge mode $\eta_g = \mathrm{const}$ at a given time as was mentioned in Sec. 2. In addition, it should be emphasized that the normal mode $\eta_{1(6)}^{(0)}$, which is also constant at any x, is a physical normal mode because the corresponding perturbation M_1 depends on x in the range $0 \leq x \leq 1$.

From Fig. 1, we note that the amplitude of all the stable normal modes (i.e., the normal modes for $n \geq 5$) at the sonic point $x = 1$ remains non-zero and the amplitude of the normal modes for $n \geq 7$ rather increases towards the sonic point $x = 1$ from the center $x = 0$. The ratio $\eta_{1(n)}^{(0)}(1)/\eta_{1(n)}^{(0)}(0)$ increases as n becomes larger and the decay rate $-\mathrm{Im}(\omega_n)$ given by Eq. (14) has the same tendency. This implies that the density perturbation generated near the sonic point is rapidly carried away to the supersonic region $x > 1$ by the background transonic flow and the growth of such a density perturbation in the subsonic region is prevented. It is remarkable that only for $n = 3$, the value of $\eta_{1(n)}^{(0)}$ vanishes at $x = 1$. This seems to be the most favorable configuration of η_1 to allow the growth of the density perturbation due to the effect of its own self-gravitation.

It should be emphasized that only the single normal mode giving an inhomogeneous density profile drawn as Fig. 1 for $n = 3$ is allowed to grow with the lapse of time in homogeneous self-similar collapse of a sufficiently low pressure perfect fluid. This result strongly suggests that critical phenomena can be observed at least for sufficiently small α in spherically symmetric perfect fluid collapse characterized by one parameter p representing inhomogeneity of the initial density profile (see Fig. 2). In such critical phenomena, the critical collapse will be described by the flat Friedmann solution. If the general relativistic Larson-Penston solution is confirmed to be stable also in our analytical scheme, a transition from the flat Friedmann stage to the general relativistic Larson-Penston stage may occur in the collapse for $p > p_*$. Because the general relativistic Larson-Penston solution for $0 < \alpha \lesssim 0.0105$ describes naked singularity formation, the critical collapse may correspond to the threshold of the naked singularity formation. What critical phenomena are relevant to the flat Friedmann solution will be an interesting problem to be investigated in future works.

References

[1] T. Koike, T. Hara, and S. Adachi, Phys. Rev. Lett. **74**, 5170 (1995).

[2] T. Koike, T. Hara, and S. Adachi, Phys. Rev. D **59**, 104008 (1999).

[3] T. Harada and H. Maeda, Phys. Rev. D **63**, 084022 (2001).

[4] E. Mitsuda and A. Tomimatsu, Phys. Rev. D **73**, 124030 (2006).

[5] E. Mitsuda and A. Tomimatsu, Phys. Rev. D **74**, 104019 (2006).

Doubly Spinning Black Rings and Beyond

Hideaki Kudoh [1]

Department of Physics, UCSB, Santa Barbara, CA 93106, USA

Abstract

We study a method to solve stationary axisymmetric vacuum Einstein equations numerically. As an illustration, the five-dimensional doubly spinning black rings that have two independent angular momenta are formulated in a way suitable for fully nonlinear numerical method. Expanding for small second angular velocity, the formulation is solved perturbatively upto second order involving the backreaction from the second spin. The obtained solutions are regular without conical singularity, and the physical properties are discussed with the phase diagram of the reduced entropy vs the reduced angular momenta. Possible extensions of the present approach to constructing the higher dimensional version of black ring and the ring with the cosmological constant are also discussed.

0.1 Introduction

At the level of classical theory of gravity, black holes are simple but general vacuum state of spacetime itself. This is a noteworthy consequence in the four-dimensional black hole physics by the uniqueness theorems. Nevertheless, corresponding to the fact that the number of degrees of freedom of gravity increases with spacetime dimensions, such simplicity of spacetime seems to hold only in four-dimensions, as was realized by the discovery of five-dimensional black rings (BRs) with horizon topology $S^1 \times S^2$ [1]. The BRs are in good contrast with the higher-dimensional Kerr solution, and many aspects have been studied so far including extensions of the solution, partial stability, role in string theory, etc.

At present, one of important aspects concerning BRs is to find out new type of "black ring" in higher dimensions. To tackle the issue, we need a new approach or tool. After the original investigation of BR, several systematic methods which can rederive the vacuum black ring solution have been developed. An outcome is the discovery of vacuum BRs with rotation on the S^2 but without rotation along the S^1 circle [2]. (An independent work based on tractable coordinates is [3].) The five-dimensional BRs have two independent rotational planes and the two rotations can generate two independent angular momenta. Thus we expect doubly spinning BRs that have the rotation on both S^2 and S^1. However, the exact solution of doubly spinning BRs has not yet been discovered, and no concrete procedure to find it has been available. The black ring with two angular momenta is known for supersymmetric case, but the two angular momenta are not independent conserved charges[4].

The present paper aims at exploring a new approach to search for new type of black holes. A numerical approach has been employed and developed to discover static axisymmetric solutions over the past several years. In this paper, we adopt the canonical form of metric for stationary axisymmetric spacetimes [5] as suitable coordinates for numerics, and we will work on five dimensions. Although the so-called ring-coordinates is the most adopted coordinate system for BRs, it is not rectangular at the asymptotic infinity (boundary) and less useful. As a good example to test such approach, we focus on the issue of doubly spinning BRs. We formulate the doubly spinning BRs in a numerically manageable manner, and solve it in a perturbative way. Based on the solutions, some of physical properties of the doubly spinning BRs are discussed. This specific example helps us to clarify subtle issues related to numerics, and we discuss how we can deal with fully nonlinear stationary solutions in the present approach. The details of the present study is given in [6].

0.2 Stationary axisymmetric spacetimes

Following to the formulation in [5], we introduce the canonical form of metric and collect necessary ingredients for later discussions. Stationary axisymmetric D-dimensional spacetimes can be put in the

---

following form,

$$ds^2 = \sum_{a,b=1}^{D-2} g_{ab} dx^a dx^b + e^{2\nu}(dr^2 + dz^2). \tag{1}$$

If this spacetimes has $D-2$ commuting Killing vectors, the metric is in a special class. For such cases, the canonical coordinates in which the coordinate r satisfies $r^2 = \det(-g)$, are available. This canonical form of metric simplifies the Einstein equations considerably.

The canonical coordinates have rectangular boundary, and they are suited for numerics. Under the canonical form of metric, the field equations are non-linear coupled equations with elliptic second-order partial differential operator. Besides, the boundary conditions are well imposed by the rod-structure, once we fix the type of black holes. Thus we will be able to apply a numerical method for stationary cases. In this section, we formulate the black ring with two spins and discuss the necessary boundary conditions, including the basic strategy to solve the equations.

To deal with general black rings carrying two spins, we define the general metric in the following form;

$$e^{2\nu} = e^{2\nu^{(bg)}} M_\nu, \qquad g_{\phi\phi} = g_{\phi\phi}^{(bg)} M_{\phi\phi}, \qquad g_{\psi\psi} = g_{\psi\psi}^{(bg)} M_{\psi\psi},$$

$$g_{t\phi} = g_{t\phi}^{(bg)} M_{t\phi} M_{\phi\phi}, \qquad g_{t\psi} = g_{t\psi}^{(bg)} M_{t\psi} M_{\psi\psi}, \qquad g_{\phi\psi} = M_{\phi\psi}. \tag{2}$$

Although we define $g_{tt} = g_{tt}^{(bg)} M_{tt}$, it is solved from the canonical condition. $g_{t\psi}^{(bg)}$ is defined by $g_{t\psi}^{(bg)} = -\left(\frac{2c\kappa^2}{R_1 + R_2}\right)^2 g_{\psi\psi}^{(bg)}$. Here, $M_{ab}(r, z)$ and $M_\nu(r, z)$ are unknown functions which we solve. We adopt the Emperan-Reall's solution as the "background" metric $g_{ab}^{(bg)}$. Our metric ansatz, in particular $g_{t\phi}$ and $g_{t\psi}$, are chosen in order to yield simple expression for physical quantities, such as the angular velocity of horizon. Besides, as we will see below, an advantage of adopting the above ansatz is that the full metric will automatically satisfy the desired rod-structured as long as M_{ab} are smooth functions.

The coupled non-linear PDEs for the functions M_{ab} are symbolically written as $\nabla^2 M = S(M)$, with the non-linear source term S, where $M = M_{ab}$ or M_ν. To solve this system as a boundary value problem, we specify the boundary conditions by explicitly analyzing the rod structure and the asymptotic behavior for the assumed general metric [6].

0.3 Perturbative doubly spinning black rings

We have numerically solved this problem perturbatively, up to the second order. The perturbative solutions are constructed with respect to the thin black rings ($c < 1/2$) and their physical properties are briefly discussed in below.

By the perturbations upto second order, we have incorporated the backreaction from the second spin. The backreaction affects the spacetime geometry, and so we can investigate the physical properties of the doubly spinning black rings based on our solutions for thin black rings. We adopt the so-called reduced spin variable j and reduced horizon entropy,

$$j^2 = \frac{27\pi}{32} \frac{J_\phi^2 + J_\psi^2}{M^3}, \quad s = \frac{3\sqrt{3}}{4\sqrt{\pi}} \frac{S}{M^{3/2}}. \tag{3}$$

Here we have introduced the reduced spin by a sum of squared angular momentum. This is useful variable to draw a phase diagram of doubly spinning BRs in a two-dimensional plane, instead of in a three-dimensional space. j^2 does not depend on the periodicity ϵ by its construction, while the reduced entropy does depend on it. However, expanding these quantities upto second order, we find

$$j^2 = \frac{(c+1)^3}{8c} + \omega_\psi^2(j_{\psi[2]}^2 + j_{\phi[2]}^2), \quad s = 2\sqrt{c(1-c)} + \omega_\psi^2 s_{[2]}. \tag{4}$$

In Fig. 1, $s_{[2]}$ and $(j^2)_{[2]}$ are shown. Both of them are negative, implying that the doubly spinning black rings have less entropy for given mass. It is a general process to decrease the horizon area as a spin increases, as are the cases in the Kerr and MP black holes. However, we have no reason to expect smaller

(a)   (b)
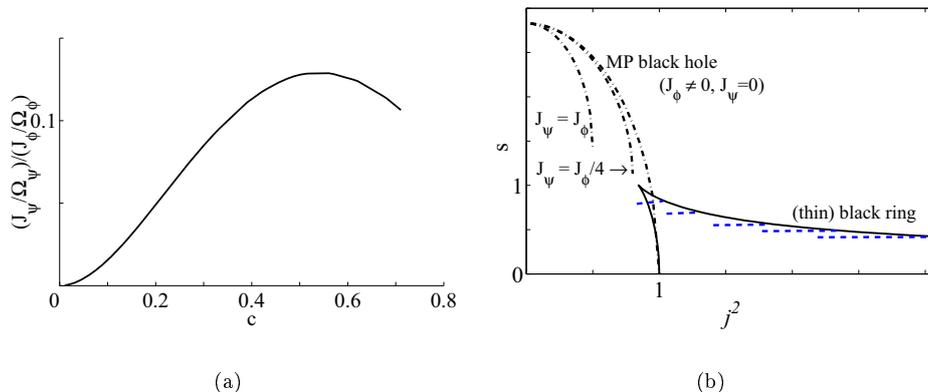
Figure 1: (a) Plot of $(J_\psi/\Omega_\psi)(J_\phi/\Omega_\phi)^{-1}$. (b) Reduced entropy vs $j^2(= j_\phi^2 + j_\psi^2)$ for the black rings (solid) and Myers-Perry black holes (dot-dashed). The curves for MP black holes correspond to $J_\psi = 0$, $J_\psi = J_\psi/4$, and $J_\psi = J_\psi$ cases. Since the existence of horizon requires $j_\phi^2 + j_\psi^2 + 2|j_\psi j_\phi| \le 1$, the latter branch ends at some point. Each dashed lines emanating from the sequence of thin black ring indicates the sequence of doubly spinning black rings.

reduced angular momentum, and so a question is why $(j^2)_{[2]}$ is negative. In the evaluation of $(j^2)_{[2]}$, $j_{\psi[2]}^2$ gives small positive contribution while $j_{\phi[2]}^2$ gives dominant negative contributions, i.e. $|j_{\phi[2]}^2| \gg j_{\psi[2]}^2$. Thus the negative value of $(j^2)_{[2]}$ comes from the backreaction to j_ϕ^2 and we have $(j^2)_{[2]} \approx j_\phi^2 < 0$. By comparing with the MP black holes (Fig. 1), the present result might suggest that there is a maximum reduced angular momentum j^2 and its maximum value is achieved by the single spinning BRs. This does not necessarily mean that the maximum total angular momentum $J^2 = J_\phi^2 + J_\psi^2$ is saturated by the single spinning black rings. We expect that the angular momentum of the single spinning black rings provides lower limit of the total angular momentum, because the second angular momentum would have no significant role for the radial balance of forces in such black rings. Therefore, the negative reduced angular momentum means that the increase of mass due to the backreaction is more rapid than the increase of spins in these perturbations.

0.4   Extensions of the approach

So far, we have focused on the perturbations to understand how we solve the boundary value problem for a given rod-structure. Besides, by the example of doubly spinning black rings, we have made it clear that the rod-structure can be actually specified by requiring physical properties of an expected black hole. Clearly, it is possible to extend the perturbative solutions to fully nonlinear solutions by directly solving the PDE.

Another interesting possibility to apply fully nonlinear numerical method is the search for black rings in higher dimensions. There have been no known feasible approaches to find such objects so far. Here we discuss a possible approach to construct such object based on numerics. A crucial point to construct higher dimensional black rings and other objects is to find an appropriate coordinate system, as is often the case in general relativity. In particular, it is best in numerics to find rectangular coordinates in which all boundaries coincide with the coordinate lines. For higher dimensional black rings, the canonical coordinates is no longer available in $D \ge 6$, but the general conformal form of the metric is still valid. The metric (1) can be written as $ds^2 = \sum_{\alpha,\beta=1}^{D-n-2} g_{\alpha\beta}(r,z)dx^\alpha dx^\beta + e^{2\lambda(r,z)}d\sigma_{(n)}^2 + e^{2\nu(r,z)}(dr^2 + dz^2)$. Here $d\sigma_{(n)}^2 = \gamma_{ij}dx^i dx^j$ is the metric of n-sphere. This form of metric will be suited for describing a black object with $S^i \times S^j$ topology. In fact, the Minkowski spacetimes for $D \ge 5$ can be embedded in this form:

$$\sum_{\alpha,\beta=1}^{D-n-2} g_{\alpha\beta}dx^\alpha dx^\beta = -dt^2 + (\sqrt{r^2 + z^2} - z)d\Omega_{(D-n-3)}^2, \quad e^{2\lambda} = \sqrt{r^2 + z^2} + z, \quad e^{2\nu} = \frac{1}{2\sqrt{r^2 + z^2}}.$$

Taking these Minkowski metric as a background metric and assuming a general form of metric, like Eq.

(2), the PDEs are reduced to coupled elliptic PDEs with the Laplace operator $\vec{\nabla}^2$ in three-dimensional cylindrical coordinates. The canonical condition is not available anymore, and important properties of rod-structure is also unavailable. For instance, as we notice from the above example, the principle of "one eigenvalue of g_{ab} becomes zero for a given z" is broken explicitly on axes, since multiple angular components, say $d\Omega_n^2$, vanishes at the same time. However, we can still require physical (or regularity) conditions on the axes and other portion of $r = 0$. Then it is possible to set up a problem of constructing higher dimensional black rings as a well-defined (numerical) problem. (This is analogous to finding a black hole localized on the KK circle in $D = 5$, whose construction in numerics had been done without relying on the rod-structure.)

Finally, we end this section with another interesting possible extension of the present approach. From the point of view of numerics, the cosmological constant is not an essential problem once a good coordinate system is provided. In fact, we can provide the metric of five-dimensional AdS in the conformal form. Such metric is found by coordinate transformation from the static coordinates of AdS.

0.5   Summary

We have discussed the formulation of solving stationary axisymmetric spacetimes and focused on the example of doubly spinning BRs. The doubly spinning BRs are distinguished from the BRs with single spin by the new independent asymptotic conserved charge.

This example shows that we can formulate the problem in a form suitable for numerical implementation. As a first step, we have expanded the nonlinear equations for small second angular velocity and obtained the perturbative equations for the doubly spinning BRs. Separation of variables is not available for some set of equations, and we have integrated the perturbative equations numerically. The perturbations have been solved upto second order in small angular velocity. The constructed doubly spinning BRs are regular and free from the conical singularity. However, the absolute value of periodicity of axes, $\Delta\phi = \Delta\psi = 2\pi\epsilon$, cannot be determined for each solution in the present approach. The ambiguity comes from the constant mode in $e^{2\nu}$.

To discuss the physical properties of doubly spinning BRs, we have evaluated the reduced entropy and reduced angular momentum for each perturbative solution. As peculiar to rotating black holes, the second spin associated to the S^2-sphere deceases the entropy for a fixed mass and angular momenta. On the other hand, the sum of reduced angular momenta decreases. Our construction of doubly spinning BRs is only for the branch of thin black rings, and it is unclear how the fat black rings behave with the second spin. An interesting question is whether the region where the Myers-Perry (MP) black holes and black rings overlap disappears or not. Presumably, the overlapped region will disappear for some range of second spin, because the branch of doubly spinning MP black holes with regular horizon leaves the overlapped region and its reduced entropy is bounded below (see Fig. 1). If the doubly spinning BRs have smaller reduced entropy all the way down to its (expected) maximum spin, they can never reach the parameter region of MP black hole in some range of j^2 (or in three-dimensional space of $\{j_1^2, j_2^2, s\}$).

References

[1] Roberto Emparan and Harvey S. Reall. A rotating black ring in five dimensions. *Phys. Rev. Lett.*, 88:101101, 2002.

[2] Takashi Mishima and Hideo Iguchi. New axisymmetric stationary solutions of five-dimensional vacuum einstein equations with asymptotic flatness. *Phys. Rev.*, D73:044030, 2006.

[3] Pau Figueras. A black ring with a rotating 2-sphere. *JHEP*, 07:039, 2005.

[4] Henriette Elvang, Roberto Emparan, David Mateos, and Harvey S. Reall. A supersymmetric black ring. *Phys. Rev. Lett.*, 93:211302, 2004.

[5] Troels Harmark. Stationary and axisymmetric solutions of higher-dimensional general relativity. *Phys. Rev.*, D70:124002, 2004.

[6] Hideaki Kudoh. Doubly spinning black rings. 2006.

Superposition of five-dimensional black rings and black holes

Takashi Mishima[1], Hideo Iguchi[2]

Laboratory of Physics, College of Science and Technology, Nihon University,
Narashinodai, Funabashi, Chiba 274-8501, Japan

Abstract

First we briefly review a solitonic solution-generating method to construct single-rotational, axisynmetric and stationary vacuum solutions in five-dimensional Einstein equations, by which S^2-rotating and S^1-rotating black rings was generated previously. Then using this method we give further new five-dimensional solutions corresponding to superposition of S^1-rotating black rings and a black hole.

1 Introduction

Since the remarkable discovery of a S^1-rotating black ring solution by Emparan and Reall [1], numerous investigations have been concentrated on the five-dimensional black objects and have clarified several features of such objects (for example, see the review by Emaparan and Reall [2] and the references therein).

Previously as further steps towards systematic construction of further new solutions in five-dimensional case, we introduced the new solitonic solution-generating method in five dimensions and succeeded in obtaining the S^2-rotating black ring solution which is complementary to the S^1-rotating black ring solution [3, 4]. Successively we also rederived S^1-rotating black ring solution [5] and gave some relationhsip between the method mentioned here and some inverse scattering technique [6]. In this ariticle, we briefly address the solution-generating method developed by us and present how to superpose black rings and a black hole. Then we give the full metric of di-ring

2 Solitonic solution-generating method

We concentrate on the spacetimes which satisfy the following conditions: (c1) five dimensions, (c2) asymptotically flat spacetimes, (c3) the solutions of vacuum Einstein equations, (c4) having three commuting Killing vectors including time translational invariance and (c5) having a single nonzero angular momentum component. Under the conditions (c1) − (c5), the following Weyl-Papapetrou metric form can be adopted as a starting point[7],

$$ds^2 = -e^{2U_0}(dx^0 - \omega d\phi)^2 + e^{2U_1}\rho^2(d\phi)^2 + e^{2U_2}(d\psi)^2 + e^{2(\gamma+U_1)}\left(d\rho^2 + dz^2\right) \tag{1}$$

where U_0, U_1, U_2, ω and γ are functions of ρ and z and also U_1 is set to $-(U_0 + U_2)$. After introducing new functions $S := 2U_0 + U_2$ and $T := U_2$, the metric form (1) is rewritten into

$$ds^2 = -e^{-T}\left[e^S(dx^0 - \omega d\phi)^2 + e^{-S}\rho^2(d\phi)^2 + e^{2(\gamma-S)}\left(d\rho^2 + dz^2\right)\right] + e^{2T}(d\psi)^2. \tag{2}$$

Then the five-dimensional Einstein equations are reduced to the following set of equations,

(i) $\quad \nabla^2 T = 0,$

(ii) $\quad \begin{cases} \partial_\rho \gamma_T = \dfrac{3}{4}\,\rho\,\left[(\partial_\rho T)^2 - (\partial_z T)^2\right] \\[2mm] \partial_z \gamma_T = \dfrac{3}{2}\,\rho\,\left[\partial_\rho T\,\partial_z T\right], \end{cases}$

---

[1] E-mail:tmishima@phys.ge.cst.nihon-u.ac.jp
[2] E-mail:iguchi.h@phys.ge.cst.nihon-u.ac.jp

(iii) $\quad \nabla^2 \mathcal{E}_S = \dfrac{2}{\mathcal{E}_S + \bar{\mathcal{E}}_S} \, \nabla \mathcal{E}_S \cdot \nabla \mathcal{E}_S,$

(iv) $\quad \begin{cases} \partial_\rho \gamma_S = \dfrac{\rho}{2(\mathcal{E}_S + \bar{\mathcal{E}}_S)} \left(\partial_\rho \mathcal{E}_S \partial_\rho \bar{\mathcal{E}}_S - \partial_z \mathcal{E}_S \partial_z \bar{\mathcal{E}}_S \right) \\ \partial_z \gamma_S = \dfrac{\rho}{2(\mathcal{E}_S + \bar{\mathcal{E}}_S)} \left(\partial_\rho \mathcal{E}_S \partial_z \bar{\mathcal{E}}_S + \partial_\rho \mathcal{E}_S \partial_z \bar{\mathcal{E}}_S \right), \end{cases}$

(v) $\quad (\partial_\rho \Phi, \, \partial_z \Phi) = \rho^{-1} e^{2S} \left(-\partial_z \omega, \, \partial_\rho \omega \right),$

(vi) $\quad \gamma = \gamma_S + \gamma_T,$

where Φ is defined through the equation (v) and the function $\mathcal{E}_S$ is defined by $\mathcal{E}_S := e^S + i\,\Phi$. The equaiton (iii) is exactly the same as the well-known Ernst equation, so that we call $\mathcal{E}_S$ Ernst potential. The most crucial point to obtain new metric forms is to solve the equation (iii) because of it's non-linearity. For the actual analysis in the following, we take some generalized Weyl solutions [7] as seeds and use the formulas shown in the paper by Castejon-Amened and Manko [8].

The procedure to generate a new metric is the following: **i.** choose an appropriate generalized Weyl solution, **ii.** extract seed functions $S^{(0)} = 2U_0^{(0)} + U_2^{(0)}$ and $T^{(0)} = U_2^{(0)}$ from the seed metric, **iii.** determine the auxiliary functions a and b by solving simple first-order linear differential equations [3], **iv.** introduce further the following new functions

$$\begin{cases} A := (x^2 - 1)(1 + ab)^2 - (1 - y^2)(b - a)^2 \\ B := [(x + 1) + (x - 1)ab]^2 + [(1 + y)a + (1 - y)b]^2 \\ C := (x^2 - 1)(1 + ab)[(1 - y)b - (1 + y)a] + (1 - y^2)(b - a)[x + 1 - (x - 1)ab], \end{cases}$$

where x and y are defined by $(R_\sigma + R_{-\sigma})/(2\sigma)$ and $(R_{-\sigma} - R_\sigma)/(2\sigma)$ with $R_{\pm\sigma} = \sqrt{\rho^2 + (z \mp \sigma)^2}$, respectively, **v.** give the corresponding Ernst potential

$$\mathcal{E}_S = e^{S^{(0)}} \frac{x(1 + ab) + iy(b - a) - (1 - ia)(1 - ib)}{x(1 + ab) + iy(b - a) + (1 - ia)(1 - ib)},$$

vi. integrate (ii) and (iv) to determine the function γ (see the previous paper [4] for the explicit expression). Finally we can obtain the full metric with the following formulae

$$e^S \quad = \quad e^{S^{(0)}} \frac{A}{B} \tag{3}$$

$$\omega \quad = \quad 2\sigma e^{-S^{(0)}} \frac{C}{A} + C_1 \tag{4}$$

$$e^{2\gamma} \quad = \quad C_2 (x^2 - 1)^{-1} A e^{2\gamma'}, \tag{5}$$

where γ' have been already derived in the step **vi.** and C_1 and C_2 are fixed from some physical conditions.

3 Generation of a multi-ring and a hole sytems

It is very helpful to use the viewpoint of the rod-structure analisys [7, 9] to describe what the method mentioned above does. By applying our method to a seed, the finite spacelike rods in the interval $-\sigma < z < \sigma$ is lifted from the ϕ-axis to the 'axis' of time-translation (i.e. horizon) and ϕ-rotation is added to the timelike rods which correspond to the static black objects around the interval.

Hence we can generate the spacetime of a black multi-ring and a black hole with the ϕ-rotation if the generalized Weyl solution corresponding to the spacetime with a static black multi-black ring, a black hole and a local Kaluza-Klein bubble are appropriately prepared as a seed. As a necessary condition to obtain a regular solution the K-K bubble should be put on the interval $-\sigma < z < \sigma$.

4 Black di-ring

In the rest we discuss the black di-ring system as the simplest black multi-ring case. The rod structure of the seed for the di-ring is given in the left figure of Fig.2. The resultant rod structure is given in

the right after applying the solitonic method. We have five parameters to make distinction between the multi-rings up to global scaling, which are $\eta_1, \eta_2, \delta_1, \delta_2, \lambda$. These parameters should satisfy the condition $-1 < \eta_1 < \eta_2 < 1 < \delta_1 < \delta_2 < \lambda$ for the di-ring solution. The following facts are noteworthy : when we set $\delta_2 = \lambda$, the inner ring shrinks to S^3 sphere ; when $\delta_1 = \delta_2$, the corresponding rod structure is exactly the same as the case of single S^1-rotating black ring.
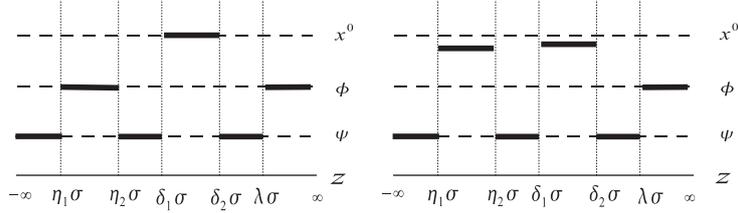

Figure 1: Schematic pictures of rod structure of black di-ring and its seed. The left which corresponds to the seed is transformed to the right which corresponds to the di-ring by the solitonic method.

The seed functions of the black di-ring can be easily extracted from Fig.1,

$$T^{(0)} = (\tilde{U}_{\lambda\sigma} - \tilde{U}_{\eta_2\sigma} + \tilde{U}_{\eta_1\sigma}) - (\tilde{U}_{\delta_2\sigma} - \tilde{U}_{\delta_1\sigma}), \tag{6}$$

$$S^{(0)} = (\tilde{U}_{\lambda\sigma} - \tilde{U}_{\eta_2\sigma} + \tilde{U}_{\eta_1\sigma}) + (\tilde{U}_{\delta_2\sigma} - \tilde{U}_{\delta_1\sigma}). \tag{7}$$

The auxiliary functions a and b are given systematically [4] as

$$a = \frac{\alpha}{2\sigma^{1/2}} \frac{e^{2U_\sigma} + e^{2\bar{U}_{\lambda\sigma}}}{e^{\bar{U}_{\lambda\sigma}}} \frac{e^{\bar{U}_{\eta_2\sigma}}}{e^{2U_\sigma} + e^{2\bar{U}_{\eta_2\sigma}}} \frac{e^{2U_\sigma} + e^{2\bar{U}_{\eta_1\sigma}}}{e^{\bar{U}_{\eta_1\sigma}}} \frac{e^{2U_\sigma} + e^{2\bar{U}_{\delta_2\sigma}}}{e^{\bar{U}_{\delta_2\sigma}}} \frac{e^{\bar{U}_{\delta_1\sigma}}}{e^{2U_\sigma} + e^{2\bar{U}_{\delta_1\sigma}}}, \tag{8}$$

$$b = 2\sigma^{1/2}\beta \frac{e^{\bar{U}_{\lambda\sigma}}}{e^{2U_{-\sigma}} + e^{2\bar{U}_{\lambda\sigma}}} \frac{e^{2U_{-\sigma}} + e^{2\bar{U}_{\eta_2\sigma}}}{e^{\bar{U}_{\eta_2\sigma}}} \frac{e^{\bar{U}_{\eta_1\sigma}}}{e^{2U_{-\sigma}} + e^{2\bar{U}_{\eta_1\sigma}}} \frac{e^{\bar{U}_{\delta_2\sigma}}}{e^{2U_{-\sigma}} + e^{2\bar{U}_{\delta_2\sigma}}} \frac{e^{2U_{-\sigma}} + e^{2\bar{U}_{\delta_1\sigma}}}{e^{\bar{U}_{\delta_1\sigma}}}, \tag{9}$$

where $\tilde{U}_d := \frac{1}{2}\ln\left[\sqrt{\rho^2 + (z-d)^2} + (z-d)\right]$ and $U_d := \frac{1}{2}\ln\left[\sqrt{\rho^2 + (z-d)^2} - (z-d)\right]$. Then following the procedure describd in the previous section, we obtain the corresponding full metric.

To extract the regular di-ring solutions, the following conditoins must be introduced. For the constants C_1 and C_2 of Eq.(4) and (5),

$$C_1 = \frac{2\sigma^{1/2}\alpha}{1 + \alpha\beta}, \quad C_2 = \frac{1}{\sqrt{2}(1 + \alpha\beta)^2}.$$

These conditions eliminate the global rotation and adjust the periods of ϕ and ψ to 2π at the infinity. To assure the regulariy of the metirc component $g_{\phi\phi}$ and to eliminate the closed timelike curves, α and β must be given by

$$\alpha = \pm\sqrt{\frac{2(\delta_1 - 1)(1 - \eta_2)}{(\lambda - 1)(\delta_2 - 1)(1 - \eta_1)}}, \quad \beta = \pm\sqrt{\frac{(\lambda + 1)(\delta_2 + 1)(1 + \eta_1)}{2(\delta_1 + 1)(1 + \eta_2)}}. \tag{10}$$

Another set of conditions comes from curing conical singularities. We must adjust both the periods about ψ-axis on the interval $\eta_2 < z/\sigma < \delta_1$ and about ψ-axis on the interval $\delta_2 < z/\sigma < \lambda$ to 2π. Both the periods of rotations about ϕ-axis corresponding to $\lambda < z/\sigma$ and about ψ-axis corresponding to $z/\sigma < \eta_1$ have been already adjusted to 2π. Hence we obtain the following two conditions,

$$2\pi = \frac{2\pi}{1 + \alpha\beta}\sqrt{\frac{(\lambda + 1)(\lambda - \delta_2)}{(\lambda - 1)(\lambda - \delta_1)}}\left(\frac{\lambda - \eta_2}{\lambda - \eta_1}\right)\left(1 + \frac{\lambda - 1}{\lambda + 1}\alpha\beta\right) \tag{11}$$

$$2\pi = \frac{2\pi}{1 + \alpha\beta}\sqrt{\frac{(\lambda + 1)(\delta_1 - 1)(\delta_2 + 1)(\delta_1 - \eta_2)(\delta_2 - \eta_1)}{(\lambda - 1)(\delta_1 + 1)(\delta_2 - 1)(\delta_1 - \eta_1)(\delta_2 - \eta_2)}}$$
$$\times \left(\frac{\lambda - \eta_2}{\lambda - \eta_1}\right)\left(1 + \frac{(\lambda - 1)(\delta_1 + 1))(\delta_2 - 1)}{(\lambda + 1)(\delta_1 - 1))(\delta_2 + 1)}\alpha\beta\right). \tag{12}$$

Here we just say that some continuous set of parameters satisfies these conditions simultaneously and seems to assure the global regularity of the corresponding spacetime at least by numerical confirmation.

The mass parameter m^2 and rotational parameter $m^2 a_0$ are the followings

$$m^2 = \sigma \frac{P}{(1+\alpha\beta)^2}, \quad m^2 a_0 = 4\sigma^{3/2} \frac{Q}{(1+\alpha\beta)^3}.$$

where

$$
\begin{aligned}
P &= 4(1+\alpha^2 - \alpha^2\beta^2) \\
Q &= \alpha(2\alpha^2 - \delta_1 + \delta_2 + \eta_1 - \eta_2 + \lambda + 3) - 2\alpha^2\beta^3 \\
&\quad - \beta\left[2(2\alpha\beta+1)(\alpha^2+1) + (\delta_1 - \delta_2 - \eta_1 + \eta_2 - \lambda - 1)\alpha^2(\alpha\beta+2)\right].
\end{aligned}
$$

The angular velocities Ω_1 and Ω_2 of event horizons of the inner and outer rings are obtained from the direction vectors $\mathbf{v}$ of finite timelike rods,

$$\mathbf{v} = (1, \Omega_1, 0), \quad \Omega_1 = -\frac{2\beta(1+\alpha\beta)}{\sqrt{\sigma}((\lambda-1)\alpha\beta + \lambda + 1)((\delta_2-1)\alpha\beta + \delta_2 + 1)} \tag{13}$$

for inner ring $[\delta_1 < z < \delta_2]$,

$$\mathbf{v} = (1, \Omega_2, 0), \quad \Omega_2 = \frac{(1+\alpha\beta)((2\beta(\delta_1+1)(1+\eta_2) - \alpha(\lambda+1)(\delta_2+1)(1-\eta_1))}{2\sqrt{\sigma}(2\alpha\beta(\delta_1+1)(1+\eta_2) - (\lambda+1)(\delta_2+1)(\alpha^2(1-\eta_1) + 2\alpha\beta + 2))} \tag{14}$$

for outer ring $[\eta_1 < z < \eta_2]$.

5 Summary and discussion

We showed the possibility of construction of black multi-ring system, using the method developed previously. Especially the full metrics of the di-ring were given. With some adjusted parameters, we also showed the possibility of regular black di-ring.

As the most important matter we can show the continuous non-uniqueness of neutral black holes in five-dimensions (here the term 'black holes' are not restricted to the spherical black holes) by using the regular di-ring system. we have six independent parameters η_1, η_2, δ_1, δ_2, λ and σ. On the other hand, there are two regularity conditions (11) and (12). Hence we can easily expect that the di-rings which have the same mass and angular momentum generate two-dimensional surface in three-dimensional parameter space. If one of the parameters are fixed (for example $\eta_2 = 1$), degree of non-uniqueness is reduced from two dimensions to one dimension. In this case we can numerically confirm that Emparan and Reall's single fat ring and thin ring with the same mass and angular momentum are continuously connected by the one-dimensional path in di-ring solution space. The detailed analysis are given in [10].

References

[1] R. Emparan and H. S. Reall, Phys. Rev. Lett. **88**, 101101 (2002).

[2] R. Emparan and H. S. Reall, Class. Quantum Grav. **23**, R169 (2006).

[3] T. Mishima and H. Iguchi, Phys. Rev. D **73**, 044030 (2006).

[4] H. Iguchi and T. Mishima, Phys. Rev. D **74**, 024029 (2006).

[5] H. Iguchi and T. Mishima, Phys. Rev. D **73**, 121501(R) (2006).

[6] S. Tomizawa, H. Iguchi and T. Mishima, Phys. Rev. D **74**, 104004 (2006).

[7] R. Emparan and H. S. Reall, Phys. Rev. D **65**, 084025 (2002).

[8] J. Castejon-Amenedo and V. S. Manko, Phys. Rev. D **41**, 2018 (1990).

[9] T. Harmark, Phys. Rev. D **70**, 124002 (2004).

[10] H. Iguchi and T. Mishima, arXiv:hep-th/0701043.

Evaporating (2+1)-dimensional black strings

Keiju Murata[1], Jiro Soda[2] and Sugumi Kanno[3]

[1,2]*Department of Physics, Kyoto University, Kyoto 606-8501, Japan*
[3]*Department of Physics, McGill University, Montréal, QC H3A 2T8, Canada*

Abstract

We investigate (2+1)-dimensional black strings in the Kaluza-Klein spacetime. The system is classically stable as long as the horizon size is much larger than the size of the compact space. Semiclassically, however, the horizon size shrinks gradually due to the energy loss through the Hawking radiation. Eventually, the system will enter into the regime of the Gregory-Laflamme instability and get destabilized. Subsequently, the spherically symmetric black hole is formed and evaporated in the usual manner. This standard picture may be altered by the dynamics of the internal space which induced by the Hawking radiation. We argue that the black string is excised from the Kaluza-Klein spacetime before the onset of the Gregory-Laflamme instability and therefore before the evaporation.

1 Introduction

In the conventional 4-dimensional spacetime, the black hole is considered as the blackbody which emits the Hawking radiation. Because of this radiation, the size of the horizon gradually shrinks and finally the black hole evaporates. Although there still exists debate on the final state after evaporation, the total picture is simple.

From the point of view of the super string theory, it is natural to consider higher dimensional spacetime. In this picture, the event horizon of the black hole would be the direct product of the usual event horizon and the compact internal space. It is interesting to investigate the evaporation process of the black hole in the Kaluza-Klein spacetime. In this paper, for simplicity, we consider the (2+1)-dimensional spacetime with S^1 as the compact internal space. The resulting Kaluza-Klein black hole is called the black string. The evaporation processes of the black strings could be different from the 4-dimensional one due to the Gregory-Laflamme instability [1]. It is known that the black string is unstable when the horizon radius is smaller than the scale of compactification. This instability changes the spacetime structure. The evaporation process taking into account this instability is depicted in the Figure 1. Soon after the onset of the Gregory-Laflamme instability, the spherically symmetric black hole would be formed. Subsequent evaporation process is very similar to the standard one.

Previously, we have considered the interplay between the radion and the Gregory-Laflamme instability [2, 3, 4]. There, the radion has played an important role. It is natural to expect the radion also makes a significant contribution to the evaporation process of the black strings. To the best of our knowledge, however, the interplay between the Hawking radiation and the radion dynamics has not been considered at all. Here, we study the role of the radion dynamics in the evaporation process of the (2+1)-dimensional black string.

The back reaction of the Hawking radiation could destabilize the radion. In fact, the energy of the Hawking radiation attracts the space around it. Thus, the radion is deformed by the Hawking radiation. In general, this deformation would be inhomogeneous. Hence, the spacetime is pinched at some radius. Consequently, assuming the singularity resolution, the black string might be excised from the spacetime. If this speculation is true, the radion dynamics would change the naive evaporation process completely. It should be stressed that the black string excision from the spacetime could occur before the onset of the Gregory-Laflamme instability and hence before the evaporation through the conventional process.
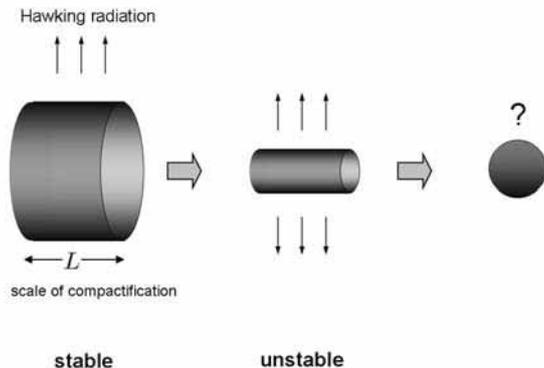
Figure 1: A naive picture of the evaporation process of the black string. Because of the Gregory-Laflamme instability, the black string becomes the spherically symmetric black hole.

2 (2+1)-dimensional Black Strings

In this section, we present our model and show the black string exists in this simple set up. We start with the (2+1)-dimensional dilaton gravity of the form

$$S[A, g] = M_3 \int d^3x \sqrt{-G}[AR^{(3)} + \frac{\lambda^2}{A}] \ , \tag{1}$$

where $G_{\mu\nu}$ is the 3-dimensional metric, $R^{(3)}$ is the 3-dimensional scalar curvature, A is the dilaton field, M_3 is the 3-dimensional Planck mass and λ is the parameter which have the mass dimension. The solution of the equation of motion obtained from the action (1) is

$$A = \lambda r \ , \quad ds^2 = -\alpha(r)dt^2 + \alpha(r)^{-1}dr^2 + dy^2 \ , \quad \alpha(r) \equiv \ln\left(\frac{r}{r_H}\right) \ , \tag{2}$$

where the period of the internal coordinate y is taken to be L. This solution represents the black string with horizon radius r_H and this spacetime is asymptotically flat because the curvature reads $R = 1/r^2$. It is known that the black string is unstable when $r_H \lesssim L$. The other way around, the black hole is stable as long as r_H is much larger than L. It is common to ignore the radion dynamics when we discuss this classical instability. However, once we take into account the semiclassical effect, we cannot ignore the radion dynamics. We need to study the evaporation process of this black string with the non-trivial radion dynamics.

3 Back Reaction of the Hawking Radiation

We consider quantum effect of the scalar field f in the black string background with the action

$$S[A, g, f] = M_3 \int d^3x \sqrt{-G}[AR^{(3)} + \frac{\lambda^2}{A}] + \int d^3x \sqrt{-G}[-\frac{1}{2}(\nabla f)^2] \ . \tag{3}$$

To take into account the radion dynamics, we parametrize the metric as

$$ds^2 = g_{ab}(x^a)dx^a dx^b + e^{-2\chi(x^a)}dy^2 \ , \tag{4}$$

where χ is the radion field. Here, we assume $r_H \gg L$ and all fields do not depend on y. Then, we can carry out the y integration in the action (3) to obtain

$$S[A, g, \chi, f] = M_3 L \int d^2x \sqrt{-g} \, e^{-\chi}[AR - 2\nabla A \cdot \nabla \chi + \frac{\lambda^2}{A}] + \int d^2x \sqrt{-g} \, e^{-\chi}[-\frac{1}{2}(\nabla f)^2] \ , \tag{5}$$

where R represents the 2-dimensional scalar curvature. We can study the evaporation process of the black string using the above effective 2-dimensional dilaton gravity. We treat the scalar field quantum mechanically, because we want to study the back reaction of the Hawking radiation. We define the effective action

$$W[A, g, \chi] = -i \ln \left(\int \mathscr{D} f \, \exp(i \int d^2 x \sqrt{-g} \, e^{-\chi} [-\frac{1}{2} (\nabla f)^2]) \right)$$ (6)

and semiclassical energy momentum tensor

$$\langle T_{ab} \rangle = \frac{-2}{\sqrt{-g}} \frac{\delta W}{\delta g^{ab}} \ .$$ (7)

We can treat the back reaction perturbatively, that is, we regard the source T_{ab} as the small quantity. The master equation for the perturbed radion $\delta \chi$ is given by

$$-\Box \delta \chi - \frac{1}{A} \nabla A \cdot \nabla \delta \chi = \frac{1}{4M_3 L} \frac{1}{A} \langle T^a_a \rangle \ .$$ (8)

Note that the perturbed radion is gauge invariant as $\chi = 0$. Therefore, the gauge mode cannot appear in the master equation (8). Since the classical action of the matter field is Weyl invariant, the trace part of the energy-momentum tensor T^a_a should be zero. As is well known, however, Weyl symmetry has the anomaly in the quantum theory, namely,

$$\langle T^a_a \rangle = \frac{1}{24\pi} R = \frac{1}{24\pi r^2}.$$ (9)

Now, we can discuss the radion dynamics.
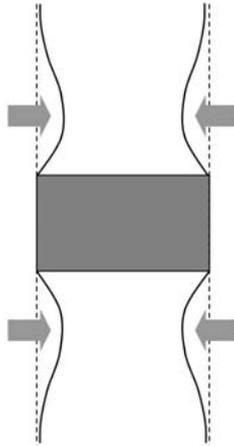
Figure 2: The radion has inhomogeneous profile due to the Hawking flux.

4   Excision of Black Strings

We set the initial conditions $\delta \chi(t = 0, r) = \delta \chi_{,t}(t = 0, r) = 0$. Then, we can deduce the radion dynamics for small t from master equation (8);

$$\delta \chi = \frac{1}{8M_3 L} \frac{\alpha(r)}{A} \langle T^a_a \rangle t^2 = \frac{1}{192\pi \lambda M_3 L} \frac{\ln(r/r_H)}{r^3} t^2 \ .$$ (10)

We gave a schematic picture of the radion dynamics in the Figure 2.

Now, we shall speculate the non-linear radion dynamics. The radion dynamics Eq.(10) can be understood from analogy to the cosmic dynamics. In cosmology, the matter tends to shrink the space
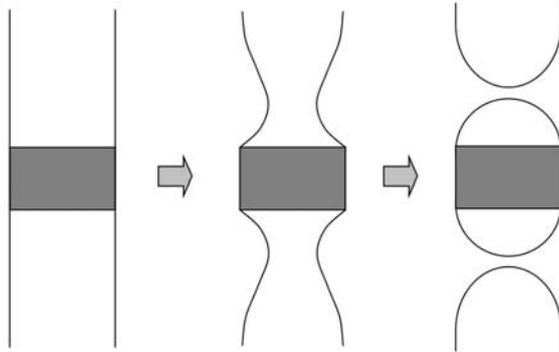
Figure 3: The speculative non-linear radion dynamics is shown. The black string is excised from the spacetime at the end of the day.

and, finally, makes the singularity. Similarly, the internal space may collapse due to the Hawking flux. Moreover, this occurs inhomogeneously. So we expect that the internal space is pinched off due to the Hawking radiation (Figure 3). Though the pinched point is classically singular, this is expected to be regularized by quantum effect. Thus, the black string region is excised from our spacetime. It looks like the evaporation of the black string from the observer outside. However, this evaporation process is completely different from the naive evaporation process in Figure 1.

5   Conclusion

We have investigated the (2+1)-dimensional black strings in the Kaluza-Klein spacetime. The solution of the master equation tells us that the internal space shrinks inhomogeneously (Figure 2). From this result, we can give the speculation for the non-linear radion dynamics. The black string may be excised from the spacetime due to the Hawking radiation (Figure 3). This can be interpreted as the evaporation of the black string from the observer outside. This evaporation process is different from that naively considered so far. Of course, at the present level of the analysis, we can not insist it strongly. However, it is worth to reconsider the evaporation process of black strings with taking into account the radion dynamics [5].

We need to analyze the non-linear radion dynamics to examine if our expectation in Figure 3 is correct. Furthermore, it is intriguing to consider the present issue in the context of the string theory.

References

[1] R. Gregory and R. Laflamme, Phys. Rev. Lett. **70**, 2837 (1993) [arXiv:hep-th/9301052].

[2] S. Kanno and J. Soda, Class. Quant. Grav. **21**, 1915 (2004) [arXiv:gr-qc/0311074].

[3] T. Tamaki, S. Kanno and J. Soda, Phys. Rev. D **69**, 024010 (2004) [arXiv:hep-th/0307278].

[4] S. Kanno and J. Soda, Gen. Rel. Grav. **37**, 1651 (2005) [arXiv:gr-qc/0508084].

[5] K. Murata, J. Soda, and S.Kanno, in preparation.

Time-symmetric initial data of brane-localized black hole in RS-II model

Norihiro Tanahashi[1] and Takahiro Tanaka[2]

Department of Physics, Kyoto University, Kyoto 606–8502, Japan

Abstract

Based on the AdS/CFT correspondence, it was conjectured that brane-localized static black holes larger than the bulk curvature scale do not exist in Randall-Sundrum II braneworld model. In order to investigate the properties of brane-localized black holes, we study time-symmetric initial data with apparent horizon. We find that the size of the apparent horizon can be much larger than the bulk curvature scale. We discuss implications of our results to the issue of brane-localized black hole.

1   Introduction

Randall-Sundrum II (RS-II) model is a braneworld model which contains a single brane with positive tension. The bulk is infinitely extending and is asymptotically anti de-Sitter (AdS). In this model gravity propagates in five dimensions. Thus it is not so obvious what kind of gravity is effectively realized on the brane. This has been studied much in weak gravity regime. Linear analysis shows that ordinary 4D Einstein gravity with small corrections is realized on the brane. On the other hand, in non-linear strong gravity regime, not much has been known yet. Here we would like to focus on gravitational collapse in braneworld, in which the effect of strong gravity is important. In ordinary 4D gravity black holes will form after gravitational collapses. It is no wonder that almost the same process will occur also in RS-II model. However, no one certainly knows what will happen after a gravitational collapse in braneworld in detail.

In RS-II model, no static black hole solution has not been found so far. This may suggest that exactly static black hole solution might be really absent in RS-II model. If so, one can say that gravity in this model is significantly different from the ordinary one in strong gravity regime. As an interpretation of the lack of static black hole solution in RS-II model, a conjecture was proposed that the black hole formed after gravitational collapse in RS-II model is not completely static [1, 2]. This conjecture is a kind of extension of the well-known AdS/CFT correspondence conjecture in superstring theory.

AdS/CFT correspondence is a conjecture based on the duality between the closed string and open string descriptions [3, 4]. One version of this conjecture states that the supergravity theory in AdS bulk background spacetime corresponds to the strongly coupled conformal field theory (CFT) defined on the boundary geometry of the bulk. A vast number of evidences support this correspondence, but a complete proof has not been obtained.

Although there are a few subtle points, one can interpret the AdS/CFT correspondence in the context of RS-II model. In RS-II model, the "boundary spacetime" is identified with the positive tension brane. Then, the AdS/CFT correspondence states that classical gravity realized on the brane in RS-II model corresponds to 4D Einstein gravity corrected by the coupling to "strongly coupled" CFT with a large number of degrees of freedom [5]. Again there is no proof for this correspondence, but there are a few supporting evidences for it. First of all, these two theories share the same correction to the Newton's law [6]. In RS-II model, gravity realized on the 4D brane deviates from the ordinary Einstein gravity due to the effects of the extra dimension [7]. The same deviation can be reproduced by CFT 1-loop correction to the graviton propagator. Another example is the tensor perturbation in the Friedmann-Lemaître-Robertson-Walker universe. It satisfies the same equation in these two theories [8].

If this correspondence also applies to the black holes, the following statements stands: *a classical black hole realized on the brane in RS-II model corresponds to a 4D black hole with quantum correction*

---

[1]E-mail:tanahashi@tap.scphys.kyoto-u.ac.jp
[2]E-mail:tama@tap.scphys.kyoto-u.ac.jp

due to CFT. A 4D black hole under CFT correction cannot be static since CFT particles extract the energy of the black hole through Hawking radiation. Then, the above statement leads to the conjecture, "the black hole realized on the brane in RS-II model also cannot be static".

In RS-II picture gravity is classical. Namely, the decrease of the black hole mass measured on the brane has to be explained by classical dynamics, such as deformation of the horizon in the 5D bulk. We call this phenomenon "classical evaporation" of the brane black hole into the bulk. This is the conjecture made by Tanaka [1] and independently by Emparan et al. [2].

2   Numerical analysis of brane-localized BH

There are already several works on static brane-localized black holes. There is a lower dimensional exact solution of brane-localized black hole [9]. But its existence does not contradict with the classical evaporation conjecture as was explained in Ref.[2]. Numerically, static black holes smaller than the curvature scale of the AdS bulk were constructed in Ref.[10]. The presence of a small static black hole does contradict with the above mentioned conjecture because CFT picture does not work when the size of the black hole is smaller than the length scale determined by the CFT cut-off. In this work static brane black hole whose size is much larger than the bulk curvature scale was not found. This does not directly mean that there is no static large black hole solution. It seems more appropriate to say that it takes too much time to obtain large black hole solutions by the method adopted there. There is a good reason why a larger black hole is harder to construct. We have to resolve the bulk curvature scale numerically even when the black hole horizon size is much bigger. This means that a larger number of grids are necessary for a larger black hole.

Roughly speaking, there are the following three possibilities. Large brane-localized black holes (1) do not exit, (2) exist but are unstable, or (3) exist and are stable. To study which one is correct, we examine time-symmetric initial data of brane-localized black holes following the method used by Shiromizu and Shibata [11]. Initial data will be easier to obtain compared with static solutions. Thus we expect that we can study larger black holes relatively easily by focusing on the initial data.

We solve the constraint equations on an initial surface. By the assumption of time-symmetry, the extrinsic curvature vanishes. Then, the only non-trivial constraint is the Hamiltonian constrain, which reduces to one equation requiring the intrinsic scalar curvature of that surface to be zero, $^{(4)}R = 0$. Since the time-symmetric initial configuration is not unique, we have to impose additional conditions that restrict the form of the metric. We try the following two simplest possibilities.

1. Shiromizu & Shibata's ansatz

   First one is the metric ansatz adopted by Shiromizu and Shibata:

$$dl^2 = \frac{1}{z^2} \left[l^2 dz^2 + (1 + \varphi(r, z))^4 \left(dr^2 + r^2 d\Omega^2 \right) \right].$$
(1)

   Here l is a constant corresponding to the bulk curvature scale. The brane is located at $z = l$. This metric ansatz is compatible with black string solutions. A pure AdS bulk corresponds to $\varphi = 0$.

2. Conformal-flat ansatz

   The second one is conformally flat metric ansatz:

$$dl^2 = \frac{l^2}{z^2} \left(1 + \frac{\zeta(r, z)}{r} \right)^2 \left[dz^2 + dr^2 + r^2 d\Omega^2 \right].$$
(2)

   The brane is placed at $z = l$. This ansatz is compatible with 5D Schwarzschild black hole solutions in the limit $\ell \to \infty$. A pure AdS bulk spacetime is realized when $\zeta = 0$.

In both cases, the Hamiltonian constraint becomes a two-dimensional elliptic partial differential equation of the form,

$$\mathcal{L}(\varphi \text{ or } \zeta) + (\text{non-linear terms of } \varphi \text{ or } \zeta) = (\text{Source}).$$
(3)

where $\mathcal{L}$ is a linear elliptic partial differential operator. We solve this equation by relaxing the associated diffusion equation.

To characterize the black hole horizon, we use apparent horizon (AH), which is the 3-surface on which the expansion of outgoing null geodesics vanishes: $\nabla_i s^i|_{\text{AH}} = 0$. Here s^i is the unit normal of the AH and ∇^i is the covariant derivative associated with the induced 3D metric on the AH. To obtain a non-trivial solution, we placed source term in Eq. (3) by hand in the bulk spacetime region near $r = 0$ and $z = \ell$. As far as the source is confined inside the AH, the obtained initial data can be interpreted as the one for vacuum case.

The boundary conditions are given as follows. At $r = 0$ the regularity conditions $\partial_r \varphi = 0$ and $\partial_r \zeta = 0$ are imposed. On the brane the boundary conditions are derived from the Israel's junction conditions [12] as

$$\partial_z \varphi|_{z=l} = 0, \quad \partial_z \zeta|_{z=l} = 0. \tag{4}$$

The boundary conditions at $z \gg l$ and at $r \gg l$ are determined from the linear analysis. We can rewrite Eq. (3) as

$$\mathcal{L}(\varphi \text{ or } \zeta) = (\text{Source}) - (\text{non-linear terms of } \varphi \text{ or } \zeta) \tag{5}$$

Then, this equation can be regarded as a linear equation with a new source term defined by the right hand side as a whole. This linear equation can be solved analytically when the source is given by $M\delta^4(\mathbf{x}, z)$. the asymptotic forms of φ and ζ are, respectively,

$$\varphi(\mathbf{x}, z) \xrightarrow{r, z \to \infty} \frac{G_5 M}{4 z_b^3} \frac{2r^2 + 3R^2 z^2}{(r^2 + R^2 z^2)^{3/2}}, \tag{6}$$

$$\zeta(\mathbf{x}, z) \xrightarrow{r, z \to \infty} \frac{1}{4\pi r} \frac{l^2 \kappa_5^2 M}{3 z_b^5} \left[\frac{3 z_b^3}{2} \left\{ 1 - \frac{2}{\pi} \arctan\left(\frac{z - z_b}{r} \right) \right\} + \frac{z_b^3 \left[r(z - z_b) \left\{ 3r^2 + 5(z - z_b)^2 \right\} \right]}{\pi \left\{ r^2 + (z - z_b)^2 \right\}^2} \right]. \tag{7}$$

As long as the non-linear terms vanish rapidly enough at $r, z \to \infty$, the asymptotic behavior of the solution of Eq. (3) is expected to be given by the above form. In more general cases, the parameter M can be represented by volume integral with the aid of Gauss' law.

Under Shiromizu-Shibata's metric ansatz (1), we succeeded in constructing time-symmetric initial data which contains the AH much larger than l (Fig. 1(a)). The heavier the source is, the larger the AH became. It seems that the AH can be arbitrarily large, although the computational time grows exponentially. On the other hand, under the conformal-flat metric ansatz (2), we could not construct such initial data. However, under the same metric ansatz we could construct initial data with a large AH if we adopt simpler boundary conditions, $\zeta = 0$ at $r, z \gg l$ (Fig. 1(b)), which are analogous to the conditions used previously in obtaining static brane black hole solutions.

3 Summary and future works

In RS-II model, static black hole solutions have not been found yet analytically. Numerical solutions were obtained for small black holes, but black holes larger than the bulk curvature scale have not been constructed. These facts are consistent with the conjecture that large brane black holes are not static.

In order to investigate the properties of brane-localized black holes in RS-II model, we focused on time-symmetric initial data of brane black holes. We obtained initial data with an AH much larger than the bulk curvature scale l in the case of Shiromizu-Shibata's metric ansatz. Definitely, time evolution of these initial data is an interesting issue. We would like to study it as a future work. However, the computation time to construct initial data increases exponentially as the AH size increases. The same problem happened in the construction of static solutions. Thus, we think that one can use the initial data construction as a test problem for blushing up the techniques necessary to construct static solutions. This will be another direction of our future work.

In contrast, in the case of the conformal-flat metric ansatz we could not construct such initial data. Interestingly, by adopting simpler boundary conditions setting $\zeta = 0$ on the boundaries, initial data could be constructed. Although we do not have enough space to explain it here, we can understand this dependence on the boundary conditions analytically, too. This fact suggests that the boundary conditions
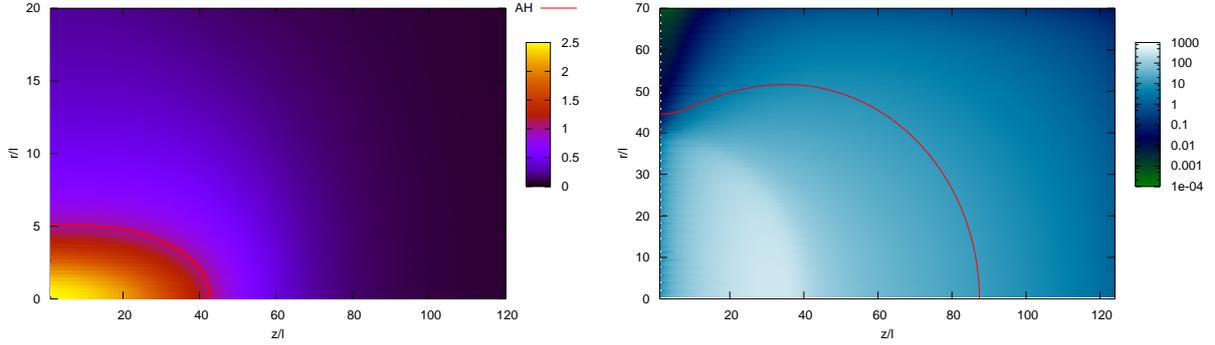
(a) value of $\varphi(r, z)$ in Shiromizu-Shibata's metric ansatz

(b) value of $\zeta(r, z)$ in conformal-flat metric ansatz. The boundary condition at $r, z \gg l$ is taken to be $\zeta = 0$.

Figure 1: The numerical solutions φ, ζ of the Hamiltonian constraint under each metric ansatz. The red lines show the position of the AH.

are crucial in this type of calculation. It should be noted that analogous simpler boundary conditions are adopted in the previous calculation for static solutions [10].

References

[1] T. Tanaka, Prog. Theor. Phys. Suppl. **148**, 307 (2003)

[2] R. Emparan, A. Fabbri and N. Kaloper, JHEP **0208**, 043 (2002)

[3] J. M. Maldacena, Adv. Theor. Math. Phys. **2**, 231 (1998) [Int. J. Theor. Phys. **38**, 1113 (1999)]

[4] O. Aharony, S. S. Gubser, J. M. Maldacena, H. Ooguri and Y. Oz, Phys. Rept. **323**, 183 (2000)

[5] S. W. Hawking, T. Hertog and H. S. Reall, Phys. Rev. D **62**, 043501 (2000)

[6] M. J. Duff and J. T. Liu, Class. Quant. Grav. **18**, 3207 (2001) [Phys. Rev. Lett. **85**, 2052 (2000)]

[7] J. Garriga and T. Tanaka, Phys. Rev. Lett. **84**, 2778 (2000)

[8] T. Tanaka, arXiv:gr-qc/0402068.

[9] R. Emparan, G. T. Horowitz and R. C. Myers, JHEP **0001**, 007 (2000)

[10] H. Kudoh, T. Tanaka and T. Nakamura, Phys. Rev. D **68**, 024035 (2003)

[11] T. Shiromizu and M. Shibata, Phys. Rev. D **62**, 127502 (2000)

[12] W. Israel, Nuovo Cimento Soc. Ital. Fis., B **44**, 1 (1996)

Gravitating Q-balls

Nobuyuki Sakai[1] and Misao Sasaki[2]

[1] *Department of Education, Yamagata University, Yamagata 990–8560, Japan*
[2] *Yukawa Institute for Theoretical Physics, Kyoto University, Kyoto 606–8502, Japan*

Abstract

We study properties of Q-balls in flat spacetime and in curved spacetime. (1) By energy analysis with catastrophe theory we obtain a clear picture of stability change of equilibrium solutions. (2) Numerical analysis of dynamical equations as a whole confirms the stability obtained by the energy analysis. However, even if we give perturbed initial conditions with the same charge, a part of charge is radiated away and approaches a different equilibrium solution with lower charge. (3) We study gravitating Q-balls as well. If the mass of the scalar filed is close to Planck mass, equilibrium solutions are nonexistent; a Q-ball either approaches a stable configuration or collapses to a black hole. We also argue that Q-ball inflation does not occur.

1 Introduction

Q-balls [1] are natural consequences of many models of a scalar field and could be dark matter [2]. To understand basic properties of Q-balls, we address the following issues.

(1) In flat spacetime stability against infinitesimal perturbations is well understood both in the thin-wall limit and in the thick-wall limit by energy analysis [1]-[6]. Here we investigate how stability changes in between the two limits by numerical analysis and catastrophe theory.

(2) To explore the fate of Q-balls with finite perturbations, we numerically solve dynamical field equations. We argue limitations of energy analysis in discussing finite perturbations.

(3) If the mass of the scalar field is so large, gravitational effects are not negligible. Therefore, we extend our investigations to gravitating Q-balls in curved spacetime.

2 Q-balls in flat spacetime

Consider an SO(2)-symmetric scalar field, whose action is given by

$$\mathcal{S} = \int d^4x \left[-\frac{1}{2}\eta^{\mu\nu}\partial_\mu \boldsymbol{\phi} \cdot \partial_\nu \boldsymbol{\phi} - V(\phi) \right], \tag{1}$$

with $\boldsymbol{\phi} = (\phi_1, \ \phi_2)$ and $\phi \equiv \sqrt{\boldsymbol{\phi} \cdot \boldsymbol{\phi}} = \sqrt{\phi_1^2 + \phi_2^2}$. Due to the symmetry there is a conserved charge:

$$Q \equiv \int_{\Sigma_t} d^3x (\phi_1 \partial_t \phi_2 - \phi_2 \partial_t \phi_1), \tag{2}$$

where Σ_t is the 3-hyperspace at $t =$const. Supposing homogeneous phase rotation,

$$\boldsymbol{\phi} = \phi(r)(\cos \omega t, \ \sin \omega t), \tag{3}$$

we obtain the field equation,

$$\frac{d^2\phi}{dr^2} = -\frac{2}{r}\frac{d\phi}{dr} - \omega^2\phi + \frac{dV}{d\phi}, \tag{4}$$

which is equivalent to the static field equation of a single scalar field with the potential $V - (\omega^2/2)\phi^2$. Monotonically decreasing solutions $\phi(r)$ with the boundary condition $d\phi/dr(0) = 0$, $\phi(\infty) = 0$ exist if

---

[1] E-mail:nsakai@e.yamagata-u.ac.jp
[2] E-mail:misao@yukawa.kyoto-u.ac.jp
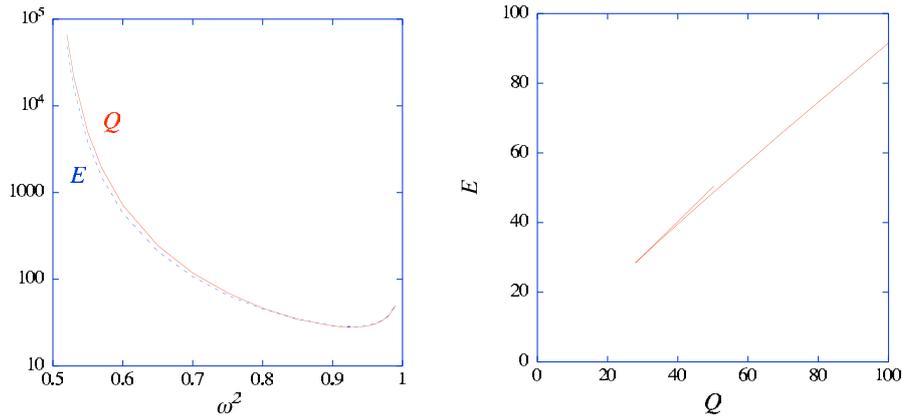
Figure 1: Relation among ω^2, Q and E for equilibrium solutions in flat spacetime.

$$\omega^2_{\min} < \omega^2 < m^2, \quad \text{with} \quad \omega^2_{\min} \equiv \min\left(\frac{2V}{\phi^2}\right), \quad m^2 \equiv \frac{d^2V}{d\phi^2}(0). \tag{5}$$

The condition $\omega^2_{\min} < m^2$ is not so severe because it is satisfied if the potential has the form,

$$V = \frac{m^2}{2}\phi^2 - \lambda\phi^n + O(\phi^{n+1}), \quad m^2 > 0, \quad \lambda > 0, \quad n \geq 3 \tag{6}$$

In the literature the stability of equilibrium solutions has been studied by energetics argument as follows. The total energy of the system for equilibrium solutions is given by

$$E = \frac{Q^2}{2I} + \int_{\Sigma_t} d^3x \left\{\frac{1}{2}\left(\frac{d\phi}{dr}\right)^2 + V\right\}, \quad Q = \omega I, \quad I \equiv \int_{\Sigma_t} d^3x \ \phi^2 \tag{7}$$

Its first variation by fixing the integral boundary and charge yields the field equation (4). Analysis of the second variation gives the stability of the equilibrium solutions; the main results which have already been obtained are as follows.

- In the thin wall limit ($\omega^2 \to \omega^2_{\min}$) they are stable [1, 5, 6].

- In the thick wall limit ($\omega^2 \to m^2$) they are stable if $n = 3$ [3, 5, 6] and unstable if $n \geq 4$ [5, 6].

- For any ω, if $\dfrac{\omega}{Q}\dfrac{dQ}{d\omega}$ is negative (positive), equilibrium solutions are stable (unstable) [6].

Here we analyze equilibrium solutions for the whole range $\omega^2_{\min} < \omega^2 < m^2$ numerically and then discuss their stability. For definiteness we assume a sextic function,

$$V(\phi) = \frac{\phi^6}{M^2} - \lambda\phi^4 + \frac{m^2}{2}\phi^2 \quad \text{with} \quad 0 < \lambda, \ M < \infty. \tag{8}$$

By rescaling the field variables, we can set $M = \lambda = 1$ without loss of generality. Then the existing condition (5) reduces to $m^2 - 1/2 < \omega^2 < m^2$. Fixing $m^2 = 1$, we numerically solve (4) for $0.5 < \omega^2 < 1$, and obtain a series of equilibrium solutions $\phi(r)$. For each equilibrium solution we calculate charge (2) and energy (7). We depict the relation among ω^2, Q and E in Figure 1. There is a minimum charge, which we denote by $Q_{\min}$, and near the minimum there are two equilibrium solutions for each Q.

To discuss the stability near $Q = Q_{\min}$ by analogy with a mechanical system, let us consider the one-parameter family of field configuration $\phi_{\xi;Q}(r)$ for each Q in such a way that $\phi_{\xi;Q}(r)$ contains all equilibrium solutions. Note that we do not impose any restriction on perturbation type. Then the
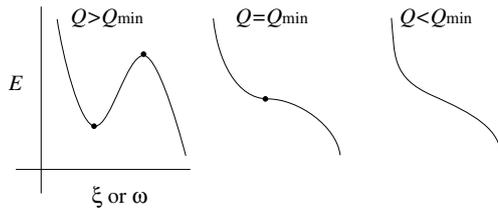
Figure 2: Behavior of the "potential" E for $Q \approx Q_{\min}$.
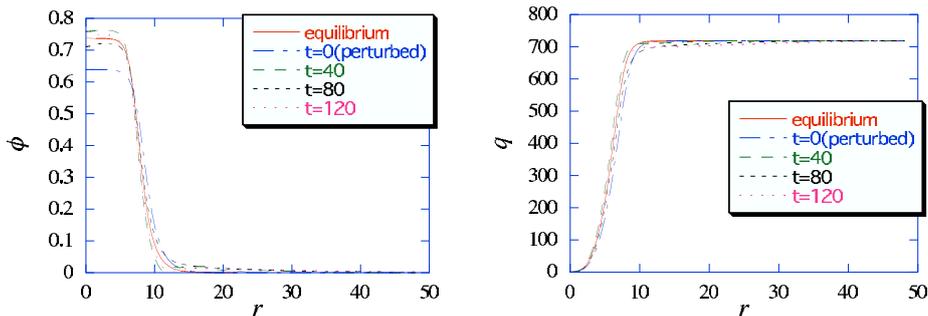
Figure 3: Dynamics of a Q-ball with a perturbed initial condition. $\omega^2 = 0.6$ and $Q = 718$. The right panel shows the evolution of the local charge, which is defined by $q \equiv 4\pi \int_0^r dr r^2 (\phi_1 \partial_t \phi_2 - \phi_2 \partial_t \phi_1)$.

energy is written as $E_Q(\xi) \equiv E[\phi_{\xi;Q}]$. Equilibrium solutions are realized when $dE_Q(\xi)/d\xi = 0$, and their stability is determined by the sign of $d^2 E_Q(\xi)/d\xi^2$. Therefore, the system completely corresponds to a mechanical system with the "potential" $E_Q(\xi)$, where ξ is a dynamical variable (or a "behavior variable" in catastrophe theory) and Q is a "control parameter" which is given by hand. Because ω is a function of ξ through $Q = \omega I[\phi_{\xi;Q}]$ for fixed Q, unless $d\xi/d\omega = 0$, ω also can be regarded as a behavior variable. Figure 2 shows how equilibrium points of $E_Q(\xi)$ change as Q varies near $Q = Q_{\min}$. This behavior is just a "fold catastrophe" in catastrophe theory.

Next, to explore the dynamics of Q-balls with finite deformation, we analyze numerically the dynamical field equations with perturbed initial conditions. Figure 3 shows an example of dynamical solutions. Although we give the initial configuration with the same Q and $\partial_t \phi = 0$, a part of charge is radiated away together with energy dispersion, and the Q-ball approaches to a different equilibrium solution with smaller Q. This shows a limitation of energy analysis with fixing Q when we discuss the dynamics of Q-balls with finite perturbations.

Coleman claimed that Q-balls with large Q are absolutely stable, not just stable under small deformation. Mathematically his statement is correct within energy-variation analysis for fixed Q. In a physical situation, however, charge is conserved but not necessarily confined in a local system. Therefore, we should not discuss finite perturbations by energy analysis with fixing Q.

3 Q-balls in curved spacetime

In this section we consider gravitating Q-balls. The action is given by

$$\mathcal{S} = \int d^4 x \sqrt{-g} \left[\frac{m_{\mathrm{Pl}}^2}{16\pi} \mathcal{R} - \frac{1}{2} g^{\mu\nu} \partial_\mu \phi \cdot \partial_\nu \phi - V(\phi) \right]. \tag{9}$$

To obtain equilibrium solutions, we assume a spherically symmetric and static spacetime,

$$ds^2 = -\alpha^2(r) dt^2 + A^2(r) dr^2 + r^2(d\theta^2 + \sin^2 \theta d\varphi^2). \tag{10}$$
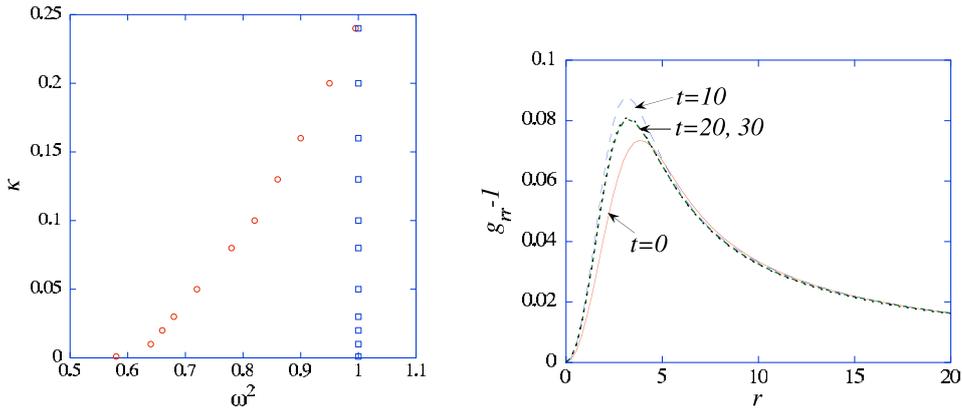
Figure 4: (left) Parameters which allow equilibrium solutions. A square denotes the maximum of ω^2 for a fixed κ, and a circle denotes the minimum.

Figure 5: Evolution of a Q-ball for $\kappa = 0.3$. In this case the metric approaches a stable configuration.

Supposing homogeneous phase rotation (3) again, we numerically solve the field equations, which follows from (9) and (10), with regularity conditions at the origin and at infinity. The model contains three independent parameters: m^2, ω^2 and $\kappa \equiv 8\pi\lambda M^2/m_{\mathrm{Pl}}{}^2$. Fixing $m^2 = 1$, we survey equilibrium solutions. The parameter range (ω^2, κ) which allow equilibrium solutions are summarized in Fig. 3. As κ becomes larger, the range of ω^2 which allows equilibrium solutions becomes smaller. If $\kappa \gtrsim 0.24$, equilibrium solutions are nonexistent regardless of ω^2.

Next, we investigate the stability of the equilibrium solutions. Becuase the energy defined by (7) does not have a definite meaning in curved spacetime, we adopt the gravitational (Misner-Sharp) mass, which is defined by $E_g \equiv m_{\mathrm{Pl}}{}^2 r(1 - a^2)/2$. We find the relation among ω^2, Q and E_g of equilibrium solutions are similar to that in Fig. 1. Therefore, we can understand their stability in the same way.

Finally, we consider the fate of Q-balls for $\kappa > 0.24$, where equilibrium solutions are nonexistent. For several initial conditions we solve the dynamical field equations numerically. We obtain two types of solutions: a Q-ball either approaches a stable solution (as shown in Fig. 5) or collapses to a black hole.

Contrary to the claim in [7], Q-ball inflation does not occur. In the core of an equilibrium Q-ball, the effective potential $V - \omega^2\phi^2/2$ must be negative, and accordingly $-T_t^t + T_i^i \propto \omega^2\phi^2 - V > 0$, which induces attractive nature of gravity. Although inflation may occur if $\omega^2\phi^2$ is sufficiently small and the slow-roll condition is satisfied, it is perhaps inappropriate to call such a configuration a Q-ball.

References

[1] S. Coleman, Nucl. Phys. **B262**, 263 (1985).

[2] A. Kusenko, M. Shaposhnikov, Phys. Lett. B **418**, 46 (1998).

[3] A. Kusenko, Phys. Lett. B **404**, 285 (1997).

[4] M. Axenides, S. Komineas, L. Perivolaropoulos & M. Floratos, Phys. Rev. D **61**, 085006 (2000).

[5] T. Multamaki & I. Vilja, Nucl. Phys. B **574**, 130 (2000).

[6] F. Paccetti Correia & M. G. Schmidt, Eur. Phys. J. **C21**, 181 (2001).

[7] T. Matsuda, Phys. Rev. D **68**, 127302 (2003).

Bubbles and Quantum Tunnelling in Inflationary Cosmology

Stefano Ansoldi[1]

International Center for Relativistic Astrophysics (ICRA), Italy, and
Istituto Nazionale di Fisica Nucleare (INFN), Sezione di Trieste, Italy, and
Dipartimento di Matematica e Informatica, Università degli Studi di Udine,
via delle Scienze 206, I-33100 Udine (UD), Italy [Mailing address]

Abstract

We review a procedure to use semiclassical methods in the quantization of General Relativistic shells and apply these techniques in some simplified models of inflationary cosmology. Some interesting open issues are introduced and the relevance of their solution in the broader context of Quantum Gravity is discussed.

The interplay of the gravitational and quantum realms is a fundamental topic in the research landscape of the last decades and is still waiting for a consolidate answer. While waiting, it is sometimes also tempting to study simplified models, that are well known from the classical point of view and that can be turned into virtual laboratories to test our present level of understanding. Concerning quantum gravitational systems, it is safe to say that, if not most, certainly many of these models use *general relativistic shells*. To make a first, quick, contact with this interesting system, we will restrict to a highly symmetric case and consider two four-dimensional spherically symmetric spacetimes $\mathcal{S}_\pm$; let us also choose the coordinates $(t_\pm, r_\pm, \theta_\pm, \phi_\pm)$ which are static and adapted to the spherical symmetry, so that in both $\mathcal{S}_\pm$ the two metrics can be written as $g_{ab}^{(\pm)} = \mathrm{diag}(g_{00}^{(\pm)}, g_{11}^{(\pm)}, g_{22}^{(\pm)}, g_{33}^{(\pm)}) = \mathrm{diag}\left(-f_\pm(r_\pm), 1/f_\pm(r_\pm), r_\pm^2, r_\pm^2 \sin^2\theta_\pm\right)$. Let us then consider the situation in which a part $\mathcal{M}_-$ of $\mathcal{S}_-$ and a part $\mathcal{M}_+$ of $\mathcal{S}_+$ are joined together across a timelike hypersurface Σ whose constant time slices are spherically symmetric, so that we obtain a new spherically symmetric spacetime $\mathcal{S} = \mathcal{M}_- \cup \Sigma \cup \mathcal{M}_+$. The dynamics of this system is described by Israel *junction conditions* [1], which, in the case we are considering, reduce to just one equation

$$R\left(\epsilon_+\sqrt{\dot{R}^2 + f_+(R)} - \epsilon_-\sqrt{\dot{R}^2 - f_-(R)}\right) = M(R); \tag{1}$$

$M(R)$ is a function describing the matter content of Σ (i.e. it is related to the stress energy tensor of the infinitesimally thin matter-energy distribution which is *joining* $\mathcal{M}_-$ and $\mathcal{M}_+$); $\epsilon_\pm$ are the signs of the radicals which follow them: when $\epsilon_\pm$ are positive (resp. negative) it means that the normal to the shell (which by convention we choose directed from $\mathcal{M}_-$ to $\mathcal{M}_+$) points in the direction of increasing (resp. decreasing) $r_\pm$. Finally, $R = R(\tau)$ is the radius of the shell (or *bubble*) expressed as a function of the proper time τ of an observer that lives on the bubble itself. Most of the popularity of shell models (particularly in the spherically symmetric version) is likely due to the direct geometrical meaning of the junction conditions, as well as to the fact that in spherical symmetry, it is possible to reduce (1) to

$$\dot{R}^2 + V(R) = 0, \quad V(R) = -\{(R^2 f_-(R) + R^2 f_+(R) - M^2(R))^2 - 4R^4 f_-(R) f_+(R)\}/(4M^2(R)R^2). \tag{2}$$

The solutions of (1) are equivalent to the solutions of (2) when the classical looking equation is complemented by the results $\epsilon_\pm = \mathrm{sign}\{M(R)(R^2 f_-(R) - R^2 f_+(R) \mp M^2(R))\}$, which are required to obtain the global spacetime structure of $\mathcal{S}$ starting from the knowledge of the trajectory $R(\tau)$. Thanks to the fact that the classical dynamics can be exactly solved (at least numerically), it is then tempting to proceed and study its quantum regime [2, 3, 4, 5]. In particular, since it is often the case that $V(R)$ in (2) acts as a potential barrier between bounded and unbounded solutions, it can be interesting to study, both, the semiclassical states corresponding to the bounded solutions [6] as well as the tunnelling under the potential barrier. Both these approaches have been considered, but here we will concentrate only on the second one, i.e. the tunnelling process: while waiting for quantum gravity, the natural framework for a its

---

[1]E-mail: `ansoldi@trieste.infn.it` — Web-page: `http://www-dft.ts.infn.it/∼ansoldi`
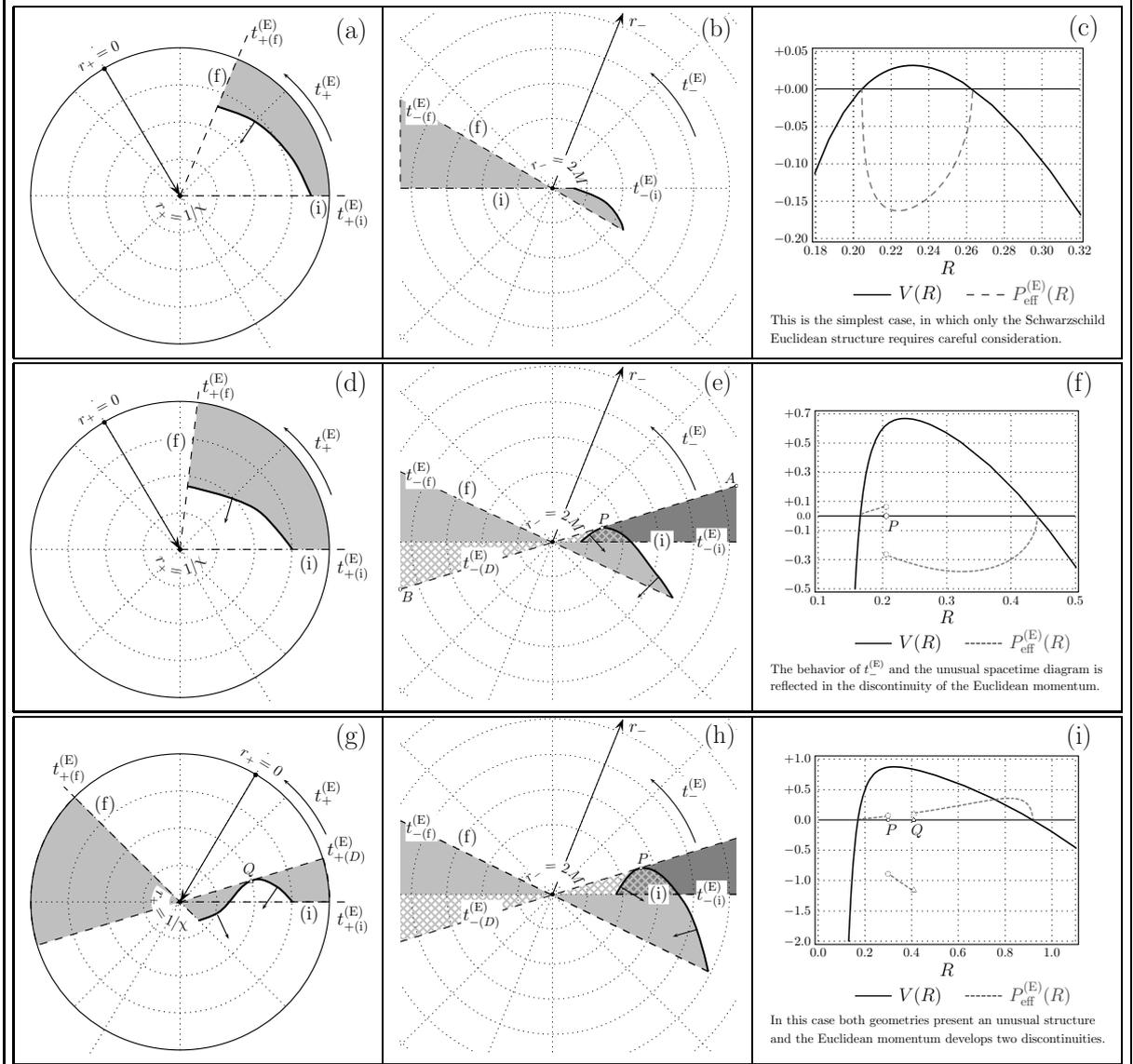
Figure 1: Various possibilities for tunnelling geometries and behavior of the Euclidean momentum. The instanton *should* be obtained joining across the shell trajectory (thick black curve) the shaded part of Euclidean de Sitter on the left with the part of Euclidean Schwarzschild on the same row in the middle. There are cases (as (a), (d)) where it is natural to identify the region to use. This is not always the case. For the tunnelling (a), (b), (c), the choice of Euclidean Schwarzschild region (b) is non-trivial and, if the Euclidean Schwarzschild time $t_-^{(E)}$ changes for more than π, multiple covering occurs [10]. At least, we see that in (c) no problem arises: in this case, path-integral and canonical approaches give the same result for the action. On the contrary, for the tunnelling (d), (e), (f), although Euclidean de Sitter (d) is again free of troubles, Euclidean Schwarzschild (e) develops an additional complication: at the point P the sign ϵ_- vanishes, passing from negative to positive values: this changes the part of the constant time section that participates in the junction ($\overline{PB}$ instead than $\overline{PA}$); *only after* P the point $r_- = 2M$ is included; moreover, $P_{\text{eff}}^{(E)}$ develops a discontinuity at P (see (f), cf. equation (4)). Using path-integrals methods, a proposal has been made to make sense of the diagram and to obtain the tunnelling action [10]: this proposal spoils the equivalence with the canonical approach although the reason is not clear. Note also that, the discontinuity in the momentum can be *cured* by carefully choosing the arctan branch in (4): the price to pay is a non-vanishing momentum at the second turning point. Coming, then, to the tunnelling (g), (h), (i), it shows that the Euclidean de Sitter part can also be affected by similar problems. $t_{\pm(i)/(f)}^{(E)}$ and $t_{\pm(D)}^{(E)}$ denote the initial/final time slices (also shown as (i) and (f)) and those corresponding to discontinuities of the momentum. The parts of spacetime selected for the junctions are chosen naively, but consistently with the amount of information provided in the main text; more refined and subtle choices can be made, without changing the conclusions.

complete analysis, many studies have already been performed at the semiclassical level. In particular, for these tunnelling processes we would like to determine: i) the geometry (instanton) interpolating between, for instance, the bounded initial configuration and the unbounded final one (if this instanton exists); ii) a general procedure to calculate the probability for the process. In this contribution we will summarize some problems that appear when trying to implement the above program and which resist, unsolved, since more than fifteen years [7], hoping to shed some light on possible successful approaches. In more detail, the problem of determining the Euclidean solution mediating the tunnelling can be formulated in the framework that we briefly depicted above. The Euclidean junction can be proved to be described by an equation very similar to (1); formally it can be obtained by simply Wick rotating the Euclidean time τ: $\tau \to \tau^{(\mathrm{E})} = -\imath\tau$ and correspondingly, $t_\pm^{(\mathrm{E})} = -\imath t_\pm$. This gives the Wick rotated equation

$$R\left(\epsilon_+ \sqrt{f_+(R) - (R')^2} - \epsilon_- \sqrt{f_-(R) - (R')^2}\right) = M(R) \quad \Rightarrow \quad (R')^2 - V(R) = 0, \tag{3}$$

where a prime denotes a derivative with respect to $\tau^{(\mathrm{E})}$. Under Wick rotation, the results for $\epsilon_\pm$ are clearly unchanged. It is also worth remembering the relations $\left(t_\pm^{(\mathrm{E})}\right)' = \epsilon_\pm \sqrt{f_\pm(R) - (R')^2}/f_\pm(R)$, as well as the fact that it is possible to provide an effective Lagrangian formulation [8, 9] to derive (1) and (3). Incidentally, we observe that (1) and (3) are, in fact, first order equations: they are a first integral of the second order Euler-Lagrange equations obtained from the effective Lagrangian L_{eff}. From L_{eff} the effective momentum P_{eff} can be derived with standard techniques and its Euclidean counterpart is

$$P_{\mathrm{eff}}^{(\mathrm{E})} = -R\left\{\arctan\left(\frac{R'}{\epsilon_+ \sqrt{f_+(R) - (R')^2}}\right) - \arctan\left(\frac{R'}{\epsilon_- \sqrt{f_-(R) - (R')^2}}\right)\right\}. \tag{4}$$

We have, now, at least two choices to determine the transition amplitude: use the path-integral approach with the Lagrangian L_{eff} or proceed *via* canonical quantization using the Euclidean momentum $P_{\mathrm{eff}}^{(\mathrm{E})}$ and the standard result for the probability amplitude $\mathcal{A}$

$$\mathcal{A} \sim \exp(-S), \quad S = \int_{R_1}^{R_2} P(R)dR, \quad R_1, R_2 \text{ extrema of the tunneling trajectory.} \tag{5}$$

For concreteness, let us now specialize to the case considered in [10] where this analysis has been performed by choosing $f_+(r_+) = 1 - \chi^2 r_+^2$, i.e. de Sitter spacetime, $f_-(r_-) = 1 - 2M/r_-$, i.e. Schwarzschild spacetime, and the shell has a constant tension ρ, i.e. $M(R) = 4\pi\rho R^2$. This is a special, important case often considered in the studies of vacuum bubbles/decay [11, 4, 5]. This specific model allows a description of inflation in early universe cosmology avoiding the initial singularity problem. Indeed, it turns out that for a wide range of values of the parameters χ, M and ρ, there are bounded inflating solutions that can be created without an initial singularity; although they do not inflate enough to be a good model of the present universe, it is suggestive to consider the possibility that they will *tunnel* into an unbounded solution which will eventually evolve and resemble the present universe. This idea becomes even more stimulating in view of some issues which appear at a careful analysis of the process [10] and which have not yet found a satisfactory solution/explanation. They are i) the fact that the Euclidean manifold which should mediated the transition between the two Lorentzian junctions (the one before the tunnelling and the one after) can not be easily defined and ii) a discordance between the results provided by a path-integral approach and those obtained with a canonical one. If in the seminal paper of Farhi *et al.* [10] an interesting proposal for the construction of the instanton has been put forward and its generalization to generic junctions might provide the sought answer, the second issue is mostly disturbing in view of the fact that canonical methods are known to reproduce well known results in vacuum decay (in particular the canonical approach has been shown to reproduce [9] the results of Coleman *et al.* [3] and Parke [12]). A slightly more detailed analysis of this point with additional technical details can be found in figure 1. Then, we would like to conclude this contribution with just a few, more speculative, considerations. In particular, what is the physical counterpart of these open issues in the Euclidean sector? Is the tunnelling process really allowed or not? If yes, is there an instanton mediating the process? What is the meaning of the discrepancy between path-integral and canonical formulations? Could it be of interest for quantum gravity? And more, how can we interpret all the above questions in

view of the initial singularity problem? For instance, we could take the point of view that transitions which do not satisfy all the standard properties of the Euclidean momentum are forbidden; but then we would forbid many transitions which would help us to evade classical singularity theorems! If, instead, we can make sense of the unusual properties of the (Euclidean) spacetime structure, we could easily develop a lot of other (solvable) examples in which, already at the semiclassical level, quantum effects can be effectively used to remove singularities.... The search for an answer to these and other similar (interesting) questions is, currently, work in progress, and its results will be reported elsewhere.

Acknowledgements

References

[1] W. Israel, *Nuovo Cimento B* **XLIV B**:1, 1966; err. ibid. **IIL**:463(E), 1967; C. Barrabes and W. Israel, *Phys. Rev.* **D43**:1129, 1991.

[2] S. Coleman, *Phys. Rev.* **D15**:2929, 1977; C. G. Callan Jr. and S. Coleman, *Phys. Rev.* **D16**:1762, 1977; V. A. Berezin, *Phys. Lett. B* **241**:194, 1990; W. Fischler, D. Morgan and J. Polchinski, *Phys. Rev.* **D42**:4042, 1990; M. Visser, *Phys. Rev.* **D43**:402, 1991; M. Visser, *Lorentzian wormholes: from Einstein to Hawking*, American institute of Physics, Woodbury, 1995; K. Nakamura, Y. Oshiro and A. Tomimatsu, *Phys. Rev.* **D53**:4356, 1996; A. D. Dolgov and I. B. Khriplovich, *Phys. Lett. B* **400**:12, 1997; G. L. Alberghi, R. Casadio, G. P. Vacca and G. Venturi, *Class. Quantum Grav.* **16**:131, 1999; N. Sakai, K. Nakao, H. Ishihara and M. Kobayashi, *Phys. Rev.* **D74**:024026, 2006.

[3] S. Coleman and F. de Luccia, *Phys. Rev.* **D21**:3305, 1980.

[4] V. A. Berezin, N. G. Kozimirov, V. A. Kuzmin and I. I. Tkachev, *Phys. Lett. B* **212**:415, 1988.

[5] W. Fischler, D. Morgan and J. Polchinski, *Phys. Rev.* **D41**:2638, 1990.

[6] S. Ansoldi, *Class. Quantum Grav.* **19**:6231, 2002; S. Ansoldi, *AIP Conf. Proc.* **751**:159, 2005; S. Ansoldi, "Braneworlds and quantum states of relativistic shells", *To appear in the proceedings of the 11th Marcell Grossman Meeting on General Relativity*, Berlin, July 23-29, 2006; S. Ansoldi, E. I. Guendelman, and H. Ishihara, In preparation.

[7] A. Aguirre and M. C. Johnson, *Phys. Rev.* **D72**:103525, 2005; A. Aguirre and M. C. Johnson, *Phys. Rev.* **D73**:123529, 2006; S. Ansoldi and L. Sindoni, "Gravitational tunnelling of relativistic shells", in *Frontiers in Fundamental Physics*, Springer, 2006.

[8] J. L. Friedman, J. Louko and S. N. Winters-Hilt, *Phys. Rev.* **D56**:7674, 1997; P. Hajicek and J. Bicak, *Phys. Rev.* **D56**:4706, 1997; P. Hajicek, *Phys. Rev.* **D58**:084005, 1998; P. Hajicek, *Phys. Rev.* **D57**:936, 1998; P. Hajicek and J. Kijowski, *Phys. Rev.* **D57**:914, 1998; err. ibid. **D61**:129901(E), 2000; J. Kijowski, *Acta Phys. Pol. B* **29**:1001, 1998; S. Mukohyama, *Phys. Rev.* **D65**:024028, 2002; V. D. Gladush, *J. Math. Phys.* **42**:2590, 2000; V. D. Gladush, *Gen. Rel. Grav.* **36**:1821, 2004; C. Barrabes and W. Israel, *Phys. Rev.* **D71**:064008, 2005.

[9] S. Ansoldi, A. Aurilia, R. Balbinot and E. Spallucci, *Physics Essays* **9**:556, 1996; S. Ansoldi, A. Aurilia, R. Balbinot and E. Spallucci, *Class. Quantum Gravity* **14**:2727, 1997.

[10] E. Farhi, A. H. Guth and J. Guven, *Nucl. Phys. B* **339**:417, 1990; A. H. Guth, *Phys. Scr.* **T36**:237, 1991.

[11] K. Sato, M. Sasaki, H. Kodama and K. Maeda, *Progr. Theor. Phys.* **65**:1443, 1981; H. Kodama, M. Sasaki, K. Sato and K. Maeda, *Progr. Theor. Phys.* **66**:2052, 1981; K. Sato, H. Kodama, M. Sasaki and K. Maeda, *Phys. Lett. B* **108**:103, 1982; H. Kodama, M. Sasaki and K. Sato, *Progr. Theor. Phys.* **68**:1979, 1982; K. Maeda, K. Sato, M. Sasaki and H. Kodama, *Phys. Lett. B* **108**:98, 1982; S. K. Blau, E. I. Guendelman and A. H. Guth, *Phys. Rev.* **D35**:1747, 1987; V. A. Berezin, V. A. Kuzmin and I. I. Tkachev, *Phys. Rev.* **D36**:2919, 1987; A. Aurilia, M. Palmer and E. Spallucci, *Phys. Rev.* **D40**:2511, 1989; M. Sasaki, T. Tanaka, K. Yamamoto and J. Yokoyama, *Phys. Lett. B* **317**:510, 1993; T. Tanaka, *Nucl. Phys. B* **556**:373, 1999; A. Khvedelidze, G. V. Lavrelashvili and T. Tanaka, *Phys. Rev.* **D62**:083501, 2000.

[12] S. Parke *Phys. Lett. B* **121**:313, 1983.

Large-scale magnetic fields from inflation

Kazuharu Bamba[1] [2] and Misao Sasaki[3]

Yukawa Institute for Theoretical Physics, Kyoto University, Kyoto 606-8502, Japan

Abstract

The generation of large-scale magnetic fields is studied in the inflationary cosmology. We consider a very general situation in which the conformal invariance of the Maxwell field is violated through a coupling of the form IF^2 where I can be a function of any non-trivial background fields that vary in time. We derive general formulas for the spectrum of large-scale magnetic fields and the spectral index. As a result, we obtain the general, model-independent necessary condition for the generation of magnetic fields with sufficiently large amplitude. Then the implications of our result are discussed.

1 Introduction

It is well known that there exist magnetic fields with the field strength $\sim 10^{-6}$G on $1 - 10$kpc scale in galaxies of all types and in galaxies at cosmological distances. Furthermore, magnetic fields in clusters of galaxies with the field strength $10^{-7} - 10^{-6}$G on 10kpc$-$1Mpc scale have been observed. It is very interesting that magnetic fields in clusters of galaxies are as strong as galactic ones and that the coherence scale may be as large as $\sim$Mpc. The origin of these magnetic fields is not well understood yet. Galactic dynamo mechanisms have been proposed to amplify very weak seed magnetic fields up to $\sim 10^{-6}$G. In fact, however, galactic dynamo mechanisms require initial seed magnetic fields to feed on, and the effectiveness of the dynamo amplification mechanism in galaxies at high redshifts or clusters of galaxies is not well established.

It is difficult to generate the magnetic fields on megaparsec scales with the sufficient field strength to account for the observed magnetic fields in galaxies and clusters of galaxies without requiring any dynamo amplification. The problem is essentially the same as the problem of the large-scale structure formation for which one needed the adiabatic curvature perturbation of non-negligible amplitude on superhorizon scales, the so-called horizon problem. Then, just as this problem is solved by the inflationary cosmology, it is natural to look for the possibility of generating such a large-scale magnetic field during inflation [1]. However, the Friedmann-Robertson-Walker (FRW) universe is conformal flat and the Maxwell theory is conformal invariant. Therefore, the conformal invariance must be broken to generate non-trivial magnetic fields. Various conformal symmetry breaking mechanisms have been proposed so far [1, 2, 3].

In the present paper [4], we consider the generation of large-scale magnetic fields in a very general situation in which the conformal invariance is violated through the coupling of the form IF^2 where I can be a function of any non-trivial background fields that vary in time. We derive the general formula for the spectrum of large-scale magnetic fields and the spectral index formula. As a result, we obtain the general, model-independent necessary condition for the generation of large-scale magnetic fields with a sufficiently large amplitude.

2 MODEL

We consider a conformal violating Maxwell theory with the action,

$$S \;=\; \int d^4x \sqrt{-g} \left(-\frac{1}{4} I \, F_{\mu\nu} F^{\mu\nu} \right) \, , \tag{1}$$

---

[1] Research Fellow of the Japan Society for the Promotion of Science
[2] E-mail:bamba@yukawa.kyoto-u.ac.jp
[3] E-mail:misao@yukawa.kyoto-u.ac.jp

where I is an arbitrary function of non-trivial background fields at the moment. Naturally the argument of I will include the inflaton if the dilaton Φ does not play the role of the inflaton.

From the action (1), the electromagnetic field equation is given by

$$-\frac{1}{\sqrt{-g}}\partial_\mu \left[\sqrt{-g}IF^{\mu\nu}\right] = 0. \tag{2}$$

We assume a spatially flat universe with the metric

$$ds^2 = -dt^2 + a^2(t)d\boldsymbol{x}^2 = a^2(\eta)(-d\eta^2 + d\boldsymbol{x}^2), \tag{3}$$

where a is the scale factor and η is the conformal time. We consider the evolution of the $U(1)$ gauge field in this background. Its equation of motion in the Coulomb gauge, $A_0(t, \boldsymbol{x}) = 0$ and $\partial^j A_j(t, \boldsymbol{x}) = 0$, becomes

$$\ddot{A}_i(t, \boldsymbol{x}) + \left(H + \frac{\dot{I}}{I}\right)\dot{A}_i(t, \boldsymbol{x}) - \frac{1}{a^2}\overset{(3)}{\Delta} A_i(t, \boldsymbol{x}) = 0, \tag{4}$$

where $H = \dot{a}/a$, and a dot denotes a time derivative, $\dot{} = \partial/\partial t$.

3   generic slow-roll inflation

In this section, we consider the evolution of the $U(1)$ gauge field and that of the magnetic fields in generic slow-roll inflation.

3.1   Spectrum from quantum fluctuations

To begin with, we shall quantize the $U(1)$ gauge field $A_\mu(t, \boldsymbol{x})$. It follows from the electromagnetic part of our model Lagrangian in Eq. (1) that the canonical momenta conjugate to $A_\mu(t, \boldsymbol{x})$ are given by

$$\pi_0 = 0, \qquad \pi_i = Ia(t)\dot{A}_i(t, \boldsymbol{x}). \tag{5}$$

We impose the canonical commutation relation between $A_i(t, \boldsymbol{x})$ and $\pi_j(t, \boldsymbol{x})$,

$$[A_i(t, \boldsymbol{x}), \pi_j(t, \boldsymbol{y})] = i\int \frac{d^3k}{(2\pi)^3}e^{i\boldsymbol{k}\cdot(\boldsymbol{x}-\boldsymbol{y})}\left(\delta_{ij} - \frac{k_ik_j}{k^2}\right), \tag{6}$$

where $\boldsymbol{k}$ is comoving wave number and $k = |\boldsymbol{k}|$. From this relation, we obtain the expression for $A_i(t, \boldsymbol{x})$ as

$$A_i(t, \boldsymbol{x}) = \int \frac{d^3k}{(2\pi)^{3/2}}\sum_{\sigma=1,2}\left[\hat{b}(\boldsymbol{k}, \sigma)\epsilon_i(\boldsymbol{k}, \sigma)A(t, k)e^{i\boldsymbol{k}\cdot\boldsymbol{x}} + \hat{b}^\dagger(\boldsymbol{k}, \sigma)\epsilon_i^*(\boldsymbol{k}, \sigma)A^*(t, k)e^{-i\boldsymbol{k}\cdot\boldsymbol{x}}\right], \tag{7}$$

where $\epsilon_i(\boldsymbol{k}, \sigma)$ ($\sigma = 1, 2$) are the two orthonormal transverse polarization vector, and $\hat{b}(\boldsymbol{k}, \sigma)$ and $\hat{b}^\dagger(\boldsymbol{k}, \sigma)$ are the annihilation and creation operators which satisfy

$$\left[\hat{b}(\boldsymbol{k}, \sigma), \hat{b}^\dagger(\boldsymbol{k}', \sigma')\right] = \delta_{\sigma, \sigma'}\delta^3(\boldsymbol{k} - \boldsymbol{k}'), \qquad \left[\hat{b}(\boldsymbol{k}, \sigma), \hat{b}(\boldsymbol{k}', \sigma')\right] = \left[\hat{b}^\dagger(\boldsymbol{k}, \sigma), \hat{b}^\dagger(\boldsymbol{k}', \sigma')\right] = 0. \tag{8}$$

It follows from Eq. (4) that the mode function $A(k, t)$ satisfies the equation

$$\ddot{A}(k, t) + \left(H + \frac{\dot{I}}{I}\right)\dot{A}(k, t) + \frac{k^2}{a^2}A(k, t) = 0, \tag{9}$$

with the normalization condition,

$$A(k, t)\dot{A}^*(k, t) - \dot{A}(k, t)A^*(k, t) = \frac{i}{Ia}. \tag{10}$$

Replacing the independent variable t by η, we find that Eq. (9) becomes

$$A''(k,\eta) + \frac{I'}{I}A'(k,\eta) + k^2 A(k,\eta) = 0, \tag{11}$$

where the prime denotes differentiation with respect to the conformal time η.

Although it is impossible to obtain the exact solution of Eq. (11) for the case when I is given by a general function of η, we can obtain an approximate solution with sufficient accuracy by using the WKB approximation on subhorizon scales and the long wavelength approximation on superhorizon scales, and match these solutions at the horizon crossing $\eta = \eta_k \approx -/k$.

As a result, we find that an approximate solution for $|A(k,\eta)|^2$ at late times is given by

$$|A(k,\eta)|^2 = |C(k)|^2 = \frac{1}{2kI(\eta_k)}\left|1 - \left(\frac{1}{2}\frac{I'(\eta_k)}{kI(\eta_k)} + i\right)e^{-ik\eta_k}k\int_{\eta_k}^{\eta_{\rm R}}\frac{I(\eta_k)}{I(\eta')}d\eta'\right|^2, \tag{12}$$

where $\eta_{\rm R}$ is the conformal time at the time of reheating after inflation. The proper magnetic field is given by

$$B_i{}^{\rm proper}(t,\boldsymbol{x}) = a^{-1}B_i(t,\boldsymbol{x}) = a^{-2}\epsilon_{ijk}\partial_j A_k(t,\boldsymbol{x}), \tag{13}$$

where $B_i(t,\boldsymbol{x})$ is the comoving magnetic field, and ϵ_{ijk} is the totally antisymmetric tensor ($\epsilon_{123} = 1$). Thus the spectrum of the magnetic field is given by

$$|B^{\rm proper}(k,\eta)|^2 = 2\frac{k^2}{a^4}|A(k,\eta)|^2 = 2\frac{k^2}{a^4}|C(k)|^2, \tag{14}$$

where the factor 2 comes from the two polarization degrees of freedom. Thus the energy density of the generated magnetic field per unit logarithmic interval of k is given by

$$\rho_B(k,\eta) \equiv \frac{1}{2}\frac{4\pi k^3}{(2\pi)^3}|B^{\rm proper}(k,\eta)|^2 I(\eta) = \frac{k|C(k)|^2}{2\pi^2}\frac{k^4}{a^4}I(\eta), \tag{15}$$

and the density parameter per unit logarithmic interval of k after reheating becomes

$$\Omega_B(k,\eta) = \frac{\rho_B(k,\eta_{\rm R})}{\rho(\eta_{\rm R})}\frac{I(\eta)}{I(\eta_{\rm R})} = \frac{k^4}{T_{\rm R}^4 a_{\rm R}^4}\frac{15k|C(k)|^2}{N_{\rm eff}\pi^4}I(\eta); \quad \rho(\eta_{\rm R}) = N_{\rm eff}\frac{\pi^2}{30}T_{\rm R}^4, \tag{16}$$

where $T_{\rm R}$ is the reheating temperature, $a_{\rm R}$ is the scale factor at reheating, and $N_{\rm eff}$ is the effective massless degrees of freedom (2 for photons) which are thermalized at reheating. The spectral index of $\Omega_B(k)$ is then given by

$$n_B \equiv \frac{d\ln\Omega_B(k)}{d\ln k} = 4 + \frac{d\ln k|C(k)|^2}{d\ln k}. \tag{17}$$

3.2 Semi-quantitative estimate

Using Eq. (12) for $|C(k)|^2$, one may derive a general expression for the density parameter and the spectral index of the magnetic field in terms of I. However, the result will be very complicated and hence will not be very illuminating. To gain more insight into semi-quantitative nature of the generated magnetic field, let us therefore a specific form for the function I. We set

$$I(\eta) = I_*\left(\frac{\eta}{\eta_*}\right)^{-\alpha}, \tag{18}$$

where η_* is some fiducial time during inflation, and α is a constant. As we shall see shortly, in order to obtain a cosmologically interesting result, we need a monotonically increasing I during the stage of inflation when the relevant comoving scales leave the horizon. So, we assume $\alpha > 0$ in the following. Then $|C|^2$ in Eq. (12) can be explicitly evaluated to be

$$k|C|^2 = \frac{1}{2I(\eta_k)}\left|1 - \frac{\alpha+2i}{2(\alpha+1)}e^{-ik\eta_k}\right|^2 \equiv \frac{\mathcal{C}}{2I(\eta_k)}, \tag{19}$$

where $k\eta_k = O(1)$ and $\mathcal{C}$ is a constant of order unity.

Then, inserting the above equation to Eqs. (16) and (17), we obtain the explicit expressions for the density parameter and the spectral index at present η_0:

$$\Omega_B(k, \eta_0) = \frac{k^4}{T_{\rm R}^4 a_{\rm R}^4} \frac{15\mathcal{C}}{2 N_{\rm eff} \pi^4 I_*} \left(\frac{\eta_k}{\eta_*} \right)^\alpha , \qquad n_B = 4 - \alpha , \qquad (20)$$

where $I(\eta_k) \propto k^\alpha$ and $I(\eta_0) = 1$ have been used. We see that for a spectrum with a sufficiently large amplitude, I_* must be sufficiently small, and for a spectral index close to a scale-invariant one, we need $\alpha \sim 4$.

To proceed further to make a more quantitative estimate, let us assume that the reheating takes place almost instantaneously so that η_R can be identified with the conformal time at the end of inflation, and $I(\eta)$ is given by Eq. (18) until the end of inflation. Noting that $a_{\rm R}^2 \eta_{\rm R}^2 \approx H_{\rm R}^{-2}$ and $3H_{\rm R}^2 = \rho_{\rm R}/M_{pl}^2$, where $M_{pl} = 1/\sqrt{8\pi G}$, from Eq. (16) we obtain

$$\Omega_B(k, \eta_0) = \mathcal{C} \frac{N_{eff}}{1080} \left(\frac{T_{\rm R}}{M_{pl}} \right)^4 (-k\eta_{\rm R})^{4-\alpha} \frac{1}{I(\eta_{\rm R})} . \qquad (21)$$

We see that higher the reheating temperature is, larger the density parameter of the magnetic field becomes. But given the fact that T_R cannot be made arbitrarily large, there is a limit to this mechanism. Instead the most important point of the above formula is the presence of the factor $1/I(\eta_{\rm R})$. It means one can make Ω_B arbitrarily large by choosing $I(\eta_{\rm R})$ arbitrarily small. An explicit example of this case was discussed in [3], where I was a function of a dilaton which is assumed to be rolling even after the end of inflation. It was found that the present magnetic field with rms amplitude as large as 10^{-9} Gauss can be obtained.

4 Conclusion

In the present paper we have studied the generation of large-scale magnetic fields in the inflationary cosmology, by breaking the conformal invariance of the electromagnetic field through the coupling of the form IF^2, where I can be a function of any non-trivial background fields that vary in time. In other words, we have given a model-independent analysis on the generation of large-scale magnetic fields due to the violation of the conformal invariance through the coupling IF^2. Then we have derived the general formula for the spectrum of large-scale magnetic fields and the formula for the spectral index. As a result, we have obtained the general, model-independent necessary condition for the generation of magnetic fields with large amplitude. Namely, the coupling function I must be extremely small in the beginning and increases rapidly in time during inflation. This is our most important result. Any model with a coupling of the form IF^2 must satisfy this condition if it should generate large-scale magnetic fields with sufficiently large amplitude. Such a coupling seems very unnatural and hard to be realized. Nevertheless, considering the recently much discussed issue of the string landscape, which tells us that infinitely many different low energy theories are possible [5], the naturalness may not be a crucial issue, and it may worth searching for a model that realizes a successful inflationary universe and satisfies the necessary condition for the generation of a large magnetic field at the same time.

References

[1] M. S. Turner and L. M. Widrow, Phys. Rev. D **37**, 2743 (1988).

[2] B. Ratra, Astrophys. J. **391**, L1 (1992); Report No. GRP-287/CALT-68-1751.

[3] K. Bamba and J. Yokoyama, Phys. Rev. D **69**, 043507 (2004).

[4] K. Bamba and M. Sasaki, arXiv:astro-ph/0611701.

[5] L. Susskind, arXiv:hep-th/0302219.

Classical and quantum radiation from a moving charge in expanding universe

Hidenori Nomura[1], Misao Sasaki[2] and Kazuhiro Yamamoto[3]

[1, 3]*Department of Physical Science, Hiroshima University, Higashi-Hiroshima 739-8526, Japan*
[2]*Yukawa Institute for Theoretical Physics, Kyoto University, Kyoto 606–8502, Japan*

1 Introduction

One of the notable feature of quantum fields in curved spacetime is that quantum processes prohibited in the Minkowski spacetime is allowed. For example, the emission of a photon from a moving massive charged particle occurs in an expanding universe, though such a process is prohibited by the energy momentum conservation in the Minkowski spacetime due to the Lorentz invariance. This subject was studied by several authors [1, 2, 3, 4]. These previous works, however, focused on the transition probability of the process. While, in the present work, we calculate the radiation energy emitted through the process. Our point of view is as follows: The motion of a massive charge in an expanding or contracting universe can be regarded as an accelerated motion, because the physical momentum of the particle decreases (increased) as the universe expands (contracts). Then, the photon emission process can be regarded as the well-known classical radiation process from an accelerated charge [5]. The present work aims to clarify the correspondence between the classical and quantum approaches to photon emission from a moving charge in expanding universe.

2 Derivation of the radiation formula with the WKB approximation

In what follows, we focus on the spatially flat Friedmann-Robertson-Walker spacetime, whose line element is expressed as

$$ds^2 = a(\eta)^2[-d\eta^2 + d\mathbf{x}^2] = a(\eta)^2 \eta_{\mu\nu} dx^\mu dx^\nu, \tag{1}$$

where η is the conformal time, and $a(\eta)$ is the scale factor. We consider the scalar QED Lagrangian conformally coupled to the curvature,

$$\mathcal{S} = \int d^4 x \sqrt{-g} \left[-g^{\mu\nu} \left(\nabla_\mu - \frac{ieA_\mu}{\hbar} \right) \Phi^\dagger \left(\nabla_\nu + \frac{ieA_\nu}{\hbar} \right) \Phi - \left(\frac{m^2}{\hbar^2} + \xi_{\rm conf} R \right) \Phi^* \Phi - \frac{1}{4\mu_0} F^{\mu\nu} F_{\mu\nu} \right], \tag{2}$$

where $F_{\mu\nu} = \nabla_\mu A_\nu - \nabla_\nu A_\mu$ is the field strength, and μ_0 is the magnetic permeability of vacuum. In this work, we use the unit light velocity equals 1 but explicitly include the Planck constant $\hbar$. Introducing the conformally rescaled field $\phi(= a(\eta)\Phi)$, we may rewrite the Lagrangian as

$$\mathcal{S} = \int d^4 x \left[-\eta^{\mu\nu} \left(\partial_\mu - \frac{ieA_\mu}{\hbar} \right) \phi^\dagger \left(\partial_\nu + \frac{ieA_\nu}{\hbar} \right) \phi - \frac{m^2 a(\eta)^2}{\hbar^2} \phi^* \phi - \frac{1}{4\mu_0} f^{\mu\nu} f_{\mu\nu} \right], \tag{3}$$

where $f_{\mu\nu} = \partial_\mu A_\nu - \partial_\nu A_\mu$. Thus the system is mathematically equivalent to the scalar QED in the Minkowski spacetime with the time-variable mass $m\, a(\eta)$.

We follow a general prescription for interacting fields, based on the interaction picture approach. We focus on the radiation energy emitted through the process described by the Feynman diagram in Fig. 1.

---

[1]E-mail:hide@theo.phys.sci.hiroshima-u.ac.jp
[2]E-mail:misao@yukawa.kyoto-u.ac.jp
[3]E-mail:kazuhiro@hiroshima-u.ac.jp
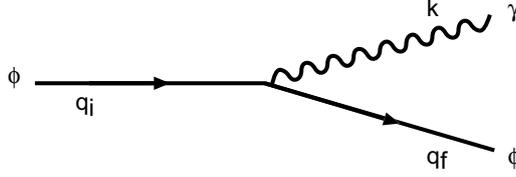
Figure 1: Feynman Diagram of the photon emission process

The radiation energy is

$$
\begin{aligned}
E &= \frac{(2\pi)^3}{L^3} \sum_{r=1,2} \sum_{\mathbf{k}} \sum_{\mathbf{q}} \hbar\omega(k)|\text{Transition Amplitude}|^2 \\
&= \frac{2e^2}{\varepsilon_0} \int \frac{d^3\mathbf{k}}{(2\pi)^3} \left(\mathbf{q}_i^2 - \frac{(\mathbf{q}_i \cdot \mathbf{k})^2}{k^2} \right) \left| \int d\eta e^{ik\eta} \varphi_{\mathbf{q}_f}^*(\eta) \varphi_{\mathbf{q}_i}(\eta) \right|^2 ,
\end{aligned}
$$

where $\mathbf{q}_f = \mathbf{q}_i - \mathbf{k}$, and ε_0 is the permittivity of vacuum, which is related to μ_0 as $\varepsilon_0\mu_0 = 1/c^2 = 1$. In the computation of the above radiation energy, we need to know the form of the mode function of the scalar field, namely the solution of the equation of motion of the scalar field. In this section, we adopt the WKB approximation in order to derive the classical formula for the radiation energy. The mode function of the scalar field, $\varphi_{\mathbf{q}}(\eta)$, is given as

$$
\varphi_{\mathbf{q}}(\eta) = \sqrt{\frac{1}{2\Omega_{\mathbf{q}}(\eta)}} \exp\left[-i \int_{\eta_*}^{\eta} \Omega_{\mathbf{q}}(\eta')d\eta' \right], \quad \text{where} \quad \Omega_{\mathbf{q}}(\eta) = \frac{\sqrt{m^2 a(\eta)^2 + \hbar^2 \mathbf{q}^2}}{\hbar}. \tag{5}
$$

We can write the condition that the WKB formula is valid, as

$$
\Omega_{\mathbf{q}}^2 \gg \frac{1}{2} \left| \frac{\ddot{\Omega}_{\mathbf{q}}}{\Omega_{\mathbf{q}}} - \frac{3}{2} \frac{\dot{\Omega}_{\mathbf{q}}^2}{\Omega_{\mathbf{q}}^2} \right|, \tag{6}
$$

where the dot means the differentiation with respect to η.

The integration in Eq.(5) requires some technique but is straghtforward. Finally, using the WKB mode functions, the integration with respect to $\mathbf{k}$ yields

$$
E = \frac{e^2}{6\pi\varepsilon_0} \int d\eta \frac{\ddot{z}^2}{(1 - \dot{z}^2)^3}. \tag{7}
$$

This result is the same as the Larmor formula in the case when the particle moves along a straight line [5]. Note that this is the energy in the conformally rescaled spacetime, which is not the physical energy. From this expression, however, we can read the physical radiation energy as $\mathcal{E} = E/a$, and the physical rate of the radiation energy per unit time as

$$
\frac{d\mathcal{E}}{dt} = \frac{1}{a^2} \frac{dE}{d\eta} = \frac{e^2 p_{phys}^2 H^2}{6\pi\varepsilon_0 m^2}, \tag{8}
$$

where t is the cosmic time, $p_{phys}(= p_i/a)$ is the physical momentum and H is the Hubble expansion rate. This result is consistent with that in ref. [3], which is obtained from consideration of the classical electromagnetic radiation formula of a moving charge in an expanding universe.

Finally in this section, let us summarize the necessary condition for reproducing the radiation formula in the classical electromagnetic theory. We started with the WKB formula of the mode function, for which Eq. (6) is needed. In addition, we assumed an additional condition as follows

$$
k(= |\mathbf{k}|) \ll q_f(= |\mathbf{q}_f|), \quad \text{and} \quad q_i(= |\mathbf{q}_f|). \tag{9}
$$

Although this condition is independent of the necessary condition for the WKB approximation, Eq. (6), we assumed it because this additional assumption is necessary to recover the conventional picture for the classical radiation from a charged massive particle, in which the massive field should behave like a particle and the photon field should behave like a wave.

3 Quantum radiation

In this section, we consider an exactly solvable model in order to address the validity of the WKB formula. We consider a time-symmetric bounce universe which asymptotically approaches a contracting and expanding radiation-dominated universe. The scale factor is given in terms of the conformal time η by [6]

$$a(\eta) = \sqrt{\varrho^2\eta^2 + \epsilon^2} \qquad (-\infty < \eta < \infty), \tag{10}$$

which recovers a radiation-dominated Friedmann universe in the asymptotic regions, $a(t) \propto t^{1/2}$ ($\eta \to \pm\infty$). In this background spacetime, the equation of motion of the scalar field is reduced to the Weber's differential equation and therefore the mode functions are constructed by the parabolic cylinder function.

Using the exact mode function, we can calculate the radiation energy exactly and represent it as following form [7]:

$$E = E_{cl} \times F\left(\frac{p_i}{\epsilon m}, \frac{\hbar\varrho}{\epsilon^2 m}\right), \tag{11}$$

where E_{cl} is the WKB formula (7) calculated in the background spacetime (10), and we defined

$$F\left(\frac{p_i}{\epsilon m}, \frac{\hbar\varrho}{\epsilon^2 m}\right) = \frac{12}{\pi} \int_0^\infty d\hat{k}\hat{k}^2 \int_{-1}^1 d\cos\theta \frac{1-\cos^2\theta}{(1-e^{-2\pi\lambda})(1-e^{-2\pi\bar{\lambda}})} e^{\pi(\lambda-2\bar{\lambda})}$$
$$\times \left|U\left(i\lambda + \frac{1}{2}, 1 + i(\lambda-\bar{\lambda}), -i\frac{\hbar\varrho\hat{k}^2}{2m\epsilon^2}\right)\right|^2, \tag{12}$$

with

$$p_i = \hbar q_i, \tag{13}$$

$$\hat{k} = \frac{\epsilon}{\varrho}k, \tag{14}$$

$$\lambda = \frac{\mathbf{q}_i^2 + m^2\epsilon^2/\hbar^2}{2m\varrho/\hbar}, \quad \bar{\lambda} = \frac{(\mathbf{q}_i - k)^2 + m^2\epsilon^2/\hbar^2}{2m\varrho/\hbar}. \tag{15}$$

Note that the function F describes the deviation from the WKB formula. Figure 2 plots F as a function of $p_i/m\epsilon$ with fixed as $\hbar\varrho/m\epsilon^2 = 1$, 0.1 and 0.01. Figure 3 plots F as a function of $\hbar\varrho/m\epsilon^2$ with fixed as $p_i/m\epsilon = 0.01$ and 1. These figures show $F = 1$ for $p_i/m\epsilon \lesssim 1$ and $\hbar\varrho/m\epsilon^2 \ll 1$, and the suppression $F < 1$ for the other region.

We consider the classical limit of the function F by taking the limit $\hbar \to 0$, or $\hbar\varrho/m\epsilon^2 \to 0$. Then, by numerical analysis of the function F, we find

$$\lim_{\hbar\to 0} F = 1. \tag{16}$$

This means that the exact formula in the limit of $\hbar \to 0$ agrees with the WKB approximate formula. Then, the decrease of F from 1 comes from the term in proportion to $\hbar$, hence the suppression is understood as the quantum effect.

Now let us consider the physical meaning of the condition $\varrho\hbar/m\epsilon^2 \ll 1$. Around the bounce regime $a \sim \epsilon \sim \varrho\eta$, where the classical radiation rate becomes maximum, we can write

$$\frac{\hbar\varrho}{m\epsilon^2} \simeq \lambda_C H\Big|_{\text{bounce}}, \tag{17}$$

where $\lambda_C = \hbar/m$ is the Compton wavelength, and $H|_{\text{bounce}} = \varrho/\epsilon^2$ is the Hubble expansion rate, respectively. Thus $\hbar\varrho/m\epsilon^2$ can be regarded as the the ratio of the Hubble horizon length to the Compton wavelength of the charged particle, around the bouncing regime.
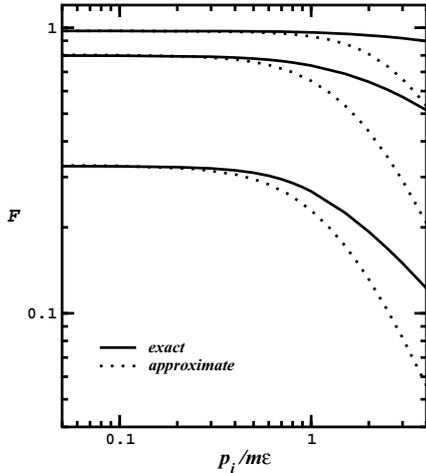
Figure 2: F as function of $p_i/m\epsilon$ with fixed as $\hbar\varrho/m\epsilon^2 = 0.01$, 0.1, 1, from top to bottom.
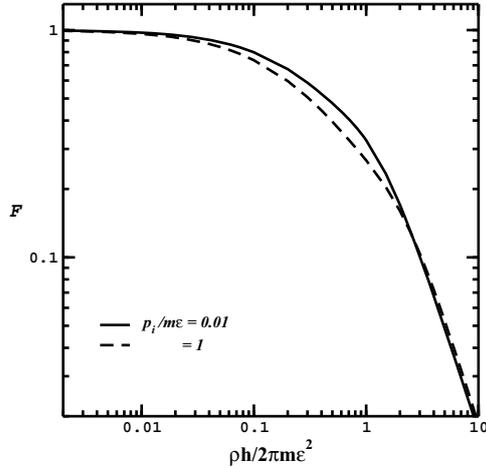
Figure 3: F as function of $\hbar\varrho/m\epsilon^2$ with fixed as $p_i/m\epsilon = 0.01$(dashed curve) and 1(solid curve).

4 Summary and Conclusions

In the present paper, we investigated photon emission from a moving massive charge in an expanding universe. We considered the scalar QED model for simplicity, and focused on the energy radiated by the process. First we showed how the Larmor formula for the radiation energy in the classical electromagnetic theory can be reproduced under the WKB approximation in the framework of the quantum field theory in curved spacetime.

We also investigated the limits of the validity of the WKB formula, by deriving the radiation formula in a bouncing universe in which the mode functions are exactly solvable. The result using the exact mode function shows the suppression of the radiation energy compared with the WKB formula. The suppression depends on the ratio of the Compton wavelength λ_C of the charged particle to Hubble length H^{-1}. Namely, the larger the ratio λ_C/H^{-1} is, the stronger the suppression becomes. In the limit the Compton wavelength is small compared with the Hubble length, the radiation formula is found to agree with the WKB formula. Since this limit is equivalent to the limit $\hbar \to 0$, the suppression we found is a genuine quantum effect in an expanding (or contracting) universe, which is due to the finiteness of the Hubble length. Whether the quantum effect on the radiation from a accelerated charge always leads suppression or not is an interesting question. This would be understood by analyzing higher order terms of the WKB approximation.

References

[1] I. L. Buchbinder and L. I. Tsaregorodtsev, Int. J. Mod. Phys. A **7**, 2055 (1992)

[2] K-H. Lotze, Class. Quantum Grav. **5**, 595 (1988)

[3] T. Futamase, M. Hotta, H. Inoue, and M. Yamaguchi, Prog. Theor. Phys. **96**, 113 (1996)

[4] M. Hotta, H. Inoue, I. Joichi, and M. Tanaka, Prog. Theor. Phys. **96**, 1103 (1996)

[5] J. D. Jacson, *Classical electrodynamics* (Wiley, New York, 1975)

[6] J. Audretsch and G. Schäfer, Phys. Lett. **66A**, 459 (1978)

[7] H. Nomura, M. Sasaki, K. Yamamoto, JCAP 0611, 013 (2006)

Matter without matter: pure gravitational creation

^{a,b,c}Hideki Maeda[1] and ^{d}Naresh Dadhich[2]

^{a}*Graduate School of Science and Engineering, Waseda University, Tokyo 169-8555, Japan*
^{b}*Department of Physics, Rikkyo University, Tokyo 171-8501, Japan*
^{c}*Department of Physics, International Christian University, 3-10-2 Osawa, Mitaka-shi, Tokyo 181-8585, Japan*
^{d}*Inter-University Centre for Astronomy & Astrophysics, Post Bag 4, Pune 411 007, India*

Abstract

We obtain a new exact black-hole solution in Einstein-Gauss-Bonnet gravity with a cosmological constant which bears a specific relation to the Gauss-Bonnet coupling constant. The spacetime is a product of the usual 4-dimensional manifold with a $(n-4)$-dimensional space of constant negative curvature, i.e., its topology is locally $\mathcal{M}^n \approx \mathcal{M}^4 \times \mathcal{H}^{n-4}$. The solution has two parameters and asymptotically approximates to the field of a charged black hole in anti-de Sitter spacetime. The most interesting and remarkable feature is that the Gauss-Bonnet term acts like a Maxwell source for large r while at the other end it regularizes the metric and weakens the central singularity. It is a pure gravitational creation including Maxwell field in four-dimensional vacuum spacetime. The solution has been generalized to make it radially radiate null radiation representing gravitational creation of charged null dust. This paper is based on the results in [1].

1 Model and basic equation

Throughout this paper we use units such that $c = 1$. The Greek indices run $\mu = 0, 1, \cdots, n-1$. We write action of Einstein-Gauss-Bonnet gravity with a cosmological constant for $n \geq 5$,

$$S = \int d^n x \sqrt{-g} \left[\frac{1}{2\kappa_n^2}(R - 2\Lambda + \alpha L_{GB}) \right] + S_{\text{matter}}, \tag{1}$$

where α is the Gauss-Bonnet (GB) coupling constant and all other symbols having their usual meaning. The GB Lagrangian is given by

$$L_{GB} = R^2 - 4R_{\mu\nu}R^{\mu\nu} + R_{\mu\nu\rho\sigma}R^{\mu\nu\rho\sigma}. \tag{2}$$

This form of action follows from low-energy limit of heterotic superstring theory [2]. In that case, α is identified with the inverse string tension and is positive definite, so we assume $\alpha \geq 0$ in this paper. It should be noted that L_{GB} makes no contribution in the field equations for $n \leq 4$.

The gravitational equation following from the action (1) is given by

$$\mathcal{G}^\mu{}_\nu \equiv G^\mu{}_\nu + \alpha H^\mu{}_\nu + \Lambda \delta^\mu{}_\nu = \kappa_n^2 T^\mu{}_\nu, \tag{3}$$

where

$$G_{\mu\nu} \equiv R_{\mu\nu} - \frac{1}{2}g_{\mu\nu}R, \tag{4}$$

$$H_{\mu\nu} \equiv 2\left[RR_{\mu\nu} - 2R_{\mu\alpha}R^\alpha{}_\nu - 2R^{\alpha\beta}R_{\mu\alpha\nu\beta} + R_\mu{}^{\alpha\beta\gamma}R_{\nu\alpha\beta\gamma} \right] - \frac{1}{2}g_{\mu\nu}L_{GB}. \tag{5}$$

We consider the n-dimensional spacetime locally homeomorphic to $\mathcal{M}^4 \times \mathcal{K}^{n-4}$ with the metric, $g_{\mu\nu} = \text{diag}(g_{AB}, r_0^2 \gamma_{ab})$, $A, B = 0, \cdots, 3$; $a, b = 4, \cdots, n-1$. Here g_{AB} is an arbitrary Lorentz metric on

---

^{1}E-mail:hideki@gravity.phys.waseda.ac.jp
^{2}E-mail:nkd@iucaa.ernet.in

$\mathcal{M}^4$, r_0 is a constant and γ_{ab} is the unit metric on the $(n-4)$-dimensional space of constant curvature $\mathcal{K}^{n-4}$ with its curvature $\bar{k} = \pm 1, 0$. Then $\mathcal{G}^\mu{}_\nu$ gets decomposed as follows:

$$
\begin{aligned}
\mathcal{G}^A{}_B &= \left[1 + \frac{2\bar{k}\alpha(n-4)(n-5)}{r_0^2} \right] {}^{(4)}G^A{}_B \\
&\quad + \left[\Lambda - \frac{\bar{k}(n-4)(n-5)}{2r_0^2} - \frac{\bar{k}^2\alpha(n-4)(n-5)(n-6)(n-7)}{2r_0^4} \right] \delta^A{}_B,
\end{aligned}
\tag{6}
$$

$$
\begin{aligned}
\mathcal{G}^a{}_b &= \delta^a{}_b \left[-\frac{1}{2}{}^{(4)}R + \Lambda - \frac{(n-5)(n-6)\bar{k}}{2r_0^2} \right. \\
&\quad \left. -\alpha \left\{ \frac{\bar{k}(n-5)(n-6)}{r_0^2}{}^{(4)}R + \frac{1}{2}{}^{(4)}L_{GB} + \frac{(n-5)(n-6)(n-7)(n-8)\bar{k}^2}{2r_0^4} \right\} \right],
\end{aligned}
\tag{7}
$$

where the superscript (4) means the geometrical quantity on $\mathcal{M}^4$.

The decomposition leads to a general result in terms of the following no-go theorem on $\mathcal{M}^4$:

Theorem 1 *If (i) $r_0^2 = -2\bar{k}\alpha(n-4)(n-5)$ and (ii) $\alpha\Lambda = -(n^2-5n-2)/[8(n-4)(n-5)]$, then $\mathcal{G}^A{}_B = 0$ for $n \geq 6$ and $\bar{k}$ and Λ being non-zero.*

The proof simply follows from substitution of the conditions (i) and (ii) in Eq. (6).

These conditions also imply for $\alpha > 0$, $\bar{k} = -1$ and $\Lambda < 0$. Hereafter we set $\bar{k} = -1$, i.e., the local topology of the extra dimensions is $\mathcal{H}^{n-4}$, and obtain the vacuum solution ($T^\mu{}_\nu \equiv 0$) satisfying the conditions (i) and (ii). The governing equation is then a single scalar equation on $\mathcal{M}^4$, $\mathcal{G}^a{}_b = 0$, which is given by

$$
\frac{1}{n-4}{}^{(4)}R + \frac{\alpha}{2}{}^{(4)}L_{GB} + \frac{2n-11}{\alpha(n-4)^2(n-5)} = 0.
\tag{8}
$$

2 Exact solutions

2.1 Schwarzschild-like solution

We seek a static solution with the metric on $\mathcal{M}^4$ reading as:

$$
g_{AB}dx^A dx^B = -f(r)dt^2 + \frac{1}{f(r)}dr^2 + r^2 d\Sigma_{2(k)}^2,
\tag{9}
$$

where $d\Sigma_{2(k)}^2$ is the unit metric on $\mathcal{K}^2$ and $k = \pm 1, 0$. Then, Eq. (8) yields the general solution for the function $f(r)$:

$$
f(r) = k + \frac{r^2}{2(n-4)\alpha} \left[1 \mp \sqrt{1 - \frac{2n-11}{3(n-5)} + \frac{4(n-4)^2\alpha^{3/2}\mu}{r^3} - \frac{4(n-4)^2\alpha^2 q}{r^4}} \right],
\tag{10}
$$

where μ and q are arbitrary dimensionless constants. The solution does not have the general relativistic limit $\alpha \to 0$. There are two branches of the solution indicated by sign in front of the square root in Eq. (10), which we call the minus- and plus-branches.

There exists a central curvature singularity at $r = 0$ as well as the branch singularity at $r = r_{\rm b} > 0$ where the term inside the square root in Eq. (10) is zero. This solution can represent a black hole depending on the parameters. The n-dimensional black hole with $(n-4)$-dimensional compact extra dimensions is called the Kaluza-Klein black hole. The warp-factor of the submanifold r_0^2 is proportional to GB parameter α which is supposed to be very small. Thus, compactifying $\mathcal{H}^{n-4}$ by appropriate identifications, we obtain the Kaluza-Klein black-hole spacetime with small and compact extra dimensions.

The function $f(r)$ is expanded for $r \to \infty$ as

$$
f(r) \approx k \mp \frac{\alpha^{1/2}\mu\sqrt{3(n-4)(n-5)}}{r} \pm \frac{\alpha q \sqrt{3(n-4)(n-5)}}{r^2} + \frac{r^2}{2(n-4)\alpha} \left(1 \mp \sqrt{\frac{n-4}{3(n-5)}} \right).
\tag{11}
$$

This is the same as the Reissner-Nordström-anti-de Sitter (AdS) spacetime for $k = 1$ in spite of the absence of the Maxwell field. This suggests that μ is the mass of the central object and q is the charge-like new parameter.

Further, the solution (10) agrees with the solution in the Einstein-GB-Maxwell-Λ system having the topology of $\mathcal{M}^n \approx \mathcal{M}^2 \times \mathcal{K}^{n-2}$ although it does not admit $n = 4$. The solution is given for $n \geq 5$ by

$$ds^2 = -g(r)dt^2 + \frac{1}{g(r)}dr^2 + r^2 d\Sigma_{n-2(k)}^2 \tag{12}$$

with

$$g(r) = k + \frac{r^2}{2(n-3)(n-4)\alpha}\left[1 \mp \sqrt{1 + \frac{8(n-3)(n-4)\alpha\Lambda}{(n-1)(n-2)} + \frac{8(n-3)(n-4)\kappa_n^2 \alpha M}{(n-2)V_{n-2}^{\bar{k}} r^{n-1}} - \frac{(n-4)\alpha\kappa_n^2 Q^2}{(n-2)\pi g_c^2 r^{2(n-2)}}}\right], \tag{13}$$

where g_c is the coupling constant of the Maxwell field, and M and Q are mass and charge respectively [3]. k is the curvature of $\mathcal{K}^{n-2}$ and a constant V_{n-2}^k is its surface area on compactifications. The non-zero component of the Maxwell field reads as

$$F_{rt} = \frac{Q}{r^{n-2}} \tag{14}$$

representing the coulomb force of a central charge in n-dimensional spacetime.

Thus the parameters μ and q act as mass and "charge" respectively in spite of the absence of the Maxwell field. The new "gravitational charge" q is generated by our choice of the topology of spacetime, splitting it into a product of the usual 4-spacetime and a space of constant curvature. Thus, the solution (10) manifests gravitational creation of the Maxwell field, i.e., "matter without matter".

Clearly the global structure of our solution (10) will be similar to that of the solution (13). Note that $f(0) = k \mp \sqrt{-q}$, which produces a solid angle deficit and it represents a spacetime of global monopole. This means that at $r = 0$ curvatures will diverge only as $1/r^2$ and so would be density which on integration over volume will go as r and would therefore vanish. This indicates that singularity is weak as curvatures do not diverge strongly enough.

2.2 Vaidya-like solution

It is well known that Schwarzschild spacetime could be made to radiate null (Vaidya) radiation by transforming the metric into retarded/advanced time coordinate and then making mass parameter function of the time coordinate. It is interesting to note that the same procedure also works here. This solution (10) can thus be generalized to include Vaidya radiation and it would be given by

$$\begin{aligned}
g_{AB}dx^A dx^B &= -\tilde{f}(v,r)dv^2 + 2dvdr + r^2 d\Sigma_{2(k)}^2, \tag{15} \\
\tilde{f}(v,r) &\equiv k + \frac{r^2}{2(n-4)\alpha}\left[1 \mp \left\{1 - \frac{2n-11}{3(n-5)}\right.\right. \\
&\left.\left. + \frac{4(n-4)^2 \alpha^{3/2}\tilde{M}(v)}{r^3} - \frac{4(n-4)^2 \alpha^2 \tilde{q}(v)}{r^4}\right\}^{1/2}\right], \tag{16}
\end{aligned}$$

where $\tilde{M}(v)$ and $\tilde{q}(v)$ are arbitrary functions. As expected, this solution is quite similar to the null dust solution with the topology of $\mathcal{M}^2 \times \mathcal{K}^{n-2}$ [4].

This solution manifests gravitational creation of an ingoing charged null dust as another complete example of "matter without matter". Using this solution and the solution (10), we can construct completely vacuum spacetime representing the formation of a black hole from an AdS spacetime by gravitational collapse of a gravitationally created charged null dust.

3 Discussions and conclusion

In this paper, we obtained new exact solutions in Einstein-Gauss-Bonnet gravity which offer direct and purely classical examples of curvature manifesting as matter, i.e., "matter without matter". The origins of the Maxwell field and a null dust fluid have been proposed.

We have found a new Kaluza-Klein vacuum black hole solution (10) of Einstein-Gauss-Bonnet gravity with topology of product of the usual 4-spacetime with a negative constant curvature space. In this solution we have brought the GB effects down on four dimensional black hole. This solution manifests gravitational creation of the Maxwell field and asymptotically resembles a charged black hole in AdS background. What really happens is that GB term regularizes the metric and weakens the singularity while the presence of extra dimensional hyperboloid space generates the Kaluza-Klein modes giving rise to the Weyl charge. This is indeed the most interesting and remarkable feature of the new solution which needs to be probed further for greater insight and application. The global structure of the solution (10) depending on the parameters will be shown in the forthcoming paper. Also, we have successfully generalized this solution into Vaidya-like metric on $\mathcal{M}^4$. That solution manifests gravitational creation of an ingoing charged null dust.

Now we explain the origin of "matter without matter". For the metric in the form of Eq. (9), one just requires one second-order differential equation (8) to determine the metric fully and it will in general have two constants of integration. On the other hand, the trace of the Einstein-Gauss-Bonnet equation (3) is given by

$$-\frac{n-2}{2}R - \frac{(n-4)\alpha}{2}L_{GB} + n\Lambda = \kappa_n^2 T. \tag{17}$$

The basic equation (8) for g_{AB} resembles this equation with $T = 0$ and $\Lambda = \Lambda_{\text{eff}}$ defined by

$$\Lambda_{\text{eff}} \equiv -\frac{C(2n-11)}{\alpha(n-4)^2(n-5)}, \tag{18}$$

where C is some positive constant. Thus, Eq. (8) will generate a Maxwell-like charge as well as a null dust because vanishing trace is characteristic of a null dust and the Maxwell field in four dimensions. That is why it is not surprising that there occur Maxwell-like additional gravitational charge or a gravitationally created null dust in our solution. It is noted that this happens only in four dimensions because electromagnetic stress tensor is not trace-free in other dimensions.

In the original Kaluza-Klein theory, the origin of the Maxwell field is the extra-dimensional component of the five-dimensional metric with which the five-dimensional vacuum Einstein equation is decomposed into the four-dimensional Einstein-Maxwell equation [5]. Here on the other hand, we have given completely different and novel generation of Maxwell field as well as of null dust fluid in the framework of Einstein-Gauss-Bonnet gravity. This is a partial success to explain origin of all matter in our four-dimensional universe. Since our mechanism works only for trace free matter fields, creation of other matter, especially with non-zero trace remains a very important open problem. Undoubtedly its solution will have a great bearing on our understanding of spacetime and matter.

References

[1] H. Maeda and N. Dadhich, Phys. Rev. D **74**, 021501(R) (2006); hep-th/0611188, accepted for publication in Physi. Rev. D.

[2] D.J. Gross and J.H. Sloan, Nucl. Phys. **B291**, 41 (1987);
    M.C. Bento and O. Bertolami, Phys. Lett. **B368**, 198 (1996).

[3] R. -G. Cai, Phys. Rev. D **65**, 084014 (2002); D. L. Wiltshire, Phys. Lett. **B169**, 36 (1986); D. G. Boulware and S. Deser, Phys. Rev. Lett. **55**, 2656 (1985); J. T. Wheeler, Nucl. Phys. **B268**, 737 (1986).

[4] T. Kobayashi, Gen. Rel. Grav. **37**, 1869 (2005); H. Maeda, Class. Quantum Grav. **23**, 2155 (2006); A.E. Dominguez and E. Gallo, Phys. Rev. D **73**, 064018 (2006).

[5] T. Kaluza, Sitzungsber. Preuss. Akad. Wiss. Berlin (Math. Phys.) **K1**, 966 (1921); O. Klein, Z. Phys. **37**, 895 (1926); J.M. Overduin and P.S. Wesson, Phys. Rep. **283**, 303 (1997).

Gravitational Wave Background from Population III Stars

Yudai Suwa[1*], Tomoya Takiwaki[1], Kei Kotake[2], and Katsuhiko Sato[1,3]

[1] *Department of Physics, School of Science, the University of Tokyo, 7-3-1 Hongo, Bunkyo-ku,Tokyo 113-0033, Japan*
[2] *National Astronomical Observatory of Japan, Mitaka, Tokyo 181-8588, Japan*
[3] *Research Center for the Early Universe, School of Science, the University of Tokyo,7-3-1 Hongo, Bunkyo-ku, Tokyo 113-0033, Japan*

Abstract

We have simulated the collapse of rotating Population III stars with numerical simulation and extracted the gravitational waves from the mass motions via the quadrupole formula. In addition, we estimate the gravitational wave emission by anisotropic neutrino radiation. With these wave forms, we calculate the gravitational wave background from Population III stars. As a result, we have found that the gravitational wave background from Population III stars is large enough to be detected by interferometers such as BBO and DECIGO without correlation.

1 Introduction

The observation of gravitational waves (GWs) is one of the most important tasks for exploring the trackless parts of the Universe. Already several ground-based laser interferometers (TAMA300, LIGO, and GEO600) are now operating and taking data. The Laser Interferometer Space Anntena (LISA) will be launched in the near future, and, moreover, future space missions such as DECIGO and BBO are in planning. These interferometers will open up a new era of exploring the Universe.

Recently, [2] pointed out that cosmological population of core-collapse supernovae could contribute to gravitational wave background (GWB) in low-frequency range as a result of the GWs associated with neutrino emissions. Moreover, [13] calculate the spectrum of GWB from Population III (Pop III) stars with the star formation rate (SFR) of the result of their computation and show that the GWB from Pop III stars could be observable by next generation interferometer LIGO III. However, these studies assumed that the wave spectrum of GW from a single Pop III star has the same shape of the result of the simulation of ordinary core-collapse supernovae [11] and amplified such wave form on the basis of several supposition. The validity of this assumption should be confirmed by the simulation of core-collapse Pop III stars.

The purpose of this paper is to give an estimate of the gravitational wave spectrum from the Pop III stars by a single Pop III star collapse simulation. In addition, we calculate the GWB spectrum with the result of single star simulation.

The paper is organized as follows: In the next section the numerical model is described. In §3, we calculate the gravitational wave signal and its spectrum of a single Pop III star collapse. In §4, we present the numerical result of the gravitational wave background from Pop III stars. Section 5 is devoted to the discussion.

2 Method

The numerical methods employed in this paper are essentially the same as those used in our previous paper [16]. We employed the ZEUS-2D code [15] as a base and added major changes to include the microphysics. First we added an equation for electron fraction to treat electron captures and neutrino transport by the so-called leakage scheme [7]. Furthermore, we extend the scheme to include all 6 species of neutrino ($\nu_e, \bar{\nu}_e, \nu_X$), which is indispensable for the computations of the Pop III stars. Here ν_X means $\nu_\mu, \bar{\nu}_\mu, \nu_\tau$ and $\bar{\nu}_\tau$. As for the reactions of neutrinos, pair, photo, and plasma processes are included using

---

the rates by [6]. We assume neutrino emission is radial. As for the equation of state, we have incorporated the tabulated one based on relativistic mean field theory instead of the ideal gas EOS assumed in the original code [14]. Spherical coordinates (r, θ) are employed with logarithmic zoning in the radial direction and regular zoning in θ. One quadrant of the meridian section is covered with 300 $(r) \times$ 30 (θ) mesh points. We also calculated some models with 60 angular mesh points, however, any significant difference was not obtained. Therefore, we will report in the following the results obtained from the models with 30 angular mesh points. In our 2D calculations, axial symmetry and reflection symmetry across the equatorial plane are assumed.

The initial condition are provided in the same manner of [16]. We produced hydrostatic core with the assumption of isentropic, which the values of entropy are taken from [1], and constant electron fraction of $Y_\mathrm{e} = 0.5$. The supposed rotation law is cylindrical rotation, which the strength of rotational energy is 0.5% of gravitational energy in all models. In this paper, we don't note the effect of magnetic fields, therefore, the injected magnetic fields are negligibly small. We calculate some mass range from $300 M_\odot$ to $1000 M_\odot$.

3   Gravitational Wave of a single Population III Star Collapse

In this section, we consider the gravitational wave emission of a single $300 M_\odot$ Population III star collapse. In this study, we estimate the gravitational wave from aspherical mass motions in our models via the Newtonian quadrupole formalism as described in [9]. In addition, we compute the gravitational wave strain from anisotropic neutrino emission employing the formalism introduced by [4] and developed by [10] and [8]. Using the standard quadrupole formula, we can estimate for the neutrinos the expression

$$Dh^{TT}(t) = \frac{2G}{c^4} \int_{-\infty}^{t} \alpha(t') L_\nu(t') dt', \tag{1}$$

where D is the distance to the source, h^{TT} is the transverse-traceless and dimensionless metric strain, G is the gravitational constant, c is the speed of light, $\alpha(t)$ is the time-dependent anisotropy parameter, and $L_\nu(t)$ is the total neutrino luminosity. To derive Equation (1), we assumed that the observer is positioned perpendicular to the source's rotational axis.

Figure 1 depicts the strain versus time after bounce of $300 M_\odot$ star. First, the matter contribution to changes in h^{TT} dominates during first 70 ms. Afterward, the anisotropic neutrino radiation begins to contribute because the thermal shock occurs and the neutrino luminosity increases in the hot region, backward of the shock surface. 120 msec after bounce, the neutrino contribution converges to a constant value and the matter contribution dumps to zero. This is due to the black hole formation. After the black hole formation, we don't calculate of the GW from matter but dump with the timescale of light crossing time $\sim O(R_\mathrm{BH}/c)$, where R_BH is the radius of black hole. This procedure does not affect the discussion of following section because the matter contribution of total GW is only in the high frequency region, which is not the main remarkable point of this letter. Population III stars have high temperature so that the dynamics of collapse is different from ordinary supernovae. The high temperature causes bounce by thermal pressure not by nuclear pressure as ordinary supernovae [5]. Such thermal bounce make the central density lower at the time of bounce $(O(10^{12})\mathrm{g\ cm}^{-3})$ so that the dynamical timescale $(\sim 1\ \mathrm{msec}(\rho/10^{14}\mathrm{g\ cm}^{-3})^{-1/2})$ becomes longer and the time evolution of gravitational waves are slower in Population III stars. The total energy emitted in gravitational waves is $\sim 4 \times 10^{50}$ erg, which is smaller than [5] because their peak amplitude is larger than our result by a factor of 100.

Figure 2 shows the Fourier transformation of the GW signal. The solid line, which means total spectrum of signal, is larger than the wave form assumed in the previous works in low frequency region. This is because [2] assumed that the wave spectrum of GW from a single Population III star has the same shape of the result of the simulation of ordinary core-collapse supernovae [11]. They amplified such wave form with the normalization of total energy emitted in GW as $10^{-3} M_\odot c^2$ as argued by [5]. However, the feature of gravitational collapse of Population III stars is different from ordinary supernovae ,as we already mentioned. Thus, the wave form is also different. The dotted line means the neutrino contribution, which is dominant in the low frequency region, meanwhile, the dashed line means the matter contribution, which dominates the high frequency region. In should be noted that the matter's spectrum overwhelms total

signal for the frequency above ~ 50Hz because the quadrupole moment of neutrinos have opposite sign to the quadrupole moment of matter [see 3]. Current numerical simulations are done for $O(1)$ sec and do not cover the strain spectrum below fractions of Hertz. However, for the low frequency region, we can deduce the GW signal by applying the zero-frequency limit [4]. In this calculation, we employed the same manner of [2].
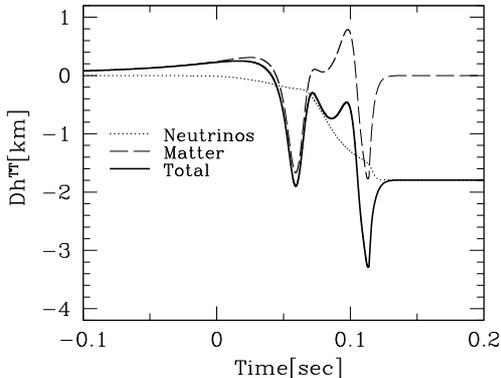
Figure 1: The gravitational wave strain,h^{TT}, times the distance to the Population III, D, versus time after bounce (in seconds). The neutrino, matter, and total wave forms are plotted with dotted, dashed, and solid lines, respectively.
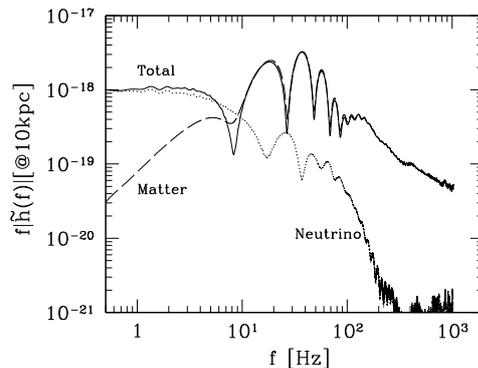
Figure 2: GW source spectra. The solid line is the total GW, the dtted line is the neutrino GW, and the dashed line is the matter GW for model $300M_\odot$ at D=10kpc.

4   Gravitational Wave Background from Population III Stars

We are now in a position to discuss the contribution of GWs from the Population III stars to the background radiation. According to [12], the sum of the energy densities radiated by a large number of independent Population III stars at each redshift is given by the density parameter $\Omega_{\mathrm{GW}}(f) \equiv \rho_c^{-1}(d\rho_{\mathrm{GW}}/d\log f)$ as

$$\Omega_{\mathrm{GW}}(f) = \frac{16\pi^2 cD^2}{15G_N\rho_c} \int \frac{dz}{1+z} \left|\frac{dt}{dz}\right| \int dm \ \phi(m)\psi(z)f'^3|\tilde{h}(f')|^2, \tag{2}$$

where ρ_c is the critical density $(3H_0^2/(8\pi G))$, $\phi(m)$ is the initial mass function (IMF) of Population III, $\psi(z)$ is the SFR, and f' is the red shifted frequency, $(1+z)f$. We employ the model 2b of [13] as the SFR, which is for the very massive stars, from $270M_\odot$ to $500M_\odot$. As for the IMF, we employ the same parameterization with [13] as follows,

$$\phi(m) \propto m^{-2.3}, \tag{3}$$

which is normalized by $\int dm\phi(m) = 1$. The cosmological model enters with $|dt/dz| = [(1+z)H(z)]^{-1}$ and, for a flat geometry,

$$H(z) = H_0[\Omega_\Lambda + \Omega_m(1+z)^3]^{1/2}. \tag{4}$$

We use the parameters $\Omega_\Lambda = 0.73, \Omega_m = 0.27$, and $H_0 = 100 \ h_0$km s^{-1} Mpc^{-1} with $h_0 = 0.71$.

In Figure 3, the calculated Ω_{GW} is plotted with the sensitivity curves of the future detectors. The GWB is broadly distributed with peak amplitude $h_0^2\Omega_{\mathrm{GW}} \sim 10^{-10}$ near 20 Hz. It can be seen that, in low frequency region, our result exceeds the foregoing research about GWB of Population III stars [2, 13], which assumed the wave form of gravitational collapse of Population III stars to be the similar shape of normal supernovae [11] and amplified by a factor ~ 1000 (see Eq. (8) in [2]). On the other hand, our result is much smaller than previous studies in high frequency region. The GWB of [2] is calculated with assumption that all Population III stars collapse at one time on $z = 15$. [13] took in the evolution of Population III stars formation. We employed the same SFR with [13], therefore, the differences of wave form of GWB are entirely owing to the single Population III star's wave form. The GWB from Population

III can give a particularly contribution, masking completely the GWB generated in the inflationary epoch constrained by *COBE* observations (the horizontal dashed line). It can be seen that the gravitational wave from the anisotropic radiation of neutrinos, which are dominated low frequency region, seem within the detection limit of the planning detectors BBO and DECIGO without correlation. In contrast, detection by LIGO III, which is the ground based detector, is difficult because the amplitude in high frequency region is smaller than the detection limit of LIGO III ($\sim 10^{-11}$ at $O(10)$ Hz).
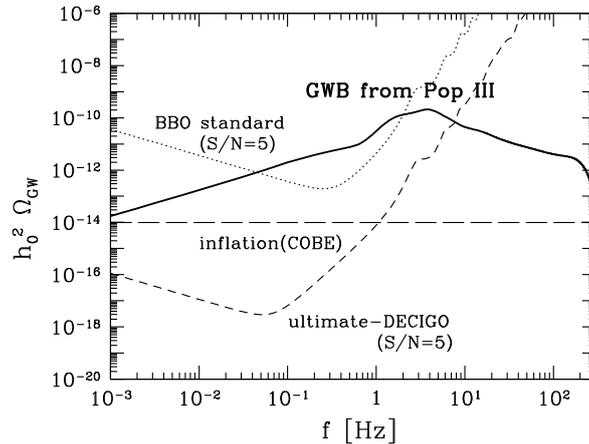
Figure 3: The energy density parameter of GWB. The horizontal dashed line shows the GWB from the inflationary epoch constrained by *COBE* observations.

References

[1] Bond, J. R., Arnett, W. D., & Carr, B. J. 1984, ApJ, 280, 825

[2] Buonanno, A., Sigl, G., Raffelt, G. G., Janka, H.-T., & Müller, E. 2005, Phys. Rev. D, 72, 084001

[3] Burrows, A. & Hayes, J. 1996, Phys. Rev. Lett., 76, 352

[4] Epstein, R. 1978, ApJ, 223, 1037

[5] Fryer, C. L., Woosley, S. E., & Heger, A. 2001, ApJ, 550, 372

[6] Itoh, N., Adachi, T., Nakagawa, M., Kohyama, Y., & Munakata, H. 1989, ApJ, 339, 354

[7] Kotake, K., Yamada, S., & Sato, K. 2003, Phys. Rev. D, 68, 044023

[8] —. 2006b, submitted to MNRAS

[9] Mönchmeyer, R., Schaefer, G., Müller, E., & Kates, R. E. 1991, A&A, 246, 417

[10] Müller, E. & Janka, H.-T. 1997, A&A, 317, 140

[11] Müller, E., Rampp, M., Buras, R., Janka, H.-T., & Shoemaker, D. H. 2004, ApJ, 603, 221

[12] Phinney, E. S. 2001, astro-ph/0108028

[13] Sandick, P., Olive, K. A., Daigne, F., & Vangioni, E. 2006, Phys. Rev., D73, 104024

[14] Shen, H., Toki, H., Oyamatsu, K., & Sumiyoshi, K. 1998, Nucl. Phys., A637, 435

[15] Stone, J. M. & Norman, M. L. 1992, ApJS, 80, 753

[16] Suwa, Y., Takiwaki, T., Kotake, K., & Sato, K. 2007, submitted to PASJ

Periodic gravitational waves from a 3-body system

Tatsunori Imai, Takamasa Chiba and Hideki Asada

Faculty of Science and Technology, Hirosaki University, Hirosaki 036-8561, Japan

Abstract

We make a proposal about a possible link between a 3-body system and periodic gravitational waves. None of N-body gravitating systems have been considered to emit periodic gravitational waves because of their chaotic orbits when N=3 (or more). However, by employing a figure-eight orbit as a toy model, we show that a 3-body system is capable of generating periodic waves, thereby suggesting that the true number of sources detectable by large-scale interferometers such as LIGO, VIRGO, GEO600 and TAMA300 may be larger than previously thought. A waveform generated by the special 3-body system is volcano-shaped and different from that of a binary system. Therefore, it will be possible to distinguish it in future observations.

1   Introduction

As you know very well, gravitational waves (GWs) are ripples in a curved spacetime generated by accelerated masses, predicted by General Relativity (GR). An evidence of GWs (though indirect) came in 1974 by discovery of binary pulser 'PSR1913+16' (J. Taylor, R. Hulse [Nobel Prize 1993]). The observed decrease in orbital period agrees with the theoretical value by GR. However, the amplitude is too small. No one has ever detected directly GWs.

The detection of GWs will open up new observation fields, especially concerning the physics of stellar central parts, black holes, the early universe, a test of GR and so on. The detection will lead to the Nobel Prize possibly in 20XX. There are several GWs detectors all over the world.

Most likely sources for the first detection are supposed to be (quasi-)periodic such as a single star in rotation and/or oscillation, and a binary star in inspiral and finally merging phases.

There are existing works on a binary plus the third body [1, 2, 3]. On the other hand, much less attention has been paid to N-body gravitating systems, because when $N = 3$(or more), orbits will be chaotic.

Our purpose is to show that a 3-body system can generate (quasi-)periodic GWs [4].

2   3-body Problem

3-body problem was investigated crucially by Jules-Henri Poincare (1854-1912): He gave a proof of being unintegralable. At present, there seems need of numerical computations. Furthermore, chaotic orbits seem to be unsuitable for periodic GWs. However, we know the existence of periodic orbits in 3-body system; Euler's a collinear solution (1765) and Lagrange's an equilateral triangle solution (1772).

We employ a figure-eight solution as a new model of a periodic orbit. It was found firstly by Cristopher Moore (1993) [5] via numerical computations, and secondly with a mathematical proof of existence by Alain Chenciner and Richard Montgomery (2000) [6].

One of its features are a stable orbit in the Newtonian gravity in spite of 3-body system [6, 7]. Each star chases each other on the same orbit with the total angular momentum = 0.

Our assumption:

- the orbital plane is taken as the x-y plane.

- 3-body system with three particles with equal mass.

- compact star like a neutron star or black hole.
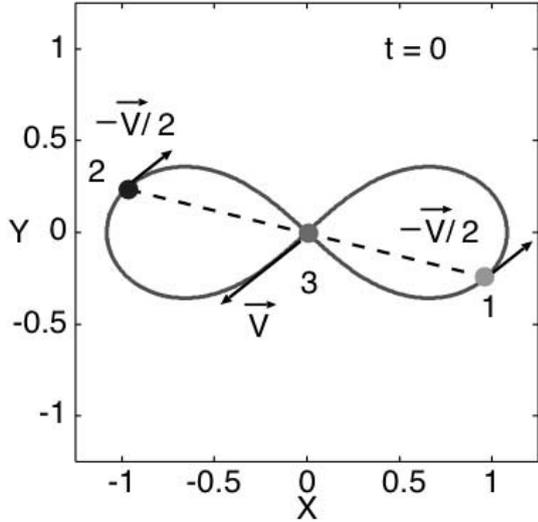
Figure 1: Three masses in a figure-eight at the initial time. Each mass is labeled by 1, 2 and 3. The initial velocity of each mass is denoted by an arrow. The distance between 1 and 3 is denoted by ℓ. In this plot, we take $\ell = 1$.

- when one mass arrives at the center of the 'figure-eight', ℓ (length parameter) is defined as a half of the separation between the remaining two masses.

The equation of motion of 3-body system is

$$m_i' \frac{d^2 \vec{r_i}'}{dt'^2} = -\frac{m_i' m_j'(\vec{r_i}' - \vec{r_j}')}{|\vec{r_i}' - \vec{r_j}'|^3} - \frac{m_i' m_k'(\vec{r_i}' - \vec{r_k}')}{|\vec{r_i}' - \vec{r_k}'|^3}, \tag{1}$$

where $i, j, k = 1 \sim 3$, $i \neq j \neq k$, and we define

$$m_i' \equiv \frac{m_i}{M_\odot}, \tag{2}$$

$$\vec{r_i}' \equiv \frac{\vec{r_i}}{\ell}, \tag{3}$$

$$t' \equiv \frac{t}{\sqrt{\ell^3/GM_\odot}}. \tag{4}$$

The orbital period becomes

$$T = 6.32591398\sqrt{\frac{\ell^3}{GM_\odot}}. \tag{5}$$

3 Gravitational Waves

The quadrupole formula in the wave zone is

$$h_{ij}^{TT} = \frac{2G \bar{I}_{ij}}{rc^4} + O(\frac{1}{r^2}), \tag{6}$$

where we define

$$\bar{I}_{ij} = I_{ij} - \delta_{ij}\frac{I_{kk}}{3}, \tag{7}$$

$$I_{ij} = \sum_{A=1}^{N} m_A x_A^i x_A^j. \tag{8}$$
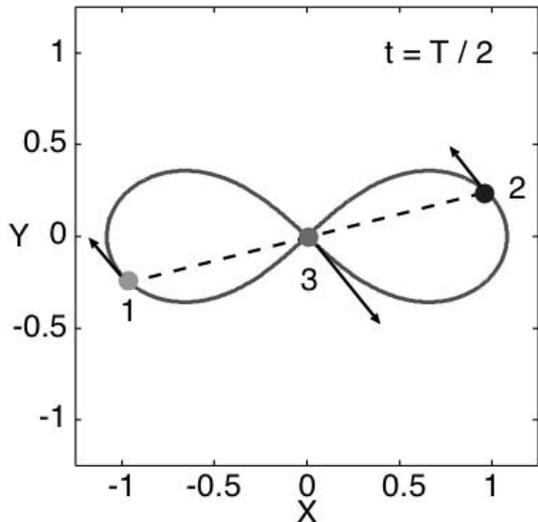
Figure 2: A figure-eight at $t = T/2$. The velocity of each mass is denoted by an arrow.

Here, we denote the Newtonian constant by G, the light speed by c, the space distance from an observer to a source by r, and Transverse and Traceless by TT.

The waveform is shown by Fig. 3. The amplitude of the GWs ($\ell = R_\odot$) is

$$h_{ij}^{TT} \sim 10^{-23} \left(\frac{m}{M_\odot} \right) \left(\frac{R_\odot}{\ell} \right) \left(\frac{10 kpc}{r} \right), \tag{9}$$

which is of the same order as that of a binary system.

Next, we consider the angular momentum loss. $L^x = L^y = 0$, because a figure-eight orbit is on the x-y plane. The angular momentum loss rate dL^z/dt vanishes. This is because the total orbital angular momentum $= 0$.

Let us compare a figure-eight with the head-on collision of two non-spinning black holes [8, 9]. For this case, the angular momentum is not carried away. A crucial difference is that for two black holes in head-on collision, each black hole moves without any orbital angular momentum with respect to the common center of mass. On the other hand, in a figure-eight, each star has the angular momentum.

The energy loss rate is expressed as

$$
\begin{aligned}
\frac{dE}{dt} &= \frac{G}{5c^5} < I_{ij}^{(3)} I_{ij}^{(3)} > \\
&= 1.2 \times 10^{19} \left(\frac{m}{M_\odot} \right)^5 \left(\frac{R_\odot}{\ell} \right)^5 \text{ erg/s} \quad \text{(figure-eight)} \\
&= 2.0 \times 10^{18} \left(\frac{m}{M_\odot} \right)^5 \left(\frac{R_\odot}{\ell} \right)^5 \text{ erg/s} \quad \text{(binary)}
\end{aligned}
\tag{10}
$$

where $\langle \cdots \rangle$ denotes the time average.

The radiation reaction time scale becomes

$$
\begin{aligned}
t_{GW} &\equiv \frac{E}{dE/dt} \\
&= 0.13 \left(\frac{M_\odot}{m} \right)^3 \left(\frac{\ell}{R_\odot} \right)^4 \text{ Gyr} \quad \text{(figure-eight)} \\
&= 0.15 \left(\frac{M_\odot}{m} \right)^3 \left(\frac{\ell}{R_\odot} \right)^4 \text{ Gyr} \quad \text{(binary)}
\end{aligned}
\tag{11}
$$

Finally, we make comments on "three black holes just before merging" as a speculation. We take each mass as $10 \times M_\odot$, and ℓ as $10 \times$ Schwarzschild radius denoted by $M_{sch} = 2GM_\odot/c^2$. The frequency of
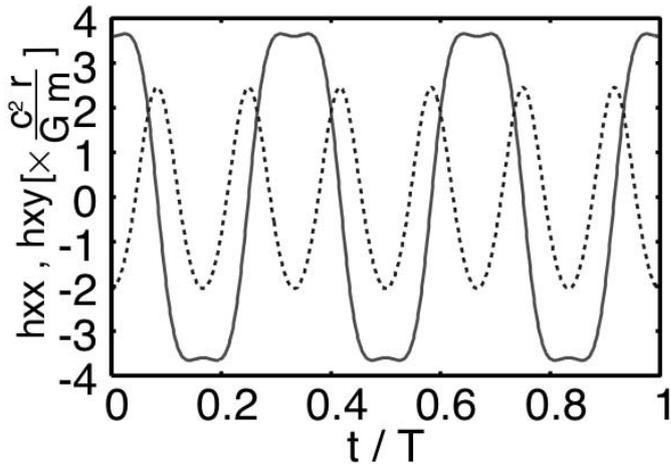
Figure 3: Gravitational waves from three masses in a figure-eight orbit. The dashed curve and the solid one denote h_{xx}^{TT} and h_{xy}^{TT}, respectively.

GWs is about a few kHz, around which the large-scale interferometric detectors are most sensitive. The amplitude of GWs becomes

$$h_{ij}^{TT} \sim 10^{-17} \left(\frac{m}{10 M_\odot} \right) \left(\frac{10 M_{sch}}{\ell} \right) \left(\frac{10 kpc}{r} \right).$$

(12)

4   Conclusion

It is possible for 3-body system to generate periodic GWs. One example is a figure-eight orbit. A difference from a binary system is a waveform which is volcano-shaped. The emitted GWs carry away no total angular momentum. Our result may be encouraging; the true number of sources may be larger than previously thought, though would be very few such systems in the universe.

References

[1] K. Ioka, T. Chiba, T. Tanaka, T. Nakamura, Phys. Rev. D **58**, 063003 (1998).

[2] Z. E. Wardell, Mon. Not. R. Astron. Soc. **334**, 149 (2002).

[3] M. Campanelli, M. Dettwyler, M. Hannam, C. O. Lousto, Phys. Rev. D **74**, 087503 (2006).

[4] T. Chiba, T. Imai, H. Asada, submitted to PRL, (astro-ph/06097773).

[5] C. Moore, Phys. Rev. Lett. **70**, 3675 (1993).

[6] A. Chenciner, R. Montgomery, Ann. Math. **152**, 881 (2000).

[7] J. Galan, F. J. Munoz-Almaraz, E. Freire, E. Doedel, A. Vanderbauwhede, Phys. Rev. Lett. **88**, 241101 (2002).

[8] L. L. Smarr, in *Sources of Gravitational Radiation*, (Cambridge University Press, Cambridge, 1979).

[9] R. H. Price, J. Pullin, Phys. Rev. Lett. **72**, 3297 (1994).

An efficient method for the computation of gravitational wave snapshots of generic extreme mass ratio inspirals

Wataru Hikida[1], Ryuichi Fujita[2], and Hideyuki Tagoshi[3]

[1,2,3] *Department of Earth and Space Science, Graduate School of Science,*
Osaka University, Toyonaka 560-0043, Japan

Abstract

Recently, we developed a numerical code to calculate the gravitational wave for generic extreme mass ratio inspirals. In this paper, for simplicity, we focus on the Schwarzschild case and calculate the energy fluxes explicitly. We also demonstrate the computational costs and accuracy.

1 Introduction

Gravitational radiation is one of the most important predictions of general relativity. It has been detected indirectly through its effect on the orbital period of the Hulse-Taylor binary pulsar but it has not yet been directly detected. Thanks to recent advances in technology, an era of gravitational wave astronomy has almost arrived. Several ground-based interferometric gravitational wave detectors are in various stages of development. R&D studies of a space-based gravitational wave observatory project, the Laser Interferometer Space Antenna (LISA) [1] have also been done.

One of the most promising sources of gravitational waves that can be detected by future space-based interferometric detectors such as LISA is a compact star orbiting a super-massive black hole. In order to do astronomy of such systems by gravitational waves, we have to know the precise waveforms. For this type of binary, i.e., an extreme mass ratio inspiral (EMRI), the standard post-Newtonian approximation [2] seems inappropriate, because the extension of the post-Newtonian approximation to higher Post-Newtonian(PN) orders is not straightforward. However, in such a system, there is another natural perturbation parameter, that is, mass ratio. As a result, the black hole perturbation approach is suited for EMRI.

The black hole perturbation theory was originally developed as a metric perturbation theory on a black hole spacetime. For non-spherically symmetric black holes, there are presently no simple, coupled equations for metric coefficients. Instead the perturbed geometry must be analyzed by means of the equations that Teukolsky derived, using gauge-invariant variables corresponding to some tetrad components of the perturbed Weyl curvature [3].

By using this Teukolsky formalism, there are many numerical calculations of gravitational waves induced by a particle. See Chandrasekhar [4], and Nakamura, Oohara and Kojima [5], for reviews and for references on earlier papers. Now the computations of gravitational waves induced by a particle moving on eccentric non-equatorial orbits are available [6]. However a lot of time are needed for computation and their results have a few order of accuracy. We, therefore, have to develop a numerical code which works more efficiently and accurately.

In this paper, we use the method based on Fujita and Tagoshi [8] for numerical computation of the homogeneous Teukolsky equations and compute the gravitational flux induced by a particle moving on eccentric equatorial orbits around Schwarzschild black hole. We also demonstrate that our method is very efficient and can be evaluated very accurately.

This paper is organized as follows. In Sec. 2, we describe how to compute gravitational wave emitted by a point particle orbiting Schwarzschild black hole. In Sec. 3, we explain briefly our method and compute the gravitational wave energy. In Sec.4, we summarize this paper.

---

[1]E-mail:hikida@vega.ess.sci.osaka-u.ac.jp
[2]E-mail:draone@vega.ess.sci.osaka-u.ac.jp
[3]E-mail:tagoshi@vega.ess.sci.osaka-u.ac.jp

2 Formulae to evaluate gravitational waves

We consider a point particle mass μ moving in the Schwarzschild background

$$ds^2 = -\left(1 - \frac{2Mr}{\Sigma}\right)dt^2 + \frac{\Sigma}{\Delta}dr^2 + \Sigma d\theta^2 + r^2\sin^2\theta d\varphi^2, \tag{1}$$

where $\Sigma = r^2$ and $\Delta = r^2 - 2Mr$. Here M is the mass of the black hole. In the Teukolsky formalism, gravitational perturbation is described by a master variable ψ, which is decomposed into Fourier-harmonic components according to

$$r^4\psi_4 = \sum_{\ell m}\int d\omega\, e^{-i\omega t + im\varphi}\,_{-2}Y_{\ell m}(\theta)R_{\ell m\omega}(r) \tag{2}$$

The radial function $R_{\ell m\omega}$ and the angular function $_sY_{\ell m}(\theta)$ satisfy the Teukolsky equations with $s = -2$ as

$$\Delta^2\frac{d}{dr}\left(\frac{1}{\Delta}\frac{dR_{\ell m\omega}}{dr}\right) - V(r)R_{\ell m\omega} = T_{\ell m\omega},$$

$$\left[\frac{1}{\sin\theta}\frac{d}{d\theta}\left\{\sin\theta\frac{d}{\theta}\right\} - \frac{(m - 2\cos\theta)^2}{\sin^2\theta} - 2 + \ell(\ell+1) - 2\right]_{-2}Y_{\ell m} = 0 \tag{3}$$

The potential $V(r)$ is given by

$$V(r) = -\frac{K^2 + 4i(r - M)K}{\Delta} + 8i\omega r + \ell(\ell+1) - 2, \tag{4}$$

where $K = r^2\omega$ and λ is the eigenvalue of $_{-2}Y_{\ell m}$. We define a homogeneous solution of the radial Teukolsky equation:

$$_sR_{\ell m\omega}^{in} \rightarrow \begin{cases} B_{\ell m\omega}^{\mathrm{trans}}\Delta^{-s}e^{-i\omega r^*} & \text{for } r \rightarrow 2M \\ r^{-2s-1}B_{\ell m\omega}^{\mathrm{ref}}e^{i\omega r^*} + r^{-1}B_{\ell m\omega}^{\mathrm{inc}}e^{-i\omega r^*} & \text{for } r \rightarrow \infty \end{cases} \tag{5}$$

where $r^* = r + 2M\ln(r - 2M)/2M$. Then a solution which has purely out-going property at infinity and has purely in-going property at the horizon is expressed at infinity as

$$R_{\ell m\omega}(r \rightarrow \infty) \rightarrow \frac{r^3 e^{i\omega r^*}}{2i\omega B_{\ell m\omega}^{\mathrm{inc}}}\int_{2M}^{\infty}dr'\frac{T_{\ell m\omega}R_{\ell m\omega}^{in}}{\Delta^2} \equiv Z_{\ell m\omega}r^3 e^{i\omega r^*}. \tag{6}$$

Now let us discuss the form of the source term $T_{\ell m\omega}$. It is given by

$$T_{\ell m\omega} = 4\int d\Omega dt\, r^6(B_2' + B_2'^*)e^{-im\varphi + i\omega t}\frac{_{-2}Y_{\ell m}}{\sqrt{2\pi}}, \tag{7}$$

where

$$B_2' = -\frac{1}{2}r^{-9}\mathcal{L}_{-1}[r^4\mathcal{L}_0(r^3 T_{nn})] - \frac{1}{2\sqrt{2}}r^{-9}\Delta^2\mathcal{L}_{-1}[r^6\mathcal{J}_+(r^4\Delta^{-1}T_{\bar{m}n})],$$

$$B_2'^* = -\frac{1}{4}r^{-9}\Delta^2\mathcal{J}_+[r^4\mathcal{J}_+(rT_{\bar{m}\bar{m}})] - \frac{1}{2\sqrt{2}}r^{-9}\Delta^2\mathcal{J}_+[r^2\Delta^{-1}\mathcal{L}_{-1}(r^4 T_{\bar{m}n})], \tag{8}$$

with

$$\mathcal{L}_s = \partial_\theta + \frac{m}{\sin\theta} + s\cot\theta, \quad \mathcal{J}_\pm = \partial_r \pm iK/\Delta. \tag{9}$$

In the above, T_{nn}, $T_{\bar{m}n}$ and $T_{\bar{m}\bar{m}}$ are the tetrad components of the energy momentum tensor. Since we consider a point particle limit, the energy momentum tensor takes the form

$$T^{\mu\nu} = \frac{\mu}{\Sigma\sin\theta dt/d\tau}\frac{dz^\mu}{d\tau}\frac{dz^\nu}{d\tau}\delta(r - r_z(t))\delta(\theta - \pi/2)\delta(\varphi - \varphi_z(t)), \tag{10}$$
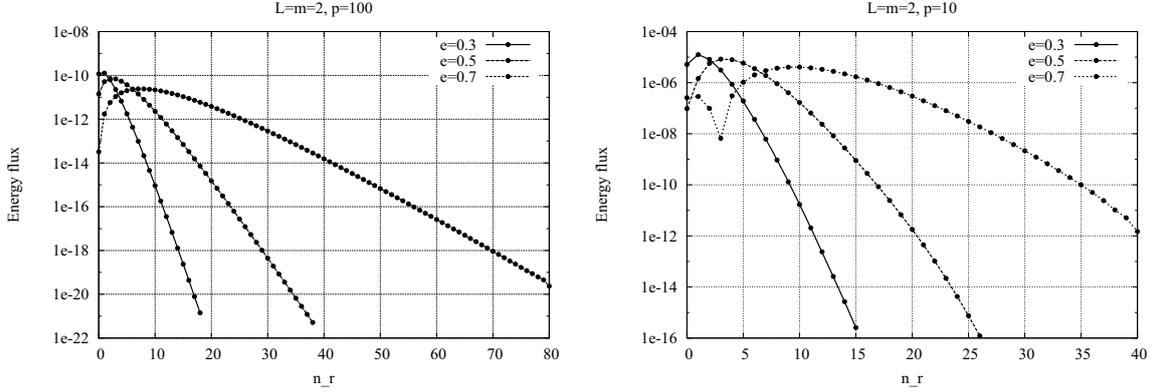
Figure 1: Energy flux at infinity. Results are $\ell = m = 2$. The orbit has eccentricity $e = 0.3$, 0.5, 0.7, and semi-latus rectum $p = 10$ and 100, respectively.

where $z^\mu = (t_z(\tau), r_z(\tau), \pi/2, \varphi_z(\tau))$. Here τ is the proper time along the orbit. Using a new parameter along the trajectory λ defined by $d\lambda = d\tau/\Sigma$, the geodesic equation become

$$\left(\frac{dr_z}{d\lambda}\right)^2 = R(r_z), \quad \frac{dt_z}{d\lambda} = \frac{r_z^2}{\Delta}P(r_z), \quad \frac{d\varphi_z}{d\lambda} = \mathcal{L}, \tag{11}$$

where $\mathcal{E}$ and $\mathcal{L}$ are the energy and angular momentum of a test particle, respectively, and

$$P(r) = \mathcal{E}r^2, \quad R(r) = [P(r)]^2 - \Delta[r^2 + \mathcal{L}^2]. \tag{12}$$

Using these notations, the amplitude of partial wave is rewritten as

$$Z_{\ell m\omega} = \frac{\mu}{2i\omega B^{\mathrm{inc}}} \int_{-\infty}^{\infty} d\lambda e^{i\omega t - im\langle d\varphi/d\lambda\rangle} \left(\frac{-1}{2\sqrt{2\pi}}\right) \left[\frac{D_r^2}{\Delta^2}{}_0\Xi R_{\ell m\omega}\right.$$
$$\left. -\frac{2D_rD_\theta}{\Delta}({}_1\Xi(\mathcal{J}_- - 2r^{-1})R_{\ell m\omega} + D_\theta^2{}_2\Xi(\mathcal{J}_-^2 - 2r^{-1}\mathcal{J}_-)R_{\ell m\omega}\right]_{r=z_r(\lambda)} \tag{13}$$

where

$${}_2\Xi := {}_{-2}Y_{\ell m}(\theta = \pi/2), \quad {}_1\Xi := \mathcal{L}_2^\dagger{}_{-2}Y_{\ell m}(\theta = \pi/2), \quad {}_0\Xi := \mathcal{L}_1^\dagger\mathcal{L}_2^\dagger{}_{-2}Y_{\ell m}(\theta = \pi/2),$$
$$D_r := \mathcal{E}r^2 + dr/d\lambda, \quad D_\theta := -i\mathcal{L}. \tag{14}$$

Furthermore, since the orbits have the periodic properties, $Z_{\ell m\omega}$ is just a sum of delta functions as

$$Z_{\ell m\omega} = \sum_{n_r} Z^{\ell m n_r}\delta(\omega - \omega_{mn_r}), \quad \text{with } \omega_{mn_r} := \left\langle\frac{dt_z}{d\lambda}\right\rangle^{-1}\left(m\left\langle\frac{d\varphi_z}{d\lambda}\right\rangle + n_r\Omega_r\right). \tag{15}$$

And the gravitational wave and energy flux can be obtained as

$$h_+ - ih_\times = -\frac{2}{r}\sum_{\ell m n_r}\frac{Z_{\ell m n_r}}{\omega_{mn_r}}\frac{{}_{-2}Y_{\ell m}(\theta)}{\sqrt{2\pi}}e^{i\omega_{mn_r}(r^*-t)+im\varphi}, \quad \frac{d\mathcal{E}}{dt} = \sum_{\ell m n_r}\frac{|Z_{\ell m n_r}|^2}{4\pi\omega_{mn_r}^2}. \tag{16}$$

3 Our method and results

Let us summarize our method briefly. The numerical method to evaluate the homogeneous Teukolsky equation is based on Mano, Suzuki and Takasugi [7]. They formulated a method to express a homogeneous solution in a series of hypergeometric functions or Coulomb wave functions. Later, Fujita and Tagoshi [8]

Table 1: Energy flux at infinity for dominant mode $(\ell, m) = (2, 2)$. p and e represent semi-latus rectum and eccentricity, respectively. We also show total computation time to obtain the energy flux.

p	e	number	time[s]	p	e	number	time[s]
100	0.1	3.116891971556e-10	1.84	10	0.1	2.710478149233e-05	2.73
100	0.5	3.533573687511e-10	9.55	10	0.5	3.642014430939e-05	13.75
100	0.7	2.891426491398e-10	53.10	10	0.7	3.665044597464e-05	124.59

applied their method to numerical calculations. They found that the convergence of hypergeometric functions was very fast and the accuracy of their code was very high. Therefore, we use the numerical method based on their formalism. In the evaluation of the orbit of a particle, the conventional method is to solve the ordinary differential equations numerically. We find that for the r- and θ-component, the solutions of the orbital motion are expressed in terms of the elliptic integral of the first kind, which can be easily computed numerically. The numerical integration to evaluate Eq. (13) is done by using the trapezium rule in evaluating each modes of the amplitude of partial wave. This is because the trapezium rule tends to become extremely accurate when periodic functions are integrated over their periods.

Based on these techniques, we develop a numerical code which works very efficiently. To demonstrate the efficiency of our code, we evaluate the gravitational wave energy flux explicitly.

In Fig. 1, we plot the energy flux for $\ell = m = 2$. Beyond the dominant modes, the mode magnitudes fall exponentially. The value of the energy flux bottom out at about $n \simeq 80$ and $n \simeq 40$ for $(p, e) = (100, 0.7)$ and $(p, e) = (10, 0.7)$, respectively. The exponential decay stops at these mode. The energy flux for modes larger than these mode seem to be dominated by numerical error. As a result, we can estimate the accuracy of our code to be 7 significant figures for $(p, e) = (10, 0.7)$ and 11-12 significant figures for the other cases. In Table 1, we show the computational costs for $\ell = m = 2$ mode. We present energy flux and the total computation time. The accuracy is better than the previous results, and the computation time is faster than the previous works.

4 Summary

So far a large number of studies have been made on numerical calculations of gravitational waves induced by a particle. However a lot of computation time are needed and their results have only a few order of accuracy for general orbits.

In this paper, we have developed an efficient method for the computation of gravitational waves from generic EMRI. By using our method, we found we could compute faster and more accurately than before, though we have focused on the Schwarzschild case. We emphasize that our method is applicable to the Kerr case as well. An extension of our method to the Kerr case is now in progress.

References

[1] LISA web page: http://lisa.jpl.nasa.gov/

[2] L. Blanchet, Living Rev. Rel. **5** (2002) 3.

[3] S. A. Teukolsky, Astrophys. J. **185** (1973) 635.

[4] S. Chandrasekhar, *Mathematical Theory of Black Holes*, Oxford University Press, 1983.

[5] T. Nakamura, K. Oohara, and Y. Kojima, Prog. Theor. Phys. Suppl. (1987) no. 90.

[6] S. A. Hughes, S. Drasco, E. E. Flanagan, and J. Franklin, Phys. Rev. Lett. **94** (2005) 221101.
    S. Drasco and S. A. Hughes, arXiv:gr-qc/0509101.

[7] S. Mano, H. Suzuki, and E. Takasugi, Prog. Theor. Phys. **95** (1996) 1079.

[8] R. Fujita and H. Tagoshi, Prog. Theor. Phys. **112** (2004) 415. ibid., **113** (2005) 1165.

Displacement noise-free gravitational-wave detection

Atsushi Nishizawa[1], Shuichi Sato[2], Seiji Kawamura[2], Keiko Kokeyama[3],
Kentaro Somiya[4], Yanbei Chen[4], Masa-aki Sakagami[1]

[1] *Graduate School of Human and Environmental Studies, Kyoto University, Kyoto 606-8501, Japan*
[2] *TAMA Project, National Astronomical Observatory of Japan, 2-21-1 Osawa, Mitaka, Tokyo 181-8588, Japan*
[3] *The Graduate School of Humanities and Sciences, Ochanomizu University, 2-1-1 Otsuka, Bunkyo-ku, Tokyo 112-8610, Japan*
[4] *Max-Planck Institut für Gravitationsphysik, Am Mühlenberg 1, 14476 Potsdam, Germany*

Abstract

The major design of current GW detector is Fabry-Perot Michelson interferometer, which uses laser interferometry. In order to reach high sensitivity, it needs to decrease all displacement noises of mirrors. Recently, new idea that combines many signals and cancels all displacement noises, was suggested. However, this has serious problems: (i) sensitive frequency-band is too high to apply to a ground-based GW interferometer. (ii) GW response function becomes f^2 in low frequency. We naively extended the design with Fabry-Perot cavity and tried resolving these problems. We found that, unfortunately, the results were negative and no improvement in the sensitivity compared with the design without FP cavity, obtained.

1 Introduction

The first generation of kilometer-scale, ground-based laser interferometer gravitational-wave (GW) detectors, located in the United States (LIGO), Europe (VIRGO and GEO 600), and Japan (TAMA 300), has begun its search for gravitational wave radiation and has yielded scientific results. The development of interferometers of the next-generation, such as Advanced-LIGO (in U.S.) and LCGT (in Japan), is underway. These current major design of GW detectors is called Fabry-Perot (FP) Michelson interferometer, in which laser is split into two directions at the beam splitter, is reflected by FP cavities, and then, is combined again at the beam splitter[1]. The output light from the photodetector contains the phase shift due to the change of an arm length in each direction, including GW signals, the displacement noise of mirrors and other noise. So far, much effort to improve sensitivity has been devoted to reducing the displacement noise, caused by seismic oscillation, thermal Brownian motion, radiation pressure of light, and etc.

Recently, the new idea, that cancels the displacement noise by combining the signals, is suggested[2]. This design of an interferometer is called displacement noise-free interferometer (DFI). DFI is similar to time-delay interferometry (TDI), which cancels all laser noise by combining the signals and will be used in Laser Interferometer Space Antenna (LISA), but there is a difference in the way of combining the signals. Extending the previous idea, it was showed that not only displacement noise but also laser noise could be canceled at the same time[3].

DFI is possible because the responses of the GW and the displacement noise is different on the frequency band higher than the frequency corresponding to the size of a detector. The displacement of a mirror acts at the time of the emission and reflection of light. On the other hand, the GW acts during the light trip between the mirrors. It should be noted that, of course, we cannot distinguish them in lower frequency than the size of a detector because GW can be regarded as the tidal force to act on the mirrors.

There is serious problems to apply DFI to a ground-based interferometer. As mentioned above, GWs

---

[1] E-mail:atsushi.nishizawa@nao.ac.jp
[2]
[3]
[4]
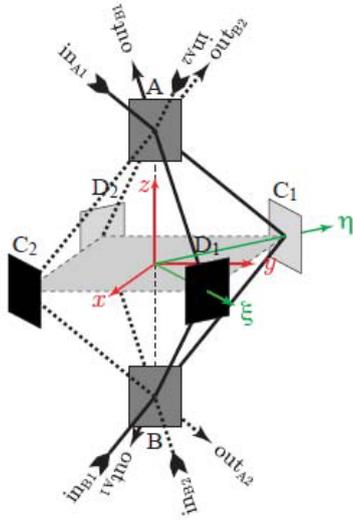
Figure 1: Design of DFI without FP cavity[4].
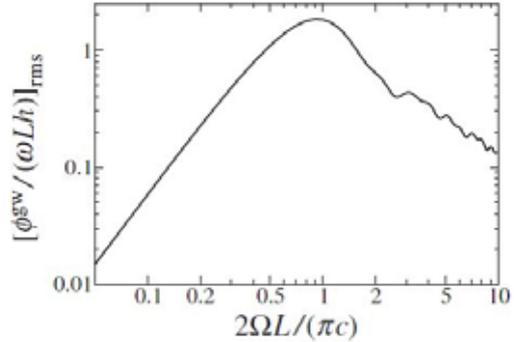
Figure 2: rms response function of DFI without FP cavity[4].

and the displacement of mirrors cannot be distinguished in low frequency. This worsens the response function for GWs in low frequency, which has the frequency dependence f^2. In addition, the peak of response function located around $100kHz$, corresponding to the arm length of the detector, for example, $3km$. Thus, the sensitivity worsens in our interested observational frequency, in which GWs from astrophysical objects can exist. To resolve this problem, we tried constructing DFI design with FP cavity. First, we will review the previous design of DFI without FP cavity briefly. Next, we will describe the design with FP cavity.

2 DFI without FP cavity

First, in order to take a brief look at the principle of DFI, let us consider N-detector system. Suppose that there are N test masses, located in D-dimensions and lights are emitted and receipted between each test mass. In this case, $N(N-1)$ signals can be acquired. On the other hand, the number of displacement noise is $N \times D$ and the number of laser noise is N. Thus, all noise can be canceled if the number of the signal is larger than that of the noise. In other words, this is expressed as the condition, $N \geq D + 2$.

In practice, however, it is difficult to realize a composite mirror, which emits or reflects light in more than two directions. So, more practical design without composite mirrors, are proposed[4]. This consists of two Machzender interferometers, in which lasers are injected from the top and bottom, as showed in Fig2. In the figure, beam splitters are located at the top and bottom, and the mirrors are at four vertices in the middle. The phase shift of light from the start $(ct_0, \mathbf{x}_0)$ to the end $(ct, \mathbf{x})$ is expressed to the linear order of h as,

$$\phi^{gw} = \frac{\omega L}{2c} \int_0^1 d\zeta h_{ij}^{TT}(t_0 + L\zeta, \mathbf{x}_0 + \mathbf{N}\ell\zeta)N_i N_j \tag{1}$$

where c is the speed of light, ω is the angular frequency of light, $|\mathbf{x} - \mathbf{x}_0| = c|t - t_0| = L$ is a nonperturbed distance between two test masses and $\mathbf{N}$ is defined as $\mathbf{N} \equiv (\mathbf{x} - \mathbf{x}_0)/L$. GW is written as h_{ij}^{TT} in Transvers-Traceless gauge.

Let us define the phase shift of signal for a Machzender interferometer,

$$\delta\phi_{A1} \equiv \phi_{(A \to C1 \to B)} - \phi_{(A \to D1 \to B)}, \qquad \delta\phi_{A2} \equiv \phi_{(A \to D2 \to B)} - \phi_{(A \to C2 \to B)}, \tag{2}$$

$$\delta\phi_{B1} \equiv \phi_{(B \to C1 \to A)} - \phi_{(B \to D1 \to A)}, \qquad \delta\phi_{B2} \equiv \phi_{(B \to D2 \to A)} - \phi_{(B \to C2 \to A)}. \tag{3}$$

Combining these signals to cancel the all displacements of mirrors and beam splitters, gives following the signal,

$$\phi_{DFI} \equiv [\delta\phi_{A1} - \delta\phi_{B1}] - [\delta\phi_{A2} - \delta\phi_{B2}]. \tag{4}$$

Fourier-transforming ϕ_{DFI} and taking average for GWs from all directions on the celestial sphere, we can obtain the root-mean-squared GW response function of DFI, as showed Fig2. The behavior of the response function is different in above and below the frequency corresponding to the size of the detector, L. Above the characteristic frequency, the response becomes f^{-1} because the contribution of GW in a phase shift during the light trip, is integrated and canceled partially. Below the frequency, the response becomes f^2 because we cannot distinguish the effects of GW and the displacement of a mirror, and DFI combination also cancels GW signals. Due to this fact, the sensitivity worsens in our interested observational frequency even though the only noise is white shot noise.

3 DFI with FP cavity
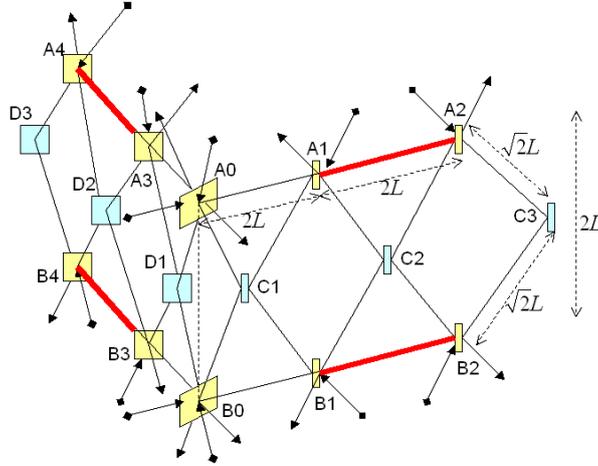
Figure 3: Design of DFI with FP cavity.

In order to figure out the problem of DFI in the previous section, we introduced the FP cavity into DFI and thought out the design like Fig3. The yellow objects are mirrors and beam splitters and the light blue are completely reflecting mirrors. The parts $A1 - A2$, $B1 - B2$, $A3 - A4$, $B3 - B4$ are FP cavities.

In Fourier domain, the phase shift due to GW and the displacement of mirrors from $(t - L_{12}, \mathbf{X}_1 + \mathbf{x}_1)$ to $(t, \mathbf{X}_2 + \mathbf{x}_2)$, is given as[3],

$$
\begin{aligned}
\tilde{\delta\phi}_{12}(\Omega) &= \omega/c \times [\, \mathbf{n}_{12} \cdot \{\tilde{\mathbf{x}}_2 - e^{-i\Omega L_{12}}\tilde{\mathbf{x}}_1\} \\
&+ \mathbf{n}_{12} \otimes \mathbf{n}_{12} \,:\, \frac{1}{2}\{\sum_p \mathbf{e}^p \tilde{h}_p \frac{e^{i\Omega(-\mathbf{e}_z \cdot \mathbf{X}_2)} - e^{-i\Omega(L_{12} + \mathbf{e}_z \cdot \mathbf{X}_1)}}{i\Omega(1 - \mathbf{e}_z \cdot \mathbf{n}_{12})}\}\,]
\end{aligned}
\tag{5}
$$

where L_{12} is the arm length between test mass 1 and 2, $\mathbf{X}_i$ and $\mathbf{x}_i$, $i = 1, 2$ are the nonperturbed and perturbed positions of test masses respectively. $\mathbf{n}_{12}$ is defined as $\mathbf{n}_{12} \equiv (\mathbf{X}_2 - \mathbf{X}_1)/L_{12}$. Noted that $\mathbf{x}_i$ depends on the time of light emission and reception. GW is propagating in the direction of $\mathbf{e}_z$. The polarization tensors of GW are difined as

$$
\mathbf{e}_+ \equiv \mathbf{e}_x \otimes \mathbf{e}_x - \mathbf{e}_y \otimes \mathbf{e}_y, \qquad \mathbf{e}_\times \equiv \mathbf{e}_x \otimes \mathbf{e}_y + \mathbf{e}_y \otimes \mathbf{e}_x.
\tag{6}
$$

The response of the FP cavity is well known. Using the above expression and taking the sum of the signals for each travels in FP cavity, we can derive the phase shift due to GW and the displacements of mirrors and obtain the simple form,

$$
\tilde{\Phi}_{12} = \alpha \tilde{\delta\phi}_{12}
\tag{7}
$$

where

$$
\alpha \equiv \frac{e^{-i\Omega L_{12}}}{1 - R^2 e^{-2i\Omega L_{12}}}
\tag{8}
$$
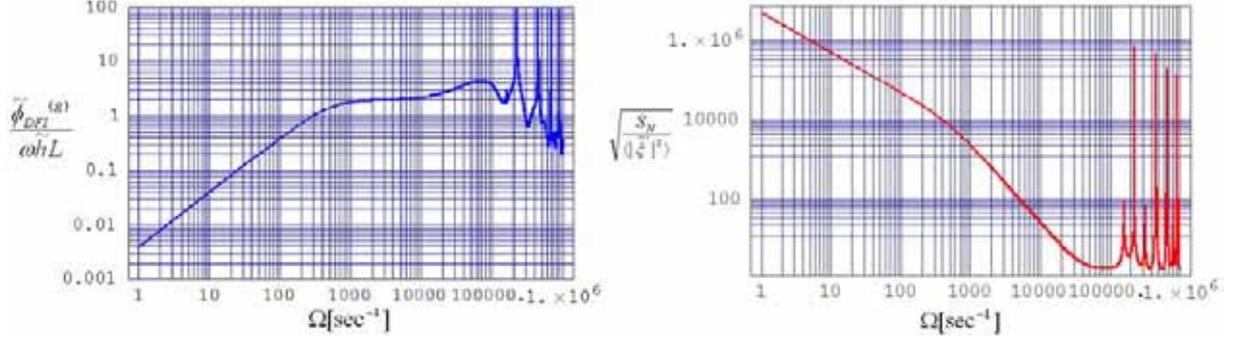
Figure 4: GW responce function (left) and shot noise spectrum (right) of DFI with FP cavity. Here we selected the parameters $R = 0.99$ and $L = 3km$. This correspons to $\Omega_{FP} \approx 6.3 \times 10^5 sec^{-1}$ and $\Omega_L \approx 500 sec^{-1}$. The values in the vertical axis are normalized by some factor.

R is the reflectivity of the mirrors of FP cavity.

Now we are ready to construct DFI signal. Using arbitrary coefficients, we can write down it like,

$$\tilde{\delta\phi}_{DFI}(\Omega) \equiv \tilde{\delta\phi}_{FPM1}(\Omega) - \tilde{\delta\phi}_{FPM2}(\Omega) + \sum_{i=0}^{4} \gamma_i \, \tilde{\delta\phi}_{MZi}(\Omega). \tag{9}$$

where $\tilde{\delta\phi}_{FPM1}$ and $\tilde{\delta\phi}_{FPM2}$ are the signals of Fabry-Perot Michelson interferometer at the top and bottom in Fig3 respectively, and $\tilde{\delta\phi}_{MZi}$, $i = 0, \cdots, 4$ are the signals of Machzender interferometer concerning A_i and B_i respectively. γ_i, $i = 0, \cdots, 4$ are arbitrary coefficients, determined by the condition that all displacement noise are canceled, and become

$$\gamma_0 = \frac{\sqrt{2}}{1 - e^{-2\sqrt{2}i\Omega L}}, \quad \gamma_1 = \frac{\{2\alpha \, cos(2\Omega L) \, e^{-2i\Omega L} + 1\}e^{-2i\Omega L}}{\sqrt{2}(1 - e^{-2\sqrt{2}i\Omega L})}, \quad \gamma_2 = \frac{-\sqrt{2}\alpha e^{-4i\Omega L}}{1 - e^{-2\sqrt{2}i\Omega L}}$$

$$\gamma_3 = -\gamma_1, \quad \gamma_4 = -\gamma_2 \tag{10}$$

Thus, the signal $\tilde{\delta\phi}_{DFI}$ has no displacement noise and is limited only by shot noise. The results are shown in Fig4. GW response function is shifted toward low frequency by virtue of FP cavity, and flat region appears between the characteristic frequency determined by the size of the detector and that determined by FP cavity, in the spectrum. These are $\Omega_L = c/L$ and $\Omega_{FP} = T^2 c/(4L)$ respectively, where T is the transmissivity of the mirrors of FP cavity. In this case, however, the spectrum of shot noise after the cancellation has nontrivial dependence on frequency, though the spectrum of an original shot noise has flat frequency dependence. So, in total, shot noise sets off the advantage of GW response and the sensitivity shows the same frequency dependence as that of DFI without FP cavity! Unfortunately, we had negative results.

In this work, we found that the naive attempt to lower the peak frequency in the sensitivity with FP cavity, doesn't work well. In order to apply the DFI to a ground-based GW interferometer, it needs other ideas to shift the peak frequency of the sensitivity.

References

[1] P.R.Saulson, Fundamentals of Interferometric Gravitational Wave Detectors, World Scientific (1994)

[2] S.Kawamura and Y.Chen, Phys. Rev. Lett., 93, 211103 (2004)

[3] Y.Chen and S.Kawamura, Phys. Rev. Lett., 96, 231102 (2006)

[4] Y.Chen, A.Pai, K.Somiya, S.Kawamura, S.Sato, K.Kokeyama, R.L.Ward, K.Goda and E.E.Mikhailov, Phys. Rev. Lett., 97, 151103 (2006)

Pulsars as Gravitational Probes

Richard N Manchester[1]

Australia Telescope National Facility, CSIRO PO Box 76, Epping NSW 1710, Australia

Abstract

Pulsars are remarkably stable clocks which have a variety of applications covering a wide range of physics and astrophysics. In particular, their occurrence as members of binary systems, in orbit with another star, opens up the possibility of tests of gravitational theories. About 1750 pulsars are now known and about 10% of these are millisecond pulsars (MSPs) which have the best rotational stability. About half of the known pulsars have been discovered in the past few years using the 20cm multibeam system on the Parkes radio telescope. They include the first-known double pulsar, PSR J0737−3039A/B, which is a remarkable test-bed for gravitational physics. Current timing results show that Einstein's general theory of relativity is accurate at the 0.05% level in strong gravitational fields. Timing measurements of an ensemble of pulsars widely distributed on the celestial sphere can be used to make a direct detection of gravitational waves with frequencies in the nanoHertz region. The Parkes Pulsar Timing Array project is observing 20 MSPs at three frequencies and at intervals of 2 – 3 weeks with the aim of detecting gravitational waves. It will also establish a pulsar timescale which has comparable stability to the best terrestrial timescales over intervals of months and years.

1 Introduction

Pulsars are generally believed to be rotating neutron stars formed in supernova explosions. They have a mass comparable to that of the Sun but a diameter of only about 30 km and so the gravitational force at their surface is incredibly strong, corresponding to a gravitational redshift $GM/cR^2 \sim 0.2$. Because of this, they can rotate very rapidly with a minimum spin period of order 1 ms. Furthermore, because of the large moment of inertia ($\sim 10^{45}$ g cm^2) and small radius, the spin rate is extremely stable and so pulsars are remarkably good clocks. This, together with the fact that some pulsars are found in compact binary systems with a relatively massive companion, makes them highly effective probes of a range of gravitational effects.

About 1750 pulsars are now known, almost all of which are located in our Milky Way galaxy. These pulsars fall into two main classes: "normal" pulsars and "millisecond" pulsars (MSPs). Most normal pulsars have spin periods of between 30 ms and 5 s, relatively large spin-down rates, $\dot{P} \sim 10^{-15}$, correspondingly low characteristic ages, $\tau_c = P/(2\dot{P}) \lesssim 10^7$ yr, and are mostly single (i.e., not members of binary systems). MSPs, on the other hand, typically have spin periods of between 1 and 20 ms, very low spin-down rates giving characteristic ages of $\gtrsim 10^9$ yrs and most of them are members of binary systems. MSPs are believed to be old neutron stars which have been "recycled" to short periods by accretion from an evolving companion star [1]. Fig. 1 gives the period distribution of known pulsars, showing that MSPs are about 10% of the known sample.

Precise pulsar periods are measured by recording pulse times of arrival (TOAs), typically over data spans of several years. In practice, a mean pulse profile obtained from an observation of duration typically a few minutes to an hour is cross-correlated with a standard template to produce a TOA at the telescope. This is then corrected for propagation delays and time transformations to give a corresponding TOA at the Solar-system barycentre. This transformation involves a knowledge of the pulsar position. A set of barycentric TOAs is then compared with TOAs predicted from a model for the pulsar timing and astrometric properties to give a set of timing "residuals", i.e., differences between observed and predicted TOAs. Systematic deviations of these timing residuals from zero can be fitted to improve the model parameters. Residuals remaining after the model fitting are either random receiver noise (including sky

---

[1]E-mail:dick.manchester@csiro.au
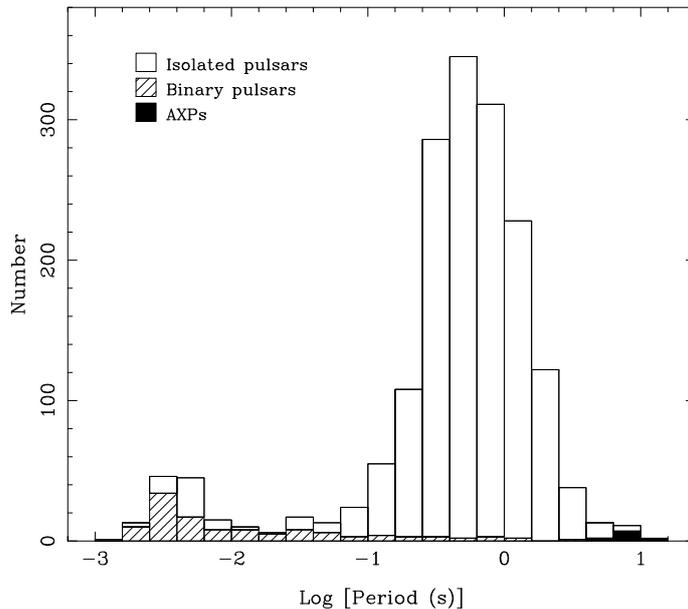
Figure 1: Period distribution of the 1750 known pulsars. Pulsar which are members of a binary system and the so-called "anomalous X-ray pulsars" are identified. Data are from the ATNF Pulsar Catalogue [30] (http://www.atnf.csiro.au/research/pulsar/psrcat)

and ground noise) or from unmodelled effects, most of which are potentially interesting. Table 1 lists possible sources of timing residuals, illustrating the wide variety of effects which can be investigated using pulsar timing. Of most interest in the present context are orbital perturbations, especially those due to relativistic effects, and perturbations of local space-time due to gravitational waves (GW) passing over the Earth.

2 The Hulse-Taylor binary pulsar

In 1975 Russell Hulse and Joeseph Taylor announced the discovery of the first-known binary pulsar, PSR B1913+16 [16]. The short orbital period (7.75 hours) and high orbital velocities observed ($\sim 0.1\%$ of the velocity of light) suggested that the companion was another neutron star and that relativistic effects would be observable in this system and, indeed, they soon were [43]. Three effects were detected: the relativistic precession of periastron, gravitational redshift and time dilation as the pulsar moved in its eccentric orbit, and orbit decay due to emission of gravitational radiation from the system. Together these determined the masses of the two stars, confirming that the companion is a neutron star, and provided a check on the validity of the theory used to predict the effects, namely Einstein's general theory of relativity (GR). These results have been confirmed by more recent observations, giving values for the mass of the pulsar $M_p = 1.4408 \pm 0.0003$ M$_\odot$, the mass of the companion $M_c = 1.3873 \pm 0.0003$ M$_\odot$ and the ratio of observed to predicted orbital period decay $\dot{P}_{b,obs}/\dot{P}_{b,pred} = 1.0013 \pm 0.0021$ [45]. Differential acceleration of the binary system and the Solar system in the gravitational field of the Galaxy introduces a bias into the measured value of $\dot{P}_b$ and the precision of the test of GR is limited by the uncertainty in this correction. Fig. 2 shows the outstanding agreement of the predicted and observed shift in periastron time due to orbit decay, confirming that GR is an accurate theory of gravity in the strong-field regime.

3 The Parkes Multibeam Pulsar Surveys

The Parkes 64-m radio telescope in New South Wales, Australia, has been outstandingly successful as an instrument for finding pulsars. In fact, it has found more than twice as many pulsars as the rest

Table 1: Sources of pulsar timing residuals

Intrinsic noise:	
	• Period fluctuations, glitches
	• Pulse shape changes
Perturbations at the pulsar:	
	• Gravitational wave background
	• Globular cluster acceleration
	• Orbital perturbations: planets, classical Doppler, relativistic effects
Propagation effects:	
	• Scattering and dispersion in a wind from a binary companion
	• Variations in interstellar or Solar-system dispersion
	• Interstellar scattering
Perturbations at the Earth:	
	• Gravitational wave background
	• Errors in the Solar-system ephemeris
Clock errors:	
	• Timescale errors
	• Errors in time transfer
Instrumental errors:	
	• Radio-frequency interference and receiver non-linearities
	• Digitisation artifacts or errors
	• Calibration errors and signal-processing artifacts or errors
Noise sources:	
	• Sky and ground noise
	• Receiver thermal noise

of the world's telescopes put together. What are the reasons for this success? Firstly, the Galactic Centre passes almost overhead at Parkes and, since the concentration of pulsars is much higher in the quadrants toward the Galactic Centre compared to those in the anti-centre direction, the telescope is very favourably located for pulsar searching. Secondly, owing to the foresight and skill of the ATNF engineers and scientists, the telescope has been equipped with state-of-the-art receiver systems. In particular, the 20cm 13-beam multibeam receiver, operating at frequencies close to 1400 MHz, is an outstanding system for blind searches, increasing the efficiency of the telescope by more than an order of magnitude over single-beam systems [42]. Thirdly, the international team responsible for the Parkes searches is very experienced and has developed and refined the data acquisition and analysis techniques over many years.

The Parkes Multibeam Pulsar Survey used the 13-beam receiver to survey a 10°-wide strip along the southern Galactic plane from longitude 260° to 50°. A bandwidth of 288 MHz centred on 1374 MHz and split into 96 3-MHz channels was sampled every 250 μs with an observation time per pointing of approximately 35 min. The survey required 3080 pointings to cover the 1500 square degrees. Observations commenced in 1997 and were completed in 2003. Following confirmation of a pulsar, at least 18 months of timing data were obtained in order to precisely determine the pulsar astrometric and timing parameters. The survey and its results are described in a series of papers [31, 35, 25, 13, 9, 27]. It has been outstandingly successful, detecting 1031 pulsars of which 743 are new discoveries.

A companion survey, the Parkes High Latitude Survey, was carried out by the same team. This survey, described by Burgay et al. [3], covered a region extending to latitudes $|b| < 60°$ between longitudes of 220° and 260°. While the number of pulsars found in this survey was more modest (42 pulsars detected, 18 new discoveries), they included the remarkable double-pulsar system, PSR J0737−3039A/B. Another companion survey using the multibeam receiver was carried out by a group based at Swinburne University. This survey covered the same longitude range as the Parkes Multibeam Pulsar Survey but higher latitudes $5° < |b| < 30°$ [6, 17]. This survey discovered 95 pulsars and detected 230.
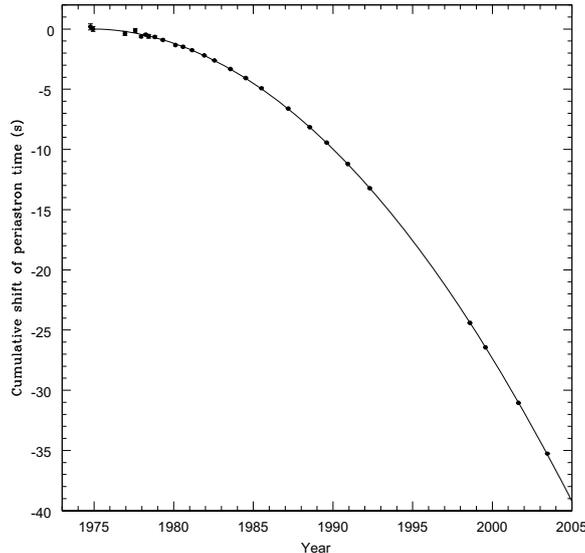
Figure 2: Observed shift of the time of periastron of PSR B1913+16 together with the predicted variation based on general relativity [45]

4   The Double Pulsar PSR J0737−3039A/B

This system, discovered in the Parkes High Latitude Survey [2, 28], is remarkable in a number of ways. Firstly it is a double-neutron-star (DNS) system with a very short orbital period, just 2.4 hours. As a consequence, orbital velocities are a significant fraction of the velocity of light and relativistic perturbations to the orbit are readily detectable. It also means that the system will coalesce in a relatively short time (85 Myr); its detection has raised the expected rate of such coalescences detectable by laser-interferometer gravitational-wave detectors by nearly an order of magnitude [21, 22]. Secondly, it is the only known double-pulsar system, i.e., the only DNS where the second neutron star is detectable as a pulsar. This immediately give a measure of the mass ratio of the two stars, which is an important constraint in tests of theories of relativistic gravity since it is theory independent, at least to 1PN order. The properties of the system, namely a pulsar (A) with a 22-ms period and small $\dot{P}$ and hence large τ_c, and a slow pulsar (B) with a period of 2.7 s which is much younger, are exactly those expected from the recycling mechanism. Thirdly, the orbit is very close to edge-on, which means that the Shapiro delay of the signal from MSP (A) as it passes through the gravitational field of B is easily detectable. (The delay of B as it passes behind A is not so easy to measure because of B's much longer period and hence less precise TOAs.) Another consequence of the near-edge-on orbit is that eclipses of the A pulsar by the magnetosphere of B are observable, giving a fascinating insight into pulsar magnetospheric physics [34, 29].

Periastron advance in the double pulsar system is ∼ 16°.9 per year, more than four times as large as in the PSR B1913+16 system. Measurement of this and the mass ratio defines the masses of the two stars. Based on analysis of 2.5 years of timing data, Kramer et al. [26] obtain $M_A = 1.3381 \pm 0.0007$ M$_\odot$ and $M_B = 1.2489 \pm 0.0007$ M$_\odot$, showing that B is a very low-mass neutron star. Four other relativistic or "Post-Keplerian" parameters have been measured for PSR J0737−3039A/B, more than for any other system. They are the gravitational-redshift/time-dilation term, orbit decay, and two parameters describing the Shapiro delay, the "shape" s and "range" r. Fig. 4 shows that the measurements are fully consistent with GR. The tightest constraint comes from the measurement of s which in GR is identical to $\sin i$, where i is the inclination angle of the orbit. This measurement confirms that GR is an accurate theory of gravity in the strong-field regime with an uncertainty of only 0.05%, the most precise test so far. Currently, the measurement of orbital decay is less precise than the corresponding measurement for PSR B1913+16, but since the precision of this measurement improves approximately as $T^{2.5}$, where T is
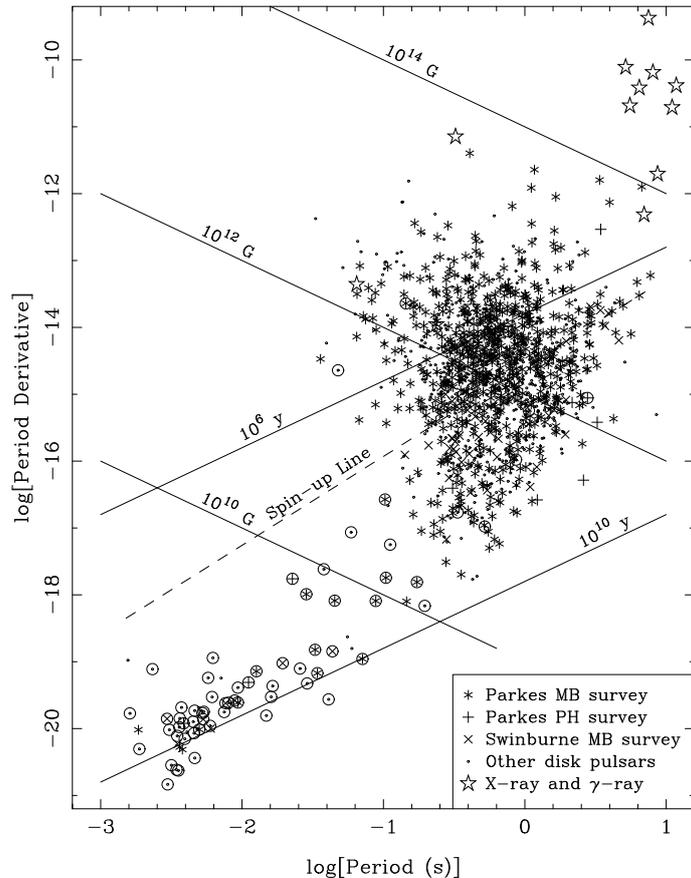
Figure 3: Plot of the slowdown rate $\dot{P}$ versus pulse period P for all known pulsars in the Galactic disk. Pulsars which are members of a binary system are marked by a circle around the point. The group of pulsars in the top right-hand corner of the plot are the anomalous X-ray pulsars (AXPs) which also include pulsating soft gamma-ray repeaters (SGRs). Lines of constant implied surface dipole magnetic field ($\propto P\dot{P}$) and characteristic age (τ_c) are shown on the plot along with the minimum period attainable by accretion from a binary companion. Data are from the ATNF Pulsar catalogue.

the data span, PSR J0737−3039A/B will provide a more accurate test of the radiative predictions of GR in a few years. Furthermore, since PSR J0737−3039A/B is much closer to the Sun than PSR B1913+16, the uncertainty in differential Galactic acceleration will not be a limiting factor for this system. We also expect to detect a number of other relativistic effects, including relativistic orbit deformation and higher-order terms in the periastron precession, testing new aspects of GR and giving additional information about the system. In particular, detection of spin-orbit coupling affecting periastron precession has the potential give a measurement of the neutron-star moment of inertia and hence constrain the equation of state for neutron-star matter [36].

5 Tests of Equivalence Principles

Binary pulsars can be used to test other aspects of relativity, specifically the equivalence principles. These tests are the strong-field analogues of weak-field tests done in Solar system using techniques such as lunar laser ranging. They are usually described in terms of the parameterised post-Newtonian (PPN) formalism in which different theories of gravity have different values of the parameters compared to GR in which they are either zero or one [46]. Many of these tests rely on the difference in self-gravitation of the two stars in the binary system, so DNS systems are not optimal and better limits are obtained from
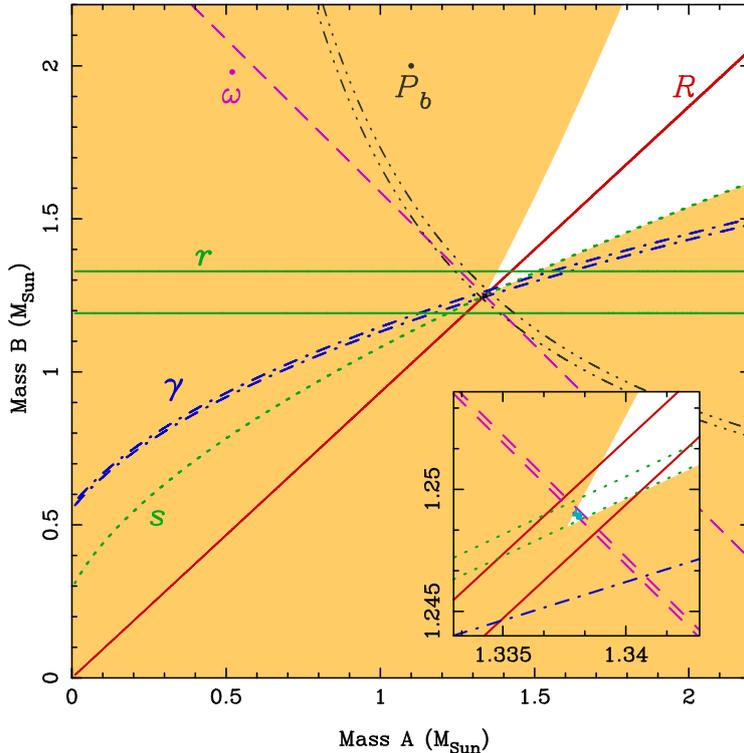
Figure 4: Mass-mass diagram for the PSR J0737−3039A/B binary system based on interpretation of the Post-Keplerian parameters within general relativity. The shaded regions are excluded by the mass-function constraint $\sin i \leq 1$ for each pulsar. The mass ratio R and the periastron advance $\dot{\omega}$ are both accurately measured and give nearly orthogonal constraints on this diagram. Other constraints come from measurement of the Shapiro shape s and range r and the orbit decay $\dot{P}_b$. The inset shows that all constraints are consistent with a very small region in the $M_A - M_B$ plane [26].

neutron-star – white-dwarf systems [39]. As an example, long-period binary pulsars with white-dwarf companions and very low eccentricity may be used to set limits on the differential acceleration of the two stars in the Galactic gravitational potential, thereby testing the Strong Equivalence Principle. From observations of 21 wide-orbit low-eccentricity pulsars, Stairs et al. [40] place a limit on the parameter $\Delta < 5 \times 10^{-3}$, not as strong as the LLR limit, but in the strong-field regime.

   Another interesting limit obtained from pulsars is a limit on the time variation of the gravitational constant $|\dot{G}/G| < 4.8 \times 10^{-12}$ yr^{-1} obtained by comparing the neutron-star masses in old and (relatively) young DNS systems [44].

6   Detection of Gravitational Waves using Pulsars

An important prediction of GR (and other theories of gravity) is that accelerated masses generate gravitational waves. The DNS binary systems provide excellent evidence for the existence of these waves at the level predicted by GR. However, despite huge efforts over many decades, efforts to make a direct detection of them at the Earth have so far not been successful. Ground-based laser-interferometer systems such as LIGO in the United States, VIRGO in Europe and TAMA in Japan are now beginning operation although their sensitivity is still being improved. These systems are most sensitive to GW with frequencies in the range $10 - 500$ Hz with the coalescence of DNS systems being the astrophysical source most likely to be detected. LISA is an ambitious ESA-NASA project consisting of a constellation of three spacecraft trailing the Earth around its orbit and forming a laser-interferometer triangle with arms 5×10^6 km in length. LISA is currently in its design and planning phase and launch is planned

for 2017. It will be most sensitive to GW in the range $10^{-4} - 10^{-1}$ Hz with the dominant sources being coalescing binary super-massive black holes in the cores of galaxies and compact stellar binary systems in our Galaxy.

Pulsars offer an alternative method of directly detecting the GW background in our Galaxy. GW passing over the pulsar and the Earth will introduce variable gravitational redshifts into the observed pulsar period. For a stochastic GW background in the Galaxy, the effects at the pulsar and at the Earth are uncorrelated. Because of the possible presence of other sources of irregularity in the observed periods, observations of a single pulsar can only put a limit on the strength of a stochastic GW background. Since pulsar timing analyses essentially measure the pulse phase, the detected signal is the integral of the effective gravitational strain and the highest sensitivity is obtained for GW signals with frequency comparable to $1/T$, that is, in the nano-Hz region for data spans of order several years. Analysis of an 8-year span of Arecibo data on PSR B1855+09 gave a limit on the energy density of a GW background in the Galaxy relative to the closure density of the Universe, $\Omega_g[1/8 \text{ yr}]h^2 < 10^{-7}$, where $H_0 = 100h$ km s^{-1} Mpc^{-1} [23, 33].

A stochastic gravitational wave background can in principle be *detected* using observations of many pulsars distributed across the celestial sphere. The timing signatures resulting from GW passing over the different pulsars are uncorrelated for a stochastic background, but for waves passing over the Earth, there is a correlation between the timing residuals in different pulsars. A set of such observations, known as a pulsar timing array, can also be used to detect possible long-term irregularities in the terrestrial timescale and errors in the Solar system planetary ephemeris [38, 10].

How are these different effects separated? If there are errors in the timescale to which the pulsar measurements are referred, normally TT(TAI) which is based on a world-wide network of atomic clocks, then all pulsars will be observed to speed up or slow down in synchronism. As a function of direction in space, this can be described as a monopole signature. Errors in the Solar system ephemeris result in errors in the predicted velocity of the Earth with respect to an inertial frame, normally assumed to be the barycentre (centre of mass) of the Solar system. Such errors will result in a dipole signature in the residuals, with opposite redshifts in opposite directions. Similarly, a gravitational wave passing over the Earth will have a quadrupolar signature with opposite redshifts in directions separated on the celestial sphere by 90°. Fig. 5 shows the predicted correlation for the sample of pulsars used in the Parkes Pulsar Timing Array (PPTA) [12, 19]. For a stochastic GW background, the actual position of the pulsars on the sky is not important, the correlation depends only their angular separation. For pulsars which are close together on the sky, the correlation is close to 0.5 since GW passing over the pulsars and over the Earth contribute equally to the residuals, but those from GW passing over the pulsars are uncorrelated.

The PPTA project is a realisation of the pulsar timing array idea in which 20 MSPs are being timed using the Parkes radio telescope with observations in three frequency bands around 685 MHz (50cm), 1400 MHz (20cm) and 3100 MHz (10cm), where the wavelength band designations are given in parentheses. The project is a collaboration principally between the ATNF, the Swinburne University pulsar group led by M. Bailes and a group at the University of Texas led by F. Jenet. Observations commenced in mid-2004 and the pulsars are observed at the three frequencies at intervals of $2 - 3$ weeks. Observations times per pulsar are typically 64 min. Observations at 50cm and 10cm are made simultaneously using the dual-band coaxial 10cm/50cm receiver. Data are recorded using the CPSR2 baseband system which has two 64-MHz bandwidths, each dual polarisation, and a digital filterbank system which has 256 MHz of bandwidth, also dual polarisation. Offline processing uses the PSRCHIVE pulsar data analysis system [15] and the TEMPO2 timing analysis program [14, 7] with the JPL DE405 Solar system ephemeris [41].

Table 2 lists the 20 pulsars, all MSPs, being observed in the PPTA project and Fig. 6 shows their sky distribution. Basic pulsar parameters are listed, including the dispersion measure (DM) characterising the amount of interstellar dispersion. All of the pulsars are located in the Galactic disk except PSR J1824-2452 (PSR B1821-24) which is associated with the globular cluster M28. These pulsars are chosen to give a good distribution over the celestial sphere, to have relatively short periods, narrow pulses and high flux densities in order to maximise the precision of the observed TOAs. The final column in Table 2 gives the rms timing residual for two years of data at the band which gives the best timing performance, usually 20cm. These results are preliminary in the sense that they have not been corrected for variations in interstellar dispersion and nor has a full polarisation calibration been done. Never-the-less, nearly half the sample has sub-microsecond rms timing residuals and all are less than 2.5 μs.
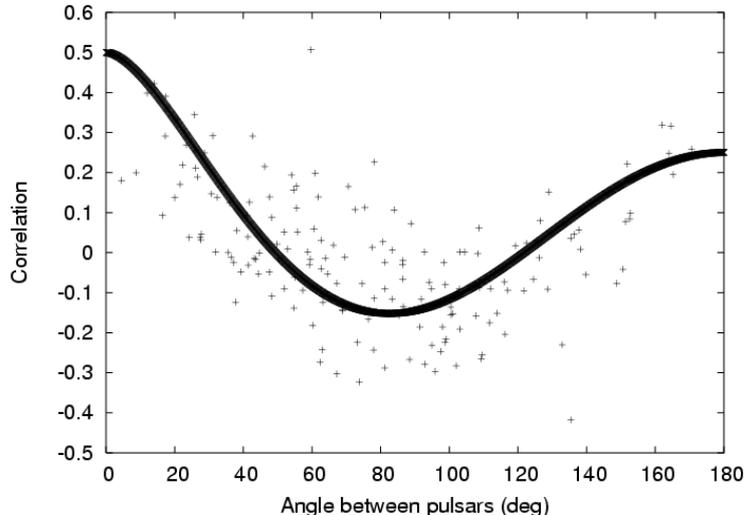
Figure 5: Simulation of the effect of a stochastic background of gravitational waves on pair-wise correlations between timing residuals for pulsars being observed in the PPTA project as a function of the angular separation between the pulsar pairs. (Hobbs & Jenet, unpublished)

The astrophysical sources of GW most likely to be detectable with a pulsar timing array are stochastic backgrounds from supermassive black-hole binary systems in the cores of galaxies [18, 47, 8], fluctuations of cosmic strings [5] and relic radiation from the inflation era [11]. Of these, the first is the most predictable, although even in this case there are large uncertainties, principally concerning the number of such systems with masses and orbital periods in the range relevant for pulsar GW detection. Jenet et al. [19] discussed techniques for detecting a stochastic GW background and showed that to have a realistic chance of a positive detection, weekly observations of at 20 pulsars over five years with rms timing residuals of order 100 ns are required.

It is clear from Table 2 that we have not yet achieved this goal although we are within a factor of a few of doing so. Considerable effort is going into improving our observing and data analysis systems and techniques with the aim of reaching this goal. A new digital filterbank system with improved time and frequency resolution is about to be commissioned. This should improve our timing precision, especially for the shorter-period pulsars. A new timing analysis program, TEMPO2 in which known errors in time transfer and propagation delays have been kept at the 1 ns level or below and which has a versatile graphical user interface has been developed [14, 7]. Radio frequency interference is an important limiting factor, especially in the 50cm band, and techniques to mitigate its effect, including real-time adaptive filtering, are being implemented [24]. We are also actively exploring international collaborations in order to obtain access to data for northern hemisphere pulsars and to improve our coverage of pulsars in the equatorial zone.

By combining the existing 2 – 3 years of PPTA data for seven of our best timing pulsars with the publically available Kaspi et al. [23] 8-year Arecibo data set for PSR B1855+09 and using a statistically rigorous analysis procedure, Jenet et al. [20] obtained a limit on $\Omega_g[1/8 \text{ yr}]h^2 < 1.9 \times 10^{-8}$. This limit, a factor of five better than the limit obtained by Kaspi et al., allows us to constrain the equation of state in the inflation era, $P/\epsilon = w > -1.3$, where P is the pressure and ϵ is the energy density. It also allows us to limit the dimensionless tension of cosmic strings, $G\mu < 1.5 \times 10^{-8}$, already ruling out some proposed models. Our limit does not constrain existing models for GW from super-massive black-hole binaries in the Universe. However, as illustrated in Fig. 7, projections for the full (five-year) PPTA show that it will either make a positive detection of GW from binary super-massive black holes or rule out all current models for their formation and evolution.

Fig. 8 shows the pulsar limiting sensitivities in the context of other gravitational-wave detectors, emphasizing the complementary nature of the three classes of detectors: pulsar timing arrays, space-
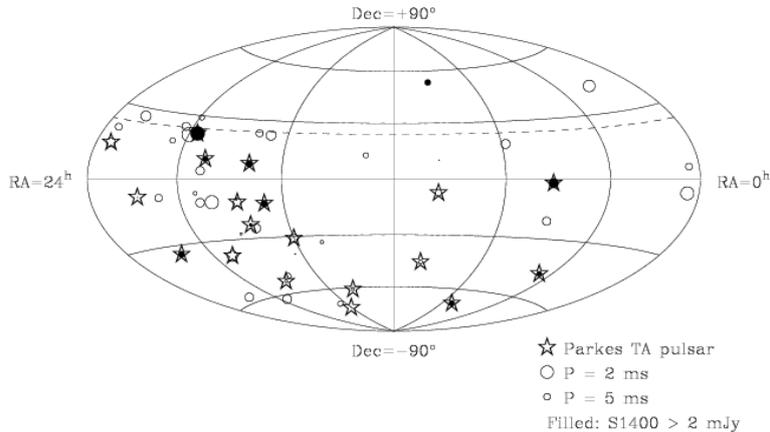
Figure 6: Sky distribution of Galactic disk MSPs with periods less than 20 ms. The size of the circle is logarithmically related to the pulsar period and stronger pulsars have filled symbols. Pulsars selected for the Parkes Pulsar Timing Array are indicated.

based laser interferometers and ground-based laser interferometers. A projected limit for pulsar timing using the next-generation radio telescope, the Square Kilometer Array (SKA) [4], is also shown. The SKA will detect the GW background predicted by all of the models discussed in this paper.

7   A Pulsar Timescale

The standard of terrestrial time, TT(TAI), is defined by the weighted average of about 200 caesium clocks at time-standard laboratories around the world. This timescale is available in near real-time through the Circular T of the BIPM (see http://www.bipm.org/en/publications). A more precise timescale can be established retroactively by a more careful adjustment of the weights given to various clocks; the latest of these timescales is TT(BIPM06), also available on the BIPM website. These revisions differ from each other by amounts of order $10 - 50$ ns and from TT(TAI) by significant trends and fluctuations of order 1 μs.

A pulsar timescale is fundamentally different from TT(TAI) in that it depends on a different physical property (rotational inertia) and is effectively isolated from all terrestrial phenomena [37]. It is not absolute in the sense that TT(TAI) is (being tied to the definition of the second through the frequency of a hyperfine transition of the Cs 133 atom) but it can be used to detect irregularities in the terrestrial timescale. Because of the nature of pulsar timing, only relatively long-timescale irregularities, with duration of months to years, can be detected. Fig. 9 shows the sigma-z statistic [32] for clock stability for two pulsars with the longest data spans and good timing properties, as well as the difference between two of the best atomic timescales. It is clear that for intervals of order a few years or more, the pulsars have a stability comparable to that of the atomic timescales. With averaging over a large number of pulsars and increased timing precision, the PPTA should be able to define a pulsar timescale having a precision of 50 ns or better over intervals of a few weeks and longer-term trends to higher precision. This will be a valuable check on the integrity of the timescales based on terrestrial atomic clocks.

Acknowledgements

Name	Period (ms)	DM (cm^{-3} pc)	Orbital Period (d)	Timing Residual (μs)
J0437−4715	5.757	2.65	5.74	0.12
J0613−0200	3.062	38.78	1.20	0.83
J0711−6830	5.491	18.41	−	1.56
J1022+1001	16.453	10.25	7.81	1.11
J1024−0719	5.162	6.49	−	1.20
J1045−4509	7.474	58.15	4.08	1.44
J1600−3053	3.598	52.19	14.34	0.35
J1603−7202	14.842	38.05	6.31	1.34
J1643−1224	4.622	62.41	147.02	2.10
J1713+0747	4.570	15.99	67.83	0.19
J1730−2304	8.123	9.61	−	1.82
J1732−5049	5.313	56.84	5.26	2.40
J1744−1134	4.075	3.14	−	0.65
J1824−2452	3.054	119.86	−	0.88
J1857+0943	5.362	13.31	12.33	2.09
J1909−3744	2.947	10.39	1.53	0.22
J1939+2134	1.558	71.04	−	0.17
J2124−3358	4.931	4.62	−	2.00
J2129−5721	3.726	31.85	6.63	0.91
J2145−0750	16.052	9.00	6.84	1.44
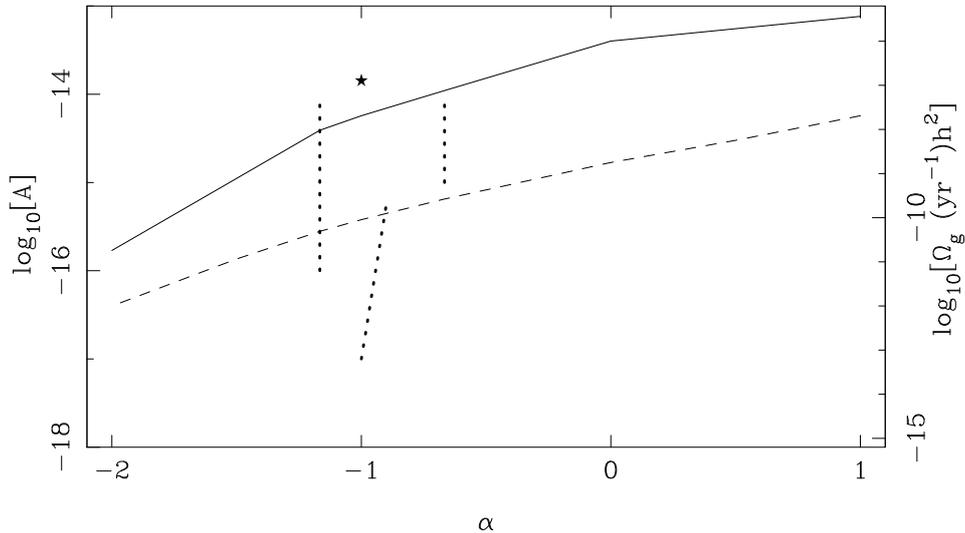
Figure 7: Current limit on the amplitude of a stochastic gravitational-wave background in the Galaxy $A = \Omega_g[1 \text{ yr}^{-1}] \, h^2$ as a function of the spectral index of the characteristic strain spectrum. The near-vertical dotted lines are the expected range of amplitudes and spectral indices for GW from (left to right) cosmic strings, the inflationary era and supermassive binary black holes. The dashed line is the expected limit from the full 5-year PPTA.
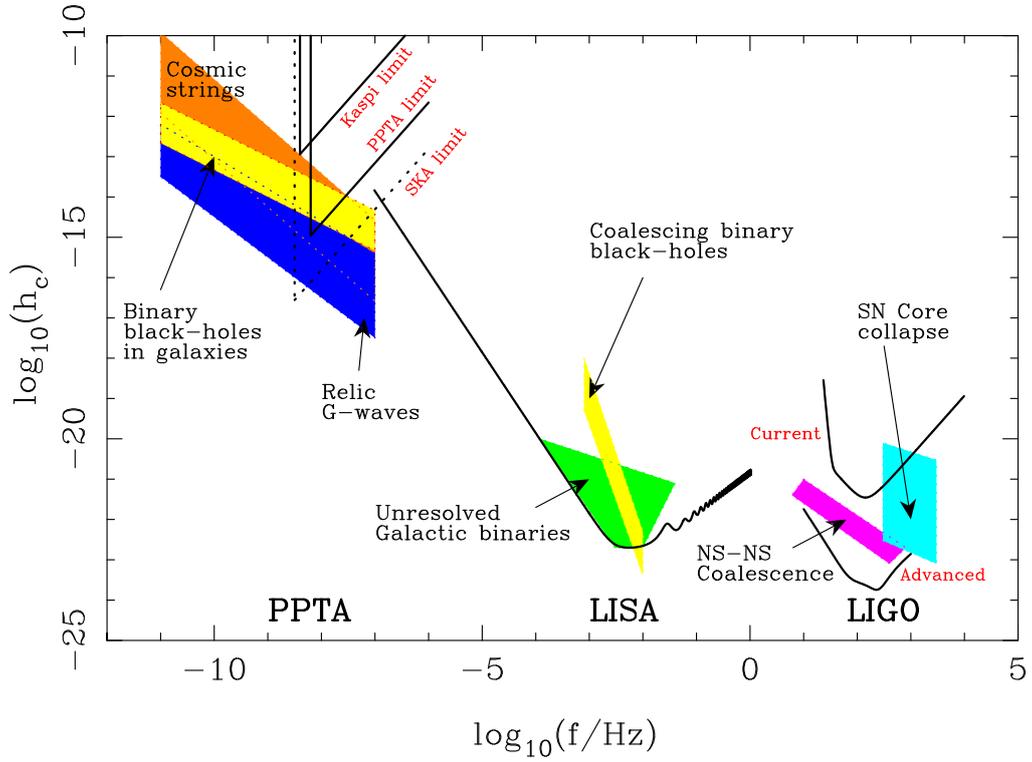
Figure 8: Sensitivities of gravitational-wave detectors in terms of characteristic strain as a function of frequency. Expected ranges of characteristic strain for likely astrophysical sources in the frequency ranges of the three classes of detectors are shown.
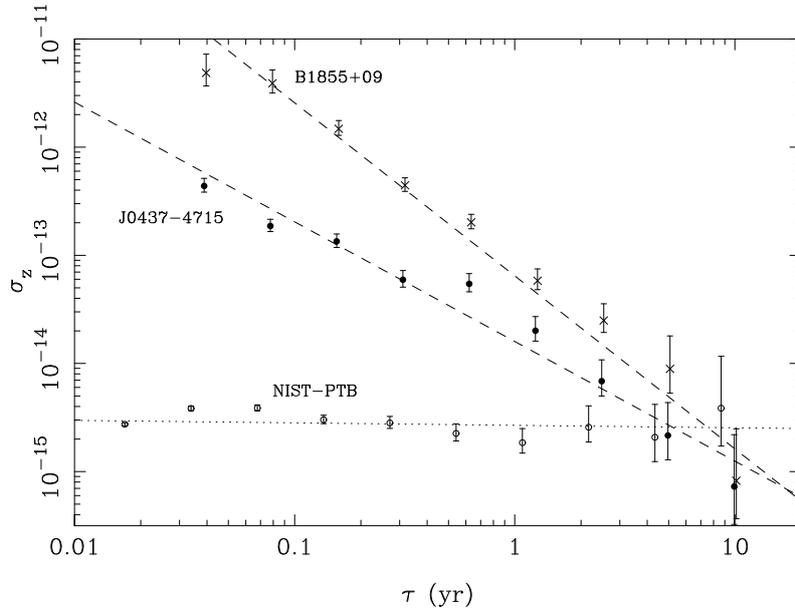
Figure 9: Sigma-z statistic as a function of averaging interval for two pulsars and the difference between two of the best atomic timescales, TT(NIST) and TT(PTB), respectively from the US and German time-standards laboratories (Hobbs & Verbiest, unpublished).

References

[1] Bhattacharya, D. & van den Heuvel, E. P. J. 1991, Phys. Rep., 203, 1

[2] Burgay, M., D'Amico, N., Possenti, A., Manchester, R. N., Lyne, A. G., Joshi, B. C., McLaughlin, M. A., Kramer, M., Sarkissian, J. M., Camilo, F., Kalogera, V., Kim, C., & Lorimer, D. R. 2003, Nature, 426, 531

[3] Burgay, M., Joshi, B. C., D'Amico, N., Possenti, A., Lyne, A. G., Manchester, R. N., McLaughlin, M. A., Kramer, M., Camilo, F., & Freire, P. C. C. 2006, MNRAS, 368, 283

[4] Cordes, J. M., Kramer, M., Lazio, T. J. W., Stappers, B. W., Backer, D. C., & Johnston, S. 2004, New Astron. Rev., 48, 1413

[5] Damour, T. & Vilenkin, A. 2005, Phys. Rev. D, 71, 063510

[6] Edwards, R. T., Bailes, M., van Straten, W., & Britton, M. C. 2001, MNRAS, 326, 358

[7] Edwards, R. T., Hobbs, G. B., & Manchester, R. N. 2006, MNRAS, 372, 1549

[8] Enoki, M., Inoue, K. T., Nagashima, M., & Sugiyama, N. 2004, ApJ, 615, 19

[9] Faulkner, A. J., Stairs, I. H., Kramer, M., Lyne, A. G., Hobbs, G., Possenti, A., Lorimer, D. R., Manchester, R. N., McLaughlin, M. A., D'Amico, N., Camilo, F., & Burgay, M. 2004, MNRAS, 355, 147

[10] Foster, R. S. & Backer, D. C. 1990, ApJ, 361, 300

[11] Grishchuk, L. P. 2005, Phys. Uspekhi, 48, 1235

[12] Hellings, R. W. & Downs, G. S. 1983, ApJ, 265, L39

[13] Hobbs, G., Faulkner, A., Stairs, I. H., Camilo, F., Manchester, R. N., Lyne, A. G., Kramer, M., D'Amico, N., Kaspi, V. M., Possenti, A., McLaughlin, M. A., Lorimer, D. R., Burgay, M., Joshi, B. C., & Crawford, F. 2004, MNRAS, 352, 1439

[14] Hobbs, G. B., Edwards, R. T., & Manchester, R. N. 2006, MNRAS, 369, 655

[15] Hotan, A. W., van Straten, W., & Manchester, R. N. 2004, PASA, 21, 302

[16] Hulse, R. A. & Taylor, J. H. 1975, ApJ, 195, L51

[17] Jacoby, B. A. 2004, PhD thesis, Calfornia Institute of Technology

[18] Jaffe, A. H. & Backer, D. C. 2003, ApJ, 583, 616

[19] Jenet, F. A., Hobbs, G. B., Lee, K. J., & Manchester, R. N. 2005, ApJ, 625, L123

[20] Jenet, F. A., Hobbs, G. B., van Straten, W., Manchester, R. N., Bailes, M., Verbiest, J. P. W., Edwards, R. T., Hotan, A. W., Sarkissian, J. M., & Ord, S. M. 2006, ApJ, 653, 1571

[21] Kalogera, V., Kim, C., Lorimer, D. R., Burgay, M., D'Amico, N., Possenti, A., Manchester, R. N., Lyne, A. G., Joshi, B. C., McLaughlin, M. A., Kramer, M., Sarkissian, J. M., & Camilo, F. 2004a, ApJ, 601, L179

[22] —. 2004b, ApJ, 614, L137

[23] Kaspi, V. M., Taylor, J. H., & Ryba, M. 1994, ApJ, 428, 713

[24] Kesteven, M., Hobbs, G., Clement, R., Dawson, B., Manchester, R., & Uppal, T. 2005, Radio Sci., 40, RS5S06:1

[25] Kramer, M., Bell, J. F., Manchester, R. N., Lyne, A. G., Camilo, F., Stairs, I. H., D'Amico, N., Kaspi, V. M., Hobbs, G., Morris, D. J., Crawford, F., Possenti, A., Joshi, B. C., McLaughlin, M. A., Lorimer, D. R., & Faulkner, A. J. 2003, MNRAS, 342, 1299

[26] Kramer, M., Stairs, I. H., Manchester, R. N., McLaughlin, M. A., Lyne, A. G., Ferdman, R. D., Burgay, M., Lorimer, D. R., Possenti, A., D'Amico, N., Sarkissian, J. M., Hobbs, G. B., Reynolds, J. E., Freire, P. C. C., & Camilo, F. 2006, Science, 314, 97

[27] Lorimer, D. R., Faulkner, A. J., Lyne, A. G., Manchester, R. N., Kramer, M., McLaughlin, M. A., Hobbs, G., Possenti, A., Stairs, I. H., Camilo, F., Burgay, M., D'Amico, N., Corongiu, A., & Crawford, F. 2006, MNRAS, 372, 777

[28] Lyne, A. G., Burgay, M., Kramer, M., Possenti, A., Manchester, R. N., Camilo, F., McLaughlin, M. A., Lorimer, D. R., D'Amico, N., Joshi, B. C., Reynolds, J., & Freire, P. C. C. 2004, Science, 303, 1153

[29] Lyutikov, M. & Thompson, C. 2005, ApJ, 634, 1223

[30] Manchester, R. N., Hobbs, G. B., Teoh, A., & Hobbs, M. 2005, AJ, 129, 1993

[31] Manchester, R. N., Lyne, A. G., Camilo, F., Bell, J. F., Kaspi, V. M., D'Amico, N., McKay, N. P. F., Crawford, F., Stairs, I. H., Possenti, A., Morris, D. J., & Sheppard, D. C. 2001, MNRAS, 328, 17

[32] Matsakis, D. N., Taylor, J. H., & Eubanks, T. M. 1997, A&A, 326, 924

[33] McHugh, M. P., Zalamansky, G., Vernotte, F., & Lantz, E. 1996, Phys. Rev. D, 54, 5993

[34] McLaughlin, M. A., Lyne, A. G., Lorimer, D. R., Possenti, A., Manchester, R. N., Camilo, F., Stairs, I. H., Kramer, M., Burgay, M., D'Amico, N., Freire, P. C. C., Joshi, B. C., & Bhat, N. D. R. 2004, ApJ, 616, L131

[35] Morris, D. J., Hobbs, G., Lyne, A. G., Stairs, I. H., Camilo, F., Manchester, R. N., Possenti, A., Bell, J. F., Kaspi, V. M., Amico, N. D., McKay, N. P. F., Crawford, F., & Kramer, M. 2002, MNRAS, 335, 275

[36] Morrison, I. A., Baumgarte, T. W., Shapiro, S. L., & Pandharipande, V. R. 2004, ApJ, 617, L135

[37] Petit, G. & Tavella, P. 1996, A&A, 308, 290

[38] Romani, R. W. 1989, in Timing Neutron Stars, ed. H. Ögelman & E. P. J. van den Heuvel (Dordrecht: Kluwer), 113

[39] Stairs, I. H. 2003, 5, uRL (Cited on 2007/02/01): http://www.livingreviews.org/Irr-2005-5

[40] Stairs, I. H., Faulkner, A. J., Lyne, A. G., Kramer, M., Lorimer, D. R., McLaughlin, M. A., Manchester, R. N., Hobbs, G. B., Camilo, F., Possenti, A., Burgay, M., D'Amico, N., Freire, P. C. C., Gregory, P. C., & Wex, N. 2005, ApJ, 632, 1060

[41] Standish, E. M. 1998, JPL Planetary and Lunar Ephemerides, DE405/LE405, Memo IOM 312.F-98-048 (Pasadena: JPL), http://ssd.jpl.nasa.gov/iau-comm4/de405iom/de405iom.pdf

[42] Staveley-Smith, L., Wilson, W. E., Bird, T. S., Disney, M. J., Ekers, R. D., Freeman, K. C., Haynes, R. F., Sinclair, M. W., Vaile, R. A., Webster, R. L., & Wright, A. E. 1996, PASA, 13, 243

[43] Taylor, J. H., Fowler, L. A., & McCulloch, P. M. 1979, Nature, 277, 437

[44] Thorsett, S. E. 1996, Phys. Rev. Lett., 77, 1432

[45] Weisberg, J. M. & Taylor, J. H. 2003, in Radio Pulsars, ed. M. Bailes, D. J. Nice, & S. Thorsett (San Francisco: Astronomical Society of the Pacific), 93–98

[46] Will, C. 2006, Living Reviews in Relativity, 9, 1, uRL (Cited on 2007/02/01): http://www.livingreviews.org/Irr-2006-3

[47] Wyithe, J. S. B. & Loeb, A. 2003, ApJ, 590, 691

Gravitational waves from a particle in bound geodesic orbits around a Kerr black hole

Ryuichi Fujita[1], Wataru Hikida[2] and Hideyuki Tagoshi[3]

[1,2,3]*Department of Earth and Space Science, Graduate School of Science, Osaka University, Toyonaka 560-0043, Japan*

Abstract

We show an efficient numerical method to compute gravitational waves radiated by a particle orbiting around a Kerr black hole. In this work, we compute the homogeneous solutions of the Teukolsky equation using formalism developed by Mano, Suzuki and Takasugi. We also compute various modes of gravitational waves using trapezoidal rule in numerical integration. We check our code in the case of simple orbits and report our current status.

1 Introduction

Gravitational waves radiated from a particle orbiting around a Kerr black hole are one of the main targets of LISA. Such systems are called the extreme mass ratio inspirals(EMRI). Observing gravitational waves from EMRI, we may be able to obtain information of the central black hole's spacetime such as mass, spin and the mass distribution of compact objects in the center of galaxy. In order to obtain information from EMRI, we have to achieve the phase accuracy of theoretical gravitational wave forms within one radian over the total cycle of wave, $\sim 10^5$.

There are a lot of previous works which numerically compute gravitational waves from EMRI. For simple orbits such as circular or equatorial orbits around black hole, they achieved the accuracy 10^{-5} which may be sufficient to detect gravitational waves. For more general orbits, Drasco and Hughes computed gravitational waves from EMRI[3]. However, their computational time and numerical accuracy seem to be insufficient to detect gravitational waves. It might be useful if we can compute gravitational waves more efficiently.

In this paper, we show such an efficient method which may be applicable for LISA data analysis.

2 Gravitational waves from EMRIs

Gravitational waves from EMRI are well approximated by the black hole perturbation theory. The basic equation of the black hole perturbation is the Teukolsky equation[1] which is a master equation for Weyl scalars, Ψ_4. The Weyl scalars are related to the amplitudes of gravitational wave as

$$\Psi_4 \to \frac{1}{2}(\ddot{h}_+ - i\,\ddot{h}_\times),\ \text{for}\ r \to \infty. \tag{1}$$

Teukolsky showed that the master equation can be separated into a radial and a angular part if we expand Weyl scalars in Fourier-harmonic modes as

$$\Psi_4 = \sum_{\ell m} \int_{-\infty}^{\infty} d\omega e^{-i\omega t + im\varphi}\ _{-2}S_{\ell m}^{a\omega}(\theta) R_{\ell m\omega}(r). \tag{2}$$

where the angular function $_{-2}S_{\ell m}^{a\omega}(\theta)$ is a spin-weighted spheroidal harmonic with spin s. The radial function $R_{\ell m\omega}(r)$ satisfies radial part of the Teukolsky equation as

$$\Delta^2 \frac{d}{dr}\left(\frac{1}{\Delta}\frac{dR_{\ell m\omega}}{dr}\right) - V(r)R_{\ell m\omega} = T_{\ell m\omega}. \tag{3}$$

---

[1]E-mail:draone@vega.ess.sci.osaka-u.ac.jp
[2]E-mail:hikida@vega.ess.sci.osaka-u.ac.jp
[3]E-mail:tagoshi@vega.ess.sci.osaka-u.ac.jp

The potential is given by

$$V(r) = -\frac{K^2 - 2is(r - M)K}{\Delta} - 4is\omega r + \lambda, \tag{4}$$

where $K = (r^2 + a^2)\omega - ma$ and λ is the eigenvalue of $_{-2}S_{\ell m}^{a\omega}(\theta)$.

We solve the radial Teukolsky equation using the Green function method. Then, the solutions of the Teukolsky equation are derived as

$$R_{\ell m\omega}(r) = R_{\ell m\omega}^{\mathrm{up}}(r)Z_{\ell m\omega}^{\infty}(r) + R_{\ell m\omega}^{\mathrm{in}}(r)Z_{\ell m\omega}^{\mathrm{H}}(r), \tag{5}$$

where $R_{\ell m\omega}^{\mathrm{in/up}}(r)$ satisfy ingoing/outgoing wave conditions at the horizon/infinity and

$$Z_{lm\omega}^{\infty,\mathrm{H}} = \int_{-\infty}^{\infty} dt\, e^{i[\omega t - m\phi(t)]} I_{lm\omega}^{\infty,\mathrm{H}}[r(t), \theta(t)]. \tag{6}$$

The function $I_{lm\omega}^{\infty,\mathrm{H}}[r(t), \theta(t)]$ is constructed from the source term of the Teukolsky equation and depends on the orbital worldline of the star perturbing the black hole spacetime. If the trajectory of the star is eccentric and inclined from equatorial plane around a black hole, it is difficult to evaluate Eq. (6) because integrand is multi periodic function and each mode couples. These problems comes from the fact that radial motion and polar motion of the star couple in observer time. They can be solved by introducing a new parameter of time[2, 3]. Then the geodesic equations of the star are given by

$$
\begin{aligned}
\left(\frac{dr}{d\lambda}\right)^2 &= \left[(r^2 + a^2)E - aL_z\right]^2 - \Delta[r^2 + (L_z - aE)^2 + C] \equiv R(r), \\
\left(\frac{d\theta}{d\lambda}\right)^2 &= C - \left[(1 - E^2)a^2 + \frac{L_z^2}{\sin^2\theta}\right]\cos^2\theta \equiv \Theta(\theta), \\
\frac{d\phi}{d\lambda} &= \frac{a}{\Delta}\left[E(r^2 + a^2) - aL_z\right] - aE + \frac{L_z}{\sin^2\theta} \equiv \Phi_{\mathrm{r}}(r) + \Phi_{\theta}(\theta), \\
\frac{dt}{d\lambda} &= \frac{r^2 + a^2}{\Delta}\left[E(r^2 + a^2) - aL_z\right] - a\left[aE\sin^2\theta - L_z\right] \equiv T_{\mathrm{r}}(r) + T_{\theta}(\theta),
\end{aligned}
\tag{7}
$$

where E, L_z and C are the energy, the z-component of the angular momentum and the Carter constant of a test particle respectively. Since the equations of radial and polar motion are decouple with time parameter λ, the radial and the polar motion are independently periodic functions. The frequencies are given by

$$\frac{2\pi}{\Upsilon_r} = 2\int_{r_{\min}}^{r_{\max}} \frac{dr}{\sqrt{R(r)}}, \quad \frac{2\pi}{\Upsilon_\theta} = 4\int_0^{\theta_{\min}} \frac{d\theta}{\sqrt{\Theta(\theta)}}. \tag{8}$$

Here, Υ_r and Υ_θ are the frequency of the radial and the polar motion respectively. The frequencies of the time and the azimuthal motion are also derived respectively as

$$
\begin{aligned}
\Gamma &\equiv \frac{1}{2\pi}\int_0^{2\pi} dw^\theta\, T_\theta\left[\theta(w^\theta)\right] + \frac{1}{2\pi}\int_0^{2\pi} dw^r\, T_r\left[r(w^r)\right], \tag{9} \\
\Upsilon_\phi &\equiv \frac{1}{2\pi}\int_0^{2\pi} dw^\theta\, \Phi_\theta\left[\theta(w^\theta)\right] + \frac{1}{2\pi}\int_0^{2\pi} dw^r\, \Phi_r\left[r(w^r)\right], \tag{10}
\end{aligned}
$$

where w^r and w^θ are action-angle variables for r and θ motion respectively.

Using new parameterization of time λ, we can evaluate Eq. (6) as

$$Z_{lm\omega}^{\infty,\mathrm{H}} \equiv \sum_{kn} \tilde{Z}_{lmkn}^{\infty,\mathrm{H}} \delta(\omega - \omega_{mkn}), \tag{11}$$

where

$$\tilde{Z}_{lmkn}^{\infty,\mathrm{H}} = \frac{1}{(2\pi)^2}\int_0^{2\pi} dw^\theta \int_0^{2\pi} dw^r\, e^{i(kw^\theta + nw^r)} Z_{lm\omega_{mkn}}^{\infty,\mathrm{H}}[r(w^r), \theta(w^\theta)], \tag{12}$$

and

$$\omega_{mkn} \equiv \Upsilon_{mkn}/\Gamma \equiv (m\Upsilon_\phi + k\Upsilon_\theta + n\Upsilon_r)/\Gamma \,. \tag{13}$$

Computing Eq. (12), we can obtain gravitational wave forms and energy flux to infinity as

$$h_+ - i\, h_\times = -\frac{2}{r} \sum_{lmkn} \frac{Z^\infty_{lmkn}}{\omega^2_{mkn}} \frac{{}_{-2}S^{a\omega_{mkn}}_{lm}(\theta)}{\sqrt{2\pi}}\, e^{i\omega_{mkn}(r^*-t)+im\phi}, \quad \left\langle \frac{dE}{dt} \right\rangle^\infty_{GW} = \sum_{lmkn} \frac{|Z^\infty_{lmkn}|^2}{4\pi\omega^2_{mkn}}. \tag{14}$$

3 An efficient numerical method and results

As explained in the previous section, we have to compute Eq. (12) in order to evaluate gravitational waves. From the points of views of LISA data analysis, it is important to find efficient methods to compute Eq. (12). In order to compute Eq. (12) efficiently, we compute the homogeneous solutions of the Teukolsky equation with the formalism developed by Mano, Suzuki and Takasugi(MST)[4] and use the trapezoidal rule to compute Eq. (12).

In MST formalism, the homogeneous solutions of the Teukolsky equation are expressed in terms of two kinds of series of special functions. Although the application of this method was previously limited to the analytical evaluation of the homogeneous solutions, Fujita and Tagoshi found that it was also useful for numerical calculation[5] because the convergence of the homogeneous solutions are very rapid and the accuracy of gravitational waves were achieved about machine accuracy. Then, we use trapezoidal rule to compute Eq. (12) because the convergence of numerical integration of periodic function over one cycle is very rapid and the accuracy is also very high if we use trapezoidal rule.

As a demonstration, we compute the energy fluxes of gravitational waves radiated to infinity and compare with past results. We show our numerical results in Table 1, 2 and Fig. 3.

l	$|m|$	Fujita and Tagoshi(2005)	This work	Relative error
2	2	$1.78401657716943627674 \times 10^{-2}$	$1.78401657717214383314 \times 10^{-2}$	1.5×10^{-12}
3	3	$1.07647967139507787920 \times 10^{-2}$	$1.07647967139685510340 \times 10^{-2}$	1.7×10^{-12}
4	4	$6.15270976286638737740 \times 10^{-3}$	$6.15270976287798920801 \times 10^{-3}$	1.9×10^{-12}
5	5	$3.62992493707918690085 \times 10^{-3}$	$3.62992493685125290973 \times 10^{-3}$	6.3×10^{-11}
6	6	$2.20229967982856367908 \times 10^{-3}$	$2.20229967906702657834 \times 10^{-3}$	3.5×10^{-10}
7	7	$1.36347483334188827007 \times 10^{-3}$	$1.36347483181112750887 \times 10^{-3}$	1.1×10^{-9}

Table 1: Energy fluxes radiated to the infinity in the case of a circular and the equatorial orbit around a Kerr black hole. In this table, the orbital radius is $1.55M$ and spin of the black hole is $a = 0.99$. We compare our numerical results with the results of high precision calculation[5] which are about 13–14 significant figures in double precision calculation. In order to check the accuracy of our numerical code, we evaluate the energy fluxes by computing Eq. (??) with numerical integration though we can compute it without numerical integration. These results shows that accuracy of our code is limited by the accuracy of the numerical integration. In this case, we set the accuracy of the numerical integration about 10 significant figures.

4 Summary

In this paper, we show an efficient numerical method to compute gravitational waves produced by a particle orbiting around a Kerr black hole. We compute the homogeneous solutions of the Teukolsky equation with the formalism developed by Mano, Suzuki and Takasugi and also evaluate Fourier mode of gravitational waves with trapezoidal rule of numerical integration. Numerical accuracy and computational time derived here are more useful for LISA data analysis than past works.

Future work is to develop our code for more general orbits such that the star move across the north and south poles. At the same time, we evaluate gravitational waves including effects of adiabatic evolution of orbital parameter by computing energy fluxes, angular momentum fluxes and change rate of the Carter constants.

e	inclination	Sago et al.(2006)	This work	Relative error
0.01	3°	$6.211124676 \times 10^{-10}$	$6.205511895774004 \times 10^{-10}$	9.0×10^{-4}
0.01	5°	$6.211194911 \times 10^{-10}$	$6.205582654583145 \times 10^{-10}$	9.0×10^{-4}
0.01	7°	$6.211301135 \times 10^{-10}$	$6.205687847727640 \times 10^{-10}$	9.0×10^{-4}
0.03	3°	$6.268368982 \times 10^{-10}$	$6.213139168623904 \times 10^{-10}$	8.8×10^{-3}
0.03	5°	$6.268440256 \times 10^{-10}$	$6.213210249941237 \times 10^{-10}$	8.8×10^{-3}
0.03	7°	$6.268548068 \times 10^{-10}$	$6.213315925452469 \times 10^{-10}$	8.8×10^{-3}
0.05	3°	$6.382857572 \times 10^{-10}$	$6.228283030987133 \times 10^{-10}$	2.4×10^{-2}
0.05	5°	$6.382930950 \times 10^{-10}$	$6.228354756012462 \times 10^{-10}$	2.4×10^{-2}
0.05	7°	$6.383041917 \times 10^{-10}$	$6.228461394314896 \times 10^{-10}$	2.4×10^{-2}

Table 2: Energy fluxes radiated to the infinity in the case of slightly eccentric and inclined orbit around a Kerr black hole. In this table, the semilatus rectum is $100M$ and spin of the black hole is $a = 0.9$. We compare the numerical results with analytical post-Newtonian expansions of the energy fluxes[6] which truncate Taylor expansion to 2.5PN, v^5, order. These results shows that accuracy of our code in the case of eccentric and inclined orbits are consistent with the results of the analytical post-Newtonian expansion.
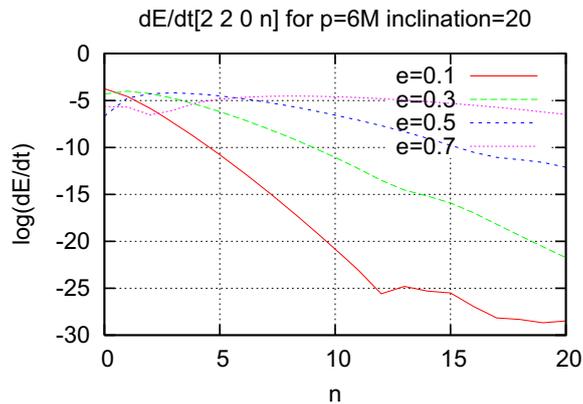
Figure 1: Modal energy fluxes radiated to the infinity in the case of eccentric and inclined orbit around a Kerr black hole. The mode indices are $\ell = M = 2$ and $k = 0$. In this figure, the semilatus rectum is $6M$ and spin of the black hole is $a = 0.9$. Computational time to calculate date for $e = 0.7$ in this figure is about 10 seconds.

References

[1] S. A. Teukolsky, Astrophys. J. **185**, 635(1973).

[2] Y. Mino, Phys. Rev. D **67**, 084027(2003).

[3] S. Drasco and S. A. Hughes, Phys. Rev. D **69**, 044015(2004).

[4] S. Mano, H. Suzuki and E. Takasugi, Prog. Theor. Phys. **95**, 1079(1996).

[5] R. Fujita and H. Tagoshi, Prog. Theor. Phys. **112**, 415(2004),;Prog. Theor. Phys. **113**, 1165(2005).

[6] N. Sago, T. Tanaka, W. Hikida, K. Ganz and H. Nakano, Prog. Theor. Phys. **115**, 873(2006).

Second-Order Quasi-Normal Mode of the Schwarzschild Black Hole

Kunihito Ioka[1] and Hiroyuki Nakano[2]

[1]*Department of Physics, Kyoto University, Kyoto 606-8502, Japan*
[2]*Department of Physics and Astronomy, and Center for Gravitational Wave Astronomy, The University of Texas at Brownsville, Brownsville, Texas 78520, USA*

Abstract

We formulate and calculate the second-order Quasi-Normal Modes (2nd-order QNMs) of the Schwarzschild black hole (BH). We derive a master Zerilli equation for the metric perturbations to 2nd-order and explicitly regularize it at the horizon and spatial infinity. The 2nd-order QNM frequencies are found to be twice the first-order ones, and the gravitational wave amplitude could go up to $\sim 10\%$ of the 1st-order one for the mergers of binary BHs. Since the 2nd-order QNMs always exist, their detections could test the nonlinearity of the general relativity.

1 Introduction

In the 21 century, the gravitational waves (GWs) will open a new eye to the universe and also provide a direct test of the general relativity. One of the most important GW sources are the Quasi-Normal Modes (QNMs) of black holes (BHs) [1]. The QNMs represent perturbations of BH metrics that damp due to the GW emission. It is important to study QNMs because we can determine the mass and angular momentum of BHs by observing the QNM frequencies.

A promising source that excites QNMs is a merger of binary BHs. In these events we may detect QNMs with high Signal-to-Noise Ratio (SNR) (e.g., SNR$\sim 10^5$ for $\sim 10^8 M_\odot$ BH mergers at $\sim$ 1Gpc by LISA) [2] since a large fraction of energy (~ 1–$5\% \times M$) is emitted as GWs of QNMs. (We use the units $c = G = 1$.) Numerical simulations have recently succeeded in calculating the entire phase of BH mergers [3], and found that the $l = 2$, $m = 2$ mode actually dominates, carrying away ~ 1–5% of the initial rest mass of the system.

In the BH mergers the BH deforms appreciably, so that the higher-order QNMs could be prominent. As an order of magnitude estimate, if the GW energy is $\sim 1\% \times M$, i.e.,

$$E_{GW} \sim [\psi^{(1)}]^2/M \sim 1\% \times M, \tag{1}$$

the relative amplitude of the metric perturbation is $\psi^{(1)}/M \sim 10\%$, and hence the 2nd-order amplitude goes up to $[\psi^{(1)}/M]^2 \sim 1\%$ ($\sim 10\%$ of the 1st-order amplitude), which is detectable for high SNR events (i.e., the SNR of the 2nd-order QNMs is ~ 10 if SNR~ 100 for the 1st-order QNMs). The essence of higher-order QNMs has already been discussed in "Mechanics" by Landau & Lifshitz [4] as an anharmonic oscillation. In general, an oscillation with small amplitude x is described by an equation, $\ddot{x} + \omega^2 x = 0$, which gives a solution, $x = a\cos(\omega t + \phi)$. Including the 2nd-order with respect to the amplitude, the equation has a correction, $\ddot{x} + \omega^2 x = -\alpha x^2$, and so the solution is $x = a\cos(\omega t + \phi) + x^{(2)}$ where

$$x^{(2)} = -\frac{\alpha a^2}{2\omega^2} + \frac{\alpha a^2}{6\omega^2}\cos 2\omega t \propto a^2. \tag{2}$$

Here the first term has a frequency $(\omega - \omega)$ and the second term has a frequency $(\omega + \omega)$. The important point is that the 2nd-order oscillation always exists and is completely determined by the 1st-order one. Note also that the frequency does not have a correction at this order.

In this paper we formulate the method to calculate the 2nd-order QNMs of BHs for the first time. As a first step we consider the Schwarzschild BH. We show that the 2nd-order QNMs appear at $\omega^{(2)} = 2\omega^{(1)}$. Since the 2nd-order QNMs always exist, their detections can be used as a new test of the general relativity.

---

[1]E-mail:ioka@tap.scphys.kyoto-u.ac.jp
[2]E-mail:nakano@phys.utb.edu

2   1st-order Zerilli equation

We consider the 2nd-order metric perturbation, $\tilde{g}_{\mu\nu} = g_{\mu\nu} + h^{(1)}_{\mu\nu} + h^{(2)}_{\mu\nu}$, where $g_{\mu\nu}$ is the background Schwarzschild metric. Expanding the Einstein's vacuum equation, we obtain basic equations order by order [5].

For the 1st-order problem we use the Regge-Wheeler-Zerilli formalism [6, 7]. Separating angular variables with tensor harmonics of indices (ℓ, m), the equations decouple to the even (or polar) part with parity $(-1)^\ell$ and the odd (or axial) part with $(-1)^{\ell+1}$. We impose the Regge-Wheeler (RW) gauge conditions. Seven equations for the even part can be reduced to a single Zerilli equation for a function $\psi^{(1)}(t, r)$, and the other three equations for the odd part to a single RW equation.

The Zerilli equation is given by

$$\left[-\frac{\partial^2}{\partial t^2} + \frac{\partial^2}{\partial r_*^2} - V_Z(r) \right] \psi^{(1)}(t, r) = 0, \quad V_Z(r) = \frac{2\lambda^2(\lambda+1)r^3 + 6\lambda^2 M r^2 + 18\lambda M^2 r + 18 M^3}{r^3(\lambda r + 3M)^2} \left(1 - \frac{2M}{r} \right), \quad (3)$$

where $r_* = r + 2M \ln\left(\frac{r}{2M} - 1\right)$ and $\lambda = (\ell-1)(\ell+2)/2$. All 1st-order perturbations can be reconstructed from $\psi^{(1)}(t, r)$. If $\psi^{(1)}(t, r)$ is Fourier analyzed, $\psi^{(1)}(t, r) = \int e^{-i\omega t} \psi^{(1)}_\omega(r) d\omega$, the Zerilli equation gives a one-dimensional scattering problem with a potential. The QNMs are obtained by imposing the boundary conditions with purely ingoing waves $\psi^{(1)}_\omega(r) \sim e^{-i\omega r_*}$ at the horizon and purely outgoing waves $\psi^{(1)}_\omega(r) \sim e^{i\omega r_*}$ at infinity. Such boundary conditions are satisfied at discrete QNM frequencies, which are complex with the real part representing the actual frequency of the oscillation and the imaginary part representing the damping. There is an infinite number of QNMs for each harmonic index ℓ.

In the following we only consider the $\ell = 2, m = \pm 2$ even mode as the 1st-order perturbations because this mode dominates for binary BH mergers. Note that we need to specify m when we consider the 2nd-order perturbations. The first three QNM frequencies for $\ell = 2$ are [11]

$$M\omega^{(1)}_{\ell=2,n=0} = 0.373671684418041835793492000298 - 0.0889623156889356982804609271 8i,$$
$$M\omega^{(1)}_{\ell=2,n=1} = 0.346710996879163439717675359 73 - 0.2739148752912348173495602221 4i,$$
$$M\omega^{(1)}_{\ell=2,n=2} = 0.301053454612366393802003608 88 - 0.4782769832230718099841828307 2i.$$

3   2nd-order Zerilli equation

For the 2nd-order perturbations, we also separate angular variables by tensor harmonics and choose the RW gauge. We introduce a function

$$\chi^{(2)}(t, r) = \frac{r - 2M}{\lambda r + 3M} \left[\frac{r^2}{r - 2M} \frac{\partial K^{(2)}(t, r)}{\partial t} - H^{(2)}_1(t, r) \right], \quad (4)$$

where we note that $\chi^{(1)}(t, r) = \partial \psi^{(1)}(t, r)/\partial t$ is satisfied for the 1st-order perturbations, and the dimensions are $\psi(t, r) \sim O(M)$ and $\chi(t, r) \sim O(M^0)$. All 2nd-order perturbations can be reconstructed from $\chi^{(2)}(t, r)$. The equations for the even mode is reduced to a Zerilli equations with a source term,

$$\left[-\frac{\partial^2}{\partial t^2} + \frac{\partial^2}{\partial r_*^2} - V_Z(r) \right] \chi^{(2)}(t, r) = S(t, r), \quad (5)$$

where the source term $S(t, r)$ is quadratic in the 1st-order perturbations.

We are sufficient to consider the $\ell = 4$, $m = \pm 4$ even mode for the 2nd-order perturbations if the dominant 1st-order perturbations are the $\ell = 2$, $m = \pm 2$ even mode, as shown below. The source term may contain products, $(\ell = 2, m = 2) \times (\ell = 2, m = 2), (\ell = 2, m = -2) \times (\ell = 2, m = -2), (\ell = 2, m = -2) \times (\ell = 2, m = 2)$ and $(\ell = 2, m = 2) \times (\ell = 2, m = -2)$. Then the source term has $m = 0, \pm 4$ modes. Only $\ell = 4$ modes can make $m = \pm 4$. We can find that the $m = 0$ source does not depend on time because of the symmetry $\omega_{l,m} = -\omega_{l,-m}$, and hence this mode is not related to GWs. Note that the source terms for $l = 2$ axisymmetric perturbations are obtained by [8, 9], although these are not dominant terms for binary BH mergers.

4 Regularization

Although it is straightforward to calculate the $\ell = 4$, $m = \pm 4$ source term $S(t,r)$ in terms of $\psi^{(1)}(t,r)$, the raw expression $S(t,r)$ does not behave well at infinity and it is useless for numerical calculations. We can find $S(t,r) \sim O(r^0)$ at infinity because the 1st-order function behaves as

$$\psi^{(1)}(t,r) = \frac{1}{3}F_I''(t-r_*) + \frac{1}{r}F_I'(t-r_*) + \frac{1}{r^2}\left[F_I(t-r_*) - MF_I'(t-r_*)\right] + O(r^{-3}), \tag{6}$$

where $F_I(x)$ is some function. We have to make at least $S(t,r) \sim O(r^{-2})$ [i.e., the same order of the potential $V_Z(r) \sim O(r^{-2})$] by some regularization. At horizon the source behaves well, $S(t,r) \sim O(r^0)$, since

$$\psi^{(1)}(t,r) = F_H'(t+r_*) + \frac{1}{4}\frac{F_H(t+r_*)}{M} + \frac{27}{56}\frac{F_H(t+r_*)}{M^2}(r-2M) + O[(r-2M)^2], \tag{7}$$

where $F_H(x)$ is some function.

We can regularize the source term by using the regularized function,

$$\chi^{(2)}_{reg}(t,r) = \chi^{(2)}(t,r) - \frac{\sqrt{70}}{126\sqrt{\pi}}\frac{(r-2M)^2}{r}\left(\frac{\partial}{\partial r}\psi^{(1)}(t,r)\right)\frac{\partial^2}{\partial r \partial t}\psi^{(1)}(t,r), \tag{8}$$

which satisfies the Zerilli equation (5) with a well-behaved source term, i.e., $S_{reg}(t,r) \sim O(r^{-2})$ at infinity and $S_{reg}(t,r) \sim O[(r-2M)]$ at horizon. Note that such a regularization is not unique, and for example we can replace $\partial/\partial r$ with $\partial/\partial t$ in Eq. (8). The regularization is equivalent to adding quadratic terms in the 1st-order gauge invariant function to the 2nd-order gauge invariant function, so that it preserves the gauge invariance [10].

The explicit expression for the regularized source term is given by

$$
\begin{aligned}
S_{reg}(t,r) = \frac{r-2M}{42}\frac{\sqrt{70}}{\sqrt{\pi}}\Bigg\{ &\frac{1}{r^6\,(M+3r)^2\,(2r+3M)^3}\Big(-72\,r^8 - 3936\,r^7M - 2316\,r^6M^2 \\
+ \ & 2030\,r^5M^3 + 7744\,r^4M^4 + 9512\,r^3M^5 + 3540\,r^2M^6 + 1119\,rM^7 + 144\,M^8\Big)\,\psi'\dot\psi \\
- \ & \frac{1}{r^3\,(M+3r)^2\,(2r+3M)^2\,(-r+2M)^2}\Big(48\,M^7 + 237\,rM^6 - 77\,r^2M^5 - 120\,r^3M^4 \\
+ \ & 771\,r^4M^3 + 872\,r^5M^2 - 344\,r^6M - 24\,r^7\Big)\,\ddot\psi\dot\psi \\
- \ & \frac{\left(-66\,r^4 + 106\,Mr^3 + 220\,M^2r^2 + 156\,M^3r + 45\,M^4\right)}{r\,(M+3r)^2\,(2r+3M)\,(-r+2M)}\ddot\psi'\psi \\
+ \ & \frac{3}{r^7\,(2r+3M)^4\,(M+3r)^2}\Big(-2160\,r^9 - 11760\,r^8M - 30560\,r^7M^2 - 41124\,r^6M^3 \\
- \ & 31596\,r^5M^4 - 11630\,r^4M^5 + 1296\,r^3M^6 + 4182\,r^2M^7 + 1341\,rM^8 + 144\,M^9\Big)\,\psi\dot\psi \\
- \ & \frac{1}{r^5\,(M+3r)^2\,(2r+3M)^2}\Big(-228\,r^7 - 8\,r^6M + 370\,r^5M^2 - 142\,r^4M^3 + 384\,r^3M^4 \\
+ \ & 514\,r^2M^5 + 273\,rM^6 + 48\,M^7\Big)\,\dot\psi'\psi' \\
+ \ & \frac{\left(24\,M^5 + 127\,M^4r + 458\,M^3r^2 + 664\,M^2r^3 + 318\,Mr^4 - 198\,r^5\right)}{3r^2\,(M+3r)^2\,(2r+3M)\,(-r+2M)}\dddot\psi\psi' \\
+ \ & \frac{2\,(-r+2M)\,M^2}{3\,(M+3r)^2\,r^2}\ddot\psi\dot\psi' - \frac{(4M+7r)}{3r}\ddot\psi'\dot\psi' + \frac{(7r+4M)\,r}{3\,(r-2M)^2}\ddot\psi\,\ddot\psi \\
+ \ & \frac{1}{r^6\,(M+3r)^2\,(2r+3M)^3}\Big(-216\,r^8 - 4296\,r^7M - 1992\,r^6M^2 + 3488\,r^5M^3 \\
+ \ & 8716\,r^4M^4 + 9512\,r^3M^5 + 3540\,r^2M^6 + 1119\,rM^7 + 144\,M^8\Big)\,\psi\dot\psi' \\
- \ & \frac{\left(24\,M^6 + 171\,rM^5 + 524\,r^2M^4 + 730\,r^3M^3 + 674\,r^4M^2 + 636\,r^5M + 252\,r^6\right)}{r^3\,(M+3r)^2\,(2r+3M)^2\,(-r+2M)}\psi\,\dddot\psi\Bigg\},
\end{aligned}
\tag{9}
$$

where $\dot{\psi} = \partial\psi^{(1)}(t,r)/\partial t$, $\psi' = \partial\psi^{(1)}(t,r)/\partial r$ etc. We can find that the source term is quadratic in $\psi^{(1)}(t,r) \sim e^{-i\omega t}$ and hence the 2nd-order perturbations have a form $\chi_{reg}^{(2)} \sim e^{-2i\omega t}$. Therefore the 2nd-order QNMs have frequencies at $\omega^{(2)} = 2\omega^{(1)}$. Since the 2nd-order frequencies are not different from the 1st-order ones, we can in principle identify the 2nd-order QNMs.

5   Discussions

With the regularization in Eqs. (8) and (9) and Fourier expansions, the 2nd-order Zerilli equation (5) provides a two-point boundary value problem. However a simple numerical integration like Runge-Kutta method fails because the outgoing waves $\sim e^{-i\omega(t-r_*)}$ diverge at infinity and the ingoing waves $\sim e^{-i\omega(t+r_*)}$ diverge at horizon since Im $\omega < 0$ (QNMs damp). Furthermore, since the irregular singularity is at $r = \infty$, an expansion around $r = \infty$ is not well-behaved. To overcome these problems, we modify the Leaver's method, which transforms the RW's differential equation to algebraic recurrence equations for the 1st-order [11]. (We use a Chandrasekhar transformation to make the Zerilli equations to the RW ones [12].) For the 2nd-order case, the recurrence equations have source terms, which we first calculate algebraically by Maple or Mathematica and then evaluate numerically. Once the source terms are obtained numerically we can solve the recurrence equations. More details will be presented elsewhere.

The solutions for the Zerilli equations do not directly give us the observed GW amplitude since the RW gauge is not asymptotically flat (AF). In order to calculate the observed GW amplitude we have to make a transformation from the RW gauge to a gauge that is AF. This is straightforward and will be presented elsewhere.

In order to verify that the 2nd-order QNMs actually exist, we have to not only demonstrate numerical calculations of 2nd-order QNMs directly but also formulate a mathematically rigorous definition of 2nd-order QNMs [1]. Direct numerical calculations of 2nd-order QNMs may be challenging because the mesh size should be less than $\sim 1\%M$ to resolve $\sim 1\%$ metric perturbations. This requires more than $(10^3)^3$ meshes if we use a simulation box of size $> (10M)^3$ to cover several GW lengths.

We also have to show that the 2nd-order QNMs can be actually detected when the 1st-order QNMs are present in the GW analysis. A correlation between the 1st and 2nd-order QNMs may reduce the detected SNR. Future problems include the odd mode case, the Kerr BH case, and the 3rd-order QNM case. The odd mode appears when BHs have spin before mergers. A correction to the QNM frequencies will appear at the 3rd-order according to the analysis of an anharmonic oscillation [4].

References

[1] K. D. Kokkotas and B. G. Schmidt, Living Rev. Relativity 2, 2 (1999).

[2] É. É. Flanagan and S. A. Hughes, Phys. Rev. D 57, 4535 (1998).

[3] F. Pretorius, Phys. Rev. Lett. 95, 121101 (2005).

[4] L. D. Landau and E. M. Lifshitz, Mechanics (Butterworth, Heinemann, Oxford, 1976), 3rd ed.

[5] K. Nakamura, gr-qc/0612040

[6] T. Regge and J. Wheeler, Phys. Rev. 108, 1063 (1957).

[7] F. J. Zerilli, Phys. Rev. D 2, 2141 (1970).

[8] R. J. Gleiser, C. O. Nicasio, R. H. Price, and J. Pullin, Phys. Rep. 325, 41 (2000).

[9] C. O. Nicasio, R. Gleiser, and J. Pullin, Gen. Relativ. Gravit. 32, 2021 (2000)

[10] A. Garat and R. H. Price, Phys. Rev. D 61, 044006 (2000)

[11] E. W. Leaver, Proc. R. Soc. A 402, 285 (1985).

[12] S. Chandrasekhar, Proc. R. Soc. A 343, 289 (1975).

Quasinormal ringing of acoustic black holes

Satoshi Okuzumi[1] and Masa-aki Sakagami[2]

Graduate School of Human and Environmental Studies, Kyoto University, Kyoto, 606-8501, Japan

Abstract

The quasinormal modes of acoustic black holes in Laval nozzles are discussed. The equation for sound waves in transonic flow is rewritten into a Schrödinger-type equation with a potential barrier, and quasinormal frequencies are calculated by the WKB method. The results of numerical simulations show that the quasinormal modes are excited when the background flow in the nozzle is externally perturbed, as well as in the real black hole case. Also, we discuss how the quasinormal modes change when the outgoing waves are partially reflected at the boundary. It is found that the partially reflected quasinormal modes damp more slowly than the ordinary ones. Using this fact, we propose an experimental setup for detecting the quasinormal ringing of an acoustic black hole efficiently.

1 Introduction

When the geometry around a black hole is slightly perturbed, a characteristic ringdown wave is emitted. This kind of phenomenon is known as *quasinormal ringing*, which is expressed as a superposition of *quasinormal modes*, The central frequencies and the damping times of the quasinormal modes are determined by the geometry around the black hole, and thus the gravitational quasinormal ringing of a black hole is expected to play the important role of connecting gravitational-wave observation to astronomy.

Although quasinormal modes are themselves linear perturbations, they are in many cases excited after a *nonlinear* oscillation of a black hole, such as the black hole formation by the coalescence of the binary neutron stars. Therefore, when we want to study the excitation of the quasinormal modes in such a complicated situation, we have to resort to numerical relativity, which needs extremely powerful computatioal resources.

Here we present an alternative way for studying the quasinormal ringing of black holes by using a transonic fluid flow, called an *acoustic black hole* [2, 5]. In a transonic flow, sound waves can propagate from the subsonic region to the supersonic region, but cannot in the opposite way. Therefore, the sonic point of a transonic flow can be considered as the "event horizon" for sound waves, and the supersonic region as the "black hole region". Furthurmore, it is shown that the wave equation for a sound wave in an inhomogeneous flow is precisely equivalent to the wave equation for a massless scalar field in a curved spacetime [2]. This implies that an acoustic black hole has the quasinormal modes, which makes it possible for us to study the quasinormal ringing of black holes *in laboratories*.

In this paper, we show some results of out numerical simulations to prove that the quasinormal ringing of sounds occurs actually , and propose a feasible way to demonstrate QN ringing in a laboratory. For future experiments in laboratories, we treat one of the most accessible models of acoustic black holes: transonic airflow in a *L*aval nozzle [3]. A Laval nozzle is a wind tunnel that is pinched in the middle, and makes it possible to create a stable transonic flow in a laboratory.

A quasinormal mode is characterized by a complex frequency (called *q*uasinormal frequency) ω_Q, or equivalently, a pair of the central frequency $f_c \equiv \mathrm{Re}(\omega_Q)/2\pi$ and the quality factor $Q \equiv |\mathrm{Re}(\omega_Q)/2\mathrm{Im}(\omega_Q)|$. The quality factor is a quantity that is propotional to the number of cycles of the oscillation within the damping time. In experiments, damping oscillation like quasinormal ringing is inevitably buried in noise within a few damping times. Therefore, in order to detect quasinormal ringing efficiently, it is important to design a Laval nozzle which gives large quality factor.

We also discuss the quasinormal modes when the outgoing waves are *p*artially reflected at the boundary. In this situation, the quasinormal modes are found to decay *m*ore slowly than in the case where the reclection at the boundary does not occur.

---

[1]E-mail:okuzumi_phys@ybb.ne.jp

[2]E-mail:sakagami@grav.mbox.media.kyoto-u.ac.jp

K	α	ω_Q $[c_{s0}/L]$		
		(1st WKB)	(2nd WKB)	(3rd WKB)
2	0.1	$2.10 - 0.85i$	$1.78 - 1.01i$	$1.73 - 0.91i$
	0.03	$3.00 - 0.99i$	$2.65 - 1.11i$	$2.61 - 1.02i$
	0.01	$4.00 - 1.20i$	$3.57 - 1.34i$	$3.54 - 1.26i$
	0.003	$5.44 - 1.57i$	$4.86 - 1.76i$	$4.83 - 1.68i$
4	0.1	$3.36 - 1.25i$	$3.09 - 1.36i$	$3.15 - 1.48i$
	0.03	$4.24 - 1.14i$	$4.10 - 1.17i$	$4.12 - 1.23i$
	0.01	$5.02 - 1.10i$	$4.86 - 1.13i$	$4.85 - 1.09i$
	0.003	$5.91 - 1.15i$	$5.69 - 1.20i$	$5.66 - 1.09i$

Table 1: The quasinormal frequency ω_Q of the least-damped mode for different Laval nozzles, calculated by the third order WKB formula [7]. To show the convergence, the first lower order WKB values are also shown.

2   Quasinormal Modes of Acoustic Black Holes in Laval Nozzles

In what follows, we assume that flow in the nozzles is isentropic and one-dimensional. Thus, the wave equation for sound reads

$$\left[\left(\partial_t + \partial_x v\right)\frac{\rho A}{c_s^2}\left(\partial_t + v\partial_x\right) - \partial_x(\rho A\partial_x)\right]\phi = 0 \ , \tag{1}$$

where ρ, v, c_s, A, ϕ are the background density and fluid velocity, the speed of sound, the cross section of the nozzle, and the vecocity potential perturbation. Note that c_s depends on the background state, and is therefore a function of x.

Assuming steady background, the wave equation of sound (1) can be rewritten into the form of Eq. (2):

$$\left[\frac{d^2}{dx^{*2}} + \left(\frac{\omega}{c_{s0}}\right)^2 - V(x^*)\right]H_\omega = 0, \qquad V(x^*) = \frac{1}{g^2}\left[\frac{g}{2}\frac{d^2g}{dx^{*2}} - \frac{1}{4}\left(\frac{dg}{dx^*}\right)^2\right], \tag{2}$$

where $x^* = c_{s0}\int\frac{dx}{c_s(1-M^2)}$, $M = v/c_s$, $g = \rho A/c_s$, $H_\omega(x^*) = g^{\frac{1}{2}}\ e^{i\omega F(x)}\int e^{i\omega t}\phi(t,x)dt$, and $F(x) = \int\frac{v\,dx}{c_s^2(1-M^2)}$. Here we have also introduced the stagnation speed of sound c_{s0}, which is constant over the isentropic region of the flow.

In this study, we consider a family of Laval nozzles which have the following form:

$$A(x) = \pi\,r(x)^2 \ , \tag{3}$$
$$r(x) = r_\infty - r_\infty(1-\alpha)\exp[-(x/2L)^{2K}] \ , \tag{4}$$

where K is a positive integer and $\alpha \equiv r(0)/r_\infty \in (0,1)$.

Having obtained the form of the potential $V(x^*)$, we can compute quasinormal frequencies by solving the Schrödinger-type wave equation (2) under the outgoing boundary conditions. In this study, we adopt the WKB approach, which was originally proposed by Schutz and Will [6] and has been developed in some works [7, 8].

Table 1 shows the least-damped quasinormal frequency ω_Q for Laval nozzles with different (K, α) up to the 3rd order WKB values. We have found that the WKB method converge well for $K > 1$. It is noted that $f_c \sim c_{s0}/L$ and $1 \lesssim Q \lesssim 3$.

3   Numerical Simulations

In the case of astrophysical black holes, quasinormal ringing occurs when a black hole is formed or when a test particle falls into a black hole. Hence, let us consider analogous situations for our acoustic black holes: (i)*acoustic black hole formation* and (ii)*weak-shock infall*. In simulations of type (i), the initial
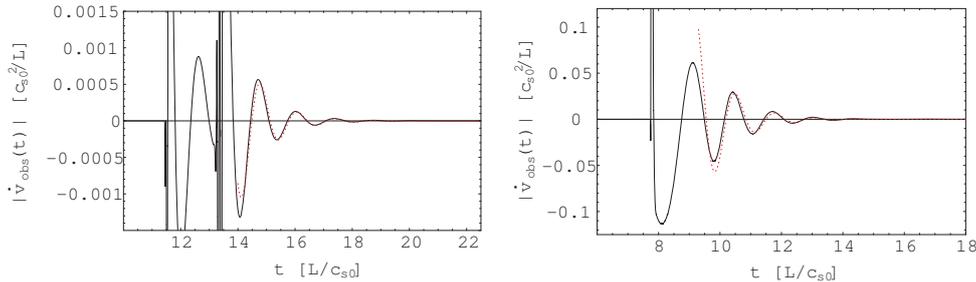
Figure 1: The numerical waveforms $\dot{v}(t)$ obtained by numerical simulations of acoustic black hole formation (left) and weak-shock infall (right). In both simulations, the nozzle parameters are set to $(K, \alpha) = (4, 0.01)$, which give the peak of the potential $V(x^*)$ at $x = 0.632$, and the observer is located at $x = 2.0$. Each waveform is compared to the analytic waveform of the damping oscillaton (dotted line) with the 3rd WKB value of the least-damped quasinormal mode frequency, $\omega_{\mathrm{Q}} = 3.54 - 1.26i$.

state of the flow in the nozzle is set to be steady and homogeneous. At time $t = 0$, a sufficiently large pressure difference is set between both ends of the nozzle, and the fluid in the nozzle starts to flow. In type (ii), the initial state is set to stationary transonic flow. At $t = 0$, the upsteream pressure is slightly raised, and a weak shock starts to fall into the sonic horizon. In both cases, we observe sound waves emitted from the potential barrier at a fixed position until the flow sufficiently settles down into a stationary transonic state.

In Fig. 1(a), the waveform observed in a numerical simulation of type (i) is plotted. For $t \lesssim 11L/c_{s0}$, nonlinear oscillation dominates, which corresponds to the "merger phase" oscillation in real black hole formation. At $t \simeq 11L/c_{s0}$, the background state begins to settle down into the statonary transonic state, and the oscillation enters into the ringdown phase. In this phase, the numerical waveform agrees in good accuracy with the analytic waveform of the least-damped quasinormal mode obtained by the third order WKB analysis. We have also performed some simulations of type (ii), and obtained the similar results, except that the nonlinear phase does not exist in the case (see Fig. 1(b)).

4   Effect of Reflection at the Boundary

It turns out from our numerical simulations that the quality factor for the quasinormal ringing of our acoustic black holes is typically $1 \lesssim Q \lesssim 2$. This means that the ringing oscillates by only a few cycles before it is substantially buried in noise. Thus, if one wants to observe it in experiments, this feature is quite unfavorable.

Now let us consider that the upstream tank has a finite length and the outgoing waves are *partially reflected* at the boundary wall of the tank. The existence of the reflection at the boundary effectively generalize the boundary condition for quasinormal modes. Assuming the boundary is located at $x = x_c$, the generalized boundary conditions are

$$H_\omega(x^*) \sim \qquad\qquad e^{-i\frac{\omega}{c_{s0}}x^*}, \qquad\qquad x^* \to -\infty, \tag{5}$$

$$H_\omega(x^*) \sim \quad e^{+i\frac{\omega}{c_{s0}}(x^*-x_c^*)} + \mathcal{R}_\omega\, e^{-i\frac{\omega}{c_{s0}}(x^*-x_c^*)}, \quad x^* \to x_c^*, \tag{6}$$

where $\mathcal{R}_\omega \in [-1, 1]$ is the reflection coefficient of the boundary wall. Sicne the solutions of the wave equation (2) with these boundary conditions are in a narrow sense no more the quasinormal modes, we shall refer to them as the *Partially Reflected QuasioNormal Modes* (PRQNMs).

Under the third order WKB approximation, the frequencies of PRQNMs ω_{PQ} are given by the solutions of simultaneous equations

$$\frac{(2\pi)^{1/2}}{R(\nu)^2\Gamma(-\nu)} = \mathcal{R}_\omega \exp[i\pi\nu + 2i\frac{\omega}{c_{s0}}\Delta_\omega], \tag{7}$$

$$\left(\frac{\omega}{c_{s0}}\right)^2 = V(x_0^*) + \left(-2V''(x_0^*)\right)^{\frac{1}{2}}\tilde{\Lambda}(\nu) - i\left(\nu + \frac{1}{2}\right)\left(-2V''(x_0^*)\right)^{\frac{1}{2}}(1 + \tilde{\Omega}(\nu)), \tag{8}$$

$\mathcal{R}$	$\omega_{\mathrm{PQ}}\ [c_{s0}/L]$	$\mathcal{R}$	$\omega_{\mathrm{PQ}}\ [c_{s0}/L]$
0	$3.54 - 1.26i$	0	$3.54 - 1.26i$
10^{-4}	$3.46 - 1.20i$	-10^{-4}	$3.64 - 1.22i$
10^{-3}	$3.39 - 1.01i$	-10^{-3}	$3.72 - 1.01i$
0.01	$3.35 - 0.73i$	-0.01	$3.76 - 0.73i$
0.1	$3.34 - 0.41i$	-0.1	$3.76 - 0.42i$
1.0	$3.38 - 0.05i$	-1.0	$3.72 - 0.14i$

Table 2: The least-damped PRQNMs ω_{PQ} for nozzle parameters $(K, \alpha) = (2, 0.01)$ and different values of $\mathcal{R}$, calculated by using the 3rd WKB formulae, Eqs. (7) and (8). The position of the half mirror, or contact surface, is set to $x_c = 3.0$.

where $\Gamma(-\nu)$ is the Gamma function, and Δ_ω is the distance between the half mirror and the classical turning point on the potential barrier. The functions $R(\nu)$, $\tilde{\Lambda}(\nu)$ and $\tilde{\Omega}(\nu)$ are shown in [7]. Note that, for $\mathcal{R}_\omega \equiv 0$, Eq. (7) gives $\nu = 0, 1, 2, ...$, which results the ordinary quasinormal mode case.

Table 2 shows how the frequency of the least-damped PRQNM ω_{PQ} deviates from the ordinary quasinormal frequency ω_{PQ} depending on $\mathcal{R}$. It is clear that $\mathrm{Im}(\omega_{\mathrm{PQ}})$ decreases drastically as $\mathcal{R}$ increases, although $\mathrm{Re}(\omega_{\mathrm{Q}})$ does not vary greatly with $\mathcal{R}$. This means that the reflection at the boundary *enhances* the quality factor of the quasinormal ringing. This fact is intuitively understandable if one notes that $\mathrm{Im}(\omega_{\mathrm{Q}})$ represents the energy dissipation rate, while $\mathrm{Re}(\omega_{\mathrm{Q}})$ characterizes the curvature of the background geometry. A partially-reflecting boundary wall suppress the dissipation of wave energy to infinity, but does not directly deform the background geometry.

5 Conclusion

We have analyzed the quasinormal modes of transonic fluid flow in Laval nozzles by WKB calculations and numerical simulations, and shown that the quasinormal ringing does arise in responce to some external perturbation. We have also argued the effect of a boundary wall which reflects the outgoing waves on quasinormal modes, and found that the existence of such a wall enhances the damping time of the ringing.

The results of our numerical study suggests a effective experimental setup for detecting the quasinormal ringing of transonic airflow in a laboratory. First, prepare a Laval nozzle and an air tank which is filled with sufficiently high-pressure air, and connect them with a shock tube. Then, remove a diaphragm in the shock tube to generate a transonic flow in the nozzle, and observe the sound waves coming out of the nozzle until the background flow sufficiently settles down. In this situation, the damping time of the quasinormal ringing will be enhanced in the upstream air tank, which will make the detection of the ringdown wave easier.

References

[1] S. W. Hawking, Nature **248**, 30 (1974); Commun. Math. Phys. **43**, 199 (1975).

[2] W. G. Unruh, Phys. Rev. Lett. **46**, 1351 (1981).

[3] M. a. Sakagami and A. Ohashi, Prog. Theor. Phys. **107**, 1267 (2002).

[4] M. Visser, Class. Quant. Grav. **15**, 1767 (1998).

[5] B. F. Schutz and C. M. Will, Astrophys. J. **291**, L33 (1985).

[6] S. Iyer and C. M. Will, Phys. Rev. D **35**, 3621 (1987); S. Iyer, Phys. Rev. D **35**, 3632 (1987).

[7] R. A. Konoplya, Phys. Rev. D **68**, 024018 (2003); J. Phys. Stud. **8**, 93 (2004).

Non-existence of self-similar black hole in a universe with a scalar field or quintessence

Tomohiro Harada[1]

Department of Physics, Rikkyo University, Toshima, Tokyo 171-8501, Japan

Abstract

We consider the growth of black holes due to mass accretion in a universe containing a scalar field or a quintessence field. The latter is especially motivated by the currently accelerating universe which is strongly suggested by several cosmological observations. We take the cosmological expansion into account in general relativity. We show that there is no self-similar black hole solution surrounded by an exact or asymptotically flat Friedmann background containing a massless scalar field. This applies even if there is a scalar potential, as in the quintessence scenario. This extends the result previously found in the perfect fluid case. It also contradicts recent claims that such black holes can grow appreciably by accreting quintessence.

1 Introduction

For a stationary black hole in an asymptotically flat vacuum spacetime in the Einsteinian gravity, the spacetime is uniquely given by the Kerr solution. This is called the black hole uniqueness theorem. This means that under these assumptions, the properties of the Kerr solution must be the properties of general black holes. However, our universe is expanding and filled with matter fields. Hence, realistic black holes would not be in vacuum. They exist in the expanding universe and hence are not asymptotically flat. Moreover, they could accrete surrounding mass and hence grow in time. The Kerr solution will give a very good approximation in some cases but not in the other. Here, we focus on the effects of the expanding universe filled with matter fields on black hole dynamics. We would call black holes in an expanding universe *cosmological black holes* to put an emphasis on this particular aspect of astrophysical black holes.

Among cosmological black holes, *primordial black holes* have been intensively studied because of their important roles as probes into the early universe, high energy physics, quantum gravity and relativistic gravity in the expanding universe. See a recent review [2] for details and references therein. It should be noted that the primordial black holes would have been born with the mass of the same order as the mass contained within the cosmological horizon at the formation epoch.

2 Accretion onto cosmological black holes

The problem of accretion rate or growth rate of black holes in the expanding universe was studied about forty years ago [3]. This discussion based on the Newtonian gravity was recently refined and generalised [4]. The mass growth rate is given by

$$\frac{dM}{dt} = 4\pi\alpha r_{\rm A}^2 c_{\rm s}\rho_{\rm FRW}(t) \simeq \frac{GM^2}{c^3 t^2},\tag{1}$$

where $r_{\rm A} \equiv GM/c_{\rm s}^2$ is the accretion radius and α is a constant of order unity which depends on the equation of state. This equation can be easily integrated. Then, we can find a critical mass of the same order as the horizon mass, which divides the evolution of black hole mass qualitatively. If the initial mass is smaller than this critical value, the accretion soon becomes insignificant. If the initial mass is equal to the critical value, the solution is self-similar and the mass of the black hole grows in proportion to the cosmological time due to the effective accretion. If the initial mass is larger than the critical value, the

---

[1]E-mail:harada@rikkyo.ac.jp

mass accretion is so significant that the mass of the black hole diverges in a finite time, which would be unphysical. It should be noted that the existence of self-similar solution plays a key role for this analysis.

The general relativistic numerical simulation strongly suggests that the growth of black holes in the universe containing a scalar field is not significant [5]. On the other hand, the above quasi-Newtonian discussion of black hole growth has been applied to a quintessence field [6], a scalar field which slowly roles down its flat potential and enables the universe to accelerate due to its large negative pressure. Then, based on the equation analogous to Eq. (1), it has been claimed that the accretion onto black holes could be so significant in the quintessence-dominated era preceding the radiation-dominated era that primordial black holes may provide the seeds for the formation of supermassive black holes in the galactic nuclei.

3 Non-existence of cosmological self-similar black holes

Indeed, it was shown that there is no self-similar solution of the Einstein field equation which contains a black hole event horizon in the expanding universe with a dust, radiation fluid [7], a perfect fluid for $p = k\rho$ $(0 < k < 1)$ [8] or a stiff fluid $(p = \rho)$ [9]. However, it has not yet been clear whether a self-similar black hole can exist or not in an accelerating universe. Because the accelerating universe is strongly favoured by the recent observational data, it would be very important to answer this question.

The self-similar (homothetic) spacetime is defined by the existence of a vector field ξ satisfying

$$\mathcal{L}_\xi g_{ab} = 2g_{ab}. \tag{2}$$

We here consider a scalar field as a matter field because it very often appears in many aspects of modern cosmology and also provides one of the simplest and physically reasonable model to accelerate the universe. It is remarkable that, from self-similarity assumption, the scalar field is restricted to be massless or with a potential of the following exponential form:

$$V(\phi) = V_0 e^{\sqrt{8\pi}\lambda\phi}, \tag{3}$$

which is parametrised by λ. Here we assume the potential is not negative. For the flat Friedmann solution, the scalar field with the exponential potential can accelerate the universe if $0 < \lambda^2 < 2$ and hence can be regarded as a quintessence model.

With the assumption of self-similarity and spherical symmetry, the line element is given in the form:

$$ds^2 = -g(r/v)\bar{g}(r/v)dv^2 + 2g(r/v)dvdr + r^2(d\theta^2 + \sin^2\theta d\phi^2), \tag{4}$$

in the Bondi coordinates. A similarity surface Σ is defined as a surface on which r/v=const. A similarity horizon is defined as a null similarity surface on which ξ is also null. A similarity horizon can be identified with an event horizon or a particle horizon. Figure 1 gives the schematic diagram of a possible self-similar black hole embedded into the flat Friedmann universe.

The Einstein equation reduces to the set of ordinary differential equations (ODEs) with respect to $\xi = \ln(r/|v|)$. The characteristic surfaces correspond to the singular points of the ODEs, as do in the case of a perfect fluid of $p = k\rho$ $(0 < k < 1)$. They are classified into nodes, saddles and foci as equilibrium points in dynamical systems theory. Figure 2 illustrates a node and a saddle. The uniqueness may break down at the singular points. The non-existence of black hole solution even with an exact Friedmann exterior is therefore highly nontrivial. Moreover, the singular points coincide with similarity horizons for the scalar field case.

We have proved the following non-existence theorem.

Theorem 1 *Let a spherically symmetric self-similar spacetime with a scalar field satisfy one of the following two conditions: (a) it coincides with the flat Friedmann solution outside some finite radius; (b) it is asymptotic to the decelerating Friedmann solution at spatial infinity. Then it has no black hole event horizon.*

The sketch of the proof is the following. For the massless case and the decelerating potential case, the Friedmann particle horizon corresponds to a nodal point. In this case, we can show the monotonicity of
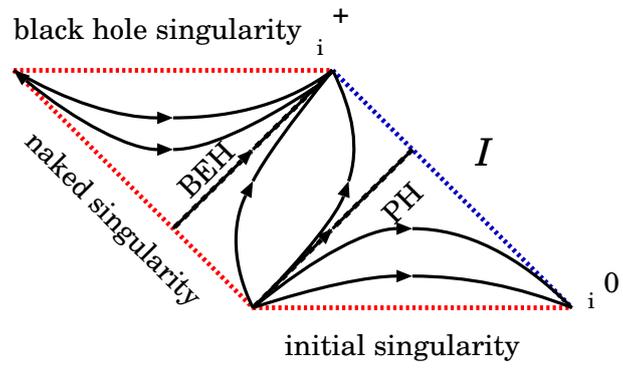
Figure 1: The schematic diagram of a possible cosmological self-similar black hole.
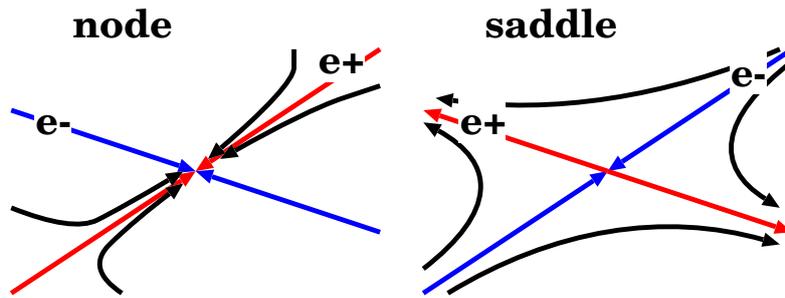
Figure 2: Node and saddle.
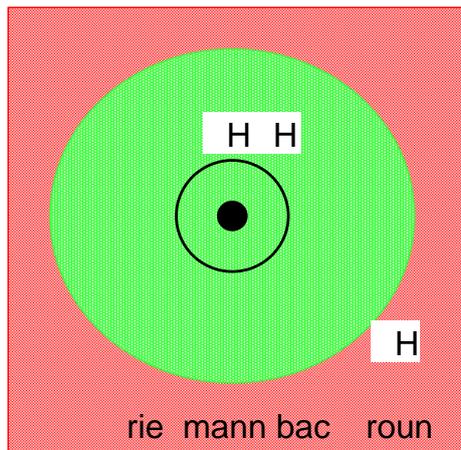
Figure 3: A black hole embedded in the Friedmann universe.

z by investigating the ODEs. For the accelerating potential case, the flat Friedmann universe does not have a particle horizon but a cosmological event horizon. This cosmological event horizon corresponds to a saddle point. We can match only the Friedmann solution or the pure shock-wave solution with the Friedmann exterior. The shock-wave solution cannot be an interior solution. See [1] for the details of the proof.

4   Summary

There is no self-similar black hole in a flat Friedmann universe containing a scalar field or quintessence field. This strongly suggests that the accretion onto black holes in the quintessence-dominant phase is not very effective even for horizon-scale black holes. However, recall that we have here adopted two nontrivial assumptions. One is that a scalar field is responsible for the acceleration of the universe and the other is that the universe is described exactly by the flat Friedmann solution outside some finite radius for the accelerating case. It would be interesting to relax these assumptions and see whether the conclusion changes or not. Finally, it should be cautioned that there could exist a self-similar black hole in a very contrived situation where a massless scalar field is suddenly converted to a null dust [9]. This means that it is impossible to prove non-existence with energy conditions alone.

References

[1] T. Harada, H. Maeda and B. J. Carr, Phys. Rev. D**74**, 024024 (2006).

[2] B. J. Carr, to appear in the Proceedings of "Inflating Horizon of Particle Astrophysics and Cosmology", (Universal Academy Press Inc and Yamada Science Foundation, Tokyo, 2005), *Preprint* astro-ph/0511743.

[3] Y. B. Zeldovich and I. D. Novikov Sov. Astron. **10**, 602 (1967).

[4] T. Harada and B. J. Carr, Phys. Rev. D**71**, 104009 (2005).

[5] T. Harada and B. J. Carr, Phys. Rev. D**71**, 104010 (2005).

[6] R. Bean and J. Magueijo, Phys. Rev. D**66**, 063505 (2002).

[7] B. J. Carr and S. W. Hawking, Mon. Not. R. Astron. Soc. **168**, 339 (1974).

[8] B. J. Carr, Ph.D. thesis, Cambridge University (1976).

[9] G. V. Bicknell and R. N. Henriksen, Astrophys. J. **225**, 237 (1978).

Topology Change of Black Holes

Daisuke Ida[1] and Masaru Siino[2]

[1]*Department of Physics, Gakushuin University, Tokyo 171–8588, Japan*
[2]*Department of Physics, Tokyo Institute of Technology, Tokyo 152–8550, Japan*

Abstract

The topological structure of the event horizon has been considered in terms of the Morse theory. The elementary process of topology changes can be understood as a handle attachment. It has been found that there are certain constraints on the black hole topology changes.

The black holes in space-time dimensions ≥ 5 have rich topological structure. The well-known results by Hawking for topology of black holes in four-dimensional space-time states that the apparent horizon or the stationary event horizon is necessarily diffeomorphic with 2-sphere. This follows from the fact that the total curvature which is the integral of the intrinsic scalar curvature over the horizon becomes positive under the dominant energy condition and from the Gauss-Bonnet theorem. On the other hand, an apparent horizon in higher dimensional space-time may not be topological sphere, because one fails to apply Gauss-Bonnet theorem there. Nevertheless, the positivity of the total curvature of the horizon still holds. This puts a certain topological restrictions on the black hole topology, though they are rather week ones. For example, the apparent horizon in five-dimensional space-time can be finite connected sums of copies of S^3/Γ and copies of $S^2 \times S^1$. In fact, the exact solutions representing black hole space-time possessing a horizon of nonspherical topology are recently found in five-dimensional general relativity. When such black holes with nontrivial topology are regarded as formed in the course of gravitational collapse, one naturally asks the topological structure of black holes. Our purpose here is to understand the time evolution of topology of event horizons in general settings.

Our approach is to utilize the Morse theory in differential topology. The Morse theory is useful in understanding the topology of smooth manifold. The basic tool is the smooth function on the differentiable manifold. The event horizon however is not differentiable manifold but has a cusp structure at the past end points of the null geodesic generators of the horizon. Hence we first smoothen the cusp. Then, the time function which is assumed to exist plays a role of the smooth function on the smoothed event horizon. According to the Morse theory, the topology change of the event horizon can be then decomposed into elementary processes called handle-attachment. Starting with spherical horizon, one adds several handles each characterized by the index which is an integer ranging from 0 to n the dimension of the smoothed horizon as differentiable manifold.

Our main result is that not all handle-attachment is possible, but there are three types of restrictions as follows:

1. The handle attachment of index n does not occur.

2. The domain of outer communication has only one connected component at each time. Hence, it does not bifurcate nor collide.

3. The handle is classified into either black or nonblack, and the only former is realized.

The detail will appear in forthcomming paper.

References

[1] D. Ida and M. Siino, "Topology Change of Black Holes." in preperation.

---

[1]E-mail:daisuke.ida@gakushuin.ac.jp
[2]E-mail:msiino@th.phys.titech.ac.jp

Nonequilibrium Phenomena in Black Hole Evaporation

Hiromi Saida[1]

Department of Physics, Daido Institute of Technology, Minami-ku, Nagoya 457–8530, Japan

Abstract

While the black hole formation (gravitational collapse) has been studied well in detail, the black hole evaporation has not been studied in detail. When a black hole evaporates, there arises a net energy flow from black hole into its outside environment. The existence of energy flow means that the thermodynamic state of the whole system, which consists of a black hole and its environment, is in a nonequilibrium state. Therefore, in order to study the detail of evaporation process, the nonequilibrium effects of the energy flow should be taken into account. Using the nonequilibrium thermodynamics which has been formulated recently, this report shows the following: (1) the negative heat capacity of black hole gives the physical essence of the generalized 2nd law of black hole thermodynamics, (2) nonequilibrium effects of the energy flow tends to make the time scale of black hole evaporation be shorter, and consequently specific nonequilibrium phenomena are suggested.

This report is a brief summary of three papers [4], [5] and [6].

1 Challenge to nonequilibrium nature of black hole evaporation

The black hole evaporation is one of interesting phenomena in black hole physics. Because a direct treatment of time evolution of the evaporation process suffers from mathematical and conceptual difficulties (e.g. dynamical Einstein eq., quantum expectation value of stress tensor, definition of dynamical horizon and so on), an approach based on the black hole thermodynamics [1] is useful. There are two important issues of black hole evaporation from thermodynamic viewpoint; the generalized 2nd law (GSL) [2] and the black hole phase transition [3] (black hole evaporation in a heat bath). Although the black hole evaporation is a dynamical/nonequilibrium process (see abstract), the existing approaches to those issues have been based on equilibrium thermodynamics. Because of the lack of complete nonequilibrium thermodynamics, the physical essence of GSL has remained unclear, and few analyses have been done about the black hole evaporation under the effects of interactions with the outside environment around black hole. That is, the study of nonequilibrium nature of black hole evaporation is the challenging topic. Then, for the first, we need to construct a nonequilibrium thermodynamics [4] suitable to the nonequilibrium nature of black hole evaporation. (Hereafter Planck units are used, $c = \hbar = G = k_B = 1$.)

2 Basic consideration and Steady state thermodynamics (SST)

According to the black hole thermodynamics [1], a stationary black hole can be treated as a *black body*. For simplicity, let us consider a Schwarzschild black hole. Its equations of states as a black body are

$$E_g = \frac{1}{8\pi T_g} = \frac{R_g}{2} \quad , \quad S_g = \frac{1}{16\pi T_g^2} = \pi R_g^2, \tag{1}$$

where E_g is mass energy, R_g is areal radius of horizon, T_g is the Hawking temperature, and S_g is the Bekenstein-Hawking entropy. It is obvious that the heat capacity of a black hole is negative, $C_g = dE_g/dT_g = -1/8\pi T_g^2 = -2\pi R_g^2 < 0$. The negative heat capacity is a peculiar property to self-gravitating systems. Therefore the equations of states (1) encode well the self-gravitational effects of black hole on its own thermodynamic state.

As mentioned abstract, the nonequilibrium nature arises in the matter fields around black hole due to energy flows by Hawking radiation and by matter accretion from the outside environment into the black hole. For simplicity, let us consider massless free fields as the matter field of Hawking radiation and

---

[1] E-mail: saida@daido-it.ac.jp

accretion. Here note that the study on nonequilibrium phenomena is one of the most difficult subjects in physics, and it is impossible at present to treat the nonequilibrium nature of black hole evaporation in a full general relativistic framework. Hence we resort to a simplified model which reflects the nonequilibrium effects of energy exchange between a black hole and its environment [6]:

Nonequilibrium Evaporation (NE) model: Put a spherical black body of temperature T_g in a heat bath of temperature $T_h(< T_g)$, where the equations of states of the black body is given by eq.(1) and we call the black body *the black hole*. Let the heat bath be made of ordinary materials of positive heat capacity. Then hollow a spherical region out of the heat bath around the black hole. The hollow region is a shell-like region which is concentric with the black hole and separates the black hole and the heat bath, and filled with matter fields emitted by them. Further, in order to make it valid to utilize the "equilibrium (static)" equations of states (1), we assume the following:

Quasi-equilibrium assumption: Time evolution in the NE model is not so fast that the thermodynamic states of black hole and heat bath at each moment of their evolution are approximated well by equilibrium states individually. That is, the time evolution of black hole is expressed as that its thermodynamic state changes along a sequence of equilibrium states in the state space during the time evolution of the whole system. The same is true of the heat bath. (Recall a quasi-static process in ordinary thermodynamics). Then, it is valid to use the eq.(1) of a Schwarzschild black hole. And, since Schwarzschild black hole is not a quantum one, the relation $R_g > O(1)$ is required.

It should be noted that, the temperature difference $(T_g > T_h)$ causes a net energy flow from the black hole to the heat bath (a relaxation process). This relaxation process describes the black hole evaporation process in the framework of NE model.

Hereafter we assume for simplicity that the matter fields in the shell-like hollow region of NE model are massless non-self-interacting fields (gas of collisionless particles), and call the matter fields *the radiation fields*. When the number of independent helicities in radiation fields is N, then the Stefan-Boltzmann constant becomes $\sigma = N\pi^2/120$ ($N = 2$ for photon). Note that, due to the quasi-equilibrium assumption $(R_g > O(1))$, the NE model describes a semi-classical stage of evaporation, $T_g < 1$. Therefore it is appropriate to evaluate N by the number of independent states of standard particles (quarks, leptons and gauge particles of four fundamental interactions), $N = O(10)$.

In the hollow region, the nonequilibrium state of radiation fields (at each moment of its time evolution) are described by a simple superposition of a state of temperature T_g and that of T_h, since the radiation fields are collisionless gas. That is, the radiation fields are in a two-temperature nonequilibrium state at each moment of time evolution. Because of the quasi-equilibrium assumption, the two-temperature nonequilibrium state of radiation fields (at each moment of time evolution) can be described well by a nonequilibrium state which possesses a stationary energy flow from the black hole to the heat bath. We call this macroscopically stationary nonequilibrium state *the steady state*. Then the time evolution of radiation fields is expressed as that the thermodynamic state of radiation fields changes along a sequence of steady states in the state space. Hence, we need a thermodynamic formalism of two-temperature steady states for radiation fields in order to analyze the black hole evaporation process in the framework of NE model. The steady state thermodynamics (SST) has already been formulated, and the 0th, 1st, 2nd and 3rd laws are established in reference [4]. By the SST for radiation fields, the energy E_{rad} and entropy S_{rad} of the radiation fields are given as

$$E_{rad} = \int dx^3\, 4\sigma \left(g_g(\vec{x})\, T_g^4 + g_h(\vec{x})\, T_h^4 \right) \quad , \quad S_{rad} = \int dx^3\, \frac{16\sigma}{3} \left(g_g(\vec{x})\, T_g^3 + g_h(\vec{x})\, T_h^3 \right) , \qquad (2)$$

where $\vec{x}$ is a spatial point in the hollow region, $g_g(\vec{x})$ is given by the solid-angle (divided by 4π) covered by the black hole seen from $\vec{x}$, and $g_h(\vec{x})$ is that given by the heat bath. By definition, $g_g(\vec{x}) + g_h(\vec{x}) = 1$.

3 Negative heat capacity is the essence of Generalized 2nd law

For simplicity, consider a black hole evaporation in an empty space. Then the black hole entropy S_g decreases as the mass energy E_g decreases along the evaporation process. Then the generalized second law (GSL) *conjectures* that the total entropy $S_{tot} = S_g + S_m$ increases ($dS_{tot} > 0$) as the evaporation process

proceeds, where S_m is the entropy of matter fields of Hawking radiation. There are three candidates for the physical origin of $dS_{tot} > 0$: (a) self-interaction of matter fields of Hawking radiation (collision of particles and self-gravitational interaction), (b) gravitational interaction between black hole and matter fields of Hawking radiation (curvature scattering, lens effect, gravitational redshift and so on), and (c) the increase of temperature T_g along the evaporation process due to the negative heat capacity $C_g < 0$ ($dE_g < 0 \Rightarrow dT_g = dE_g/C_g > 0$). In the existing proofs of GSL, all of these candidates are considered and it has remained unclear which of these dominates over the others. If the GSL would be proven by considering a situation keeping one of them and discarding the others, then we can conclude that the one kept is the essence of GSL. In reference [5], it has been revealed that the third candidate (c) is the essence of GSL. The outline of discussion in [5] is summarized as follows.

Let us consider about the candidates (a) and (b). The (a), self-interaction of matter fields of Hawking radiation, denotes clearly the positive entropy production rate inside the matter fields. That is, the self-relaxation (self-production of entropy) of the matter fields occurs due to the self-interactions. The (b), gravitational interaction between the black hole and the matter fields, causes the relaxation of the matter fields as well and the matter entropy is produced. Therefore, (a) and (b) give a positive entropy production rate inside the matter fields of Hawking radiation. In other words, matter entropy increases by (a) and (b) during propagating in the outside space of black hole. On the other hand, the candidate (c), increase of black hole temperature T_g, does not cause the entropy production inside the matter fields like (a) and (b). However the (c) denotes that the entropy of the matter fields just at the moment of emission at the black hole horizon ("inherent" entropy of matter fields) increases as the black hole evaporation process proceeds, because the temperature T_g of the "entropy source" increases. This is not the self-production of entropy by matter fields, but the emission of entropy by the black hole.

The NE model includes (c) due to the equation of state (1), but not (a) because the radiation fields are massless and non-self-interacting. Here recall that (b) causes a relaxation of matter fields. That is, the heat bath in NE model can be understood as a very simple and rough model representing (b). Therefore, the black hole evaporation which reflects only (c) can be obtained by removing the heat bath from the NE model and makes the radiation fields spread out into an infinitely large space (black hole evaporation in empty space). Then the total entropy $S_{tot} = S_g + S_{rad}$ is calculated concretely using S_g in eq.(1) and S_{rad} in eq.(2). Finally $dS_{tot} > 0$ is found and it is concluded that (c) is the essence of GSL.

Conclusion by [5]: It is not the interactions of matter fields around black hole, but the self-gravitation of the black hole (negative heat capacity) which guarantees the validity of GSL.

4   Black hole evaporation interacting with outside environment

In general, a black hole evaporation proceeds under the effects of interactions with the outside environment around black hole (e.g matter accretion, curvature scattering and so on). The heat bath in NE model can be considered as a simple model of such interactions, and it is expected that the analysis of time evolution of NE model gives a thermodynamic understanding of black hole evaporation interacting with outside environment.

Hereafter assume that the whole system of NE model (the black hole, the heat bath and the radiation fields) is isolated from the outside world around heat bath (micro-canonical ensemble). It is useful to divide the whole system into two sub-systems X and Y. The X consists of the black hole and the "outgoing" radiation fields emitted by black hole, which share the temperature T_g. The Y consists of the heat bath and the "in-going" radiation fields emitted by heat bath, which share the temperature T_h. Then the energy transport between X and Y is given by the Stefan-Boltzmann law,

$$\frac{dE_X}{dt} = -\sigma \left(T_g^4 - T_h^4\right) A_g \quad , \quad \frac{dE_Y}{dt} = \sigma \left(T_g^4 - T_h^4\right) A_g \,, \tag{3}$$

where $A_g = 4\pi R_g^2$, $E_X = E_g + E_{rad}^{(out)}$ ($E_{rad}^{(out)} = \int dx^3 4\sigma g_g T_g^4$) is the energy of X, $E_Y = E_h + E_{rad}^{(in)}$ ($E_{rad}^{(in)} = \int dx^3 4\sigma g_h T_h^4$, $E_h(T_h) =$ energy of heat bath) is the energy of Y, and $E_{rad}^{(out)} + E_{rad}^{(in)} = E_{rad}$ by definition (see eq.(2)). In order to analyze these nonlinear equations (3), it is useful to consider the energy emission rate (luminosity) by the black hole, $J_{ne} = -dE_g/dt$. The larger the value of J_{ne}, the more rapidly the energy E_g of black hole decreases along its evaporation process. That is, the stronger

emission rate J_{ne} denotes the acceleration of the evaporation process. Further we compare J_{ne} with $J_{empty} = \sigma T_g^4 A_g$ which is the energy emission rate by a black hole of the same mass E_g evaporating in an empty space (as considered in previous section). Then, applying eq.(3) to J_{ne}, we obtain a relation, $J_{ne}/J_{empty} = (C_g/C_X)(1 - T_h^4/T_g^4)$, where $C_X = dE_X/dT_g (< 0)$ is the heat capacity of sub-system X [6]. By a careful analysis of J_{ne}/J_{empty} with a support of numerical solutions of eq.(3), reference [6] has found a non-trivial result (where t_{ne} denotes the time scale of evaporation in the framework of NE model, and t_{empyt} denotes that in an empty space):

Conclusion by [6]: When the thickness of the hollow region in the NE model is thin enough, then $J_{ne}/J_{empty} < 1$ holds along the black hole evaporation in NE model and $t_{ne} > t_{empty}$ is obtained. When the hollow region is thick enough, then $J_{ne}/J_{empty} > 1$ holds along the black hole evaporation in NE model and $t_{ne} < t_{empty}$ is obtained.

One may naively think that the existence of the heat bath always decelerates the evaporation and $t_{ne} < t_{empty}$ does not occur. However the above result states that this naive sense does not work. In order to understand the failure of naive sense, it is helpful to note the following two points: The first point is that the evaporation in an empty space (see previous section) is regarded as a relaxation process of "isolated" sub-system X, since the heat bath and consequently the in-going radiation fields are removed. That is, $E_X = constant$ has to hold during the evaporation process in an empty space. On the other hand, in the NE model, the sub-system Y extracts energy from X due to the temperature difference $T_h < T_g$. Further the energy extraction from X by Y becomes stronger as the nonequilibrium region around black hole (the volume of the hollow region in NE model) is set larger, since a strong nonequilibrium effect causes a strong dynamical effect. That is, for the case of a sufficiently large volume of the hollow region, the energy emission rate J_{ne} is enhanced by the energy extraction by Y, and then it results in $t_{ne} < t_{empty}$. The second point of understanding the failure of naive sense is that the energy transport equation $dE_g/dt = -J_{empty}$ of the evaporation in an empty space can not be obtained from those of NE model (3). One may expect that the empty case would be recovered by a limit operation, $T_h \to 0$ and $V_{rad} \to \infty$, where V_{rad} is the volume of the hollow region. However this operation gives $R_g = \infty$ (see [6] for derivation) which is unphysical. Therefore, the evaporation in an empty space can not be described as some limit situation of NE model. Hence, the naive sense which is based on a limit operation of NE model leads a mistake.

Finally turn our discussion to the suggestion by the NE model. Because of the quasi-equilibrium assumption, the NE model is valid only in a semi-classical evaporation stage. The SST for the radiation fields enables us to estimate the quantities like J_{ne}, E_g and S_g at the end of semi-classical stage (at the onset of quantum evaporation stage) more precisely than the method based on ordinary thermodynamics. Then, we can guess physically what happens in the quantum evaporation stage without referring to present incomplete theories of quantum gravity. In reference [6], the followings have been suggested:

Suggestion 1 by [6]: The black hole evaporation in the framework of NE model will end with a huge energy burst which is stronger than that of the evaporation in an empty space.

Suggestion 2 by [6]: A remnant of Planck size may remain at the end of the quantum evaporation stage in order to guarantee the increase of total entropy along the whole process of evaporation. This implies that the so-called information loss problem may disappear due to the nonequilibrium effect of energy flow.

References

[1] S.W.Hawking, *Commun.Math.Phys.* **43**(1975) 199–220
    J.M. Bardeen, B. Carter and S.W. Hawking, *Commun. Math. Phys.* **31**(1973) 161–170

[2] J.D. Bekenstein, *Phys.Rev.* **D7**(1973) 2333–2346 , *Phys.Rev.* **D9**(1974) 3292–3300

[3] S.W.Hawking, *Phys.Rev.* **D13** (1976) 191–197 ; J.W.York, *Phys.Rev.* **D33** (1986) 2092–2099

[4] H.Saida, *Physica* **A356** (2005) 481–508 (cond-mat/0505223)

[5] H.Saida, *Class.Quant.Grav.* **23** (2006) 6227–6243 (gr-qc/0609022)

[6] H.Saida, *Class.Quant.Grav.* **24** (2007) accepted for publication (gr-qc/0701030)

Impact of Lorentz Violation on Cosmology

Jiro Soda[1] and Sugumi Kanno[2]

[1] *Department of Physics, Kyoto University, Kyoto 606-8501, Japan*
[2] *Department of Physics, McGill University, Montréal, QC H3A 2T8, Canada*

Abstract

We discuss the impact of Lorentz violation on the cosmology. Firstly, we show that the Lorentz violation affects the dynamics of the chaotic inflationary model and gives rise to an interesting feature. Secondly, we propose the Lorentz violating DGP brane models where the Lorentz violating terms on the brane accelerate the current universe. We conjecture that the ghost disappears in the Lorentz violating DGP models.

1 Introduction

Various observations suggest the existence of two accelerating stages in the universe, namely, the past inflationary universe and the current acceleration of the universe. In cosmology, therefore, how to accelerate the universe in the past and present is a big issue. Many attempts to resolve this issue have been performed and failed. Given the difficulty of the problem, it would be useful to go back to the basic point and reexamine it. Here, we consider the possibility to break the Lorentz symmetry.

Typically, the Lorentz violation yields the preferred frame. In the case of the standard model of particles, there are strong constraints on the existence of the preferred frame. In contrast, there is no reason to refuse the preferred frame in cosmology. Rather, there is a natural preferred frame defined by the cosmic microwave background radiation (CMB). Therefore, there is room to consider the gravitational theory which allows the preferred frame.

Now, we present our model with which we discuss the cosmological acceleration problems. Suppose that the Lorentz symmetry is spontaneously broken by getting the expectation values of a vector field u^μ as $< 0|u^\mu u_\mu|0 > = -1$. We do not notice the existence of this field because the frame determined by this field coincides with the CMB frame. However, in the inhomogeneous universe, both frames can fluctuate independently. Hence, we can regard the spatial hypersurface of our universe as a kind of membrane characterized by the extrinsic curvature K_{ij} with a time like vector field u^μ. Based on this observation, we propose the model

$$
\begin{aligned}
S &= \int d^4x \sqrt{-g} \left[\frac{1}{16\pi G} R + \beta_1(\phi) K^{ij} K_{ij} - \beta_2(\phi) K^2 - \gamma_1(\phi) \nabla^\mu u^\nu \nabla_\mu u_\nu \right. \\
&\quad - \gamma_2(\phi) \nabla^\mu u^\nu \nabla_\nu u_\mu - \gamma_3(\phi) \left(\nabla_\mu u^\mu \right)^2 - \gamma_4(\phi) u^\mu u^\nu \nabla_\mu u^\alpha \nabla_\nu u_\alpha \\
&\quad \left. + \lambda \left(u^\mu u_\mu + 1 \right) - \frac{1}{2} \left(\nabla \phi \right)^2 - V(\phi) \right] ,
\end{aligned}
\tag{1}
$$

where $g_{\mu\nu}$, R, and λ are the 4-dimensional metric, the scalar curvature, and a Lagrange multiplier, respectively. Here, we also considered the scalar field ϕ with the potential V and it couples to other terms with the coupling function $\beta_i(\phi)$ and $\gamma_i(\phi)$. This is a generalization of the Einstein-Ether gravity [1]. Since β_i, γ_i at present can be different from those in the very early universe, we do not have any constraint on these parameters in the inflationary stage. Of course, ultimately, they have to approach the observationally allowed values at present. Here, the Lorentz symmetry is violated both spontaneously and explicitly.

The purpose of this paper is to discuss the impact of the Lorentz violation both on the inflationary scenario and the current acceleration. In the former case, the Lorentz violation merely modifies the scenario. In the latter case, however, the impact of Lorentz violation could be appreciable. The inclusion of Lorentz violation may give rise to a resolution of the ghost problem in the DGP brane model [2].

2 Impact of Lorentz Violation on Inflationary Scenario

Now, let us consider the chaotic inflationary scenario and clarify to what extent the Lorentz violation affects the inflationary scenario [3]. We take the model

$$S = \int d^4x \sqrt{-g} \left[\frac{1}{16\pi G} R - \beta(\phi) K^2 - \frac{1}{2} (\nabla\phi)^2 - V(\phi) \right] . \tag{2}$$

Let us consider the homogeneous and isotropic spacetime

$$ds^2 = -dt^2 + e^{2\alpha(t)} \delta_{ij} dx^i dx^j . \tag{3}$$

The scale of the universe is determined by α. Now, let us deduce the equations of motion. First, we define the dimensionless derivative Q' by $\dot{Q} = \frac{dQ}{d\alpha}\frac{d\alpha}{dt} \equiv Q'\frac{d\alpha}{dt}$. Then, the equations of motion are

$$\left(1 + \frac{1}{8\pi G\beta}\right) H^2 = \frac{1}{3} \left[\frac{1}{2}\frac{H^2\phi'^2}{\beta} + \frac{V}{\beta} \right] \tag{4}$$

$$\left(1 + \frac{1}{8\pi G\beta}\right) \frac{H'}{H} + \frac{1}{2}\frac{\phi'^2}{\beta} + \frac{\beta'}{\beta} = 0 \tag{5}$$

$$\phi'' + \frac{H'}{H}\phi' + 3\phi' + \frac{V_{,\phi}}{H^2} + 3\beta_{,\phi} = 0 , \tag{6}$$

where $\beta_{,\phi}$ denotes the derivative with respect to ϕ. We have taken $H = \dot{\alpha}$ as an independent variable. As is usual with gravity, these three equations are not independent. Usually, the second one is regarded as a redundant equation.

The above equation changes its property at the critical value ϕ_c defined by $8\pi G\beta(\phi_c) = 1$. When we consider the inflationary scenario, we usually require the enough e-folding number, say $N = 70$. Let ϕ_i be the corresponding initial value of the scalar field. If $\phi_c > \phi_i$, the effect of Lorentz violation on the inflationary scenario would be negligible. However, if $\phi_c < \phi_i$, the standard scenario should be modified. It depends on the models. To make the discussion more specific, we choose the model $\beta = \xi\phi^2$, $V = \frac{1}{2}m^2\phi^2$, where ξ and m are parameters. For this model, we have $\phi_c = \frac{M_{pl}}{\sqrt{8\pi\xi}}$. As $\phi_i \sim 3M_{pl}$ approximately in the standard case, the condition $\phi_i > \phi_c$ implies the criterion $\xi > 1/(72\pi) \sim 1/226$ for the Lorentz violation to be relevant to the inflation. For other models, the similar criterion can be easily obtained.

Now, we suppose the Lorentz violation is relevant and analyze the two regimes separately.

For a sufficiently larger value of ϕ, both the coupling function β and the potential function V are important in the model (2). During this period, the effect of Lorentz violation on the inflaton dynamics must be large. In the Lorentz violating regime, $8\pi G\beta \gg 1$, we have

$$H^2 = \frac{1}{3\beta} \left[\frac{1}{2}H^2\phi'^2 + V \right] \tag{7}$$

$$\frac{H'}{H} + \frac{1}{2\beta}\phi'^2 + \frac{\beta'}{\beta} = 0 \tag{8}$$

$$\phi'' + \frac{H'}{H}\phi' + 3\phi' + \frac{V_{,\phi}}{H^2} + 3\beta_{,\phi} = 0 . \tag{9}$$

To have the inflation, we impose the condition $H^2\phi'^2 \ll V$ as the slow roll condition. Consequently, Eq.(7) is reduced to

$$H^2 = \frac{1}{3\beta}V . \tag{10}$$

Using Eq.(10), the slow roll condition can be written as $\phi'^2 \ll \beta$. Now, we also impose the condition $H'/H \ll 1$ as the quasi-de Sitter condition. Then, Eq.(8) gives us the condition $\beta' \ll \beta$. We also require the standard condition $\phi'' \ll \phi'$. Thus, we have the slow roll equations (10) and

$$\phi' + \frac{V_{,\phi}}{3H^2} + \beta_{,\phi} = 0 . \tag{11}$$

For our example, we can easily solve Eqs.(10) and (11) as $\phi(\alpha) = \phi_i e^{-4\xi\alpha}$. For this solution to satisfy slow roll conditions, we need $\xi < 1/16$. Thus, we have the range $1/226 < \xi < 1/16$ of the parameter for which the Lorentz violating inflation is relevant. Note that, in our model, the Hubble parameter (10) becomes constant

$$H^2 = \frac{m^2}{6\xi} \ , \tag{12}$$

even though the inflaton is rolling down the potential. This is a consequence of Lorentz violation.

After the inflaton crosses the critical value ϕ_c, the dynamics is governed entirely by the potential V. In the standard slow roll regime $8\pi G\beta \ll 1$, the evolution of the inflaton can be solved as

$$\phi^2(\alpha) = \phi_c^2 - \frac{\alpha}{2\pi G} \ . \tag{13}$$

The scale factor can be also obtained as $a(t) = \exp\left[2\pi G(\phi_c^2 - \phi^2(t))\right]$. The standard inflation stage ends and the reheating commences when the slow roll conditions violate.

Now it is easy to calculate e-folding number. Let ϕ_i be the value of the scalar field corresponding to the e-folding number $N = 70$. The total e-folding number reads

$$N = \frac{1}{4\xi} \log \frac{\phi_i}{\phi_c} + 2\pi G \left(\phi_c^2 - \phi_e^2\right) \ , \tag{14}$$

where $\phi_e \sim 0.3 M_{pl}$ is the value of scalar field at the end of inflation. Note that the first term arises from the Lorentz violating stage. As an example, let us take the value $\xi = 10^{-2}$. Then, $\phi_c \sim 2M_{pl}$. The contribution to the e-folding number from the inflation end is negligible. Therefore, we get $\phi_i \sim 12M_{pl}$.

In this simple example, the coupling to the Lorentz violating sector disappears after the reheating. Hence, the subsequent homogeneous dynamics of the universe is the same as that of Lorentz invariant theory of gravity. However, it is possible to add some constants to β, which are consistent with the current experiments. In that case, the effect of the Lorentz violation is still relevant to the subsequent history.

The tensor part of perturbations can be described by

$$ds^2 = -dt^2 + a^2(t) \left(\delta_{ij} + h_{ij}(t, x^i)\right) dx^i dx^j \ , \tag{15}$$

where the perturbation satisfy $h^i{}_i = h_{ij}{}^{,j} = 0$. The quadratic part of the action is given by

$$S = \int d^4x \frac{a^3}{16\pi G} \left[\frac{1}{4}\dot{h}_{ij}\dot{h}'^{ij} - \frac{1}{4a^2}h_{ij,k}h^{ij,k}\right] \ . \tag{16}$$

In the case of chaotic inflation model, the Hubble parameter is constant (12) during Lorentz violating stage. The spectrum is completely flat although the inflaton is rolling down the potential. This is a clear prediction of the Lorentz violating chaotic inflation.

3   Impact of Lorentz Violation on Current Acceleration

To solve the current acceleration problem is much more difficult than the past one. The most interesting proposal is the DGP model [2]. However, it suffers from the ghost. Hence, it is not a stable model. Here, we would like to argue the Lorentz violation may resolve the instability problem.

Our basic observation is that the Lorentz violating term itself can accelerate the universe. Let us consider the simplest braneworld model:

$$S = \frac{1}{2\kappa_5^2} \int d^5x \sqrt{-G}R - \int d^4x \sqrt{-g}\beta K^2, \tag{17}$$

where G is the determinant of the 5-dimensional metric and κ_5 is the 5-dimensional gravitational coupling constant. Here, we have assumed the scalar field is stabilized at present. Let us assume the Z_2 symmetry. Then the junction condition $K_{\mu\nu} - g_{\mu\nu}K = \kappa_5^2 T_{\mu\nu}$ gives the effective Friedman equation:

$$\pm H = \frac{\kappa_5^2}{6} \left[3\beta H^2 - \rho\right] \ . \tag{18}$$

If we take the positive sign, in the late time, we have the de Sitter spacetime with

$$H = \frac{2}{\kappa_5^2 \beta} \ .$$ (19)

Thus, the late time accelerating universe can be realized due to the Lorentz violation.

More generally, we propose the following model

$$
\begin{aligned}
S \ = \ & \frac{1}{2\kappa_5^2} \int d^5 x \sqrt{-G} R \\
& + \int d^4 x \sqrt{-g} \left[\frac{1}{16\pi G} R + \beta_1 K^{ij} K_{ij} - \beta_2 K^2 - \gamma_1 \nabla^\mu u^\nu \nabla_\mu u_\nu \right. \\
& \left. - \gamma_2 \nabla^\mu u^\nu \nabla_\nu u_\mu - \gamma_3 \left(\nabla_\mu u^\mu \right)^2 - \gamma_4 u^\mu u^\nu \nabla_\mu u^\alpha \nabla_\nu u_\alpha + \lambda \left(u^\mu u_\mu + 1 \right) \right] \ .
\end{aligned}
$$ (20)

It should be stressed that any term on the brane can generate the current acceleration. As the tensor structure in the action is very different from the original DGP model, we can expect the above action contains no ghost. In fact, we have many parameters here, hence there is a chance to remove the ghost from our models. Thus, we expect that some of the above Lorentz violating brane models does not contain any ghost. If this is so, one can say the Lorentz violation explains the current stage acceleration of the universe.

4 Conclusion

We have discussed the impact of Lorents violation on cosmology. In the first place, we found that the Lorentz violating inflation shows an interesting feature. In the second place, we proposed a Lorentz violating DGP model which have a possibility to avoid the ghost problem.

It would be interesting to study the evolution of fluctuations completely. If the vector modes of perturbations can survive till the last scattering surface, they leave the remnant of the Lorentz violation on the CMB polarization spectrum. It is also intriguing to seek for a relation to the large scale anomaly discovered in CMB by WMAP. The calculation of the curvature perturbation is much more complicated. However, it must reveal more interesting phenomena due to Lorentz violating inflation. The tensor-scalar ratio of the power spectrum would be also interesting. These are now under investigation.

More importantly, we need to show the stability of Lorentz violating DGP model. If the Lorentz violation kills the ghost, this is a great progress in the cosmology. Even in case that it turns out that all of the models are unstable, it makes our understanding of the ghost issue profound.

References

[1] T. Jacobson and D. Mattingly, Phys. Rev. D **64**, 024028 (2001) [arXiv:gr-qc/0007031].

[2] G. R. Dvali, G. Gabadadze and M. Porrati, Phys. Lett. B **485**, 208 (2000) [arXiv:hep-th/0005016].

[3] S. Kanno and J. Soda, Phys. Rev. D **74**, 063505 (2006) [arXiv:hep-th/0604192].

Stability of a de Sitter brane in a six-dimensional braneworld

Shunichiro Kinoshita[1] , Shinji Mukohyama[2] and Yuuiti Sendouda[3]

[1,2,3]*Department of Physics, Graduate School of Science, The University of Tokyo, Hongo 7-3-1, Bunkyo-ku, Tokyo 113-0033, Japan*
[2]*Research Center for the Early Universe, Graduate School of Science, The University of Tokyo, Hongo 7-3-1, Bunkyo-ku, Tokyo 113-0033, Japan*

Abstract

We investigate the dynamical stability of a six-dimensional braneworld solution with warped flux compactification recently found by the authors. We consider linear perturbations around this background spacetime, assuming the axisymmetry in the extra dimensions. Perturbations are decomposed into scalar-, vector- and tensor-sectors according to the representation of the 4D de Sitter symmetry, and analyzed separately. It is found that when the four-dimensional spacetime has a large Hubble expansion rate, there appear are tachyonic modes in the scalar sector. This fact means that in this regime the spacetime becomes dynamically unstable. We interpret this result via thermodynamics of the spacetime.

1   6D warped flux compactification braneworld model

When we reduce a higher dimensional spacetime to the 4D universe, a compactification of extra dimensions is necessary. However, this compactification yields moduli fields (e.g. radion field), and in order to recover the 4D Einstein gravity we must stabilize these fields. In other words, we need to stabilize the shape and the volume of the extra dimensions. Recently some authors suggest that when the Hubble expansion rate of the 4D spacetime is too large, it is hard to stabilize all moduli [1, 2]. So we would like to study stability of a de Sitter brane universe in the context of a simple 6D braneworld solution found by us [3].

We consider the 6D Einstein-Maxwell system described by the action

$$I = \frac{1}{16\pi} \int \mathrm{d}^6 x \sqrt{-g} \left(R - 2\Lambda_6 - \frac{1}{2} F_{MN} F^{MN} \right), \tag{1}$$

where Λ_6 is the 6D bulk cosmological constant ($\Lambda_6 > 0$), and $F_{MN} = \partial_M A_N - \partial_N A_M$ is the field strength associated with the $U(1)$ gauge field A_M to stabilize the extra dimensions. The braneworld solution is

$$\mathrm{d}s_6^2 = r^2 g_{\mu\nu} \mathrm{d}x^\mu \mathrm{d}x^\nu + \frac{\mathrm{d}r^2}{f(r)} + f(r) \mathrm{d}\phi^2,$$
$$A_M \mathrm{d}x^M = A(r) \mathrm{d}\phi, \tag{2}$$

where $g_{\mu\nu}$ is the metric of the 4D de Sitter space with the Hubble parameter h and

$$f(r) = h^2 - \frac{\Lambda_6}{10} r^2 - \frac{\mu}{r^3} - \frac{b^2}{12 r^6}, \quad A(r) = \frac{b}{3 r^3}. \tag{3}$$

When $h = 0$ the 4D spacetime reduces the Minkowski spacetime. Two branes are located at $r = r_\pm$ ($0 < r_- < r_+$) which are two positive roots for $f(r) = 0$. The tension of each brane characterizes a conical deficit of the angular coordinate ϕ in the extra dimensions. To be precise, the period of the angular coordinate ($\phi \sim \phi + \Delta\phi$) is given by

$$\Delta\phi = \frac{2\pi - \sigma_+}{|f'(r_+)/2|} = \frac{2\pi - \sigma_-}{|f'(r_-)/2|}, \tag{4}$$

---

[1] E-mail:kinoshita@utap.phys.s.u-tokyo.ac.jp
[2] E-mail:mukoyama@phys.s.u-tokyo.ac.jp
[3] E-mail:sendouda@utap.phys.s.u-tokyo.ac.jp

where $\sigma_\pm$ are tensions of the branes at $r = r_\pm$, respectively.

In this braneworld model the spacetime has two compact extra dimensions and two 3-branes at $r = r_\pm$. The geometry on the brane at $r = r_\pm$ is the 4D de Sitter spacetime with the Hubble expansion rate $h_\pm = h/r_\pm$, respectively. The role of the $U(1)$-field is to stabilize extra dimensions by magnetic flux.

For a fixed cosmological constant Λ_6 in the bulk, this solution is locally parameterized by two parameters b and μ. It is convenient to introduce two dimension-less parameters determining the geometry instead of these original parameters. One is the ratio of the warp factors at the branes $\alpha \equiv r_-/r_+$. This parameter describes how the geometry of the 2D extra dimensions is warped. Note that in the special case $\alpha = 1$ the geometry is non-warped and locally a round sphere. The other is β defined by

$$\beta \equiv \frac{h_+^2}{h_{\max}(\alpha)^2} = \frac{10(1 + \alpha + \alpha^2)}{\Lambda_6(1 + \alpha + \alpha^2 + \alpha^3 + \alpha^4)} \frac{h^2}{r_+^2}, \tag{5}$$

which is the Hubble parameter squared on the brane at $r = r_+$ normalized by its maximum value $h_{\max}^2(\alpha)$ for a given α. In the following we parametrize the solutions by the pair of two parameters (α, β), both of which run over the finite interval $[0, 1]$.

2 Dynamical stability

In order to investigate the dynamical stability of this spacetime, we consider linear perturbations around the background spacetime. Perturbations are decomposed into scalar-, vector- and tensor-sectors according to the representation of the 4D de Sitter symmetry. In this presentation we consider the scalar sector only. The vector and tensor sectors are easier to analyze and turn out to be stable in the whole range of parameters. The scalar sector is expanded by scalar-type harmonics on the 4D de Sitter space, as

$$g_{MN}dx^M dx^N = r^2(1 + \Phi_2 Y)g_{\mu\nu}dx^\mu dx^\nu + [1 + (\Phi_1 + \Phi_2)Y]\frac{dr^2}{f} + [1 - (\Phi_1 + 3\Phi_2)Y]f d\phi^2,$$
$$A_M dx^M = (A + a_\phi Y)d\phi, \tag{6}$$

where Y is the scalar harmonics on the 4D de Sitter space. The Einstein equation and the Maxwell equation are reduced to two perturbation equations,

$$\Phi_1'' + 2\left(\frac{f'}{f} + \frac{5}{r}\right)\Phi_1' - \frac{4\Lambda_6}{f}(\Phi_1 + \Phi_2) + \frac{m^2 + 18h^2}{r^2 f}\Phi_1 = 0,$$
$$\Phi_2'' + \frac{4}{r}\Phi_2' + \frac{m^2}{2r^2 f}(\Phi_1 + 2\Phi_2) = 0, \tag{7}$$

where a prime denotes derivative with respect to r and m^2 is the eigenvalue of harmonics on the de Sitter space with the Hubble parameter h:

$$\nabla_{(4)}^2 Y - m^2 Y = 0. \tag{8}$$

Here, $\nabla_{(4)}$ is the covariant derivative associated with $g_{\mu\nu}$ which is the 4D de Sitter space with the Hubble parameter h. The boundary conditions at $r = r_\pm$ obtained by requiring the regularities at the brane positions. An alternative and more rigorous derivation of the boundary conditions is possible by using the formalism developed in [5]. If the Kaluza-Klein mass square m^2 is negative, then the mode is tachyonic and the scalar sector is unstable.

Since the background spacetime is a two-parameter family of solutions, the system of the perturbation equations depend on two parameters. We investigate the lowest KK mass of the scalar-type perturbation for different values of two parameters. Our strategy to attack the problem is as follows. First, we analytically solve the perturbation equations in the $\alpha = 1$ case for any β in the region $[0, 1]$, and obtain the lowest KK mass $m^2(\alpha = 1, \beta)$. Next, we numerically calculate $m(\alpha, \beta)^2$ as α changes from 1 to 0 for a fixed β by the relaxation method.

Fig. 1 shows the lowest KK mass square of the scalar perturbation. For $\beta = 0$ which means the 4D spacetime is the Minkowski, we have shown that there is no unstable (i.e. neither massless nor tachyonic) mode in the scalar perturbation [4]. We find that as β becomes larger, namely as the Hubble
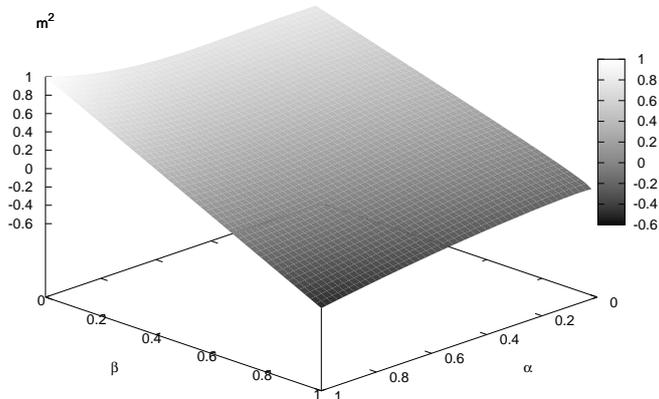
Figure 1: The lowest KK mass square of the scalar perturbation. When $\beta = 0$ the 4D spacetime is the Minkowski. As β becomes larger (i.e. the 4D Hubble becomes larger), m^2 decreases and eventually becomes negative at some value of β.

parameter on the brane becomes larger, the lowest KK mass square m^2 decreases and eventually becomes negative. Therefore we conclude that when the Hubble on the brane is too large the extra-dimensions are destabilized and such configurations are unstable.

3   Summary and discussion

We have studied the stability of the 6D braneworld solution with 4D de Sitter branes, considering linear perturbations around it. We have explored the lowest KK mass for the scalar perturbations and found that for large values of the 4D Hubble parameter on the brane tachyonic modes appear and the geometry becomes unstable.

We can interpret this instability from a different viewpoint via thermodynamics of the spacetime. Since the de Sitter space has the cosmological horizon, it has entropy given by one quarter of the area of the horizon. This is an analogue of the well-known black hole entropy. In the 6D braneworld background solution which we have considered, each point in the 2D extra dimensions corresponds to a 4D de Sitter spacetime. Therefore, we shall define the entropy by one quarter of the area of the cosmological horizon integrated over the extra dimensions. We can represent the entropy S as a function of conserved quantities η and Φ up to the normalization depending only on $\Delta\phi$, where η is given by

$$\eta \equiv \frac{2\pi - \sigma_-}{2\pi - \sigma_+}, \tag{9}$$

and Φ is the total magnetic flux. We see from Fig. 2 that $S(\eta, \Phi)$ is not single-valued but actually has two values for some values of η and Φ. Thus we find that the spacetime has two branches, which we call the high-entropy branch and the low-entropy branch, respectively, and these two branches merge at the critical curve. Beyond the critical curve there is no solution. Since the upper branch has a greater entropy than the lower one, we expect that the upper high-entropy branch is thermodynamically preferred than the lower branch and the spacetime becomes marginally stable on the critical line where two branches merge. Indeed, we can show that the massless mode of the scalar sector in linear perturbations appears on this critical curve. Furthermore, we can show that the high-entropy and the low-entropy branches in Fig. 2 exactly agree with the positive and negative m^2 regions in Fig. 1, respectively [6]. This fact implies that in this spacetime the onset of dynamical instability coincides with the onset of thermodynamic instability. This is similar to the Gubser-Mitra conjecture for extended black objects [7]. More generally
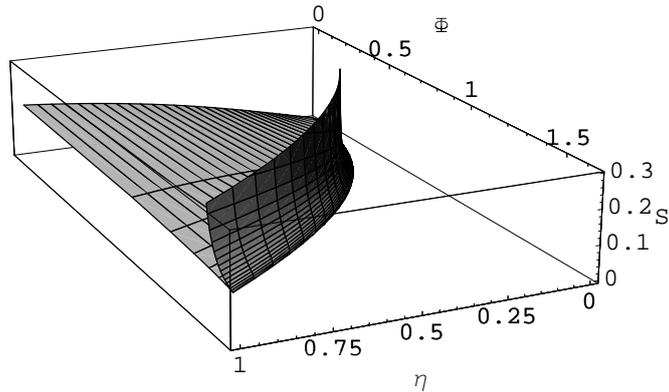
Figure 2: The entropy as a function for η and Φ.

speaking, we should be able to understand our result in the language of the catastrophe theory. Further studies in this line are certainly worthwhile pursuing.

References

[1] A. V. Frolov and L. Kofman, Phys. Rev. D **69**, 044021 (2004) [arXiv:hep-th/0309002].

[2] R. Kallosh and A. Linde, JHEP **0412**, 004 (2004) [arXiv:hep-th/0411011].

[3] S. Mukohyama, Y. Sendouda, H. Yoshiguchi and S. Kinoshita, JCAP **0507**, 013 (2005) [arXiv:hep-th/0506050].

[4] H. Yoshiguchi, S. Mukohyama, Y. Sendouda and S. Kinoshita, JCAP **0603**, 018 (2006) [arXiv:hep-th/0512212].

[5] Y. Sendouda, S. Kinoshita and S. Mukohyama, Class. Quant. Grav. **23**, 7199 (2006) [arXiv:hep-th/0607189].

[6] S. Kinoshita, S. Mukohyama and Y. Sendouda, in preparation

[7] S. S. Gubser and I. Mitra, JHEP **0108**, 018 (2001) [arXiv:hep-th/0011127]; S. S. Gubser and I. Mitra, arXiv:hep-th/0009126.

Inflaton perturbations in brane-world cosmology with induced gravity

Shuntaro Mizuno[1] and Kazuya Koyama[2]

[1] *Research Center for the Early Universe (RESCEU), Graduate School of Science, The University of Tokyo, Tokyo 113-0033, Japan*
[2] *Institute of Cosmology and Gravitation, University of Portsmouth, Portsmouth PO1 2EG, UK*

Abstract

We study cosmological perturbations in the brane models with an induced Einstein-Hilbert term on a brane. We consider an inflaton confined to a de Sitter brane in a five-dimensional Minkowski spacetime. There are two branches ($\pm$ branches) of solutions for the background spacetime. In the $+$ branch, which includes the self-accelerating universe, a resonance appears. In the $-$ branch, which can be thought as the Randall-Sundrum type brane-world with the high energy quantum corrections, there is no resonance. At high energies, we analytically confirm that four-dimensional Einstein gravity is recovered, which is related to the disappearance of van Dam-Veltman-Zakharov discontinuity in de Sitter spacetime. On sufficiently small scales, we confirm that the lineariaed gravity on the brane is well described by the Brans-Dicke theory with $\omega = 3Hr_c$ in $-$ branch and $\omega = -3Hr_c$ in $+$ branch, respectively, which confirms the existence of the ghost in $+$ branch.

1 Introduction

There has been much interest over the last several years in the brane-world scenario where we are assumed to be living on a four-dimensional hypersurface (brane) in a higher-dimensional spacetime (bulk) [1].

One of the most promising tools to extract the information of the extra-dimension is the primordial density fluctuations generated in the period of inflation in the early universe. In the inflation model where inflation is driven by an inflaton field confined to the brane, the amplitude of the curvature perturbation is calculated in the extremely slow-roll limit where the coupling between inflaton field fluctuation and bulk perturbations can be neglected [2].

This work is proceeded to go beyond the zero-th order slow-roll approximation by solving the bulk metric perturbations classically [3, 4]. It is shown that we could have significant effects from the back-reaction due to the coupling to five-dimensional gravitational perturbations.

On the other hand, it was pointed out that the localized matter on a brane can induce gravity on the brane via quantum loop corrections at high energies [5]. This induced gravity can act as the ultra-violet cut-off for the inflaton perturbations.

Based on the induced gravity scenario, Dvali, Gabadadze, and Porrati (DGP) proposed a brane-world model with induced gravity [6] in which the four-dimensional brane is embedded in a five-dimensional Minkowski spacetime. In this paper, we study the behavior of five-dimensional metric perturbations excited by the inflaton perturbations confined to the brane in DGP model.

2 Bulk gravitons with a de Sitter brane

2.1 Background cosmology

We consider a four-dimensional brane-world model with a five-dimensional infinite-volume bulk. The action is given by

$$S = \frac{1}{2\kappa^2} \int d^5x \sqrt{-g}^{(5)}R + \int d^4x \sqrt{-\gamma} \left[\frac{1}{\kappa^2} K + L_{\text{brane}} + \frac{1}{2\kappa_4^2} R \right], \tag{1}$$

---

where κ^2 is the fundamental five-dimensional gravitational constant, K is the trace of extrinsic curvature K_{AB} on the brane and L_{brane} is a Lagrangian for brane-localized matter. In addition, we consider the last term, an intrinsic curvature term on the brane which plays a crucial role in this model. Here, $\kappa_4^2 = 8\pi G$ is the four-dimensional gravitational constant. We define a crossover scale r_c as $r_c = \kappa^2/2\kappa_4^2$. We are interested in the gravitational property of this model in a cosmological setting. By assuming the flat Friedmann-Robertson-Walker metric on the brane and neglecting the effect from the five-dimensional Weyl tensor in the background, the following Friedmann like equation is derived [7];

$$H^2 - \frac{\epsilon}{r_c}H = \frac{\kappa_4^2}{3}\rho, \tag{2}$$

where H is a Hubble parameter on the brane and $\epsilon = \pm 1$, which is the parameter related to the embedding of the brane in the bulk. We call the case with $\epsilon = 1 +$ branch, while $\epsilon = -1 -$ branch.

2.2   Master variable for perturbations in the Minkowski bulk

Now let us consider the scalar perturbation. In order to solve the perturbations in this background, it is convenient to use five-dimensional longitudinal gauge, given by

$$ds^2 = (1 + 2A_{yy})dy^2 + 2N(y)A_y dy dt + N(y)^2\Big[-(1+2A)dt^2 + a(t)^2(1+2\mathcal{R})\delta_{ij}dx^i dx^j\Big], \tag{3}$$

where $a(t) = \exp(Ht)$.

In the absence of bulk matter perturbations, five-dimensional perturbed Einstein equations $^{(5)}\delta G^A{}_B = 0$ are solved in a Minkowski background if the metric perturbations are derived from a 'master variable', Ω [8], [9]. The perturbed five-dimensional Einstein equations yield a single wave equation governing the evolution of the master variable Ω in the bulk. Solutions for the master equation can be separated into eigenmodes of the time-dependent equation on the brane and bulk mode equation for de Sitter brane:

$$\Omega(t, y; \vec{x}) = \int d^3\vec{k} dm g_m(t) f_m(y) e^{ikx}, \tag{4}$$

where

$$\ddot{g}_m - 3H\dot{g}_m + \left[m^2 + \frac{k^2}{a^2}\right]g_m = 0, \quad f_m'' - 2\frac{N'}{N}f_m' + \frac{m^2}{N^2}f_m = 0. \tag{5}$$

3   Scalar field on the brane

3.1   Boundary conditions

In the following, we model the matter on the brane as a canonical scalar field ϕ with potential $V(\phi)$ whose homogeneous part gives approximately de Sitter universe on the brane [3, 4]. In this case, combining the junction conditions we get an evolution equation for $\mathcal{G}$:

$$\ddot{\mathcal{G}} - \left(H + 2\frac{\ddot{\phi}}{\dot{\phi}}\right)\dot{\mathcal{G}} + \frac{k^2}{a^2}\mathcal{G} = 0, \quad \text{where } \mathcal{G} = (1 - 2\epsilon H r_c)(\Omega' - \epsilon H\Omega) - r_c(2H^2 - m^2)\Omega. \tag{6}$$

This gives the boundary condition for the time dependence of the master variable Ω. Assuming that ϕ is slow-rolling, so that $|\ddot{\phi}/\dot{\phi}| \ll H$ in Eq. (6), which is valid for the de Sitter universe, the solution for $\mathcal{G}$ is

$$\mathcal{G} = C_1\frac{\cos(-k\eta)}{-k\eta} + C_2\frac{\sin(-k\eta)}{-k\eta}. \tag{7}$$

We use the formulae for summation of Bessel functions,

$$\sum_{\ell=0}^{\infty}(-1)^\ell\left(2\ell + \frac{3}{2}\right)z^{-\frac{3}{2}}J_{2\ell+\frac{3}{2}}(z) = \sqrt{\frac{1}{2\pi}}\frac{\sin z}{z},$$

$$\sum_{l=0}^{\infty}(-1)^\ell\left(2\ell + \frac{1}{2}\right)z^{-\frac{3}{2}}J_{2\ell+\frac{1}{2}}(z) = \sqrt{\frac{1}{2\pi}}\frac{\cos z}{z}. \tag{8}$$

These show that an infinite sum of mode functions

$$g_m = (-k\eta)^{-3/2} J_\nu(-k\eta), \quad \text{where} \ \nu^2 = \frac{9}{4} - \frac{m^2}{H^2}, \tag{9}$$

can satisfy the boundary condition imposed on $\mathcal{G}$, where the spectrum of KK modes is given by

$$\frac{m^2}{H^2} = -2(2\ell - 1)(\ell + 1) \quad \text{for} \ \ C_1, \quad \frac{m^2}{H^2} = -2\ell(2\ell + 3) \quad \text{for} \ \ C_2. \tag{10}$$

3.2 Curvature perturbation on the brane

Making use of the boundary condition obtained above, we can obtain the general solutions for Ω which yield the metric perturbations in the five-dimensional longitudinal gauge. Since we can show the curvature perturbation on the brane $\mathcal{R}_{(b)}$ is related with A and $\mathcal{R}$ as

$$\mathcal{R}_{(b)} \ = \ \frac{1}{1 - 2\epsilon H r_c} \Big[(1 - \epsilon H r_c)\mathcal{R} + \epsilon H r_c A \Big], \tag{11}$$

the general solutions for $\mathcal{R}_{(b)}$ is obtained. We show only the results − branch ($\epsilon = -1$) and + branch ($\epsilon = 1$) separately.

− branch ($\epsilon = -1$)

$$
\begin{aligned}
\mathcal{R}_{(b)} \ = \ & -\frac{\sqrt{2\pi}}{6}\frac{C_1}{k}\frac{H^2}{(2Hr_c + 1)}\sum_{\ell=0}^{\infty}\frac{(-1)^\ell(2\ell + \frac{1}{2})}{(2\ell + 1)\{2(\ell + 1)Hr_c + 1\}} \\
& \times [6(\ell + 1)(2\ell + 1)Hr_c(-k\eta)^{-\frac{1}{2}}J_{2\ell+\frac{1}{2}}(-k\eta) + 2(2\ell + 1)(-k\eta)^{\frac{1}{2}}J_{2\ell-\frac{1}{2}}(-k\eta) - (-k\eta)^{\frac{3}{2}}J_{2\ell-\frac{3}{2}}(-k\eta)] \\
& -\frac{\sqrt{2\pi}}{6}\frac{C_2}{k}\frac{H^2}{(2Hr_c + 1)}\sum_{\ell=0}^{\infty}\frac{(-1)^\ell(2\ell + \frac{3}{2})}{2(\ell + 1)\{(2\ell + 3)Hr_c + 1\}} \\
& \times [6(\ell + 1)(2\ell + 3)Hr_c(-k\eta)^{-\frac{1}{2}}J_{2\ell+\frac{3}{2}}(-k\eta) + 2(2\ell + 2)(-k\eta)^{\frac{1}{2}}J_{2\ell+\frac{1}{2}}(-k\eta) - (-k\eta)^{\frac{3}{2}}J_{2\ell-\frac{1}{2}}(-k\eta)].
\end{aligned}
\tag{12}
$$

In + branch ($\epsilon = 1$), the curvature perturbation on the brane is given as

$$
\begin{aligned}
\mathcal{R}_{(b)} \ = \ & \mathcal{R}_{(b)(m^2=2H^2)} \\
& -\frac{\sqrt{2\pi}}{6}\frac{C_1}{k}\frac{H^2}{(2Hr_c - 1)}\sum_{\ell=1}^{\infty}\frac{(-1)^\ell(2\ell + \frac{1}{2})}{2\ell\{(2\ell - 1)Hr_c + 1\}} \\
& \times [\{6\ell(2\ell - 1)Hr_c + 12\ell + 3\}(-k\eta)^{-\frac{1}{2}}J_{2\ell+\frac{1}{2}}(-k\eta) - 2(2\ell + 1)(-k\eta)^{\frac{1}{2}}J_{2\ell-\frac{1}{2}}(-k\eta) + (-k\eta)^{\frac{3}{2}}J_{2\ell-\frac{3}{2}}(-k\eta)] \\
& -\frac{\sqrt{2\pi}}{6}\frac{C_2}{k}\frac{H^2}{(2Hr_c - 1)}\sum_{\ell=0}^{\infty}\frac{(-1)^\ell(2\ell + \frac{3}{2})}{(2\ell + 1)\{2\ell Hr_c + 1\}} \\
& \times [\{6\ell(2\ell + 1)Hr_c + 12\ell + 9\}(-k\eta)^{-\frac{1}{2}}J_{2\ell+\frac{3}{2}}(-k\eta) - 4(\ell + 1)(-k\eta)^{\frac{1}{2}}J_{2\ell+\frac{1}{2}}(-k\eta) + (-k\eta)^{\frac{3}{2}}J_{2\ell-\frac{1}{2}}(-k\eta)],
\end{aligned}
\tag{13}
$$

+ branch ($\epsilon = 1$)

where

$$
\begin{aligned}
\mathcal{R}_{(b)(m^2=2H^2)} \ = \ & -\frac{C_1}{6k}\frac{H^2}{(2Hr_c - 1)(Hr_c - 1)}\Big[3(Hr_c - 1)(-k\eta)^{-1}\sin(-k\eta) \\
& + \frac{\alpha(-k\eta)}{2}\{-3(-k\eta)^{-1}\sin(-k\eta) + 3\cos(-k\eta) + (-k\eta)\sin(-k\eta)\} \\
& + \frac{\beta(-k\eta)}{2}\{-3(-k\eta)^{-1}\cos(-k\eta) - 3\sin(-k\eta) + (-k\eta)\cos(-k\eta)\}\Big],
\end{aligned}
\tag{14}
$$

for $Hr_c \neq 1$ and

$$
\begin{aligned}
\mathcal{R}_{(b)(m^2=2H^2)} \;=\; & \frac{C_1 H^2}{12k}\Big[-6(-k\eta)^{-1}\sin(-k\eta) \\
& +\tilde{\alpha}(-k\eta)\{-3(-k\eta)^{-1}\sin(-k\eta)+3\cos(-k\eta)+(-k\eta)\sin(-k\eta)\} \\
& +\tilde{\beta}(-k\eta)\{-3(-k\eta)^{-1}\cos(-k\eta)-3\sin(-k\eta)+(-k\eta)\cos(-k\eta)\}\Big],
\end{aligned}
\tag{15}
$$

for $Hr_c = 1$.

We should note that there are homogeneous solutions that satisfy $\mathcal{G}=0$. These homogeneous solutions also induce curvature perturbations on the brane.

4 Conclusion

In this paper, we studied inflaton perturbations confined to a de Sitter brane with induced gravity in a five-dimensional Minkowski spacetime.

For a vacuum brane, the spin-0 mode appears as a discrete bulk mode with $m^2 = 2H^2$ in the $+$ branch, while in the $-$ branch there are no normalizable solutions for the spin-0 modes. Since there is another discrete bulk mode (helicity-0 mode of spin-2 perturbation) with mass $m^2 = H^2(3Hr_c-1)(Hr_c)^{-2}$ in the $+$ branch, there is a resonance between the spin-0 mode and the helicity-0 mode of spin-2 perturbation for $Hr_c = 1$. In this paper we introduced inflaton perturbations on a brane. Then an infinite ladder of discrete modes with $m^2 = -2(2\ell-1)(\ell+1)H^2$ and $m^2 = -2\ell(2\ell+3)H^2$ are excited. Since there is a mode with $m^2 = 2H^2$ regardless of the value of Hr_c, in the $+$ branch the resonance inevitably appears. We obtained the solutions for the curvature perturbation on the brane $\mathcal{R}_{(b)}$ and studied their behavior.

We make comments on future applications of our results. In $-$ branch, if $r_c \ll H^{-1}$, small scale perturbations $a/k \ll r_c$ can be described by the four-dimensional Brans-Dicke theory. If the perturbations approaches to r_c, the gravity becomes five-dimensional and we expect significant effects from the coupling to five-dimensional metric perturbations [4]. Unlike the Randall-Sundrum model where the small scales perturbations are always coupled to five-dimensional perturbations and a quantum vacuum state is hard to be specified [4, 10, 11], we can specify a vacuum state without ambiguity based on the four-dimensional BD theory on sufficiently small scales. Then we can estimate the effect of the coupling to five-dimensional gravity without ambiguity.

For the discussion of the behavior of metricperturbation in several limits, please see Ref. [12]

References

[1] R. Maartens, Living Rev. Rel. **7**, 7 (2004).

[2] R. Maartens, D. Wands, B. A. Bassett and I. Heard, Phys. Rev. D **62**, 041301 (2000).

[3] K. Koyama, D. Langlois, R. Maartens and D. Wands, JCAP **0411** (2004) 002.

[4] K. Koyama, S. Mizuno and D. Wands, JCAP **0508**, 009 (2005).

[5] S. L. Adler, Phys. Rev. Mod. Phys. **54**, 729 (1982) [Erratum-ibid. **55**, 837 (1983)].

[6] G. R. Dvali, G. Gabadadze and M. Porrati, Phys. Lett. B **485**, 208 (2000).

[7] C. Deffayet, Phys. Lett. B **502**, 199 (2001).

[8] S. Mukohyama, Phys. Rev. D **62**, 084015 (2000).

[9] H. Kodama, A. Ishibashi and O. Seto, Phys. Rev. D **62**, 064022 (2000).

[10] K. Koyama, A. Mennim and D. Wands, Phys. Rev. D **72**, 064001 (2005).

[11] H. Yoshiguchi and K. Koyama, Phys. Rev. D **71** (2005) 043519.

[12] K. Koyama and S. Mizuno, JCAP **0607**, 013 (2006).

Scalar cosmological perturbations in the Gauss-Bonnet braneworld

Tsutomu Kobayashi[1] and Masato Minamitsuji[2]

[1]*Department of Physics, Tokyo Institute of Technology, Tokyo 152–8551, Japan*
[2]*Yukawa Institute for Theoretical Physics, Kyoto University, Kyoto 606–8502, Japan*

Abstract

We study scalar cosmological perturbations in a braneworld model with a bulk Gauss-Bonnet term. For an anti-de Sitter bulk, the five-dimensional perturbation equations share the same form as in the Randall-Sundrum model, which allows us to obtain metric perturbations in terms of a master variable. We derive the boundary conditions for the master variable from the generalized junction conditions on the brane. We then investigate several limiting cases in which the junction equations are reduced to a feasible level. In the low energy limit, we confirm that the standard result of four-dimensional Einstein gravity is reproduced on large scales, whereas on small scales we find that the perturbation dynamics is described by the four-dimensional Brans-Dicke theory. In the high energy limit, all the non-local contributions drop off from the junction equations, leaving a closed system of equations on the brane. We show that, for inflation models driven by a scalar field on the brane, the Sasaki-Mukhanov equation holds on the high energy brane in its original four-dimensional form. This article is a short summary of [1].

1 Introduction

One of the simplest realizations of braneworld is proposed by Randall and Sundrum (RS) [2], assuming that the bulk involves five-dimensional (5D) Einstein gravity with a negative cosmological constant. The RS model can be naturally extended to include the *Gauss-Bonnet* (GB) term:

$$\mathcal{L}_{\mathrm{GB}} := \mathcal{R}^2 - 4\mathcal{R}_{AB}\mathcal{R}^{AB} + \mathcal{R}_{ABCD}\mathcal{R}^{ABCD}, \tag{1}$$

where $\mathcal{R}$, $\mathcal{R}_{AB}$, and $\mathcal{R}_{ABCD}$ denote the Ricci scalar, Ricci tensor, and Riemann tensor in five dimensions, respectively. Cosmology on a GB brane is important because one of the possible ways to test the braneworld idea is studying cosmological perturbations from inflation. In this direction, Minamitsuji and Sasaki [3] have examined linearized effective gravity on a de Sitter brane, and Dufaux *et al.* [4] investigated tensor and scalar perturbations generated from de Sitter inflation in the GB braneworld (The authors of [4] have performed an exact analysis for the tensor perturbations, but they have neglected bulk effects for the scalar perturbations without any justification). In the present article, we study scalar cosmological perturbations on a more general (flat) Friedmann-Robertson-Walker cosmological brane.

2 Gauss-Bonnet braneworld

We start with providing the basic equations that describe the GB braneworld. Our action is

$$S = \frac{1}{2\kappa^2} \int d^5x \sqrt{-g}\left[\mathcal{R} - 2\Lambda + \alpha\mathcal{L}_{\mathrm{GB}}\right] + \int d^4x \sqrt{-q}\left[2K + \frac{4\alpha}{3}Q + \mathcal{L}_m - \sigma\right], \tag{2}$$

where Λ is the cosmological constant in the bulk, $\mathcal{L}_m$ is the matter Lagrangian on the brane, and σ is the brane tension. The GB Lagrangian $\mathcal{L}_{\mathrm{GB}}$ was already defined in Eq. (1) and the coupling constant α has dimension of (length)^2. The surface term is given by $2K + (4\alpha/3)Q$, where K is the trace of the extrinsic curvature $K_\mu{}^\nu$ of the brane and $Q := Q_\mu{}^\mu$ with $Q_\mu{}^\nu$ defined below in Eq. (6).

---

[1]E-mail:tsutomu@th.phys.titech.ac.jp
[2]E-mail:masato@yukawa.kyoto-u.ac.jp

The 5D field equations following from the above action are

$$\mathcal{G}_{AB} - \frac{\alpha}{2}\mathcal{H}_{AB} = -\Lambda g_{AB}, \tag{3}$$

where $\mathcal{G}_{AB} := \mathcal{R}_{AB} - \mathcal{R}g_{AB}/2$ is the Einstein tensor and $\mathcal{H}_{AB}$ is the GB tensor defined by

$$\mathcal{H}_{AB} := \mathcal{L}_{\mathrm{GB}}g_{AB} - 4\left(\mathcal{R}\mathcal{R}_{AB} - 2\mathcal{R}_{AC}\mathcal{R}^C_B - 2\mathcal{R}_{ACBD}\mathcal{R}^{CD} + \mathcal{R}_{ACDE}\mathcal{R}_B^{\ CDE}\right). \tag{4}$$

Assuming a Z_2 symmetry across the brane, the junction conditions at the brane are given by [5]

$$K_\mu^{\ \nu} - K\delta_\mu^{\ \nu} = -\frac{\kappa^2}{2}\left(T_\mu^{\ \nu} - \sigma\delta_\mu^{\ \nu}\right) - 2\alpha\left(Q_\mu^{\ \nu} - \frac{1}{3}Q\delta_\mu^{\ \nu}\right), \tag{5}$$

where $T_{\mu\nu}$ is the matter energy-momentum tensor and

$$\begin{aligned}
Q_\mu^{\ \nu} &:= 2KK_\mu^{\ \alpha}K_\alpha^{\ \nu} - 2K_\mu^{\ \alpha}K_\alpha^{\ \beta}K_\beta^{\ \nu} + \left(K_\alpha^{\ \beta}K_\beta^{\ \alpha} - K^2\right)K_\mu^{\ \nu} \\
&\quad + 2KR_\mu^{\ \nu} + RK_\mu^{\ \nu} - 2K_\alpha^{\ \beta}R_{\mu\beta}^{\ \ \nu\alpha} - 2R_\mu^{\ \alpha}K_\alpha^{\ \nu} - 2R_\alpha^{\ \nu}K_\mu^{\ \alpha},
\end{aligned} \tag{6}$$

with $R_{\mu\nu\alpha\beta}$, $R_{\mu\nu}$ and R being the Riemann tensor, Ricci tensor and Ricci scalar with respect to the 4D induced metric. The main difference in the junction conditions from those in Einstein gravity is that they include intrinsic curvature terms as well as external ones. Using the Codacci equation, we can show that the conservation law holds on the brane.

The field equations (3) admit an anti-de Sitter (AdS) bulk with the curvature radius ℓ ($=: \mu^{-1}$). The 5D cosmological constant and μ are related by $\Lambda = -6\mu^2\left(1 - 2\alpha\mu^2\right)$. It is useful to define a dimensionless parameter $\beta := 4\alpha\mu^2$. In this paper, we assume the parameter range $0 \le \beta < 1$. To present a cosmological background solution which has a flat 3D geometry [6], we write the AdS metric in the Gaussian normal coordinates as $g^{(0)}_{AB}dx^Adx^B = -n^2(t,y)dt^2 + a^2(t,y)\delta_{ij}dx^idx^j + dy^2$. We may set $n(t,0) = 1$, so that t is the proper time on the brane at $y = y_b = 0$ and $a_b(t) := a(t,0)$ is the scale factor. Then the 5D field equations are solved to give

$$n(t,y) = \dot{a}(t,y)/\dot{a}_b(t), \tag{7}$$

$$a(t,y) = a_b(t)\left[\cosh(\mu y) - \sqrt{1 + \frac{H^2}{\mu^2}}\sinh(\mu y)\right]. \tag{8}$$

Although the 5D field equations include the GB term, the metric functions $n(t,y)$ and $a(t,y)$ have the same form as in the cosmological solution in the RS braneworld based on the Einstein-Hilbert action. What is manifestly different is the Friedmann equation that relates the Hubble expansion rate H and the energy-momentum components on the brane. The Friedmann equation derived from the generalized junction conditions at the brane is [6]

$$2\sqrt{H^2 + \mu^2}\left(3 - \beta + 2\beta\frac{H^2}{\mu^2}\right) = \kappa^2(\rho + \sigma). \tag{9}$$

The critical brane tension, which allows for a Minkowski brane, is obtained by setting $H \to 0$ as $\rho \to 0$: $\kappa^2\sigma = 2\mu(3 - \beta)$. There are three regimes for the dynamical history of the GB brane universe, two of which are basically the same as those found in the context of the RS braneworld. When $H^2 \ll \mu^2/\beta[= (4\alpha)^{-1}]$, we recover the RS-type Friedmann equation, $H^2 \simeq 8\pi G/3\left(\rho + \rho^2/2\sigma\right)$, where we defined the 4D gravitational constant as $8\pi G := \kappa^2\mu/(1 + \beta)$. At very high energies, $H^2 \gg \mu^2/\beta$, the effect of the GB term becomes prominent. In this regime, we find $H^2 \simeq \left(\kappa^2\mu^2\rho/4\beta\right)^{2/3}$.

3 Summary of cosmological perturbation theory in the Gauss-Bonnet braneworld

Now let us consider linear perturbations about the cosmological brane background discussed in the previous section. If the background geometry is given by AdS, the perturbed GB tensor has a following nice property:

$$\delta\mathcal{H}_A^{\ B} = 8\mu^2\delta\mathcal{G}_A^{\ B} \quad \Rightarrow \quad (1 - \beta)\delta\mathcal{G}_A^{\ B} = 0, \tag{10}$$

which, aside from the factor $(1 - \beta)$, give the same perturbation equations as in Einstein gravity. This allows us to make full use of the previously known results on cosmological perturbations in the RS model.

We write the perturbed metric in an arbitrary gauge as

$$
\begin{aligned}
\left(g_{AB}^{(0)} + \delta g_{AB}\right) dx^A dx^B = \ & -n^2(1 + 2A)dt^2 + 2a^2 B_{,i} dt dx^i + a^2 \left[(1 - 2\psi)\delta_{ij} + 2E_{,ij}\right] dx^i dx^j \\
& + 2nA_y dt dy + 2a^2 B_{y,i} dx^i dy + (1 + 2A_{yy})dy^2.
\end{aligned}
\tag{11}
$$

The 5D perturbation equations will be solved most easily in the so-called *5D longitudinal gauge* [7], which is defined by $\tilde{\sigma} = -\tilde{B} + \dot{\tilde{E}} = 0$, and $\tilde{\sigma}_y = -\tilde{B}_y + \tilde{E}' = 0$. We use a master variable, Ω, which was originally introduced by Mukohyama [8] in the Einstein gravity case. The perturbed 5D field equations are solved if the metric perturbations are written in terms of this master variable:

$$
\tilde{A} = -\frac{1}{6a}\left[2\Omega'' - \frac{n'}{n}\Omega' - \mu^2\Omega + \frac{1}{n^2}\left(\ddot{\Omega} - \frac{\dot{n}}{n}\dot{\Omega}\right)\right], \quad \tilde{A}_y = \cdots, \quad \tilde{A}_{yy} = \cdots, \quad \tilde{\psi} = \cdots,
\tag{12}
$$

where Ω is a solution of the master equation

$$
\Omega'' + \left(\frac{n'}{n} - 3\frac{a'}{a}\right)\Omega' - \frac{1}{n^2}\left[\ddot{\Omega} - \left(\frac{\dot{n}}{n} + 3\frac{\dot{a}}{a}\right)\dot{\Omega}\right] + \left(\mu^2 + \frac{1}{a^2}\Delta\right)\Omega = 0,
\tag{13}
$$

with $\Delta := \delta^{ij}\partial_i\partial_j$.

From the junction conditions (5) we obtain

$$
\kappa^2\delta\rho = -6(1 - \beta)\delta K_T + \frac{2\beta}{\mu^2}\frac{a_b'}{a_b}\delta G_0{}^0,
\tag{14}
$$

$$
\kappa^2\delta q_{,i} = -2(1 - \beta)\delta K_i{}^0 - \frac{2\beta}{\mu^2}\frac{a_b'}{a_b}\delta G_i{}^0,
\tag{15}
$$

$$
\kappa^2\delta p = 2(1 - \beta)\left(\delta K_0{}^0 + 2\delta K_T\right) + \frac{2\beta}{\mu^2}\left[\frac{1}{3}\left(\frac{a_b'}{a_b} - \frac{n_b'}{n_b}\right)\delta G_0{}^0 - \frac{a_b'}{a_b}\delta G_T\right],
\tag{16}
$$

$$
\kappa^2\delta\pi = -2(1 - \beta)\delta K_{TL} - \frac{2\beta}{\mu^2}\frac{1}{a_b^2}\left[\frac{n_b'}{n_b}\Psi - \frac{a_b'}{a_b}\Phi\right].
\tag{17}
$$

The perturbations of the extrinsic curvature and the Einstein tensor can be written in terms of the master variable Ω and the *brane bending* (the perturbed location of the brane) ξ. In Eq. (17) the metric potentials are defined by $\Phi := \tilde{A} + (n'/n)_b\xi$ and $\Psi := \tilde{\psi} - (a'/a)_b\xi$. This equation relates Ω with ξ. Thus the above equations (14)–(17) give the boundary conditions for Ω at the brane.

3.1 Low energy limit

3.1.1 Perturbations larger than the bulk curvature radius

We can show that the standard 4D result is reproduced if $H^2 \ll \mu^2$ and $\mu^2\Omega \gg \Delta\Omega/a_b^2$.

3.1.2 Small scale perturbations

We now consider scales much smaller than the typical GB scale, $\left|\Delta\Omega/a_b^2\right| \gg \left|\mu^2\Omega/\beta\right|$, by requiring that $\xi \sim (\beta/\mu)\Delta\Omega/a_b^3$. In this regime, the junction equations are equivalent to

$$
\delta G_\mu{}^\nu = \frac{1}{2\varphi_0}\delta T_\mu{}^\nu + \frac{1}{\varphi_0}\left(\nabla_\mu\nabla^\nu - \nabla_\lambda\nabla^\lambda\delta_\mu{}^\nu\right)\delta\varphi, \quad \nabla_\lambda\nabla^\lambda\delta\varphi = \frac{1}{6 + 4\omega}\delta T,
\tag{18}
$$

with the identifications

$$
\frac{1}{\varphi_0} \to \frac{\kappa^2\mu}{\beta}, \quad \frac{\delta\varphi}{\varphi_0} \to -\mu\left(\frac{1 - \beta}{\beta}\right)\xi, \quad \omega \to \frac{3\beta}{1 - \beta}.
\tag{19}
$$

This is nothing but the linearized Brans-Dicke theory with terms of $\mathcal{O}(H^2\delta\varphi)$ neglected.

3.2 High energy limit

Let us take the high energy limit, $H^2 \gg \mu^2/\beta$. In this regime, the right hand side of the junction equations (14)–(16) is dominated by the perturbed 4D Einstein tensor and so we have

$$\delta G_0{}^0 = -\frac{\kappa^2 \mu^2}{2\beta H}\delta\rho, \quad \delta G_i{}^0 = \frac{\kappa^2 \mu^2}{2\beta H}\delta q_{,i}, \quad \delta G_T = \frac{\kappa^2 \mu^2}{2\beta H}\left(\delta p - \frac{\epsilon_H}{3}\delta\rho\right), \tag{20}$$

where we defined $\epsilon_H := -\dot{H}/H^2$. Similarly, it is easy to show that the right hand side of Eq. (17) is dominated by the metric potentials. Thus we obtain

$$(1 - \epsilon_H)\Psi - \Phi = \frac{\kappa^2 \mu^2}{2\beta H}a_b^2 \delta\pi. \tag{21}$$

The set of equations (20) and (21) governs the perturbation dynamics at very high energies.

Consider braneworld inflation driven by a single scalar field ϕ which is confined on the brane. For this background we have $\rho = \dot{\phi}^2/2 + V(\phi)$ and $p = \dot{\phi}^2/2 - V(\phi)$, where $V(\phi)$ is the potential of the inflaton. For perturbations generated by fluctuations of the scalar field, it is quite easy to describe the evolution of perturbations in the high energy limit by introducing the Sasaki-Mukhanov variable and invoking the energy conservation equation. The perturbations of the energy-momentum components are given by $\delta\rho = \dot{\phi}\left(\dot{\delta\phi} - \dot{\phi}\bar{A}_b\right) + (dV/d\phi)\,\delta\phi$, $\delta q = -\dot{\phi}\delta\phi$, and $\delta p = \dot{\phi}\left(\dot{\delta\phi} - \dot{\phi}\bar{A}_b\right) - (dV/d\phi)\,\delta\phi$. The equation of motion for the scalar field perturbation $\delta\phi$ follows from the energy conservation equation, $\delta\left(\nabla_\nu T^{\mu\nu}\right) = 0$. Introducing a scalar field perturbation in the spatially flat gauge, $\delta\phi_\psi := \delta\phi + \dot{\phi}/H\bar{\psi}_b$, and defining new variables $v := a_b\delta\phi_\psi, z := a_b\dot{\phi}/H$, the Klein-Gordon equation for the scalar field perturbation can be rewritten in a familiar form

$$v'' + \left(k^2 - \frac{z''}{z}\right)v = 0, \tag{22}$$

where a prime denotes a derivative with respect to conformal time. This exactly coincides with the Sasaki-Mukhanov equation derived in the standard 4D context.

References

[1] T. Kobayashi and M. Minamitsuji, JCAP **0612**, 008 (2006).

[2] L. Randall and R. Sundrum, Phys. Rev. Lett. **83**, 3370 (1999), L. Randall and R. Sundrum, Phys. Rev. Lett. **83**, 4690 (1999).

[3] M. Minamitsuji and M. Sasaki, Prog. Theor. Phys. **112**, 451 (2004).

[4] J. F. Dufaux, J. E. Lidsey, R. Maartens and M. Sami, Phys. Rev. D **70**, 083525 (2004).

[5] G. W. Gibbons and S. W. Hawking, Phys. Rev. D **15**, 2752 (1977), R. C. Myers, Phys. Rev. D **36**, 392 (1987), S. C. Davis, Phys. Rev. D **67**, 024030 (2003), E. Gravanis and S. Willison, Phys. Lett. B **562**, 118 (2003).

[6] C. Charmousis and J. F. Dufaux, Class. Quant. Grav. **19**, 4671 (2002).

[7] H. A. Bridgman, K. A. Malik and D. Wands, Phys. Rev. D **65**, 043502 (2002).

[8] S. Mukohyama, Phys. Rev. D **62**, 084015 (2000), S. Mukohyama, Class. Quant. Grav. **17**, 4777 (2000), S. Mukohyama, Phys. Rev. D **64**, 064006 (2001) [Erratum-ibid. D **66**, 049902 (2002)].

Fermions on Colliding Branes

Yu-ichi Takamizu [1], Gary Gibbons [2] and Kei-ichi Maeda [3]

[1,3] *Department of Physics, Waseda University, Okubo 3-4-1, Shinjuku, Tokyo 169-8555, Japan*
[2] *DAMTP, Centre for Mathematical Sciences, University of Cambridge, Wilberforce Road, Cambridge CB3 0WA, UK*

Abstract

We study the behaviour of five-dimensional fermions localized on branes, which we describe by domain walls, when two parallel branes collide in a five-dimensional Minkowski background spacetime. We find that most fermions are localized on both branes as a whole even after collision. However, how much fermions are localized on which brane depends sensitively on the incident velocity and the coupling constants unless the fermions exist on both branes.

1 Introduction

In the 80's, one may regard our universe as a domain wall, or more generally a brane in a higher dimensional universe. The idea is that the fermionic chiral matter making up the standard model is composed of trapped zero modes. A similar mechanism is used in models, such as the Horawa-Witten model, in which two domain walls are present. The existence of models with more than one brane suggests that branes may collide, and it is natural to suppose that the Big Bang is associated with the collision [1]. This raises the fascinating questions of what happens to the localized fermions during such collisions? In this study we shall embark on what we believe is the first study of this question by solving numerically the Dirac equation for a fermions coupled via Yukawa interaction to a system of two colliding domain walls. Kink-anti-kink collisions, have recently been studied numerically [2, 3]. One may extend the treatment to include gravity [4, 5] but in this paper we shall, for the sake of our preliminary study, work throughout with gravity switched off.

2 Fermions on moving branes

We start with a discussion of five-dimensional (5D) four-component fermions in a time-dependent domain wall in 5D Minkowski spacetime. As a domain wall, we adopt a 5D real scalar field Φ with an appropriate potential $V(\Phi)$. The 5D Dirac equation with a Yukawa coupling term $g\Phi\bar{\Psi}\Psi$ is given by

$$(\Gamma^{\hat{A}}\partial_{\hat{A}} + g\Phi)\Psi = 0, \quad (\hat{A} = 0, 1, 2, 3, 5), \tag{1}$$

where Ψ is a 5D four-component fermion. $\Gamma^{\hat{A}}$ are the Dirac matrices in 5D Minkowski spacetime satisfying the anticommutation relations. We introduce two chiral fermion states

$$\Psi_{\pm} = \frac{1}{2}\left(1 \pm \Gamma^{\hat{5}}\right)\Psi, \quad \Psi_{+} = \begin{pmatrix} \psi_{+} \\ \psi_{+} \end{pmatrix}, \quad \Psi_{-} = \begin{pmatrix} \psi_{-} \\ -\psi_{-} \end{pmatrix}, \tag{2}$$

where ψ_{+} and ψ_{-} are two-component spinors. The Dirac equation (1) is now reduced to

$$\left(\pm\partial_{\hat{5}} + g\Phi\right)\psi_{\pm} + \Gamma^{\hat{\mu}}\partial_{\hat{\mu}}\psi_{\mp} = 0. \tag{3}$$

As for a domain wall, now we assume the potential form is given by $V(\Phi) = \frac{\lambda}{4}\left(\Phi^2 - \eta^2\right)^2$. Then a domain wall solution is given by $\Phi = \epsilon \tanh(z/D)$ where $\epsilon = \pm$ correspond to a kink and an anti-kink

---

[1]E-mail:takamizu@gravity.phys.waseda.ac.jp
[2]E-mail:G.W.Gibbons@damtp.cam.ac.uk
[3]E-mail:maeda@waseda.jp

solutions and $D = \sqrt{2/\lambda}$ is the width of a domain wall. As for a fermion, in the case of a static domain wall, separating variables as $\psi_\pm = \overset{(4)}{\psi}_\pm(x^\mu) f_\pm(z)$ and assuming massless chiral fermions on a brane, i.e. $\Gamma^{\hat{\mu}} \partial_\mu \overset{(4)}{\psi}_\pm(x^\mu) = 0$, we find the solutions are

$$f_\pm \propto \left[\cosh\left(\frac{z}{D}\right)\right]^{\mp \epsilon g D}. \tag{4}$$

Hence the positive-chiral (the negative-chiral) fermion is localized for a kink (an anti-kink) but is not localized for an anti-kink (a kink). To discuss fermions at collision of branes, we first discuss fermions on a domain wall moving with a constant velocity. Since 3-space is flat, we expand the wave functions by Fourier series. In what follows, we shall consider only low energy fermions, that is, we assume that $\vec{k} \approx 0$. The equations we have to solve are now

$$i\partial_0 \psi_\pm = (\mp \partial_5 + g\Phi) \psi_\mp. \tag{5}$$

Since up- and down-components of $\psi_\pm$ are decoupled, we discuss only up-components here. With this ansatz, we can construct a localized fermion wave function on a moving domain wall with a constant velocity v. We find for a kink with velocity v,

$$\psi_+^{(\mathrm{K})}(z,t;v) = \sqrt{\frac{\gamma+1}{2}} \tilde{\psi}^{(\mathrm{K})}(\gamma(z-vt)), \quad \psi_-^{(\mathrm{K})}(z,t;v) = i\frac{\gamma v}{\gamma+1}\sqrt{\frac{\gamma+1}{2}} \tilde{\psi}^{(\mathrm{K})}(\gamma(z-vt)) \tag{6}$$

and we also find solution for an anti-kink, where $\tilde{\psi}^{(\mathrm{K})}(\tilde{z}) = f_+(\tilde{z})$ are static wave functions of chiral fermions localized on static kink. If a domain wall is given by a kink [an anti-kink], we have only the positive-chiral fermions in a comoving frame [the negative-chiral fermions]. However, from Eqs (6), we find that the negative-chiral modes [positive-chiral modes] also appear in this boosted Lorentz frame. The above wave functions on a moving domain wall can be used for setting the initial data for colliding domain walls.

3 Fermions on colliding domain wall

We construct our initial data as follows. Provide a kink solution at $z = -z_0$ and an anti-kink solution at $z = z_0$, which are separated by a large distance and approaching each other with the same speed v. We can set up as an initial profile for the scalar field Φ and fermions Ψ;

$$\Phi(z,t) = \Phi^{(\mathrm{K})}(z+z_0,t;v) + \Phi^{(\mathrm{A})}(z-z_0,t;-v) - 1, \tag{7}$$

$$\hat{\Psi} = \Psi_{\mathrm{in}}^{(\mathrm{K})}(x,z+z_0;v)a_{\mathrm{K}} + \Psi_{\mathrm{in}}^{(\mathrm{A})}(x,z-z_0;-v)a_{\mathrm{A}} + \Psi_{\mathrm{in}}^{(\mathrm{B})}(x,z)a_{\mathrm{B}}, \tag{8}$$

where $\Phi^{(\mathrm{K,A})}(z,t;v) = \pm \tanh(\gamma(z-vt)/D)$, and $\Psi_{\mathrm{in}}^{(\mathrm{K})}(x,z;v)$ and $\Psi_{\mathrm{in}}^{(\mathrm{A})}(x,z;-v)$ are the wave function of right-moving localized fermion on a kink and those of left-moving one on an anti-kink. We also denote the bulk fermions symbolically by $\Psi_{\mathrm{in}}^{(\mathrm{B})}(x,z)$. To quantize the fermion fields, we define annihilation operators of localized fermions on a kink and on an anti-kink by

$$a_{\mathrm{K}} = \langle \Psi^{(\mathrm{K})}, \Psi \rangle \quad \text{and} \quad a_{\mathrm{A}} = \langle \Psi^{(\mathrm{A})}, \Psi \rangle \tag{9}$$

Now we can set up an initial state for fermion by creation-annihilation operators. We shall call a domain wall associated with fermions a fermion wall, and a domain wall in vacuum a vacuum wall. We shall discuss two cases: one is collision of two fermion walls, and the other is collision of fermion and vacuum walls. For initial state of fermions, we consider two states;

$$|\mathrm{KA}\rangle \equiv a_{\mathrm{A}}^\dagger a_{\mathrm{K}}^\dagger |0\rangle \quad \text{and} \quad |\mathrm{K0}\rangle \equiv a_{\mathrm{K}}^\dagger |0\rangle \tag{10}$$

where $|0\rangle$ is a fermion vacuum state. We discuss behaviour of fermions at collision. After collision of two domain walls, each wall will recede to infinity with almost the same velocity as the initial one v. We define final fermion states as

$$\hat{\Psi} = \Psi_{\mathrm{out}}^{(\mathrm{K})}(x,z;-v)b_{\mathrm{K}} + \Psi_{\mathrm{out}}^{(\mathrm{A})}(x,z;v)b_{\mathrm{A}} + \Psi_{\mathrm{out}}^{(\mathrm{B})}(x,z)b_{\mathrm{B}}, \tag{11}$$

where $b_{\rm K}$, $b_{\rm A}$ and $b_{\rm B}$ are annihilation operators of those fermion states. We find the relations between ingoing and outgoing states by solving the Dirac equation (5);

$$b_{\rm K} = \alpha_{\rm K}a_{\rm K} + \beta_{\rm A}a_{\rm A} , \quad b_{\rm A} = \alpha_{\rm A}a_{\rm A} + \beta_{\rm K}a_{\rm K} , \tag{12}$$

Using the Bogoliubov coefficients $\alpha_{\rm K}, \beta_{\rm K}$ and $\alpha_{\rm A}, \beta_{\rm A}$, we obtain the expectation values of fermion number on a kink and an anti-kink after collision as

$$\langle N_{\rm K}\rangle \equiv \langle {\rm KA}|b_{\rm K}^{\dagger}b_{\rm K}|{\rm KA}\rangle = |\alpha_{\rm K}|^2 + |\beta_{\rm A}|^2 , \tag{13}$$

$$\langle N_{\rm A}\rangle \equiv \langle {\rm KA}|b_{\rm A}^{\dagger}b_{\rm A}|{\rm KA}\rangle = |\alpha_{\rm A}|^2 + |\beta_{\rm K}|^2 , \tag{14}$$

for the case of $|{\rm KA}\rangle$. If the initial state is $|{\rm K0}\rangle$, we find

$$\langle N_{\rm K}\rangle \equiv \langle {\rm K0}|b_{\rm K}^{\dagger}b_{\rm K}|{\rm K0}\rangle = |\alpha_{\rm K}|^2 , \tag{15}$$

$$\langle N_{\rm A}\rangle \equiv \langle {\rm K0}|b_{\rm A}^{\dagger}b_{\rm A}|{\rm K0}\rangle = |\beta_{\rm K}|^2 . \tag{16}$$

In order to obtain the Bogoliubov coefficients, we have to solve the equations for domain wall Φ [3] and fermion Ψ numerically. From the solution (4), we find the fermions are localized within the domain wall width D if $g \gtrsim 2/D$. When $g < 2/D$, fermions leak out from the domain wall. Hence, in this paper, we analyze for the case of $g \geq 2$ with setting $D = 1$, but leave v free. To obtain the Bogoliubov coefficients, we solve the Dirac equation for the collision of fermion-vacuum walls. We shall give numerical results only for the case that positive chiral fermions are initially localized on a kink. Because of z-reflection symmetry, we find the same Bogoliubov coefficients for the case that negative chiral fermions are initially localized on an anti-kink, i.e. $|\alpha_{\rm K}|^2 = |\alpha_{\rm A}|^2$. The Bogoliubov coefficients depend on the initial wall velocity. In Table 1, we summarize our results for different values of velocity and Yukawa coupling constant.

v	$g = 2$			$g = 2.5$		
	$|\alpha_{\rm K}|^2$	$|\beta_{\rm K}|^2$	$|\gamma_{\rm K}|^2$	$|\alpha_{\rm K}|^2$	$|\beta_{\rm K}|^2$	$|\gamma_{\rm K}|^2$
0.3	0.94	0.056	0.004	0.47	0.53	0.00
0.4	0.87	0.12	0.01	0.57	0.40	0.03
0.6	0.69	0.30	0.01	0.78	0.17	0.05
0.8	0.42	0.55	0.03	0.88	0.02	0.10

Table 1: The Bogoliubov coefficients of fermion wave functions localized on each domain wall after collision ($|\alpha_{\rm K}|^2$ and $|\beta_{\rm K}|^2$) with respect to the initial velocity v. We also show the amount of fermions escaped into bulk space ($|\gamma_{\rm K}|^2 = 1 - (|\alpha_{\rm K}|^2 + |\beta_{\rm K}|^2)$).

For the coupling constant $g = 2$, $|\alpha_{\rm K}|^2$ and $|\beta_{\rm K}|^2$ are almost equal (0.44 and 0.55), but for $g = 2.5$, most fermions remain on the kink ($|\alpha_{\rm K}|^2 = 0.88$ and $|\beta_{\rm K}|^2 = 0.02$). We find that the Bogoliubov coefficients depend sensitively on the coupling constant g as well as the velocity v. In Fig. 1, we shows the g-dependence. Since the wave function is changed at collision, when the background scalar field evolves in a complicated way, one might think that the behaviour of wave function would be difficult to describe analytically. However, we may understand the qualitative behaviour in terms of the naive estimation. As a result, we obtain the formula;

$$|\alpha_{\rm K}|^2, |\beta_{\rm K}|^2 \approx \frac{1}{2}\left[1 \pm \sin\left(2\varepsilon g \Phi_c \Delta t + C_0\right)\right] , \tag{17}$$

where $\varepsilon = \pm 1$ and C_0 is an integration constant. Comparing the numerical data and the formula (17) with $\Phi_c \approx -1.5$, we find the fitting curves in Fig. 1 ($\varepsilon = -1$, $\Delta t \approx 1.4$ and $C_0 = -1.2$). This fitting formula explains our numerical results very well.

Finally, we can evaluate the expectation values of fermion numbers after collision as follows. For the initial state of fermions, we consider two cases: case (a) collision of two fermion walls $|{\rm KA}\rangle$ and case (b) collision of fermion and vacuum walls $|{\rm K0}\rangle$. In the case (a), we find

$$\langle N_{\rm K}\rangle = |\alpha_{\rm K}|^2 + |\beta_{\rm A}|^2 = |\alpha_{\rm K}|^2 + |\beta_{\rm K}|^2 \approx 1 , \quad \langle N_{\rm A}\rangle = |\alpha_{\rm A}|^2 + |\beta_{\rm K}|^2 = |\alpha_{\rm A}|^2 + |\beta_{\rm A}|^2 \approx 1 . \tag{18}$$
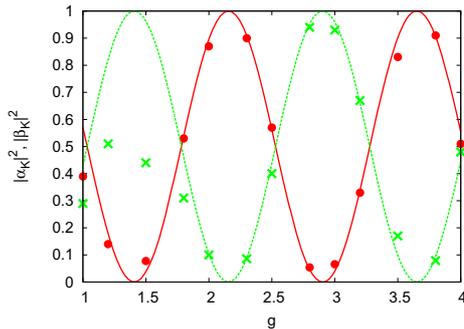
Figure 1: The Bogoliubov coefficients $(|\alpha_K|^2, |\beta_K|^2)$ with $v = 0.4$ in terms of a coupling constant g. The circle and the cross denote $|\alpha_K|^2$ and $|\beta_K|^2$ respectively. Two sine curves $(|\alpha_K|^2, |\beta_K|^2 \approx [1 \pm \sin(4.2g - 1.2))]/2$ show the formula (17) with the best-fit parameters.

We find that most fermions on domain walls remain on both walls even after the collision. A small amount of fermions escapes into the bulk spacetime at collision. In the case (b), however, we obtain

$$\langle N_K \rangle = |\alpha_K|^2 \ , \quad \langle N_A \rangle = |\beta_K|^2 \, . \tag{19}$$

Since the Bogoliubov coefficients depend sensitively on both the velocity v and the coupling constant g, the amount of fermions on each wall is determined by the fundamental model as well as the details of the collision of the domain walls.

4   Conclusion

We have studied the behaviour of five-dimensional fermions localized on domain walls, when two parallel walls collide in five-dimensional Minkowski background spacetime. We analyzed the dynamical behaviour of fermions during the collision of fermion-fermion branes (case (a)) and that of fermion-vacuum walls (case (b)). In case (a), we find that most fermions are localized on both branes even after collision. In case (b), however, some fermions jump up to the vacuum brane at collision. The amount of fermions localized on which brane depends sensitively on the incident velocity v and the coupling constants $g/\sqrt{\lambda}$. The detailed discussion is shown in [6].

References

[1] J. Khoury, B. A. Ovrut, P. J. Steinhardt and N. Turok, Phys. Rev. D **64**, 123522 (2001) [hep-th/0103239]

[2] P. Anninos, S. Oliveira and R. A. Matzner, Phys. Rev. D **44**, 1147 (1991).

[3] Y. Takamizu and K. Maeda, Phys. Rev. D **70** (2004) 123514 [hep-th/0406235].

[4] Y. Takamizu and K. Maeda, Phys. Rev. D **73** (2006) 103508 [hep-th/0603076].

[5] G.W. Gibbons, H. Lu, C.N. Pope, Phys. Rev. Lett. **94**, 131602 (2005) [hep-th/0501117].

[6] G. Gibbons, K. Maeda and Y. Takamizu, arXiv:hep-th/0610286.

Algebraic quantum gravity

Masaru Siino[1]

Department of Physics, Tokyo Institute of Technology,
Oh-Okayama 1-12-1, Megro-ku, Tokyo 152-8550, Japan

Abstract

Field theory is reformulated on the algebraically defined system. Here we argue the algebraic construction of field theory by a Dirac operator and its quantization. Also gravitational field is investigated. As a simple example, we develop the gravitational field theory on the two-point lattice spacetime.

1 Introduction

From the progresses of quantum mechanics, we have a wavy images of quantum particle, which posseses both aspects of a particle and a stochastic wave. In the study of quantum theory of gravity, what can we have the image about the microscopic spacetime. Most speculative is Wheeler's wormhole which combined the paticle and microscopic topology of spacetime. Hawking's suggestion is in small scale the spacetime has some topological nontoriviality in addition to some smooth fluctuation, which are small handle with π_1-nontriviality and virtrual black hole with π_2-nontriviality.

Since the smoothness is the essential concept of theoritical physics since standard physical theory is analytical theory. Without the differentiation on a continuous manifold we surrender the physical analysis of system. However, algebraic formulation is possible to extend the analysis to the discrete space or noncommutative space. For example, the author demonstrated that the analytical dynamics and general relativity is extended. It encourage us to have a image of microscopic spacetime with discrete topology of any other topological nontriviality. There are no reason prevent that. We should go further and watch the new horizon of the theoritical physics.

There is no doubt that the essence of quantum theory is the noncommutativity of operator algebra for physical variables. Usually, this noncommutativity reflects the ordering of quantum observations. In quantum gravity, how can we understand the noncommutativity? A standard answer would be the framework of field theory where the gravitational field is decomposed into a fluctuation of potential and background geometry. As long as the gravity is sufficiently weak, that will promise to treat spacetime geometry. However, strong gravity drastically changes background geometry, since general relativity is remarkably non-linear theory. Indeed, the topological instanton of quantum gravity implies the microscopic nontriviality of topology for spacetime. In this sense one should care the topological structure as a physical variable, for example, the Wilson loop and moduli parameter. If we want to completely enumerate the topological variables, one might treat the open neighborhoods of spacetime points, whose set and coordinate transformation yields a concept of manifold. Roughly speaking, considering all open neighborhoods as physical variable is similar to regarding their own spacetime points as physical variables by themselves. This will realize any noncommutativity through quantization of spacetime dynamics. Of course, though such an idea is an imaginary picture without mathematical background, if we once reproduce the geometry in an algebraic language, noncommutativity will be given to all the geometrical concepts, e.g., to spacetime points, by changing the commutative algebra into the noncommutative algebra.

The most successful framework of the noncommutative space has been established by A. Connes and is well known by his textbook[1]. In the study of the noncommutative geometry, the most important concept is algebraic abstraction of conventional commutative geometry. While ordinary commutative geometry has been established on a space with any mathematical structure, noncommutative geometry is constructed on the basis of the operator algebra which acts on a Hilbert space. Therefore we need algebraic abstraction of gravity theory when we consider noncommutative gravity theory. We will have

---

[1]E-mail:msiino@th.phys.titech.ac.jp

corresponding algebraic objects instead of the conventional objects like curvatures by which we characterize geometry, that is, topological space, differentiable manifold and Riemannian manifold. The algebraic counterparts are a set of continuous function, pseudodifferential operators and a Dirac operator; and are defined in the framework of a commutative operator algebra. Once this algebraic abstraction has been made, the operator algebra naturally extends from commutative to noncommutative one.

One might worry that by the noncommutative extension, space may lose its continuity or differentiability. The most worrisome thing might be missing of reasonable measure which is indispensable to develop physical theory there. Nevertheless, the framework of the spectral geometry established by Connes[2][3] provides the substantial structure that is appropriate to define a trace of operators.

Although people believe that our world is commutative and relativists study the dynamics of commutative spacetime, there are two motivations to consider noncommutative space. One is interest about the characteristic of real noncommutative space. For example, the noncommutative torus or the space of irreducible Penrose tiling is a well-known model of noncommutative space. The noncommutative torus of irrotational ring[4] is known as not Lebesgue measurable space. The set of the Penrose tiling is a quotient set of the Cantor set[1]. The other is physical interest concerning quantization of gravitational theory. Recently many authors study the noncommutative gravity, in the standpoint that at Planckian scale spacetime should be noncommutative. Most of them expect that the noncommutative space gives the quantization of spacetime geometry in the context of deformation quatization. On the other hand, the aim of the algebraic gravity is to rewrite general relativity in an algebraic language. Since the algebraically formulated theory makes it possible to extend general relativity into the spacetime without differential structure, it is expected that one can develop a consistent quantum theory of gravitation as a continuous limit of the theory on a discritized spacetime[5].

In these sense, a discretized spacetime is one of model of microscopic spacetime. In the present task, we attempt to extend the fundamental notion about the field theory to such a topologically nontrivial spacetime discribed by algebraic manner. Important concept is the function algebra and Clifford algebra on a spacetime. From Gelfand Naimark, the function algebra determine the topology of spacetime. Alain Connes establish the way to relate the Riemannian geometry and the Clifford algebra on it. Since the analytical dynamics was extended to discritized space[5], also the field theory is extended to the discritized spacetime in the present work. Some concept is prepared for the quantum theory formulated in the comvined work[6].

The detail will appear in forthcomming papers. There we develop the algebraic formulations for:

- field theory.

- Nether theorem.

- gravitational perturbation

- canonical quantization

- QFT

- quantum theory of gravitational perturbation.

References

[1] A. Connes, *Non Commutative Geometry,* Academic Press, London and San Diego 1994

[2] A. Connes, *Commun. Math. Phys.* **117**(1988) 673-683.

[3] J. C. Várilly and J. M. Gracia-Bondía, *J. Geom. Phys.* **12** (1993) 223-301.

[4] M. A. Rieffel, *Pac. J. Math.* **93** (1981) 415-429.

[5] M. Siino," Operator geometry and algebraic gravity" hep-th/0602256.

[6] M. Siino, "Algebraic gravity I: field theory" and "Algebraic gravity II: quantum theory" in preperation.

Time dependent solutions in six dimensional supergravity

Osamu Seto

Instituto de Física Teórica, Universidad Autónoma de Madrid, Cantoblanco, Madrid 28049, Spain

Edmund J. Copeland

School of Physics and Astronomy, University of Nottingham, University Park, Nottingham NG7 2RD, United Kingdom

Abstract

We derive exact time dependent solutions in a six dimensional supergravity model. Of particular interest would be models where four dimensions expand whereas the compact internal dimensions remain static. We show that under the assumptions we make for the form of the fields, this is impossible and find that the only consistent time dependent solutions lead to all six dimensions evolving (expanding) in time, implying the decompactification of the extra dimensions.

1 Introduction

Six dimensional supergravity models have several interesting properties. Salam and Sezgin obtained static solutions in which the six dimensional gauged supergravity compactifies on a product spacetime of four dimensional Minkowski and a two dimensional sphere, $\mathcal{M}_4 \times S^2$ [1]. Remarkably this supergravity model admits the supersymmetric Minkowski vacuum while many other supergravity models do not. The modern interpretation of this remarkable property is that the solution of this theory is compatible with the introduction of branes into the spacetime. As with any massive defect, this then leads of course to the appearance of a deficit angle in the two internal spatial dimensions, as a gravitational response to the tensions of branes [2]. The resulting geometry looks a rugby ball solution where the branes are located at the north and south pole of the ball. It was later revealed that the Salam-Sezgin vacuum is the unique one with a four dimensional maximal symmetry and general solutions with an axisymmetric internal space were obtained by Gibbons, Guven and Pope (GGP) [3].

The observation that the four dimensional spacetime is always Minkowski even in the presence of branes with tensions in Ref. [3] is a basis of the interesting supersymmetric large extra dimension (SLED) scenario, an approach to solving the cosmological constant and dark energy problems [2]. If only for this reason, such is the prize at stake, it makes this six dimensional supergravity interesting from a cosmological point of view, although we note that cosmology in six dimensional supergravity has previously been studied in the context of Kaluza-Klein cosmology [4, 5]. One of the neatest aspects of the SLED model is that a 3-brane with any tension in six dimensional spacetime induces only the corresponding deficit angle and does not lead to a non-vanishing four dimensional cosmological constant. This feature is often referred to as a "self-tuning mechanism" of the effective four dimensional cosmological constant and would be expected to be part of the solution to the cosmological constant problem (we still have to account for the affect of quantum corrections).

Although the SLED scenario has enjoyed a number of successes, open questions still remain. We are particularly interested in establishing whether the self-tuning mechanism really works in a time dependent evolving Universe. Previous authors have argued that the self-tuning of the four dimensional cosmological constant does not work at least in non-supersymmetric six dimensional Einstein Maxwell theories [6, 7, 8]. Our work has a number of overlaps with some of the solutions obtained by Tolley et al [9], who have obtained a series of solutions to the dynamical system, although we believe the explicit expressions of exact solution we present is done so for the first time.

In this short proceedings we search for time dependent exact solutions to the six dimensional supergravity model, as a first step toward understanding the cosmological evolution. Full details of the work will be published shortly [10].

2 The basic field equations

Concentrating on the bosonic field contents of this model, we have the metric g_{MN}, dilaton ϕ, a $U(1)$ gauge field A_M with field strength F_{MN} and an antisymmetric tensor field B_{MN} whose corresponding field strength is expressed as

$$G_{MNP} = \partial_M B_{NP} + F_{MN} A_P + \text{cyclic permutations.} \tag{1}$$

The lagrangian density for the bosonic sector is given by

$$\mathcal{L}_{\text{SUGRA}} = \frac{1}{2} R - \frac{1}{2} \partial^M \phi \partial_M \phi - \frac{e^{-2\phi}}{12} G^{MNP} G_{MNP} - \frac{e^{-\phi}}{4} F^{MN} F_{MN} - 2g^2 e^{\phi}, \tag{2}$$

where g is the $U(1)$ gauge coupling. Here M, N runs over all the spacetime indices and we work on the sphere with the six dimensional (reduced) Planck scale $M_6 = 1$.

For simplicity we consider an ansatz $G^{MNP} = 0$, namely the vanishing of the three form field strength. With that assumption the field equations are

$$D^M D_M \phi + \frac{e^{-\phi}}{4} F^{MN} F_{MN} - 2g^2 e^{\phi} = 0, \tag{3}$$

$$D_M \left(e^{-2\phi} F^{MN} \right) = 0, \tag{4}$$

$$-R_{MN} + \partial_M \phi \partial_N \phi + e^{-\phi} \left(F_M{}^P F_{NP} - \frac{1}{8} F^{PQ} F_{PQ} g_{MN} \right) + g^2 e^{\phi} g_{MN} = 0. \tag{5}$$

The metric ansatz we adopt is

$$ds^2 = W(x^m, t)^2 ds_4 + r(t)^2 ds_2^2,$$
$$ds_4^2 = -dt^2 + \delta_{ij} dx^i dx^j, \quad ds_2^2 = \gamma_{mn}(x^m) dx^m dx^n, \tag{6}$$

where i, j run over the usual three spatial indices and m, n run over the extra two spatial indices. Under this metric, the two form field strength takes a form of

$$F_{\mu\nu} = F_{\mu m} = 0$$
$$F_{mn} = F(t, x^m) \epsilon_{mn}, \tag{7}$$

with ϵ_{mn} being the anti-symmetric tensor. Here, the use of Greek indices denote the four spacetime coordinates (i.e. $\mu = (0, i)$).

3 Static Internal spaces are not solutions

3.1 Case1: Time dependent W

Ideally what we want to obtain is a solution which describes the expansion of our three space dimensions with a static extra dimensional space. As a first step towards obtaining it, we make the ansatz of a static internal space $r = 1$, a static dilaton $\phi = \phi(x^m)$ and assume a separable form for $W = W(t)W(x^m)$. The field equations can then be reduced to

$$C(x^m) - \frac{1}{4W^4} D_m(\gamma^{mn} \partial_n W^4) + \frac{e^{-\phi}}{8} F^{PQ} F_{PQ} - g^2 e^{\phi} = 0 \tag{8}$$

$$\frac{3}{W^2} \left(\frac{\partial_0 W}{W} \right)_{,0} = \frac{1}{W^2} \left(\frac{\partial_0 W}{W} \right)_{,0} + \frac{2}{W^2} \left(\frac{\partial_0 W}{W} \right)^2 = C(x^m). \tag{9}$$

which after some algebra leads to [10]

$$W(t) = \frac{W_0}{t - t_0}, \quad C(x^m) = \frac{3}{W_0^2 W(x^m)^2} \tag{10}$$

with W_0 and t_0 being integration constants.

However, from the other field equations, we also know that

$$D_m \left(\gamma^{mn} W^4 \partial_n (\ln W^4 + 2\phi) \right) - 4W^4 C(x^m) = 0, \tag{11}$$

which is conflict, for any non-vanishing W on the internal space, with the fact that the extra two dimensional space is compact. In other words, if we integrate both sides of Eq. (11) over the compact extra space, we see that the first term on the left hand side vanishes as it is a total derivative while the second terms does not. Hence, there is an inconsistency and so we conclude there is no solution static solution for the compact space with this ansatz for W.

3.2 Case 2: Time dependent r and ϕ, but static W.

Next, we tried to find a solution of the static three space with a dynamical extra dimensional space. However, unfortunately, we found that there is no consistent solution under this ansatz as well.

4 Time dependent solutions with dymanical r, W and ϕ

Having tried unsuccessfully to obtain static solutions for r and W, we now look for dynamical solutions where all the key fields r, W and ϕ are time dependent. We again make a series of ansatz, in this case $\phi(t, x^m) = \phi(t) + \phi(x^m)$, $e^{\phi(t)} r^2 = 1$ and assume the separable form of $W = W(t)W(x^m)$. We then obtain

$$\partial_m \phi = -2 \frac{\partial_m W}{W} \tag{12}$$

as in the GGP solution. Here, we note that the relation $r^2 \propto e^{-\phi}$ has been indicated by previous works [2]. If we assume that the Field strength F is static and only depends on x^m, then from the field equations we obtain [10]

$$C(x^m) - \frac{D_m(\gamma^{mn}\partial_n W^4)}{4W^4} + \frac{e^{-\phi}r^2}{8} F^{PQ} F_{PQ} - g^2 e^{\phi} r^2 = 0, \tag{13}$$

which depends on only x^m. Here, $C(x^m)$ is given by

$$
\begin{aligned}
C(x^m) &= \frac{r^2}{W^2} \left[3\left(\frac{\partial_0 W}{W}\right)_{,0} + 2\left(\frac{\partial_0 r}{r}\right)_{,0} - 2\frac{\partial_0 r}{r}\frac{\partial_0 W}{W} + 2\left(\frac{\partial_0 r}{r}\right)^2 + \partial_0\phi\partial_0\phi \right] \\
&= \frac{r^2}{W^2} \left[\left(\frac{\partial_0 W}{W}\right)_{,0} + 2\left(\frac{\partial_0 W}{W}\right)^2 + 2\frac{\partial_0 W}{W}\frac{\partial_0 r}{r} \right] \\
&= -\frac{1}{W^4}\partial_0\left(r^2 W^2 \partial_0\frac{\phi}{2}\right). \tag{14}
\end{aligned}
$$

and a function only of x^m, because all other terms in Eq. (13) also only depends on x^m.

4.1 Case a: Power law solutions for r and W

Eqns. (13) and (14) still look very difficult to solve directly from first principles, and so instead we will try to obtain solutions by assuming the form of r and W, and looking for consistency with the solutions. As a first attempt we assume power law behavior for them, namely:

$$W \propto t^{n_W}, \quad r \propto t^{n_r}. \tag{15}$$

Substitution into the field equations yields the non trivial expanding solution

$$n_W = \frac{2 - \sqrt{3}}{4}, \quad n_r = \frac{\sqrt{3}}{2}, \tag{16}$$

which in turn leads to $C(x^m) = 0$. Notice that in this case, we obtain identical solutions for F, ϕ and the x^m dependent part of W as found in the in the GGP solution. This is as expected, since the x^m dependent part of the field equations are identical to that of the GGP solution.

4.2 Case b: Exponential solutions for r and W

The next obvious step is to assume an exponential form

$$W(t) = e^{h_W t}, \quad r(t) = e^{h_r t}, \tag{17}$$

where h_W and h_r are constants. In this case, the non trivial solution turns out to be $h_W = h_r$. Then, $C(x^m)$ is given by

$$C(x^m) = \frac{4h^2}{W(x^m)^2} \tag{18}$$

with $h \equiv h_W(= h_r)$. Thus, we obtain the equations of motion of the x^m dependent part of the fields to be

$$\frac{4h^2}{W(x^m)^2} - \frac{D_m(\gamma^{mn}\partial_n W^4)}{4W^4} + \frac{e^{-\phi(x^m)}}{8}F^{PQ}F_{PQ} - g^2 e^{\phi(x^m)} = 0, \tag{19}$$

$$\frac{4h^2}{W(x^m)^2}\gamma_{mn} - \partial_m\phi\partial_n\phi - e^{-\phi(x^m)}\left(F_m{}^P F_{Pn} - \frac{1}{8}F^{PQ}F_{PQ}\gamma_{mn}\right) - g^2 e^{\phi(x^m)}\gamma_{mn} = 0. \tag{20}$$

Something significant can now be see. Recall that we have equation (12), relating ϕ and $W(x^m)$. Given the solution we have just obtained, we see that in Eqn. (20), by introducing $\tilde{g}^2 \equiv g^2 - 4h^2$, we see that the original x^m part of the GGP solution with our redefined gauge coupling $\tilde{g}^2$ instead of g^2 is a solution of this system. Obviously, the $h \to 0$ limit corresponds to the original static GGP solution. The line element of this solution with non-vanishing h is rewritten as

$$ds^2 = W(x^m)^2[-d\tau^2 + (h\tau)^2\delta_{ij}dx^i dx^j] + (h\tau)^2 ds_2^2, \tag{21}$$

in terms of the cosmic time. This solution (21) is found by Tolley et al too [9].

5 Conclusions

We have derived a class of exact time dependent solutions in a six dimensional gauged supergravity compactified on a two dimensional axisymmetric space. Under the assumption of a separable form of W we showed that there is no solution expressing the expanding four dimensional universe with a static internal space. Exact solutions we obtained involved all the dimensions expanding which means the eventual decompactification of the extra dimension, indicating an instability of Salam-Sezgin, (Minkowski)$_4 \times S^2$, spacetime for the case with the absence of the maximal symmetry in the four dimensional spacetime.

Acknowledgments

References

[1] A. Salam and E. Sezgin, Phys. Lett. B **147**, 47 (1984).

[2] Y. Aghababaie, C. P. Burgess, S. L. Parameswaran and F. Quevedo, Nucl. Phys. B **680**, 389 (2004) [arXiv:hep-th/0304256].

[3] G. W. Gibbons, R. Guven and C. N. Pope, Phys. Lett. B **595**, 498 (2004) [arXiv:hep-th/0307238].

[4] K. i. Maeda and H. Nishino, Phys. Lett. B **154**, 358 (1985).

[5] K. i. Maeda and H. Nishino, Phys. Lett. B **158**, 381 (1985).

[6] H. P. Nilles, A. Papazoglou and G. Tasinato, Nucl. Phys. B **677**, 405 (2004) [arXiv:hep-th/0309042].

[7] J. Vinet and J. M. Cline, Phys. Rev. D **70**, 083514 (2004) [arXiv:hep-th/0406141].

[8] J. Garriga and M. Porrati, JHEP **0408**, 028 (2004) [arXiv:hep-th/0406158].

[9] A. J. Tolley, C. P. Burgess, C. de Rham and D. Hoover, New J. Phys. **8**, 324 (2006) [arXiv:hep-th/0608083].

[10] E. J. Copeland and O. Seto, in preparation.

[11] G. W. Gibbons and K. i. Maeda, Nucl. Phys. B **298**, 741 (1988).

[12] Y. Aghababaie *et al.*, JHEP **0309**, 037 (2003) [arXiv:hep-th/0308064].

Global properties of some homogeneous spacetimes in the Einstein-Yang-Mills-dilaton system

Makoto Narita[1]

Department of Mathematics, National Taiwan University
1, Sec. 4, Roosevelt Rd., Taipei, 106, Taiwan

Abstract

We prove theorems which support the validity of the strong cosmic censorship for some homogeneous spacetimes in the Einstein-Yang-Mills-dilaton system.

Introduction   The strong cosmic censorship (SCC) conjecture states that the maximal Cauchy development of generic initial data for the Einstein(-matter) equations is inextendible [EM81]. To prove this conjecture in terms of nonlinear partial differential equations two steps are needed; as the first step, a global existence theorem of solutions for the Einstein(-matter) equations in a suitable (e.g. constant mean curvature) time coordinate should be shown and as the second step, inextendibility should be checked. To do the second step, analysis of asymptotic behavior of spacetimes is needed. Recently, global existence theorems for some classes of spacetimes with or without matter are proven (see review article [RA05]).

By the discovery of spherical symmetric and static particle-like (numerical) solutions to the Einstein-Yang-Mills equations by Bartnik and McKinnon [BM], study of classical solutions to gravitational field coupled with the Yang-Mills filed turned out to be an interest research field. Also, the success of gauge field theory in connection with accelerated expanding universe [FL] and the evidence of chaotic behavior near asymptotic regions of spacetimes [BL], lead us to study the Einstein-Yang-Mills system in cosmological setting. From the viewpoint of nonlinear differential equation problems, since global existence theorem for the Yang-Mills-Higgs system has been shown on the Minkowski background [EM82], it is interesting to study extension to system of the Yang-Mills field coupled with scalar and gravitational fields. For cosmological spacetimes, there are few results on this problem. Thus, we will consider locally rotational symmetric (LRS) Bianchi type I spacetimes, which is one of the most simplest cosmological models, and use the form of $SU(2)$-Yang-Mills gauge field given by Darian and Künzle [DK].

In this paper, motivated by higher-dimensional unified theories, e.g. superstring/M-theory, where a dilaton field arises naturally, the Einstein-Yang-Mills-dilaton theory is considered and we investigate global properties of the Einstein-Yang-Mills-dilaton system in LRS Bianchi I spacetimes with an $SU(2)$-Yang-Mills field. Our main result is a proof of the validity of the SCC in the spacetimes. In summary,

Theorem 1 ([NM]) *The strong cosmic censorship holds for LRS Bianchi I spacetimes in the Einstein-Yang-Mills-dilaton system, that is, there exists a maximal Cauchy development of generic initial data for the system of the Einstein-Yang-Mills-dilaton equations and it is inextendible.*

Einstein-Yang-Mills-dilaton system   Four dimensional string vacua emerging from heterotic superstring theories, correspond to $\mathcal{N} = 1$ non-minimal supergravity and super Yang-Mills model [GSW]. The low-energy effective bosonic action arising the string theory, called the Einstein-Yang-Mills-dilaton (EYMD) system, is given by

$$S = \int d^4x \sqrt{-g} \left[R - e^{a\kappa} \text{Tr}(\mathcal{F}_{\mu\nu}\mathcal{F}^{\mu\nu}) - \frac{1}{2}(\nabla\kappa)^2 \right], \tag{1}$$

with the Yang-Mills field strength

$$\mathcal{F}_{\mu\nu} = \partial_\mu \mathcal{A}_\nu - \partial_\nu \mathcal{A}_\mu + [\mathcal{A}_\mu, \mathcal{A}_\nu], \tag{2}$$

where $g_{\mu\nu}$ is the metric of four dimensional spacetimes, R is the Ricci scalar, κ is the dilaton field with a coupling constant a, $\mathcal{A}_\mu = A_\mu^{(a)} T_{(a)}$ is the gauge potential of the Yang-Mills field and $\{T_{(a)}\}$ is a generator

---

[1] E-mail:narita@math.ntu.edu.tw

of Lie group G with $[T_{(a)}, T_{(b)}] = f_{(a)(b)}^{(c)} T_{(c)}$, where $f_{(a)(b)}^{(c)}$ is the structure constant of G. In terms of components, the Yang-Mills field strength becomes

$$F_{\mu\nu}^{(a)} = \partial_\mu A_\nu^{(a)} - \partial_\nu A_\mu^{(a)} + f_{(b)(c)}^{(a)} A_\mu^{(b)} A_\nu^{(c)}. \tag{3}$$

We have assumed that a cosmological constant and potentials of dilaton field are zero. Varying this action with respect to $g_{\mu\nu}$, $\mathcal{A}_\mu$ and κ, we have the system of the EYMD equations as follows:

$$R_{\mu\nu} - \frac{1}{2} g_{\mu\nu} R = T_{\mu\nu}, \tag{4}$$

$$D_\mu \left(e^{a\kappa} \mathcal{F}^{\mu\nu} \right) = 0, \tag{5}$$

$$\nabla_\lambda \nabla^\lambda \kappa - a e^{a\kappa} \text{Tr}(\mathcal{F}_{\mu\nu} \mathcal{F}^{\mu\nu}) = 0, \tag{6}$$

where $T_{\mu\nu}$ is the energy-momentum tensor

$$T_{\mu\nu} = \nabla_\mu \kappa \nabla_\nu \kappa - \frac{1}{2} g_{\mu\nu} \nabla_\lambda \kappa \nabla^\lambda \kappa + e^{a\kappa} \left(\text{Tr}(\mathcal{F}_{\mu\lambda} \mathcal{F}_\nu^\lambda) - \frac{1}{4} g_{\mu\nu} \text{Tr}(\mathcal{F}_{\mu\nu} \mathcal{F}^{\mu\nu}) \right), \tag{7}$$

and D_α is the gauge-covariant derivative

$$D_\mu \mathcal{F}^{\mu\nu} := \nabla_\mu \mathcal{F}^{\mu\nu} + [\mathcal{A}_\mu, \mathcal{F}^{\mu\nu}], \tag{8}$$

with the covariant derivative ∇ with respect to $g_{\mu\nu}$.

LRS Bianchi I spacetime   A generic form of the metric for LRS Bianchi type I spacetimes is given as follows:

$$ds = -N^2 dt^2 + b^2 (dx^2 + dy^2) + c^2 dz^2, \tag{9}$$

where metric functions b and c are depend only on time t and N is the lapse function, which will be supposed $N \equiv 1$ after getting the field equations. Here we put

$$e^\alpha := (b^2 c)^{1/3}, \qquad e^\gamma := (bc^{-1})^{1/3}.$$

e^α is the averaged scale factor and e^γ implies the anisotropy of three dimensional spacelike hypersurfaces, $t =$ constant. In this coordinate, the metric becomes

$$ds = -N^2 dt^2 + e^{2(\alpha+\gamma)} (dx^2 + dy^2) + e^{2(\alpha-2\gamma)} dz^2. \tag{10}$$

We also define the momentum for α and γ to obtain the first-order differential equations as follows.

$$p_\alpha := \partial_t \alpha \qquad p_\gamma := \partial_t \gamma.$$

Yang-Mills field   We assume the following form for the gauge potential,

$$A = T_1 u dx + T_2 u dy + T_3 v dz, \tag{11}$$

for the Yang-Mills field [DK]. Functions u and v are depend only on time t and T_i are $SU(2)$ generators $[T_1, T_2] = iT_3$. From this, we can obtain the field strength as follows:

$$\begin{aligned} F = {} & \partial_t u \left(T_1 dt \wedge dx + T_2 dt \wedge dy \right) + \partial_t v T_3 dt \wedge dz \\ & + u^2 T_3 dx \wedge dy + uv \left(T_2 dz \wedge dx + T_1 dy \wedge dz \right). \end{aligned} \tag{12}$$

We will define the following quantities:

$$\psi := \frac{u}{b} = u e^{-(\alpha+\gamma)}, \qquad \phi := \frac{v}{c} = v e^{-(\alpha-2\gamma)},$$

and

$$p_\psi := \frac{\partial_t u}{b} = \partial_t u e^{-(\alpha+\gamma)} = \partial_t \psi + (p_\alpha + p_\gamma)\psi, \qquad p_\phi := \frac{\partial_t v}{c} = \partial_t v e^{-(\alpha-2\gamma)} = \partial_t \phi + (p_\alpha - 2p_\gamma)\phi.$$

Dilaton field   The dilaton field κ also depends only on time and the momentum will be defined as follows:

$$p_\kappa := \partial_t \kappa.$$

The coupling constant a is arbitrary. In the case of $a = 0$, the system becomes the Einstein-Yang-Mills-scalar one and this scalar filed is decoupled with the Yang-Mills field.

Field equations   Now, the Lagrangian density in terms of $(N, \alpha, \gamma, \psi, \phi, \kappa)$ is of the form:

$$L := L_K + L_P, \tag{13}$$

where L_K is the kinetic part

$$L_K = \frac{e^{3\alpha}}{2N} \left\{ 3 \left[-(\partial_t \alpha)^2 + (\partial_t \gamma)^2 \right] + (\partial_t \kappa)^2 + e^{a\kappa} \left[2e^{-2(\alpha+\gamma)}(\partial_t u)^2 + e^{-2(\alpha-2\gamma)}(\partial_t v)^2 \right] \right\},$$

and L_P is the potential part

$$L_P = -\frac{1}{2} e^{a\kappa} e^{3\alpha} N \left(2e^{-2(2\alpha-\gamma)} u^2 v^2 + e^{-4(\alpha+\gamma)} u^4 \right).$$

By varying this action with respect to $(\alpha, \gamma, \psi, \phi, \kappa)$ and putting $N \equiv 1$, we have the system of the dynamical part of the EYMD equations, which is the first-order nonlinear ordinary differential equations as follows:

$$\partial_t w = f(w), \tag{14}$$

where $w := (\alpha, p_\alpha, \gamma, p_\gamma, \psi, p_\psi, \phi, p_\phi, \kappa, p_\kappa)^T$ and

$$f(w) := \begin{bmatrix} p_\alpha \\ -p_\gamma^2 - 2p_\alpha^2 - \frac{1}{3}p_\kappa^2 \\ p_\gamma \\ -3p_\alpha p_\gamma + \frac{2}{3}e^{a\kappa}(-p_\psi^2 + p_\phi^2 - \psi^2\phi^2 + \psi^4) \\ p_\psi - (p_\alpha + p_\gamma)\psi \\ -(2p_\alpha - p_\gamma + ap_\kappa)p_\psi - \psi(\psi^2 + \phi^2) \\ p_\phi - (p_\alpha - 2p_\gamma)\phi \\ -[ap_\kappa + 2(p_\alpha + p_\gamma)]p_\phi - 2\psi^2\phi \\ p_\kappa \\ -3p_\alpha p_\kappa + \frac{a}{2}e^{a\kappa}\left(2p_\psi^2 + p_\phi^2 - 2\psi^2\phi^2 - \psi^4\right) \end{bmatrix}. \tag{15}$$

By varying the action with respect to N and putting $N \equiv 1$, we have the Hamiltonian constraint equation

$$-3p_\alpha^2 + 3p_\gamma^2 + e^{a\kappa}\left(2p_\psi^2 + p_\phi^2 + 2\psi^2\phi^2 + \psi^4\right) + p_\kappa^2 = 0. \tag{16}$$

The momentum constraint is trivial. Note that the constant mean curvature time slices is equivalent to the hypersurfaces of homogeneity in spatially homogeneous spacetimes. Thus, the mean curvature H of spacelike hypersurfaces

$$H = -3p_\alpha, \tag{17}$$

serves as *time*. Now we can fix the time direction as $H < 0$ into the future [RA94]. This means that the universe is expanding along the time. To see this, consider the constraint equation (16). This equation means that H cannot become zero except in very special conditions. That is, $H = 0$ implies that p_γ and matter fields are zero and then, the spacetime must be Minkowski space. Therefore, $H < 0$ for all time if the spacetime is not flat.

Results Theorem 1 is proved from the following theorems, whose proofs are given in [NM].

Theorem 2 *For any positive constant M, there exists a positive constant $t_0 = t_0(M)$, which is independent of τ, and the following holds: If w_τ satisfies $|w_\tau| \leq M$, Cauchy problem*

$$\begin{cases} \partial_t w = f(w), & t \geq \tau, \\ w(\tau) = w_\tau \in \mathrm{R}^{10}, \end{cases} \tag{18}$$

has a unique solution $w \in C^1(I)$ on $I = [\tau, \tau + t_0]$ such that

$$\sup_{t \in I} |w(t)| \leq 2M \tag{19}$$

is satisfied, and thus there exists a unique corresponding maximal spacetime on the interval.

Theorem 3 *For any $w_0 \in \mathrm{R}^{10}$, which satisfies the constraint equation (16), there is a positive number $C(w_0)$ which depends only on w_0 and the Cauchy problem (18) has a unique global solution $w \in C^1((T^*, \infty))$ such that*

$$\sup_{t > T^*} |w(t)| \leq C(w_0),$$

is satisfied, and thus there exists a corresponding maximal spacetime globally.

Theorem 4 *The Kretschmann scalar for the spacetime become infinite as t goes to the time T^*.*

Theorem 5 *The spacetime is future geodesic complete.*

References

[BM] Bartnik, R. and McKinnon, J., *Particlelike solutions of the Einstein-Yang-Mills equations*, Phys. Rev. Lett. **61**, (1988) 141-144.

[BL] Barrow, J. D. and Levin, J., *Chaos in the Einstein-Yang-Mills equations*, Phys. Rev. Lett. **80**, (1998) 656-659.

[DK] Darian, B. K. and Künzle, H. P., *Axially symmetric Bianchi I Yang-Mills cosmology as a dynamical system*, Classical Quantum Gravity **13**, (1996), 2651-2662.

[EM81] Eardley D. and Moncrief, V., *The global existence problem and cosmic censorship in general relativity*, Gen. Rel. Grav. **13**, (1981), 887-892.

[EM82] Eardley D. and Moncrief, V., *The global existence of Yang-Mills-Higgs fields in 4-dimensional Minkowski space. I. Local existence and smoothness properties*, Comm. Math. Phys. **83**, (1982), 171-191; *The global existence of Yang-Mills-Higgs fields in 4-dimensional Minkowski space. II. Completion of proof*, Comm. Math. Phys. **83**, (1982), 193-212.

[FL] Ford, L. H., *Inflation driven by a vector field*, Phys. Rev. **D40**, (1989) 967-972.

[GSW] Green, M. B., Schwarz, J. H. and Witten, E., *Superstring theory. Vol. 2*, Cambridge Monographs on Mathematical Physics, (Cambridge University Press, Cambridge, 1988).

[NM] Narita, M., *Global properties of locally rotational symmetric Bianchi I cosmology in the Einstein-Yang-Mills-dilaton system*, Class. Quantum Grav. **23**, 7531-7540, (2006).

[RA94] Rendall, A. D., *Cosmic censorship for some spatially homogeneous cosmological models*, Ann. Physics **233**, (1994) 82-96.

[RA05] Rendall, A. D., *Theorems on existence and global dynamics for the Einstein equations*, Living Rev. Relativity **8**, (2005), 6.

Cosmological Constraints on Generalized Dark Energy Models

Kiyotomo Ichiki[1] and Tomo Takahashi[2]

[1] *Research Center for the Early Universe, University of Tokyo, Tokyo 113-0033, Japan*
[2] *Department of Physics, Saga University, Saga 840-8502, Japan*

Abstract

A puzzling question in modern cosmology has been the nature and origin of dark energy for the apparent acceleration of the universe in the present epoch. In most researches of dark energy, one often parameterizes dark energy with its equation of state 'w', and cosmological observations have tried to put constraint on this parameter as severe as possible. The equation of state parameter can only be relevant to the back ground evolution, and therefore, one needs to specify the fluctuation properties of dark energy to compare its theoretical predictions with observational data derived from density inhomogeneity such as cosmic microwave background anisotropies (CMB) and galaxy clustering. Here we parameterize the dark energy fluctuation in a general manner and investigate their effect on the final result of the constraint on the equation of state of dark energy. We found that a different assumption of the fluctuation property of dark energy can lead a different result of constraint on 'w' by at most $\lesssim 20$ %.

Almost all cosmological observations today suggests that the present universe is accelerating. To account for the present cosmic acceleration, one usually assumes an enigmatic component called dark energy. In most researches of dark energy, one often parameterizes dark energy with its equation of state $w_X = p_X/\rho_X$ where p_X and ρ_X are pressure and energy density of dark energy. Current cosmological observations can give a severe constraint on w_X. When the equation of state is assumed to be constant in time, it is constrained as $w_X = -0.941^{+0.087}_{-0.101}$ [1][3].

The parameterization mentioned above can only be relevant to the background evolution. In fact, in various models of dark energy, dark energy can fluctuate and then its fluctuation can affects the cosmic density perturbations such as cosmic microwave background (CMB). When one specifies a model for dark energy, one can investigate its effects of fluctuation using the perturbation equation in the model. However, there are many models proposed to date, one may prefer to describe it in a phenomenological way. To describe the nature of fluctuation of dark energy, the (effective) speed of sound c_s^2 has been used in many works so far. Some authors have investigated the constraints on the equation of state varying the speed of sound [2] and on the speed of sound itself [3]. Since the fluctuation of dark energy mostly come into play after when dark energy becomes the dominant component of the universe, the effects of it appears on large scales. Hence, when one tries to constrain the speed of sound from observations of CMB, we do not obtain a severe constraint on it because the cosmic variance error is large there. However, some studies have shown that the constrains on the equation of state can vary with the assumption for the perturbation property of dark energy. For example, the constraint we mentioned above is obtained by assuming no fluctuation for dark energy, however, when one take into account the perturbation of dark energy, the constraint becomes $w_X = -1.00^{+0.17}_{-0.19}$ where $c_s^2 = 1$ is assumed [1]. Thus, in this sense, it is important to investigate the properties of dark energy fluctuation from the viewpoint not only from to reveal its fluctuation nature but also from constraining the equation of state for dark energy.

In fact, to parameterize the perturbation property of dark energy, the use of the speed of sound is not enough. If one considers the possibilities of imperfect fluid models for dark energy, we also need to specify its anisotropic stress in some way. In fact, there have been proposed that some models have such anisotropic stress [4] and also there are a few works which accommodate such possibilities from a phenomenological point of view [5, 6]. Although they investigated its effects in some detail, cosmological constrains in such models did not given. Since now we have precise measurements of cosmology, it is

---

[1] E-mail:ichiki@resceu.s.u-tokyo.ac.jp
[2] E-mail:tomot@cc.saga-u.ac.jp
[3] This constraint is given for the fluctuation of dark energy being neglected.

worth to investigate constraints for dark energy in such a general setting. The purpose of the present paper is to discuss a generalized dark energy including the possibilities of imperfect fluids and give the constraints on various parameters assuming such a generalized dark energy.

The background evolution of dark energy can be parameterized by its equation of state $w_X = p_X/\rho_X$. The evolution of the energy density of dark energy is given by solving

$$\rho'_X = -3\mathcal{H}(1 + w_X)\rho_X \tag{1}$$

where the prime denotes the derivative with respect to the conformal time η and $\mathcal{H} = a'/a$ is the conformal Hubble parameter with a being the scale factor. As far as the background evolution is concerned, this equation specifies it.

To specify the nature of dark energy perturbation, we need to give its pressure perturbation and anisotropic stress. For the pressure perturbation, it may be useful to separate it to adiabatic and non-adiabatic parts. When the dark energy fluid is adiabatic, the evolutions of pressure perturbation can be specified with the adiabatic sound speed c_a^2 which is

$$c_a^2 \equiv \frac{p'_X}{\rho'_X} = w_X - \frac{w'_X}{3\mathcal{H}(1 + w_X)}. \tag{2}$$

Then pressure perturbation is given as $\delta p = c_a^2 \delta\rho$. However, in general, non-adiabatic pressure perturbation may arise. Such a degrees of freedom can be parameterized with the so-called speed of sound which is defined as

$$c_s^2 \equiv \frac{\delta p_X}{\delta\rho_X}\Big|_{\rm rest}. \tag{3}$$

This quantity is usually defined in the rest frame of dark energy. A famous example of dark energy models with non-adiabatic pressure is quintessence which has the speed of sound $c_s^2 = 1$. Other models such as k-essence can have different values for the speed of sound. In the adiabatic case, c_s^2 and c_a^2 coincide.

In fact, to consider a general fluid model for dark energy, the speed of sound is not enough to specify its nature. We still have to specify an anisotropic stress for dark energy. Including the anisotropic stress, perturbation equations for density and velocity fluctuations are

$$\delta'_X = -(1 + w_X)\left[k^2 + 9\mathcal{H}^2(c_s^2 - c_a^2)\right]\frac{\theta_X}{k^2} - 3\mathcal{H}(c_s^2 - w_X)\delta_X - (1 + w_X)\frac{h'}{2} \tag{4}$$

$$\theta'_X = -\mathcal{H}(1 - 3c_s^2)\theta_X + \frac{c_s^2 k^2}{1 + w_X}\delta_X - k^2\sigma_X \tag{5}$$

where δ_X, θ_X and σ_X represent density, velocity and anisotropic stress perturbations for a general fluid, respectively. The anisotropic stress can be obtained by solving

$$\sigma'_X + 3\mathcal{H}\frac{c_a^2}{w_X}\sigma_X = \frac{8}{3}\frac{c_{\rm vis}^2}{1 + w_X}\left(\theta_X + \frac{h'}{2} + 3\eta'\right) \tag{6}$$

where $c_{\rm vis}^2$ is "the viscosity parameter" which can specify the nature of an anisotropic stress for dark energy. We modified CAMB code [7] and CMBFAST code [8] to include a general dark energy fluid to calculate CMB power spectra.

In Figure 1, we show the CMB power spectrum with several values of $c_{\rm vis}^2$. As seen from the figure, increasing the values of $c_{\rm vis}^2$, the low multipole region are more enhanced, which is driven by the ISW effect. In fact, for the case with $c_{\rm vis}^2 = 1$ and 0.1, the tendency becomes the opposite. This is because of the non-trivial cancellation between the ISW effect and the cross correlation of the SW with the ISW effects.

By including the sound speed and viscous effects of dark energy, we now investigate how these fluctuation properties can affect the result of constraint on the equation of state of dark energy w_X. To do this, we first fix the two parameters related to the fluctuation of dark energy (c_s^2 and $c_{\rm vis}^2$) to some values, and compare the result with the standard (quintessential) dark energy model parameterized by $(c_s^2, c_{\rm vis}^2) = (1, 0)$. Here we investigate three cases: $(c_s^2, c_{\rm vis}^2) = (0, 0)$, $(0, 1)$, and $(1, 1)$.

To obtain the result of constraint on the equation of state of dark energy w_X, we employ a Markov Chain Monte Carlo (MCMC) engine which has been a standard method to explore the likelihood. The
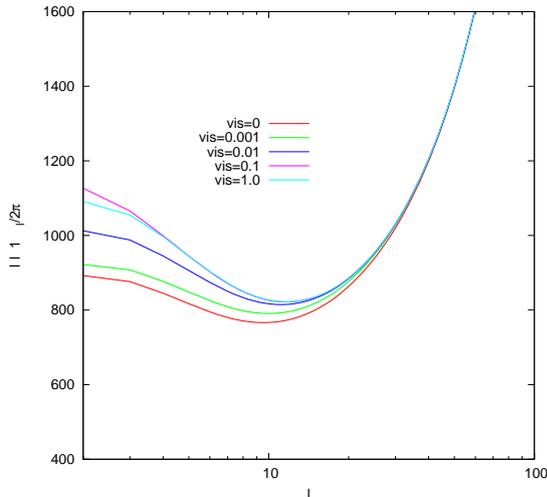
Figure 1: Calculated angular power spectrum of CMB temperature anisotropy for several values of c_{vis}^2. Lines are for the model with (from bottom to top) $c_{\mathrm{vis}}^2 = 0$, 0.001, 0.01, 1.0, 0.1 as indicated. In the figure, we fixed dark energy parameters as $w_X = -0.8$ and $c_s^2 = 0$. Other cosmological parameters are fixed to $\Omega_m h^2 = 0.02, \Omega_b h^2 = 0.11, h = 0.68, \tau = 0$ and $n_s = 1$ only for an illustration. We assume that the universe is flat and no tensor mode contribution.

other cosmological parameters are all marginalized. The likelihood functions we calculate are given by WMAP3 term [9] for the CMB anisotropies and 2dF term [10] for the matter power spectrum. Our results are shown in figures 2 and 3.
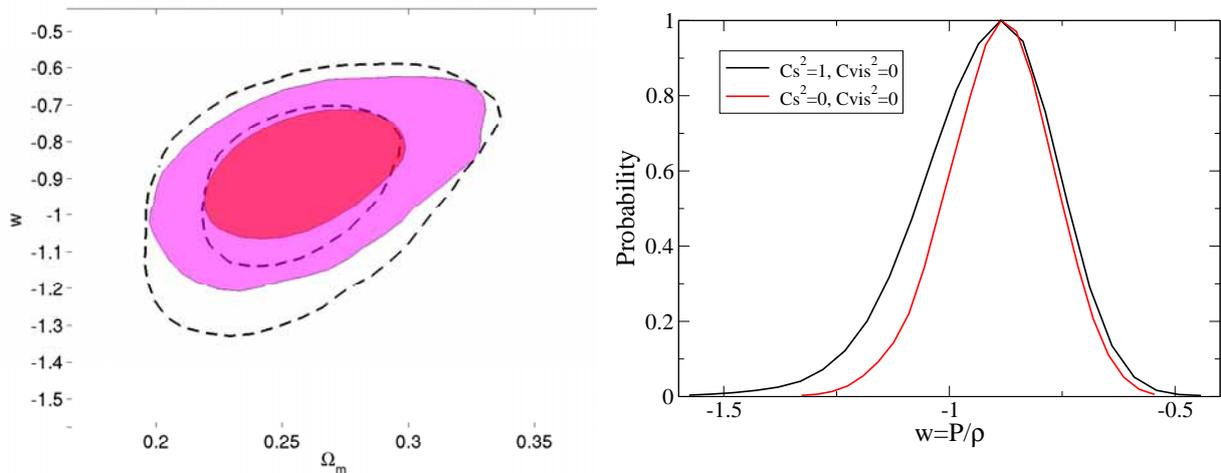

Figure 2: Left: Marginalized 68% and 95% confidence regions from CMB and $P(k)$ for an $(c_s^2, c_{\mathrm{vis}}^2) = (0, 0)$ dark energy component (dashed) and $(c_s^2, c_{\mathrm{vis}}^2) = (0, 0)$ (colored). The confidence region is smaller for preassureless dark energy model. Right: One dimensional distribution function of w_X obtained by marginalizing all the other cosmological parameters.

Interestingly, we found that the confidence region in the parameters plane of Ω_M and w_X is significantly smaller for the $(c_s^2, c_{\mathrm{vis}}) = (0, 0)$ case than the fiducial standard case $(c_s^2, c_{\mathrm{vis}}) = (1, 0)$ (figure 2). This fact leads to the different conclusion on the constraint on the equation of state w_X as $w_X = -0.89^{+0.21}_{-0.24}$, while w_X is limited as $w_X = -0.92^{+0.25}_{-0.32}$ for the fiducial case (errors are 2 σ). In this particular case, the confidence limits on w_X can differ by $\sim 20\%$. Notice that these constraints are obtained from the same observational data set. On the other hand, we found no evidence that the limits for the other two cases, i.e., for $(c_s^2, c_{\mathrm{vis}}) = (0, 1)$ and $(1, 1)$, differ from that for the fiducial case (figure 3).

In this presentation we parameterized the dark energy fluid with its equation of state w_X, speed of sound c_s^2 and viscosity c_{vis}^2 and calculate CMB angular and matter power spectra to compare with recent
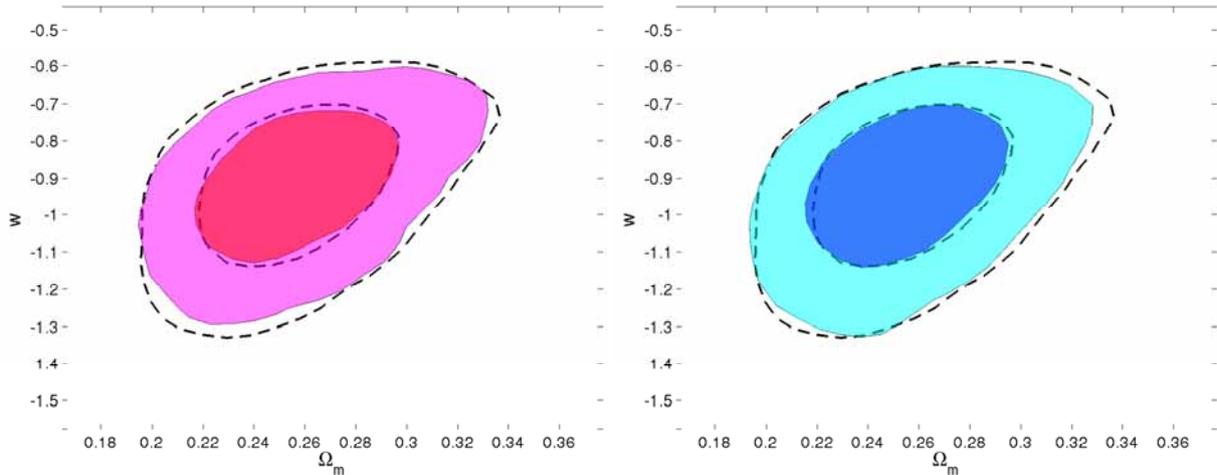
Figure 3: Same as figure 2, but for $(c_s^2, c_{\mathrm{vis}}^2) = (0, 1)$ (left) and $(c_s^2, c_{\mathrm{vis}}^2) = (1, 1)$ (right).

observations. The larger speed of sound and/or viscosity lead to the smaller gravitational potentials and hence the larger ISW effect. We found that different assumption of the fluctuation property of dark energy resulted in a different result of constraint on the equation of state parameter by at most $\lesssim 20\%$, even though current observational data can not put any significant constraint on the fluctuation properties. Thus we suggest that it is important to specify the fluctuation property when putting constraint on the equation of state of dark energy. More details will be found elsewhere soon [11].

References

[1] M. Tegmark *et al.*, arXiv:astro-ph/0608632.

[2] R. Bean and O. Dore, Phys. Rev. D **69**, 083503 (2004) [arXiv:astro-ph/0307100].

[3] S. Hannestad, Phys. Rev. D **71**, 103519 (2005) [arXiv:astro-ph/0504017].

[4] C. Armendariz-Picon, JCAP **0407**, 007 (2004) [arXiv:astro-ph/0405267].

[5] W. Hu, Astrophys. J. **506**, 485 (1998) [arXiv:astro-ph/9801234].

[6] T. Koivisto and D. F. Mota, Phys. Rev. D **73**, 083502 (2006) [arXiv:astro-ph/0512135].

[7] A. Lewis, A. Challinor and A. Lasenby, Astrophys. J. **538**, 473 (2000) [arXiv:astro-ph/9911177].

[8] U. Seljak and M. Zaldarriaga, Astrophys. J. **469**, 437 (1996) [arXiv:astro-ph/9603033].

[9] G. Hinshaw *et al.*, arXiv:astro-ph/0603451.

[10] S. Cole *et al.* [The 2dFGRS Collaboration], Mon. Not. Roy. Astron. Soc. **362**, 505 (2005) [arXiv:astro-ph/0501174].

[11] K. Ichiki and T. Takahashi, in preparation.

Analysis of the evolution of curvature perturbations in preheating by using δN formalism

Teruaki Suyama[1] and Shuichiro Yokoyama[2]

[1,2] *Department of Physics, Kyoto University, Kyoto 606–8502, Japan*

Abstract

We study the evolution of the curvature perturbation during preheating for a simple preheating model whose potential is given by $V(\phi, \chi) = \frac{1}{4}\lambda\phi^4 + \frac{1}{2}g^2\phi^2\chi^2$ with $g^2/\lambda = 2$. We make use of the δN formalism and compare our results with the previous studies which make use of the Hartree approximation. We find that the final amplitude of the curvature perturbation after preheating obtained by the δN formalism is smaller than that obtained in the previous studies.

1 Introduction

The primordial curvature perturbations which are coherent over the horizon scales at recombination epoch are seeds for large scale structure. A simple scenario to explain the origin of curvature perturbations is that vacuum fluctuations of inflaton driving inflation convert into classical perturbations at around the time of horizon crossing.

As another candidate for the mechanism of generating curvature perturbations, preheating model has also been considered.

Preheating is a process in which the coherent oscillation of the inflaton excites the fluctuations of fields coupled to the inflaton by parametric resonance. This process was investigated in detail without metric perturbations, which is valid in dealing processes occurring well within the horizon scale. It has now been widely accepted that particle production in preheating occurs much more efficiently than in the old reheating scenario where inflaton decays perturbatively to other particles.

In this paper, we study the issue of the generation of the curvature perturbation on super-horizon scales during preheating for the two-field preheating model with potential

$$V(\phi, \chi) = \frac{\lambda}{4}\phi^4 + \frac{g^2}{2}\phi^2\chi^2, \tag{1}$$

with $g^2/\lambda = 1 \sim 3$, where the fluctuations of χ-field is not suppressed at the end of inflation due to the small effective mass of χ-field during inflation. In a previous work by Finelli and Brandenberger, by using the standard cosmological perturbation theory, they found that the curvature perturbation (on constant energy density hypersurface) on superhorizon scales shows the exponential growth during preheating.

Because the non-linear effects become important at the late stage of preheating, a method beyond linear perturbation theory is required in order to obtain the final amplitude of the curvature perturbation after preheating which is relevant to the COBE normalization. This is a difficult problem because this requires a full numerical study of non-linear perturbation dynamics. Following this work by Finelli and Brandenberger, by including the effects of backreaction in the Hartree approximation, the authors in [1] showed that the final amplitude of the curvature perturbation considerably exceeds the COBE normalization. However in the Hartree approximation, introduction of the backreaction terms such as $\langle \delta\phi^2 \rangle, \langle \delta\chi^2 \rangle$, where $\langle \cdots \rangle$ denotes the spatial average, breaks the law of causality and hence unphysical acausal energy transfer occurs.

Then in this paper, we take a different approach than the Hartree approximation in order to obtain the final amplitude of the curvature perturbation. We make use of the δN formalism [4]. In δN formalism, we can evaluate the evolution of curvature perturbations on superhorizon scales only by the knowledge of the homogeneous background solutions and also as was emphasized in [2], unphysical acausal energy transfer

---

does not occur in this formalism. The purpose of this paper is to evaluate the curvature perturbation after preheating by δN formalism and compare the results with those obtained by the Hartree approximation.

There are some studies [2, 3] which applied δN formalism to preheating. However even the issue of generation of the curvature perturbation in preheating remains unresolved due to the numerical problems in [2, 3].

This work is an extension of the paper [2]. In this paper, we numerically solve background equations for the model given by Eq. (1) during preheating for large number of different initial values of χ-field, which is needed in order to obtain the final amplitude of the curvature perturbation on large scales. Then we show that the final amplitude of the curvature perturbation obtained by using the δN formalism is smaller than the one obtained by the Hartree approximation [1]. We also discuss about this discrepancy.

2　Numerical results

2.1　Background equations

The background equations which we should solve numerically are given by

$$\ddot{\phi} + (3H + \Gamma)\dot{\phi} + \lambda\phi^3 + g^2\phi\chi^2 = 0, \tag{2}$$

$$\ddot{\chi} + (3H + \Gamma)\dot{\chi} + g^2\phi^2\chi = 0, \tag{3}$$

$$\dot{\rho_R} + 4H\rho_R = \Gamma(\dot{\phi}^2 + \dot{\chi}^2), \tag{4}$$

$$H^2 = \frac{8\pi}{3M_p^2}(\rho_S + \rho_R), \tag{5}$$

$$\rho_S \equiv \frac{1}{2}\dot{\phi}^2 + \frac{1}{2}\dot{\chi}^2 + \frac{\lambda}{4}\phi^4 + \frac{g^2}{2}\phi^2\chi^2. \tag{6}$$

Here ρ_R is the energy density of the radiation. We have included the radiation fluid in order to realize the radiation dominated universe after preheating. Γ is a decay rate from scalar fields to the radiation. We assume that both the decay rates of ϕ and χ to the radiation are the same for simplicity.

2.2　Dependence of δN on the initial value of χ.

In order to evaluate curvature perturbations generated during preheating by using the δN formalism, we first study the dependence of the e-folding number, $N \equiv \int H dt$, until the Hubble parameter H reaches a given value H_{fin} varying the initial values of fields, that is, fields values at the end of inflation. Perturbation of ϕ approximately corresponds to the adiabatic perturbation in the linear regime of preheating. Hence the variation of ϕ at the end of inflation does not newly-generate curvature perturbations during preheating and we only vary the initial value of χ in the numerical simulations.

We show in Fig. 1 plots of e-folding number as a function of the initial value of χ which we denote as χ_{ini} for two different values of the sample size of χ_{ini} (10^2 and 10^4 for the left and right panel respectively). The parameters used in the simulations are $g^2 = 2\lambda = 0.04$, $\phi_{\mathrm{ini}} = M_p, \dot{\phi}_{\mathrm{ini}} = \dot{\chi}_{\mathrm{ini}} = 0, \Gamma = 10^{-4}H_{\mathrm{ini}}, H_{\mathrm{fin}} = 10^{-1}\Gamma$.

From both plots, we find that the e-folding number N is very sensitive to χ_{ini}. This feature is also seen in [2] though the sample size is limited to 10^2 and the parameters such as decay rate Γ are different from those used in our simulations. Hence we expect that this feature is characteristic of preheating itself. We have increased the sample size to 10^6 (we cannot show the plot in this case because the file size becomes too large.) and found similar feature to the case of the smaller sample size. The dependence on the initial value of χ is also seen in Ref. [1].

As we mentioned above, $\delta N(\chi)$ is very sensitive to χ and the dependence of $\delta N(\chi)$ on χ seems almost random. If this dependence is completely random, then $\delta\hat{N}(\vec{x})$, which is the perturbation of the e-folding number at a point $\vec{x}$ in the real space (we use $\delta\hat{N}(\vec{x})$ rather than $\delta N(\vec{x})$ in order to avoid confusion because we use δN as the perturbation in χ-field space.), is also random regardless of the shape of the power spectrum of χ at the end of inflation. In such a case, $\delta\hat{N}(\vec{x})$ smoothed over the scale R with the window function $W(\vec{x}; R)$,

$$\delta\hat{N}(\vec{x}; R) \equiv \int d^3x' W(\vec{x}' - \vec{x}; R)\,\delta\hat{N}(\vec{x}), \tag{7}$$
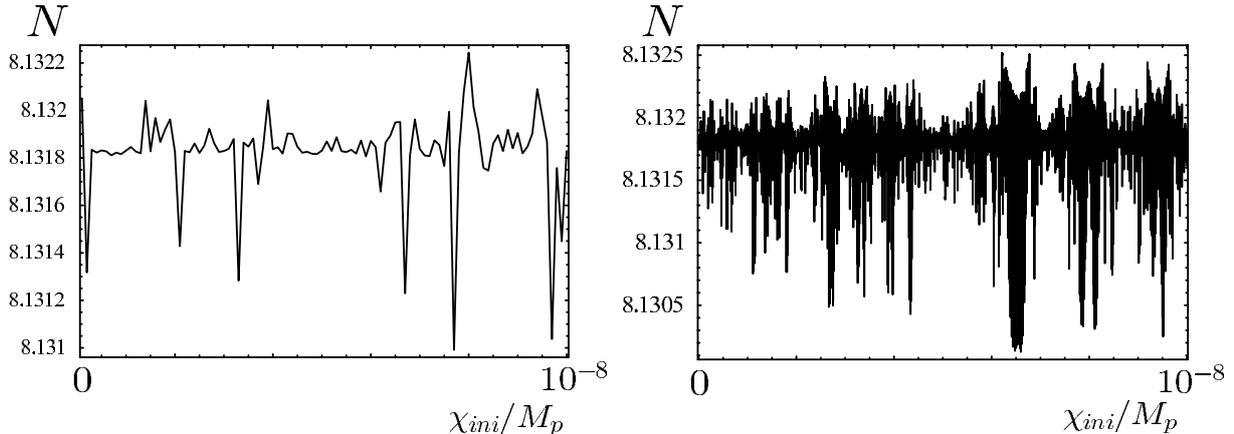
Figure 1: Plots showing the initial value dependence of the e-folding number N. In left and right panel, 100 and 10000 discrete points are plotted respectively within the same interval of the horizontal axis. The parameters used in both panels are $g^2 = 2\lambda = 0.04$, $\phi_{\text{ini}} = M_p, \dot{\phi}_{\text{ini}} = \dot{\chi}_{\text{ini}} = 0, \Gamma = 10^{-4} H_{\text{ini}}, H_{\text{fin}} = 10^{-1}\Gamma$.

would have a typical magnitude given by the statistical fluctuations as

$$\sim \sqrt{\langle \delta N(\chi)^2 \rangle_\chi} \left(\frac{R}{r_H} \right)^{-3/2}, \tag{8}$$

where r_H is the horizon scale at the time of preheating. Hence the smoothed $\delta \hat{N}(\vec{x})$ is significantly suppressed and the generation of curvature perturbations on super-horizon scales does not occur.

On the other hand, if $\delta N(\chi)$ is not completely randomized and have some dependence on χ besides random component, then $\delta \hat{N}(\vec{x}; R)$ would be dominated by the residual component rather than the random component on sufficiently large scales.

In order to see whether $\delta N(\chi)$ is randomized or not, we divided the region of χ_{ini} which contains one million sampling points into ten bins (hence there are 10^5 sampling points in each bin) and took the average of $\delta N(\chi)$ for each bin with the same parameters as in Fig. 1. Figure 2 is the result. We see that the fluctuations of points in the plot exceed 10^{-5}. If $\delta N(\chi)$ is completely random, then the fluctuations of points in Fig. 2 should be bounded by the statistical fluctuations

$$\sim 2 \times 10^{-4} \times \frac{1}{\sqrt{10^5}} \approx 10^{-6}, \tag{9}$$

which is much smaller than the result (this is shown in a gray band in the figure). Hence $\delta N(\chi)$ is not completely randomized.

Next, we compare our results with the previous results obtained by the Hartree approximation [1].

In [1], the authors found that the amplitude of Φ which is the metric perturbation in the longitudinal gauge becomes about 10^{-3} after preheating, which is much larger than the COBE normalization.

From Fig. 2, we see that the amplitude of δN is at most 10^{-4}. This means that the amplitude of the curvature perturbation on sufficiently large scales must be at 10^{-4} which is one order of magnitude smaller than that obtained by the Hartree approximation. Hence the amplitude of the curvature perturbation obtained by the δN formalism is suppressed than that obtained by the Hartree approximation.

The discrepancy of results between by the Hartree approximation and by the δN formalism is due to the difference of the treatment of non-linear dynamics of preheating. As emphasized in [2], in the Hartree approximation, the introduction of the backreaction terms such as $\langle \delta\phi^2 \rangle$, $\langle \delta\chi^2 \rangle$ breaks the law of causality. In δN formalism, because each patch of the universe separated by distance larger than the horizon scale evolves independently as the homogeneous Friedmann universe, violation of the law of causality does not occur in this formalism.

averaged N in each bin
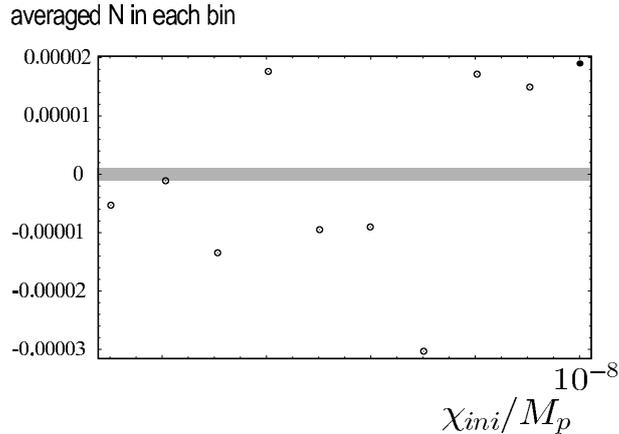
Figure 2: Plot showing the e-folding number N averaged in each bin in which 10^5 sampling points are contained. Gray band represents the amplitude of the statistical fluctuation. We see that the fluctuation of the averaged e-folding number exceeds the statistical fluctuation. Hence N is not completely randomized.

In this paper, we have assumed fluctuations of fields on horizon scales are suppressed during preheating which is a crucial assumption to apply the δN formalism. It is interesting to study the validity of the assumption and this is a future issue.

3 Conclusion

The main purpose of this paper is to evaluate the curvature perturbation after preheating by using the δN formalism and compare our results with those obtained by the Hartree approximation [1].

We studied two-field preheating model whose potential is given by $\frac{\lambda}{4}\phi^4 + \frac{g^2}{2}\phi^2\chi^2$. Then we have analyzed the dependence of the e-folding number during preheating on the iso-curvature perturbations at the end of inflation which corresponds to perturbations of χ-field. We verified that the e-folding number during preheating is very sensitive to the initial value of χ due to the chaotic nature of the background trajectory in field space, which has been already observed in [2]. Though the e-folding number seems almost random as a function of χ_{ini}, we found that the fluctuation of the smoothed e-folding number over a large number of initial values of χ exceeds the statistical fluctuation, which is one of the new results beyond [2]. In particular, we found that though $\delta N(\chi)$ fluctuates almost randomly in a local region of χ space, it grows in proportion to $\chi^{1/3}$ as a general trend. Hence the e-folding number is not completely randomized.

Then we compared our results with the previous study [1]. The amplitude of the curvature perturbation after preheating evaluated by the δN formalism is smaller than that evaluated by the Hartree approximation.

We would like to thank Takahiro Tanaka for continuously encouraging us to pursue our study and giving us useful comments.

References

[1] J. P. Zibin, R. H. Brandenberger and D. Scott, Phys. Rev. D **63**, 043511 (2001).

[2] T. Tanaka and B. Bassett, Proc. 12th JGRG Meeting.

[3] Y. Nambu and Y. Araki, Class. Quant. Grav. **23**, 511 (2006).

[4] M. Sasaki and E. D. Stewart, Prog. Theor. Phys. **95**, 71 (1996).

Weak lensing of galaxy clusters in relativistic MOND theory

Ryuichi Takahashi[1] and Takeshi Chiba[2]

[1]*Division of Theoretical Astronomy, National Astronomical Observatory of Japan, Mitaka, Tokyo 181-8588, Japan*
[2]*Department of Physics, College of Humanities and Sciences, Nihon University, Tokyo 156-8550, Japan*

Abstract

We study weak gravitational lensing of galaxy clusters in relativistic MOND (MOdyfied Newtonian Dynamics) theory proposed by Bekenstein (2004). We calculate shears of background galaxies for three clusters (A1689, CL0024+1654, CL1358+6245) and compare them with observational data. For the shear as a function of the angle from the lens center, MOND predicts a shallower slope than the data irrespective of the critical acceleration parameter g_0. The dark halo is necessary to explain the data for any g_0. If the dark halo is composed of massive neutrinos, its mass should be heavier than $2 - 3$ eV. However, it is still difficult to explain a small core $(100 - 300$ kpc) determined by the lensing data in the neutrino halo model.

1 Introduction

MOND (MOdyfied Newtonian Dynamics) is an alternative theory to Newtonian dynamics proposed by Milgrom (1983). It makes gravitational force stronger at large distance (or small acceleration) to explain galactic dynamics without dark matter. The equation of motion is changed if the acceleration is lower than the critical value $g_0 \simeq 1 \times 10^{-8} \mathrm{cm/s^2} \approx H_0$. It is well known that this theory can explain galactic rotation curves with only one free parameter: the mass-to-light ratio (see review Sanders & McGaugh 2002). Bekenstein (2004) recently proposed a relativistic covariant formula of MOND (called TeVeS) by introducing several new fields and parameters. After his work, several authors have discussed the relativistic phenomena. In this paper, we discuss weak gravitational lensing of galaxy clusters.

The weak lensing provides an important observational method to test MOND. This is because the weak lensing probes the lens potential outside of the Einstein radius, $r_E \sim (MD)^{1/2} \simeq 150 \mathrm{kpc}(M/10^{14}M_\odot)^{1/2}$ $(D/H_0^{-1})^{1/2}$, where M is the lens mass and D is the distance to the source. The gravitational law is changed outside of the MOND radius, $r_M = (M/g_0)^{1/2}$, where the acceleration is less than g_0. Since $g_0 \approx H_0 \approx 1/D$, the Einstein radius r_E is comparable to the MOND radius r_M. Hence, we can test the MOND-gravity regime by the weak lensing.

The gravitational lensing in MOND have been studied by many authors. Just after Bekenstein proposed the relativistic formula, Chiu et al. (2006) and Zhao et al. (2006) first studied the lensing in detail and tested MOND with strong lensing data of galaxies. In this paper, we calculate shears for three clusters (A1689, CL0024+1654, CL1358+6245) and compare them with the observational data. We perform a χ^2 fit of the data to give a constraint on the dark halo profile and the neutrino mass. Throughout this paper, we use the units of $c = G = 1$.

2 Basics

We briefly review the basics of gravitational lensing based on the relativistic MOND theory for a spherical symmetric lens model. The detailed discussions are given in Bekenstein (2004) and Zhao et al. (2006).

When a light ray passes through a lens with the impact parameter b, the deflection angle is

$$\alpha(b) = 2b \int_{-\infty}^{\infty} dl \frac{g(r)}{r}, \tag{1}$$

---

where l is the distance along the light path and r is the distance from the lens center, $r = \sqrt{l^2 + b^2}$.

The gravitational force due to the lens is $\tilde{\mu}(g/g_0)g(r) = g_N(r) = M(<r)/r^2$, where g_N is the usual Newtonian acceleration and $M(<r)$ is the lens mass enclosed inside a radius r. We use a standard interpolation function $\tilde{\mu}(x) = x/\sqrt{1+x^2}$ with $g_0 = 1 \times 10^{-8}$cm s^{-2}. Then, $\tilde{\mu}(x) = 1$ (i.e. $g = g_N$) for $g \gg g_0$, while $\tilde{\mu}(x) = x$ (i.e. $g = \sqrt{g_N g_0}$) for $g \ll g_0$.

The lens equation is $\theta_s = \theta - (D_{LS}/D_S)\alpha(\theta)$. Here, θ_s and $\theta(= b/D_L)$ are the angular positions of the source and the image, and D_L, D_S and D_{LS} are the angular diameter distances between the observer, the lens and the source.[3] The shear γ and the convergence κ are given by, $\gamma = (\theta_s/\theta - d\theta_s/d\theta)/2$; $1 - \kappa = (\theta_s/\theta + d\theta_s/d\theta)/2$. We note that if the mass increases as $M \propto r^p$ with $p \geq 0$, the shear and the convergence decrease as

$$\begin{aligned} \gamma \propto \kappa \propto \quad & \theta^{p-2} \quad && \text{for } g \gg g_0, \\ \propto \quad & \theta^{p/2-1} \quad && \text{for } g \ll g_0. \end{aligned} \qquad (2)$$

The slopes of γ and κ for $g \gg g_0$ are steeper than that for $g \ll g_0$. This is because the gravitational force is proportional to $g_N^{1/2}$ for $g \ll g_0$, and hence the force decreases more slowly at larger distance. Comparing the slope in Eq.(2) with the observational data, we can test MOND.

3   Results for Individual Clusters

We calculate the shear γ and the convergence κ based on the MOND theory for the three clusters, A1689, CL0024+1654, CL1358+6245. The mass profiles of these clusters have been measured by gravitational lensing for wider range of angular diameters, and hence these clusters are appropriate system to investigate the angle dependence of the shear and the convergence. In this section, we assume the source redshift is $z_S = 1$.

3.1   A1689

The mass profile of the cluster A1689[4] is shown in Fig.1(a). The hot gas mass profile was directly determined from X-ray observational data [2]. The galaxy mass profile was given from the surface brightness profile with assuming the constant mass-to-light ratio $8M_\odot/L_\odot$ (B-band) [12]. The total baryonic mass (gas + galaxies) is shown in the solid line. We also show the dark halo profile which will be needed to match the observational data (we will discuss later).

The panel (c) shows the reduced shear data $\gamma/(1-\kappa)$ from Broadhurst et al. (2005). The solid line is the MOND theoretical prediction. We note that for $\theta < 10'$ the solid line is clearly smaller than the data. This indicates that the gravitational force is too weak to explain the data. In the dotted line, for the critical acceleration g_0 we use 40 times larger than the usual value $(= 1 \times 10^{-8}$cm s$^{-2})$. In this case, for the central region $(\theta < 4')$ the theory can explain the data, but for larger radius it cannot. This is because that the slope of shear is shallow from Eq.(2) for $g < g_0$. The slope is shallower than $\gamma \propto \theta^{-1}$ for $g < g_0$ (since $p \geq 0$ in Eq.(2)) and the data in the panel (c) clearly shows steeper profile than this. Hence MOND cannot explain the data for any mass model and any acceleration parameter g_0 in the low acceleration region $g < g_0$.

Previously, Aguirre, Schaye & Quataert (2001) and Sanders (2003) reached the same conclusion as ours by studying temperature profiles of clusters. They indicated that the temperature data near the core is higher than the MOND prediction. Sanders (2003) noted that if the dark matter core is added this discrepancy could be resolved. Following the previous studies, we include the dark halo to explain the observational data. We take the Hernquist profile,

$$M(<r) = M_0 r^2/(r+r_0)^2, \qquad (3)$$

as the dark halo profile. We perform a χ^2 fit of the data in order to determine the parameters M_0 and r_0. The χ^2 is given by $\chi^2 = \sum_i (x_i - x_i^{data})^2/\sigma_i^2$ where x_i is the reduced shear $\gamma/(1-\kappa)$ at the i-th angle,

---

[3] We use the distance in the usual FRW (Friedmann-Robertson-Walker) model with $\Omega_M = 1 - \Omega_\Lambda = 0.3$ and $H_0 = 70$km/s/Mpc. The distance in MOND is almost the same with that in FRW model [3].

[4] Its redshift is $z = 0.183$ and $1'$ corresponds to 184kpc.
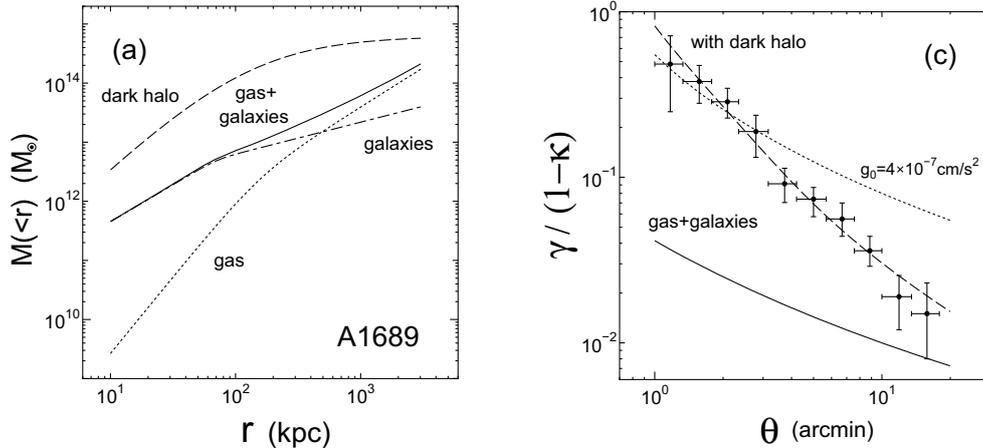
Figure 1: Results for the cluster A1689. The left panel (a): The mass profiles of the gas (dotted line), the galaxies (dot-dashed line), the gas + galaxies (solid line), and the dark halo (dashed line). The quantity $M(< r)$ is the mass enclosed within the radius r. The right panel (c): The reduced shear $\gamma/(1 - \kappa)$ as a function of an angle from the cluster center. The data is from Broadhurst et al. (2005). The solid line is the MOND prediction. In the dotted line we use the value of g_0, 40 times larger than usual one ($= 1 \times 10^{-8} \text{cm/s}^2$). In the dashed line the dark halo is added. From the panel (c), the MOND can not explain the data unless the dark halo is added, because the gravitational force is too weak near the core.

x_i^{data} is the data and σ_i is the standard deviation. The best fitted model is $M_0 = (6.2 \pm 1.2) \times 10^{14} M_\odot$ and $r_0 = 125 \pm 52$ kpc (see Table 1). The minimized χ^2-value per degree of freedom (dof) is $\chi^2_{min}/\text{dof} = 3.0/8$. The results are insensitive to the mass-to-light ratio. As shown in the panel (c), this model (dashed line) fits the data well. The dashed line in the panel (c) is steeper than the solid and dotted lines, since $\theta < 5' (\leftrightarrow r < 1000\text{kpc})$ is the high acceleration region $g > g_0$ and hence the slope is steeper as seen from Eq.(2).

3.2 CL0024+1654 & CL1358+6245

Fig.2 shows the reduced shear for the cluster CL0024+1654 [7] and CL1358+6245 [6]. Similar to the previous case of A1689, the solid line is clearly smaller than the data near the core. The best fitted halo model is $M_0 = (3.5 \pm 1.0) \times 10^{14} M_\odot$ and $r_0 = 309 \pm 93$ kpc with $\chi^2_{min}/\text{dof} = 9.9/8$ for CL0024 and $M_0 = (8.1 \pm 3.6) \times 10^{13} M_\odot$ and $r_0 = 134 \pm 68$ kpc with $\chi^2_{min}/\text{dof} = 4.5/7$ for CL1358. Same as the previous case of A1689, the dark halo is needed to fit the data.

4 Discussion

In previous studies, several authors assumed a massive neutrino with a mass of ~ 2 eV as the dark matter to explain the observational data [10]. In this section, we put a constraint on its mass from the weak lensing.

The neutrino oscillation experiments provide the mass differences between different families : $\Delta m_\nu^2 \lesssim 10^{-3} \text{eV}^2$. Here we consider massive neutrinos whose masses are much heavier than Δm_ν and assume they are degenerate: they have (almost) the same mass independent of their families. Using the maximum phase space density h^{-3}, the maximum density of the neutrino dark halo is given by $\rho_{\nu max} = 4.8 \times 10^{-27} \text{g cm}^{-3} (m_\nu/2\text{eV})^4 (T/\text{keV})^{3/2}$ [11, 10]. The core density of the Hernquist profile is $\rho_c = 3M(< r_0)/(4\pi r^3)$ from Eq.(3). Since $\rho_c < \rho_{\nu max}$, we obtain the minimum neutrino mass,

$$m_\nu > 6.1\text{eV} \left(\frac{M_0}{10^{14} M_\odot} \right)^{1/4} \left(\frac{r_0}{100\text{kpc}} \right)^{-3/4} \left(\frac{T}{\text{keV}} \right)^{-3/8}, \tag{4}$$
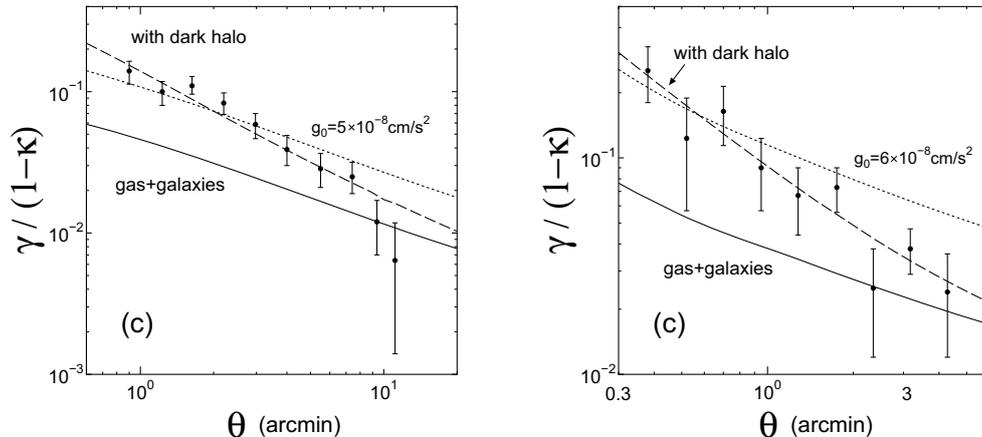
Figure 2: The reduced shear for the cluster CL0024+1654 (left) and CL1358+6245 (right).

where T is the X-ray temperature. The results are shown in Table 1. The minimum neutrino mass is $2-3$ eV for these three clusters. Since the current limit is $m_\nu < 2$ eV from tritium β decay[5], our results in Table 1 are comparable to or larger than this limit.

Sanders (2003) derived a core radius of neutrino virialized halo, $r_\nu \gtrsim 700\mathrm{kpc}(m_\nu/2\mathrm{eV})^{-2}(T/\mathrm{keV})^{-1/4}$. But this is much larger than the core radius in Table 1. Hence, it is difficult to explain the small core in the neutrino halo model.

	M_0 $(M_\odot)$	r_0 (kpc)	T (keV)	m_ν (eV)
A1689	$(6.2 \pm 1.2) \times 10^{14}$	125 ± 52	9.00 ± 0.13	$> 3.6 \pm 1.1$
CL0024	$(3.5 \pm 1.0) \times 10^{14}$	309 ± 93	3.52 ± 0.17	$> 2.2 \pm 0.5$
CL1358	$(8.1 \pm 3.6) \times 10^{13}$	134 ± 68	7.16 ± 0.10	$> 2.2 \pm 0.9$

References

[1] Aguirre, A., Schaye, J. & Quataert E. 2001, ApJ, 561, 550

[2] Andersson, K.E. & Madejski, G.M. 2004, ApJ, 607, 190

[3] Bekenstein, J.D. 2004, PRD, 70, 083509

[4] Broadhurst, T. et al. 2005, ApJ, 619, L143

[5] Chiu, M.-C., Ko, C.-M. & Tian, Y. 2006, ApJ, 636, 565

[6] Hoekstra, H., Franx, M., Kuijken, K., & Squires, G. 1998, ApJ, 504, 636

[7] Kneib, J.P. et al. 2003, ApJ, 598, 804

[8] Milgrom, M. 1983, ApJ, 270, 365

[9] Sanders, R.H. & McGaugh S.S. 2002, ARA&A, 40, 263

[10] Sanders, R.H. 2003, MNRAS, 342, 901

[11] Tremaine, S. & Gunn, J.E. 1979, PRL, 42, 408

[12] Zekser, K.C. et al. 2006, ApJ, 640, 639

[13] Zhao, H.S. et al. 2006, MNRAS, 368, 171

---

[5]Particle Data Group Home Page : http://pdg.lbl.gov/

Lensing Effects on SNe Observations due to Extended Lenses

Chul-Moon Yoo[1] , Hideki Ishihara[2] and Ken-ichi Nakao[3]

Department of Mathematics and Physics, Graduate School of Science, Osaka City University, Osaka 558-8585, Japan

Abstract

Lensing effects on point light sources are simulated in a clumpy universe model. In our universe model, it is assumed that all of the matter in the universe constitutes randomly distributed extended transparent objects each of which has the identical mass M_L and the typical size L. We suppose that the density distribution of the objects is axially symmetric, non-singular, and smooth. Numerical calculations are performed for three different density distributions, and we compute probability distribution functions of the magnification. In the large $L/\sqrt{M_L}$ case, the magnification distribution functions are well fitted by the gamma distribution. This result suggests that we might obtain information about $L/\sqrt{M_L}$ through the probability distribution function of the magnification comparing it with the gamma distribution.

1 Introduction

Many cosmological observations suggest that our universe is globally homogeneous and isotropic, in other word, that the time evolution of the global aspect is well approximated by the Friedmann-Lemaître (FL) cosmological model. However our universe is apparently locally inhomogeneous. Recent cosmological observations draw our attention to the effects of the inhomogeneity on our universe as one of the most important issues in cosmology. One of the useful tools of obtaining information on the inhomogeneities is to examine gravitational lensing.

Our main target of this work is the TypeIa supernovae observation. In this paper, we clarify the effect of gravitational lensing on high redshift supernovae observation. There are several works for this purpose [1][2][4]. In these works, the main purpose is to supply the method for investigation of the fraction of compact objects in our universe through the observation of TypeIa supernovae. They have not taken into account the size of clumps. However, the configuration of dark matter is not well known in small scales. Hence further investigation with finite size clumps is needed.

In this paper, we assume that light sources can be treated as point sources. This assumption is valid only when the width of a light beam emitted by the source is much thiner than the Einstein radius of lens objects. In the case of supernovae, the light beam width is given by the order of the size of supernovae at peak brightness $\sim 10^{15}$cm. The Einstein radius of lens objects is the order of $\sqrt{M_L D}$, where D is typical distance to supernovae given as ~ 1Gpc in high redshift supernova events. Therefore we assume the following inequality: $\sqrt{M_L D} \gg 10^{15}$cm $\Leftrightarrow M_L \gg 10^{-2} M_\odot$.

We focus on the magnification probability distribution function (MPDF) and the distance redshift relation. If the size of lenses L is sufficiently large, we can expect that the MPDF and the distance redshift relation agree with those of homogeneous universe model. On the other hand, when the lenses are point masses, observed distances have large dispersion, and the MPDF has a broad tail in high magnification with a sharp peak at the value which is corresponding to the distance of the undisturbed beam. This fact indicates that the MPDF or the distance redshift relation depends a lot on L. Therefore we expect that we may find the typical length scale of dark matter clumps through lensing effects on the MPDF or the distance redshift relation. As the first step for this purpose, we investigate lensing effects on the observation in very simple situations.

This paper is organized as follows: In § 2, we show definitions of the observed distance and magnification in this paper. In § 3, the calculation method and settings are introduced. The results are shown in § 4. Finally, § 5 is devoted to the conclusion and summary.

---

[1]E-mail:c_m_yoo@sci.osaka-cu.ac.jp

[2]E-mail:ishihara@sci.osaka-cu.ac.jp

[3]E-mail:knakao@sci.osaka-cu.ac.jp

2 Magnification and the distance

In this study, we assume that multiple images can not be separated within the observational limit and we can only observe the total flux of light rays. The magnification $\mu_{(p)}$ of the p-th image of a source is defined by

$$\mu_{(p)} = \frac{S_{(p)}}{S_0},\tag{1}$$

where $S_{(p)}$ is the flux of the p-th image. Then the observed magnification μ is given by

$$\mu = \frac{\sum_p S_{(p)}}{S_0} = \sum_p \mu_{(p)}.\tag{2}$$

Since the flux is inversely proportional to the square of the distance, we define the observed angular diameter distance by

$$D_A = \frac{D_{DR}(0, z_S)}{\sqrt{\sum_p \mu_{(p)}}},\tag{3}$$

where D_{DR} is Dyer-Roeder (DR) distance which represents the angular diameter distance for undisturbed beam [3].

3 Settings and the calculation method

In very simple terms, our universe model is globally FL universe, and all of the matter in this universe takes the form of randomly distributed lens objects each of which has identical mass M_L. The multiple lensing calculation method is basically same as Ref.[5]. The brief description of the procedure is follows: 1. We ignore clumps far from the ray. 2. Lens mappings are calculated with the multiple lens plane method [3] and the Newton-Raphson method. 3. Summing up the magnifications of all images, we obtain the total magnification.

For simplicity, we assume that all of the clumps satisfy following properties. 1. They are transparent. 2. They have axially symmetric density distributions which is non-singular and smooth surface mass density at the center of symmetry, and the axis of symmetry is identical to the line-of-sight. 3. The total mass of each lens object $2\pi \int_0^\infty \xi \Sigma(\xi)$ is finite, where ξ is the distance from the axis of symmetry on the lens plane and $\Sigma(\xi)$ is the surface mass density. 4. The surface mass density $\Sigma(\xi)$ is a monotonically decreasing function of ξ.

In this paper, we pick up following three lens models.

$$\text{(a)Homogeneous disk} \quad \Sigma(\xi) = \begin{cases} \frac{M_L}{\pi L^2} & \text{for} \quad \xi < L, \\ 0 & \text{for} \quad \xi \geq L. \end{cases}\tag{4}$$

$$\text{(b)Homogeneous sphere} \quad \Sigma(\xi) = \begin{cases} \frac{3M_L}{2\pi L^2}\left(1 - \frac{\xi^2}{L^2}\right)^{1/2} & \text{for} \quad \xi < L, \\ 0 & \text{for} \quad \xi \geq L. \end{cases}\tag{5}$$

$$\text{(c)Power low tail model} \quad \Sigma(\xi) = \frac{M_L}{\pi L^2 \left(1 + \left(\frac{\xi}{L}\right)^2\right)^2}.\tag{6}$$

4 Results

Through the distance-redshift relations, we can overview the dependence of lensing effects on L. We have calculated distance-redshift relations of 2,000 samples in each case. We only show the case of lens model (b) (see the left and the center figures in Fig.1). We have set $L/\sqrt{M_L} = 2$ and 10 $[H_0^{-1/2}]$. For small L, several plot points are scattered in wide area of figures. And, many samples are plotted in the vicinity of the DR distance. On the other hand, for large L, most of samples are plotted in the vicinity of the FL distance. These are expected results as mentioned in § 1.
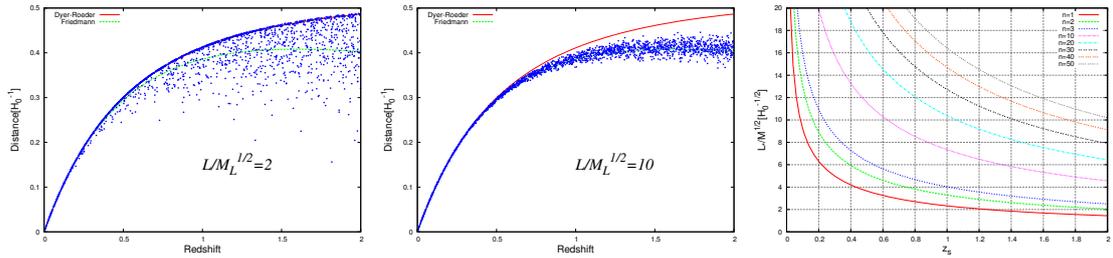
Figure 1: The left and the center figures: Distance-redshift relation of 2000 samples, depicted in the case of lens model (b) for $L/\sqrt{M_L} = 2$ and 10 $[H_0^{-1/2}]$. The solid line and dashed line represent the DR and the FL distance. The right figure: The values of L_{*n} are depicted as functions of the source redshift.

In order to find the typical value of L which gives a criterion for whether the distance-redshift relations become like the center figure in Figure1, we consider the lens size L_{*n} for which a light ray receive lensing averagely n times during the propagation. Using the probability of receiving lensing during the propagation shown in Ref.[5], we find

$$\frac{L_{*n}}{\sqrt{M_L}} = \left(\frac{8n}{3H_0\Omega_{\mathrm{m0}}} \left(\int_0^{z_S} \frac{(1+z)^2}{\sqrt{\Omega_{\mathrm{m0}}(1+z)^3 + 1 - \Omega_{\mathrm{m0}}}} dz \right)^{-1} \right)^{1/2}, \tag{7}$$

where we have set $\Omega_{\mathrm{K0}} = 0$ (see the right figure in Fig.1). From the results, we can find that most of samples are plotted in the vicinity of the FL distance only in the case of $L \gg L_{*1}$.

In order to see the details of the L dependence of lensing effects, we investigate the MPDF. The MPDFs given by our calculations are shown in Figure 2. In this figure, we also depict the gamma distributions
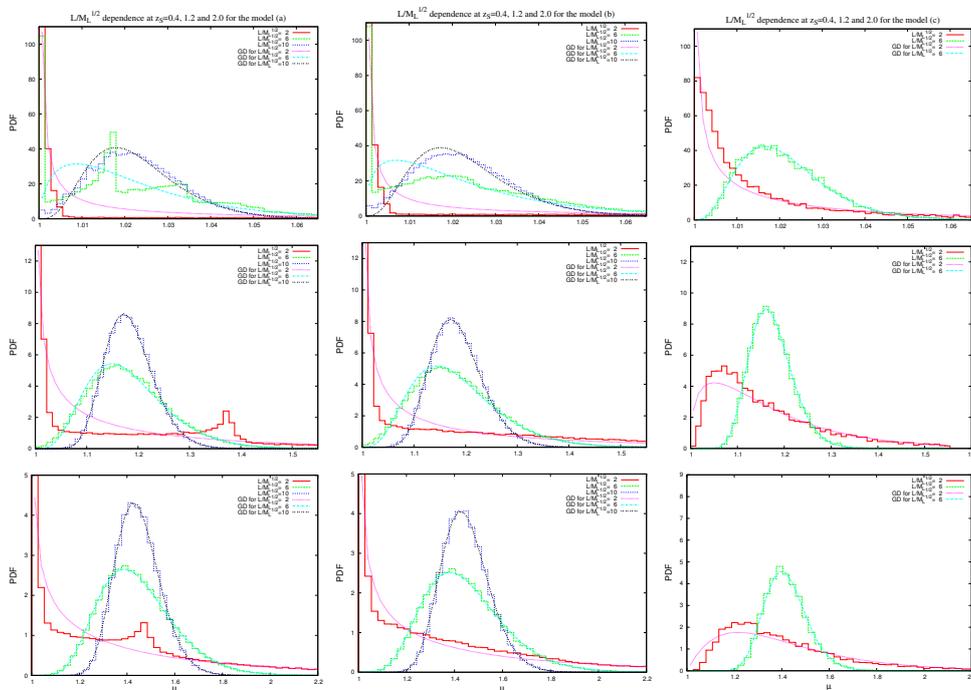

Figure 2: The MPDFs in lens model (a), (b), and (c) are shown here. The smooth lines are gamma distributions which have same averages and second moments as those given by the each ensemble.

which have same means and variances as those given by each ensemble. The gamma distribution is defined by follows:

$$f(\mu - 1; k, \theta) = \mu^{k-1} \frac{e^{-(\mu-1)/\theta}}{\theta^k \Gamma(k)}, \tag{8}$$

where $k > 0$ and $\theta > 0$ called the shape parameter and the scale parameter respectively, and $\Gamma(k)$ is the gamma function. The mean μ_m and the variance σ^2 are given by $\mu_\mathrm{m} = k\theta + 1$ and $\sigma^2 = k\theta^2$. At first glance, we can see the following common property; in $L \gg L_{*1}$ cases, MPDFs are well fitted by the gamma distributions, and one cannot see these properties in $L \lesssim L_{*1}$ cases. This result implies that, in sufficiently large $L/\sqrt{M_L}$, effects of gravitational lensing due to different lens models are degenerate.

Since the gamma distribution is identified by two parameters :mean and variance, we are interested in the dependence of these parameters on the source redshift. In our calculations, the ensemble averages of the magnification $\langle \mu \rangle$ are almost equal to that of filled beam value D_{DR}^2/D_{FL}^2 (see the left figure in Fig.3). It is consistent with the concept of the clumpy universe model. Hence, the variance is only non-trivial
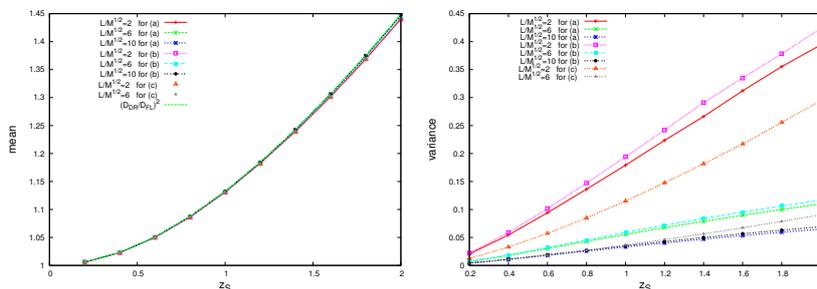

Figure 3: Means and variances of the magnification are depicted as functions of the source redshift.

variable. The variances are depicted as functions of the source redshift in the right side of Figure 3. The gradient of the lines in this figure seems to be sensitive to the value of $L/\sqrt{M_L}$ and the lens model.

5   Conclusion and Summary

We have calculated lensing effects on point source observations such as TypeIa supernovae observations. We have assumed very simple situations in order to understand basic properties of multiple gravitational lensing effects. We have shown the MPDFs in each source redshift and $L/\sqrt{M_L}$. We can divide the results into two main categories through whether the MPDF is well approximated by the gamma distribution or not. If our universe model well approximate the actual universe, in later case, one can conclude that the typical size of dark matter clumps L satisfy $L \lesssim L_{*1}$. In this case, the shape of MPDF depend a lot on the lens model, therefore we might obtain the information about mass distribution through the shape of the MPDF. On the other hand, if L satisfy $L \gtrsim L_{*1}$, the effects of gravitational lensing due to different lens models degenerate. However, the variance of the MPDF depends on the value of $L/\sqrt{M_L}$ and lens models. Hence, it might be possible to obtain the information about typical value of $L/\sqrt{M_L}$ or lens model from the variance of magnifications which are given by observations even if $L \gtrsim L_{*1}$.

References

[1] R. Benton Metcalf and Joseph Silk. *Astrophys. J.*, 519:L1–4, 1999.

[2] E. Moertsell, A. Goobar, and L. Bergstrom. *Astrophys. J.*, 559:53, 2001

[3] Elers J. Schneider, P. and E. E. Falco. Gravitational lenses. 1992. New York : Springer.

[4] U. Seljak and D. E. Holz. *Astronomy and Astrophysics*, 351:L10–L14, November 1999.

[5] Chul-Moon Yoo, Ken-ichi Nakao, Hiroshi Kozaki, and Ryuichi Takahashi. astro-ph/0604123.

1/f fluctuations in spinning-particle motions near Schwarzschild black hole

Hiroko Koyama[1], Kenta Kiuchi[2] and Tetsuro Konishi[3]

[1,2]*Department of Physics, Waseda University, Shinjuku-ku, Tokyo 181–8555, Japan*
[3]*Department of Physics, Nagoya University, Chikusa-ku, Nagoya 464–8602, Japan*

Abstract

We study the property of chaos in spinning-particle motions in Schwarzschild space-times. We characterize the chaos in the motions using the power spectrum. We find that the power spectrum is not only white noise but also $1/f$ fluctuation, depending on the value of the spin and the angular momentum of the test particle. We obtain the phase diagram for the properties of the chaos. Furthermore, we suggest that the origin of the $1/f$ fluctuations is the "stagnant motions" around the different tori.

1   Introduction

Nature is filled with phenomena that exhibit chaotic behavior. In the chaotic systems we cannot predict the state in the future exactly [1]. Such chaotic behaviors have also been found in some relativistic systems. For example, in Schwarzschild spacetime, the motions of a spinning test particle can be chaotic [2]. They found that, as the magnitude of spin increases, the motions switch from periodic to chaotic. exponents. However, they just classified the motions as regular or chaotic according to the Lyapunov exponents, and details of the properties of the chaotic motion were not investigated.

In this paper, we look for statistical laws in the chaotic motions in the above system. Once we find the chaotic behaviors, we can characterize the chaos to extract the specific property of the system. We can hardly know about the chaos only from the positiveness of the Lyapunov exponents. Not a few people may believe that chaotic system is just complex and unpredictable at all. Of course, we cannot predict the time evolution of the state of the spinning test particle exactly, when the system is chaotic. However, even in such cases, we can frequently find some statistical laws which is proper to the system. One of the measure of the chaos is the power spectrum of the time series. In some cases, the pattern of the power spectrum obeys power laws, so called, $1/f$ fluctuations, which can be distinguished from the white-noise type. That the power spectrum obeys some power laws means that the time evolution of the system is time-correlated. In other words, we can characterize the chaos by the pattern of the power spectrum.

In this paper, we will characterize the properties of the chaos in the spinning-particle motions in Schwarzschild spacetime, using the pattern of the power spectrum of the time series. The pattern of the power spectrum can be divided into two types, $1/f$ and white noise. We will obtain the phase diagram for the properties of the chaos, the types of the power spectrum. We will discuss the origin of the $1/f$ fluctuations of the power spectrum in this system.

2   Equations for a spinning test particle in Schwarzschild spacetime

We consider a spinning test particle in Schwarzschild spacetime,

$$ds^2 = -\left(1 - \frac{2M}{r}\right)dt^2 + \left(1 - \frac{2M}{r}\right)^{-1} dr^2 + r^2 d\theta^2 + r^2 \sin^2\theta d\phi^2, \tag{1}$$

where M is the mass of the black hole.

---

[1]E-mail:koyama@gravity.phys.waseda.ac.jp
[2]E-mail:kiuchi@gravity.phys.waseda.ac.jp
[3]E-mail:tkonishi@r.phys.nagoya-u.ac.jp

The equations of motions of a spinning test particle in a relativistic spacetime have been derived by Papapetrou [3] and then reformulated by Dixon [4]. The set of equations is given as

$$\frac{dx^\mu}{d\tau} = v^\mu, \tag{2}$$

$$\frac{Dp^\mu}{d\tau} = -\frac{1}{2}R^\mu{}_{\nu\rho\sigma}v^\nu S^{\rho\sigma}, \tag{3}$$

$$\frac{DS^{\mu\nu}}{d\tau} = 2p^{[\mu}v^{\nu]}, \tag{4}$$

where τ, v^μ, p^μ and $S^{\mu\nu}$ are an affine parameter of the orbit, the four-velocity of a particle, the momentum, and the spin tensor, respectively. p^μ deviates from a geodesic due to the coupling of the Riemann tensor with the spin tensor. We also need an additional condition which gives a relation between p^μ and v^μ. We adopt the condition formulated by Dixon [4]

$$p_\mu S^{\mu\nu} = 0. \tag{5}$$

This condition consistently determines the center of mass in the present system. The mass of the particle μ is defined by

$$\mu^2 = -p_\mu p^\mu. \tag{6}$$

To make clear the freedom of this system, we have to check the conserved quantities. Regardless of the symmetry of the background spacetime, it is easy to show that μ and the magnitude of spin S defined by

$$S^2 \equiv \frac{1}{2}S_{\mu\nu}S^{\mu\nu}, \tag{7}$$

are constants of motion. If a background spacetime possesses some symmetry described by a Killing vector ξ^μ,

$$C_\xi \equiv \xi^\mu p_\mu - \frac{1}{2}\xi_{\mu;\nu}S^{\mu\nu} \tag{8}$$

is also conserved [4].

Because the spacetime is static and spherically symmetric, there are two Killing vector fields, $\xi^\mu_{(t)}$ and $\xi^\mu_{(\phi)}$. From (8), we find the constants of motion related with those Killing vectors as

$$E \equiv -C_{(t)} = -p_t - \frac{M}{r^2}S^{tr}, \tag{9}$$

$$J_z \equiv C_{(\phi)} = p_\phi - r(S^{\phi r} - rS^{\theta\phi}\cot\theta)\sin^2\theta. \tag{10}$$

E and J_z are interpreted as the energy of the particle and the z component of the total angular momentum, respectively. Because the background is spherically symmetric, without loss of generality we can choose the z axis in the direction of total angular momentum as

$$(J_x, J_y, J_z) = (0, 0, J), \tag{11}$$

where $J > 0$.

3 $1/f$ fluctuations of the power spectrum

In this section, we characterize the chaos in the spinning particle motions using the power spectrum. First, we plot the Poincaré maps with the different sets of the parameters in Fig.1. To draw the Poincaré map, we adopt the equatorial plane ($\theta = \pi/2$) as a Poincaré section and plot the point (r, v^r) when the particle crosses the Poincaré section with $v^\theta < 0$. If the orbit is chaotic, some of the tori are broken and the Poincaré map does not consist of a set of closed curves. As shown in Fig.1, the orbits with both sets of the parameters are chaotic, and we cannot distinguish them apparently.

Next we plot the power spectrum of the time series of z components of the particle in Fig.2 with the same set of the parameters as Fig.1. From Fig.2 we find that one is $1/f$, and the other is white noise. Therefore we can distinguish them clearly using the pattern of the power spectrum. That is, the property of the chaos depends on the system parameters, the angular momentum and the spin of the test particle. A preliminary result is summarized in the phase diagram in Fig.3.
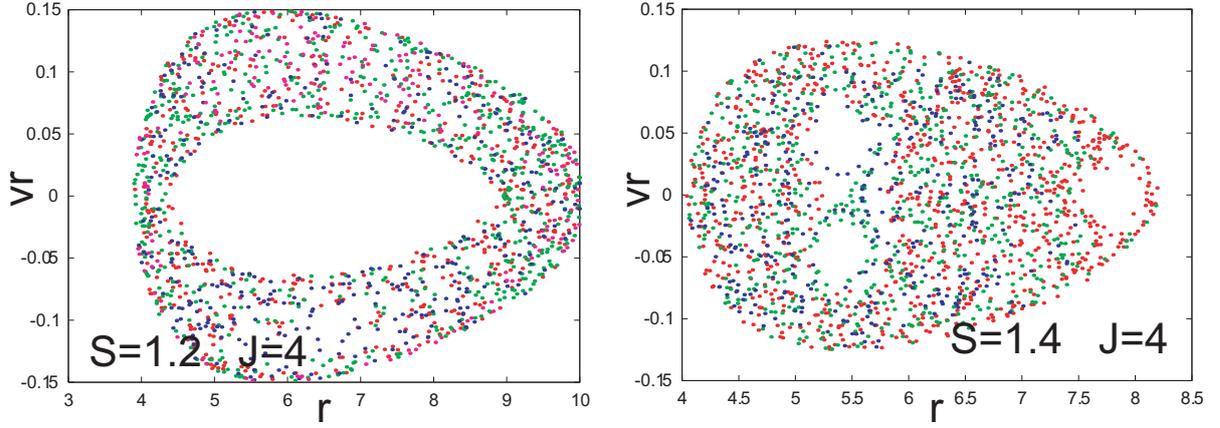
Figure 1: The Poincaré maps. All orbits have the total angular momentum $J = 4.0\mu M$. The magnitude of spin and the total energy are $S = 1.2\mu M$ and $E = 0.93545565\mu$ in the left panel, and $S = 1.4\mu M$ and $E = 0.92292941\mu$ in the right panel, respectively.
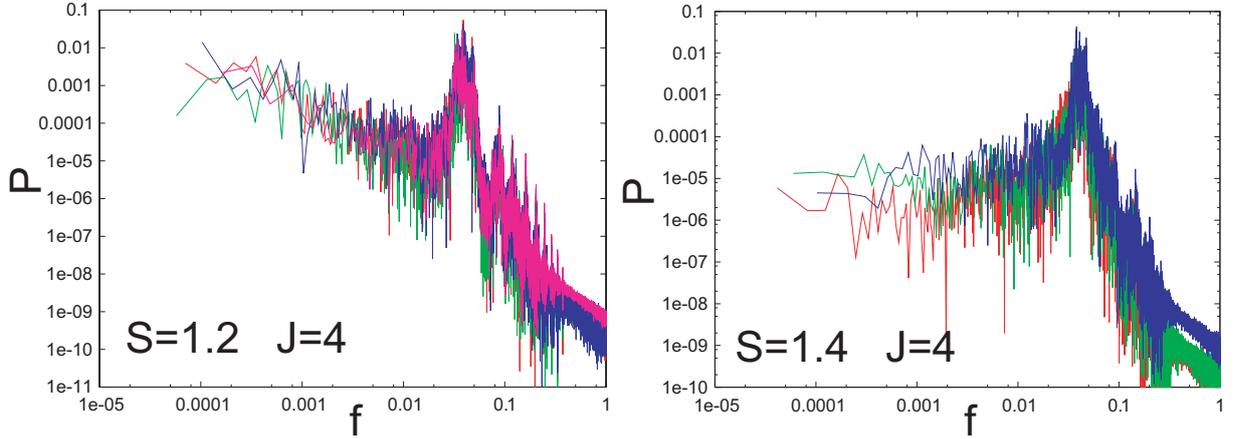
Figure 2: The power spectrum of the time series of z components of the particle. The sets of the parameters are same as Fig.1.
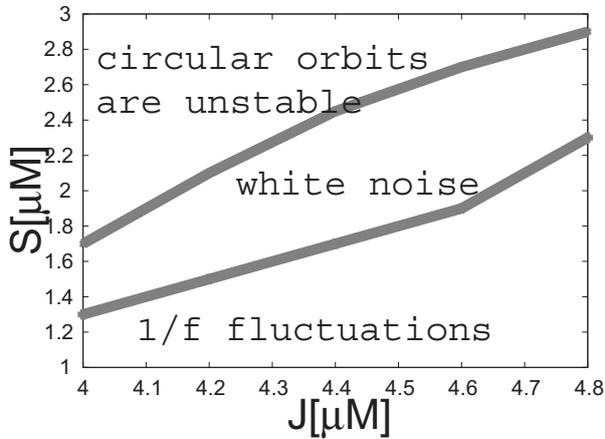
Figure 3: The phase diagram for the type of the pattern of the power spectrum. The spectrum is $1/f$ or white noise in the bottom or middle regions, respectively. The energy surface is unbounded in the upper region.
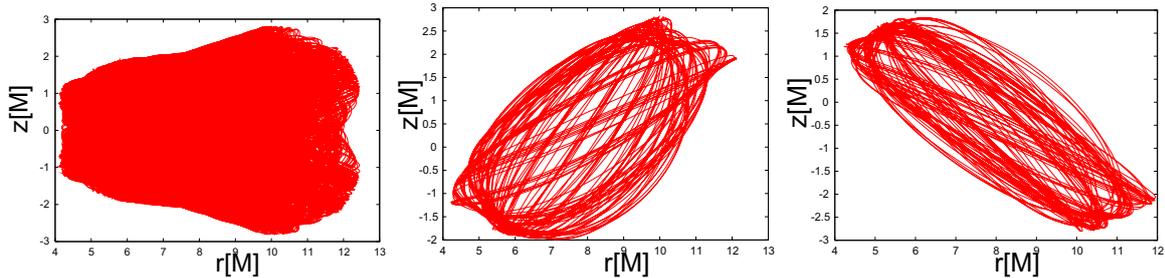
Figure 4: The orbit in the two-dimensional configuration space with $J = 4.2\mu M$, $S = 1.4\mu M$ and $E = 0.943$. The period is $0 < t < 110000$ in the left panel, $20000 < t < 32000$ in the middle panel, and $100000 < t < 110000$ in the right panel.

4　Summary and Discussion

In this paper we have investigated the properties of chaos in a spinning test particle in Schwarzschild spacetime. We have calculated the power spectrum of the time series of z components of the position of the test particle. We have found that the pattern of the power spectrum is $1/f$ or white noise, depending on the spin S and the angular momentum J of the test particle. We have obtained the phase diagram for the character of the chaos, the type of the pattern of the power spectrum. To put it another way, we can guess the properties of the system (S and J) by observing the dynamics of the test particle, even if the motion is chaotic.

Finally we discuss the origin of the $1/f$ fluctuations we found for the spinning test particle. We plot the orbit in the two-dimensional configuration space in Fig.4. Instead of filling the phase space uniformly, we find that the orbit (left panel in Fig.4) have two significant components (center and right panels in Figs.4), which stagnate around different tori. This type of motion where the phase point in chaotic orbit stays close to some regular orbits (tori) for some long time is known as "stagnant motion", and is often observed in Hamiltonian dynamical systems [5]. Stagnant motions are usually accompanied with $1/f$ fluctuations and are considered to be due to the fractal structure of the phase space. We expect that the $1/f$ fluctuations we observed in the system are also generated by such stagnant motions, itinerating among regular orbits in the Schwarzschild spacetime.

References

[1] A. J. Lichtenberg and M. A. Lieberman, "Regular and Chaotic Dynamics", (Springer 1992)

[2] S. Suzuki, K. Maeda, Phys. Rev. D**55**, 4848 (1997).

[3] A. Papapetrou, Proc. Roy. Soc. **A209**, 248 (1951).

[4] W. G. Dixon, Proc. Roy. Soc. **A314**, 499 (1970); *ibid* **A319**, 509 (1970); Journ. Gen. Rel. Grav. **4**, 193 (1973); Phil. Trans. Roy. Soc. **277**, 59 (1974); *in Isolated Gravitating Systems in General Relativity*, edited by J. Ehlers, (North-Holland, Amsterdam, 1979), 156.

[5] Y. Aizuchi, Y. Kikuchi, T. Harayama, K. Yamamoto, M. Ota and K. Tanaka, Prog. Theor. Phys. Suppl. **98**, 36(1989).

3-body problem in GR

Takamasa Chiba, Tatsunori Imai and Hideki Asada

Faculty of Science and Technology, Hirosaki University, Hirosaki 036-8561, Japan

Abstract

We discuss a 3-body problem in general relativity. It is impossible to describe all the solutions to the three-body problem even for the $1/r$ potential. For the Newtonian gravity, a special solution was found firstly by Moore (1995) and re-discovered with a rigorous proof by mathematicians Chenciner and Montgomery (2000). This solution is that three massive particles chase each other in a figure-eight orbit. We try to find out a figure-eight orbit of three masses by taking account of the post-Newtonian corrections. In a 2-body system, the post-Newtonian corrections cause the famous periastron shift. Therefore, we investigate whether or not the periastron shift appears in our post-Newtonian 3-body system.

1 Introduction

There are exact solutions for a 3-body problem in Newtonian gravity; a collinear solution (Euler, 1765), an equilateral triangle solution (Lagrange, 1772) and so on. The 3-body problem has not yet been solved completely in the sense that it is impossible to describe all the solutions to the 3-body problem even for the $1/r$ potential.

However, we shall investigate the 3-body problem in general relativity. From a different point of view, a binary plus the third body have been investigated so far regarding chaotic behaviors [1, 2, 3]. For our purpose, we take a figure-eight orbit in the Newton gravity as one example. This particular solution in the Newtonian gravity was found firstly by Moore (1995) [4] and re-discovered with a rigorous proof by mathematicians Chenciner and Montgomery (2000) [5].

What happens for the figure eight in GR? In a 2-body system by taking account of the post-Newtonian corrections, the famous periastron shift occurs. For instance, one may thus ask, "Is there a periastron shift?" or "Does the Figure-eight survive?" We will give an answer to these questions below [7]. The emitted gravitational waves have been computed [6].

2 The post-Newtonian corrections

Our assumption is as follows.

- Each mass is $m = 1$.

- The orbital plane is taken as the x - y plane.

- The position of each mass is denoted by (x_K, y_K) for $K = 1, 2, 3$.

- initial conditions

$$\boldsymbol{\ell} \equiv (x_1, y_1), \tag{1}$$
$$\ell = 100, \tag{2}$$
$$(x_1, y_1) = (-x_2, -y_2) \tag{3}$$
$$= (97.000436, -24.308753), \tag{4}$$
$$(x_3, y_3) = (0, 0), \tag{5}$$
$$(\dot{x}_3, \dot{y}_3) = (-2\dot{x}_1, -2\dot{x}_1) \tag{6}$$
$$= (-2\dot{x}_2, -2\dot{x}_2) \tag{7}$$
$$= (0.093240737, -0.086473146), \tag{8}$$
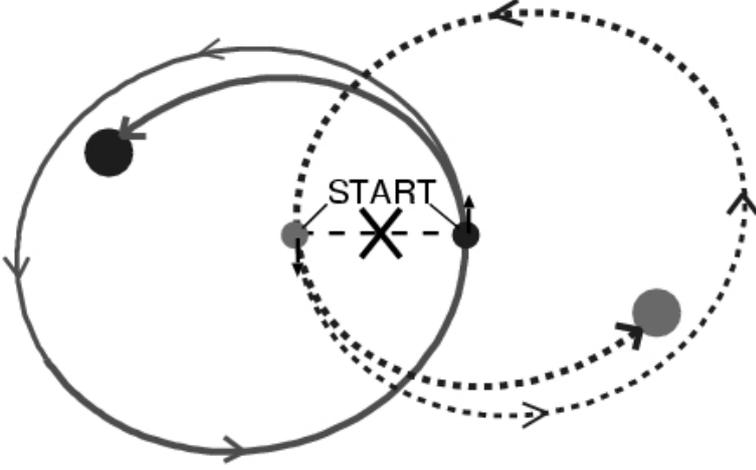
Figure 1: A binary orbit in the general relativity. The orbit is not closed any more, because a periastron shift occurs.

where, a dot denotes the time derivative.

The "EIH" equations of motion for a many-body system is expressed as

$$
\begin{aligned}
\frac{d^2 \boldsymbol{x}_K}{dt^2} &= \sum_{A \neq K} \boldsymbol{r}_{CA} \frac{1}{r_{AK}^3} \left[1 - 4 \sum_{B \neq K} \frac{1}{r_{BK}} - \sum_{C \neq A} \frac{1}{r_{CA}} \left(1 - \frac{\boldsymbol{r}_{AK} \cdot \boldsymbol{r}_{CA}}{2 r_{CA}^2} \right) \right. \\
&\qquad \left. + v_K^2 + 2 v_A^2 - 4 \boldsymbol{v}_A \cdot \boldsymbol{v}_K - \frac{3}{2} \left(\frac{\boldsymbol{v}_A \cdot \boldsymbol{r}_{CA}}{r_{AK}} \right)^2 \right] \\
&\quad - \sum_{A \neq K} (\boldsymbol{v}_A - \boldsymbol{v}_K) \frac{\boldsymbol{r}_{AK} \cdot (3 \boldsymbol{v}_A - 4 \boldsymbol{v}_K)}{r_{AK}^3} \\
&\quad + \frac{7}{2} \sum_{A \neq K} \sum_{C \neq A} \boldsymbol{r}_{CA} \frac{1}{r_{AK} r_{CA}^3},
\end{aligned} \tag{9}
$$

where we define $\boldsymbol{r}_{CA} \equiv \boldsymbol{r}_C - \boldsymbol{r}_A$.

Apparently, Fig. 2 shows that a figure-eight orbit does not survive at the 1PN order. However, this is not a case. We have to carefully investigate an initial condition by taking account of 1PN corrections. We assume that both of the total linear momentum and the total angular momentum vanish ($\boldsymbol{P} = 0$ and $\boldsymbol{L} = 0$). Then, the velocity of each mass is parameterized as

$$
\boldsymbol{v}_1 = k \boldsymbol{V} + \xi \frac{m}{\ell}, \tag{10}
$$

$$
\boldsymbol{v}_1 = k \boldsymbol{V} + \xi \frac{m}{\ell}, \tag{11}
$$

$$
\boldsymbol{v}_3 = \boldsymbol{V}, \tag{12}
$$

where k and ξ are determined as

$$
k = -\frac{1}{2} + \alpha V^2 + \beta \frac{m}{\ell}, \tag{13}
$$

$$
\alpha = -\frac{3}{16}, \tag{14}
$$

$$
\beta = \frac{1}{8}, \tag{15}
$$

$$
\xi = \frac{1}{8} \frac{m}{\ell^3} (\boldsymbol{V} \cdot \boldsymbol{\ell}). \tag{16}
$$
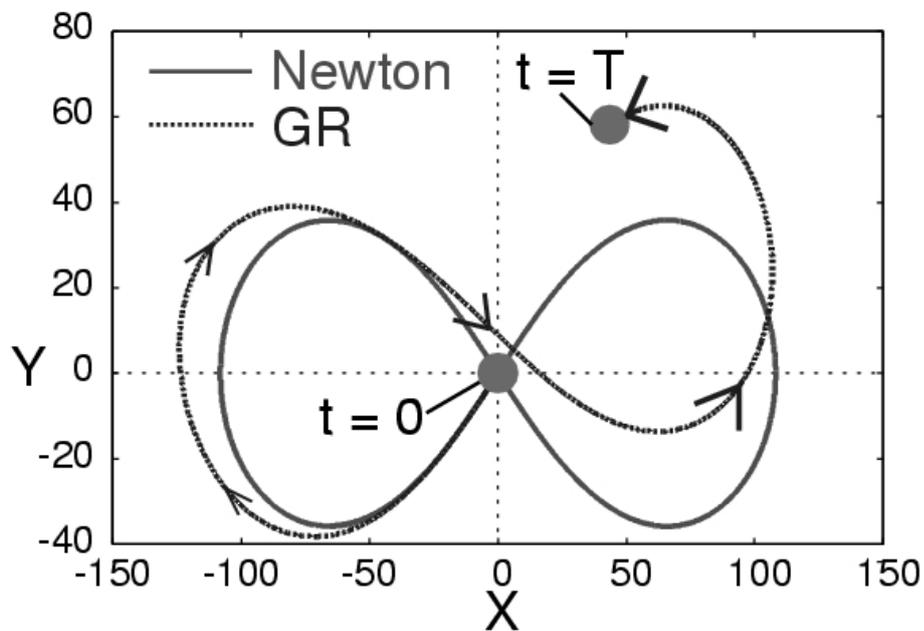
Figure 2: Figure-eights starting at the Newtonian initial condition. The solid curve denotes a figure-eight orbit in the Newtonian gravity. The dotted curve denotes a trajectory of one mass following the EIH equation of motion under the same Newtonian initial condition.
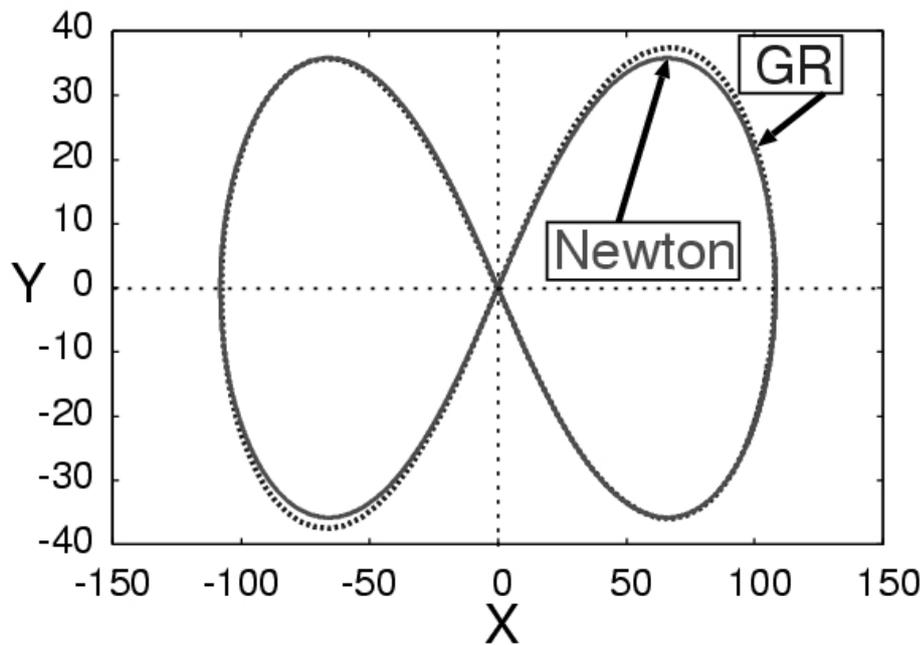
Figure 3: Figure-eight orbits. The solid curve denotes a figure-eight orbit in the Newtonian gravity. The dotted curve denotes a figure-eight orbit at the 1PN order of the general relativity.

We parameterize $\boldsymbol{V}$ as

$$\boldsymbol{V} = \left(1 + \delta \frac{m}{\ell}\right) \boldsymbol{V}_{\mathrm{Newton}} + \eta \frac{m}{\ell} \frac{\boldsymbol{\ell}}{\ell} \left(\boldsymbol{V}_{\mathrm{Newton}} \cdot \frac{\boldsymbol{\ell}}{\ell}\right). \tag{17}$$

To obtain a period orbit, we find out numerically

$$\delta = -3.28, \tag{18}$$
$$\eta = -3.82. \tag{19}$$

The orbital period becomes

$$T_{GR} \approx \left(1 + \frac{6m}{\ell}\right) \times T_{Newton}. \tag{20}$$

3   Conclusion

The figure-eight can survive also in GR! A difference is an expansion of the orbit around the upper right and lower left parts. The line symmetry in the Newton gravity is reduced to the symmetry with respect to the center.

References

[1] K. Ioka, T. Chiba, T. Tanaka, T. Nakamura, Phys. Rev. D **58**, 063003 (1998).

[2] Z. E. Wardell, Mon. Not. R. Astron. Soc. **334**, 149 (2002).

[3] M. Campanelli, M. Dettwyler, M. Hannam, C. O. Lousto, Phys. Rev. D **74**, 087503 (2006).

[4] C. Moore, Phys. Rev. Lett. **70**, 3675 (1993).

[5] A. Chenciner, R. Montgomery, Ann. Math. **152**, 881 (2000).

[6] T. Chiba, T. Imai, H. Asada, submitted to PRL, (astro-ph/06097773).

[7] T. Chiba, T. Imai, H. Asada, in preparation.

Regular second order perturbations of extreme mass ratio black hole binaries

Hiroyuki Nakano[1] and Carlos O. Lousto[2]

Department of Physics and Astronomy, and Center for Gravitational Wave Astronomy,
The University of Texas at Brownsville, Brownsville, Texas 78520, USA
and
Center for Computational Relativity and Gravitation, School of Mathematical Sciences,
Rochester Institute of Technology, 78 Lomb Memorial Drive, Rochester, New York 14623, USA

Abstract

We report on the first results of self-consistent second order metric perturbations produced by a point particle moving in the Schwarzschild spacetime. The second order waveforms satisfy a wave equation with an effective source term build up from products of first order metric perturbations and its derivatives. We have explicitly regularized this source term at the particle location as well as at the horizon and at spatial infinity.

1 Introduction

The observation of gravitational waves opens a new window onto our universe and we also expect that the observation of gravitational waves will provides a direct experimental test of general relativity.

The space mission LISA will primarily detect gravitational waves from inspiraling solar-mass compact objects captured by a supermassive black hole residing in the core of active galaxies. For these Extreme Mass Ratio Inspirals (EMRI) we use the black hole perturbation approach, where the compact object is approximated by a point particle orbiting a massive black hole. There are two nontrivial problems to consider in this approach: The self-force problem and the second order gravitational perturbations problem. Due to the self-force the orbit of the particle deviates from the background geodesic, i.e. the spacetime is perturbed by the particle itself. It is essential to take this deviation into account in order to predict the orbital evolution to the required order. For the headon configuration studied in this paper this was achieved in [1]. The gravitational self-force is, however, not easily obtainable for more general trajectories.

We require the second perturbative order calculations to derive the precise gravitational waveforms to be used as templates for gravitational wave data analysis. In general, this computation has to be done by numerical integration. Hence, it is important to derive a well-behaved second order effective source. In this paper, we will focus on this later problem.

2 Second order metric perturbations

We consider second order metric perturbations (MP), $\tilde{g}_{\mu\nu} = g_{\mu\nu} + h^{(1)}_{\mu\nu} + h^{(2)}_{\mu\nu}$, with expansion parameter μ/M corresponding to the mass ratio of the holes and where $g_{\mu\nu}$ is the Schwarzschild metric. The Hilbert-Einstein tensor and the stress-energy tensor up to the second perturbative order is given by

$$G_{\mu\nu}[\tilde{g}_{\mu\nu}] = G^{(1)}_{\mu\nu}[h^{(1)}] + G^{(1)}_{\mu\nu}[h^{(2)}] + G^{(2)}_{\mu\nu}[h^{(1)}, h^{(1)}], \quad T_{\mu\nu} = T^{(1)}_{\mu\nu} + T^{(2,SF)}_{\mu\nu} + T^{(2,h)}_{\mu\nu}, \tag{1}$$

where

$$G^{(1)}_{\mu\nu}[h] = -\frac{1}{2}h_{\mu\nu;\alpha}{}^{;\alpha} + h_{\alpha(\mu;\nu)}{}^{;\alpha} - R_{\alpha\mu\beta\nu}h^{\alpha\beta} - \frac{1}{2}h_{;\mu\nu} - \frac{1}{2}g_{\mu\nu}(h_{\lambda\alpha}{}^{;\alpha\lambda} - h_{;\lambda}{}^{;\lambda}),$$

---

[1] E-mail:nakano@phys.utb.edu
[2] E-mail:lousto@phys.utb.edu

$$G^{(2)}_{\mu\nu}[h^{(1)}, h^{(1)}] = R^{(2)}_{\mu\nu}[h^{(1)}, h^{(1)}] - \frac{1}{2}g_{\mu\nu}R^{(2)}[h^{(1)}, h^{(1)}];$$

$$R^{(2)}_{\mu\nu}[h^{(1)}, h^{(1)}] = \frac{1}{4}h^{(1)}_{\alpha\beta;\mu}h^{(1)\alpha\beta}{}_{;\nu} + \frac{1}{2}h^{(1)\alpha\beta}(h^{(1)}_{\alpha\beta;\mu\nu} + h^{(1)}_{\mu\nu;\alpha\beta} - 2h^{(1)}_{\alpha(\mu;\nu)\beta})$$
$$- \frac{1}{2}(h^{(1)\alpha\beta}{}_{;\beta} - \frac{1}{2}h^{(1);\alpha})(2h^{(1)}_{\alpha(\mu;\nu)} - h^{(1)}_{\mu\nu;\alpha}) + \frac{1}{2}h^{(1)}_{\mu\alpha;\beta}h^{(1)\alpha;\beta}_{\nu} - \frac{1}{2}h^{(1)}_{\mu\alpha;\beta}h^{(1)\beta;\alpha}_{\nu}.$$

On the other hand, the stress-energy tensor includes three parts, the first order stress-energy tensor $T^{(1)}_{\mu\nu}$ which is the one of a point particle moving along a background geodesic;

$$T^{(1)\mu\nu} = \mu \int_{-\infty}^{+\infty} \delta^{(4)}(x - z(\tau))\frac{dz^\mu}{d\tau}\frac{dz^\nu}{d\tau}d\tau, \tag{2}$$

where $z^\mu = \{T(\tau), R(\tau), \Theta(\tau), \Phi(\tau)\}$ for the particle orbit, the deviation from the geodesic by the self-force $T^{(2,SF)}_{\mu\nu}$ (See Ref. [1]), and finally $T^{(2,h)}_{\mu\nu}$, which is purely affected by the first order MP,

$$T^{(2,h)}_{\mu\nu} = -\frac{1}{2}\mu \int_{-\infty}^{+\infty} h^{(1)}\, \delta^{(4)}(x - z(\tau))\frac{dz^\mu}{d\tau}\frac{dz^\nu}{d\tau}d\tau, \tag{3}$$

where we have used the determinant $\tilde{g} = g(1 + h^{(1)})$ up to the first perturbative order.

3　First order metric perturbations in the RW gauge

Before considering the second order, it is necessary to discuss the first order MP, i.e., the Regge-Wheeler-Zerilli formalism [2, 3]. The basic formalism has been given in Zerilli's paper [3], and it has been summarized in the time domain in [4, 5]. In the following, equation numbers (Z:1), (L1:1) and (L2:1) for instance, denote the equation (1) in [3], [4] and [5], respectively.

For the first order Hilbert-Einstein equation, $G^{(1)}_{\mu\nu}[h^{(1)}] = 8\pi T^{(1)}_{\mu\nu}$, we expand $h^{(1)}_{\mu\nu}$ and $T^{(1)}_{\mu\nu}$ in ten tensor harmonics components. We then obtain the linearized field equations for each harmonic mode. For the even part, which has the even parity behavior, $(-1)^\ell$, we have seven equations. We impose the Regge-Wheeler gauge conditions (RW), the vanishing of some coefficients of the first order MP: $h^{(e)}_0 = h^{(e)}_1 = G = 0$.

We introduce the following wave-function for the even parity modes,

$$\psi^{\text{even}}_{\ell m}(t, r) = \frac{2r}{\ell(\ell+1)}\left[K^{\text{RW}}_{\ell m}(t, r) + 2\frac{(r - 2M)}{(r\ell^2 + r\ell - 2r + 6M)}\left(H^{\text{RW}}_{2\,\ell m}(t, r) - r\frac{\partial}{\partial r}K^{\text{RW}}_{\ell m}(t, r)\right)\right], \tag{4}$$

where the suffix RW stands for the RW gauge. This function $\psi^{\text{even}}_{\ell m}$ obeys the Zerilli equation,

$$\hat{Z}^{\text{even}}_\ell \psi^{\text{even}}_{\ell m}(t, r) = S^{\text{even}}_{\ell m}(t, r); \quad \hat{Z}^{\text{even}}_\ell = -\frac{\partial^2}{\partial t^2} + \frac{\partial^2}{\partial r^{*2}} - V^{\text{even}}_\ell(r), \tag{5}$$

where $r^* = r + 2M\log(r/2M - 1)$, the potential V^{even}_ℓ and the source $S^{\text{even}}_{\ell m}$ are given in Eqs. (L1:1-2) and (L1:A.3). The reconstruction of the MP under the RW gauge have been expressed in Eqs. (L2:B.9-12).

In the following, we consider a particle falling radially into a Schwarzschild black hole as the first order source. The equation of motion of the test particle is given by

$$\left(\frac{dR}{dt}\right)^2 = -\left(1 - \frac{2M}{R}\right)^3\frac{1}{E^2} + \left(1 - \frac{2M}{R}\right)^2; \quad E = \left(1 - \frac{2M}{R}\right)\frac{dT(\tau)}{d\tau}, \tag{6}$$

where E and R are the energy and the location of the particle, respectively. The non-vanishing tensor harmonics coefficients of the energy-momentum tensor are $A_{\ell m}$, $A^{(0)}_{\ell m}$ and $A^{(1)}_{\ell m}$. Because of the symmetry of the problem we have only to consider even parity modes, i.e., described by the Zerilli equation.

In the head on collision case, the MP in the RW gauge are C^0 (continuous across the particle). One can see this as follows. First, from Eqs. (Z:C7d) and (Z:C7e), we find that $H_{2\,\ell m}(= H_{0\,\ell m})$ and $K_{\ell m}$ have the same differential behavior. Then, we note that $\partial_r K_{\ell m} \sim \theta(r - R(t))$, because the left hand side of

(4) behaves as a step function near the particle. This means that $K_{\ell m}$ (and also $H_{2\,\ell m}$) is C^0. Using this, $\partial_r H_{1\,\ell m} \sim \theta(r - R(t))$ is derived from Eq. (Z:C7e), i.e., $H_{1\,\ell m}$ is C^0. (See Ref. [6].)

Using the above fact, we can take up second derivatives of the function $\psi_{\ell m}^{\rm even}$ with respect to t and r. These quantities allow us to calculate the coefficients of the δ-terms in the second order source.

Next, we consider the $\ell = 0$ perturbations ($\ell = 1$ modes can be completely eliminated in the center of mass coordinate system). In the RW gauge there are four non-vanishing coefficients of the MP, $H_{0\,00}$, $H_{1\,00}$, $H_{2\,00}$ and K_{00}. The gauge transformation has two extra degrees of freedom. We could choose the gauge so that $H_{1\,00} = K_{00} = 0$, i.e., the Zerilli gauge, but it is difficult to treat the second order source, since the MP are not C^0.

We instead consider here a new (singular) gauge transformation, chosen to make the metric perturbations C^0 and to obtain an appropriate second order source behavior. To derive this gauge transformation, we have also considered a regularization of the second order source at $r = \infty$ and the horizon at the same time [3]. Note that we succeeded in choosing the gauge such that all of the above MP behave as C^0 at the location of the particle and vanish at $r = \infty$ and $r = 2M$.

4   Second order Zerilli equation

Since the first order MP contains only even parity modes, we can discuss the second order MP for the even parity modes only, i.e. in terms of the Zerilli function,

$$\chi_{20}^{\rm Z}(t,r) \;\; = \;\; \frac{1}{2\,r + 3\,M}\left(r^2\frac{\partial}{\partial t}\mathcal{K}_{20}(t,r) - (r - 2\,M)\mathcal{H}_{1\,20}(t,r)\right). \tag{7}$$

Here, we have considered the contribution from the $\ell = 0$ and 2 modes of the first order to the $\ell = 2$ mode of the second order since this gives the leading contribution to gravitational radiation. We also choose the RW gauge to second order. This Zerilli function satisfies the equation, $\hat{\mathcal{Z}}_2^{\rm even}\chi_{20}^{\rm Z}(t,r) = \mathcal{S}_{20}^{\rm Z}(t,r)$ with

$$\begin{aligned}
\mathcal{S}_{20}^{\rm Z}(t,r) \;\; = \;\; & \frac{8\,\pi\,\sqrt{3}\,(r - 2\,M)^2}{3(2\,r + 3\,M)}\frac{\partial}{\partial t}\mathcal{B}_{20}(t,r) + \frac{8\,\pi\,(r - 2\,M)^2}{2\,r + 3\,M}\frac{\partial}{\partial t}\mathcal{A}_{20}(t,r) - \frac{8\,\sqrt{3}\,\pi\,(r - 2\,M)}{3}\frac{\partial}{\partial t}\mathcal{F}_{20}(t,r) \\[2mm]
& -\frac{4\,\sqrt{2}\,i\pi\,(r - 2\,M)^2}{2\,r + 3\,M}\frac{\partial}{\partial r}\mathcal{A}_{20}^{(1)}(t,r) - \frac{8\,\sqrt{2}\,i\pi\,(r - 2\,M)\,(5\,r - 3\,M)\,M}{r\,(2\,r + 3\,M)^2}\mathcal{A}_{20}^{(1)}(t,r) \\[2mm]
& -\frac{8\,\sqrt{3}\,i\pi\,(r - 2\,M)^2}{3(2\,r + 3\,M)}\frac{\partial}{\partial r}\mathcal{B}_{20}^{(0)}(t,r) + \frac{32\,\sqrt{3}\,i\pi\,\left(3\,M^2 + r^2\right)(r - 2\,M)}{3\,r\,(2\,r + 3\,M)^2}\mathcal{B}_{20}^{(0)}(t,r).
\end{aligned} \tag{8}$$

The functions $\mathcal{B}_{20}$ etc. are derived from the second order quantities, $G_{\mu\nu}^{(2)}[h^{(1)}, h^{(1)}]$, $T_{\mu\nu}^{(2,h)}$ (and $T_{\mu\nu}^{(2,SF)}$) by the same tensor harmonics expansion as for the first order.

The delta function $\delta^{(4)}(x - z(\tau))$ in $T_{\mu\nu}^{(2,h)}$ includes $\delta^{(2)}(\Omega - \Omega(\tau)) = \sum_{\ell m} Y_{\ell m}(\Omega)Y_{\ell m}^*(\Omega(\tau))$. We have considered only the contribution from the $\ell = 0$ and 2 modes of the first order perturbations. Consistently, we use only the three components, $h_{(\ell=2)}^{(1)}Y_{2m}(\Omega)Y_{2m}^*(\Omega(\tau))$, $h_{(\ell=2)}^{(1)}Y_{0m}(\Omega)Y_{0m}^*(\Omega(\tau))$ and $h_{(\ell=0)}^{(1)}Y_{2m}(\Omega)Y_{2m}^*(\Omega(\tau))$.

We may wander if there is any δ^2-term in the second order source. The answer is "No". This is because in the case of the head on collision, the MP under the RW gauge are C^0: $R_{\mu\nu}^{(2)}[h^{(1)}, h^{(1)}]$ includes second derivatives and we need one more derivative to construct $\mathcal{S}_{20}^{\rm Z}$. $(h^{(1)})^2$ is $C^0 \times C^0$ and its third derivative yields $C^0 \times \delta'$ and $\theta \times \delta$ as the most singular terms. On the other hand, $T_{\mu\nu}^{(2,h)}$ includes only $C^0 \times \delta$ terms.

From Eq. (8), we obtain the second order source as

$$\mathcal{S}_{20}^{\rm Z}(t,r) \;\; = \;\; {}^{(2,2)}\mathcal{S}_{20}^{\rm Z}(t,r) + {}^{(0,2)}\mathcal{S}_{20}^{\rm Z}(t,r), \tag{9}$$

where ${}^{(2,2)}\mathcal{S}_{20}^{\rm Z}$ and ${}^{(0,2)}\mathcal{S}_{20}^{\rm Z}$ are the contribution from $(\ell = 2)\cdot(\ell = 2)$ and $(\ell = 0)\cdot(\ell = 2)$, respectively.

Note that while the above source term is locally well behaved near the particle location, some terms diverge as $r \to \infty$. So, we need to consider some regularization for the asymptotic behavior [7].

---

[3]We could regularize and fix the gauge for the second order source. One could also proceed by first fixing the gauge.

In order to obtain a well behaved source for large values of r, we define a renormalized Zerilli function by

$$
\begin{aligned}
\tilde{\chi}_{20}^{\mathrm{Z}}(t,r) &= \chi_{20}^{\mathrm{Z}}(t,r) - \chi_{20}^{\mathrm{reg},(2,2)} - \chi_{20}^{\mathrm{reg},(0,2)} ; \\
\chi_{20}^{\mathrm{reg},(2,2)} &= \frac{\sqrt{5}}{7\sqrt{\pi}}\frac{r^2}{2\,r+3\,M}\left(\frac{\partial}{\partial t}K_{20}^{\mathrm{RW}}(t,r)\right)K_{20}^{\mathrm{RW}}(t,r) , \\
\chi_{20}^{\mathrm{reg},(0,2)} &= -\frac{1}{32\sqrt{\pi}}\frac{r\,(r-2\,M)}{2\,r+3\,M}\Bigg(\left(1-\frac{M}{r}\ln\left(\frac{r}{2M}\right)\right)H_{2\,00}^{\mathrm{RZ}}(t,r)\frac{\partial}{\partial r}H_{2\,20}^{\mathrm{RW}}(t,r) \\
&\quad +6\left(1-5\frac{M}{r}\right)H_{0\,00}^{\mathrm{RZ}}(t,r)\frac{\partial}{\partial r}H_{2\,20}^{\mathrm{RW}}(t,r)+4\left(1+3\frac{M}{r}\ln\left(\frac{r}{2M}\right)\right)H_{2\,00}^{\mathrm{RZ}}(t,r)\frac{\partial}{\partial t}H_{2\,20}^{\mathrm{RW}}(t,r) \\
&\quad +5\left(1-4\frac{M}{r}\right)H_{0\,00}^{\mathrm{RZ}}(t,r)\frac{\partial}{\partial t}H_{2\,20}^{\mathrm{RW}}(t,r)-18\frac{1}{r}\ln\left(\frac{r}{2M}\right)H_{0\,00}^{\mathrm{RZ}}(t,r)H_{2\,20}^{\mathrm{RW}}(t,r)\Bigg) ,
\end{aligned}
$$
(10)

where the suffix RZ means some gauge choice as discussed in Sec. 3. Finally, The best suited equation to solve numerically for $\tilde{\chi}_{20}^{\mathrm{Z}}$ is then

$$
\begin{aligned}
\hat{\mathcal{Z}}_2^{\mathrm{even}}\tilde{\chi}_{20}^{\mathrm{Z}}(t,r) &= \mathcal{S}_{20}^{\mathrm{Z,reg}}(t,r) ; \\
\mathcal{S}_{20}^{\mathrm{Z,reg}}(t,r) &= \left({}^{(2,2)}\mathcal{S}_{20}^{\mathrm{Z}}(t,r)-\hat{\mathcal{Z}}_2^{\mathrm{even}}\chi_{20}^{\mathrm{reg},(2,2)}(t,r)\right)+\left({}^{(0,2)}\mathcal{S}_{20}^{\mathrm{Z}}(t,r)-\hat{\mathcal{Z}}_2^{\mathrm{even}}\chi_{20}^{\mathrm{reg},(0,2)}(t,r)\right) .
\end{aligned}
$$
(11)

5 Discussion

In this paper, we obtained the regularized second order effective source of the Zerilli equation in the case of a particle falling radially into a Schwarzschild black hole. Using this source, we are able to compute the second order contribution to gravitational radiation by numerical integration.

To be fully second order consistent we have to include the term $T_{\mu\nu}^{(2,SF)}$ which is derived from the self-force on a particle. The self-force for a headon collision has been calculated in [1], and in a circular orbit around a Schwarzschild black hole in [8], but have not been obtained in the general case yet.

To prove that there is no δ^2 term in the second order source, we have used the fact that the first order MP in the RW gauge is C^0. In the general orbit cases (including circular orbits), the first order MP is not C^0 in the RW gauge, but it is C^0 in the Lorenz gauge [9]. This gauge choice favors the study of the second order perturbations for generic orbits.

Acknowledgments

We would like to thank K. Nakamura and T. Tanaka for useful discussions.

References

[1] L. Barack and C. O. Lousto, Phys. Rev. D **66**, 061502 (2002) [arXiv:gr-qc/0205043].

[2] T. Regge and J. A. Wheeler, Phys. Rev. **108**, 1063 (1957).

[3] F. J. Zerilli, Phys. Rev. D **2**, 2141 (1970).

[4] C. O. Lousto, Class. Quant. Grav. **22**, S543 (2005) [arXiv:gr-qc/0503001].

[5] C. O. Lousto, Class. Quant. Grav. **22**, S569 (2005) [arXiv:gr-qc/0501088].

[6] C. O. Lousto, Phys. Rev. Lett. **84**, 5251 (2000) [arXiv:gr-qc/9912017].

[7] R. J. Gleiser, C. O. Nicasio, R. H. Price and J. Pullin, Phys. Rept. **325**, 41 (2000).

[8] H. Nakano, N. Sago and M. Sasaki, Phys. Rev. D **68**, 124003 (2003) [arXiv:gr-qc/0308027].

[9] L. Barack and C. O. Lousto, Phys. Rev. D **72**, 104026 (2005) [arXiv:gr-qc/0510019].

"Black Hole Aurora" in a Black Hole Magnetosphere

Masaaki Takahashi[1]

Department of Physics and Astronomy, Aichi University of Education,
Kariya, Aichi 448–8542, Japan

Abstract

I present a model of high-energy emission sources generated by a standing magnetohydrodynamical (MHD) shock in a black hole magnetosphere. The black hole magnetosphere would be constructed around a black hole and an equatorial accretion disk, and can be considered as a model for a central engine of active galactic nuclei (AGNs) and gamma-ray bursts (GRBs). From the analysis of MHD shock conditions for accreting plasma onto a black hole, we obtain the restrictions on the flow's physical parameters, and examine the distribution of the shock front. Then, we find that an off-equatorial Aurora-like shaped hot plasma region is possible by the MHD shock formation when the magnetosphere rapidly rotates; the hot plasma region locates close to the event horizon. The emission from this off-equatorial sources would carry new information about the strong gravitational field to us.

1 Introduction

A black hole magnetosphere would be constructed around a black hole and an equatorial disk (see Fig. 1a) [1, 2]. The global magnetic field in the magnetosphere should be generated by the disk. Along the magnetic field lines, the plasma fluid ejected from the disk surface stream inward and outward by the dominant gravitational force and centrifugal force, respectively [3]. The outgoing plasma would make a relativistic jet/wind, which may be observed in systems of AGNs and GRBs. Here, to understand the astrophysical phenomena around a black hole, we consider ingoing flows and discuss the condition of MHD shocks [4]. The ingoing MHD flow ejected from a plasma source with low velocity must be supermagnetosonic at the event horizon, so that the two magnetosonic surface are require in front and behind the shock front (see Fig. 1b). By the generation of the MHD shock, a very hot plasma region can be formed near the event horizon [5]. Such a hot plasma region can be considered as a source of high energy radiation, which gives us information of the strong gravitational field in addition to the (magnetized) plasma state. Of course, some part of the radiation emitted from the hot plasma will fall into the black hole because of gravitational lens effects, but we can expect that huge energy can be released at the very hot shocked plasma region and considerable flux will be obtained. In the following sections, we introduce transmagnetosonic accretion flows [7] and apply the shock condition in §2. Then, in §3, we treat *negative* energy MHD inflows [3] and discuss the energy release of the rotational energy of the black hole at the shocked region. In §4, we present the outline of radiative MHD shocks [8] for obtaining the energy spectrum and the image of a shocked region.

2 MHD Accretion with MHD Shock

We consider MHD flows in a stationary and axisymmetric magnetosphere of a rotating black hole (see, e.g., [3, 9]). The background metric is written by the Boyer-Lindquist coordinate with $c = G = 1$. The basic equations for MHD flows are the equation of the particle number conservation, the equation of motion and Maxwell equations. We assume ideal MHD condition and the polytropic relation. In these situations, there are five field-aligned flow parameters; the total energy E, the total angular momentum L, the angular velocity of the magnetic field line Ω_F, the number flux per flux-tube η and the entropy. The critical conditions at the Alfvén point and the magnetosonic points restrict the acceptable ranges of these parameters (see [7] for the details). To obtain a shocked black hole accretion solution, it is
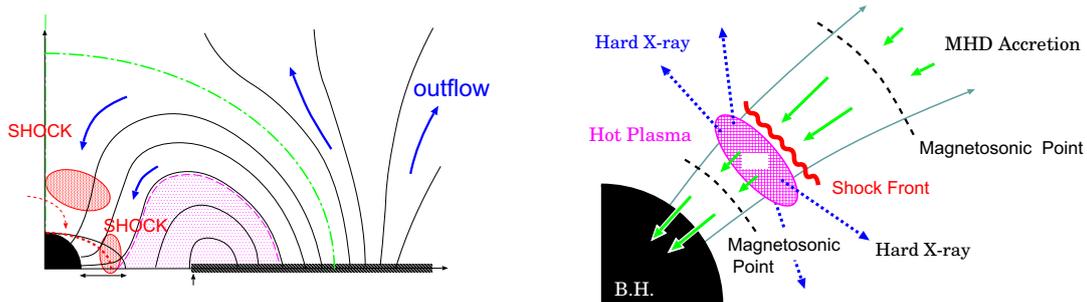

Figure 1: (a) A model of the black hole magnetosphere. Ingoing MHD flows stream along the disk–black hole connected magnetic field lines. Because of the loop-shaped magnetic field configuration, off-equatorial shock is possible. (b) MHD shock in black hole accretion. After passing through *first* magnetosonic point, the MHD inflow can make the MHD shock. The postshocked sub-magnetosonic flows must pass through the *second* magnetosonic point again before reaching the event horizon.

necessary to find the two transmagnetosonic solutions; that is, the upstream and downstream solutions. At the shock location, where the shock conditions must be satisfied, the super-magnetosonic branch of the upstream solution is connected to the sub-magnetosonic branch of the downstream solution. After the shock, the inflow must pass through the second magnetosonic point again, and then can fall into the horizon. The upstream and downstream solutions would have different energy and angular momentum because of the radiation loss, but the conservation of the angular velocity and the number flux between the upstream and downstream solutions is assumed at present. Recently, Fukumura, Takahashi & Tsuruta [6] investigates the accretion solutions with the fast MHD shock. Figure 2 shows the possible shock range in the poloidal plane. When the angular velocity of the magnetic field lines are rather faster than the Kepler velocity estimated at the footpoint of the field line, the shock can be generated, while for slowly rotating magnetic field lines there are no shock fronts. The energy E and angular momentum L are also restricted within the certain ranges of parameter spaces. It is interesting that for faster rotating case the acceptable parameter range for the shock front shifts toward the polar region; the MHD shock formation near the equatorial region is forbidden. Such a situation may not be stable when we consider inflows originated from the equatorial thin disk, which rotates with Kepler velocity. However, when high-energy MHD fluid ($E \gg m_p$) falls along faster rotating magnetic field line, the MHD shock is generated in the high-latitude region of the black hole. Thus, a ring shaped hot region would be observed close to the black hole like an aurora (see Fig. 3).

3   High Energy Radiation powered by Rotating Black Hole

Rotational energy of a black hole can be extracted by magnetic field lines [3, 10]. The extracted energy is carried to the magnetosphere in the form of outgoing Poynting flux, and would be converted to some kinds of fluid energy related to the radiative process directly. Then, the extracted hole's energy can be observable for us. However, in the treatment of the force-free (magnetically dominated limit) magnetosphere, realistic conversion mechanisms are not clear, although some ideas may be proposed. We are now discussing the MHD accretion onto a black hole. Although the MHD inflow takes the fluid energy into the hole, which is positive at the plasma source, the total (fluid + magnetic) energy can be *negative* from the plasma source to the horizon. In general, we understand that the kinetic energy of the upstream MHD flow converts to the thermal and magnetic energies of the downstream flow at the fast MHD shock. When the negative energy accrete onto the black hole (i.e., energy extraction by MHD flows), we can also expect the energy conversion from the extracted hole's energy to the radiative energy at the MHD shock. By considering the regularity condition at the Alfvén point, which is related to the amount of jump of the energy and angular momentum between the preshock and postshock solutions, we find the necessary condition for doing such a energy release process (Takahashi & Takahashi 2007, in preparation). To complete the black hole's rotational energy release at the MHD shock, we must link this
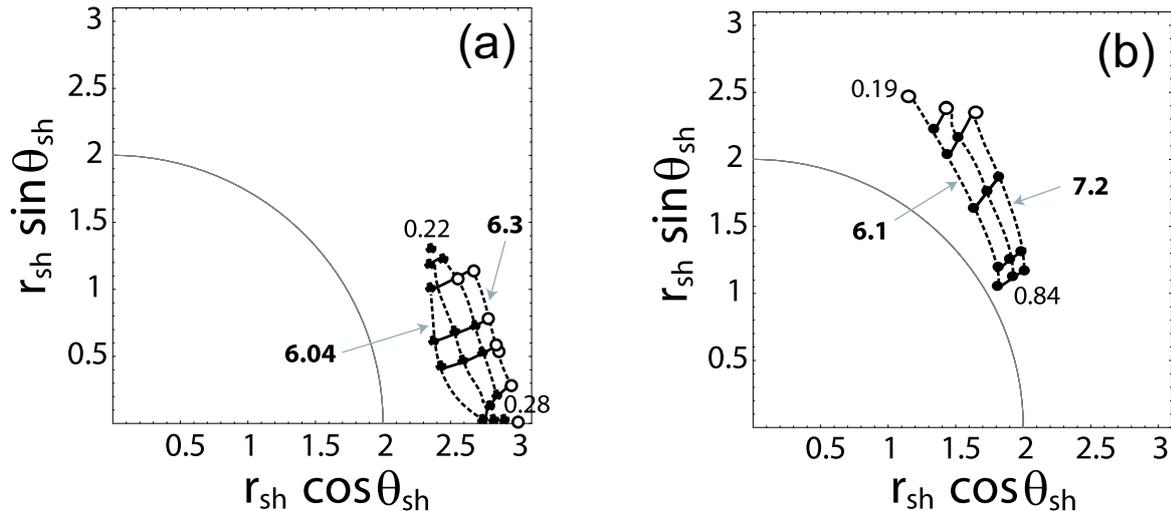
Figure 2: The possible range of the fast MHD shock front for (a) $\Omega_F = 0.1m$ and (b) $\Omega_F = 0.2m$ [6]. The solid curves show $L\Omega_F/E = $ constant, and the dotted curves show the $E/m_p = $ constant, where m_p is the particle's rest-mass energy. The radial magnetic field lines are assumed.

Alfvénic necessary condition to the requirement by the regularity conditions at the fast magnetosonic points, consistently. That remains to be proved.

4   Radiative MHD Shock

Although we discuss the activity of plasma around a black hole in the frame work of general relativity, the shocks and emission process are essentially local phenomena, which can be treated by special relativity. We have discussed the global shocked accretion solutions, which are two transmagnetosonic solutions with a MHD shock as mentioned above, in Boyer-Lindquist coordinates. To introduce the radiative process in the MHD shock solution, Takahashi & Takahashi [8] discuss this problem in the local plasma frame, and then transform the physical quantities in the local frame to that of the curved spacetime; in actual numerical calculation, three kinds of reference frames are utilized; that is, the Boyer-Lindquist frame, Zero-Angular Momentum Observer (ZAMO) frame and the fluid rest frame. Compared with the global solution (plasma density, temperature, etc) denoted in curves spacetime, the restrictions on the local plasma quantities are also determined. When radiation process (synchrotron radiation, bremsstrahlung, inverse Compton scattering, etc.) are specified, local energy spectrum at radiative shock is obtained. In order to calculate the observed spectrum and image of the radiative MHD shock around a black hole, null geodesics from the black hole area to us should be calculated exactly. Such calculations include the Doppler effects of plasma motion and general relativistic effects such as bending of light, gravitational redshift and frame dragging effects. Thus, we present a theoritical tool to find the evidence of black holes in the observed spectrum and the images (see [8] for details).

5   Summary

The general relativistic MHD is applied to a black hole magnetosphere, and transmagnetosonic ingoing flows are discussed. The MHD shock conditions are also discussed, and the possibility of very hot shocked plasma region is indicated very close to the black hole. We can expect that the high energy emission from this hot plasma bring to us *additional* information about the black hole spacetime; the polar region emission including this information can be distinct from the emissions from the equatorial plasma source, which have investigated by many authors in models of black hole accretion. In this stage, expected energy spectrum from the off-equatorial MHD shock is not clear. We need a realistic model of the black hole
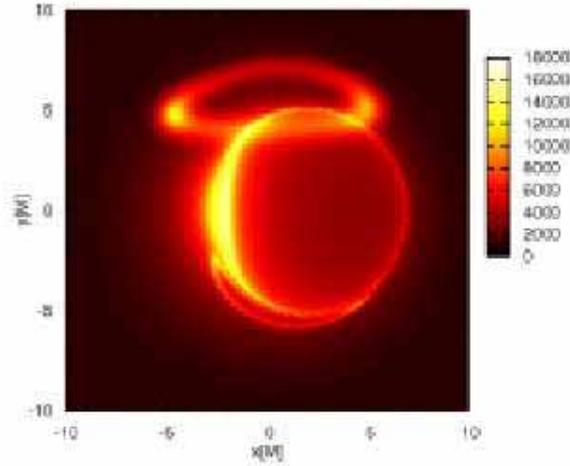
Figure 3: Image of the radiative MHD shock with radiatively inefficient accretion flows (RIAF) around a Kerr black hole [8]. The split-monopole magnetic field is assumed. The shape of the emission region is just like a aurora (black hole aurora). In this calculation, the shock in the Northern hemisphere is considered, but the ghost of the shock is also seen in the Southern hemisphere because of the gravitational lens effect. The crescent-shaped bright area, which is the radiation from RIAF, is cased by the Doppler boosting.

magnetosphere with a magnetized accretion disk. Then, we will find the evidences of the existence of *real* black holes (not the candidate) in observational data.

References

[1] Nitta, S., Takahashi, M., & Tomimatsu, A. 1991, Phys. Rev. D44, 2295

[2] Takahashi, M., & Tomimatsu, A. 2001, ApJ, 552, 710

[3] Takahashi, M., Nitta, S., Tatematsu, Y., & Tomimatsu, A. 1990, ApJ, 363, 206

[4] Lichnerowicz, A. 1967, Relativistic Hydrodynamics and Magnetohydrodynamics (New York : Benjamin Press)

[5] Takahashi, M., Goto, J., Fukumura, K., & Tsuruta, S. 2006, ApJ, 645, 1408

[6] Fukumura, K., Takahashi, M., & Tsuruta, S. 2007, ApJ, in press

[7] Takahashi, M. 2002, ApJ. 570, 264

[8] Takahashi, R., & Takahashi, M. 2007, submitted to PRD.

[9] Camenzind, M. A&A, 184, 341

[10] Blandford, R. D., & Znajek, R. L. 1977, MNRAS, 179, 433

Equilibrium configurations of magnetized rotating polytropes

Shijun Yoshida[1] and Yoshiharu Eriguchi[2]

[1] *Science and Engineering, Waseda University, Okubo, Shinjuku, Tokyo 169-8555, Japan*
[2] *Department of Earth Science and Astronomy, Graduate School of Arts and Sciences, University of Tokyo, Komaba, Meguro, Tokyo 153-8902, Japan*

Abstract

We have constructed many equilibrium sequences of magnetized polytropic stars with infinite conductivity for polytropes of indices $N = 0.5$, 1 and 3. Not only poloidal magnetic fields but also toroidal magnetic fields have been included in addition to rotation. By choosing simplified forms for arbitrary functions appearing in the formulation of magnetized barotropic equilibrium stars, we have obtained equilibrium configurations of strongly magnetized polytropes whose toroidal magnetic fields are of comparable strength to those of poloidal magnetic fields. The exterior magnetic fields of the obtained stars are consisted of dipole-like poloidal fields, which decrease as r^{-3} when $r \to \infty$. On the other hand the interior magnetic fields are mixed poloidal-toroidal fields, which are composed of tori of twisted field lines around the symmetry axis and of untwisted poloidal fields that continue to the exterior fields penetrating the surfaces of the stars.

We construct polytropic models of rotating equilibrium stars of infinite conductivity with poloidal and toroidal magnetic fields by using the numerical scheme that has been recently developed by Tomimura and Eriguchi [1]. By taking a particular functional form for the arbitrary function κ determining the magnetic field distributions, we obtain highly magnetized polytropes whose toroidal magnetic fields have comparable strengths to those of the poloidal magnetic fields. In equilibrium stars obtained, the exterior magnetic fields of the stars are dipole-like poloidal fields, which decrease as r^{-3} when $r \to \infty$. On the other hand, the interior magnetic fields of the stars are mixed poloidal-toroidal fields, which are composed of tori of twisted field lines around the symmetry axis and untwisted poloidal fields that continues outside through the surfaces of the stars. Typical distributions of the physical quantities of the magnetized stars are shown in Figure 1.

Three polytropes with $N = 0.5$, 1, and 3 are calculated for different sets of model parameters determining electro-magnetic properties. It is found that, for some sets of the model parameters, rotating and magnetized equilibrium stars can exist only for some restricted range of the axis ratio. In other words, in general, there are upper and lower limits of the axis ratio of rotating and magnetized equilibrium stars. It is also observed that magnetized rotating stars containing both the poloidal and toroidal magnetic fields can store much more magnetic energy than those containing purely poloidal magnetic fields. Basic properties observed in the present study are consistent with those of Ref.[1], who have calculated rotating and magnetized equilibrium polytropes with $N = 1.5$, assuming a functional form of κ different from ours [2]. However, it is found that detailed properties of the magnetized rotating stars are highly dependent on stiffness of the equation of state, and strength and distributions of the magnetic field.

[1] E-mail:shijun@waseda.jp
[2] E-mail:eriguchi@ae.c.u-tokyo.ac.jp
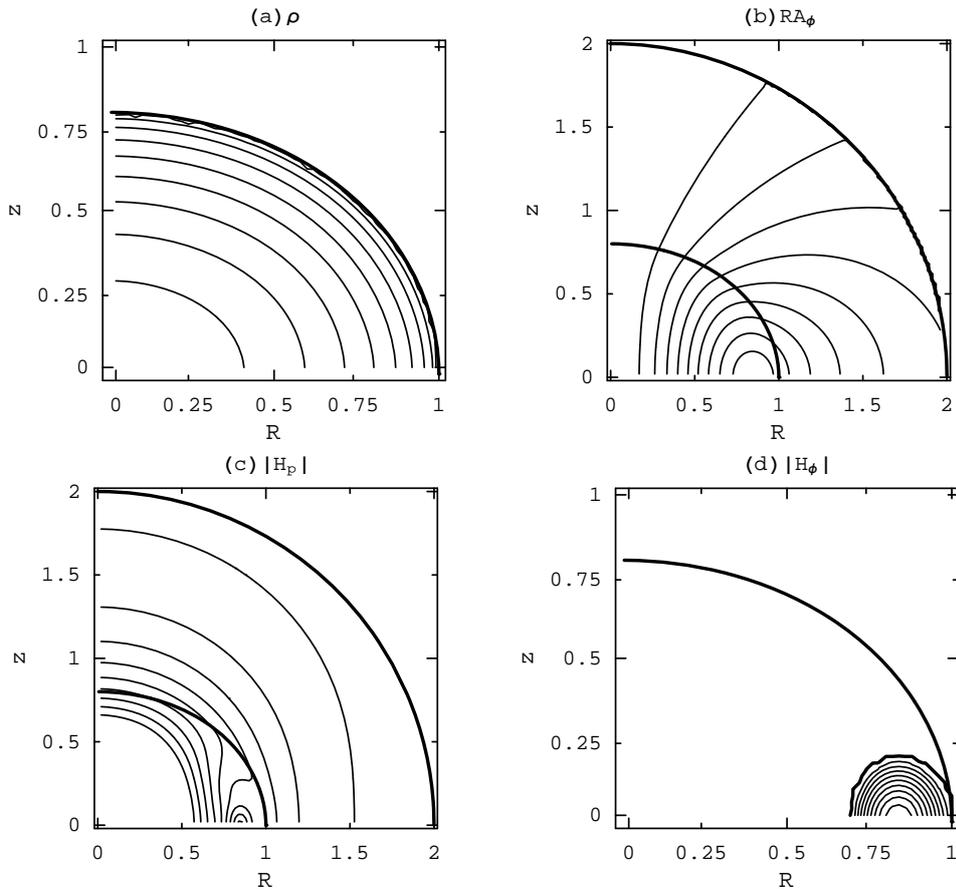
Figure 1: (a) equi-density contours, (b) magnetic field lines or equi-RA_ϕ contours, (c) equi-$|H_p|$ contours, and (d) equi-$|H_\phi|$ contours, in the meridional cross section for the $q = 0.8$, $a = 15$, $\hat{\Omega}^2 = 0.0$ and $N = 0.5$ polytropic stars. Here, $|H_p|$ stands for the magnitude of the poloidal components of the magnetic field, defined by $|H_p| = (H_R^2 + H_z^2)^{\frac{1}{2}}$. The thick eccentric quarter circle denotes the stellar surface. The contours are linearly spaced, i.e. the difference of the physical quantities between two adjacent contours is a tenth of the difference between the maximum and minimum values. In the panels (b) and (c), the larger thick quarter circle denotes the outer boundary for numerical calculations, thus outside of the circle, there is no mesh point for numerical calculations. In the panel (d), the boundary of $|H_\phi| = 0$ is shown by the smaller thick half circle, outside of which $|H_\phi| = 0$ is satisfied.

References

[1] Y. Tomimura and Y. Eriguchi, Mon. Not. R. Astron. Soc. **359**, 1117 (2005).

[2] S. Yoshida and Y. Eriguchi, Astrophys. J. Suppl. **164**, 156 (2006); S. Yoshida, S. Yoshida and Y. Eriguchi, Astrophys. J. **651**, 462 (2006).

Energy transport by MHD waves in force-free black hole magnetospheres

Kohei Onda[1] Eiji Mitsuda[2] Akira Tomimatsu[3]

Department of Physics, Graduate School of Science, Nagoya University, Nagoya 464-8602, Japan

Abstract

Propagation of low-frequency MHD waves in a force-free black hole (BH) magnetosphere is studied. We investigate axisymmetric linear perturbations on the split-monopole magnetic field. Imposing regularity conditions on the event horizon and the outer light cylinder (LC), we derive an approximate global wave solution. We find that the generation of the electromagnetic energy and angular momentum can occur in the large distance. Moreover, we point out the physical role of the outer LC.

1 Introduction

The rotating BH surrounded by magnetosphere is believed to be one of the important energy sources of active galactic nuclei and gamma-ray bursts. Blandford & Znajek demonstrated the possibility that rotational energy of the BH can be extracted through the electromagnetic process[1]. Most of the foregoing works on this subject are concerned with stationary and axisymmetric configurations and recent GRMHD simulations have been able to remove these restrictions. Nonetheless, even in some simple settings such as the force-free limit or the slow rotation limit of the BH, some analytic investigations are also important to clarified underlying physics. Especially, to investigate the behaviour of small disturbances is an important issue in terms of the wave propagation or the stability of stationary configurations, .

The importance of wave propagation analysis lies on understanding the role of MHD waves in the BH magnetospheres. Using the force-free approximation in which the plasma inertia is negligible compared to the magnetic energy density, Uchida investigated linear perturbations in the BH magnetospheres[2]. He applied Lagrangian perturbation theory to the treatment of small disturbances in the force-free stationary axisymmetric BH magnetospheres. In the high-frequency limit, he derived local dispersion relations for the Alfvén mode and the fast magnetosonic mode and clarified the physical difference between these two modes from the viewpoint of the super-radiant scattering.

On the other hand, the role of low-frequency MHD waves has not well understood. It is important to find out the phenomenon that is peculiar to low-frequency waves. The purpose of this work lies in this direction. Moreover, analysis of low-frequency waves might be important in terms of eigenvalue problems. In force-free BH magnetospheres, the regularity conditions should be imposed upon wave solutions not only on the horizon but also on the LCs (see section 2). Especially, it is known that the screw instability of the magnetic field is a prior non-axisymmetric mode which work on low-frequency waves[3]. In this sense, though we only treat axisymmetric waves as a first step, the extension of this work to non-axisymmetric ones is also important.

In the present work[4], we consider axisymmetric linear perturbations in the stationary and axisymmetric force-free BH magnetosphere. We investigate global propagation of low-frequency waves from the large distance (beyond the outer LC) to the BH. For simplicity, we choose the split-monopole magnetic field around the slowly rotating BH as the background field. Moreover, in the large distance, we only consider the propagation of waves in the polar region.

2 Background force-free field

Since the gravitational field induced by the electromagnetic field is small, the force-free BH magnetosphere is determined by Maxwell's equations $F^{\mu\nu}{}_{;\nu} = 4\pi j^\mu$, $F_{[\mu\nu,\lambda]} = 0$ and the force-free conditions

---

[1]E-mail:onda@gravity.phys.nagoya-u.ac.jp
[2]E-mail:emitsuda@gravity.phys.nagoya-u.ac.jp
[3]E-mail:atomi@gravity.phys.nagoya-u.ac.jp

$F_{\mu\nu}j^\nu = 0$ in the Kerr spacetime. For the non-stationary and axisymmetric filed, these equations reduce to more simple forms which determine the eight quantities, A_ϕ, $B_{\rm T}$, ψ_θ, ψ_r and j^μ[5]. We follow this notation.

Especially for stationary fields, the force-free BH magnetosphere is characterized by two functions, $\Omega_{\rm F}(A_\phi)$ interpreted as the electromagnetic angular velocity and $B_{\rm T}(A_\phi)$. Namely, if $\Omega_{\rm F}$ and $B_{\rm T}$ are given as functions of A_ϕ, A_ϕ is determined by the stream equation. In the slow rotation limit, the split-monopole solution was derived[1]. We only note here the relation $\Omega_{\rm F} = \Omega_{\rm H}/2 + \mathcal{O}(a/M^2)$. Here $\Omega_{\rm H}$, a and M are the angular velocity, Kerr parameter and mass of the BH respectively. We use this solution as the background fields. The reason for this choice comes from mathematical simplicity. Moreover, recent simulations suggest that their numerical solution is consistent with this solution in the polar region[6].

Here we stress that the existence of LCs causes difficulty of global analysis for force-free BH magnetospheres. LCs are two surfaces on which the velocity of magnetic field lines become light-like, i.e. defined by $g_{tt} + 2\Omega_{\rm F}g_{t\phi} + \Omega_{\rm F}^2 g_{\phi\phi} = 0$. They appear as singular surfaces in the stream equation which gives A_ϕ. For the split-monopole solution, the outer LC is defined by $r\Omega_{\rm F}\sin\theta \simeq 1$. On the other hand, we need not care the inner LC because it degenerates to the horizon.

3 Linear perturbations in force-free black hole magnetospheres

For the eight equations (B10)–(B17) given in [5], we consider axisymmetric linear perturbations δf as $f \to f + \epsilon\delta f$ and obtain perturbation equations for δf. Here f represents above eight quantities for the split-monopole solution and ϵ is a small parameter. Then, we assume the harmonic time dependency $e^{-i\sigma t}$ and the separation of variables. Because we are interested in the disturbances exited in the timescale of BH's rotational period, the order of σ is same as $\Omega_{\rm H}$ (i.e. low-frequency waves).

To solve the perturbation equations, we use the slow rotation approximation of the BH and expand δf in powers of a/M. Here, $M\Omega_{\rm F}$ is also small enough because $\Omega_{\rm F} \simeq \Omega_{\rm H}/2$ is satisfied for the split-monopole solution. However, this treatment is valid only in the region $r \ll 1/\Omega_{\rm F}$ because the term such as $r\Omega_{\rm F}$ in the perturbation equations can be large in the large distance. For this reason, in subsection 3.1, we first solve the perturbation equations around the BH in the slow rotation approximation. Then, in subsection 3.2, we extend these solutions to the large distance in the flat spacetime approximation. This treatment is justified by the fact that the overlap region $M \ll r \ll 1/\Omega_{\rm F}$ exists in this case. In the following subsections, we only show the solution δA_ϕ and omit other seven quantities. Moreover, by the symmetry, we only consider the region $0 \le \theta < \pi/2$.

3.1 accretion of waves into the black hole

To begin with, we determine the order concerning a/M and θ-dependencies for each quantities δf. In view of force-free equations $\delta F_{\mu\nu}j^\nu + F_{\mu\nu}\delta j^\nu = 0$, the natural choice is to follow the background. Of course, this choice is not unique one, but is partially limited by the boundary condition on the pole. As a result, we follow the background except for δA_ϕ. δA_ϕ arises in the order $\mathcal{O}(a^2/M^2)$ and we can separate θ as $\delta A_\phi = A(r)\sin^2\theta\cos\theta e^{-i\sigma t}$. In this way, we obtain the scattering equation for $A(r)$ as

$$\frac{d^2 A(r_*)}{dr_*^2} + \left(\sigma^2 - 6\frac{\Delta}{r^4}\right)A(r_*) = 4C_{\rm B}\Omega_{\rm F}\left(\Omega_{\rm H} - \frac{2Ma}{r^3}\right)e^{-i\sigma r_*} + O(a^4/M^6). \tag{1}$$

Here r_* is the tortoise coordinate and $C_{\rm B}$ is a constant. For the equation (1), we can find the approximate form of the solution satisfying the ingoing wave boundary condition on the horizon and also derive other seven quantities, $\delta B_{\rm T}$, $\delta\psi_r$, $\delta\psi_\theta$ and δj^μ. We only note here that these solutions satisfy the regularity of the electromagnetic fields on the horizon.

3.2 wave inflow in the large distance

As mentioned above, we consider the region $M \ll r$ and derive a solution of the perturbation in in the flat spacetime approximation and patch it to the solution of (1) in the overlap region $M \ll r \ll 1/\Omega_{\rm F}$. At the beginning, defining $\chi \equiv r\Omega_{\rm F}$, $k \equiv \sigma/\Omega_F = \mathcal{O}(1)$, $\hat{L}_1(\theta) \equiv \csc\theta\partial/\partial\theta\,(\csc\theta\partial/\partial\theta)$, $\hat{L}_2(\theta) \equiv (\partial/\partial\theta + 3\cot\theta)\,(\partial/\partial\theta - 2\cot\theta)$, we derive the perturbation equation for δA_ϕ as

$$\left[\chi^2 - \frac{1}{\sin^2\theta}\right]\delta A_{\phi,\chi\chi\chi} - \left[ik\chi^2 - 4\chi + \frac{ik}{\sin^2\theta}\right]\delta A_{\phi,\chi\chi} + \left[k^2\chi^2 - 4ik\chi + 2 - \frac{k^2}{\sin^2\theta} + \hat{L}_2(\theta) - \frac{1}{\chi^2}\hat{L}_1(\theta)\right]\delta A_{\phi,\chi}$$

$$-\left[ik^3\chi^2 + 2ik + \frac{ik^3}{\sin^2\theta} + ik\hat{L}_2(\theta) + \left(\frac{ik}{\chi^2} - \frac{2}{\chi^3}\right)\hat{L}_1(\theta)\right]\delta A_\phi \simeq 0. \quad (2)$$

We notice that the outer LC is also the singular surface of the equation (2) and other θ-dependencies of δA_ϕ arise as r glows. Difficulty of the global analysis arise in this point. For the difficulty to solve it, we restrict our treatment in the region $\theta \ll 1$. This restriction would be reasonable because our background fields might be consistent with the real astrophysical system in the polar region[6].

Moreover, we divide the region into some ones where the behavior of δA_ϕ change and solve the equation (2) in each region by the leading order analysis. Then we connect these solutions in each overlap region. Here, we omit the detail of the analysis and only show the solution. In the region where the relations $\theta \ll 1$ & $M \ll r \ll 1/(\Omega_{\mathrm{F}}\theta)$ are valid, δA_ϕ behaves as

$$\delta A_\phi = A(\chi)\theta^2 e^{-i\sigma t} \simeq \frac{4C_{\mathrm{B}}}{k^2}\left[\left\{\frac{k^2\chi^2 - 3ik\chi - 3}{k^2\chi^2}\left(ik\chi - 3\log\chi - 3\gamma + \frac{11}{2} - 3\log(2k) - \frac{3}{2}\pi i + \frac{3i}{k\chi}\right)\right.\right.$$

$$\left.\left. + \left(\frac{1}{2} - \frac{3i}{k\chi}\right)\frac{k^2\chi^2 + 3ik\chi - 3}{k^2\chi^2}\right\}e^{-ik\chi} - 3\frac{k^2\chi^2 + 3ik\chi - 3}{k^2\chi^2}\int_\chi^\infty \frac{e^{-2ik\chi}}{\chi}e^{+ik\chi}\right]\theta^2 e^{-i\sigma t} \quad (3)$$

where, γ is the Euler constant and (3) is connected with the solution of (1). In the farther region which contains the LC, the behavior of δA_ϕ changes as

$$\delta A_\phi \simeq \left(\frac{4iC_{\mathrm{B}}}{k}\chi - 2C_{\mathrm{B}}\chi^2\theta^2\right)\theta^2 e^{-i(\sigma t + k\chi)}. \quad (4)$$

As r glows larger, we also find that the direction of the propagation becomes vertical.

4 Energy and angular momentum transport

In this section, we discuss the energy and angular momentum transport induced by the wave propagation. Here, if we introduce a notation of the perturbation as $f \to f + \epsilon\delta^{(1)}f + \epsilon^2\delta^{(2)}f$, the quadratic quantities such as $\delta^{(2)}f$ or $(\delta^{(1)}f)^2$ are more important because $\delta^{(1)}f$ vanishes after they have been averaged over periods. For this reason, averaging over periods, we would treat the quadratic energy-momentum tensor

$$\delta^{(2)}T_{\mathrm{EM}}^{\mu\nu} = \frac{1}{4\pi}\left[\delta^{(1)}F^{\mu\lambda}\delta^{(1)}F^\nu{}_\lambda - \frac{1}{4}g^{\mu\nu}\delta^{(1)}F^{\lambda\tau}\delta^{(1)}F_{\lambda\tau} + F^{\mu\lambda}\delta^{(2)}F^\nu{}_\lambda + F^{\nu\lambda}\delta^{(2)}F^\mu{}_\lambda - \frac{1}{2}g^{\mu\nu}F^{\lambda\tau}\delta^{(2)}F_{\lambda\tau}\right] \quad (5)$$

in the following. However, we have obtained not $\delta^{(2)}f$ but $\delta^{(1)}f$ in the above section. To obtain $\delta^{(2)}f$, we follow the Lagrangian perturbation theory developed in [2]. In this formulation, the perturbations are expressed by the vector ξ^μ called Lagrangian displacement as $\delta^{(1)}A_\mu = F_{\mu\nu}\xi^\nu$, $\delta^{(2)}A_\mu = \delta^{(1)}F_{\mu\nu}\xi^\nu/2$. Here, these relations have been derived by the requirement that the perturbationsare given only by ξ^μ. We only stress that this requirement does not guarantee the satisfaction of the force-free condition in the second order perturbations. This means that $\delta^{(2)}T_{\mathrm{EM}}^{\mu\nu}$ is not a conserved quantity in general.

Since we have obtained the first order perturbations $\delta^{(1)}A_\mu$ and can derive ξ^μ, we can construct the second order perturbations $\delta^{(2)}A_\mu$. In this way, we obtain $\delta^{(2)}T_{\mathrm{EM}}^{\mu\nu}$ and derive the electromagnetic energy flux $\mathscr{E}^\mu = -\delta^{(2)}T_{\mathrm{EM}\,t}^\mu/(4\pi)$ and angular momentum flux $\mathscr{L}^\mu = \delta^{(2)}T_{\mathrm{EM}\,\phi}^\mu/(4\pi)$.

To begin with, we obtain the relations between intensity of the disturbances and the energy and angular momentum inflow into the BH as $\delta\mathcal{M} \simeq C_{\mathrm{B}}^2\Omega_{\mathrm{F}}^2/3$, $\delta\mathcal{J} \simeq 704C_{\mathrm{B}}^2M^2\Omega_{\mathrm{F}}^3/135$ respectively. Moreover, from the definition $\Omega_H \simeq J/4M^3$, we also found $\delta\Omega_H \simeq -94C_{\mathrm{B}}^2\Omega_{\mathrm{F}}^3/(135M) < 0$.

Next, we point out the generation of the electromagnetic energy and angular momentum can occur around $\chi = \mathcal{O}(1)$. To see this, we show the radial components of the flux in the region where the relations $\theta \ll 1$ & $M\Omega_{\mathrm{F}} \ll \chi \ll 1/\theta$ are valid,

$$\mathscr{E}^r \simeq -\frac{\Omega_{\mathrm{F}}^4\theta^2}{8\pi\chi^2}\left[C_B^2 + k^2\left(1 - \frac{8}{k^2}\right)|A(\chi)|^2\right], \quad \mathscr{L}^r \simeq -\frac{\Omega_{\mathrm{F}}^3\theta^2}{\pi\chi^2}\left[\frac{C_{\mathrm{B}}}{4}\{A(\chi)e^{+ik\chi} + A^*(\chi)e^{-ik\chi}\} - |A(\chi)|^2\right]. \quad (6)$$

Here, $A(\chi)$ is given by (3) and the terms of $|A(\chi)|^2$ are negligible for $\chi \ll 1$ and dominant for $1 \gg \chi$. This

means the generation of the electromagnetic energy and angular momentum can occur around $\chi = \mathcal{O}(1)$. Confining the discussion in this region, the generation of the energy flux can not occur for $8 \le k^2$.

Finally, we consider the energy and angular momentum flux around the outer LC (i.e. $\varrho \equiv \chi \theta = \mathcal{O}(1)$), then discuss the role of the outer LC. In this region, $\mathscr{E}^\mu$ and $\mathscr{L}^\mu$ reduce to

$$\mathscr{E}^r \simeq -\frac{2}{\pi} C_{\rm B}^2 \Omega_{\rm F}^4 \theta^2 \left[\left(\frac{k^2}{9} - 4 \right) \varrho^4 + \left(1 - \frac{8}{k^2} \right) \right] \;,\;\; \mathscr{E}^\theta \simeq \frac{2C_{\rm B}^2 \Omega_{\rm F}^5 \theta^4}{\pi \varrho} \left[\left(\frac{k^2}{12} - 2 \right) \varrho^4 - \frac{4}{3} \varrho^2 + \frac{1}{2} \left(1 - \frac{8}{k^2} \right) \right]$$

$$\mathscr{L}^r \simeq \frac{8}{\pi} C_{\rm B}^2 \Omega_{\rm F}^3 \theta^2 \left[\varrho^4 - \varrho^2 + \frac{2}{k^2} \right] \;,\;\; \mathscr{L}^\theta \simeq -\frac{4C_{\rm B}^2 \Omega_{\rm F}^4 \theta^4}{\pi \varrho} \left[\varrho^4 - \frac{2}{3} \varrho^2 + \frac{2}{k^2} \right] \tag{7}$$

where, θ-components of the flux are smaller than r-components of that (even seen in the orthonormal frame). Again, the radial outgoing flux can be realized for some values of k in some places. Especially for the energy flux, this can not occur for $36 \le k^2$. Here, we note that we can take the stationary limit $k \to 0$ of our solutions by keeping $C_{\rm B}/k$ finite. Of course, this treatment guarantees the regularity of the solution on the horizon. In this limit, from the expression (7), the radial energy and angular momentum flux are positive definite and the relation $\mathscr{E}^\mu = \Omega_{\rm F} \mathscr{L}^\mu$ are realized (Of course, this differ from the Blandford-Znajek process near the horizon because the energy and angular momentum density are positive). Moreover, these energy and angular momentum flux are conserved in this limit. Hence, we have identified a part of generation of the electromagnetic energy and angular momentum as stationary change of the state. As seen below, the another part of them is caused by dissipation.

As mentioned above, our second order perturbations do not guarantee the satisfaction of the force-free condition in the second order and $\delta^{(2)} T_{\rm EM}^{\mu\nu}$ is not a conserved quantity. In this region, we can find

$$\nabla_\nu \delta^{(2)} T_{\rm EM}^{t\nu} = \frac{16}{\pi} C_{\rm B}^2 \Omega_{\rm F}^4 \frac{\varrho^2 \theta^2}{r} \left[\varrho^2 - 1 \right] \;,\;\; \nabla_\nu \delta^{(2)} T_{\rm EM}^{r\nu} = \frac{16}{\pi} C_{\rm B}^2 \Omega_{\rm F}^4 \frac{\varrho^2 \theta^2}{r} \left[\varrho^2 - 1 \right] \tag{8}$$

$$\nabla_\nu \delta^{(2)} T_{\rm EM}^{\theta\nu} = -\frac{16}{\pi} C_{\rm B}^2 \Omega_{\rm F}^6 \theta^3 \;,\;\; \nabla_\nu \delta^{(2)} T_{\rm EM}^{\phi\nu} = \frac{16}{\pi} C_{\rm B}^2 \Omega_{\rm F}^3 \frac{\varrho^2}{r^3} \left[\varrho^2 - 1 \right] \;. \tag{9}$$

If we consider the contribution of fluids toward the energy-momentum tensor, then the total energy-momentum tensor is conserved. Hence, in the case $\nabla_\nu \delta^{(2)} T_{\rm EM}^{\mu\nu} < 0$, the electromagnetic fields lose their energy and momentum and fluids obtain them. Seeing in the orthonormal frame, $\nabla_\nu \delta^{(2)} T_{\rm EM}^{\theta\nu}$ dominates and fluids obtain the momentum in θ direction. This direction is almost vertical to the LC. Moreover, in the inner region of the LC, fluids obtain energy and momentum in r and ϕ direction. On the other hand, in the outer one, they lose them. We identify this as the effect of the LC.

5   Summary

We have obtained the approximate solution representing inflow of low-frequency waves from the large distance to the BH. The relations between intensity of the disturbances and the energy and angular momentum inflow into the BH have been derived. We have found the generation of the electromagnetic energy and angular momentum can occur around $r\Omega_{\rm F} = \mathcal{O}(1)$. We regard this effect as stationary change of the state and dissipation in the second order perturbations. We have also found that fluids obtain energy from the electromagnetic fields in the inner region of the LC and lose them in the outer one.

References

[1] R. D. Blandford and R. L. Znajek, MNRAS, **179**, 433 (1977)

[2] T. Uchida, MNRAS, **286**, 931 (1997a), T. Uchida, MNRAS, **291**, 125 (1997b)

[3] A. Tomimatsu, T. Matsuoka and M. Takahashi, Phys. Rev. D **64**, 123003 (2001)

[4] K. Onda, E. Mitsuda and A. Tomimatsu, *in preparation*

[5] A. Levinson, ApJ, **608**, 411 (2004)

[6] J. C. McKinney, MNRAS, **368**, 1561 (2006)

Numerical Construction of Pulsar Magnetosphere Models

Yasufumi Kojima[1]

Department of Physics, Hiroshima University, Higashi-Hiroshima 739–8526, Japan

Abstract

A numerical method to study pulsar magnetosphere is developed in terms of two-component plasma flow. The positive and negative charged particles are assumed to be ejected from inner simulation boundary with relativistic speed almost along the magnetic field lines. Time-dependent Maxwell equations are consistently calculated for non-zero charge density and electric current given by the plasma flow. Some preliminary results are shown.

1   Introduction

Global pulsar magnetosphere is a long-standing unsolved problem. Stationary condition is assumed in most previous works. Recently, some time-dependent numerical codes are adopted to simulate it. For example, electromagnetic field structures are calculated in the force-free approximation [1, 2, 3], and in the relativistic MHD approximation [4].

In both force-free and MHD codes, magnetically dominated conditions, $B > E$ and $\vec{B} \cdot \vec{E} = 0$ are assumed to hold everywhere. Such modeling may be physically acceptable, since the electric fields along the magnetic field lines may quickly dissipate as a result of acceleration of charged particles. However, it is important to study in the numerical simulation, how and where the conditions break down, and what physical mechanism involved changes the electro-magnetic field structure and plasma behavior. An alternative approach is necessary to address these problems, relaxing the magnetically dominated conditions.

We present a numerical approach based on two-fluid description consisted of positive and negative charged particles. Two-fluid calculation is not new [5], but is significantly improved [6]. In this approach, the electric field is solved by time-dependent Maxwell equations with the plasma source, and therefore the magnetically dominated conditions may possibly break elsewhere. Furthermore, it can naturally extend to include physical mechanism in future.

2   Method

Most important feature is that our code does not require the ideal MHD condition, $\vec{E} + \vec{v} \times \vec{B}/c = 0$, which results in $B > E$ and $\vec{B} \cdot \vec{E} = 0$. Our numerical code has the following properties. The details are given elsewhere [6].

- The code is time-dependent one to simulate the evolution of plasma flow and electromagnetic fields, with appropriate initial and boundary conditions.

- We adopt the spherical coordinates (r, θ, ϕ), and assume axial symmetry $(\partial/\partial\phi = 0)$ in the plasma flows and the electro-magnetic fields. However, the azimuthal component of a vector, is not zero in general. For example, toroidal magnetic field B_ϕ originates from poloidal currents (j_r, j_θ).

- The Maxwell equations are solved for the source terms $(\rho_e, \vec{j})$.

- Relativistic fluid dynamics is calculated for two components (electrons and positrons), i.e, charge to mass ratio is the same in magnitude, but opposite in sign, $q_-/m_- = -q_+/m_+$.

- Electromagnetic force is only taken into account, because gravity, thermal pressure, and so on are small and are ignored here.

---

[1]E-mail:kojima@theo.phys.sci.hiroshima-u.ac.jp

3 Results

Figures 1 and 2 show the magnetic flux function G in the meridian ($r\sin\theta$-$r\cos\theta$) plane, which is normalized by $\mu\Omega/(2c)$, where μ is initial magnetic dipole moment and Ω stellar angular velocity. Note that poloidal magnetic fields are given by $(B_r, B_\theta) = (\vec{\nabla}G \times \vec{e}_\phi)/(r\sin\theta)$. The magnetic field liens in these figures are almost the same, but are slightly different, since total amount of flowing currents from the inner to outer boundaries are different. The current is larger in the result of figure 2. The magnetic flux function deviates due to toroidal current.
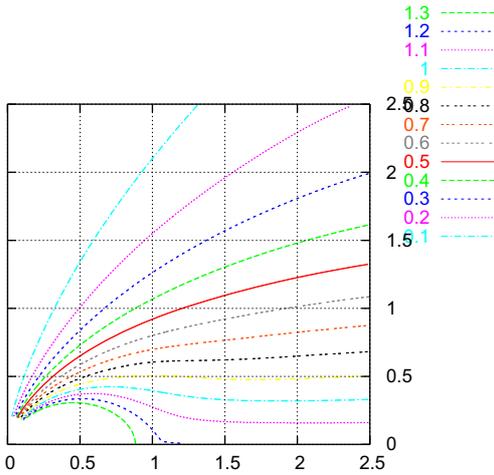
Figure 1: Magnetic flux function G. The length is normalized by c/Ω. The curves denote $2cG/(\mu\Omega) = 0.1, 0.2, \cdots, 1.3$ from the polar axis.
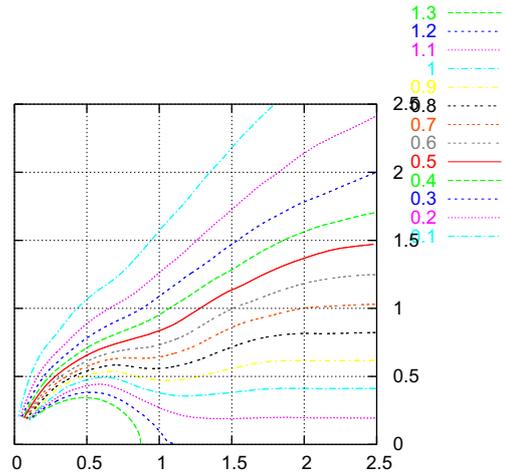
Figure 2: Magnetic flux function G. The length is normalized by c/Ω. The curves denote $2cG/(\mu\Omega) = 0.1, 0.2, \cdots, 1.3$ from the polar axis.

References

[1] Asano, E, Uchida, T., & Matsumoto, R., 2005, PASJ, 57, 409

[2] McKinney, J. C., 2006, Mon. Not. Roy. Astron. Soc., 368, L30

[3] Spitkovsky, A., 2006, Astrophys. J., 648, L51

[4] Komissarov, S. S., 2006, Mon. Not. Roy. Astron. Soc., 367, 19

[5] Kuo-Petravic, L. G., Petravic, M., & Roberts, K. V., 1975, Astrophys. J., 202, 762

[6] Kojima, Y. & Oogi, J., 2007, in preparation

Violation of Third Law of Black Hole Thermodynamics

Takashi Torii[1]

General Education of Science, Osaka Institute of Technology, Omiya, Asahi-ku, Osaka 535-8585, Japan,
and
Advanced Research Institute for Science and Engineering, Waseda University, Okubo, Shinjuku-ku,
Tokyo 169-8555, Japan

Abstract

We derive the black hole solutions in higher curvature gravitational theories and discuss their properties. In this talk Lovelock theory is mainly investigated, which includes cosmological constant, Einstein-Hilbert action, and Gauss-Bonnet term as its lower order terms. Among the solutions, there are solutions which may become extreme solutions with zero temperature through physical processes. This may be a counterexample of the third law of black hole thermodynamics. We also discuss whether an extreme black hole is formed from a regular spacetime by considering collapse of a shell.

1 Introduction

Black holes are characteristic objects to general theory of relativity. Recent observational data show the existence of one or more huge black holes in the central region of a number of galaxies. While over the past decades much concerning the nature of black hole spacetimes has been clarified, a good many unsolved problems remain. One of the most important ones is what the final state of black-hole evaporation through quantum effects is. The mid-galaxy supermassive black holes are certainly not related to this problem; however, it has been suggested that tiny black holes, whose quantum effect should not be neglected, could be formed in the early universe by the gravitational collapse of the primordial density fluctuations. Black holes may become small enough in the final stage of evaporation enough for quantum aspects of gravity to become noticeable. In other words, such tiny black holes may provide a good opportunity for learning not only about strong gravitational fields but also about of the quantum aspects of gravity.

Up to now many quantum theories of gravity have been proposed. Among them superstring/M-theory formulated in the higher dimensional spacetime is the most promising candidate. So far, however, no much is known about the non-perturbative aspects of the theory have not been To take string effects perturbatively into classical gravity is one approach to the study of the quantum effects of gravity.

We focus on the n-dimensional action with the Gauss-Bonnet terms for gravity as the higher curvature corrections to general relativity. The Gauss-Bonnet terms naturally arise as the next leading order of the α'-expansion of superstring theory, where α' is inverse string tension [1], and are ghost-free combinations [2]. The black hole solutions in Gauss-Bonnet gravity were first discovered by Boulware and Deser [3]. Since then many types of black hole solutions have been intensively studied.

In this paper, we investigate the third law of the black hole thermodynamics. In general relativity it is shown that the the 3rd law hold under the following conditions [4]; the energy-momentum tensor of infalling matters is finite, and the weak energy condition is hold in the neighborhood of outer apparent horizon. In Gauss-Bonnet gravity, however, there are exotic types of black hole solutions [5], they may be the first counter examples to the third law. As the first step, we consider the collapse of a thin dust shell and formation of the extreme black hole solution with a degenerate horizon.

---

[1]E-mail:torii@ge.oit.ac.jp

2 Black Hole Solutions

We start with the following n-dimensional action

$$S = \int d^n x \sqrt{-g} \left[\frac{1}{2\kappa_n^2} (\mathcal{R} - 2\Lambda + \alpha \mathcal{L}_{GB}) \right], \tag{1}$$

where $\mathcal{R}$ and $^{(n)}\Lambda$ are the n-dimensional Ricci scalar and the cosmological constant, respectively. $\kappa_n := \sqrt{8\pi G_n}$, where G_n is the n-dimensional gravitational constant. $\mathcal{L}_{GB} := \mathcal{R}^2 - 4\mathcal{R}_{AB}\mathcal{R}^{AB} + \mathcal{R}_{ABCD}\mathcal{R}^{ABCD}$ is Gauss-Bonnet Lagrangian, and $\alpha \geq 0$ is the coupling constant of the Gauss-Bonnet term. This type of action is derived from superstring theory in the low-energy limit. We assume the static spacetime with the following line element:

$$ds^2 = -f(r)e^{-2\delta(r)}dt^2 + f^{-1}(r)dr^2 + r^2 d\Omega_{n-2}^2, \tag{2}$$

where $d\Omega_{n-2}^2 = \gamma_{ij}dx^i dx^j$ is the metric of the $(n-2)$-dimensional Einstein space with the volume Σ_{n-2}^k.

The solution of the gravitational equations is obtained [3, 5] as

$$f = k + \frac{r^2}{2\tilde{\alpha}}(1 + \epsilon x), \quad \delta \equiv 0, \tag{3}$$

where we have defined $\tilde{\alpha} := (n-3)(n-4)\alpha$, $\Lambda = -(n-1)(n-2)/2\ell^2$,

$$x := \sqrt{1 + 4\tilde{\alpha}\left(\frac{\tilde{M}}{r^{n-1}} - \frac{1}{\ell^2} \right)}, \quad \tilde{M} := \frac{2\kappa_n^2 M}{(n-2)\Sigma_{n-2}^k}. \tag{4}$$

The integration constant M is the mass of the black hole. There are two families of solutions which correspond to $\epsilon = \pm 1$.

We focus on the family of solutions with the following parameters: $n \geq 6$, $\ell^2 = 1$, $k = -1$ and $\epsilon = +1$. Fig. 1 shows the M-r_h diagram of the solution. The curve of horizon is obtained by the condition $f(r_h) = 0$. When the mass parameter vanishes $\tilde{M} = 0$, the spacetime is pure vacuum expressed by Eq. (3) with $x = x_0 := \sqrt{1 - 4\tilde{\alpha}/\ell^2}$. For a well-defined theory, the condition $4\tilde{\alpha} \leq \ell^2$ should be satisfied. The pure vacuum solution has a black hole event horizon. However, the center is not singular but regular and spacelike. For $0 < \tilde{M} < \tilde{M}_{ex}$, the solution has a black hole and an inner horizons. The positive-mass solutions have a timelike central singularity. For $\tilde{M} = \tilde{M}_{ex}$, the solution has a degenerate horizon and represents the extreme black hole spacetime. For $\tilde{M} > \tilde{M}_{ex}$, the solution has no horizon and represents the spacetime with a globally naked singularity.

3 Motion of the Thin Dust Shell

We define the trajectory of the $(n-1)$-dimensional dust shell as $t = t(\tau)$ and $r = R(\tau)$, where τ is the proper time on the shell. The induced metric is

$$ds^2 = -d\tau^2 + R(\tau)^2 d\Omega_{n-2}^2. \tag{5}$$

Since it is shown that there is the generalized Birkhoff's theorem in Gauss-Bonnet graivty [6], we can employ the generalized thin shell formalism [7, 8]. The junction condition at the shell is

$$[K_{\mu\nu}]_{\pm} - h_{\mu\nu}[K]_{\pm} + 2\alpha\Big(3[J_{\mu\nu}]_{\pm} - h_{\mu\nu}[J]_{\pm} - 2P_{\mu\rho\nu\sigma}[K^{\rho\sigma}]_{\pm}\Big) = -\kappa_5^2 \tau_{\mu\nu}, \tag{6}$$

where

$$J_{\mu\nu} = \frac{1}{3}\Big(2KK_{\mu\rho}K^\rho_{\ \nu} + K_{\rho\sigma}K^{\rho\sigma}K_{\mu\nu}, -2K_{\mu\rho}K^{\rho\sigma}K_{\sigma\nu} - K^2 K_{\mu\nu}\Big), \tag{7}$$

$$P_{\mu\nu\rho\sigma} = R_{\mu\nu\rho\sigma} + 2h_{\mu[\sigma}R_{\rho]\nu} + 2h_{\nu[\rho}R_{\sigma]\mu} + Rh_{\mu[\rho}h_{\sigma]\nu}, \tag{8}$$
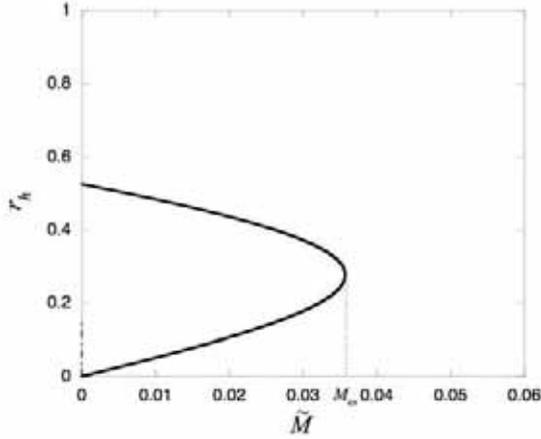
Figure 1: The $\tilde{M}$-r diagrams of the static solutions in the six-dimensional Einstein-Gauss-Bonnet-Λ system with $1/\ell^2 = 1$ (negative cosmological constant), $k = -1$, and $\epsilon = +1$. We set $\tilde{\alpha} = 0.2$. The $\tilde{M}$-r diagrams of the higher-dimensional solutions where $n > 6$ have qualitatively similar configurations.

and $\tau_{\mu\nu}$ is the energy-momentum tensor on the brane. We have introduced $[X]_\pm := X_+ - X_-$, where $X\pm$ are X's evaluated either on the plus or minus side of the shell. The shell is assumed to be dust with the surface energy density ρ. Since the surface energy density of the dust shell is conserved [8], it behaves as

$$\frac{d}{d\tau}(\rho R^{n-2}) = 0. \tag{9}$$

The proper mass of the dust shell defined as $M_s = \Sigma_{n-2}^k R^{n-2}\rho$ remains constant.

In 6-dimensional spacetime the Equation of the shell can be written in a simple way as

$$\left[D\sqrt{f + \dot{R}^2}\right]_\pm = -C, \tag{10}$$

where

$$C := \frac{\tilde{M}_s}{2R^3}, \qquad D_\pm := 1 + \frac{4\alpha k}{R^2} - \frac{2\tilde{\alpha}}{3R^2}f_\pm. \tag{11}$$

This equation can be solved with respect to $\dot{R}^2$ as

$$\dot{R}_\pm^2 = \frac{1}{(D_+^2 - D_-^2)^2}\left\{C^2(D_+^2 + D_-^2) - (D_+^2 - D_-^2)(f_+D_+^2 - f_-D_-^2)\right.$$

$$\left.\pm 2C\sqrt{D_+^2 D_-^2\left[C^2 - (f_+ - f_-)(D_+^2 - D_-^2)\right]}\right\}. \tag{12}$$

It is noted that the $\pm$ of the $\dot{R}_\pm^2$ does not mean the inner and outer value of $\dot{R}^2$ but two roots in Eq. (12).

Here we set $\tilde{\alpha} = 0.02$. Fig. 2 shows square of the velocity of the shell. The positive (negative) sign of the square root $\dot{R}_\pm = \sqrt{\dot{R}_\pm^2}$ $\left(\dot{R}_\pm = -\sqrt{\dot{R}_\pm^2}\right)$ is the speed of the expanding (collapsing) shell.

For the case with $\tilde{M}_s = 0.1\tilde{M}_{ex}$, $\dot{R}^2$ behaves as R^4 for large R. The collapsing shell from the infinity bounces at $r = 5.1648$ and expands to infinity. There is another region where the shell can move. As the shell moves inward below $r = 0.7772$, its speed decreases, and the solution curve is terminated at $r = 0.3652$. Below this radius $\sqrt{f_- + \dot{R}^2}$ takes imaginary value. This means that the shell moves spacelike. Since the radius of the extreme horizon is $r_{ex} = 0.2764$, the degenerate horizon is not formed.
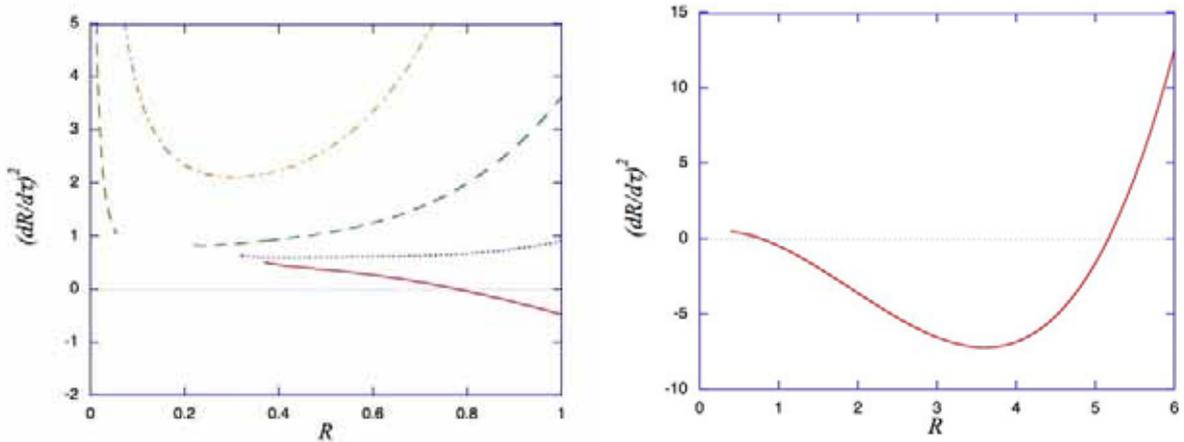
Figure 2: The motion of the thin dust shell. We set the parameters as $\tilde{\alpha} = 0.2$, $\ell^2 = 1$, $k = -1$ and $\epsilon = 1$. The interior region is pure vacuum solution with the black hole horizon at $r_h = 0.525731$, and the exterior of the shell is extreme black hole solution with the degenerate horizon at $r_{ex} = 0.276393$. The mass of the black hole is $\tilde{M}_{ex} = 0.035771$. The curves shows the velocity of the shell with $\tilde{M}_s = 0.1\tilde{M}_{ex}$ (solid curve), $\tilde{M}_s = 0.5\tilde{M}_{ex}$ (dotted curve), $\tilde{M}_s = \tilde{M}_{ex}$ (dashed curve), and $\tilde{M}_s = 2\tilde{M}_{ex}$ (dot-dashed curve).

For the case with $\tilde{M}_s = 0.5\tilde{M}_{ex}$, the region where $\dot{R}^2$ is negative disappears. The collapsing shell from the infinity does not bounce but continues to collapse to $r = 0.3154$ where the $\sqrt{f_- + \dot{R}^2}$ takes imaginary value.

For the case with $\tilde{M}_s = \tilde{M}_{ex}$, the collapsing shell from the infinity continues to collapse to $r = 0.2099$. This is inside of r_{ex}. By the generalized Birkhoff's theorem, the exterior spacetime is static extreme black hole solution. This means that the degenerate horizon is formed. However, below $r = 0.2099$, the shell moves spacelike. There is another region where the shell can move below $r = 0.05922$. However, if the shell moves in this region, the degenerate horizon exist from the beginning. This does not mean the formation of the degenerate horizon.

For the case with $\tilde{M}_s = 2\tilde{M}_{ex}$, the shell moves timelike in all the region. The shell from the infinity continues to collapse to the center and would form the central singularity. In this case the degenerate horizon is formed without any irrelevant phenomena. This can be the counter example to the third law of the black hole thermodynamics.

References

[1] D. J. Gross and J. H. Sloan, Nucl. Phys. **B291**, 41 (1987).

[2] B. Zwieback, Phys. Lett. B **156**, 315 (1985).

[3] D. G. Boulware and S. Deser, Phys. Rev. Lett. **55**, 2656 (1985).

[4] W. Israel, Phys. Rev. Lett. **28**, 397 (1986).

[5] T. Torii and H. Maeda, Phys. Rev. D **71**, 124002 (2005).

[6] B. Whitt, Phys. Rev. **D38**, 3000 (1988).

[7] S. C. Davis, Phys. Rev. **D67**, 024030 (2003).

[8] K. Maeda and T. Torii, Phys. Rev. D **69**, 024002 (2004).

Polarization analysis of gravitational-wave backgrounds

Atsushi Taruya[1], Naoki Seto[2] and Asantha Cooray[2]

[1]*Research Center for the Early Universe, School of Science, The University of Tokyo, Tokyo 113–0033, Japan*
[2]*Department of Physics and Astronomy, University of California, Irvine, California 92697, USA*

Abstract

The stochastic background of gravitational waves may be polarized by the mechanisms involving the parity violation in the early universe and/or the preferential alignment of unresolved sources. Here, we present the detection method of a polarized gravitational-wave background and discuss the sensitivity of space interferometers to the polarized gravitational waves.

1   Introduction

The stochastic background of gravitational wave contains valuable cosmological information to probe the dark side of the universe. In particular, primordial gravitational-wave background produced during inflation is one of the most fundamental prediction from the inflationary theory and detection of it provides a stringent constraint on the inflation model. Recently, several space missions to detect such a tiny signal have been proposed and feasibility of direct detection was intensively discussed. Although there still remain practical issues such as the subtraction of the overlapping signals coming from the neutron star-neutron star binaries and/or the unknown unresolved sources, aiming at the future direct detection, the infrastructure such as new characterization and/or data analysis technique of gravitational-wave signals should be developed furthermore.

Along the line of this discussion, one important aspect is the polarization character of the gravitational wave background (GWB). As it is well known, gravitational waves have polarization degree of freedom due to its spin-2 nature. While the standard prediction from inflation leads to an un-polarized GWB, there might exist some physical mechanisms to generate a polarized GWB [1]. Detection of polarized GWB may thus be important to identify the physical origin of each GWB.

In this article, based on the cross-correlation technique, we present a formalism to detect a polarized GWB. The observational characteristics for polarized GWB are discussed in a specific detector, LISA. Further, we discuss how the geometry of detectors affects the sensitivity to a polarized GWB.

2   Formalism

To begin with, let us write down the basic equation characterizing the gravitational waves. In the transverse-traceless gauge, the metric perturbation becomes

$$h_{ij}(\vec{x},t) = \sum_{A=+,\times} \int_{-\infty}^{\infty} df \int d\hat{\Omega}\, h_A(f,\hat{\Omega})\, e^{i\,2\pi\,f(t-\hat{\Omega}\cdot\vec{x})}\, e_{ij}^A(\hat{\Omega}), \tag{1}$$

where the unit vector $\hat{\Omega}$ is the propagation direction and the quantity $e_{ij}^{+,\times}$ is the polarization basis satisfying the transverse-traceless conditions. For our interest of the stochastic signals, the amplitude h_A has random nature, whose statistical properties including the polarization characters are described by the power spectra. Defining the right and the left-handed tensor amplitudes as, $h_R \equiv (h_+ - ih_\times)/\sqrt{2}$ and $h_L \equiv (h_+ + ih_\times)/\sqrt{2}$, we have [2, 3]

$$\left(\begin{matrix} \left\langle h_R(f,\hat{\Omega})\,h_R^*(f',\hat{\Omega}') \right\rangle & \left\langle h_L(f,\hat{\Omega})\,h_R^*(f',\hat{\Omega}') \right\rangle \\ \left\langle h_R(f,\hat{\Omega})\,h_L^*(f',\hat{\Omega}') \right\rangle & \left\langle h_L(f,\hat{\Omega})\,h_L^*(f',\hat{\Omega}') \right\rangle \end{matrix} \right) = \frac{\delta_D(f-f')}{2} \frac{\delta_D(\hat{\Omega},\hat{\Omega}')}{4\pi} \left(\begin{matrix} I+V & Q+iU \\ Q-iU & I-V \end{matrix} \right). \tag{2}$$

---

[1]E-mail:ataruya.at.utap.phys.s.u-tokyo.ac.jp

The quantities I, V and $(Q \pm iU)$ are the stokes parameters for gravitational waves, which are the standard notations characterizing the polarization states, in analogy to characterize those of the electromagnetic waves. While the quantity I denotes the total intensity, V represents the asymmetry between left- and right-handed gravitational waves, leading to the circular polarization. On the other hand, $(Q \pm iU)$ characterize the linear polarization states and have spin-± 4 properties. These are all functions of frequency f and the direction $\hat{\Omega}$. For later convenience, we write down the power spectra in terms of the spherical harmonics. For the intensity I and V, the harmonic expansions become

$$I(f, \hat{\Omega}) = \sum_{\ell, m} I_{\ell m}(f)\, Y_{\ell m}(\hat{\Omega}), \qquad V(f, \hat{\Omega}) = \sum_{\ell, m} V_{\ell m}(f)\, Y_{\ell m}(\hat{\Omega}). \tag{3}$$

As for the linear polarization, due to its spin-4 nature, these are expanded by the spin-weighted spherical harmonics $_{\pm 4}Y_{\ell m}$ [3]:

$$(Q \pm iU)(f, \hat{\Omega}) = \sum_{\ell, m} P_{\ell m}^{(\pm)}\, {}_{\pm 4}Y_{\ell m}(\hat{\Omega}). \tag{4}$$

Notice that the combinations $(Q \pm iU)$ are not invariant under the rotation around a specific direction. For a better characterization, we introduce the electric- and the magnetic-mode decomposition of linear polarization:

$$\mathcal{E}_{\ell m}(f) = \frac{1}{2}\left\{ P_{\ell m}^{(+)}(f) + P_{\ell m}^{(-)}(f) \right\}, \qquad \mathcal{B}_{\ell m}(f) = \frac{1}{2i}\left\{ P_{\ell m}^{(+)}(f) - P_{\ell m}^{(-)}(f) \right\}. \tag{5}$$

These two combinations behave differently under parity transformation: while $\mathcal{E}$ remains unchanged, $\mathcal{B}$ changes its sign.

With the harmonic coefficients $I_{\ell m}$, $V_{\ell m}$, $\mathcal{E}_{\ell m}$ and $\mathcal{B}_{\ell m}$, anisotropies and frequency dependence of polarized GWBs are completely characterized. We then move to discuss how one can detect such polarized GWBs. First recall that the gravitational-wave signal received at the detector α, h_α, can be written as

$$h_\alpha(\vec{x}, t) = \sum_{A=+,\times} \int_{-\infty}^{\infty} df \int d\hat{\Omega}\, D_\alpha^{ij}(f, \hat{\Omega}; t)\, e_{ij}^A(\hat{\Omega})\, h_A(f, \hat{\Omega})\, e^{i\,2\pi f(t - \hat{\Omega} \cdot vecx)}, \tag{6}$$

where the function D_α^{ij} represents the detector response tensor, which explicitly depends on time due to the (orbital) motion of detector. If we have another data set, h_β, obtained from the detector β which is located near the detector α, the cross-correlation analysis may be applied to detect a stochastic GWB and we have the non-vanishing amplitude of cross-correlation signal, $C_{\alpha\beta}(t) \equiv \langle h_\alpha(t)\, h_\beta(t) \rangle$. The Fourier counterpart of it, $\widetilde{C}_{\alpha\beta}$, which is related with $C_{\alpha\beta}$ by $C_{\alpha\beta}(t) = \int \frac{df}{2}\, \widetilde{C}_{\alpha\beta}(f; t)$, becomes [3]

$$\widetilde{C}_{\alpha\beta}(f; t) = \frac{1}{4\pi} \sum_{\ell, m, m'} \left\{ \vec{S}_{\ell m'}(f) \cdot \vec{\mathcal{F}}_{\alpha\beta, \ell m}(f) \right\} \mathcal{D}_{m'm}^{(\ell)}\big(\psi(t), \vartheta(t), \varphi(t) \big), \tag{7}$$

where $\mathcal{D}_{m'm}^{(\ell)}$ is the rotation matrix. In deriving the expression (7), we have assumed that the time variation of detector's orientation is described by the Euler rotation with angles $(\psi(t), \vartheta(t), \varphi(t))$ in the co-moving frame of rigidly moving detectors α and β. Here, the vectors $\vec{S}_{\ell m}$ and $\vec{\mathcal{F}}_{\alpha\beta, \ell m}$ are

$$\vec{S}_{\ell m}(f) = \left\{ I_{\ell m}(f),\ V_{\ell m}(f),\ \mathcal{E}_{\ell m}(f),\ \mathcal{B}_{\ell m}(f) \right\},$$
$$\vec{\mathcal{F}}_{\alpha\beta, \ell m}(f) = \left\{ a_{\ell m}^{(I)}(f),\ a_{\ell m}^{(V)}(f),\ a_{\ell m}^{(\mathcal{E})}(f),\ a_{\ell m}^{(\mathcal{B})}(f) \right\},$$

where quantities $a_{\ell m}^{(X)}$ $(X = I, V, \mathcal{E}, \mathcal{B})$ represent the multipole coefficients of antenna pattern function for each polarization state. Eq.(7) implies that polarized anisotropies of GWBs can be detected through the time variation of correlation signal $\widetilde{C}_{\alpha\beta}$ and the sensitivity to each polarization anisotropy depends on the amplitude of the multipole coefficient $a_{\ell m}^{(X)}$. The explicit expressions for each multipole coefficients are given as follows. Defining the quantity $F_\alpha^{R,L}(f, \hat{\Omega})$ by $F_\alpha^{R,L} = D_\alpha^{ij}(f, \hat{\Omega})e_{ij}^{R,L}(\hat{\Omega})$, we have [3]

$$a_{\ell m}^{(I)}(f) = \int d\hat{\Omega}\, e^{i\,2\pi f\, \hat{\Omega} \cdot (\vec{x}_\beta - \vec{x}_\alpha)} \left\{ F_\alpha^R F_\beta^{R*} + F_\alpha^L F_\beta^{L*} \right\} Y_{\ell m}(\hat{\Omega}), \tag{8}$$

$$a_{\ell m}^{(V)}(f) \quad = \quad \int d\hat{\Omega} \; e^{i\,2\pi\,f\,\hat{\Omega}\cdot(\vec{x}_\beta - \vec{x}_\alpha)} \left\{ F_\alpha^R \, F_\beta^{R*} - F_\alpha^L \, F_\beta^{L*} \right\} Y_{\ell m}(\hat{\Omega}), \tag{9}$$

$$a_{\ell m}^{(\mathcal{E})}(f) \quad = \quad \int d\hat{\Omega} \; e^{i\,2\pi\,f\,\hat{\Omega}\cdot(\vec{x}_\beta - \vec{x}_\alpha)} \left\{ F_\alpha^R \, F_\beta^{L*} \; {}_{-4}Y_{\ell m}(\hat{\Omega}) + F_\alpha^L \, F_\beta^{R*} \; {}_{4}Y_{\ell m}(\hat{\Omega}) \right\}, \tag{10}$$

$$a_{\ell m}^{(\mathcal{B})}(f) \quad = \quad i \int d\hat{\Omega} \; e^{i\,2\pi\,f\,\hat{\Omega}\cdot(\vec{x}_\beta - \vec{x}_\alpha)} \left\{ -F_\alpha^R \, F_\beta^{L*} \; {}_{-4}Y_{\ell m}(\hat{\Omega}) + F_\alpha^L \, F_\beta^{R*} \; {}_{4}Y_{\ell m}(\hat{\Omega}) \right\}. \tag{11}$$

Here, the vectors $\vec{x}_\alpha$ and $\vec{x}_\beta$ represent the position of detectors α and β, respectively. Note that the phase factor $e^{i\,2\pi\,f\,\hat{\Omega}\cdot(\vec{x}_\beta - \vec{x}_\alpha)}$ arises from the arrival-time difference of gravitational waves between detectors α and β.

3   Detector characteristic: low-frequency limit of LISA

The expressions (8)-(11) derived in previous section play a central role in detecting a polarization anisotropy of GWB. We then wish to understand the sensitivity of gravitational-wave detector to a polarized GWB in a specific detector configuration. In this section, as an illustrative example, we consider the low-frequency limit of LISA and investigate the characteristic properties of the polarization sensitivity. Here, the term, low-frequency, implies the frequency lower than the characteristic frequency f_{crit} given by $f_{\text{crit}} = c/(2\pi L)$ with L being the arm-length of detector. With $L = 5 \times 10^6$ km, low-frequency limit of LISA indicates $f \ll 0.1$ mHz. In this frequency range, LISA has effectively two output signals sensitive to the gravitational waves, called A and E variables, which are constituted by a time-delayed combination of six one-way data streams.

Adopting the coordinate system defined in Ref.[2], the projected detector responses $F_A^{R,L}$ and $F_E^{R,L}$ are explicitly written as

$$F_A^{R,L}(\hat{\Omega}) \quad = \quad \frac{1}{2}(1 + \cos^2\theta)\cos 2\phi \mp i \cos\theta \sin 2\phi \qquad (- : R, \; + : L), \tag{12}$$

$$F_E^{R,L}(\hat{\Omega}) \quad = \quad \frac{1}{2}(1 + \cos^2\theta)\sin 2\phi \pm i \cos\theta \cos 2\phi \qquad (+ : R, \; - : L). \tag{13}$$

Then, substituting the above equations into the expressions (8)-(11), we compute the multipole coefficients $a_{\ell m}^{(X)}$. Using the fact that $\vec{x}_\alpha = \vec{x}_\beta$, the resultant non-vanishing coefficients are summarized as follows:

$$I\text{-mode}: \qquad a_{00}^{(I)} = \frac{4\sqrt{\pi}}{5}, \quad a_{20}^{(I)} = \frac{8}{7}\sqrt{\frac{\pi}{5}}, \quad a_{40}^{(I)} = \frac{2\sqrt{\pi}}{105}, \qquad a_{44}^{(I)} = \pm\frac{1}{3}\sqrt{\frac{\pi}{35}},$$

$$\mathcal{E}\text{-mode}: \qquad\qquad\qquad\qquad\qquad\qquad\qquad a_{40}^{(\mathcal{E})} = \frac{2}{3}\sqrt{\frac{2\pi}{35}}, \quad a_{44}^{(\mathcal{E})} = \pm\frac{2\sqrt{\pi}}{3} \qquad (+ : \text{AA}, \; - : \text{EE})$$

for the self-correlation signals, $(\alpha, \beta) = (A, A)$ or (E, E), and

$$I\text{-mode}: \qquad a_{44}^{(I)} = i\,\frac{1}{3}\sqrt{\frac{2\pi}{35}},$$

$$\mathcal{E}\text{-mode}: \qquad a_{44}^{(\mathcal{E})} = i\,\frac{2\sqrt{\pi}}{3},$$

$$V\text{-mode}: \qquad a_{10}^{(V)} = -i\,\frac{8}{5}\sqrt{\frac{\pi}{3}}, \quad a_{30}^{(V)} = -i\,\frac{2}{5}\sqrt{\frac{\pi}{7}}$$

for the cross-correlation signals, $(\alpha, \beta) = (A, E)$. From this, important properties of polarization sensitivity in the low-frequency limit can be found:

- Visible multipole components of anisotropic GWB are restricted to $\ell = 0, 2, 4$ for I-mode, $\ell = 1, 3$ for V-mode and $\ell = 4$ for $\mathcal{E}$-mode. As for the $\mathcal{B}$-mode, all the multipole moments vanish.

- There exists degeneracy between I- and $\mathcal{E}$-modes ($\ell = 4$). To be precise, the relation $a_{4m}^{(I)}/a_{4m}^{(\mathcal{E})} = \sqrt{1/70}$ holds for the non-vanishing components $m = 0$ and 4,

which are generic properties in the low-frequency limit of co-located detectors.

4 Improving the sensitivity to a polarized GWB: worked example

The polarization sensitivity of LISA shown in previous section seems a little bit problematic in a sense that no useful information about linear polarization modes ($\mathcal{E}$ and $\mathcal{B}$) can be obtained. While this may be a generic low-frequency property, we wish to remedy this by introducing some physical effects. There are two possible effects: **(i)** finite arm-length effect on detector's response ($f \gtrsim f_{\mathrm{crit}}$) and **(ii)** effect of finite separation between two detectors $\vec{x}_\alpha \neq \vec{x}_\beta$. Here, we examine the latter case and study how the sensitivity to the linear polarized GWB can be improved.

First note that the influence of finite separation is incorporated into the phase factor in Eqs.(8)-(11). The non-vanishing contribution of the phase factor $e^{i\,2\pi\,f\,\hat{\Omega}\cdot(\vec{x}_\beta-\vec{x}_\alpha)}$ leads to the frequency-dependent polarization sensitivity and depending on the propagation direction, the response to a polarized gravitational-wave signal can be different between two detectors. As a worked example, we consider the two set of LISA-type detector labeled by I and II, which are separated by a distance d. The two detectors are assumed to be co-aligned and the position vector $\vec{x}_{\mathrm{I}} - \vec{x}_{\mathrm{II}}$ is normal to the arms of each detector. In Fig.1, specifically focusing on the $\ell = 4$ component, the resultant multipole coefficients are plotted as ratio, $a_{4m}^{(X)}/a_{4m}^{(\mathcal{E})}$, which are given by a function of normalized frequency, f/f_* with $f_* \equiv c/(2\pi|\vec{d}|)$. The left panel shows that the degeneracy between I- and $\mathcal{E}$-modes can be broken as increasing the frequency f (or the separation d), while the right panel reveals that sensitivity to $\mathcal{B}$-mode polarization can be recovered.

Although the polarization sensitivity shown in Fig.1 indicates a monotonic dependence on the frequency, the actual detector response to each polarization mode is a complicated function of the frequency f/f_*. Relaxing the assumption of co-aligned detectors, there are six parameters to characterize the geometric configuration of two detectors: orientation, alignment and separation between two detectors. Optimizing these six parameters, one can obtain the most sensitive detector set to the polarized GWB at a given frequency band. Improvement of the sensitivity is important and helpful to extract useful cosmological information. This issue will be discussed in details in a separate publication.
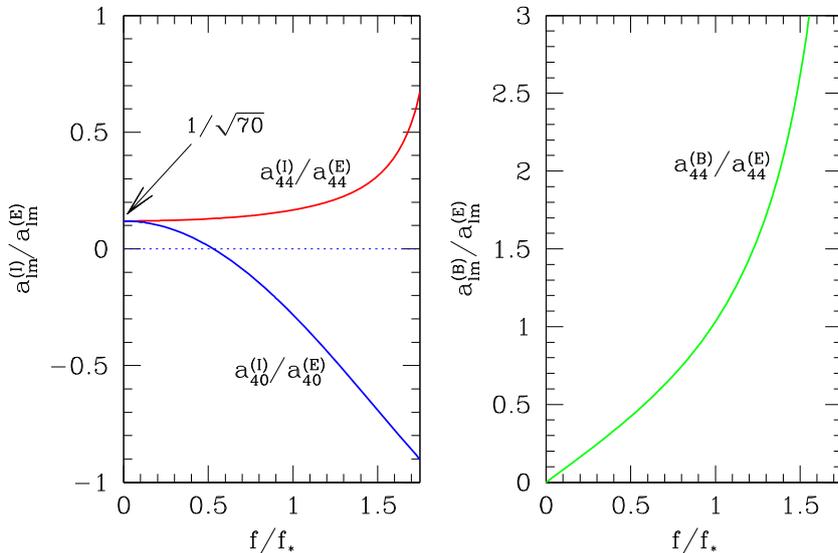

Figure 1: Ratio of the multipole coefficients for antenna pattern function, $a_{4m}^{(I)}/a_{4m}^{(\mathcal{E})}$ (*left*) and $a_{44}^{(\mathcal{B})}/a_{44}^{(\mathcal{E})}$ (*right*), as function of normalized frequency (see Eqs.(8)-(11) for definitions). In left panel, the blue and the red lines represent the ratios $a_{40}^{(I)}/a_{40}^{(\mathcal{E})}$ and $a_{44}^{(I)}/a_{44}^{(\mathcal{E})}$, respectively.

References

[1] E.g., A. Lue, L.M. Wang and M. Kamionkowski, Phys.Rev.Lett. **83**, 1506 (1999); T. Kahniashvili, G. Gogoberidze and B. Ratra, Phys.Rev.Lett. **95**, 151301 (2005).

[2] N. Seto, Phys.Rev.Lett. **97**, 151101 (2006); N. Seto, astro-ph/0609633.

[3] N. Seto, A. Taruya and A. Cooray, in preparation.

Constraint propagation revisited
— Adjusted ADM formulation for numerical relativity —

Hisa-aki Shinkai[1] and Gen Yoneda[2]

[1]*Department of Information Science, Osaka Institute of Technology Hirakata, Osaka 573-0196, Japan*
[2]*Department of Mathematical Science, Waseda University, Shinjuku, Tokyo 169-8855, Japan*

Abstract

Formulation of the Einstein equations is one of the necessary implements for realizing long-term stable and accurate numerical simulations. We re-examine our formulation scheme, that intends to construct a dynamical system which evolves toward the constraint surface as the attractor, by adjusting evolution equations with constraints. We propose an additional guideline which may delay the final blow-up. The new idea is to avoid multipliers to the evolution equations which produce non-linear growth of the constraints in the later stage. Slight but actual improvement can be seen in our test simulations.

1 Introduction

With the purpose of the predictions of precise gravitational waveforms from the coalescence of the binary neutron-stars and/or black-holes, the research field of "numerical relativity" has been developed for the past three decades. The difficulty of numerical integrations of the Einstein equations arises both from its mathematical complexity of the equations and from high-level requirements for computational skills and technology.

In 2005-2006, several groups independently announced that the success of the inspiral black-hole binary merger [1, 2, 3, 4, 5]. There are many implements for their successes, such as gauge conditions, coordinate selections, boundary treatments, singularity treatments, numerical discretization, and mesh refinements, together with the re-formulation of the Einstein equations which we will discuss here.

There are many approaches to re-formulate the Einstein equations for obtaining a long-term stable and accurate numerical evolution (e.g. see references in [6]). In a series of our works, we have proposed to construct a system that has its constraint surface as an attractor. By applying eigenvalue analysis of constraint propagation equations, we showed that there *is* a constraint-violating mode in the standard Arnowitt-Deser-Misner (ADM) evolution system [7, 8], which has been used for simulations over 20 years, when it is applied to a single non-rotating black-hole space-time [10]. We also found that such a constraint-violating mode can be compensated if we adjust the evolution equations with a particular modification using constraint terms like the one proposed by Detweiler [9].

Our predictions are borne out in simple numerical experiments using the Maxwell, Ashtekar, and ADM systems [10, 11, 12, 13]. There are also several numerical experiments to confirm our predictions are effective [14, 15].

The recent binary black-hole simulations also applies such ideas. Pretorius [1] uses harmonic decomposition of the Einstein equations with constraint damping terms. NASA/Goddard, UTB, and LSU groups applied modified BSSN formulation [16], while PSU group applied another modified BSSN formulation [15]. Here, BSSN is the widely used modification of the ADM formulation which was originally proposed by Kyoto group[17, 18].

In this report, we re-examine our formulation scheme and propose the additional guideline which may delay the final blow-up. The new idea is to avoid multipliers to the evolution equations which may produce non-linear growth of the constraints in the later stage. We applied the idea to the adjusted ADM formulation, and also show our test simulations. We think that killing or compensating the constraint violation mode is the essential to this formulation problem, and for that purpose, the ADM formulation is the best benchmark to work with.

---

[1]E-mail:shinkai@is.oit.ac.jp
[2]E-mail:yoneda@waseda.jp

2 Adjusted system and Constraint Propagation

2.1 Our idea of adjusted system

Suppose we have a dynamical system of variables $u^a(x^i, t)$, which has evolution equations,

$$\partial_t u^a = f(u^a, \partial_i u^a, \cdots), \tag{1}$$

and the (first class) constraints,

$$C^\alpha(u^a, \partial_i u^a, \cdots) \approx 0. \tag{2}$$

Note that we do not require (1) to form a first-order hyperbolic form. We propose to investigate the evolution equation of C^α (constraint propagation, CP),

$$\partial_t C^\alpha = g(C^\alpha, \partial_i C^\alpha, \cdots), \tag{3}$$

for evaluating violation features of constraints.

The character of constraint propagation, (3), will vary when we modify the original evolution equations. Suppose we modify (adjust) (1) using constraints

$$\partial_t u^a = f(u^a, \partial_i u^a, \cdots) + F(C^\alpha, \partial_i C^\alpha, \cdots), \tag{4}$$

then (3) will also be modified as

$$\partial_t C^\alpha = g(C^\alpha, \partial_i C^\alpha, \cdots) + G(C^\alpha, \partial_i C^\alpha, \cdots). \tag{5}$$

Therefore, finding a proper adjustment $F(C^\alpha, \cdots)$ is a quite important problem.

Hyperbolicity analysis may be a way to evaluate constraint propagation, (3) and (5) [19]. However, this requires (3) to be a first-order system which is easy to be broken. (See e.g. Detweiler-type adjustment [9] in the ADM formulation [10]). Furthermore hyperbolicity analysis only concerns the principal part of the equation, that may fail to analyze the detail evaluation of evolution.

Alternatively, we have proceeded an eigenvalue analysis of the whole RHS in (3) and (5) after a suitable homogenization,

$$\partial_t \hat{C}^\alpha = \hat{g}(\hat{C}^\alpha) = M^\alpha{}_\beta \hat{C}^\beta, \quad \text{where} \quad C(x, t)^\alpha = \int \hat{C}(k, t)^\alpha \exp(ik \cdot x) d^3 k, \tag{6}$$

and conjectured that the system is more stable, if the eigenvalues of $M^\alpha{}_\beta$ [we call them constraint amplification factors (CAFs)] has a *negative real-part* or *non-zero imaginary-part* [10, 11, 12, 13].

2.2 Additional idea

Suppose that RHS of the constraint propagation equation (5) accidentally includes C^2 terms,

$$\partial_t C = -aC + bC^2, \tag{7}$$

then the solution will blow-up as

$$C = \frac{-aC_0 \exp(-at)}{-a + bC_0 - bC_0 \exp(-at)}. \tag{8}$$

The blow-up will appear when C^2-term is comparable to C-term, that is, the last stage of simulation supposing the constraint surface is the attractor. We therefore have to prohibit the adjustments which simply produce self-growing terms (C^2) in constraint propagation, $\partial_t C$.

3 Adjusted ADM system

In the ADM system, we can write possible adjustments generally as [10, 11, 12]:

$$
\begin{aligned}
\partial_t \gamma_{ij} &= -2\alpha K_{ij} + \nabla_i \beta_j + \nabla_j \beta_i \\
&\quad + P_{ij}\mathcal{H} + Q^k{}_{ij}\mathcal{M}_k + p^k{}_{ij}(\nabla_k \mathcal{H}) + q^{kl}{}_{ij}(\nabla_k \mathcal{M}_l), \\
\partial_t K_{ij} &= \alpha R^{(3)}_{ij} + \alpha K K_{ij} - 2\alpha K_{ik}K^k{}_j - \nabla_i \nabla_j \alpha + (\nabla_i \beta^k)K_{kj} + (\nabla_j \beta^k)K_{ki} + \beta^k \nabla_k K_{ij} \\
&\quad + R_{ij}\mathcal{H} + S^k{}_{ij}\mathcal{M}_k + r^k{}_{ij}(\nabla_k \mathcal{H}) + s^{kl}{}_{ij}(\nabla_k \mathcal{M}_l),
\end{aligned}
$$
$$(9)$$
$$(10)$$

with constraint equations

$$
\begin{aligned}
\mathcal{H} &:= R^{(3)} + K^2 - K_{ij}K^{ij}, \\
\mathcal{M}_i &:= \nabla_j K^j{}_i - \nabla_i K.
\end{aligned}
$$
$$(11)$$
$$(12)$$

Along to the discussion in §2.2, by carefully observing the constraint propagation equations $\partial_t \mathcal{H} = \cdots$ and $\partial_t \mathcal{M}_i = \cdots$ with above adjustments, we conclude that the adjustments using p, q, P, Q-terms in the above (9) and (10) may produce non-linear terms in constraint propagation equations. Therefore, we have not to put too much confidence for adjustments using these terms. Conversely, several adjustments are *safe* for this points, and are expected to compensate such non-linear term effects.

In Fig.1, we demonstrate numerical evolutions of such an adjusted ADM system. We plot violation of Hamiltonian constraints versus time for Teukolsky wave evolution with harmonic slicing, and with periodic boundary condition, which is one of the benchmark test of the formulation problem proposed by the Mexico NR workshop in 2002 [20]. We apply two sets of adjusted ADM equations: The Case (I)

$$
\begin{aligned}
\partial_t \gamma_{ij} &= (\text{first line of (9)}) - \kappa_1 \alpha \gamma_{ij}\mathcal{H} \\
\partial_t K_{ij} &= (\text{first line of (10)}) + \kappa_2 \alpha \gamma_{ij}\gamma^{kl}\,\partial_k \mathcal{M}_l
\end{aligned}
$$
$$(13)$$
$$(14)$$

and the Case (II):

$$
\begin{aligned}
\partial_t \gamma_{ij} &= (\text{first line of (9)}) - \kappa_1 \alpha^3 \gamma_{ij}\mathcal{H} \\
\partial_t K_{ij} &= (\text{first line of (10)}) + \kappa_1 \alpha^3 (K_{ij} - (1/3)K\gamma_{ij})\mathcal{H} + \kappa_2 \alpha \gamma_{ij}\gamma^{kl}\,\partial_k \mathcal{M}_l \\
&\quad + \kappa_1 \alpha^2 [3(\partial_{(i}\alpha)\delta^k_{j)} - (\partial_l \alpha)\gamma_{ij}\gamma^{kl}]\mathcal{M}_k + \kappa_1 \alpha^3 [\delta^k_{(i}\delta^l_{j)} - (1/3)\gamma_{ij}\gamma^{ki}](\nabla_k \mathcal{M}_l),
\end{aligned}
$$
$$(15)$$
$$(16)$$

where the terms with coefficient κ_1 in Case (II) were those in Detweiler [9], while the terms with coefficient κ_2 in Case (I/II) are newly introduced adjustment along to the above discussion.

We see in Fig.1 that the evolution with the standard ADM system is the shortest lifetime in simulation, while Case (II) makes twice as much longer evolution available. Moreover, the newly added term helps to extend the lifetime of simulation. The new term works effectively, makes 10% longer evolution available, while this is not yet perfect nor drastic.

We are now investigating CAFs of these new adjustments, blow-up time estimations, together with other numerical demonstrations. These will be reported elsewhere near future.

References

[1] F. Pretorius, Phys. Rev. Lett. 95 (2005) 121101; Class. Quant. Grav. 23 (2006) S529.

[2] J. G. Baker, *et al.* Phys. Rev. Lett. 96 (2006) 111102; Phys. Rev. D 73 (2006) 104002.

[3] M. Campanelli, C. O. Lousto, P. Marronetti, Y. Zlochower, Phys. Rev. Lett. 96 (2006) 111101.

[4] P. Diener, *et al.* Phys. Rev. Lett. 96 (2006) 121101.

[5] C. F. Sopuerta, U. Sperhake, P. Laguna, Class. Quant. Grav. 23 (2006) S579.

[6] H. Shinkai and G. Yoneda, gr-qc/0209111.
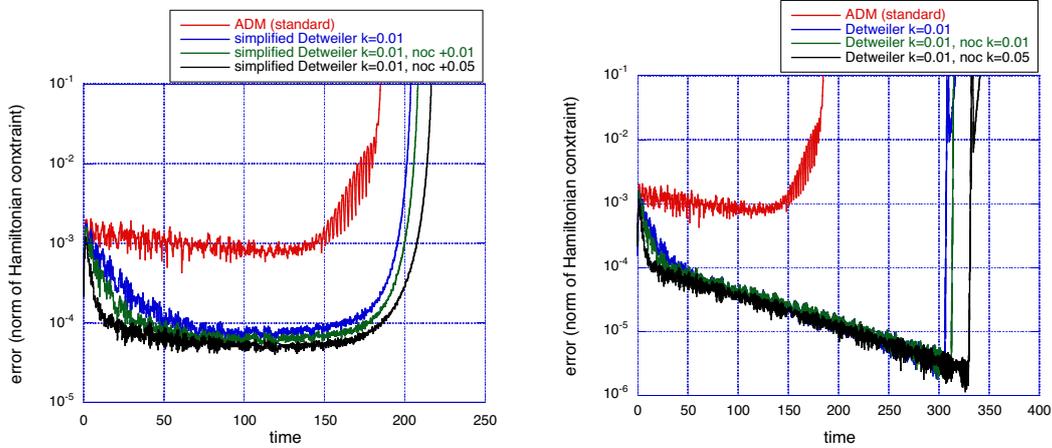
Figure 1: Comparisons of numerical evolutions of adjusted ADM systems, using Teukolsky wave propagation. L2 norm of the Hamiltonian constraint $\mathcal{H}$ is plotted. (Left panel) The Case (I). (Right panel) The Case (II). Cactus-based original (3+1)-dimensional code was applied.

[7] R. Arnowitt, S. Deser and C.W. Misner, in *Gravitation: An Introduction to Current Research*, ed. by L.Witten, (Wiley, New York, 1962).

[8] J.W. York, Jr., in *Sources of Gravitational Radiation*, ed. by L. Smarr, (Cambridge, 1979) ; L. Smarr, J.W. York, Jr., Phys. Rev. D**17**, 2529 (1978).

[9] S. Detweiler, Phys. Rev. D **35**, 1095 (1987).

[10] H. Shinkai and G. Yoneda, Class. Quantum Grav. **19**, 1027 (2002).

[11] H. Shinkai and G. Yoneda, Class. Quant. Grav. **17**, 4799 (2000). G. Yoneda and H. Shinkai, Class. Quant. Grav. **18**, 441 (2001).

[12] G. Yoneda and H. Shinkai, Phys. Rev. D **63**, 124019 (2001).

[13] G. Yoneda and H. Shinkai, Phys. Rev. D **66**, 124003 (2002).

[14] B. Kelly, *et al.*, Phys. Rev. D **64**, 084013 (2001).

[15] H-J. Yo, T.W. Baumgarte and S.L. Shapiro, Phys. Rev. D **66**, 084026 (2002).

[16] M. Alcubierre, *et al.* Phys. Rev. D 67 (2003) 084023.

[17] T. Nakamura, K. Oohara and Y. Kojima, Prog. Theor. Phys. Suppl. **90**, 1 (1987). M. Shibata and T. Nakamura, Phys. Rev. **D52**, 5428 (1995).

[18] T.W. Baumgarte and S.L. Shapiro, Phys. Rev. D **59**, 024007 (1999).

[19] S. Frittelli, Phys. Rev. D **55**, 5992 (1997).

[20] M. Alcubierre *et al.* Class. Quant. Gravity 21, 589 (2004)

Inhomogeneous charged black branes
— A novel stable phase —

Umpei Miyamoto[1] and Hideaki Kudoh[2]

[1]*Department of Physics, Waseda University, Okubo 3-4-1, Tokyo 169-8555, Japan*
[2]*Department of Physics, UCSB, Santa Barbara, CA 93106, USA*
and
Department of Physics, The University of Tokyo, Tokyo 113-0033, Japan

Abstract

The final fate of the Gregory-Laflamme (GL) instability is one of the most interesting problems in the black hole physics. To know the effects of charge in this context, we construct non-uniform black strings with a magnetic charge by higher-order perturbations. At the linear order of the perturbation, we see that the GL mode vanishes at the point where the background solution becomes thermodynamically stable. This vanishing resembles a second-order phase transition which is characterized by a universal power-law behavior. Solving the higher-order perturbations, the thermodynamical stability of the non-uniform strings in microcanonical, canonical and grandcanonical ensembles is investigated. We find that for fixed spacetime dimensions there exist critical charges at which the stability of non-uniform states changes. The charge can serve as a parameter that controls not only the stability of uniform black strings but also that of non-uniform states. Possible three dimensional (mass-tension-charge) phase diagram is proposed.

1 Introduction

It is known that black objects with translational symmetries, such as black branes and black strings, suffer from the Gregory-Laflamme (GL) instability, breaking the translational symmetries [1]. To know the endpoint of the instability, there are extensive studies to construct black objects in Kaluza-Klein (KK) spacetimes [2]. See [3] for reviews. One of the interesting features is that the phase structure, therefore the endpoint of the GL instability, would depend on the spacetime dimensions [4, 5].

Owing to the extensive studies, the phase structure of KK black holes in vacuum has been clarified gradually. However, the gravity in fundamental theories *inevitably* couples to other fields, such as gauge ones. Although we know that the linear perturbation of black branes strongly depends on the extremality of background solutions, the roles of extremality in non-linear regimes have not been known so far. Our understanding of the phase structure of charged black strings/branes is restricted to very special cases [6, 5], in which the systems can be translated to a vacuum system. The aim of this work is to see effects of a charge in non-linear regimes. We perform the higher-order static perturbations of magnetic black strings, and then investigate the thermodynamical properties of constructed solutions in detail. We see that the charge (extremality) controls the stability of black strings in non-linear regimes as well as in the linear regime [3].

2 Method: higher-order static perturbation

We consider $D = (d+1)$-dimensional spacetime in which the gravity couples to a $(d-2)$-form field $\mathcal{F}_{d-2}$. The governing equations are

$$R_{\mu\nu} = \frac{1}{2(d-3)!} \mathcal{F}_\mu{}^{\mu_2\cdots\mu_{d-2}} \mathcal{F}_{\nu\mu_2\cdots\mu_{d-2}} - \frac{d-3}{2(d-1)!} g_{\mu\nu} \mathcal{F}^2, \qquad \nabla_\mu \mathcal{F}^{\mu\mu_2\cdots\mu_{d-2}} = 0, \qquad \mathrm{d}\mathcal{F}_{d-2} = 0. \tag{1}$$

---

[1]E-mail: umpei at gravity.phys.waseda.ac.jp
[2]E-mail: kudoh at utap.phys.s.u-tokyo.ac.jp
[3]This article corresponds to a short version of paper [7] with some new results and figures added.
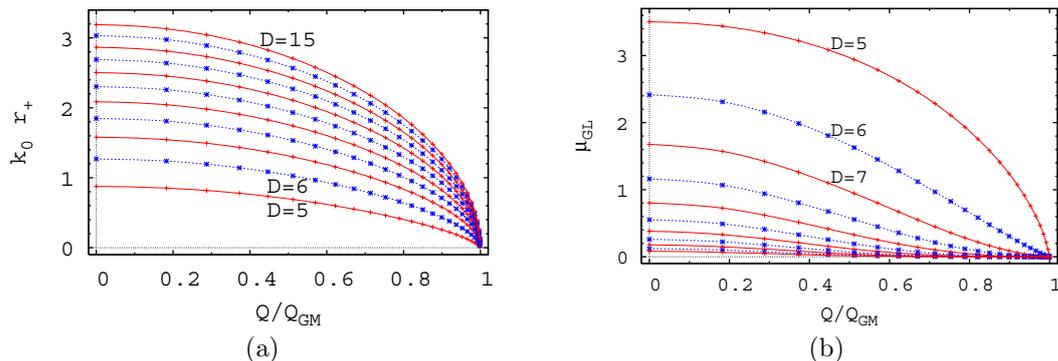
Figure 1: The charge dependance of the GL critical wavenumber, (a), and that of critical mass, (b).

We will find non-uniform black string solutions perturbatively with the metric ansatz given by

$$ds^2 = -e^{2a(r,z)}f_+ dt^2 + e^{2b(r,z)}f_- \left(\frac{dr^2}{f_+ f_-^2} + dz^2\right) + e^{2c(r,z)}r^2 d\Omega_{d-2}^2,$$

$$f_\pm(r) = 1 - \left(\frac{r_\pm}{r}\right)^{d-3}, \qquad \mathcal{F}_{d-2} = Q_m \, \text{Vol}_{\Omega_{d-2}}, \tag{2}$$

where $r = r_+$ and $r = r_-$ correspond to an outer and an inner horizons. Q_m is a constant proportional to a magnetic charge Q. By setting $a = b = c = 0$, we have a uniform black string solution. Note that the form field Eq. (2) is a *general* solution even for $a, b, c \neq 0$. This fact makes our analysis simple since we do not have to perturb the form field independently. The physical property of the background solution to be noted is that the specific heat, which specifies the thermodynamical stability, is negative for small charge $0 \leq Q < Q_{\text{GM}}$ and positive for $Q_{\text{GM}} < Q < M$, where Q_{GM} and M are a critical charge, characterized only by dimensions, and the mass, respectively. The Gubser-Mitra (or correlated stability) conjecture asserts that the GL instability exists iff the string is locally thermodynamically unstable [8]. Indeed, we will see that the GL instability does not exist for $Q > Q_{\text{GM}}$.

We expand the metric function $X(r, z)$ ($X = a, b, c$) around the uniform solution as

$$X(r,z) = \sum_{n=0}^{\infty} \epsilon^n X_n(r) \cos(nKz), \quad X_n(r) = \sum_{p=0}^{\infty} \epsilon^{2p} X_{n,p}(r), \quad K = \sum_{q=0}^{\infty} \epsilon^{2q} k_q, \tag{3}$$

where $X_{0,0}(r) = 0$ is imposed. Here, K is the GL critical wavenumber and ϵ is an expansion parameter. Substituting these expansions into the Einstein equations, we obtain ODEs for $X_{n,p}(r)$ at $\mathcal{O}(\epsilon^{n+2p})$.

3 Results: properties of non-uniform charged strings

Solving the first order perturbations, the GL critical mode for each given charge Q is obtained [10]. The charge dependence of the critical wavenumber is shown in Fig. 1(a). One can see that the critical wavenumber vanishes at $Q = Q_{\text{GM}}$. In addition, we find that the vanishing of the wavenumber obeys a power law near the GM point, $k_0 \propto |Q - Q_{\text{GM}}|^\beta$, irrespective of dimensions. The universal "critical exponent" β is nearly $1/2$, which resembles a second-order phase transition [9]. In Fig. 1(b), we show the charge dependence of the conventionally-used dimensionless mass parameter for the critical string. The mass parameter in the present case is defined by

$$\mu \equiv \frac{16\pi G_D M}{L^{D-3}}, \tag{4}$$

where G_D is a D-dimensional gravitational constant and L is the compactification length of the z-direction. The critical mass μ_{GL} is estimated by setting $L = 2\pi/k_0$. The uniform string can exist stably for a parameter region of $\mu > \mu_{\text{GL}}$ and $0 \leq Q < M$ in the (μ, Q) plane.
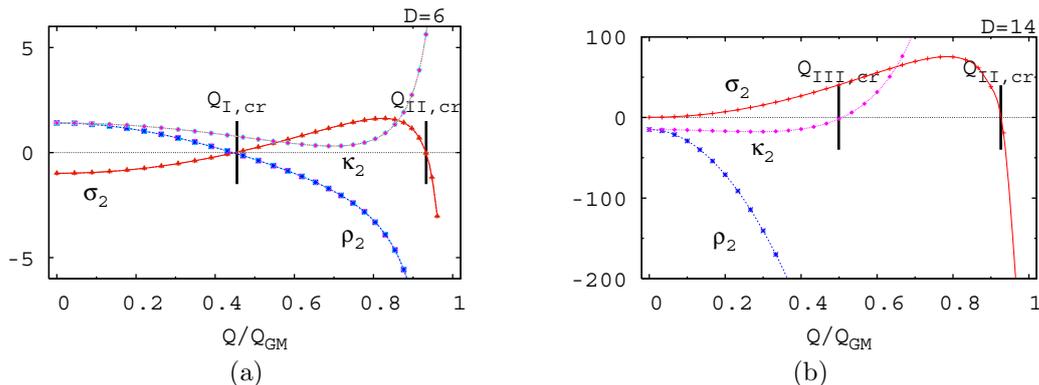
Figure 2: The difference of entropy and free energies between the uniform and non-uniform black strings in suitable ensembles. One can find three critical charges, at which the stability of non-uniform solution changes.

Solving the higher-order perturbations (up to third order), we can compare the entropy S, Helmholtz free energy F $(= M - TS)$ and Gibbs free energy G $(= M - TS - \nu Q)$ between Uniform and Non-Uniform black strings in suitable ensembles. We denote the differences of these thermodynamical functions by

$$S_{\mathrm{NU}}/S_{\mathrm{U}} \simeq 1 + \sigma_2 \epsilon^4, \quad F_{\mathrm{NU}}/F_{\mathrm{U}} \simeq 1 + \rho_2 \epsilon^4, \quad G_{\mathrm{NU}}/G_{\mathrm{U}} \simeq 1 + \kappa_2 \epsilon^4. \quad (5)$$

For example, the fourth-order coefficient of the Gibbs free energy is given by

$$\kappa_2 = -\frac{d-3}{2} \left[\delta S_1 + (d-2)\delta T_1 \right] \delta T_1 - \frac{(d-1)q^{d-3}}{2(1-q^{d-3})} \left[\delta Q_1 + 2(d-3)\delta T_1 - \frac{1-(d-2)q^{d-3}}{1-q^{d-3}} \delta \nu_1 \right] \delta \nu_1, \quad (6)$$

where $q \equiv r_-/r_+$ and $(\delta S_1, \delta T_1, \delta Q_1, \delta \nu_1)$ are the second-order changes of entropy, temperature, charge, and chemical potential, respectively. See [7] for the similar expressions for σ_2 and ρ_2. In Fig. 2, we show the charge dependence of these quantities for $D = 6$, (a), and $D = 14$, (b).

First, let us focus on the behavior of entropy difference σ_2 in $D = 6$. σ_2, being negative at $Q = 0$, increases as the background charge Q increases and become positive in an intermediate charge region, $Q_{\mathrm{I,cr}} < Q < Q_{\mathrm{II,cr}}$. For $Q_{\mathrm{II,cr}} < Q < Q_{\mathrm{GM}}$, σ_2 is negative again. The non-uniform black strings are entropically favored over the uniform one in the intermediate region. This also suggests that the phase transition from uniform to non-uniform phases is second (or higher) order. This behavior is common for $5 \le D \le 13$. For $D \ge 14$, the increase/decrease-behavior of σ_2 is similar but there is a different feature that σ_2 is positive at $Q = 0$ [4]. Therefore the first critical charge $Q_{\mathrm{I,cr}}$ does not exist for $D \ge 14$.

Next, let us see the the behavior of ρ_2. ρ_2 monotonically decreases as the charge increases for all dimensions. For vacuum cases it has been known that ρ_2 is positive for $5 \le D \le 12$ and negative for $D \ge 13$ [5, 11]. Thus, there exists a critical charge for $5 \le D \le 13$, which almost coincides with the critical charge $Q_{\mathrm{I,cr}}$.

Last, let us see the stability in a grandcanonical ensemble, which was not discussed in [7]. The Gibbs free energy is compared between the uniform and non-uniform strings with the temperature and chemical potential kept fixed. For $D = 6$, κ_2 is always positive to imply the non-uniform configuration is unstable for all non-extremal black strings. While, for $D = 14$ (in fact for $D \ge 13$) κ_2 is negative around the neutral point and increases as the background charge increases. Thus, a "third" critical charge $Q_{\mathrm{III,cr}}$, below which the non-uniform string is favored in the grandcanonical ensembles, appears.

4 Future prospects

The non-uniform charged black strings are constructed by the static perturbations for various dimensions. We have seen that the charge controls the stability of non-uniform strings as well as that of uniform strings.
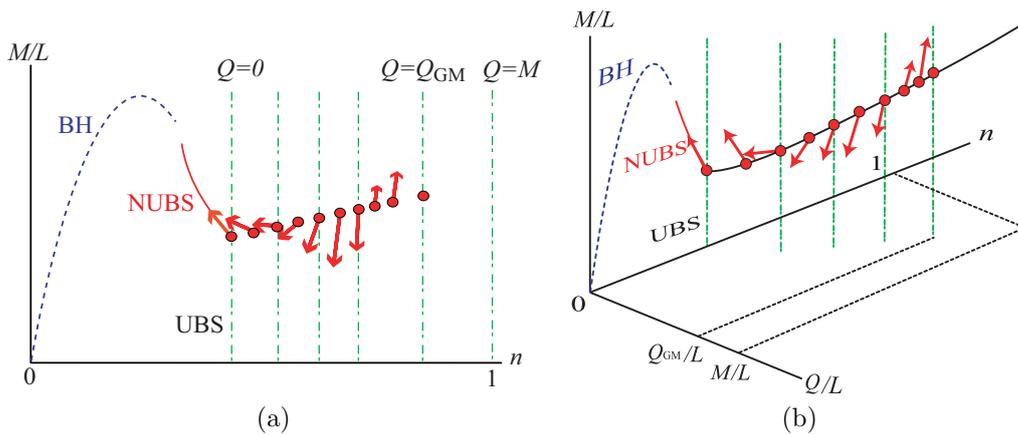
Figure 3: A possible (M, n) diagram, (a), and a (M, n, Q) diagram, (b) of Black Hole (BH), Uniform Black String (UBS) and Non-Uniform Black String (NUBS). Projecting (b) onto the $Q = 0$ plane, we obtain (a). Each arrow indicates the direction of the non-uniform string branch emanates.

We show possible phase diagrams in Fig. 3 suggested by the perturbation analysis in this paper. It is necessary to give some physical/intuitive understanding to the sign changes of $(\sigma_2, \rho_2, \kappa_2)$ and those phase diagrams. The application of the Landau-Ginzburg theory of phase transition would provide us good understanding of these [11]. The roles of the critical charges in the time evolution of GL instability and the gauge theories, predicted by the gauge/gravity dual, will be interesting [12].

References

[1] R. Gregory and R. Laflamme, *Phys. Rev. Lett.* **70**, 2837 (1993); *Nucl. Phys.* **B428**, 399 (1994); M. W. Choptuik et al., *Phys. Rev.* **D68**, 044001 (2003); G. T. Horowitz and K. Maeda, *Phys. Rev. Lett.* **87**, 131301 (2001).

[2] S. S. Gubser, *Class. Quant. Grav.* **19**, 4825 (2002); T. Harmark, *Phys. Rev.* **D69**, 104015 (2004); D. Gorbonos and B. Kol, *JHEP* 06 (2004) 053. T. Wiseman, *Class. Quant. Grav.* **20**, 1137 (2003); H. Kudoh and T. Wiseman, *Phys. Rev. Lett.* **94**, 161102 (2005); E. Sorkin, *Phys. Rev.* **D74**, 104027 (2006).

[3] B. Kol, *Phys. Rept.* **422**, 119 (2006); T. Harmark and N. A. Obers, hep-th/0503020.

[4] E. Sorkin. *Phys. Rev. Lett.* **93**, 031601 (2004).

[5] H. Kudoh and U. Miyamoto, *Class. Quant. Grav.* **22**, 3853 (2005).

[6] T. Harmark and N. A. Obers. *JHEP* 09 (2004) 022; J. L. Hovdebo and R. C. Myers, *Phys. Rev.* **D73**, 084013 (2006).

[7] U. Miyamoto and H. Kudoh, *JHEP* 12 (2006) 048.

[8] S. S. Gubser and I. Mitra, *JHEP* 08 (2001) 018.

[9] S. S. Gubser and A. Ozakin, *JHEP* 05 (2003) 010.

[10] Mathematica programs containing the numerics in this paper are available at author's website, http : //www.gravity.phys.waseda.ac.jp/~umpei.

[11] B. Kol and E. Sorkin, *Class. Quant. Grav.* **23**, 4563 (2006).

[12] O. Aharony, J. Marsano, S. Minwalla and T. Wiseman, *Class. Quant. Grav.* **21**, 5169 (2004).

Unexorcized ghost in DGP brane world

Keisuke Izumi[1], Kazuya Koyama[2] and Takahiro Tanaka[3]

[1,3]*Department of Physics, Kyoto University, Kyoto 606-8502, Japan*
[2]*Institute of Cosmology and Gravitation, University of Portsmouth, Portsmouth PO1 2EG,UK*

Abstract

The braneworld model of Dvali-Gabadadze-Porrati realizes the self-accelerating universe. However, it is known that this cosmological solution contains a spin-2 ghost. We study the possibility of avoiding the appearance of the ghost by slightly modifying the model, introducing the second brane. First we consider a simple model without stabilization of the separation of the brane. By changing the separation between the branes, we find we can erase the spin-2 ghost. However, this can be done only at the expense of the appearance of a spin-0 ghost instead. We discuss why these two different types of ghosts are correlated. Then, we examine a model with stabilization of the brane separation. Even in this case, we find that the correlation between spin-0 and spin-2 ghosts remains. As a result we find we cannot avoid the appearance of ghost by two-branes model.

1   Introduction

The present-day accelerated expansion of the Universe [1] is one of the hotest topic in cosmology. Most of ideas to explain this phenomenon are modifications of scalar (spin-0) sectors of the cosmology model. But there is another direction which has not been explored much so far. That is modifying the gravity theory in spin-2 sectors. The simplest gravity model with modified spin-2 sector would be the massive gravity theory [2]. Since the models which have the terms quadratic in metric perturbations can be regarded as a massive gravity theory, most of the modified gravity models fall into this category. If we introduce the mass of the graviton to explain the accelerated expansion of the universe, its value would be the same order as the present value of the Hubble constant, $m_g \simeq H$. However, it is known that a spin-2 graviton with mass in the range $0 < m^2 < 2H^2$ in de Sitter background has a ghost excitation in its helicity-0 component [3]. The Hubble parameter is larger in an earlier epoch of the universe. Hence it seems difficult to avoid appearance of a ghost throughout the evolution of the universe in simple models that are arranged to explain present-day accelerated expansion. Here we would like to raise a simple question whether we can build a model in which modification of the spin-2 sector explains the accelerated cosmic acceleration, simultaneously escaping from the ghost appearance.

The DGP brane world model [4] (See Ref. [5] as a recent review paper), in which the 4D Einstein-Hilbert term is assumed to be induced on the brane, is known to give a mechanism to realize the late-time accelerating expansion of the Universe without introducing additional matter [6]. The existence of a ghost excitation is pointed out in the self-accelerating branch of the DGP brane world model [7, 8, 9]. The lowest Kaluza-Klein mass of gravitons m satisfies $m^2 = 2H^2$ [8, 9]. If the analogy to the massive gravity theory could hold, this would mean that the self-acceleration branch of the DGP brane world model does not have a ghost excitation. However, it was shown by a detailed analysis that there is still a ghost in this model [9]. Based on the DGP brane world model, we attempt to build a ghost-free model which simultaneously explains the accelerated expansion of the universe due to the effect of a spin-2 sector. The first idea is to push up the lowest graviton mass by putting another boundary brane. We call this model two-branes model. We will successfully make all masses of gravitons satisfy $2H^2 < m^2$. Then, however, a spin-0 excitation, which originates from the brane bending degrees of freedom, is transmuted into a ghost [12]. We will find that a ghost excitation cannot be eliminated in this two-branes model.

---

[1]**e-mail**: ksuke@tap.scphys.kyoto-u.ac.jp
[2]**e-mail**: kazuya.koyama@port.ac.uk
[3]**e-mail**: tama@tap.scphys.kyoto-u.ac.jp

Usually spin-2 modes are decoupled from spin-0 modes at the level of linear perturbation. However, a spin-2 mode can be composed of a spin-0 mode by operating a differential operator when and only when its mass squared takes the specific critical value. At the critical mass, a spin-2 mode can exceptionally couple with a spin-0 mode. In addition to that, the critical mass corresponds to a threshold for the appearance of a ghost in spin-2 sector. If the mass of spin-2 mode is smaller than the critical mass, this spin-2 sector has a ghost excitation as previously mentioned. Moreover, a unique spin-0 mode that appears in the two-branes model has also the critical mass. Hence the spin-2 mode can couple with the spin-0 mode when it crosses the critical mass. This fact partly explains why the ghost can be transferred between spin-2 and spin-0 modes.

Then, we consider a model with stabilized brane separation by introducing a bulk scalar field in two-branes model [10, 11]. Since the mass spectrum of spin-0 mode changes, spin-0 mode at the critical mass does not remain to exist in this stabilized two-branes model. Then, it is expected that the ghost will not be transferred between spin-2 and spin-0 modes. However, by studying this stabilized two-branes model in detail, we will find that this naive expectation goes wrong.

This paper is organized as follows. In §2 we will discuss the two-branes model. In §3 extension to the stabilized two-branes model is performed. We will summarize our results in §4.

2   Two-branes model

In order to make a model which does not have spin-2 ghost modes, we introduce another brane into the DGP model. The action describing this model is given by

$$S = \frac{1}{2\kappa^2} \int d^5x \sqrt{-g}R + \sum_{\sigma=\pm} \int d^4x \sqrt{-g_\sigma^{(4)}} \left(\frac{1}{2\kappa_4^2} R_\sigma^{(4)} + \frac{1}{\kappa^2} K_\sigma - \tau_\sigma + L_{m\sigma} \right). \tag{1}$$

where R, $R_\pm^{(4)}$, $g_\pm^{(4)}$, $K_\pm$, $\tau_\pm$ and $L_{m\pm}$ are five dimensional Ricci scalar, four dimensional Ricci scalar, the trace of the four dimensional induced metric $g_{\mu\nu}$, the trace of the extrinsic curvature $K_{\mu\nu}$, the brane-tension and the matter Lagrangian on the $(\pm)$-brane, respectively. We assume $\mathbf{Z}_2$ symmetry across the brane. We assume vacuum without any matter field, $L_{m\sigma} = 0$, as an unperturbed state. The five dimensional metric is given by

$$ds^2 = dy^2 + a^2(y)\gamma_{\mu\nu}dx^\mu dx^\nu, \qquad a(y) = a_+ + y. \tag{2}$$

where $\gamma_{\mu\nu}$ is the four dimensional de Sitter metric with unit curvature radius. The range of y-coordinate is from 0 to $(a_- - a_+)$. The positions of $(+)$ and $(-)$-branes are at $y = y_+ := 0$ and at $y = y_- := a_- - a_+$, respectively. Notice that the bulk geometry of the above solution is nothing but the five dimensional Minkowski spacetime written in the spherical Rindler coordinates.

Now we study perturbations around the background mentioned above. Besides the transverse-traceless conditions, one can impose the conditions of vanishing $\{yy\}$ and $\{y\mu\}$ components of metric perturbations. Then the perturbed metric is given by

$$ds^2 = dy^2 + \left(\tilde{\gamma}_{\mu\nu} + h_{\mu\nu}^{(TT)} \right) dx^\mu dx^\nu, \qquad \text{with} \qquad \nabla^\mu h_{\mu\nu}^{(TT)} = 0, \quad h^{(TT)\mu}{}_\mu = 0, \quad \tilde{\gamma}_{\mu\nu} \equiv a^2 \gamma_{\mu\nu} \tag{3}$$

where ∇_μ is the covariant derivative operator associated with $\tilde{\gamma}_{\mu\nu}$. In raising or lowering Greek indices, we use $\tilde{\gamma}_{\mu\nu}$. Because the equations of motion of $h_{\mu\nu}^{(TT)}$ take the separable form, we expand $h_{\mu\nu}^{(TT)}$ as

$$h_{\mu\nu}^{(TT)} = \sum_j h_{\mu\nu}^{(j)}(x^\mu)u_j(y), \tag{4}$$

The induced metric on the $(+)$-brane for the solution with source is given by

$$
\begin{aligned}
\bar{h}_{\mu\nu}^{(+)} =\ & -2\kappa^2 \sum_i \frac{u_i^2(y_+)}{\Box^{(4)} - 2 - m_i^2} \left(T_{\mu\nu}^{(+)} - \frac{1}{4}\tilde{\gamma}_{\mu\nu}T^{(+)} + \frac{H_+^{-2}}{3(m_i^2 - 2)} \left(\nabla_\mu\nabla_\nu - \frac{1}{4}\gamma_{\mu\nu}\Box^{(4)} \right) T^{(+)} \right) \\
& + \frac{\kappa^2}{6H_+^2}\gamma_{\mu\nu} \left(\frac{2}{H_+}(2r_cH_+ - 1)^{-1} - \left(\sum_i \frac{u_i^2(y_+)}{m_i^2 - 2} \right) \Box^{(4)} \right) \frac{1}{\Box^{(4)} + 4}T^{(+)}.
\end{aligned} \tag{5}
$$

It is known that the equation of motion of the massive gravity is written as

$$h_{\mu\nu}^{(mg)} = -\alpha \left(\frac{T_{\mu\nu} - \frac{1}{4}\gamma_{\mu\nu}T}{(\square^{(4)} - 2 - m^2)} + \frac{(m^2 - 2)^{-1}}{3(\square^{(4)} - 2 - m^2)} \left(\nabla_\mu \nabla_\nu - \frac{1}{4}\gamma_{\mu\nu}\square^{(4)} \right) T \right) - \frac{\alpha}{12(m^2 - 2)}\gamma_{\mu\nu}T. \quad (6)$$

So $\bar{h}_{\mu\nu}^{(+)}$ has the spin-0 propagation as

$$s = \frac{\kappa^2}{6H_+^2}\gamma_{\mu\nu} \left(\frac{2}{H_+}(2r_c H_+ - 1)^{-1} + 4 \left(\sum_i \frac{u_i^2(y_+)}{m_i^2 - 2} \right) \right) \frac{1}{\square^{(4)} + 4}T^{(+)}, \quad (7)$$

where $s \equiv (\bar{h}_{\mu\nu}^{(+)} - h_{\mu\nu}^{(mg)})\gamma^{\mu\nu}/4$. This means that, when all spin-2 modes have no ghost ($m_i^2 > 2$), the sign of spin-0 propagation has wrong; namely the spin-0 mode becomes ghost.

3   Stabilization

We introduce a bulk scalar field to stabilize the brane separation [11]. The action is given by

$$S = S_2 + S_s, \qquad S_s \equiv \int d^5x \sqrt{-g} \left(-\frac{1}{2}g^{ab}\psi_{,a}\psi_{,b} - V_B(\psi) - \sum_{\sigma=\pm} V^{(\sigma)}(\psi)\delta(y - y_\sigma) \right). \quad (8)$$

By choosing the potential in the bulk $V_B(\psi)$ and the potentials on the branes $V^{(\sigma)}(\psi)$ appropriately, we can stabilize the brane separation. In the following discussion we do not need explicit form of the potential functions. The unperturbed background configuration is similar to the previous case. The bulk metric is given by (2) and the branes are located at a fixed value of $y(= y_\pm)$ as before. But the functional form of the warp factor $a(y)$ is different.

We use "Newton gauge", in which the spin-0 component of the shear of the hypersurface normal vector vanishes, following Ref. [11]. In this gauge, using the traceless part and $\{y\mu\}$-component of the Einstein equations, we find that perturbations of the metric and the scalar field are related as

$$h_{yy} = 2\phi, \quad h_{y\mu} = 0, \quad h_{\mu\nu} = h_{\mu\nu}^{(TT)} - \phi\tilde{\gamma}_{\mu\nu}, \quad \delta\psi = \frac{3}{2\kappa^2\psi'}\left[\partial_y + 2\mathcal{H}\right]\phi, \quad (9)$$

where $\mathcal{H} \equiv a'/a$ and $h_{\mu\nu}^{(TT)}$ is a tensor which satisfies transverse-traceless conditions. Transverse-traceless part $h_{\mu\nu}^{(TT)}$ takes the same form as given in Eq. (4).While the trace part is computed as

$$\phi + 2\mathcal{H}_+\hat{\xi}_{(+)}^y = \frac{2\kappa^2}{9\tilde{H}_+^4} \sum_i \frac{v_i^2(y_+)}{\mu_i^2 + 4} \frac{1}{\square^{(4)} - \mu_i^2}T^{(+)} - \frac{\kappa^2}{3\tilde{H}_+^2} \left(\frac{2\kappa^2}{3\tilde{H}_+^2} \left(\sum_i \frac{v_i^2(y_+)}{\mu_i^2 + 4} \right) + \frac{a'}{a} \right) \frac{1}{\square^{(4)} + 4}T^{(+)}, \quad (10)$$

where for brevity we have introduced

$$\tilde{H}_+^2 = H_+^2 \left(2r_c\mathcal{H}_+ - 1 \right). \quad (11)$$

The above expression for $\bar{h}_{\mu\nu}^{(+)}$ apparently contains a pole at the critical mass eigenvalue corresponding to $(\square^{(4)} + 4)^{-1}$. The term proportional to $\nabla_\mu\nabla_\nu$ in Eq. (4) is pure gauge. Hence all the contribution from the pole at the critical mass eigenvalue is in the form proportional to $\gamma_{\mu\nu}(\square^{(4)} + 4)^{-1}T^{(+)}$. Collecting such terms in $\bar{h}_{\mu\nu}^{(+)}$ coming both from the TT-part and from the scalar-part, the coefficient becomes

$$\frac{\kappa^2}{3H_+^2} \left\{ 2 \left(\sum_i \frac{u_i^2(y_+)}{m_i^2 - 2} \right) + \frac{1}{\tilde{H}_+^2} \left(\frac{2\kappa^2}{3\tilde{H}_+^2} \left(\sum_i \frac{v_i^2(y_+)}{\mu_i^2 + 4} \right) + \mathcal{H}_+ \right) \right\}. \quad (12)$$

Calculating this coefficient, we can find that it vanishes as a whole.

When the mass eigenvalue is in the range $0 < m_i^2 < 2$, such a mode contains a ghost in its helicity zero component. In contrast, the coefficients of spin-0 component, β_i, becomes negative when $\mu_i^2 < -4$. In this case this mode becomes a ghost. Hence, to realize a ghost-free model, all masses of spin-2 modes

and spin-0 modes must satisfy $m_i^2 > 2$ and $\mu_i^2 > -4$. However, it turns out to be impossible that both conditions are satisfied simultaneously.

In order to show this, we consider continuous deformation of the model potentials of the bulk scalar field. When the smallest eigenvalue of spin-2 excitations, m_0^2, approaches 2 from below, $u_0^2(y_+)/(m_0^2 - 2)$ in Eq. (12) diverges. Since this equality is always satisfied, this divergence must be compensated by the other terms. The only possible way is that one of the eigenvalues of spin-0 exitations μ_j^2 approaches -4 from above Therefore, when the value of m_0^2 exceeds 2, at least one of the valuevalues, μ_j^2, must be smaller than -4. Hence, we cannot make both conditions $m_0^2 > 2$ and $\mu_0^2 > -4$ satisfied simultaneously by a continuous deformation. Any model specified by given potentials of the bulk scalar field is connected with each other by a continuous deformation. Thus it is proved that we cannot realize a model free from a ghost within the two-brane extension of DGP model with a bulk scalar field.

4   Summary

In the present paper, we have attempted to construct a ghost-free model by modifying the self-acceleration branch of the DGP brane world model, in which a spin-2 sector drives the accelerated expansion of the universe. We first tried adding another boundary brane in §2 and stabilizing the brane separation by introducing a bulk scalar field in §3, respectively. In both cases, we found that the ghost exitation survives. As we have already mentioned in Introduction, this is caused through the degeneracy between spin-2 and spin-0 modes at the critical mass. This degeneracy enables the ghost property to transmute between these two normally decoupled modes. But this degeneracy occurs only at this special mass.

To conclude, we confirmed in this paper that it is really difficult to erase this ghost as far as we work within the standard linear analysis. However, a different way to avoid appearance of ghost is proposed in Ref. [13]. We think still further study is necessary to conclude whether this ghost is really harmful or not.

References

[1] A. G. Riess et al., Astron. J. **116**, 1009 (1998), Astron. J. **607**, 665 (2004).

[2] M. Fierz and W. Pauli, Proc. Roy. Soc. **173**, 211 (1939).

[3] A. Higuchi, Nucl. Phys. **B282**, 397 (1987).

[4] G. R. Dvali, G. Gabadadze and M. Porrati, Phys. Lett. **B485**, 208 (2000).

[5] A. Lue, Phys. Rept. **423**, 1-48 (2006).

[6] C. Deffayet, Phys. Lett. **B502**, 199 (2001).

[7] M. A. Luty, M. Porrati and R. Rattazzi, JHEP **0309**, 029 (2003).
A. Nicoils and R. Rattazzi, JHEP **0406**, 059 (2004).

[8] K. Koyama, Phys. Rev. **D72**, 123511 (2005).
C. Charmousis, R. Gregory, N. Kaloper and A. Padilla, arXiv:hep-th/0604086 (2006).

[9] D. Gorbunov, K. Koyama and S. Sibiryakov, Phys. Rev. **D73**, 044016 (2005).

[10] W. D. Goldberger and M. B. Wise, Phys. Rev. Lett. **83** 4922 (1999), Phys. Lett. **B475** 275 (2000).

[11] T. Tanaka and X. Montes, Nucl. Phys. **B528**, 259 (2000).

[12] In JGRG-15 meeting, K.I and T.T made an incorrect claim that the ghost should disappear in two-branes model. It was pointed out by N. Kaloper during the meeting that the ghost should remain in this setup.

[13] C. Deffayet, G. Gabadadze and A. Iglesias, JCAP **0608**, 012 (2006).

Volume stabilizaition in a warped flux compactification model

Masato Minamitsuji[1], Wade Naylor[2] and Misao Sasaki[3]

[1,3] *Yukawa Institute for Theoretical Physics, Kyoto University, Kyoto 606–8502, Japan*
[2] *Department of Physics, Ritsumeikan University, Kusatsu, Shiga 525-8577, Japan*

Abstract

We investigate the stability of the volume modulus in a warped, codimension two braneworld model in a 6D gauged supergravity. The braneworld solution has two 3-branes, which are located at the positions of the boundary conical singularities. For this brane solution, the *shape* modulus, i.e., the relative position of the branes, is fixed via the tension-deficit relations, once the brane tensions are specified. However, the *volume* modulus, i.e., the size of the extra dimensions, is not fixed, implying we should take quantum corrections of bulk fields into account. Hence, we discuss the one-loop quantum corrections of a massless minmally coupled bulk scalar field to stabilize the volume modulus. We show that in most cases the volume modulus is stabilized. Then, we make some suggestions on the original six-dimensional model. Finally, we close this article, after discussing some phenomenological implications.

1 Introduction

String theory implies that our universe is not actually four-dimensional (4D), but in fact a submanifold (brane) embedded into a higher-dimensional spacetime (bulk). Braneworld gravity and cosmology, especially based on the proposal by Randall and Sundrum (RS) [1], have been developed a lot in the literature in the codimension one context. String theory, however suggests that there are as many as six or seven extra dimensions and thus, one may consider braneworld models with higher codimensions.

Stability of the moduli, i.e., "volume" and "shape" of the extra-dimensions, is a significant issue in braneworld. For instance, in RS-type codimension one brane models, the interbrane distance, called the radion, should be fixed at an appropriate value to realise a large mass hierarchy between fundamental energy scales, i.e., electroweak and gravitational scales. Several stabilization mechanisms of the radion have been discussed in the RS model, both by dynamics of additional bulk fields [2] and quantum corrections to the bulk vacuum state [3]. Since the increasing number of the extra-dimensions implies increasing number of the moduli, the similar issues on moduli stabilization could arise in braneworld with higher codimension.

We focus on codimension 2 braneworld solutions [4, 5] which is based on a six-dimensional (6D) gauged supergravity [6] . Similar warped braneworld solutions have been recently discussed in [7], in the context of 6D Einstein-Maxwell theory. In these two-brane models, the magnetic flux can compactify the extra-dimension. Brane tensions are directly related to the deficit angles of the bulk, and thus, once the brane tensions are fixed, a part of the moduli is fixed. In the models discussed in [7], all the moduli are completely fixed. However, in the model, in 6D supergravity given by [4, 5], only the shape modulus is fixed even after specifying the brane tensions. Hence, to fix the volume modulus, quantum corrections of bulk fields should be taken into account. In this presentation, we introduce our recent analyses on the modulus stabilization by the quantum corrections of a massless scalar field, based on our recent paper [8].

2 Codimension 2 brane model in 6D supergravity

We consider a six-dimensional Einstein-Maxwell-dilaton theory with a non-vanishing scalar potential as

$$S_6 = \int d^6x \sqrt{-g} \left(\frac{1}{2}R - \frac{1}{2}\partial_a\varphi\partial^a\varphi - \frac{1}{4}e^{-\varphi}F_{ab}F^{ab} - 2g_1^2 e^{\varphi} \right) , \tag{1}$$

---

[1] E-mail:masato@yukawa.kyoto-u.ac.jp
[2] E-mail:naylor@se.ritsumei.ac.jp
[3] E-mail:misao@yukawa.kyoto-u.ac.jp

where φ is a dilaton field, F_{ab} represents a $U(1)$ gauge field strength and g_1 represents the dilaton potential. This theory corresponds to the bosonic part of the Salam-Sezgin, 6D gauged supergravity theory [6] with vanishing 2-form field and hypermultiplets .

This theory contains a 3-parameter family of static braneworld solutions:

$$
\begin{aligned}
ds^2 &= h(\rho)d\theta^2 + \frac{d\rho^2}{h(\rho)} + (2\rho)(-d\tau^2 + dx_2^2 + dx_3^2 + dx_4^2)\,, \\
h(\rho) &= \frac{g_1^2}{2\rho^3}\left(\rho_+^2 - \rho^2\right)\left(\rho^2 - \rho_-^2\right)\,, \\
\varphi(\rho) &= -\ln(2\rho)\,, \quad F_{\theta\rho} = -\frac{g_1\rho_+\rho_-}{\rho^3}\,,
\end{aligned}
\tag{2}
$$

where $\rho_\pm$ are integration constants [4, 5]. In this model, the branes are located at positions which are determined by the *horizon* condition $h(\rho) = 0$; and whence we also obtain the following useful relations. These give a direct relation between the mass and charge of the magnetic flux. The global period of θ is called $\Delta\theta$, which is determined by the brane tensions through the tension-deficit relations as will be discussed later.

The branes are codimension two boundaries, embedded onto conical deficits at $\rho = \rho_\pm$, whose actions are given by

$$
S_\pm = -\int d^4x \sqrt{h}\sigma_\pm \,,
\tag{3}
$$

respectively, where $\sigma_\pm$ denotes the brane tensions. These choices of the brane action are onlu ways to embed a codimension two branein the present set-up. The brane tensions are related to the conical deficit angles by $\sigma_\pm = M_6^4\delta_\pm$. Then, the angle period $\Delta\theta$ is determined by

$$
\Delta\theta(r, \delta_+) = \frac{2\pi - \delta_+}{-\frac{1}{2}h'(\rho_-)} = \frac{2\pi - \delta_-}{\frac{1}{2}h'(\rho_+)} = \frac{2(2\pi - \delta_+)}{g_1^2(1 - r^2)}\,.
\tag{4}
$$

Once the brane tensions, σ_+ and σ_- are fixed, then r is also fixed and thus, we now regard the free parameters as r and δ_+, along with the dilaton bulk coupling g_1. The remaining degree of freedom used to determine the bulk geometry is the absolute size of the bulk, i.e., ρ_+. Due to the scale invariance of the background brane solution, ρ_+ can only be fixed by quantum corrections of bulk fields. Note that there is also magnetic flux constraint given by

$$
\int_{\rho_-}^{\rho_+} d\rho \int_0^{\Delta\theta} d\theta F_{\rho\theta} = -\Delta\theta A\left(\frac{1}{\rho_-^2} - \frac{1}{\rho_+^2}\right) = -\frac{2(2\pi - \delta_+)}{g_1 r}\,,
\tag{5}
$$

but the magnetic flux only depends on r and δ_+ and does not contribute to the volume of the bulk. Thus, the overall size of the extra-dimension ρ_+ behaves as the modulus, i.e., the *volume* modulus. We also note that the dilaton is also fixed once we can fix the volume modulus and hence ρ_+ is only the modulus in the present model. We consider the modulus dynamics in a 4D effective theory in the conext of the moduli space approximation, in which we regard ρ_+ as a function of the coordinate on the brane x^μ and we get the modulus kinetic term with the correct sign [8]. This approximation should be valid for sufficiently low energy scales.

3 One-loop effective potential of the volume modulus

Next, we introduce a massless, minimally coupled scalar field as a simple analogue of the bulk gravitons. From this we can investigate the one-loop effective action for such a scalar field and thus, the effective potential of the volume modulus on the co-dimension two warped brane background. From now on, we shall work mainly in Euclidean space, rather than in the original Lorentzian frame. The action for the massless scalar field perturbations is given by

$$
S_{\text{scalar}} = -\frac{1}{2}\int d^6x \sqrt{g}\phi\Delta_6\phi\,.
\tag{6}
$$

The one-loop effective action for a massless minimally coupled scalar field is defined as

$$
W_6 = \frac{1}{2}\ln\det(-\Delta_6)\,,
\tag{7}
$$

where Δ_6 is the six-dimensional Laplacian, which is UV divergent and needs to be regularized and renormalized. We employ the zeta function regularization technique to obtain the renormalized effective action. Since there is still divergence due to the infinite volume of the 4D spacetime, it is useful to define the effective potential

$$W_{6,\mathrm{ren}} = \int \left(d^4 x \rho_+^2 \right) V_{6,\mathrm{eff}} = \int d^4 \tilde{x} V_{6,\mathrm{eff}}. \tag{8}$$

Due to symmetries of the background solution, the form of the effective potential can be reduced to the following form

$$V_{6,\mathrm{eff}}(r, \delta_+, \rho_+, \mu) = \frac{A_6(r, \delta_+) - B_6(r, \delta_+) \ln(\mu^2 \rho_+)}{\rho_+^2}, \tag{9}$$

where $A_6(r, \delta_+)$ and $B_6(r, \delta_+)$ are related to a background heat kernel coefficient. Clearly, if $B_6(r, \delta_+) > 0$, then the volume modulus is stabilized at

$$\rho_+^* = \mu^{-2} e^{(2A_6 + B_6)/(2B_6)}. \tag{10}$$

Thus, the evaluation of $B_6(r, \delta_+)$ is the first important task to judge the stability. $B_6(r, \delta_+)$ can be decomposed into the contribution of the bulk and branes (conical singularities). There are several reasonable choices of μ, such as the bulk curvature scale $g_1(\rho_+)^{-1/2}$ and the gravitational scale M_6 (these become $g(\rho_+)^{-1/2}$ and M_4 in 4D alternative model, which is discussed in the next section). However, the stability itself does not depend on the scale, because it is determined solely by the value of $B_6(r, \delta_+)$ (this is $B_4(r, \delta_+)$ in the 4D model).

4 Volume stabilization and its implication on the hierarchy problem

Due to the lack of formulations of the relevant conical heat kernel in 6D, we consider a toy model in 4D supergravity with almost the same Langrangian as the original 6D theory, only except for the number of dimensions. The coupling g_1 should be replaced by g. The corresponding coefficients in the effective potential $A_6(r, \delta_+)$ and $B_6(r, \delta_+)$ are also replaced by $A_4(r, \delta_+)$ and $B_4(r, \delta_+)$, respectively.

As $B_6(r, \delta_+)$, the function $B_4(r, \delta_+)$ is also composed of two parts; a bulk and conical brane contribution. As a result, the sign of $B_4(r, \delta_+)$ is always positive for the most of values of the parameters (r, δ_+). Thus, the volume modulus is *stabilized*. We should add comments on the stability of the volume modulus in 6D. In 6D model, only the bulk part of $B_6(r, \delta_+)$ is calculable and has very similar behavior to the 4D toy model.

After making the stabilization of the volume modulus, we can give discuss some phenomenological implications. For instance, we discuss the suggestions for the hierarchy problem between the fundamental energy scales.

In the original six-dimensional model, the *effective* four-dimensional Planck scale is

$$M_{\mathrm{pl}}^2 \simeq \frac{\rho_+(2\pi - \delta_+)}{g_1^2} M_6^4. \tag{11}$$

If we assume a brane localized field whose bare mass is given by m^2 on either brane at $\rho_\pm$ then the observed mass scales are $m_+^2 = m^2, m_-^2 = r^2 m^2$. Thus, the mass ratio between the field and the effective Planck mass is given by

$$\frac{m_+^2}{M_{\mathrm{pl}}^2} \simeq \left(\frac{\mu^2 m^2}{M_6^4} \right) \frac{g_1^2}{2\pi - \delta_+} e^{-(2A_6 + B_6)/(2B_6)}, \quad \frac{m_-^2}{M_{\mathrm{pl}}^2} \simeq \left(\frac{\mu^2 m^2}{M_6^4} \right) r^2 \frac{g_1^2}{2\pi - \delta_+} e^{-(2A_6 + B_6)/(2B_6)}, \tag{12}$$

where we have used the value of $\rho_{+,*}$, given by Eq. (10), at stabilization. We assume that the factor of $(\mu m/M_6^2)^2$ takes the optimal value of $\mathcal{O}(1)$ at the unification of the fundamental scales. At present, the best we can do is use the results obtained from the four-dimensional model

$$R(r, \delta_+) := \frac{g^2}{2\pi - \delta_+} e^{-(A_4 + B_4)/B_4} \tag{13}$$

The results of the values of $R(r, \delta_+)$ are shown in the Figure and indicate that smaller values of g and r lead to a large hierarchy on both branes.
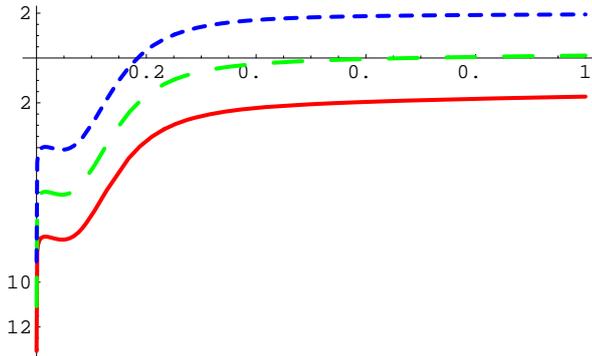
Figure 1: $\log_{10}(R(r, 0.01))$ is shown as a function of r, for $\delta_+ = 0.01$. The red (solid), green (dashed, with wider intervals) and blue (dashed, with shorter intervals) curves correspond to $g = 0.5, 5, 50$, respectively.

5   Summary

We have discussed the stability of the volume modulus of a warped codimension two brane model in 6D supergravity, by taking the one-loop quantum corrections of a massless scalar field into account.

The branes are located at the boundary conical singularities. The shape modulus is determined once one specifying the brane tensions. But, the volume modulus is not completely determined even if the flux conservation law is taken into account. In order to stabilize the volume modulus, we consider quantum corrections of a massless scalar field (as an analogue of the bulk gravitons).

The form of the one-loop effective potential can be fixed, due to scale invariance of the background solution. In the actual investigation of stability, we have used an alternative model in 4D supergravity due to the lack of formulation of the relevant conical heat kernel coefficients in 6D. We then showed that the heat kernel coefficient is positive definite for most dilaton couplings, g, independently of the choice of r and δ_+. The contribution from the bulk is positive, whereas that from the conical branes is negative for smaller r; though they are of the same order. For all of the cases with $g \sim \mathcal{O}(1)$, the bulk dominates over the brane parts and thus, the volume is *stabilized*.

We also discussed some phenomenological issues, for instance, here we pick up the hierarchy problem between the fundamental energy scales. The 6D results were extrapolated from the corresponding results in 4D. We found that in the hierarchy problem, the ratio between the energy scale of the brane localized field and the gravitational scale becomes much smaller than unity, especially for larger degrees of warping $r \ll 1$.

References

[1] L. Randall and R. Sundrum, Phys. Rev. Lett. **83**, 3370 (1999) [arXiv:hep-ph/9905221].

[2] W. D. Goldberger and M. B. Wise, Phys. Rev. Lett. **83**, 4922 (1999) [arXiv:hep-ph/9907447].

[3] J. Garriga, O. Pujolas and T. Tanaka, Nucl. Phys. B **605**, 192 (2001) [arXiv:hep-th/0004109].

[4] Y. Aghababaie *et al.*, JHEP **0309**, 037 (2003) [arXiv:hep-th/0308064].

[5] G. W. Gibbons, R. Guven and C. N. Pope, Phys. Lett. B **595**, 498 (2004) [arXiv:hep-th/0307238].

[6] A. Salam and E. Sezgin, Phys. Lett. B **147**, 47 (1984).

[7] S. Mukohyama, Y. Sendouda, H. Yoshiguchi and S. Kinoshita, JCAP **0507**, 013 (2005) [arXiv:hep-th/0506050].

[8] M. Minamitsuji, W. Naylor and M. Sasaki, arXiv:hep-th/0606238.

Ambiguity of black hole entropy in loop quantum gravity II

Takashi Tamaki[1] and Hidefumi Nomura[2]

Department of Physics, Waseda University, 3-4-1 Okubo, Shinjuku, Tokyo 169-8555, Japan

Abstract

We reexmine some proposals of black hole entropy in loop quantum gravity and consider a new possible choice of the Immirzi parameter.

1 Introduction

Loop quantum gravity (LQG) has attracted much attention because of its background independent formulation, account for microscopic origin of black hole entropy [1], etc. The spin network has played a key role in this theory [2]. Basic ingredients are edges and vertices. In Fig. 1, edges are expressed by lines lebeled by $j = 0, 1/2, 1, 3/2, \ldots$ reflecting the SU(2) nature of the gauge group. A vertex is an intersection between edges. For three edges having spin j_1, j_2, and j_3 that merges at an vertex, we have

$$j_1 + j_2 + j_3 \in N , \qquad j_i \leq j_j + j_k, \quad (i, j, k \text{ different from each other.}) \tag{1}$$

to garantee the gauge invariance of the spin network. Using this, expressions for the spectrum of the area can be derived as [3] $A = 8\pi\gamma \sum \sqrt{j_i(j_i + 1)}$, where γ is the Immirzi parameter. The sum is added up all intersections between a surface and edges as shown in Fig. 1. The number of states that determines the black hole entropy was first estimated as [1]

$$S = \frac{A \ln(2j_{\min} + 1)}{8\pi\gamma\sqrt{j_{\min}(j_{\min} + 1)}} , \tag{2}$$

where A and $j_{\min}$ are the horizon area and the lowest nontrivial representation usually taken to be $1/2$ because of SU(2), respectively. In this case, the Immirzi parameter is determined as $\gamma = \ln 2/(\pi\sqrt{3})$ to produce the Bekenstein-Hawking entropy formula $S = A/4$.

However, the formula (2) was corrected as [4, 5] $S = \frac{\gamma_M A}{4\gamma}$, where γ_M is the solution of

$$1 = \sum_{j=Z/2}^{\infty} 2\exp(-2\pi\gamma_M\sqrt{j(j+1)}) , \tag{3}$$

where j takes all the positive half-integer. In this case, $\gamma_M = 0.23753\cdots$. Interestingly, another possibility has also been argued. It is to determine γ_M as the solution of [6, 7]

$$1 = \sum_{j=Z/2}^{\infty} (2j + 1)\exp(-2\pi\gamma_M\sqrt{j(j+1)}) . \tag{4}$$

In this case, $\gamma_M = 0.27398\cdots$. These provide us with the following question: which is the best choice for the Immirzi parameter? Therefore, we reanalyze these possibilities. This is important in the following reasons. (i) In string theory, number counting for microscopic states of black holes has been considered. In future, it is desirable for us to have a connection with the number counting in string theory. Probably, we will need to proceed many steps toward this purpose. However, there is a subject which can be attacked soon. This is (ii) the possible relation to the quasinormal mode which has been argued as another consistency check of the Immirzi parameter. Using (2), an encounter between LQG and the quasinormal mode was considered first in Ref. [8]. This means that if we have $j_{\min} = 1$, we can determine γ as

---

[1]E-mail:tamaki@gravity.phys.waseda.ac.jp
[2]E-mail:nomura@gravity.phys.waseda.ac.jp
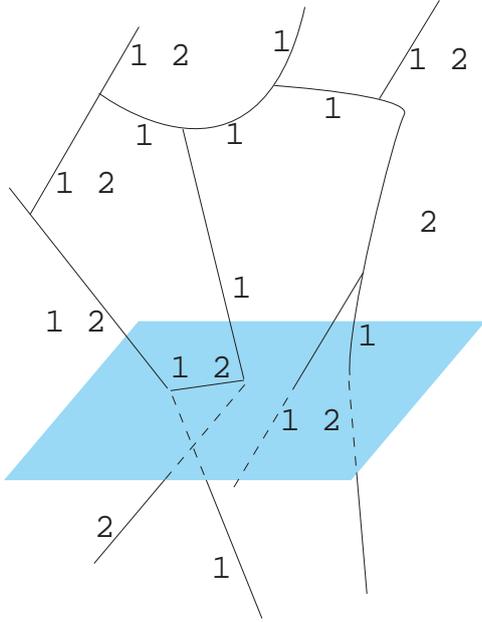
Figure 1: Spin network and a surface.

$\ln 3 / (2\pi\sqrt{2})$ which gives $A = 4\ln 3$. Moreover, the quasinormal mode analysis that originally performed in Schwarzschild black hole [9] has been extended to single-horizon black holes [10]. Thus, we also want to know which is the best choice for the Immirzi parameter in this view point.

This paper is organized as follows. In Sec. 2, we summarize the framework [1] (which we call the ABCK framework.). In Sec. 3, we argue various possibilities that determine the number of state. In Sec. 4, we summarize our results and discuss their meaning. For details, see [11].

2   Summary of the ABCK framework

First, we introduce the isolated horizon (IH) where we can reduce the SU(2) connection to the U(1) connection. Next, we imagine that spin network pierces the IH. By eliminating the edge tangential to the isolated horizon, we can decompose the Hilbert space as the tensor product of that at the IH H_{IH} and that in the bulk H_Σ, i.e., $H_{IH} \otimes H_\Sigma$. If we specify the points that are intersections of edges having spin $(j_1, j_2, \cdots, j_n)$ and the IH, we can write H_Σ as the orthogonal sum $H_\Sigma = \bigoplus_{j_i, m_i} H_\Sigma^{j_i, m_i}$, where m_i takes the value $-j_i, -j_i + 1, \cdots, j_i$. This is related to the flux operator eigenvalue $e_{s'}^{m_i} := 8\pi\gamma m_i$ that is normal to the IH (s' is the part of the IH that have only one intersection between the edge with spin j_i.). Since we eliminate the edge tangential to the IH, we have $m_i \neq 0$. The horizon Hilbert space can be written as the orthogonal by eigenstates Ψ_b of the holonomy operator $\hat{h}_i$, i.e., $\hat{h}_i \Psi_b = e^{\frac{2\pi i b_i}{k}} \Psi_b$.

Next, we consider the constraints in the bulk and at the IH, respectively. In the bulk, the Gauss constraint is already satisfied and the diffeomorphism constraint means that the place to which the edges stick the IH is not relavant. It is assumed that the bulk scalar constraint does not affect (j, m). At the IH, we do not consider the scalar constraint since the lapse function disappears. If we require that the horizon should be invariant under the diffeomorphism and the U(1) gauge transformation, The horizon area A is fixed as $A = 4\pi\gamma k$, where k is natural number and it is the level of the Chern-Simons theory. In addition, it is required that we should fix an ordering $(b_1, b_2, \cdots, b_n)$. The area operator eigenvalue A_j should satisfy (i) $A_j = 8\pi\gamma \sum \sqrt{j_i(j_i + 1)} \leq A$. From the quantum Gauss-Bonnet theorem, (ii) $\sum_{i=1}^{n} b_i = 0$. From the boundary condition between the IH and the bulk, (iii) $b_i = -2m_i \mod k$. All we need to consider in number counting are (i)(ii)(iii).

3 number counting

If we use (ii) and (iii), we obtain $(ii)'$ $\sum_{i=1}^{n} m_i = n'\frac{k}{2}$. In [5], it was shown that this condition is irrelevant in number counting. Thus, we perform number counting only concentrating on (i) below.

For this purpose, there are two different points of view. The one adopted in the original paper [1, 4, 5] counts the *surface* freedom $(b_1, b_2, \cdots, b_n)$. The second counts the freedom for both j and b [6, 7].

We first consider the second possibility since (we suppose) it is easier to understand. To simplify the problem, we first consider the set M_k by following [4], that is

$$M_k := \left\{ (j_1, \cdots, j_n) | 0 \neq j_i \in \frac{Z}{2}, \sum_i j_i \leq \frac{k}{2} \right\} . \tag{5}$$

Let N_k be the number of elements of M_k plus 1. Certainly, $N(a) \leq N_k$, where $N(a)$ ($a := \frac{A}{8\pi\gamma}$) is the number of states which account for the entropy. Note that if $(j_1, \cdots, j_n) \in M_{k-1}$, then $(j_1, \cdots, j_n, \frac{1}{2}) \in M_k$. In the same way, for natural $0 < s \leq k$,

$$(j_1, \cdots, j_n) \in M_{k-s} \Rightarrow (j_1, \cdots, j_n, \frac{s}{2}) \in M_k . \tag{6}$$

Then, if we consider all $0 < s \leq k$ and all the sequence $(j_1, \cdots, j_n) \in M_{k-s}$, we found that $(j_1, \cdots, j_n, \frac{s}{2})$ form the entire set M_k. Moreover, for $s \neq s'$, $(j_1, \cdots, j_n, \frac{s}{2}) \neq (j_1, \cdots, j_n, \frac{s'}{2}) \in M_k$. The important point to remember is that we should include the condition $m_i \neq 0$ (or equivalently $b_i \neq 0$). Thus, each j_i has freedom $2j_i$ for the j_i integer and the $2j_i + 1$ way for the j_i half-integer. They are summarized as $2[\frac{2j+1}{2}]$ where $[\cdots]$ is the integer parts. For this reason, the recursion relation is

$$N_k = \sum_{s=1} 2[\frac{s+1}{2}](N_{k-s} - 1) + 1 . \tag{7}$$

This is the point which has not been examined out so far.

As a stright forward extension of this, we can consider $N(a)$, which is

$$N(a) := \left\{ (j_1, \cdots, j_n) | 0 \neq j_i \in \frac{Z}{2}, \sum_i \sqrt{j_i(j_i + 1)} \leq \frac{k}{2} = a \right\} . \tag{8}$$

In this case, we obtain the recursion relation

$$N(a) = 2N(a - \sqrt{3}/2) + 2N(a - \sqrt{2}) + \cdots + 2[\frac{2j+1}{2}]N(a - \sqrt{j_i(j_i + 1)}) + \cdots + [\sqrt{4a^2 + 1} - 1] . \tag{9}$$

If we notice that the solution of $\sqrt{j_i(j_i + 1)} = a$ is $j_i = (\sqrt{4a^2 + 1} - 1)/2$, meaning of $[\sqrt{4a^2 + 1} - 1]$ is obvious. If we use the relation $N(a) = Ce^{\frac{A\gamma_M}{4\gamma}}$, where C is a constant, that was obtained in [5], we obtain

$$1 = \sum_{j=Z/2} 2[\frac{2j+1}{2}] \exp(-2\pi\gamma_M \sqrt{j(j+1)}) , \tag{10}$$

by taking the limit $A \to \infty$. Then if we require $S = A/4$, we have $\gamma = \gamma_M$. In this case, $\gamma_M = 0.26196\cdots$.

Next, we consider the first possibility that counts only the surface freedom. This means that even if $(j_1, j_2, \cdots, j_n)$ is different, it is regarded as the *same* surface state if the horizon area and $(b_1, b_2, \cdots, b_n)$ are same. For example, $(j_1, j_2) = (3/2, 1/2)$ and $(1/2, 3/2)$ both give the possibility $(b_1, b_2) = (-1, -1)$. Then, it should *not* be distinguished in this description. This following is the method taken in [4], i.e., we rewrite (i) as $(i)'$ $8\pi\gamma \sum_i \sqrt{|m_i|(|m_i| + 1)} \leq A$. Let us compare (6) with

$$(m_1, \cdots, m_n) \in M_{k-s} \Rightarrow (m_1, \cdots, m_n, \pm\frac{s}{2}) \in M_k . \tag{11}$$

At first glance, it might seem that we abondon the freedom $m_{n+1} = -\frac{s}{2} + 1, \cdots \frac{s}{2} - 1$. However, it is not the case since we obtain that freedom from M_{k-s+2}, M_{k-s+4}, $\cdots$. It is the crucial difference from (6) where the freedom of j is counted. In this way, we have the relation

$$N_k = \sum_{s=1} 2(N_{k-s} - 1) + 1 . \tag{12}$$

Therefore, we obtain (3).

4 Conclusions and discussion

In this paper, we have considered two possibilities for the number of states of black holes in the ABCK framework. One of them gives a new value for the Immirzi parameter. From these results, we consider whether or not there is a consistency between the area spectrum in LQG and the area spectrum in the quasinormal mode. Since the area spectrum obtained from the quasinormal mode is $dA = 4 \ln 3$, it is obvious that we do not have the same consistency if we adopt the Immirzi parameter determined by (3) or (10). Then, how about the case in which only $j = j_{\min}$ survives, as considered in [12] ? Unfortunately, both (3) and (10) do not provide consistency that is different from the case in (4). This means that if we take the consistency to the quasinormal mode seriously, we will need new considerations.

Finally, we want to consider which of the two candidates is the better choice. The reason why only surface degree was counted in [1, 4, 5] is to separate surface degree from the bulk freedom. If we admit j as an independent variable, it is difficult to separate it from other bulk freedoms since that in the bulk can communicate with infinity. However, as pointed out in [7], it is j that determines area eigenvalue and other bulk variables are irrelevant. Moreover, since quantum horizons would fluctuate [13], it may be a problem to consider the IH as a sharp boundary. For these reasons, it is too early to abondon the possibility that we could count j as an independent variable. Of course, it is also important to consider the other method in the calculating the number of freedom as in [14]. We also want to examine these possibilities in future.

References

[1] A. Ashtekar, J. Baez, A. Corichi, and K. Krasnov, Phys. Rev. Lett. **80**, 904 (1998); A. Ashtekar, J. Baez, and K. Krasnov, Adv. Theor. Math. Phys. **4**, 1 (2000).

[2] C. Rovelli and L. Smolin, Phys. Rev. D **52**, 5743 (1995).

[3] C. Rovelli and L. Smolin, Nucl. Phys. B **442**, 593 (1995); Erratum, *ibid.*, **456**, 753 (1995).

[4] M. Domagala and J. Lewandowski, Class. Quant. Grav. **21**, 5233 (2004).

[5] K. A. Meissner, Class. Quant. Grav. **21**, 5245 (2004).

[6] I.B. Khriplovich, gr-qc/0409031; gr-qc/0411109.

[7] A. Ghosh and P. Mitra, Phys. Lett. B **616**, 114 (2005); *ibid.*, gr-qc/0603029, hep-th/0605125.

[8] O. Dreyer, Phys. Rev. Lett. **90**, 081301 (2003).

[9] L. Motl, Adv. Theor. Math. Phys. **6**, 1135 (2003); L. Motl and A. Neitzke, *ibid.*, **7**, 307 (2003).

[10] T. Tamaki and H. Nomura, Phys. Rev. D **70**, 044041 (2004).

[11] T. Tamaki and H. Nomura, Phys. Rev. D **72**, 107501 (2005).

[12] O. Dreyer, F. Markopoulou and L. Smolin, Nucl. Phys. B **744**, 1 (2006)

[13] M. Bojowald and R. Swiderski, Phys. Rev. D **71**, 081501 (2005).

[14] A. Dasgupta, JCAP08, 004 (2003).

Mass, tension and thermodynamics of Kaluza-Klein black holes

Yasunari Kurita[1] and Hideki Ishihara[2]

Department of Physics, Osaka City University, Osaka 558–8585, Japan

Abstract

We study the thermodynamics of charged black holes with squashed S^3 horizons in five-dimensional Einstein-Maxwell theory. The free energy of the black hole is obtained on two different backgrounds; one is four-dimensional Minkowski times S^1 and the other is the Kaluza-Klein monopole spacetime. The black hole has different values for the Hamiltonian, the Abbott-Deser mass and the Komar mass, and each mass satisfies thermodynamic first law. It is shown that the Hamiltonian, these masses and the free energy can be related each other in terms of Legendre transformations with respect to some thermodynamic variables. We find a new couple of thermodynamic variables that represents the squashing of the outer horizon. It gives a work term to each first law. In stead of them, the gravitational tension and its conjugate are also a couple of thermodynamic variables and give a work term to each first law except for that of the Komar mass, though the Komar mass satisfies Smarr's formula and would be thought of as a thermodynamic mass. In this case, the Komar mass can not be related to the free energy and other masses using Legendre transformations. We also investigate thermodynamic stability of the black hole in many thermodynamic environment. In environment with fixed gravitational tension, the most globally stable state is the Kaluza-Klein monopole. We find a phase transition between the black hole and the four-dimensional Minkowski times S^1 in an enviromnent with fixed temperature, electric charge and gravitational tension. In isolated system, smaller extra dimension is entropically favored, and the five-dimensional Reissner-Nordströrm black hole has the smallest entropy in the sequence of the black holes with the same mass and the same electric charge. Therefore, the Reissner-Nordströrm black hole might be the most unstable state in the sequence.

1 Introduction and Summary

It has a long history to formulate black hole thermodynamics in terms of quantum theory of gravity. Especially, the Euclidean path integral for gravitational field in saddle-point approximation is successful and gives the Bekenstein-Hawking formula for black hole entropy [1]. The Euclidean path integral method is consistent formulation for black hole thermodynamics and has a feature that it gives a thermodynamic free energy. The free energy is approximately given as the Euclidean classical action of the solution times its temperature.

Recently, spacetime structure of charged static black holes with squashed S^3 horizons in five-dimensional Einstein-Maxwell theory was studied by one of the authors and his collaborator [2]. The metric has three parameters characterizing mass, electric charge and the deformation of the S^3 horizon from round S^3 or the size of the extra dimension. The squashed S^3 can be thought of as a twisted S^1 fiber over S^2 base space with different circumference radius; the circumference radius of S^1 does not equal that of S^2. The spacetime asymptotes to a twisted S^1 bundle over four-dimensional Minkowski spacetime, which is not flat spacetime and not solution of the Einstein equation. The size of S^1 is asymptotically constant and, if its size is adequately small, the spacetime is effectively asymptotically four-dimensional spacetime with one extra dimension. In this sense, the black hole has the properties of Kaluza-Klein black holes. Furthermore, the solution includes the Kaluza-Klein monopole spacetime in a no horizon limit, which is originally found by Gross and Perry [3], and Sorkin [4].

The thermodynamics of this black hole was firstly investigated by Cai et al.[5]. They showed that the mass defined by the counter-term method equals the Abbott-Deser (AD) mass [6] on the locally

---

[1] E-mail:kurita@sci.osaka-cu.ac.jp
[2] E-mail:ishihara@sci.osaka-cu.ac.jp

flat spacetime to which the black hole spacetime asymptotes. It was shown that these masses satisfy a thermodynamic first law if one parameter is treated as a constant. In the investigation, they assumed that entropy, temperature, electric charge and electric potential difference are thermodynamic variables for the black hole. Furthermore, they discussed that there might exist other thermodynamic variables representing the deformation of the horizon and its conjugate generalized pressure.

In this paper, we study the thermodynamics of the black hole in more detail. The free energy of the black hole can be evaluated using traditional background subtraction method on two different backgrounds. The free energy $(F^{BH} - F^{flat})$ is evaluated on four-dimensional Minkowski times S^1 spacetime which is a flat spacetime obtained by neglecting the twisting of the S^1 fiber in the locally flat spacetime. The other free energy $(F^{BH} - F^{GPS})$ is evaluated on the Kaluza-Klein monopole spacetime. We consider the Hamiltonian which is formulated by Hawking and Horowitz [7] and the Komar mass in addition to the AD mass. We find that the Hamiltonian is a Legendre transform of the free energy with respect to temperature,

$$H^{B-f} = (F^{BH} - F^{flat}) + TS, \quad \text{and} \quad H^{B-G} = (F^{BH} - F^{GPS}) + TS \tag{1}$$

in both cases of the flat background and the Kaluza-Klein monopole background. In the above equation, H^{B-f} and H^{B-G} are the Hamiltonian of the black hole on the flat and the Kaluza-Klein monopole background, respectively. T is temperature defined by the Hawking formula and S is entropy given by the Bekenstein-Hawking formula. The AD mass on the flat background M_{AD} is a Legendre transform of the Hamiltonian with respect to the electric potential difference

$$M_{AD} = H^{B-f} + Q\Phi, \tag{2}$$

where Q is the electric charge and Φ is the electric potential difference between that at the outer horizon and at the spatial infinity. The Hamiltonian and the AD mass satisfy the following thermodynamic first laws:

$$dH^{B-f} = TdS - Qd\Phi + \mathcal{T}_f dL \tag{3}$$
$$dH^{B-G} = TdS - Qd\Phi + \mathcal{T}_G dL \tag{4}$$
$$dM_{AD} = TdS + \Phi dQ + \mathcal{T}_f dL, \tag{5}$$

where $\mathcal{T}_f$ and $\mathcal{T}_G$ are graviational tension [8] evaluated on the flat spacetime background and the Kaluza-Klein monopole background, respectively. L is its conjugate and given by the period of the compact fifth dimension, or equivalently, the size of S^1 fiber at the spatial infinity. The Legendre transformations with respect to these variables are summarized as follows:

$$(F^{BH} - F^{flat}) \xrightarrow{T \to S} H^{B-f} \xrightarrow{\Phi \to Q} M_{AD}^{B-f}$$

for the flat background and

$$(F^{BH} - F^{GPS}) \xrightarrow{T \to S} H^{B-G} \xrightarrow{\Phi \to Q} W_1$$

for the Kaluza-Klein monopole background. W_1 is defined as $W_1 := H^{B-G} + Q\Phi$.

On the other hand, the Komar mass can not be related to other masses or the free energy in terms of Legendre transformation with respect to those already known thermodynamic variables. However, since the Komar mass satisfies Smarr's formula [9]

$$M_K - Q\Phi = \frac{3}{2}TS. \tag{6}$$

then, it would be thought of as a thermodynamic mass and would be related to the free energy by a Legendre transformation with respect to some thermodynamic variable. In order to do so, we introduce a couple of thermodynamic variables (X, Y_f) or (X, Y_G), depending on choice of the background. X is proportional to square of L and Y_f or Y_G is its conjugate on the flat background and on the Kaluza-Klein monopole background, respectively. Especially, Y_G can be written as

$$Y_G = -\frac{\pi}{16G} \frac{2}{R_+ r_+} \left(\frac{r_+}{2} - R_+ \right)^2, \tag{7}$$

where

$$R_+ = \frac{r_+}{2} \sqrt{\frac{r_\infty^2 - r^2}{r_\infty^2 - r_+^2}} \tag{8}$$

is the circumference radius of S^2 base space at the outer horizon and $r_+/2$ is the circumference radius of S^1 fiber there. Therefore, Y_G vanishes when the size of S^2 at the outer horizon equals that of S^1 and the horizon is a full-orbed three sphere as in the case of the extreme black hole. In this way, Y_G represents the squashing of the horizon. On the other hand, Y_f does not have this property because the flat background does not have any spherically symmetric limit unlike the case of the Kaluza-Klein monopole background. With these new variables, the Komar mass satisfy the following first laws:

$$dM_K = TdS + \Phi dQ + XdY_f, \quad \text{or} \quad dM_K = TdS + \Phi dQ + XdY_G. \tag{9}$$

The last terms are new thermodynamic work terms. Furthermore, the Komar mass can be related to the free energy by Legendre transformation with these new variables as

$$
\begin{aligned}
F^{BH} - F^{flat} &= M_K - TS - Q\Phi - XY_f, \tag{10} \\
F^{BH} - F^{GPS} &= M_K - TS - Q\Phi - XY_G. \tag{11}
\end{aligned}
$$

Then, the Legendre transformations are summarized as follows:

$$
\begin{array}{ccccc}
(F^{BH} - F^{fl}) & \xrightarrow{T \to S} & H^{B-f} & \xrightarrow{X_f \to Y_f} & W_2 \\
& & \Big\downarrow{\scriptstyle \Phi \to Q} & & \Big\downarrow{\scriptstyle \Phi \to Q} \\
& & M_{AD}^{B-f} & \xrightarrow{X_f \to Y_f} & M_K
\end{array}
$$

for the flat background and

$$
\begin{array}{ccccc}
(F^{BH} - F^{GPS}) & \xrightarrow{T \to S} & H^{B-G} & \xrightarrow{X \to Y_G} & W_2 \\
& & \Big\downarrow{\scriptstyle \Phi \to Q} & & \Big\downarrow{\scriptstyle \Phi \to Q} \\
& & W_3 & \xrightarrow{X \to Y_G} & M_K
\end{array}
$$

for the Kaluza-Klein monopole background. From equation (6), it is found that $W_2 = \frac{3}{2}TS$.

The new quantities X and its conjugate Y_f or Y_G also give a new work term to the first laws of the Hamiltonian and the AD mass.

$$
\begin{aligned}
dH^{B-f} &= TdS - Qd\Phi + Y_f dX \tag{12} \\
dH^{B-G} &= TdS - Qd\Phi + Y_G dX \tag{13} \\
dM_{AD} &= TdS + \Phi dQ + Y_f dX. \tag{14}
\end{aligned}
$$

Thus, thermodynamic first law for each Hamiltonian or AD mass is not unique. For example, H^{B-f} is a function of (S, Φ, X) as well as of (S, Φ, L). On the other hand, the gravitational tension does not give any work term to the first law of the Komar mass. And, it is found that any Legendre transformation with respect to the gravitational tension or its conjugate quantity can not relate the Komar mass to the free energy and the other masses.

We also investigate thermodynamic stability of the black hole. There are many thermodynamic environment depending choice of a set of independent thermodynamic variables. The specific heat of the black hole is apt to be negative and then it is unstable under thermal fluctuation. For near extremal black hole in environment with fixed electric charge, it tends to be positive and then, the black hole is locally thermodynamically stable. On the other hand, in environment with fixed electric potential difference, the specific heat is always negative and the black hole is always locally thermodynamically unstable. In environment with fixed X or L, the most globally stable state that has the minimum free energy is the flat spacetime whereas, in environment with fixed Y, the most globally stable state is degenerate both for the flat spacetime and the Kaluza-Klein monopole. With fixed gravitational tension $\mathcal{T}$, the Kaluza-Klein monopole is the most globally stable state. It is found that, there is a phase transition between the black

hole with positive specific heat and the flat spacetime in environment with fixed T, Q and $\mathcal{T}$. In this situation, the most stable state is the Kaluza-Klein monopole spacetime and the black hole is thought of as a meta-stable state. These result are summarized in the following table:

Environment	The most stable state	local stability of the BH	phase transition
(T,Q,L)	flat	only near extremal	none
(T,Q,X)			
(T,Q,Y)	flat = KK monopole	only nearextremal	none
$(T,Q,\mathcal{T})$	KK monopole	not only near extremal	BH $\leftrightarrow$ flat
(T,Φ,L)	flat	alway unstable	none
(T,Φ,X)			
(T,Φ,Y)	flat= KK monopole	alway unstable	none
$(T,\Phi,\mathcal{T})$	KK monopole	alway unstable	none

In isolated system, we have an interest in thermodynamic stability with respect to the size of the extra dimension, that is the size of the S^1 fiber at the spatial infinity L. We consider the sequence of the solutions with the same mass and the same electric charge. Then, the entropy of the black hole with the same mass and the same electric charge is a monotonically decreasing function with respect to the size of the extra dimension

$$\left(\frac{\partial S}{\partial L}\right)_{M,Q} < 0, \quad \text{or} \quad \left(\frac{\partial S}{\partial X}\right)_{M,Q} < 0. \tag{15}$$

Therefore, smaller extra dimension is entropically favored. In the limit that L becomes infinity, the black hole becomes the five-dimensional Reissner-Nordstörm (RN) black hole. Therefore, the five-dimensional RN black hole has the minimum entropy. In this sense, it might be the most unstable state in the sequence of the black hole solutions with the same mass and the same electric charge.

Acknowledgments

References

[1] G. W. Gibbons and S. W. Hawking, Phys. Rev. D **15**, 2752 (1977).

[2] H. Ishihara and K. Matsuno, Prog. Theor. Phys. **116**, 417 (2006).

[3] D. J. Gross and M. J. Perry, Nucl. Phys. B **226**, 29 (1983)

[4] R. Sorkin, Phys. Rev. Lett. **51**, 87 (1983)

[5] R. G. Cai, L. M. Cao and N. Ohta, Phys. Lett. B **639**, 354 (2006).

[6] L. F. Abbott and S. Deser, Nucl. Phys. B **195**, 76 (1982).

[7] S. W. Hawking and G. T. Horowitz, Class. Quant. Grav. **13**, 1487 (1996).

[8] T. Harmark and N. A. Obers, JHEP **0405**, 043 (2004).

[9] J. P. Gauntlett, R. C. Myers and P. K. Townsend, Class. Quant. Grav. **16**, 1 (1999).